Journal of
Composites Science

Special Issue Reprint

Carbon Fiber Composites, Volume III

Edited by
Jiadeng Zhu

mdpi.com/journal/jcs

MDPI

Carbon Fiber Composites, Volume III

Carbon Fiber Composites, Volume III

Guest Editor

Jiadeng Zhu

MDPI

Basel • Beijing • Wuhan • Barcelona • Belgrade • Novi Sad • Cluj • Manchester

Guest Editor
Jiadeng Zhu
Brewer Science Inc.
Springfield, MO
USA

Editorial Office
MDPI AG
Grosspeteranlage 5
4052 Basel, Switzerland

This is a reprint of the Special Issue, published open access by the journal *Journal of Composites Science* (ISSN 2504-477X), freely accessible at: https://www.mdpi.com/journal/jcs/special_issues/OH18YG1V78.

For citation purposes, cite each article independently as indicated on the article page online and as indicated below:

Lastname, A.A.; Lastname, B.B. Article Title. *Journal Name* **Year**, *Volume Number*, Page Range.

ISBN 978-3-7258-5871-2 (Hbk)
ISBN 978-3-7258-5872-9 (PDF)
https://doi.org/10.3390/books978-3-7258-5872-9

Contents

About the Editor

Jiadeng Zhu

Jiadeng Zhu is a materials scientist with interests primarily focused on the applications of advanced fibers, polymers, and carbon materials in energy and environmental areas, including but not limited to energy storage/conversion, lightweight structural materials, printed/wearable electronics, smart textiles, filtration, and sensor fabrication/testing. He received his B.S. degree in Chemical Engineering & Materials Science from Soochow University and Ph.D. in Fiber and Polymer Science from North Carolina State University. He is the recipient of the Distinguished Achievement Award in *Fiber Science* and the PMSE Early Investigator Award from the *Fiber Society* and the *American Chemical Society*, respectively, both in 2025. Additionally, he has received Editors' Choice of *ACS Applied Materials & Interfaces* (ACS 2023) and the *Best of Advanced Materials Technologies 2021* (Wiley-VCH, 2022).

Journal of
Composites Science

MDPI

Editorial

Editorial for the Special Issue on Carbon Fiber Composites III

Jiadeng Zhu

Smart Devices, Brewer Science Inc., Springfield, MO 65810, USA; zhujiadeng@gmail.com

Composites, which combine two or more components to produce a product with properties superior to those of their individual parts, have played a critical role in modern materials science and engineering [1]. Typically, composites consist of a reinforcing material (e.g., fibers, nanoparticles, etc.) embedded within a matrix (e.g., polymer, metal, ceramic, etc.) [2,3]. Among various reinforced materials, carbon fibers have attracted tremendous attention since they are extremely strong, light, durable, and resistant to environmental damage [4,5]. Because of these advantages, carbon fiber composites have been widely used in the aerospace, automotive, construction, and renewable energy industries, where performance, efficiency, and reliability are paramount [6,7]. Additionally, composites offer design flexibility that allows engineers to customize material properties for specific applications via adapting the proper approaches (e.g., the orientation of fiber fillers, curing conditions, surface modification, etc.) [8–10].

This Special Issue brings together studies on the design, preparation, characterization, and applications of carbon fiber composites, aiming to serve as a reference in the field by offering insights into current challenges and future research directions.

Blythe et al. studied the influence of fiber orientation and explored the random effect on longitudinal misalignment via precision fiber laying of unidirectional fabrics [11]. The fiber alignment scatter was reduced by 52% using Fill Multilayer, and the increased fiber orientation resulted in a higher flexural strength of 16.08%. Zheng et al. utilized the energy conversion principle to investigate the damage mechanism of carbon fiber-reinforced concrete [12]. They tuned the strain rates to establish an energy-based damage model, which could be used as a reference for future applications. To address the failure at the interface between the surface material and the ribs, Tanaka et al. introduced a resin layer to the rib roots when the ribs were injected, providing outstanding specific stiffness [13]. Other components, such as wedge anchorages, have prevented carbon fiber composite stress concentration and premature failure [14].

The rotational speed and grinding head design remarkably affect the machining quality, efficiency, and finishing performance [15]. The mesh size and rotational speed were studied to understand their effects on the post-machining quality of carbon fiber-reinforced polymer laminates. In addition, the surface quality of face milling parameters in the 3D-printed version was investigated [16]. Moreover, a uniform layer of graphene oxide/chitin nanocrystals was prepared by Abdel-Mohsen et al. to minimize delamination resistance [17]. On the other hand, Kocharla et al. introduced crab shell powder into the jute/carbon fiber composite [18]. Their results indicate that the composite could achieve its best mechanical properties with 5 wt.% card shell powder thanks to its well-bonded interface between the fiber and matrix.

Surface texturing was also applied by Liu et al. to strengthen metal–carbon fiber-reinforced composite joints [19]. The effects of the corresponding surface morphology and roughness on the properties were studied. In another study, Li et al. proposed using

a digital image correlation analysis to research the in-plane shear behavior and process influence on composite performance [20]. Combining carbon fiber-reinforced polymer bars and warps enhanced the reinforced concrete beams, which showed a 95% increment in flexural load capacity compared to the control sample [21].

As discussed earlier, process parameters also play a crucial role in determining the performance of the resulting carbon fiber composites. Bianchi et al. adapted a filament winding process to study the effect of heat-shrinkable tape application on composite mechanical properties, which improved the performance of the wound part because of the enhanced material compaction [22]. In addition, Mandal et al. utilized aromatic vitrimers to boost the processing and self-healing capability of carbon fiber composites [23]. A high-energy laser was introduced to explore the degradation of prepared carbon fiber-reinforced polymer composites [24]. This work proved the predictions concerning the scalable effects of high-energy laser radiation and material behavior in high-performance settings.

In addition to these experimental studies, the finite element analysis (FEA) approach was used to analyze prepared composites. For instance, Han et al. used FEA to evaluate the buckling performance of carbon and/or E-glass fiber-reinforced composite stiffened panels with various skin layups, showing that hybrid reinforcement could optimize structural efficiency and reduce costs [25]. In addition, Ceddia et al. compared carbon fiber-reinforced polymer composite (CFRPC) and Ti-6Al-4V via FEA, indicating that CFRPC exhibited mechanical properties that were close to those of bone, enabling more patient-specific implant designs [26].

Despite extensive research on carbon fiber composites from various perspectives, significant challenges remain. This Special Issue aims to help advance technology, inspire further research, and promote border applications of carbon fiber composites.

Data Availability Statement: No new data were created or analyzed in this study. Data sharing is not applicable to this article.

Conflicts of Interest: Jiadeng Zhu is employed by Brewer Science Inc. The author declares that the research was conducted in the absence of any commercial or financial relationships that could be construed as a potential conflict of interest.

References

1. Chen, Z.; Chen, J.; Ge, H.; Gao, Q.; Zhu, J.; Zhu, C.; Gao, C. Unique core-shell organogel/hydrogel fibers with tunable assembly structures for personal thermal management and human motion detection. *Chem. Eng. J.* **2025**, *518*, 164807. [CrossRef]
2. Hu, Y.; Lin, Y.; Yang, L.; Wu, S.; Tang, D.; Yan, C.; Shi, Y. Additive manufacturing of carbon fiber-reinforced composites: A review. *Appl. Compos. Mater.* **2024**, *31*, 353–398. [CrossRef]
3. Zeng, H.; Gao, C.; Yu, Y.; Jiang, M.; Deng, T.; Zhu, J. Wet spinning enabled advanced PEDOT: PSS composite fibers for smart devices. *Acc. Mater. Res.* **2025**, *6*, 952–963. [CrossRef]
4. Zhu, J.; Gao, Z.; Mao, Q.; Gao, Y.; Li, Y.; Zhang, X.; Gao, Q.; Jiang, M.; Lee, S.; van Duin, A.C.T. Advances in Developing Cost-Effective Carbon Fibers by Coupling Multiscale Modeling and Experiments: A Critical Review. *Prog. Mater. Sci.* **2024**, *146*, 101329. [CrossRef]
5. Kumar, A.; Dixit, S.; Singh, S.; Sreenivasa, S.; Bains, P.S.; Sharma, R. Recent developments in the mechanical properties and recycling of fiber-reinforced polymer composites. *Polym. Compos.* **2025**, *46*, 3883–3908. [CrossRef]
6. Zhu, J.; Li, G.; Kang, L. Editorial for the Special Issue on Carbon Fiber Composites. *J. Compos. Sci.* **2024**, *8*, 113. [CrossRef]
7. Zhu, J. Editorial for the Special Issue on Carbon Fiber Composites, Volume II. *J. Compos. Sci.* **2024**, *8*, 307. [CrossRef]
8. Wu, H.; Guo, A.; Kong, D.; Wu, J.; Qu, P.; Wang, S.; Guo, S.; Li, X.; Zhao, Z.; Liu, C.; et al. Preparation of Bouligand biomimetic ceramic composites and the effect of different fiber orientations on mechanical properties. *J. Manuf. Process.* **2024**, *132*, 789–801. [CrossRef]
9. Almeida Jr, J.H.S.; Miettinen, A.; Léonard, F.; Falzon, B.G.; Withers, P.J. Microstructure and damage evolution in short carbon fibre 3D-printed composites during tensile straining. *Compos. B: Eng.* **2025**, *292*, 112073. [CrossRef]

10. Lu, S.; Zhang, B.; Niu, J.; Yang, C.; Sun, C.; Wang, L.; Li, D. High-strength carbon fiber-reinforced polyether-ether-ketone composites with longer fiber retention length manufactured via screw extrusion-based 3D printing. *Addit. Manuf.* **2024**, *86*, 104200. [CrossRef]
11. Blythe, A.; Fox, B.; Nikzad, M. Stiffness retention in cyclic-loaded CFRP composites produced via novel automatic tape laying. *J. Compos. Sci.* **2024**, *8*, 92. [CrossRef]
12. Zheng, R.; Pang, J.; Sun, J.; Su, Y.; Xu, G. Damage model of carbon-fiber-reinforced concrete based on energy conversion principle. *J. Compos. Sci.* **2024**, *8*, 71. [CrossRef]
13. Tanaka, K.; Taniguchi, M. Effects of the Injection Material and Resin Layer on the Mechanical Properties of Carbon Fiber-Reinforced Thermoplastic (CFRTP) Press and Injection Hybrid Molded Parts. *J. Compos. Sci.* **2024**, *8*, 56. [CrossRef]
14. Alhusain, M.; Al-Mayah, A. Innovative Wedge Anchorage for CFRP Plates: Development and Testing. *J. Compos. Sci.* **2024**, *8*, 103. [CrossRef]
15. Li, L.; Song, Z.; Zhang, X.; Wang, F.; Song, P.; Jin, K.; Lee, T.; Quagliato, L. Influence of Grinding Tool Mesh Size and Rotational Speed on Post-Machining Quality of CFRP Laminates by Acceleration Signal and Surface Roughness Analyses. *J. Compos. Sci.* **2024**, *8*, 543. [CrossRef]
16. El Mehtedi, M.; Buonadonna, P.; Loi, G.; El Mohtadi, R.; Carta, M.; Aymerich, F. Surface Quality Related to Face Milling Parameters in 3D Printed Carbon Fiber-Reinforced PETG. *J. Compos. Sci.* **2024**, *8*, 128. [CrossRef]
17. Abdel-Mohsen, A.M.; Abdel-Rahman, R.M.; Kalina, L.; Vishakha, V.; Kaprálková, L.; Němeček, P.; Jančář, J.; Kelnar, I. Effect of chitin nanocrystal deacetylation on a nature-mimicking interface in carbon fiber composites. *J. Compos. Sci.* **2024**, *8*, 163. [CrossRef]
18. Kocharla, R.P.B.; Bandlamudi, R.K.; Mirza, A.A.; Kolli, M.; Shanmugam, R.; Cheepu, M. Investigation on the Mechanical and Thermal Properties of Jute/Carbon Fiber Hybrid Composites with the Inclusion of Crab Shell Powder. *J. Compos. Sci.* **2024**, *8*, 296. [CrossRef]
19. Liu, W.; Luo, Y.; Zhao, Y.; Zhou, H.; Ao, S.; Li, Y. Electrochemical Jet Machining of Surface Texture: Improving the Strength of Hot-Pressure-Welded AA6061-CF/PA66 Joints. *J. Compos. Sci.* **2024**, *8*, 263. [CrossRef]
20. Li, H.; Zhang, H.; Yue, G.; Guo, B.; Wu, Y. Determination of the In-Plane Shear Behavior of and Process Influence on Uncured Unidirectional CF/Epoxy Prepreg Using Digital Image Correlation Analysis. *J. Compos. Sci.* **2024**, *8*, 133. [CrossRef]
21. Akbarpour, A.; Volz, J.; Vemuganti, S. An Experimental study incorporating carbon fiber composite bars and wraps for concrete performance and failure insight. *J. Compos. Sci.* **2024**, *8*, 174. [CrossRef]
22. Bianchi, I.; Forcellese, A.; Mancia, T.; Mignanelli, C.; Simoncini, M.; Verdini, T. Effect of Heat-Shrinkable Tape Application on the Mechanical Performance of CFRP Components Obtained by a Filament Winding Process. *J. Compos. Sci.* **2024**, *8*, 535. [CrossRef]
23. Mandal, T.; Ozten, U.; Vaught, L.; Meyer, J.L.; Amiri, A.; Polycarpou, A.; Naraghi, M. Processing and Mechanics of Aromatic Vitrimeric Composites at Elevated Temperatures and Healing Performance. *J. Compos. Sci.* **2024**, *8*, 252. [CrossRef]
24. Schäffer, S.; Reich, S.; Heunoske, D.; Lueck, M.; Wolfrum, J.; Osterholz, J. Laser-Induced Decomposition and Mechanical Degradation of Carbon Fiber-Reinforced Polymer Subjected to a High-Energy Laser with Continuous Wave Power up to 120 kW. *J. Compos. Sci.* **2024**, *8*, 471. [CrossRef]
25. Han, H.; Dong, C. Buckling Analysis for Carbon and Glass Fibre Reinforced Hybrid Composite Stiffened Panels. *J. Compos. Sci.* **2024**, *8*, 34. [CrossRef]
26. Ceddia, M.; Solarino, G.; Giannini, G.; De Giosa, G.; Tucci, M.; Trentadue, B. A Finite Element Analysis Study of Influence of Femoral Stem Material in Stress Shielding in a Model of Uncemented Total Hip Arthroplasty: Ti-6Al-4V versus Carbon Fibre-Reinforced PEEK Composite. *J. Compos. Sci.* **2024**, *8*, 254. [CrossRef]

Journal of
Composites Science

MDPI

Article

Influence of Grinding Tool Mesh Size and Rotational Speed on Post-Machining Quality of CFRP Laminates by Acceleration Signal and Surface Roughness Analyses

Lichen Li [1], Ziyuan Song [2], Xinxin Zhang [2], Fangyuan Wang [1], Pengda Song [1], Kai Jin [1,*], Taeyong Lee [3] and Luca Quagliato [3,*]

[1] College of Material Science and Technology, Ocean University of China, Qingdao 266100, China
[2] Hisense (Shandong) Refrigerator Co., Ltd., Qingdao 266100, China
[3] Department of Mechanical and Biomedical Engineering, Ewha Womans University, Seoul 03760, Republic of Korea
* Correspondence: jinkai@ouc.edu.cn (K.J.); lucaq@ewha.ac.kr (L.Q.); Tel.: +86-0532-60891690 (K.J.); +82-02-3277-4759 (L.Q.)

Abstract: In the grinding process, acceleration signals in both the time and frequency domains are valuable for monitoring and controlling vibration patterns, as factors such as rotational speed and the grinding head design significantly influence machining quality, efficiency, and finishing performance. This study analyzes the acceleration signals by dividing them into three distinct stages, pairing this analysis with microscopic morphology to investigate the grinding behavior of carbon fiber-reinforced polymer (CFRP). The findings reveal that high-frequency and low-amplitude vibrations enhance polishing efficiency and quality, whereas low-frequency and high amplitudes adversely affect grinding quality. Acceleration vibrations are more stable during the intermediate grinding stage compared to the initial and final stages, which helps reduce surface roughness, regardless of the rotational speed or grinding head mesh size. In addition, a coarse mesh (#40) results in an uneven surface due to a large amount of removed material, whereas a fine one (#120) results in lower material removal but continuous vertical vibrations due to the impact with the grinding surface, also resulting in poor surface quality. Thus, controlling the tool's size and rotational speed is essential in reducing the amplitude of the vibration, allowing for maximizing the grinded CFRP surface quality.

Keywords: carbon fiber-reinforced polymer (CFRP); grinding mechanism; acceleration signal; frequency–amplitude control; surface quality; roughness

1. Introduction

The increasing variety of carbon fiber-reinforced polymers (CFRPs) has significantly driven the expansion of these materials across multiple fields [1,2]. Traditional CFRP composite manufacturing methods, such as hot press molding and injection molding, have been commonly used. However, the slow processing times or the high costs associated with these methods are now insufficient to meet the evolving needs of modern industries [3–5]. Consequently, additional manufacturing technologies are being explored, leveraging well-established processes from metallic materials, such as grinding, milling, drilling, and turning [6,7]. While practical and widely available in many industrial settings, these conventional machining methods are influenced by various factors, including grinding wheel speed, grit size, feed rate, and lubrication conditions. In response, recent research has begun to explore the interactions between these relatively traditional techniques when applied to the processing of CFRPs. For instance, Wang et al. [8] found that high grinding speeds enhance the surface quality of CFRP, especially when combined with industrial robots. Their study demonstrated that a grit size of #80 achieved the best grinding results and highest surface quality. Similarly, Liu et al. [9] applied the Box–Behnken design and

response surface methodology (RSM) to analyze the effects of spindle speed, cutting depth, feed rate, and grit size on grinding force and surface roughness, ultimately developing an optimization model to identify the ideal process parameters. Subsequent research has corroborated that grinding force is directly proportional to cutting depth and feed rate but inversely proportional to grinding wheel speed [10–12], showing insights into improving processing quality by selecting optimal grinding parameters.

Beyond process parameters, the choice and specifications of tools have a considerable impact on machining quality. This has led researchers to focus on tool design specifically for CFRP grinding. For instance, Nomura et al. [13] addressed the limitations of conventional grinding wheels for CFRP by developing a new type of wheel with diamond abrasive grains electrochemically deposited on a circular metal wire mesh. This innovation effectively prevents clogging during grinding and enhances surface quality. Additionally, Xu et al. [14] found that diamond-coated tools can significantly lower drilling temperatures, reducing the risk of localized glass transition within the composite matrix and thus preventing degradation of mechanical performance. Based on the tool design proposed by Nomura et al. [13], Liang et al. [15] conducted research using a robotic arm equipped with small-volume brazed diamond abrasive heads for ultrasonic-assisted grinding of CFRP. Their study established a mathematical model for grinding force to determine the optimal spacing between abrasive grains, aiming to improve both grinding outcomes and surface quality. They also demonstrated that using a robotic arm to handle the diamond grinding head offers significant advantages in processing small, intricate workpieces.

In addition to diamond abrasives, researchers have explored other abrasive particles to assess grinding quality. Soo et al. [16] investigated the performance of diamond and cubic boron nitride (CBN) abrasives on CFRP. Their study found that CBN tools experienced greater wear, cutting force, and surface roughness compared to diamond grinding heads, providing important guidance for selecting appropriate machining tools. Wang et al. [17] examined five different drill bits with ultrasonic assistance for CFRP grinding. They experimentally analyzed tool variables such as abrasive size, abrasive concentration, groove count, and tool end geometry on machining performance. Their findings showed that larger abrasive sizes, lower abrasive concentrations, and tools with two grooves reduced cutting force and torque, while smaller abrasive sizes and lower abrasive concentrations in tools with two grooves and convex end geometry produced better surface smoothness. Similarly, Tao et al. [18] developed an innovative discontinuous grinding head and studied its interactions with CFRP, creating a grinding force model for two types of discontinuous micro-grinding tools. Interest in developing new grinding tools for composite materials, particularly CFRP [19], as well as ceramic matrix composites [20,21], has surged over the past two years. These efforts continue to introduce novel grinding techniques and enhance the surface quality of manufactured components.

Recognizing the industrial trend toward robotic machining [22,23] and the need to account for the dynamic interaction between robotic movements and the machining forces involved [24], this study investigates the influence of the grinding wheel rotational speed and grit size on the acceleration signals during the grinding process of CFRP laminates, initially manufactured by hot pressing. Three head mesh sizes have also been included to establish a correlation between them and the mentioned grinding process parameters.

By analyzing the variations in vibration frequency and amplitude during the initial, middle, and final stages of the grinding process, this research examines the material removal mechanisms in CFRPs and their impact on surface quality. The results reveal that high surface quality can be achieved by increasing vibration frequency, while the number of grinding heads plays a crucial role in determining surface roughness.

2. Materials and Methods

2.1. CFRP Laminates' Manufacturing

In the experiments, 0.14 mm/layer thick plain weave USN150 (SK-Chemical, Seongnam-si, Republic of Korea) prepregs were used to manufacture CFRP laminates through curing

by hot pressing. The prepreg material was laminated and cured under a pressure of 2 MPa at 175 °C for 1.5 h. A summary of the properties is reported in Table 1. The manufactured specimens employed in the grinding process have dimensions of 200 mm (length), 20 mm (width), and 2 mm (thickness), respectively.

Table 1. Characteristic and mechanical properties of the USN150 prepreg CFRP material.

Characteristic	Value
Fiber content [vol. %]	54%
Matrix polymer	Thermoset epoxy resin
Prepreg fiber angle	0°/90°
Tensile moduli E_{11}, E_{22} [GPa]	128, 8.7
Shear modulus G_{12} [GPa]	4.74
Tensile strengths σ_{11}, σ_{22} [MPa]	2000, 61
Shear strength τ_{12} [MPa]	70

2.2. CFRP Grinding Process

For the grinding of the CFRP laminates, the tooling equipment shown in Figure 1a was employed and includes the FANUC M20id industrial robot (Rochester Hills, MI, USA), a 3D worktable, an A304EX accelerometer (Paeonian Springs, VA, USA), the SM3542B-24 spindle motor (Dongguan Tianyi Precision Electromechanical Co., Ltd., Guangzhou, China), and a diamond grinding head. The schematic diagram of the grinding process is shown in Figure 1b. A systematic study was conducted to study the relationship between the acceleration signal and grinding mechanism, considering the parameters' levels shown in Table 2. The employed A304EX acceleration sensor, as shown in Figure 1a, is connected with the BeeData software (https://www.beetech.cn/products/147.html—Accessed date: 20 November 2023) employed to record, export, and post-process the acceleration signals during the experiments. The three employed grinding tools, named #40, #80, and #120, are representative of average particle sizes of 345 µm, 181 µm, and 110 µm, respectively, all with a grinding head diameter equal to 10 mm. The microscopic images of abrasive particles from different grinding head nets are shown in Figure 2, where three particles are measured as an example and are representative of the whole distribution throughout the grinding head.

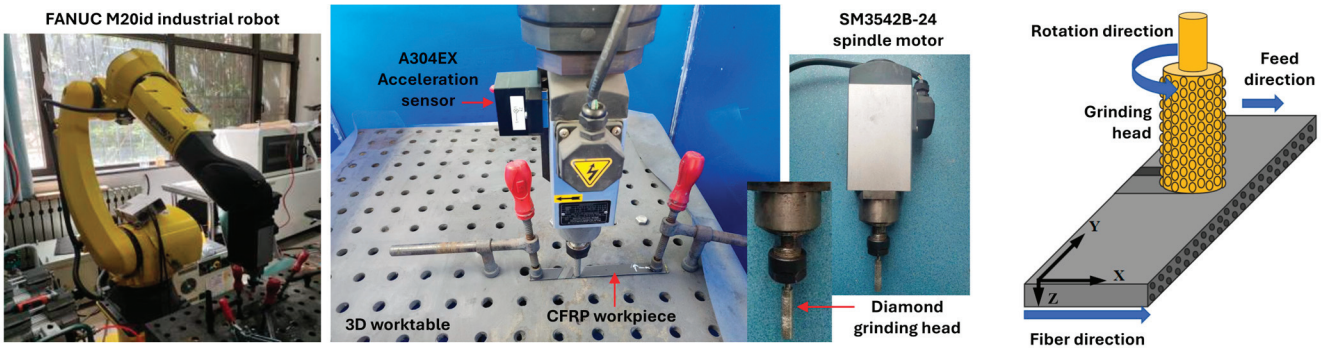

Figure 1. (**a**) Equipment and settings employed in the CFRP grinding process and (**b**) Schematic of the grinding process.

For the case of the #40 grinding head, both the abrasive particle diameter and the gap between the particles are significantly larger compared to those of #80 and #120. Consequently, the gap between abrasive particles hinders the material removal capabilities and prevents them from achieving uniform grinding. In this scenario, certain areas undergo more intense cutting while others remain insufficiently affected, leading to an uneven surface height. As a final remark, all experiments involved the utilization of deionized

water as a coolant during processing. Due to its effective heat dissipation capability and non-reactivity with the CFRP machined surface, deionized water is employed for cooling purposes.

Table 2. Process parameters and levels employed for the CFRP grinding experiments.

Parameter	Levels
Rotational speed [rpm]	2000, 3000, 4000
Peripheral speed [m/min]	62.8, 94.2, 125.7
Grinding head mesh size	#40, #80, #120
Feed speed [mm/s]	4
Grinding depth [mm]	1
Grinding width [mm]	10

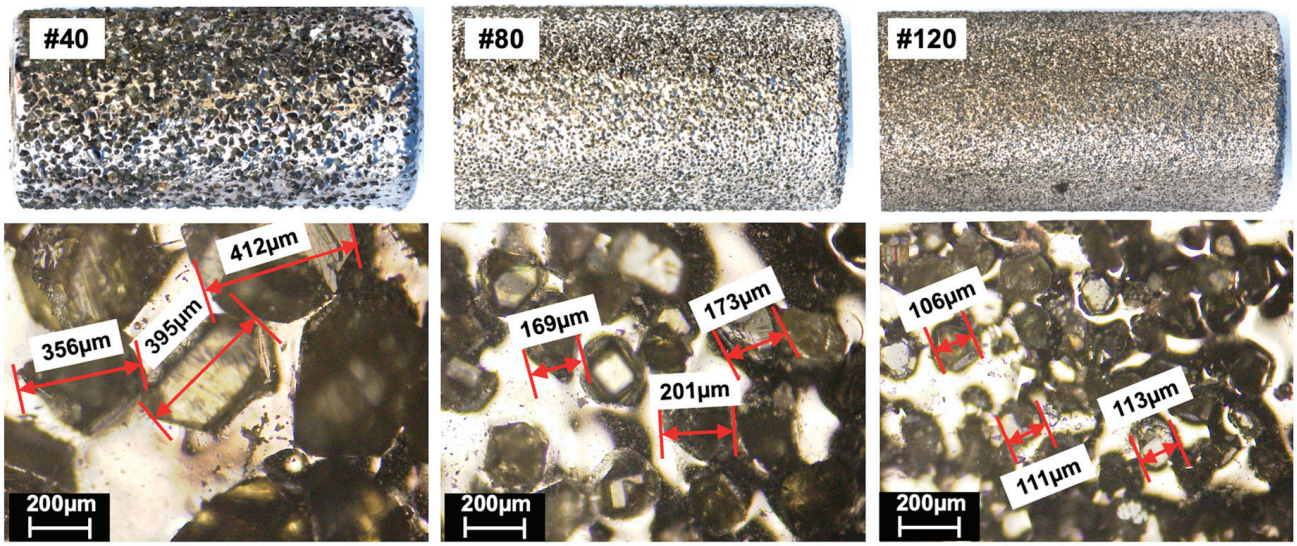

Figure 2. Microscope analysis of the employed abrasive heads with #40, #80, and #120 mesh sizes.

3. Results and Discussion

3.1. Relationship Between Speed and Acceleration Vibration Signals

The analysis presented in this section aims at showing the influence of the rotation speed of the spindle and the resulting surface quality of the grinded CFRP. To this end, only the #80 grit grinding head was considered, as it represents the intermediate mesh size. The Z-axis acceleration time domain and fast Fourier transformation (FFT) charts at grinding head rotating speeds of 2000 rpm, 3000 rpm, and 4000 rpm (#80, 0°) are shown in Figure 3. Here, "0°" refers to the angle between the fiber direction of the CFRP and the grinding feed direction.

When the rotation speed is 2000 rpm, the vibration frequencies generated during the grinding process are concentrated between 100 Hz and 300 Hz. When the rotational speed of the grinding tool increases (Figure 3a–c), both low-frequency and high-frequency vibrations occur during the grinding process, and the main forms of vibration are increasingly concentrated around 200 Hz. As shown in the FFT chart of Figure 3b, at 3000 rpm, there are low-frequency vibrations with a frequency of 43 Hz and an amplitude of 0.053 g, as well as high-frequency vibrations with a frequency of 389 Hz and an amplitude of 0.056 g. At 4000 rpm, there are low-frequency vibrations with a frequency of 25 Hz and an amplitude of 0.081 g, as well as high-frequency vibrations with a frequency of 398 Hz and an amplitude of 0.063 g.

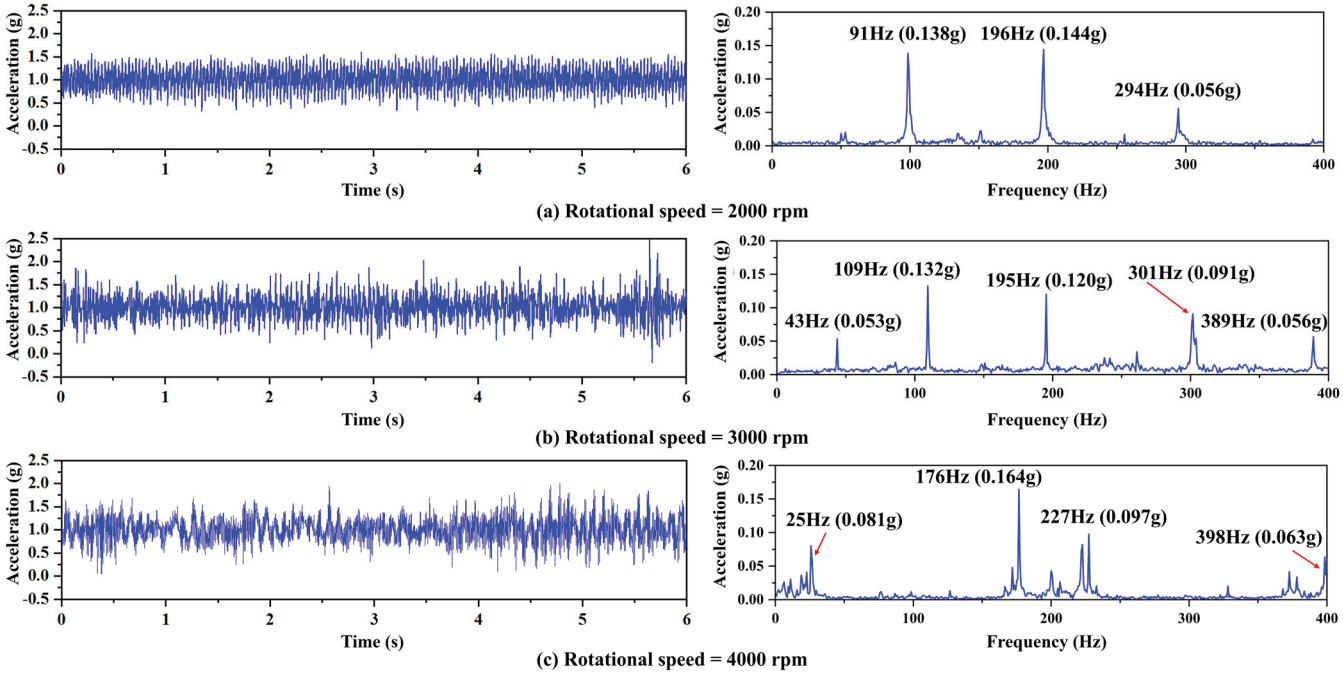

Figure 3. Z-axis acceleration signals in the time domain and FFT spectrum for (**a**) 2000 rpm, (**b**) 3000 rpm, and (**c**) 4000 rpm rotation speed of the #80 grinder during the CFRP machining process.

As the speed increases, the interaction between the tool and the workpiece becomes more intense, resulting in a faster accumulation of grinding debris. High-frequency vibrations can quickly remove the debris, thereby improving the grinding efficiency and the quality of the debris. Moreover, after the debris is vibrated out, the grinding resistance instantly decreases, resulting in low-frequency vibrations. The smaller amplitude of high-frequency vibrations is due to their auxiliary role in debris removal compared to the main vibration mode (around 200 Hz) generated by the removal of CFRP material.

The grinding mechanism at different grinding speeds is illustrated in Figure 4, where the tilting of the tool is reported to highlight the high resistance encountered by the grinding head, especially for low rotational speeds of 2000 rpm (Figure 4a) and also slightly at 3000 rpm (Figure 4b). The misalignment in the z-direction is not intentionally inputted as a grinding angle $\neq 0$ but is the result of the interaction between the coarse mesh size of the diamond grinding head and the CFRP workpiece.

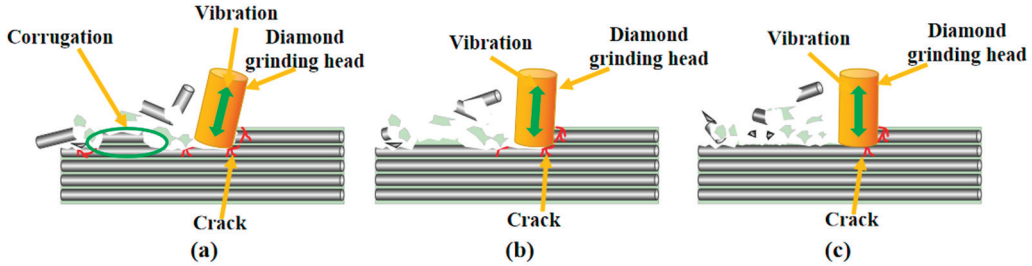

Figure 4. Grinding mechanism schematic representation at different grinding speeds: (**a**) 2000 rpm; (**b**) 3000 rpm; (**c**) 4000 rpm.

As the grinding process progresses, the fibers at the interface with the grinding head experience pressure from the Z and X directions, causing them to bend and fracture slightly. In conjunction with the low-frequency vibration peak of 0.138 g generated at 91 Hz, as shown in Figure 3a, the vibration frequency of the grinding head is relatively slow. In this scenario, the grinding head continuously impacts the grinding surface at the edge of its

bottom surface, creating a rippled grinding surface, as shown in Figure 5a, with fibers and resin remaining unremoved.

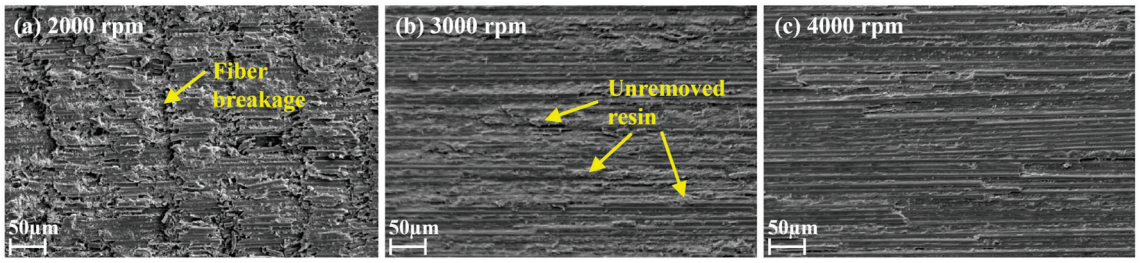

Figure 5. Microscopy images of the CFRP grinded surface at different rotational speeds (#40 grinder) for (**a**) 2000 rpm, (**b**) 3000 rpm, and (**c**) 4000 rpm.

As the speed increases, the grinding resistance decreases, and the predominant vibration mode of grinding becomes more concentrated around 200 Hz. The appearance of high-frequency, low-amplitude vibration helps alleviate the resistance caused by the grinding debris, resulting in less tilt of the diamond grinding head and the generation of continuous, closely spaced impacts. The impact amplitude in the Z-axis direction is significantly reduced, thereby improving the grinding surface, as visible by comparing Figure 5a–c. By considering Figures 3 and 5 together, for a spindle rotation speed of 3000 rpm, a significant amount of resin remains unremoved due to the grinding vibration frequency not being sufficiently concentrated.

Aiming for a deeper understanding of the reason for the variation in the surface quality shown in Figure 5, the FFT charts of the Z-axis acceleration at different speeds (#80, 0°) in the three stages of the grinding process are shown in Figure 6a–c. Figure 6 shows the acceleration peaks in the frequency domain on the left and, on the right, the confocal morphology and magnitude of surface roughness for the three speeds and the initial, intermediate, and final stages. In the same image, the post-grinding CFRP specimens are reported with the identification of the four points for each stage, employed for the measurement of the Sa roughness micrographs.

Moving from Figure 6a–c, the vibrations generated during grinding have larger amplitudes in the initial and final stages, while the amplitude decreases in the intermediate stage. Moreover, low- and high-frequency vibrations occur in all three stages of grinding with increasing speed, consistent with the frequency domain variations of the acceleration throughout the grinding process (Figure 3).

However, in the case of a 3000 rpm rotational speed for the grinding head (Figure 6b), it is found that a high-frequency vibration with a frequency of 311 Hz and an amplitude of 0.166 g occurs in the intermediate stage of grinding. This difference in the acceleration response is caused by an increase in resistance during the grinding process, which results in the generation of high-frequency vibrations that promote the improvement of grinding quality and efficiency. Accordingly, only for the case of 3000 rpm, the intermediate stage sees a higher amplitude frequency component around 300 Hz, which is fainter in both the initial and final stages, where the main vibrations are around 100 and 200 Hz.

In terms of surface quality, the micrographs of Figure 6 show the periodic textures left by the grinding head at a low rotational speed, which leads to larger roughness values. This transition is clear from the confocal micrographs reported in Figure 6a–c, and already from 3000 rpm, no impact textures are observed (Figure 6b). As shown in all micrographs of Figure 6, as we move closer to the central grinding area (left side of the micrographs), a greater proportion of red coloration is observed due to the lower linear speed at this region, resulting in incomplete grinding and higher surface roughness for CFRP materials. Conversely, towards the edges where linear speed increases, a smaller amount of red coloration is present, indicating lower surface roughness.

By combining this result with the acceleration, the FFT chart shows that the balancing of the vibration amplitude at 109 Hz, from 2000 to 3000 rpm, as well as the appearance of a

high-frequency component at 311 Hz (0.166 g) in the intermediate stage promotes a better grinding quality and a smoother surface. Finally, when the speed is 4000 rpm, significant high-frequency vibrations occur in all three stages of grinding, resulting in a smaller surface roughness compared to 2000 and 3000 rpm. The maximum surface roughness for the three speeds reported in Figure 6 is summarized in Figure 7 and shows a clear variation of the roughness from the initial to the final stages and an overall reduction from 2000 to 4000 rpm, with a clear step between 2000 and 3000 rpm.

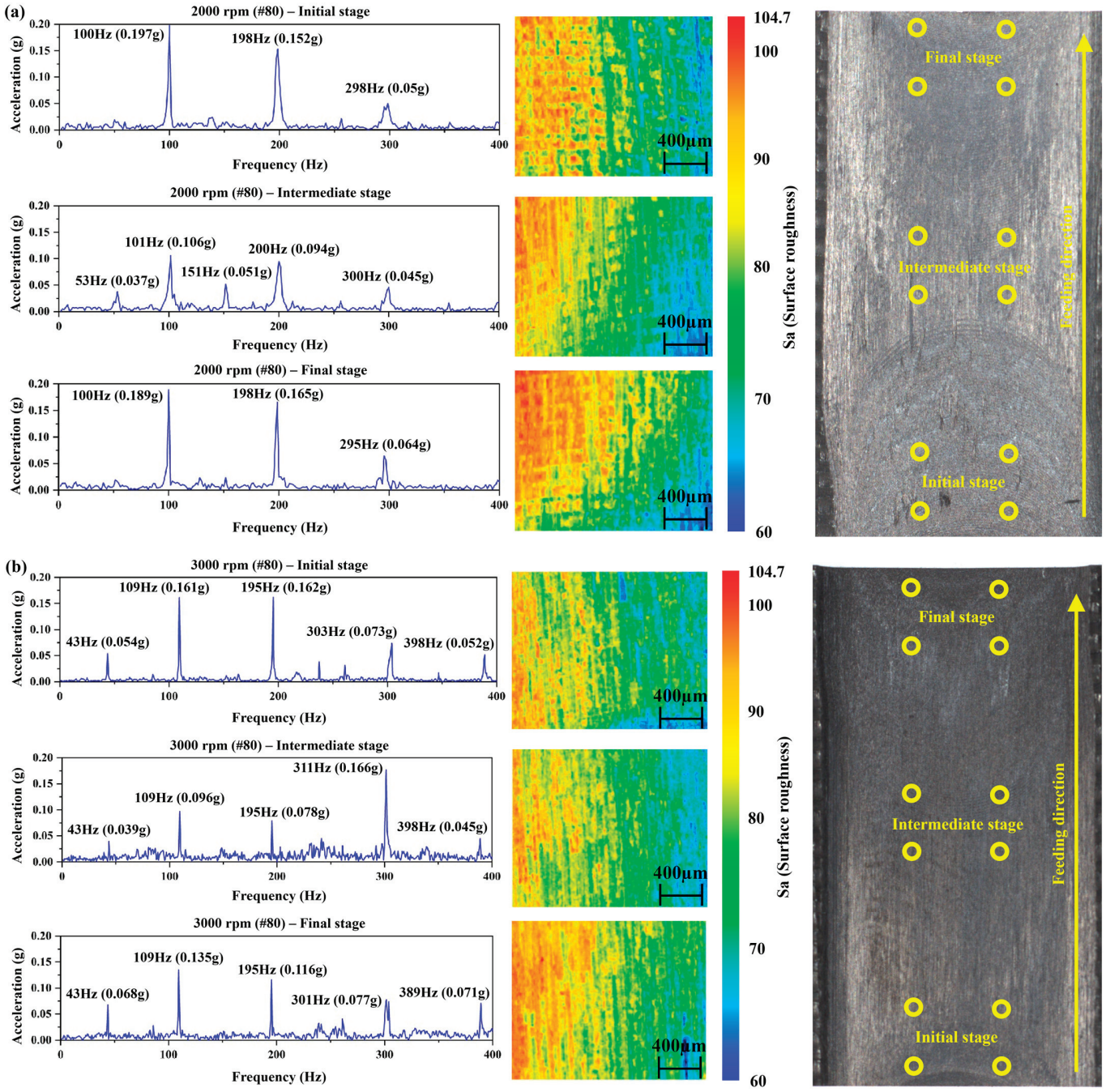

Figure 6. *Cont.*

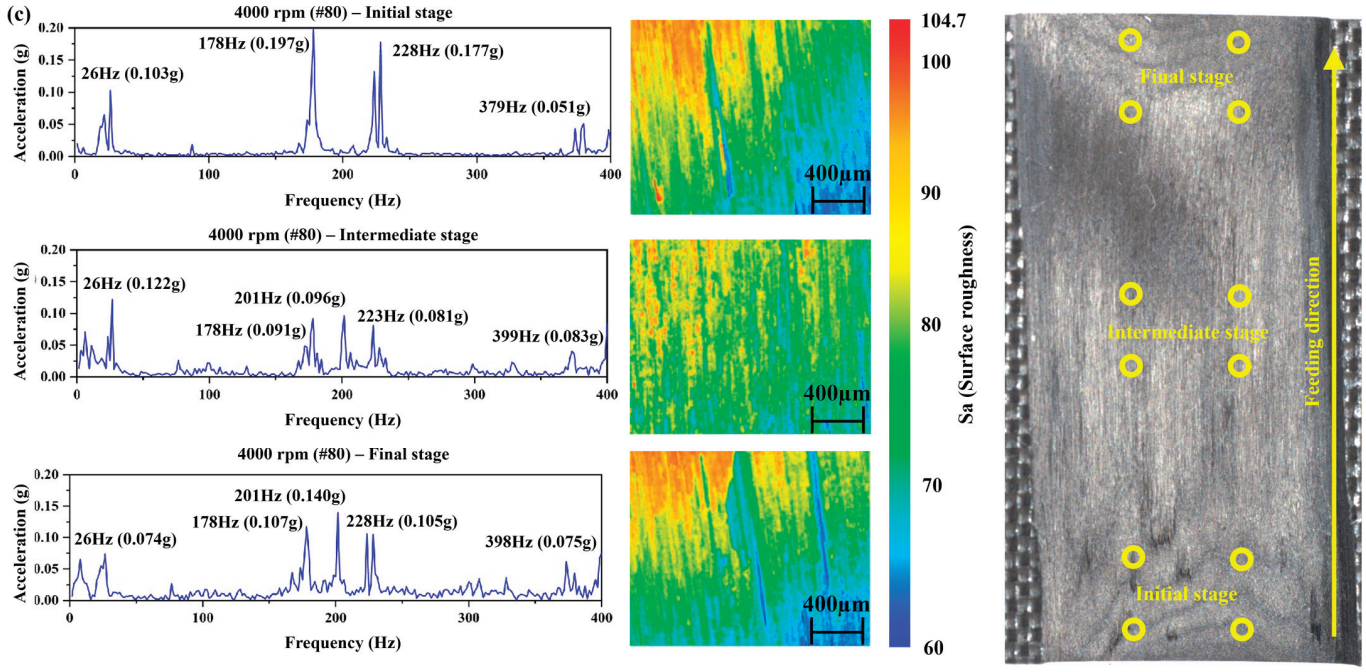

Figure 6. FFT diagram of acceleration and confocal micrographs at the initial stage, intermediate stage, and final stage of grinding at different speeds: (**a**) 2000 rpm, (**b**) 3000 rpm, and (**c**) 4000 rpm. The scale on the micrographs is in microns (µm). For all three sets of images on the right, the pictures of the post-grinding CFRP specimens are reported with the identification of the four points for each stage employed for the measurement of the Sa roughness micrographs.

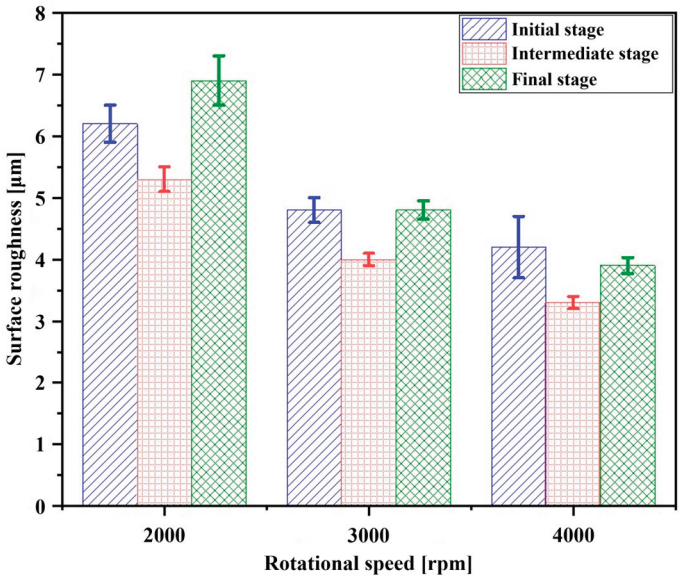

Figure 7. Roughness diagram of the initial stage, intermediate stage, and final stage of grinding at different rotational speeds (2000 rpm, 3000 rpm, and 4000 rpm).

3.2. Relationship Between the Grinding Heads Mesh Size and the Acceleration Vibration Signal

To investigate the effect of the grinding mesh size on the acceleration signals, in this section, the rotational speed has been considered as a constant equal to 4000 rpm. To this end, the temporal and spectral variations of acceleration during the grinding process for #40, #80, and #120 grit sizes are shown in Figure 8.

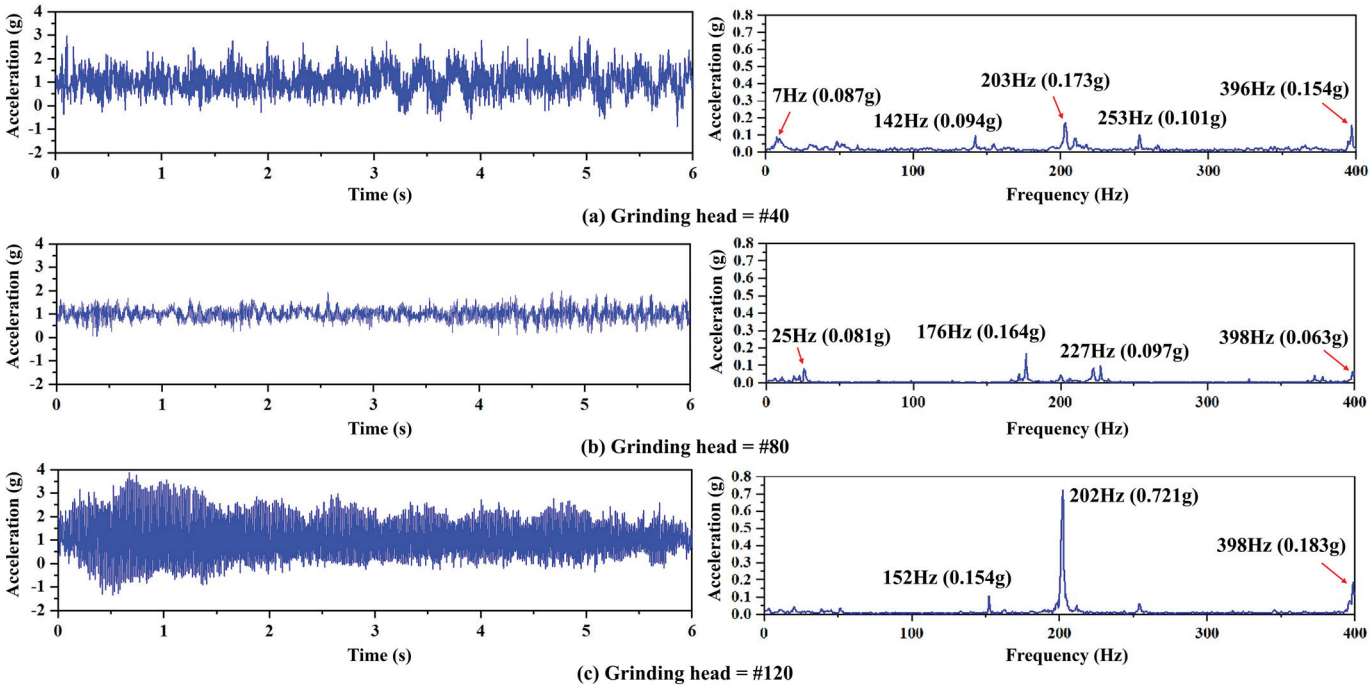

Figure 8. Z-axis acceleration signals in the time domain and FFT spectrum for (**a**) #40, (**b**) #80, and (**c**) #120 grinding head at 4000 rpm rotation speed during the CFRP machining process.

For grit size #40, the maximum amplitude in the frequency domain of acceleration is 0.173 g, which is not significantly different from the maximum amplitude of 0.164 g for grit size #80. However, the maximum amplitude for grit size #120 can reach 0.721 g, which is significantly higher and between 3.9 and 4.7 times that of the lower or higher frequencies identified in the FFT analysis, as shown in Figure 8c. As previously shown in Figure 3, an increase in the grit size results in a reduction of the size of the diamond particles and of the spacing between them. In this regard, the interaction between different grit sizes during the grinding process is shown in Figure 9. This phenomenon can be explained by a combined analysis of the grinding mechanism and microscopy analysis.

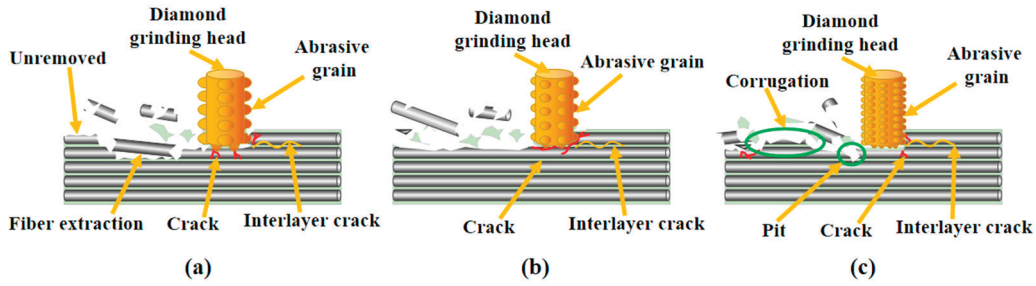

Figure 9. Grinding mechanism at different mesh sizes of grinding heads: (**a**) #40; (**b**) #80; (**c**) #120.

When the grit size is #40 (Figures 8a and 9a), the abrasive particle size and spacing are large, resulting in low grinding precision, causing leftovers of unremoved resin and fibers. In this scenario, the abrasive particles on the side and bottom surfaces of the diamond grinding head exert pressure on the CFRP in the X- and Z-directions. For the former, the fibers at the interface with the side surface undergo slight bending and develop interlayer cracks between the underlying fibers, leading to fracture under the applied force. For the latter, the fiber layer in contact with the bottom surface of the diamond grinding head fractures in the Z-direction due to the impact, and the high roughness of the #40 grit head causes it to pull out the fractured fibers from the lower layer during grinding, ultimately resulting in an uneven grinding surface, as depicted in Figure 10a.

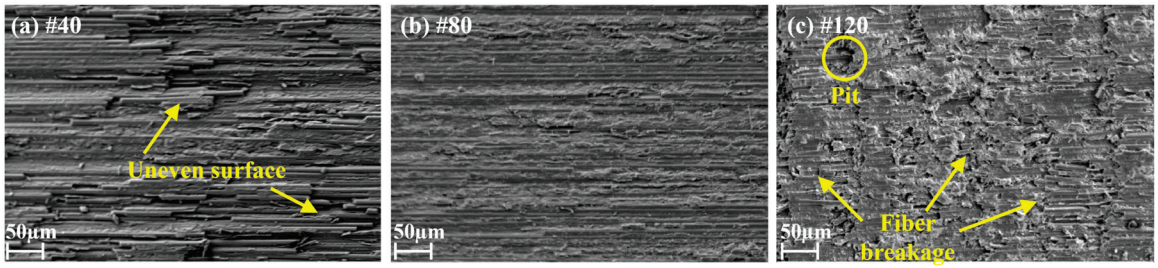

Figure 10. Microscopy images of the CFRP grinded surface for different grit mesh sizes (4000 rpm) for (**a**) #40, (**b**) #80, and (**c**) #120 grit heads.

However, when the grit size is #120 (Figures 8c and 9c), the particle-to-particle spacing is reduced, and the amount of material removed per unit time is relatively small. Under a constant feed rate, compared to grit sizes #40 and #80, the grinding head experiences increased resistance during the grinding process, leading to significant vibrations; Figure 8c. For the #120 grit size, the diamond particles are packed more tightly, causing chip clogging around the grinding head and exacerbating the vibration to facilitate chip removal. The fiber layer in contact with the bottom surface of the grinding head undergoes compressive fracture due to the edge impact of the grinding head (Figure 9c), and the fractured fibers and resin chunks are expelled under the action of vibration and coolant, leaving behind fractured pits, as shown in Figure 10c.

When the grit size is #40, the overall fiber removal effect is poor, and a significant amount of resin remains unremoved. However, when the grit size is #120, periodic fiber fracture marks can be observed. This fact indicates that excessive vibration amplitude (Figure 8c; 0.721 g) causes the grinding head to continuously impact the grinding surface, resulting in periodic fiber fracture. When the grit size is #80, the surface quality is flatter and smoother, in comparison to #40 and #120 (Figure 10), and the magnitude of the vibration is limited to 0.164 g, more than four times lower than #120 (Figure 8b vs. Figure 8c).

To investigate further the effect of different grit mesh sizes on the acceleration profile in the frequency spectrum and on the surface roughness, a similar comparison to the one proposed in Figure 6 but relevant to the #40, #80, and #120 tools' mesh, is reported in Figure 11. Under different grinding wheel grits, the vibration generated during grinding has larger amplitudes in the early and final stages but decreases in the intermediate stage.

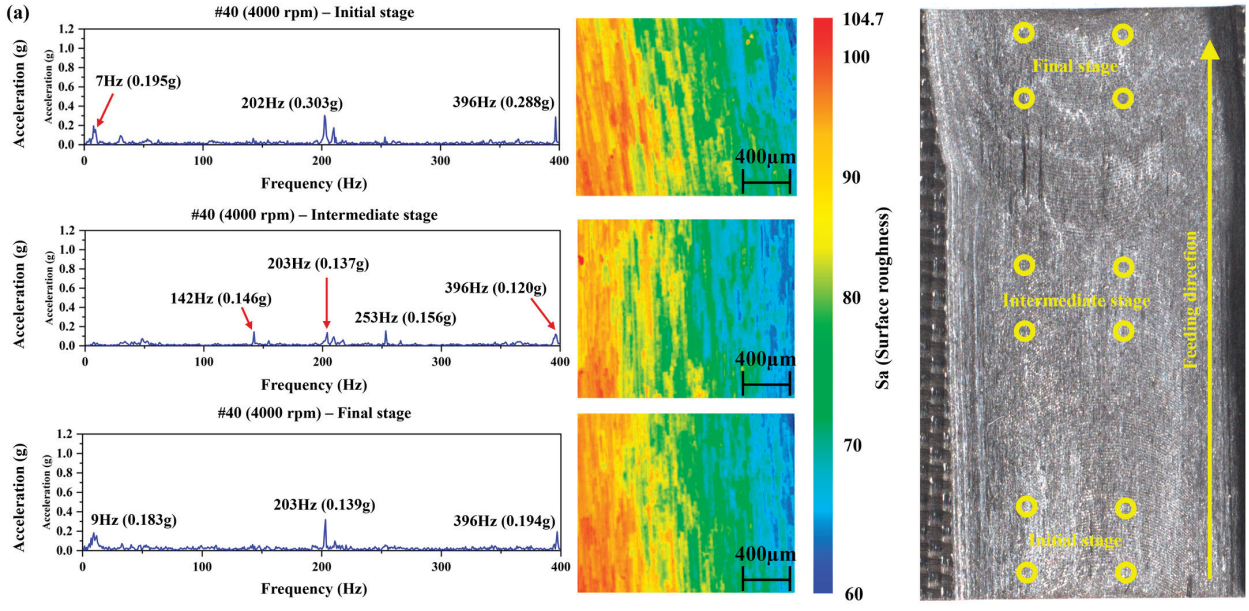

Figure 11. *Cont.*

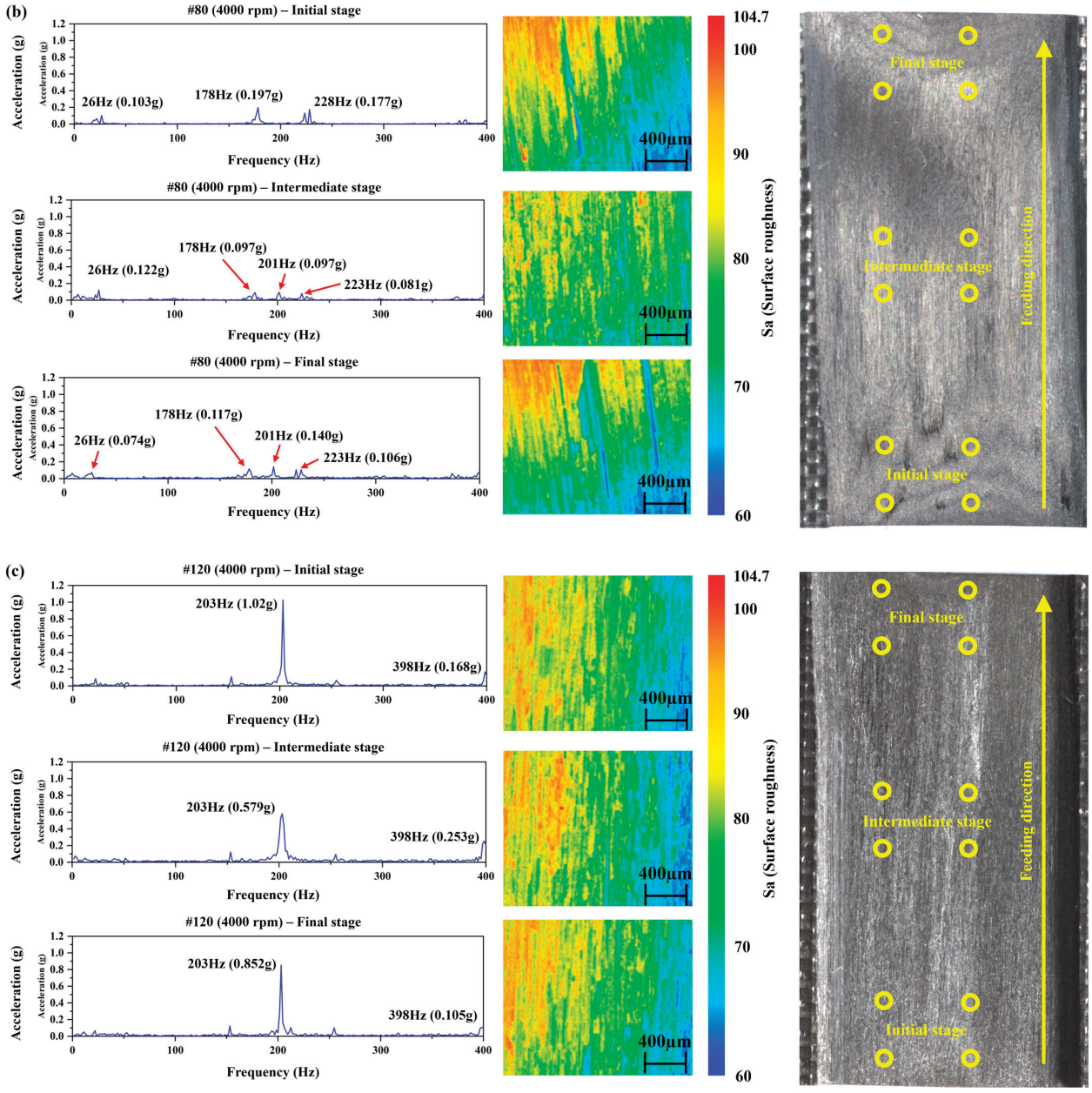

Figure 11. FFT diagram of acceleration and confocal micrographs at the initial stage, intermediate stage, and final stage of grinding for different grinding wheel grits: (**a**) #40, (**b**) #80, and (**c**) #120. The scale on the micrographs is in microns (μm). For all three sets of images on the right, the pictures of the post-grinding CFRP specimens are reported with the identification of the four points for each stage employed for the measurement of the Sa roughness micrographs.

Moreover, when using a #120 grit, the maximum amplitude in the grinding stage is much larger than that of #40 and #80 grits, and, as shown in Figure 11a,c, the Z-axis accelerations in #40 and #120 grits both exhibit high-frequency vibration, but for different reasons. By comparing the results in Figure 11 for the three grit mesh sizes combined with the same rotational speed of 4000 rpm, the high-frequency vibration for the #40 grit (Figure 10a) is due to larger abrasive particles, and thus a rougher grinding wheel, resulting in incomplete fibers and polymer matrix removal, decreased surface quality of CFRP, and high-frequency vibration caused by uneven machining surfaces hindering subsequent processes. However, when using the #120 grit (Figure 11c), the grinding removal rate per unit time is lower, so high-frequency vibrations are generated to facilitate grinding.

In the confocal image under #40 grit (Figure 11a), the rough surface area (red) is larger, whereas the red area in the confocal image under #80 grit (Figure 10b) is the smallest, indicating the lowest roughness profile and the best polishing quality. Moreover, for the #80 grit, the roughness in the intermediate stage is generally better than that of Figure 6b, mostly thanks to the properties of the tool's mesh, as well as the high rotational speed employed, resulting in smaller vibrations, which in turn results in a stable grinding and low roughness grinding.

Concerning the confocal images proposed in Figure 11, careful observation reveals periodic textures in the confocal image under #120 grit (Figure 11c), caused by large amplitudes in each stage continuously impacting the grinding surface. As mentioned for the case in Figure 6 and also for the case of Figure 11, the higher red coloration of the micrographs when moving from the right to the left of the pictures is caused by the linear speed of the grinding head, which is lower at the center and higher on the edges.

Referring to the micrographs in Figure 11, the summary of the maximum magnitudes for the three grits and the initial, intermediate, and final stages of the grinding process is reported in Figure 12, together with the relevant deviations calculated among the measurements. Therefore, both excessively large (#40) and small grinding wheel grits (#120) will affect the surface quality of grinding.

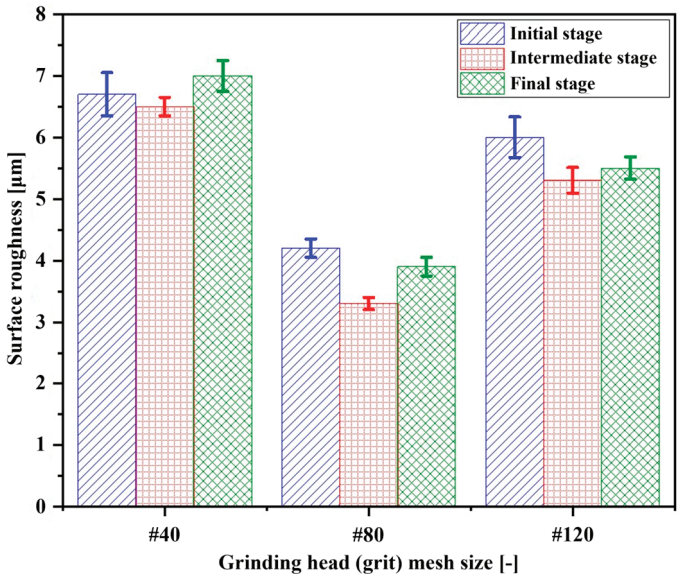

Figure 12. Roughness diagram of the initial stage, intermediate stage, and final stage of grinding for different grinding wheel grits (#40, #80, #120).

Together with the results summary proposed in Figure 7, the results in Figure 12 suggest that an intermediate grit mesh size of #80 associated with a rotational speed between 3000 and 4000 rpm is optimal in the machining of CFRP plates. If these process parameters are employed, the precision in the material removal can be optimized while the impacts of the toll on the machined surface can be minimized, resulting in a finer surface quality.

4. Conclusions

This research investigated the effect of rotational speed and grinding wheel grits on the acceleration profile and magnitude, as well as on the surface roughness of CFRP laminates initially manufactured by a hot-pressing process. Regarding the rotational speed and the number of abrasive particles, as the rotational speed increases, the vibration peak shifts to the high-frequency region, reducing grinding resistance and improving surface quality. At lower rotational speeds, low-frequency and high-amplitude vibrations occur, leading to fiber fracture and affecting surface quality. Larger particle sizes of the grinding head result

in larger vibration amplitudes of acceleration and rougher surfaces after grinding. The larger the abrasive grain size, the greater the amplitude of acceleration, and the rougher the surface after grinding. With a larger abrasive grain size, the material removal rate per unit time for each stage of grinding is lower. Therefore, high-frequency vibration is generated to facilitate grinding. However, an excessively large maximum amplitude in the Z-axis direction can reduce surface quality.

Author Contributions: Conceptualization, L.L. and K.J.; methodology, L.L., F.W. and P.S.; software, L.L., F.W. and P.S.; validation, L.L., K.J., Z.S. and X.Z.; formal analysis, L.L., F.W. and P.S.; investigation, L.L., F.W. and P.S.; resources, K.J., Z.S., X.Z. and L.Q.; data curation, Z.S., X.Z. and L.Q.; writing—original draft preparation, K.J., L.Q. and T.L.; writing—review and editing, K.J., L.Q. and T.L.; visualization, Z.S., X.Z. and L.Q.; supervision, K.J. and L.Q.; project administration, K.J.; funding acquisition, K.J., L.Q. and T.L. All authors have read and agreed to the published version of the manuscript.

Funding: This project was supported by the Qingdao Natural Science Foundation (23-2-1-246-zyyd-jch) and by the Lianyungang key research and development plan, (Grant No. CG2310). Prof. Luca Quagliato was supported by the RP-Grant 2024 of Ewha Woman's University.

Data Availability Statement: The data that support the findings of this study are not openly available due to reasons of sensitivity and are available upon request to the corresponding author.

Conflicts of Interest: Authors Ziyuan Song and Xinxin Zhang were employed by the company Hisense (Shandong) Refrigerator Co., Ltd. The remaining authors declare that the research was conducted in the absence of any commercial or financial relationships that could be construed as a potential conflict of interest.

References

1. Xu, J.; Lin, T.; Li, L.; Ji, M.; Davim, J.P.; Geier, N.; Chen, M. Numerical Study of Interface Damage Formation Mechanisms in Machining CFRP/Ti6Al4V Stacks under Different Cutting Sequence Strategies. *Compos. Struct.* **2022**, *285*, 115236. [CrossRef]
2. Wang, F.; Qian, B.; Jia, Z.; Fu, R.; Cheng, D. Secondary Cutting Edge Wear of One-Shot Drill Bit in Drilling CFRP and Its Impact on Hole Quality. *Compos. Struct.* **2017**, *178*, 341–352. [CrossRef]
3. Zhang, F.; Lin, Y.; Huang, Y.; Zhang, Z.; Wu, J.; Du, L. Forming Characteristics of Channel-Section CFRP-Aluminum Hybrid Profiles Manufactured by Inflatable Mandrel Assisted Hot-Pressing Process. *Compos. Struct.* **2022**, *296*, 115895. [CrossRef]
4. Mei, J.; Tan, P.J.; Bosi, F.; Zhang, T.; Liu, J.Y.; Wang, B.; Huang, W. Fabrication and Mechanical Characterization of CFRP X-Core Sandwich Panels. *Thin-Walled Struct.* **2021**, *158*, 107144. [CrossRef]
5. Tatsuno, D.; Yoneyama, T.; Kinari, T.; Sakanishi, E.; Ochiai, T.; Taniichi, Y. Braid-Press Forming for Manufacturing Thermoplastic CFRP Tube. *Int. J. Mater. Form.* **2021**, *14*, 753–762. [CrossRef]
6. Li, S.; Huang, S.; Li, H.; Liu, W.; Wu, W.; Liu, J. Multi-Condition Tool Wear Prediction for Milling CFRP Base on a Novel Hybrid Monitoring Method. *Meas. Sci. Technol.* **2024**, *35*, 035017. [CrossRef]
7. Guo, N.; Chen, Y.; Yan, C.; Meng, X.; Li, Y. Machinability of CFRP/Ti6Al4V Stacks with Low-Frequency-Vibration Assisted Drilling under Different Cooling Strategies. *J. Manuf. Process.* **2023**, *108*, 852–862. [CrossRef]
8. Wang, F.; Xuan, S.; Chang, Z.; Jin, K.; Gao, Y.; Wang, H.; Song, Q. Effect of Grinding Parameters on Industrial Robot Grinding of CFRP and Defect Formation Mechanism. *Int. J. Precis. Eng. Manuf. Green Technol.* **2024**, *11*, 427–438. [CrossRef]
9. Liu, S.; Zheng, K.; Li, H.; Cao, Z.; Zhao, S. Multi-Objective Optimization of Process Parameters in Longitudinal-Torsional Ultrasonic Vibration Face Grinding CFRP. *Machines* **2023**, *11*, 935. [CrossRef]
10. Wen, Z.; Zhao, H.; Yan, X.; Peng, Z.; Ding, H. Grinding Performance Study of CF/Epoxy and CF/PEEK Composites. *Polym. Compos.* **2023**, *44*, 4565–4578. [CrossRef]
11. Hu, N.S.; Zhang, L.C. Some Observations in Grinding Unidirectional Carbon Fibre-Reinforced Plastics. *J. Mater. Process. Technol.* **2004**, *152*, 333–338. [CrossRef]
12. Wang, Y.G.; Yan, X.P.; Chen, X.G.; Sun, C.Y.; Liu, G. Cutting Performance of Carbon Fiber Reinforced Plastics Using PCD Tool. *Adv. Mater. Res.* **2011**, *215*, 14–18. [CrossRef]
13. Nomura, M.; Kurashige, S.; Ito, Y.; Fukuhara, Y.; Sasahara, H. Development of Electrodeposited Wire Mesh Grinding Wheel for Cutoff and Grooving Carbon Fiber Reinforced Plastic. *Materials* **2023**, *16*, 5247. [CrossRef] [PubMed]
14. Xu, J.; Lin, T.; Davim, J.P. On the Machining Temperature and Hole Quality of CFRP Laminates When Using Diamond-Coated Special Drills. *J. Compos. Sci.* **2022**, *6*, 45. [CrossRef]
15. Liang, Y.; Chen, Y.; Chen, B.; Fan, B.; Yan, C.; Fu, Y. Feasibility of Ultrasonic Vibration Assisted Grinding for Carbon Fiber Reinforced Polymer with Monolayer Brazed Grinding Tools. *Int. J. Precis. Eng. Manuf.* **2019**, *20*, 1083–1094. [CrossRef]
16. Soo, S.L.; Shyha, I.S.; Barnett, T.; Aspinwall, D.K.; Sim, W.M. Grinding Performance and Workpiece Integrity When Superabrasive Edge Routing Carbon Fibre Reinforced Plastic (CFRP) Composites. *CIRP Ann. Manuf. Technol.* **2012**, *61*, 295–298. [CrossRef]

17. Wang, H.; Ning, F.; Hu, Y.; Fernando, P.K.S.C.; Pei, Z.J.; Cong, W. Surface Grinding of Carbon Fiber-Reinforced Plastic Composites Using Rotary Ultrasonic Machining: Effects of Tool Variables. *Adv. Mech. Eng.* **2016**, *8*, 1–14. [CrossRef]
18. Yu, T.; Cheng, J.; Gao, C.; Wu, J.; Guo, Z. Modeling and Experimental Study of Different Discontinuous Micro-Grinding Tools. *Int. J. Adv. Manuf. Technol.* **2020**, *107*, 4009–4032. [CrossRef]
19. Cao, S.; Zhang, X.; Wu, C.; Yang, M.; Xia, K. Towards Understanding the Material Removal Mechanism on the Effect of Ultrasonic Vibration and Anisotropy for Unidirectional CFRP by Scratching. *J. Mater. Process. Technol.* **2024**, *324*, 118250. [CrossRef]
20. Yao, L.; Liu, Z.; Song, Q.; Wang, B.; Cai, Y.; Zhao, J. Numerical Prediction of Surface Morphology and Roughness in Rotary Ultrasonic Face Grinding SiO2f/SiO2 Composite. *J. Mater. Res. Technol.* **2023**, *25*, 5917–5937. [CrossRef]
21. Zhang, Z.; Yuan, S.; Li, Q.; Gao, X.; Ouyang, X.; Luo, Y. Investigation on the Machined Surface Quality and Removal Mechanism of SiCf/SiC Composites in Ultrasonic-Assisted Grinding. *Int. J. Adv. Manuf. Technol.* **2022**, *123*, 4427–4445. [CrossRef]
22. Ji, W.; Wang, L. Industrial Robotic Machining: A Review. *Int. J. Adv. Manuf. Technol.* **2019**, *103*, 1239–1255. [CrossRef]
23. Makulavičius, M.; Petkevičius, S.; Rožėnė, J.; Dzedzickis, A.; Bučinskas, V. Industrial Robots in Mechanical Machining: Perspectives and Limitations. *Robotics* **2023**, *12*, 160. [CrossRef]
24. Cen, L.; Melkote, S.N. Effect of Robot Dynamics on the Machining Forces in Robotic Milling. *Procedia Manuf.* **2017**, *10*, 486–496. [CrossRef]

Journal of
Composites Science

MDPI

Article

Effect of Heat-Shrinkable Tape Application on the Mechanical Performance of CFRP Components Obtained by a Filament Winding Process

Iacopo Bianchi [1], Archimede Forcellese [1], Tommaso Mancia [2], Chiara Mignanelli [1], Michela Simoncini [1,*] and Tommaso Verdini [1]

[1] Department of Industrial Engineering and Mathematical Sciences, Università Politecnica delle Marche, Via Brecce Bianche 12, 60131 Ancona, Italy; i.bianchi@pm.univpm.it (I.B.); a.forcellese@staff.univpm.it (A.F.); c.mignanelli@pm.univpm.it (C.M.); t.verdini@pm.univpm.it (T.V.)
[2] Department of Theoretical and Applied Sciences, Università degli Studi eCampus, Via Isimbardi 10, 22060 Novedrate, Italy; tommaso.mancia@uniecampus.it
* Correspondence: m.simoncini@staff.univpm.it; Tel.: +39-071-2204443

Abstract: Carbon Fiber Reinforced Polymers (CFRPs) are widely used in aerospace, automotive, and other sectors for their high strength-to-weight ratio and adaptability. In order to reach high mechanical performance and quality for CFRP components in which a thermosetting resin is used, the curing process plays a key role, and the optimal conditions have to be identified. In this context, the present study aims to study the effect of heat-shrinkable tape application on the mechanical performance of CFRP tubular components obtained by a filament winding process. To this purpose, CFRP hoop-wound components were realized with a laboratorial filament winding machine. Half of them were directly cured in a muffle oven, while the other half were cured after the application of heat-shrinkable tape around the external surface of the component. To evaluate the effect of the heat-shrinkable tape use on the mechanical properties of the CFRP wound parts, ring specimens, obtained by the tubular components according to the ASTM D2290 standard, were subjected to ring tensile tests. The thickness uniformity and void content of the components were evaluated by means of X-ray computed tomography, whilst the fracture surfaces were observed using scanning electron microscopy. It was demonstrated that the heat-shrinkable tape application around the external surface of the CFRP tubular components allows for improved mechanical performance of the wound parts due to the enhanced material compaction, resulting in stronger and more cohesive structures characterized by a uniform thickness and reduced void content.

Keywords: filament winding; CFRP; heat-shrinkable tape application; ring tensile test; tomography; SEM

1. Introduction

Composite materials have been gaining increasing interest in the last years in many industrial sectors due to their high mechanical properties and low weights [1,2]. Among the various categories of composite materials, Carbon Fiber Reinforced Polymers (CFRPs) are the most widely used for automotive, aerospace, nautical, biomedical, and construction applications [3–5]. CFRPs allow us to realize high-performance components with a weight reduction with respect to traditional and conventional materials [6].

Over the years, many production processes have been developed to realize CFRP components, and the most used to produce axisymmetric components is the filament winding (FW) process. This technique allows us to realize composite tubular structures, which can be tailored in a wide range of properties; thus, they are suitable for several applications [7], especially in the aerospace sector and other critical sectors like pressure vessels, rocket engines, and aircraft structural components [8–11].

The FW process consists of the winding of the composite material around a rotating mandrel [12,13]. Depending on the kind of composite material used, the FW process can be classified in terms of wet-FW and dry-FW. The first one involves the use of dry continuous fibers, which enter a resin bath, by passing through a tension system, and then they are wounded around the mandrel [14]. The second one involves the use of preimpregnated fibers, which are directly wounded around the rotating mandrel, avoiding the passage in the resin bath, which is usually a critical step since it could lead to defects in the components [15].

The control of different axis speeds (e.g., mandrel and deposition head rotation, carriage, and cross-carriage translation) joined to a deposition head employed to lay down the prepregged or already impregnated fibers on the mandrel allows us to accurately define the material directions [10].

By winding the fibers with specific winding angles and following a precise path, high-performance and tailored structures can be realized. Indeed, the winding angle definition, which coincides with the fiber orientation direction, is crucial for the mechanical properties of the component since it is well known that composites' properties are greater along the direction of the fiber orientation. Thus, it is appropriate, during the design phase, to choose a winding angle that involves the fiber orientation along the load directions to obtain a high-performance composite component [16,17].

Commercially, different kinds of FW machines equipped with different configurations and numbers of numerically controlled axes can be found, which are suitable for producing complex-shaped structures. This technology avoids the labor-intensive and costly phases of traditional composite manufacturing methods by fully automating the lay-up process [18]. This also results in a reduction in the cost of composite products, making them more competitive in the market. The FW process requires a subsequent curing phase, which is crucial to consolidating the material. Most composite industries consider the autoclave curing process as the highest quality process for preimpregnated components [19,20]. Since the costs associated with the use of an autoclave are very high, several solutions can be considered to cure composites, such as oven curing, microwave curing, and the in situ process, as proved by the scientific literature [21–23].

The curing process plays a key role in the mechanical properties and the quality of a composite component; for this reason, it is important to identify which is the optimal solution to apply with respect to the applications. Therefore, in the scientific literature, there are several studies concerning this issue. As an example, Liang et al. [24] investigated the effect of the autoclave curing temperature on the mechanical properties of the composite material for the FW process, through tests performed on a pressure vessel. Betz et al. [25] studied the technical and economic aspects related to a microwave curing process for composite components obtained via FW. Moreover, Tabuchi et al. [26] investigated the influence of simultaneous heating for the curing process on the residual stress of the CFRP hoop-wound composite component. In addition, due to the high costs related to the autoclave curing process, the use of heat-shrinkable tape (HT) during oven curing processes gained a relevant interest; for this reason, some scientific literature studies concern the use of heat-shrinkable tapes during a consolidation process. Purnomo et al. [27] compared different finishing techniques, including the use of heat-shrinkable tape during the curing process of CFRP wound components, to investigate the surface quality of the obtained parts in terms of roughness, tensile stress, and stiffness. Heusinger et al. [28] investigated the effect of the number of shrink tape layers applied during an oven curing process, the shrink tape tension, and the holding time on the mechanical properties of a CFRP thermoplastic matrix tubular component.

Unfortunately, no studies concerning the effect of the heat-shrinkable tape application before the curing process on the mechanical properties and the surface quality in terms of thickness uniformity and of the CFRP thermosetting matrix wound component are available in the scientific literature.

In this context, this study aims to study the mechanical properties, the thickness uniformity, and the presence of voids of tubular hoop-wound CFRP components realized by means of the FW process. For this purpose, an X-WINDER machine was used to realize the CFRP hoop-wound components. Half of them were directly cured using a muffle furnace, while the other half of the wound parts were cured after the application of the heat-shrinkable tape around the external surface of the components. Then, cutting operations were performed to obtain ring specimens from the CFRP tubular parts obtained with and without HT. According to the D2290 ASTM standard, ring tensile tests were carried out at room temperature to evaluate the effect of the heat-shrinkable tape application on the mechanical properties of the CFRP hoop-wound components. Finally, X-ray computed tomography and scanning electron microscopy were used, respectively, to analyze the thickness uniformity and void content of the tubular components and the fracture surfaces of ring specimens obtained using the two different conditions.

The paper is organized as follows: after the Introduction, Section 2 defines the materials and methods used for this study, Section 3 shows the results and discussion; then, the Conclusions are drawn.

2. Materials and Methods

2.1. Materials

The composite tubular components were produced by means of a filament winding process using a towpreg consisting of carbon fibers (CF) as reinforcements and an epoxy resin matrix. The towpreg, composed of 30K CF filaments with a diameter of 7 μm, is characterized by a total width and thickness equal to 8 mm and 0.2 mm, respectively. The epoxy resin used in the present research (Huntsman International LLC) is characterized by a gel temperature (T_{gel}) equal to 90 °C and a glass transition temperature (T_g) of 120 °C.

The mechanical properties of the composite were calculated from the constituent data sheets using a mixture rule [29]. Table 1 reports the mechanical properties of the constituent materials and composite materials.

Table 1. Mechanical properties of CF, epoxy resin from data sheet, and CFRP calculated by using the mixture rule.

	Carbon Fiber	Epoxy Resin	Composite Material
Elastic modulus (E)	230 GPa	3.5 GPa	75 GPa
Ultimate Tensile Strength (UTS)	4900 MPa	73 MPa	750 MPa
Density (ρ)	1.8 g/cm^3	1.1 g/cm^3	1.5 g/cm^3

2.2. Filament Winding and Curing Processes

The X-winder (Arroyo Seco, NM, USA) laboratorial filament winding machine (Figure 1) was used to produce the CFRP tubular components. The machine has 4 controlled axes: the *X*-axis allows the movement of the cross carriage toward the rotating mandrel, the *Z*-axis allows the movement of the carriage along the longitudinal section of the mandrel, the W-axis allows the rotation of the mandrel around the *Z*-axis, and the U-axis allows the rotation of the deposition head around the *X*-axis. The controlled axes make it possible to wind the rotating mandrel. In particular, the X-axis is used to cover the domes of a vessel, the Z- and U-axes are used to cover the cylindrical section, and the W-axis is used to rotate the mandrel. The total movement and angle of fiber deposition is given by the combination of the translational movement of the deposition head and the rotational movement of the mandrel around its axis.

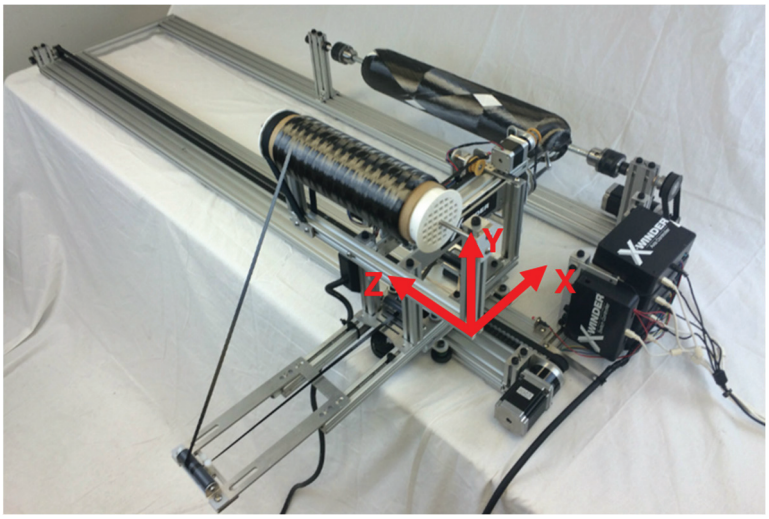

Figure 1. X-Winder filament winding machine.

In this study, the composite tubular components were obtained by winding three layers with a theoretical winding angle of 88° and carriage and mandrel maximum speeds of 101.60 mm/s and 3.14 rad/s, respectively.

The composite wound parts were then cured in a FALC muffle furnace 8.2 Lt—FM 8.2 (Treviglio, Bergamo, Italy), which allows for a maximum temperature of 1200 °C. According to the resin manufacturer, the curing process requires heating the chamber to 120 °C for 2 h. After curing, a post-cure is required to ensure all the resin is cured, at 150 °C for 2 h, followed by air cooling. Figure 2 shows the curing and post-cure cycle.

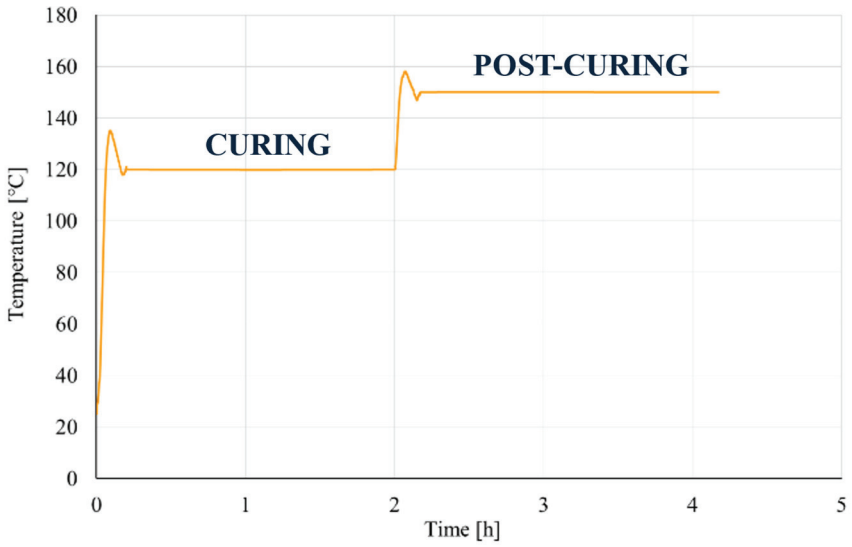

Figure 2. Composite part curing and post-curing cycle.

In order to investigate different curing conditions, half of the CFRP wound components were directly cured in the muffle furnace, while the other half of the wound parts were cured after the application of a heat-shrinkable tape (DIATEX SAS, Saint-Genis-Laval, France) around the external surface of the component. The heat-shrinkable tape is a tape that exerts a compressive force on the CFRP's underlying structure when heat is applied during the curing process. Furthermore, the tape is entirely adhesive free, so once the curing process is completed, the tape can be easily removed with no residue left behind.

Figure 3 shows the wound tubular components after curing, obtained with and without the application of the tape before the curing process.

Figure 3. CFRP wound tubular components obtained: (**a**) without and (**b**) with heat-shrinkable tape application before curing process.

2.3. X-Ray Computed Tomography and Scanning Electron Microscopy

An important issue of the FW process is related to the thickness uniformity both along the tubular component section and width and the presence of voids due to the winding strategy or process defects. For these reasons, in the present work, an X-ray computed tomography (X-CT) scan was performed using a Zeiss METROTOM 1500 CT (Zeiss, Oberkochen, Germany) system equipped with an X-ray tube with a minimum focal spot of 7 µm, a maximum accelerating voltage of 199 kV, and a maximum current leakage of 1000 µA. The source–detector distance was maintained at 1500 mm, with a maximum measuring range of 350 mm × 300 mm and a detector resolution of 2048 × 2048 pixels.

The different slices of the specimens for the investigated conditions, obtained by means of a scanning process performed with X-CT, were analyzed using National Instrument (NI) Vision Suite 2023 software. For each slice, eight benchmarks were considered along the circular section to analyze the thickness uniformity along the transversal direction, both for the specimens cured with and without the HT (Figure 4). In addition, the thickness uniformity along the longitudinal direction of the specimens was evaluated by analyzing two different slices for each specimen, obtained both with and without heat-shrinkable tape, at about a distance of 10 mm.

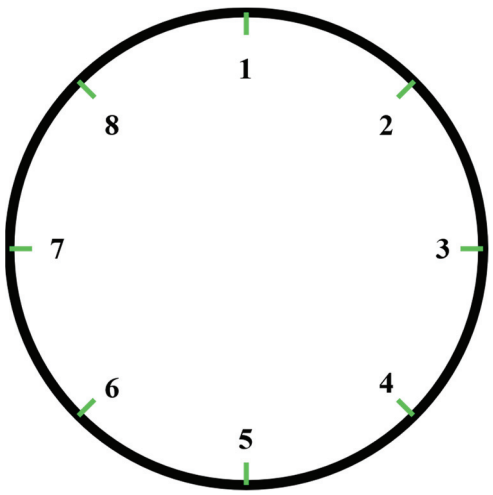

Figure 4. The eight benchmarks considered for the evaluation of specimen thickness distribution.

In addition, to achieve high-resolution imaging of the fractured surfaces of the ring specimens after tensile tests, the TESCAN VEGA 3 (TESCAN, Brno, Czech Republic) was used for a scanning electron microscopy (SEM) investigation. Before SEM analysis, the fracture surface of the samples was nanocoated with gold to have better electrical transmission during observation.

2.4. Tensile Test of Ring Specimens

The mechanical properties of the CFRP filament wound components, obtained with or without the application of an HT before the curing process, were analyzed by means of ring tensile tests performed according to ASTM D2290 [30] using a servo-hydraulic testing machine (MTS 810®, MTS Systems Corporation, Eden Prairie, MN, USA) equipped with a 250 kN load cell (Figure 5). During tests, the crosshead speed was kept constant at 0.1 mm/s. The experimental results were plotted as applied load versus displacement curves from which the hoop tensile strength (HTS) was evaluated.

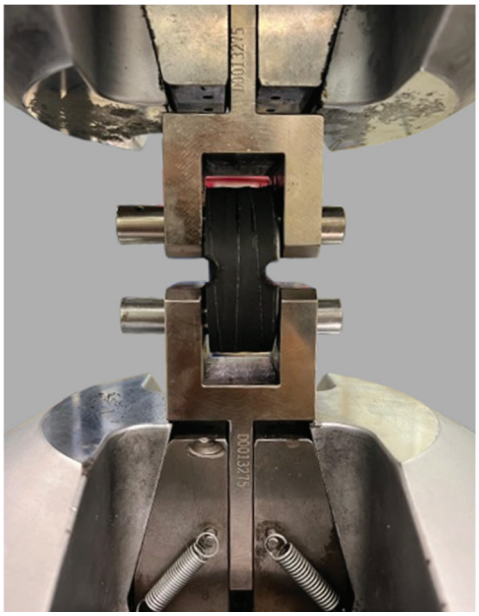

Figure 5. Tensile test of ring specimens.

In accordance with the ASTM D2290 [30] standard, Procedure A was considered to test the specimens as it is suitable for a thermoset composite ring. The rings were obtained from the composite tubular components by means of drilling and cutting operations. Five specimens, obtained both using and not using the HT, were realized and tested to obtain a reliable average test value. Specimen dimensions are reported in Figure 6.

The split disc test from ASTM D2290 [30] is used to evaluate the circumferential properties of filament wound products. Several factors have a significant effect on the results of the test. The hoop tensile strength calculation does not take into account the bending component during the test, resulting in a reduction in HTS of up to 25% [31]. Friction between the specimen and fixture disc can affect the stress/strain distribution along the circumference of the disc; in particular, the effect increases with increasing friction values [32–37].

From the results of the tensile tests, it is possible to calculate the HTS according to the standard and assuming a uniform tensile stress in the ring cross-section by using Equation (1):

$$\sigma_{HTS} = \frac{P}{2 \cdot A_{min}} \quad (1)$$

in which P [kN] is the maximum load during the tensile test and A_{min} [mm^2] is the minimum area between the two reduced sections.

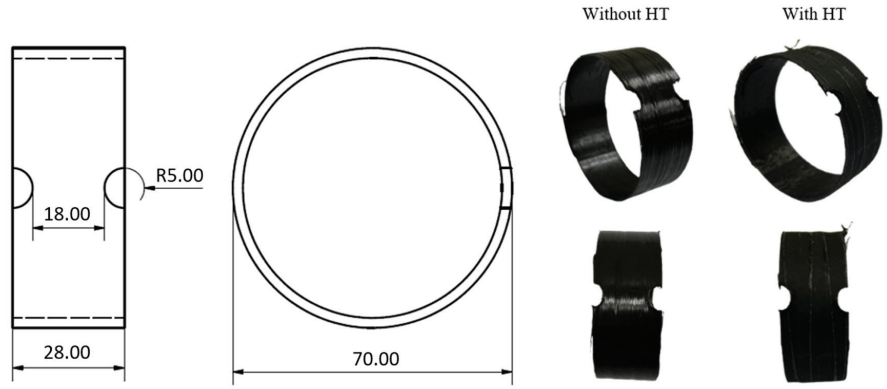

Figure 6. Ring specimen dimensions according to ASTM D2290 standard.

Since the weight can vary depending on the application or not of the heat-shrinkable tape, the specific strength and specific modulus were calculated by dividing the HTS by the weight of the specimens.

3. Results and Discussion

In order to evaluate the effect of the heat-shrinkable tape application on the mechanical properties of the CFRP wound parts, ring specimens, obtained from the tubular components by machining operations, were subjected to ring tensile tests. Figure 7 shows the tomography of typical rings obtained both using and not using the HT before the curing process. Specifically, two different slices (i.e., slice 100 and slice 200) of two typical ring specimens can be observed.

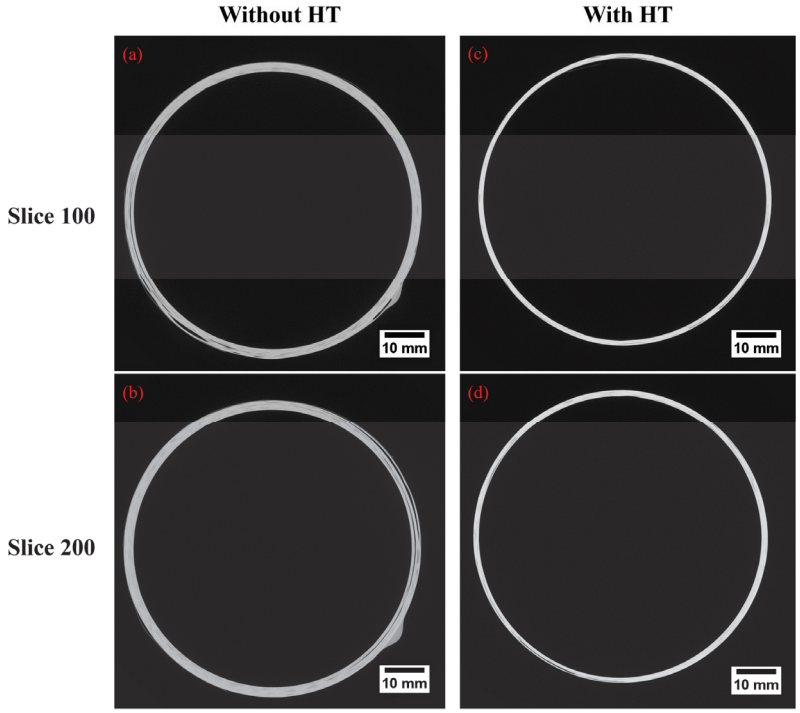

Figure 7. X-ray computed tomography images of typical ring specimens obtained from cured wound components: (**a**) without HT—slice 100, (**b**) without HT—slice 200, (**c**) with HT—slice 100, and (**d**) with HT—slice 200.

By comparing the ring specimens obtained with and without the application of the heat-shrinkable tape, a high quantity of voids can be clearly observed in the specimen obtained without HT (Figure 7a,b) as compared to that obtained using the heat-shrinkable tape (Figure 7c,d), irrespective of the X-CT slice taken into account. Such a result can be attributed to the capability of the heat-shrinkable tape to guarantee a high level of compaction of the underlying layers when it is heated. Furthermore, the application of the HT allows a good distribution of the epoxy resin on the component. As a matter of fact, the ring specimen obtained without the application of HT (Figure 7a,b) is characterized by the presence of superficial resin drops. Such a drawback occurs when the epoxy resin reaches the low viscosity point, moves along the circular section, and accumulates below the wound tubular component in the form of drops, due to gravity.

In addition to the improved compaction of the wrapped material by FW and the void reduction, the presence of the heat-shrinkable tape allows for benefits in terms of uniformity of the thickness of the wound components. As a matter of fact, Figure 7 also shows that the thickness of the ring specimen cured with the HT (Figure 7c,d) is lower than the one related to the specimen cured without HT (Figure 7a,b).

According to the experimental procedure described in Section 2.4, the thicknesses of the ring specimens, obtained using and not using HT, were measured by considering the eight benchmarks along the circular section at two different X-CT slices along the width. To this purpose, the two ring specimens, obtained with and without HT, respectively, were analyzed at the same X-CT slice using NI Vision software (Figure 8).

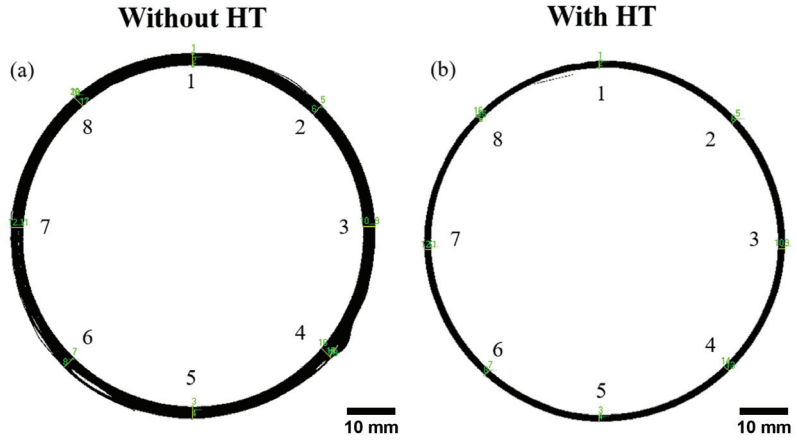

Figure 8. Comparison between the two ring specimens, analyzed at the same X-CT slice using NI Vision software, obtained: (**a**) without HT and (**b**) with HT (X-CT slice n. 100).

For a given X-CT slice, the specimens cured with the HT application are characterized by lower thickness values in all the benchmark points as compared to those cured without HT, denoting an effective compaction of CFRP layers due to the presence of the heat-shrinkable tape (Figure 9). Specifically, the reduction in mean specimen thickness is about 45% (in particular, 49% as Slice 100 is considered and about 42% in Slice 200). To this purpose, Table 2 summarizes the mean thickness values measured in the eight benchmark points of the ring specimens obtained with and without the HT application before the curing process. The mean thickness was calculated both along the circular section and the width of the ring specimens. The standard deviation of the thickness values with respect to the mean values was evaluated as well. Specifically, the standard deviation along the circular section of the ring specimens without HT is higher than that obtained from specimens with HT.

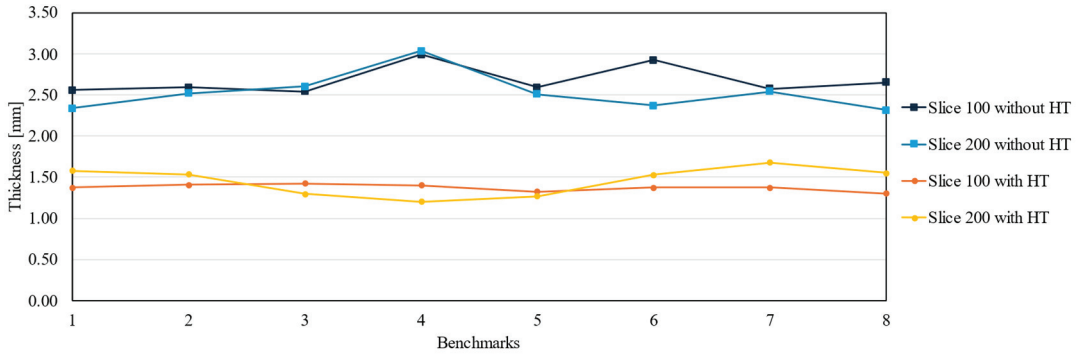

Figure 9. Thickness distribution, evaluated at two different X-CT slices, in ring specimens obtained with and without heat-shrinkable tape.

Table 2. Thickness values measured in the eight benchmark points of the ring specimens obtained with and without the HT application, mean thickness, and standard deviation values.

Benchmarks	Thickness [mm]			
	Slice 100		Slice 200	
	Without HT	With HT	Without HT	With HT
1	2.56	1.37	2.34	1.58
2	2.59	1.41	2.52	1.54
3	2.54	1.42	2.60	1.30
4	2.99	1.40	3.04	1.21
5	2.59	1.32	2.51	1.27
6	2.92	1.38	2.37	1.53
7	2.58	1.38	2.54	1.68
8	2.65	1.30	2.32	1.55
Mean (section)	2.68	1.37	2.53	1.46
Standard Deviation (section)	0.18	0.04	0.23	0.17
	Without HT		With HT	
Mean (width)	2.60		1.41	
Standard Deviation (width)	0.18		0.08	

As far as the thickness along the width is concerned, by comparing the thickness values measured at the two different slices of the same ring specimen, Figure 9 also shows that the ring specimens' thickness along the width of the components is significantly variable for specimens cured without HT, whilst a more uniform thickness distribution can be observed in ring specimens obtained using the HT. In particular, the mean thickness value of the specimen cured without HT is higher than the one of the specimens cured with HT by about 84%, with a standard deviation along the width higher for the specimen cured without HT than the one cured with HT. Such results demonstrate that the heat-shrinkable tape application before the curing process leads to a reduction in the mean thickness values and to an improvement in the thickness distribution both along the circular section and the width.

In order to evaluate the effect of heat-shrinkable tape application on the mechanical properties of the CFRP tubular components obtained by means of FW, ring tensile tests were performed at room temperature. According to ASTM standard D2290, the hoop tensile stress was evaluated as a function of the crosshead displacement, both for specimens with and without HT. The hoop tensile strength (σ_{HTS}) was obtained as the maximum value of the hoop tensile stress behavior. Table 3 summarizes the σ_{HTS} and the maximum load values obtained by the ring tensile tests. Moreover, in order to investigate the specific hoop tensile strength and the specific load, the ratio between the hoop tensile strength and weight and the one between the load and the weight, reported in Table 3, were considered.

Table 3. Typical values obtained by the tensile tests.

	Without Heat-Shrinkable Tape	With Heat-Shrinkable Tape
σ_{HTS} [MPa]	646.26	1473.28
Weight [g]	18.34	12.11
Specific σ_{HTS} [MPa/g]	35.24	121.66
Load [kN]	48.86	71.60
Specific load [kN/g]	2.66	5.91

The effect of the heat-shrinkable tape application on the typical specific load versus crosshead displacement curves and specific hoop tensile stress versus crosshead displacement curves is shown in Figure 10.

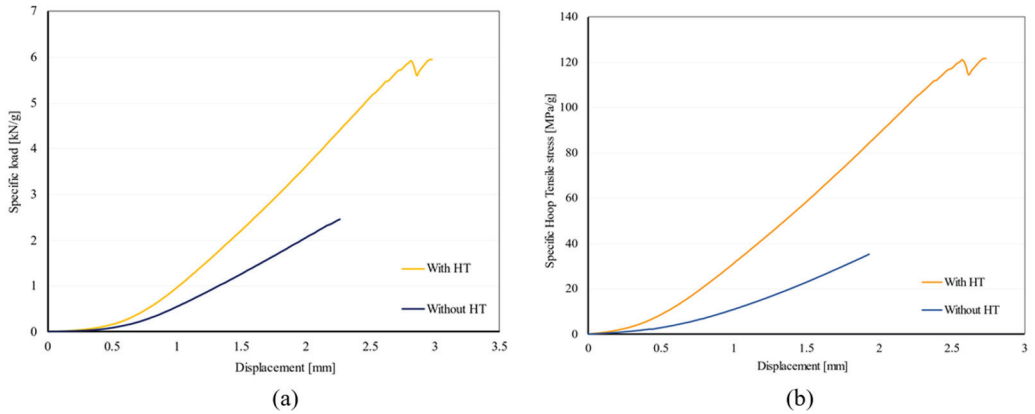

Figure 10. (**a**) Typical specific load versus crosshead displacement curves and (**b**) specific hoop tensile stress versus crosshead displacement curves obtained by testing the ring specimens obtained with and without HT.

Irrespective of the heat-shrinkable tape application, the specific load (Figure 10a) and, consequently, the specific hoop tensile stress (Figure 10b) increase with displacement until reaching a peak value at which the ring specimen fracture occurs. As far as the ring specimen with HT is considered, it can be observed that the specific load and the specific hoop tensile stress level reached by the specimen with HT are always higher than those of the specimens obtained without HT, denoting that the application of a heat-shrinkable tape before the curing process involves an improvement in the mechanical properties of the wound component. Specifically, it can be observed that the ring specimens with the heat-shrinkable tape achieved a specific load increase of about 55% with respect to the specimens without the application of the tape. As far as the specific hoop tensile stress is concerned, ring specimens obtained with HT achieve a specific HTS of about 121.66 MPa/g, which is about a 71% increase with respect to the 35.24 MPa/g obtained by specimens cured without the HT application. Furthermore, according to the scientific literature [7,38], a significant improvement in elongation can be observed in ring specimens with HT. To justify the results obtained by ring tensile tests in terms of the mechanical properties of tubular components, a scanning electron microscopy investigation was carried out to observe the fracture surfaces of ring specimens obtained with and without HT. Figure 11 shows a typical ring specimen obtained using the HT, fractured at the holes that represent stress concentration zones [39].

Figure 11. Typical ring specimen, obtained using the HT, fractured after tensile test.

Figure 12 shows SEM images of the fracture surfaces of ring specimens obtained both without (Figure 12a–c) and with (Figure 12d–f) heat-shrinkable tape at different magnifications. Irrespective of the application of heat-shrinkable tape on the external surface of tubular components before the curing process is concerned, it can be observed that the CFRP specimens are characterized by a brittle fracture. During ring tensile tests, failure begins with transverse microcracks. As the stress level further increases, in particular, corresponding to the holes in the specimens, the number of transverse microcracks increases until saturation is reached. Delamination, fiber failure, and longitudinal cracking can follow transverse crack formation. In the present study, after transverse microcracking, a marked delamination between CFRP layers appears in the ring specimens. The delamination can occur on several adjacent layers, and therefore, the debonding surface can appear as a flat stepped surface (Figure 12a,d).

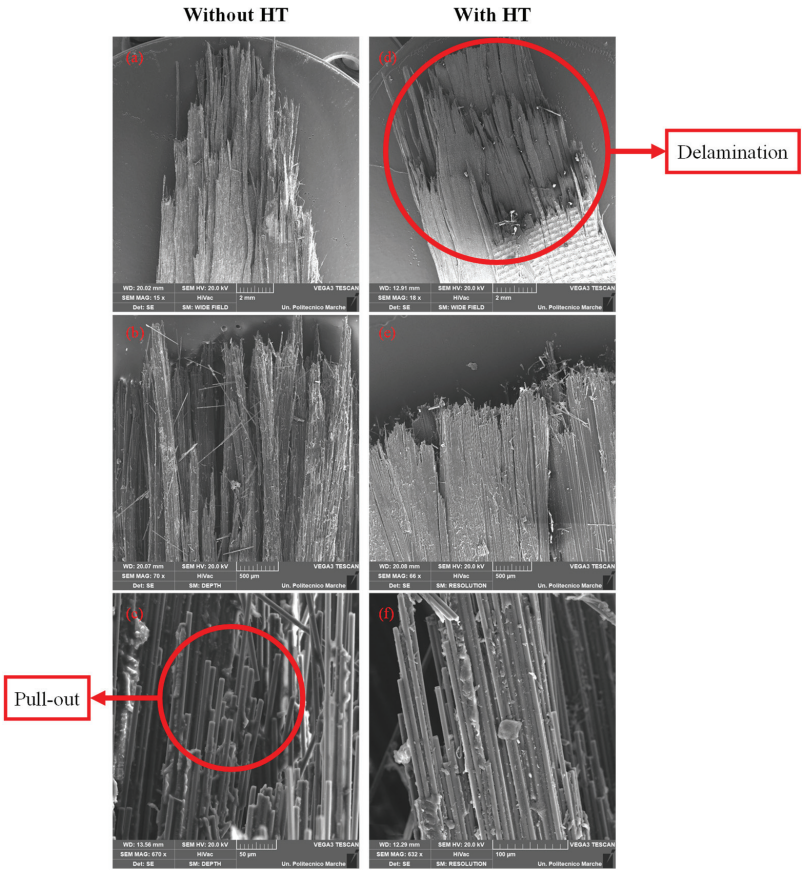

Figure 12. SEM images of the fracture surfaces of ring specimens obtained: (**a**–**c**) without HT and (**d**–**f**) with HT at different magnifications.

As far as the effect of heat-shrinkable tape application is concerned, it can be noted that the ring specimen obtained without HT (Figure 12a) is characterized by more unbound, less compacted, and more frayed fibers than those in the ring specimen obtained using the HT (Figure 12d). Such results can be attributed to the effective compaction of CFRP layers due to the heat-shrinkable tape application, shown in the X-CT images of Figure 7 and in the thickness distribution of Figure 9.

Furthermore, Figure 12d shows that the external surface layer of the ring, on which the tape has been wrapped, is characterized by a typical texture due to the compressive force exerted by the HT on the component during the curing process. Finally, the surface finish of the component will be characterized by a high roughness, which is suitable for any subsequent surface processing.

At a higher magnification (Figure 12b,e), the comparison between the fracture surfaces of the specimens highlights that, in the sample obtained by applying the heat-shrinkable tape, the fibers maintain their position in an orderly manner, as they are more bound to the matrix. This result is due to the presence of the HT, which during the curing process, contracts, ensuring a high level of compaction and greater adhesion at the fiber–matrix interface. This provides a greater capacity for the fibers to remain bound to the matrix during fracture. Figure 12c shows the presence of many dry fibers and very poor epoxy resin quantity; the amount of resin in the ring specimen obtained without the HT application is much lower than the one that can be observed in Figure 12f. This proves that a pull-out of fibers occurs during the fracture of the specimen obtained without HT. On the contrary, Figure 12f shows that many fibers are still bonded due to the matrix presence. Finally, Figure 13 shows a typical matrix cracking that occurs due to its relatively low strength in the loading direction.

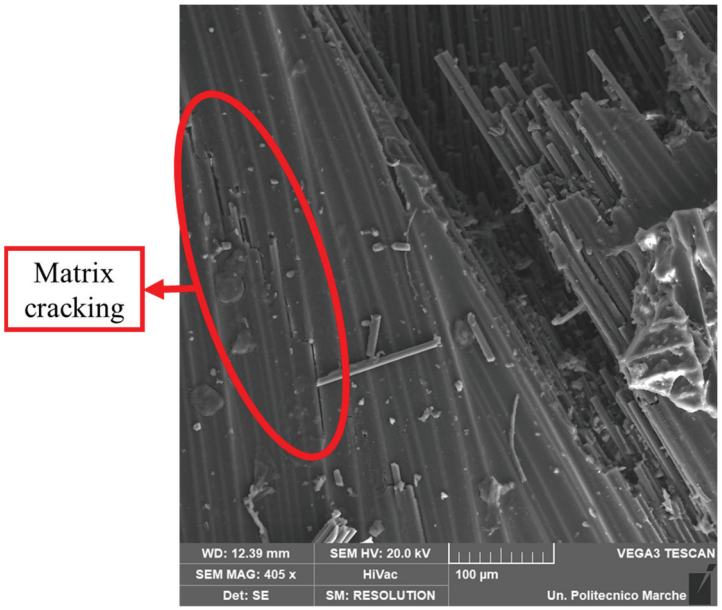

Figure 13. SEM image of the fracture surfaces of a ring specimen obtained with HT in which the matrix cracking can be observed.

In conclusion, it can be stated that the application of heat-shrinkable tape before the polymerization process of a CFRP-wrapped component improves the compaction of the material and the adhesion at the fiber–matrix interface, reduces the void content, and optimizes the thickness distribution of the tubular component. These benefits result in a significant improvement in the mechanical properties of the CFRP tubular component under tensile stress.

4. Conclusions

The present investigation aimed at studying the effect of heat-shrinkable tape application on the mechanical properties, thickness distribution, and void presence of CFRP hoop-wound components realized with a laboratorial filament winding machine. Half of the components were directly cured in a muffle oven, while the other half were cured after the application of heat-shrinkable tape around the external surface of the part. Ring tensile tests were then performed at room temperature on ring specimens manufactured by the tubular components according to the ASTM D2290 standard. The thickness distribution and void content of the components were evaluated using X-ray computed tomography, whilst the fracture surfaces were observed using scanning electron microscopy.

The main results can be summarized as follows:

- The X-CT shows that the heat-shrinkable tape application on the external surface of the CFRP tubular component involves a significant thickness reduction of about 45%. Furthermore, the HT application resulted in improved thickness distribution both along the circular cross-section of the component and across the width of the specimens, compared to the tubular component cured without HT.
- X-ray tomography shows a significant decrease in void content in the ring specimens cured with the presence of heat-shrinkable tape, indicating an improved resin distribution and reduction in defects. This contributes to improving the structural integrity of the CFRP components.
- Tensile tests show that the specific hoop tensile stress increases with displacement until reaching a peak value at which the ring specimen fracture occurs.
- Ring specimens obtained with heat-shrinkable tape exhibit a specific load of about 55% higher than the samples without the application of the tape. Furthermore, they achieve a specific hoop tensile strength of about 121.66 MPa/g, which is about 71% increased with respect to the 35.24 MPa/g obtained by specimens cured without the HT application. These results show the effectiveness of the heat-shrinkable tape in improving material compaction.
- The SEM observation shows that specimens with HT application exhibit more orderly fracture surfaces and stronger fiber–matrix bonding, whereas those obtained without HT show frayed fiber surfaces and significant fiber pull-out.
- The application of heat-shrinkable tape before the curing process improves the compaction of the material and the adhesion at the fiber–matrix interface, resulting in a significant improvement in the mechanical properties of the CFRP tubular component under tensile stress.

Future works will concern the variation in the types of tape and other parameters during the curing process and the number of layers of the winding to further optimize the mechanical performance of CFRP components. In addition, the potential of other curing tools, such as microwave-assisted tools or an autoclave, could be evaluated to provide insights into achieving higher quality and efficiency in CFRP manufacturing for high-performance applications.

Author Contributions: Conceptualization, A.F. and M.S.; methodology, I.B., C.M., T.M. and T.V.; software, I.B., C.M., T.M. and T.V.; validation, I.B., C.M., T.M. and T.V.; formal analysis, I.B., C.M., T.M., M.S. and T.V.; investigation, I.B., C.M., T.M. and T.V.; resources, A.F. and M.S.; data curation, I.B., C.M., T.M. and T.V.; writing—original draft preparation, I.B., C.M., T.M. and T.V.; writing—review and editing, A.F. and M.S.; visualization, I.B., C.M., T.M. and T.V.; supervision, A.F. and M.S.; project administration, A.F. and M.S. All authors have read and agreed to the published version of the manuscript.

Funding: This research received no external funding.

Data Availability Statement: The original contributions presented in the study are included in the article, further inquiries can be directed to the corresponding author.

Conflicts of Interest: The authors declare no conflicts of interest.

References

1. Holmes, M. Carbon composites continue to find new markets. *Reinf. Plast.* **2017**, *61*, 36–40. [CrossRef]
2. Cepero-Mejías, F.; Phadnis, V.A.; Kerrigan, K.; Curiel-Sosa, J.L. A finite element assessment of chip formation mechanisms in the machining of CFRP laminates with different fibre orientations. *Compos. Struct.* **2021**, *268*, 113966. [CrossRef]
3. Rubino, F.; Nisticò, A.; Tucci, F.; Carlone, P. Marine Science and Engineering Marine Application of Fiber Reinforced Composites: A Review. *J. Mar. Sci. Eng.* **2020**, *8*, 26. [CrossRef]
4. Singh, P.; Raghavender, V.; Joshi, S.; Vasant, N.P.; Awasthi, A.; Nagpal, A.; Jasim Abd al-saheb, A. Composite material: A review over current development and automotive application. *Mater. Today Proc.* **2023**, *in press*. [CrossRef]
5. Henning, F.; Kärger, L.; Dörr, D.; Schirmaier, F.J.; Seuffert, J.; Bernath, A. Fast processing and continuous simulation of automotive structural composite components. *Compos. Sci. Technol.* **2019**, *171*, 261–279. [CrossRef]
6. Kelly, J.C.; Sullivan, J.L.; Burnham, A.; Elgowainy, A. Impacts of Vehicle Weight Reduction via Material Substitution on Life-Cycle Greenhouse Gas Emissions. *Environ. Sci. Technol.* **2015**, *49*, 12535–12542. [CrossRef]
7. Eggers, F.; Almeida, J.H.S.; Azevedo, C.B.; Amico, S.C. Mechanical response of filament wound composite rings under tension and compression. *Polym. Test.* **2019**, *78*, 105951. [CrossRef]
8. Krikanov, A.A. Composite pressure vessels with higher stiffness. *Compos. Struct.* **2000**, *48*, 119–127. [CrossRef]
9. Iacopo, B.; Chiara, M.; Michela, S.; Tommaso, V. Life cycle analyses of a composite towbar realized via filament winding and comparison with traditional metallic alternatives. *Sustain. Mater. Technol.* **2024**, *40*, e00980. [CrossRef]
10. Bianchi, I.; Forcellese, A.; Galliani, F.; Greco, L.; Mignanelli, C.; Trevisan, G. Process and structural simulation for the development of a pressure vessel through filament winding technology. *Mater. Res. Proc.* **2023**, *28*, 347–556. [CrossRef]
11. Mignanelli, C.; Bianchi, I.; Forcellese, A.; Simoncini, M. Life cycle assessment of pressure vessels realized with thermoplastic and thermosetting matrix composites. *Int. J. Adv. Manuf. Technol.* **2024**, *135*, 4491–4509. [CrossRef]
12. Mateen, M.A.; Shankar, D.V.R.; Hussain, M.M. Design and development of low cost two axis filament winding machine. *J. Adv. Manuf. Technol.* **2018**, *12*, 117–126.
13. Ma, Q.; Rejab, M.R.M.; Idris, M.S. Dataset of the lab-scale 3-axis winding machine integrated with the portable real-time winding angle measurement system. *Data Brief* **2022**, *45*, 108731. [CrossRef]
14. Carosella, S.; Hügle, S.; Helber, F.; Middendorf, P. A short review on recent advances in automated fiber placement and filament winding technologies. *Compos. B Eng.* **2024**, *287*, 111843. [CrossRef]
15. Alimirzaei, S.; Najafabadi, M.A.; Nikbakht, A. Investigation of Mechanical Properties and Failure Behavior of CFRP Filament-Wound Composites Using an Acoustic Emission-Based Methodology and Numerical Simulation. *Fibers Polym.* **2023**, *24*, 693–707. [CrossRef]
16. Annadorai, M.E.; Ramakrishna, M.; Jyothi, Y. Effect on mechanical properties of CFRP composites in different fiber orientations. *Interactions* **2024**, *245*, 1–11. [CrossRef]
17. Pathak, A.K.; Garg, H.; Subhedar, K.M.; Dhakate, S.R. Significance of Carbon Fiber Orientation on Thermomechanical Properties of Carbon Fiber Reinforced Epoxy Composite. *Fibers Polym.* **2021**, *22*, 1923–1933. [CrossRef]
18. Vita, A.; Castorani, V.; Germani, M.; Marconi, M. Comparative life cycle assessment and cost analysis of autoclave and pressure bag molding for producing CFRP components. *Int. J. Adv. Manuf. Technol.* **2019**, *105*, 1967–1982. [CrossRef]
19. Taser, M.K.H.H. Experimental investigation of the effect of fabric wrapping method and autoclave curing on the mechanical and thermal degradation of carbon nanotube doped and undoped carbon composite pipes. *Polym. Compos.* **2024**, *45*, 12885–12898. [CrossRef]
20. Stadler, H.; Kiss, P.; Stadlbauer, W.; Plank, B.; Burgstaller, C. Influence of consolidating process on the properties of composites from thermosetting carbon fiber reinforced tapes. *Polym. Compos.* **2022**, *43*, 4268–4279. [CrossRef]
21. Bao, H.; Marguerès, P.; Olivier, P. An innovative and low-cost system for in situ and real-time cure monitoring using electrical impedancemetry for thermoset and CFRP laminate. *Meas. Sci. Technol.* **2023**, *35*, 035603. [CrossRef]
22. Rao, S.; Revgade, S.V.; Manjunath, N.M.; Prakash, M.R. Microwave Assisted Curing of CFRP Composite Laminates for Aerospace Applications. In Proceedings of the 17th ISAMPE National Conference on Composites; Springer: Berlin/Heidelberg, Germany, 2024; Volume 39, pp. 131–138. [CrossRef]
23. Collinson, M.G.; Swait, T.J.; Bower, M.P.; Nuhiji, B.; Hayes, S.A. Development and implementation of direct electric cure of plain weave CFRP composites for aerospace. *Compos. Part A Appl. Sci. Manuf.* **2023**, *172*, 107615. [CrossRef]
24. Liang, J.; Liu, L.; Qin, Z.; Zhao, X.; Li, Z.; Emmanuel, U.; Feng, J. Experimental Study of Curing Temperature Effect on Mechanical Performance of Carbon. Fiber Composites with Application to Filament Winding Pressure Vessel Design. *Polymers* **2023**, *15*, 982. [CrossRef]
25. Betz, S.; Köster, F.; Ramopoulos, V. Energy and Time Efficient Microwave Curing for CFRP Parts Manufactured by Filament Winding. *Mater. Sci. Forum* **2015**, *825–826*, 741–748. [CrossRef]
26. Tabuchi, D.; Sajima, T.; Doi, T.; Onikura, H.; Ohnishi, O.; Kurokawa, S.; Miura, T. Residual Stress of Hoop-Wound CFRP Composites Manufactured with Simultaneous Heating. *Sens. Mater.* **2012**, *24*, 99–111.
27. Purnomo, H.; Soemardi, T.P.; Budiono, H.D.S.; Wibowo, H.B.; Ibadi, M. The Filament Winding Method's Finishing Process Impact on Highfidelity Specimens: Homogenity of Density, Fiber Volume Fraction, Outer Surface Roughness and Tensile Strength. *East. Eur. J. Enterp. Technol.* **2023**, *6*, 43–51. [CrossRef]

28. Von Heusinger, J.; Grohmann, Y.; Khan, S. Methods for the Post-Consolidation of High-Speed-Wound Thermoplastic CFRP Tubes. Available online: https://www.dlr.de/sy (accessed on 1 December 2024).
29. Jacquet, E.; Trivaudey, F.; Varchon, D. Calculation of the transverse modulus of a unidirectional composite material and of the modulus of an aggregate. Application of the rule of mixtures. *Compos. Sci. Technol.* **2000**, *60*, 345–350. [CrossRef]
30. *ASTM D2290-19a*; Test Method for Apparent Hoop Tensile Strength of Plastic or Reinforced Plastic Pipe. ASTM International: West Conshohocken, PA, USA, 2019. [CrossRef]
31. Lee, S.; Kim, S.H.; Kim, S.; Choi, J.; Choi, H.J. Hoop tensile strength of tubular carbon fiber reinforced silicon carbide matrix composites. *Ceram. Int.* **2018**, *44*, 17087–17093. [CrossRef]
32. Yoon, S.H.; Cho, W.M.; Kim, C.G. Measurement of modulus in filament wound ring specimen using split disk test. *Exp. Tech.* **1997**, *21*, 25–28. [CrossRef]
33. Perillo, G.; Vacher, R.; Grytten, F.; Sørbø, S.; Delhaye, V. Material characterisation and failure envelope evaluation of filament wound GFRP and CFRP composite tubes. *Polym. Test.* **2014**, *40*, 54–62. [CrossRef]
34. Chen, J.F.; Li, S.Q.; Bisby, L.A.; Ai, J. FRP rupture strains in the split-disk test. *Compos. B Eng.* **2011**, *42*, 962–972. [CrossRef]
35. Al Ali, I.B.K.F. A procedure to determine the tangential true stress-strain behavior of pipes. *Int. J. Press. Vessel. Pip.* **2015**, *128*, 59–68. [CrossRef]
36. Zhao, Y.; Druzhinin, P.; Ivens, J.; Vandepitte, D.; Lomov, S.V. Split-disk test with 3D Digital Image Correlation strain measurement for filament wound composites. *Compos. Struct.* **2021**, *263*, 113686. [CrossRef]
37. Khalfallah, A.; Ktari, Z.; Leitão, C.; Fernandes, J.V. New Mandrel Design for Ring Hoop Tensile Testing. *Exp. Tech.* **2021**, *45*, 769–787. [CrossRef]
38. Kaynak, C.; Erdiller, E.S.; Parnas, L.; Senel, F. Use of split-disk tests for the process parameters of filament wound epoxy composite tubes. *Polym. Test.* **2005**, *24*, 648–655. [CrossRef]
39. Abbasi, R.R.F. Numerical and Experimental Analyses of the Hoop Tensile Strength of Filament-Wound Composite Tubes. *Mech. Compos. Mater.* **2020**, *56*, 423–436. [CrossRef]

Journal of
Composites Science

MDPI

Article

Laser-Induced Decomposition and Mechanical Degradation of Carbon Fiber-Reinforced Polymer Subjected to a High-Energy Laser with Continuous Wave Power up to 120 kW

Sebastian Schäffer [1,*], Stefan Reich [1], Dominic Heunoske [1], Martin Lueck [1], Johannes Wolfrum [2] and Jens Osterholz [1]

[1] Fraunhofer Institute for High-Speed Dynamics EMI, Ernst-Zermelo. 4, 79104 Freiburg, Germany; stefan.reich@emi.fraunhofer.de (S.R.); dominic.heunoske@emi.fraunhofer.de (D.H.); martin.lueck@emi.fraunhofer.de (M.L.); jens.osterholz@emi.fraunhofer.de (J.O.)
[2] Bundeswehr Research Institute for Materials, Fuels and Lubricants, Institutsweg 1, 85435 Erding, Germany; johanneswolfrum@bundeswehr.org
* Correspondence: sebastian.schaeffer@emi.fraunhofer.de

Abstract: Carbon fiber-reinforced polymer (CFRP), noted for its outstanding properties including high specific strength and superior fatigue resistance, is increasingly employed in aerospace and other demanding applications. This study investigates the interactions between CFRP composites and high-energy lasers (HEL), with continuous wave laser powers reaching up to 120 kW. A novel automated sample exchange system, operated by a robotic arm, minimizes human exposure while enabling a sequence of targeted laser tests. High-speed imaging captures the rapid expansion of a plume consisting of hot gases and dust particles during the experiment. The research significantly advances empirical models by systematically examining the relationship between laser power, perforation times, and ablation rates. It demonstrates scalable predictions for the effects of high-energy laser radiation. A detailed examination of the damaged samples, both visually and via micro-focused computed X-ray tomography, offers insights into heat distribution and ablation dynamics, highlighting the anisotropic thermal properties of CFRP. Compression after impact (CAI) tests further assess the residual strength of the irradiated samples, enhancing the understanding of CFRP's structural integrity post-irradiation. Collectively, these tests improve the knowledge of the thermal and mechanical behavior of CFRP under extreme irradiation conditions. The findings not only contribute to predictive modeling of CFRP's response to laser irradiation but enhance the scalability of these models to higher laser powers, providing robust tools for predicting material behavior in high-performance settings.

Keywords: high-energy laser; CFRP; laser impact; compound material; volume ablation; scalability; compression-after-impact; laser damage

1. Introduction

Over the last 20 years, fiber lasers have rapidly evolved in terms of output power, beam quality, and efficiency. Due to their compact solid-state design, they are suitable for maintenance-free and portable applications. Fiber-guided beams can be robustly transported over long distances to laser optics or can be remotely used by an industrial robot. Furthermore, the near-IR wavelengths of fiber lasers are well absorbed by many materials that are used for production, such as various metals and plastics. All this has led to fiber lasers now dominating the market for industrial laser processing [1].

In recent years, the performance of continuous wave (CW) fiber lasers has increased significantly, making lasers in the 100-kW range commercially available [2,3]. Such powerful CW lasers are now used not only for industry but for defense technology [4–6].

Although these systems are not usable over long distances due to their low beam quality, they are well suited to investigate HEL effects in a laboratory environment.

The main objective of this study is to investigate the degradation mechanisms of CFRP under continuous-wave high-energy laser (HEL) exposure, focusing on the effects of laser power levels up to 120 kW. By systematically analyzing thermal and mechanical responses, this research aims to improve the understanding of material behavior under extreme laser conditions and to develop empirical models that support laser-based processing and countermeasure applications.

The interaction between HELs and carbon fiber-reinforced polymer (CFRP) composites is crucial in the aerospace and defense sectors, where material integrity under extreme conditions is critical. CFRP exhibits notably high thermal insulation properties. While the carbon fibers withstand high heat fluxes, the polymer matrix provides low thermal resistance [7]. Therefore, understanding the effect of high-energy laser radiation on CFRP, especially with large beam diameters, is of particular interest [8–13].

The propagation of laser radiation over long distances is an important consideration for laser weapons. Laser beams can be scattered or absorbed by air molecules, water vapor, or dust [14–16]. In this study, we focus on the effect of the laser on the target. Considering our case with a maximum of 120 kW at the target location, it can be assumed that an actual directed energy laser system must have an output power of several hundred kilowatts tens of kilometers away due to propagation losses in the air. This loss depends strongly on the actual weather condition, in this rough estimation valid for a medium extinction and neglecting a decrease due to turbulence.

High-energy lasers are increasingly applied in both industrial and defense settings, particularly in aerospace servicing, where precision material removal and surface treatments are essential. Other applications include laser-based countermeasures, where HELs are used to neutralize threats like UAVs and drones. Understanding the response of CFRP to HEL exposure is critical for optimizing such applications, ensuring material resilience.

In the literature, welding processes in the range of 10–100 kW are extensively studied [17–21]. For example, both Krichel et al. and Kawahito et al. analyzed the process limits in laser beam welding of thick steel sheets, using a 40 kW and 100 kW laser, respectively [17,21]. Herzog et al. used a 30-kW laser to cut CFRP with a focus on minimizing the heat affected zone and maximizing the feed rate of the cutting process [22,23]. These studies, and similar studies with particularly high laser powers, are based on working with a small beam diameter well below 1 mm. In contrast to the studies in the literature, this work focuses more on the investigation of laser effects with extremely high laser powers and simultaneously large spot sizes. This aspect is not only important to understand the degradation of CFRP under HEL exposure, but also in the context of defense technology, with CFRP as a representative material.

Various sources provide information on the thermal decomposition of CFRP and the resulting temperatures. Typically, the epoxy matrix begins to degrade at temperatures around 300 °C, while the carbon fibers exhibit higher temperatures between 1000 and 3000 °C during final degradation stages [24–27]. Tranchard et al. conducted a study on decomposition processes under varying atmospheric conditions using thermogravimetric and FTIR measurements [24]. They provide a deeper insight into the damaged behavior of CFRP and developing a kinetic decomposition model.

Numerical modelling has been instrumental in understanding the interaction between CFRP and high-energy laser sources. The interaction involves complex thermal and material dynamics, which can be described by heat conduction models and finite element simulations. Heat transfer equations can be used to predict the transport of heat through the material. Existing models can be found in [28,29], simulating the effects of laser energy on composite materials by using the equation

$$\rho C \frac{\partial T}{\partial t} = \nabla \cdot (k \nabla T) + Q \tag{1}$$

where ρ is the material density, C is the specific heat capacity, k is the thermal conductivity, T is temperature, and Q represents the heat source due to laser irradiation. In the context of CFRP, the thermal properties are highly anisotropic due to the differences between the carbon fibers and the polymer matrix, and they vary significantly with temperature [28]. Similarly, Xu et al. utilized a heat conduction model, incorporating phase change processes, such as polymer pyrolysis and carbon fiber sublimation, to predict material removal in CFRP during laser milling [29]. They used a homogenized approach, which simplified the heterogeneous nature of CFRP, to predict the average ablation depth and extent of the HAZ.

Chippendale et al. [30] and Joyce et al. [31] have modelled the thermal decomposition processes and effects of high-energy laser effects on polymers and composites, offering insights into the heat-affected zones and ablation dynamics. Further, Nan et al. demonstrated the influences of the laminated structure on ablation characteristics, emphasizing how layer orientation affects thermal and mechanical responses during laser exposure [32]. Ohkubo et al. simulated laser beam cutting of CFRP, revealing the complex interactions between laser parameters and material responses [33]. The study of Schmitt and Allheily investigated thermal development within CFRP structures under laser impact, highlighting the importance of thermal radiation between carbon layers at elevated temperatures [34]. While these numerical studies form a foundation, the focus of the current study is on empirical validation and extension of these models up to higher power levels, and thus detailed numerical modelling is beyond the scope of this paper.

In laser processing of CFRP composites, the choice between CW and pulsed lasers significantly influences the outcomes. While CW lasers offer higher cutting speeds and efficiency, they often lead to greater thermal damage; on the other hand, pulsed lasers provide better control of the heat-affected zone (HAZ) through optimizing process parameters, reducing thermal degradation at the cost of slower processing rates [35,36].

In addition to continuous and pulsed lasers, Quasi-Continuous Wave (QCW) fiber lasers offer a unique approach to managing the heat affected zone (HAZ) in CFRP cutting. Leone et al. conducted a study investigating the influence of process parameters, such as pulse power and pulse duration, and the overlapping factor on kerf geometry and HAZ, suggesting that by optimizing these parameters, it is possible to achieve minimal HAZ [37]. With the use of an ultra-short pulse laser "cold processing" of the compound materials can be achieved, resulting in minimizing the HAZ. Such methods are gaining popularity for demanding CFRP applications, especially in aerospace and automotive industries, where precision and material integrity are crucial [38].

Besides HEL, other competing technologies have emerged for processing CFRP and similar composite materials. Abrasive water jet (AWJ) machining is one method that provides powerful cutting performance without thermal effects, making it suitable for applications requiring minimal heat-induced degradation [39]. However, it typically results in an increased surface roughness, or kerf taper, which limits its precision compared to laser cutting.

While the current state of the art provides a good overview of the impact processes of CW lasers on CFRP in the range up to a few kilowatts, empirical evidence at higher power scales is needed. To assess the behavior of CFRP under laser irradiation in previously unexplored power ranges, we conducted a parameter study with laser powers up to 120 kW. This study includes the design of a test environment that meets operational safety requirements for laser processing of CFRP. The test results include high-speed imaging to capture the process dynamics. The setup includes photodiode measurements for the detection of perforation times and for an automated laser shut-off mechanism and high-speed video recording for the visualization of the interaction effects. Micro-focused computed X-ray tomography (μ-CT) scans were performed after the exposure to analyze the ablation and delamination behavior caused by the laser impact. Additionally, physical properties of the irradiated samples, such as residual strength, were evaluated using compression tests in accordance with compression after impact (CAI) test regulations.

The interaction of HEL and composite materials is characterized by thermal and mechanical processes. At a fundamental level, the material's response depends on factors such as laser power density, laser wavelength, exposure time, and the material's thermal and mechanical properties. Infrared laser light is effectively absorbed by CFRP, leading to rapid heating and pyrolysis of the resin matrix, followed by potential ablation of the fibers. For CFRP, the concept of a failure threshold can be defined as a specific laser power density required to initiate irreversible changes in the material's structure. This includes, among other things, the removal of material due to vaporization and decomposition, which begins once the temperature exceeds the decomposition temperature of the resin. In this study, the relationship between laser power and perforation time provides a practical measure of the CFRP's failure threshold. By examining the time to reach perforation at different power levels, we determine the energy levels required to reach critical failure in each material.

Investigating these energy levels is essential for applications requiring rapid material removal, high precision, and minimal collateral damage under extreme conditions. By exploring this power range, we aim to establish thresholds for material failure and provide data-driven models that enhance predictive capabilities in HEL applications.

2. Materials and Methods

The setup used in this study incorporates various improvements compared to our setup used in our previous work published in Wolfrum et al. [8]. The experimental setup is depicted in Figure 1. It utilized a CW infrared fiber laser with a wavelength of 1.07 µm, capable of delivering up to 120 kW (YLS-120000, IPG Photonics Corporation, Burbach, Germany). The laser beam passed a collimator and was then focused using an adjacent lens with a focal length of 400 mm. The laser beam exhibits a beam intensity that closely resembles a Gaussian distribution, with a super-Gaussian exponent of 1.5. To protect the coated optics from dust, a cover was attached to the laser optics and purged with clean air. During the experimental series, the distance between the optics and the sample was adjusted to vary the beam diameter (D4σ) between 10 and 30 mm. The laser-matter interaction zone is captured using a high-speed framing camera (Phantom v1610, Vision Research Inc., Wayne, NJ, USA).

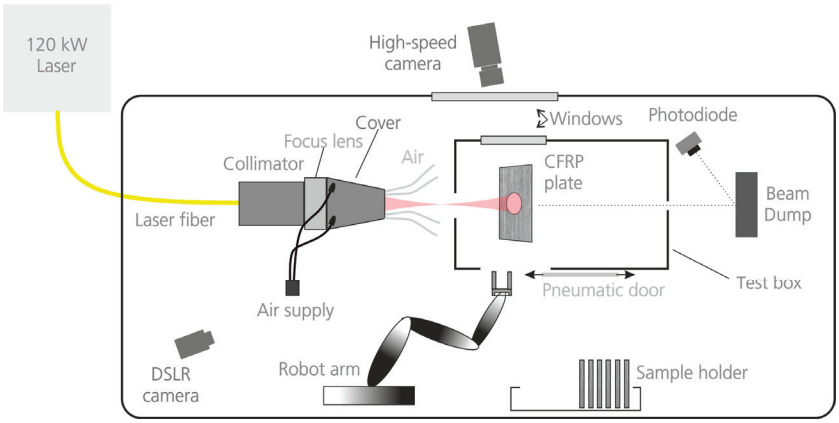

Figure 1. Experimental setup includes an automated sample exchange, operated by a robotic arm.

The experimental setup featured several characteristics aimed to mitigate the risks associated with the combustion of CFRP. To minimize human exposure to potentially hazardous by-products of CFRP combustion, an automated sample exchange system operated by a robotic arm is utilized. This allowed for a sequence of laser tests to be conducted while ensuring safety. The concern regarding human exposure to hazardous by-products of CFRP combustion has been highlighted in studies by Lacroix et al. [9]. To capture smoke and fiber fragments generated during the experiments, an enclosed measurement box with additional ventilation was designed. This helped to maintain a controlled environment and prevent the dispersion of harmful substances. Furthermore,

a shut-off automation system was implemented to immediately stop the laser irradiation after sample perforation using the automatic photodiode switch. This effectively limited the potential "afterburn effect" that could compromise experimental precision and safety. While the additional enclosure of the sample is an advantage in terms of safety, it restricted the use of additional measurement devices, such as infrared technology, due to the formation of CFRP dust.

The two CFRP materials are typically used in high-performance aerospace applications, like military aircraft construction [10]. The materials exhibit differences in fiber type, fiber volume fraction, and matrix composition. HexPly® M18-1/G939 contains G939 carbon fibers in a woven fabric form, with a fiber volume fraction of 55% and a fiber density of 1.78 g/cm^3 [11]. The M18-1 system incorporates a polyetherimide (PEI) thermoplastic within its epoxy matrix. HexPly® 8552/IM7 contains IM7 unidirectional carbon fibers, with a fiber volume fraction of about 58% and a fiber density of 1.77 g/cm^3 [11]. The 8552 system uses a toughened epoxy resin with polyethersulfone (PES) as a thermoplastic toughening agent. The 8552 composite exhibits a more homogeneous distribution of its toughened epoxy matrix compared to the layered structure of the M18-1 composite, leading to variations in matrix uniformity that may influence thermal and mechanical behavior. Further information and a detailed comparison of both material systems can be found in [10]. The dimensions and lay-up of the samples were analogous to those used in [8]. Before testing, all samples were ground at the 100 mm wide edges to provide parallelism for the compression after impact (CAI) testing. Compressive strength after impact is measured according to DIN 65561 at a universal testing machine (UPN 250 kN, ZwickRoell, Ulm, Germany) with a cross-head speed of 1 mm/min. Micro-focused computed X-ray tomography (μ-CT) is carried out on selected samples using a 300 kV micro-focus X-ray source (Phoenix VTOM XL300, Waygate Technologies, Wunstorf, Germany) and a GE Dynamic 41/100 detector. For the investigations up to six samples were combined to one package.

With a parameter variation over a large laser power range (10–120 kW), different spot sizes (10–30 mm), sample thicknesses (2–6 mm), and two different materials (HexPly® M18-1/G939 and 8552/IM7), this study aims to systematically investigate the effects of high-energy lasers on CFRP materials.

3. Results and Discussion

Direct CW laser irradiation of CFRP samples resulted in evaporation of the epoxy matrix and to some extent of the carbon fibers. This evaporation is evident from the emergence of a dust plume in front of the sample, extending up to half a meter. The expansion of the plume starts immediately after the laser emission is turned on, as observed in high-speed images (Figure 2). The experiment shown in Figure 2 was conducted using a laser power of 120 kW and a beam diameter of 20 mm on a 4 mm thick M18-1/G939 sample. In the following section, this experiment will be used to show typical results of the series of experiments carried out.

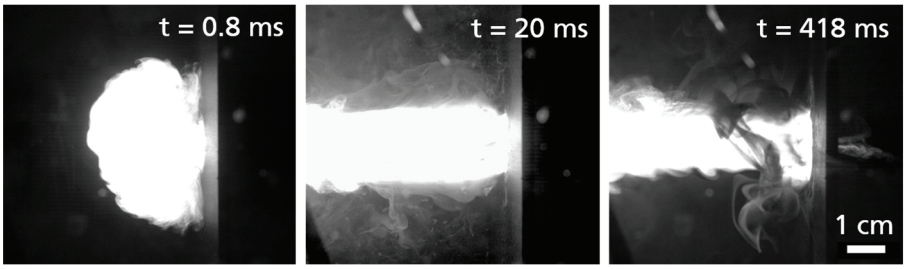

Figure 2. A gas cloud expands rapidly caused by laser irradiation of a CFRP plate with 120 kW and a beam size of 20 mm. The plate is perforated after 0.4 s.

The vapor plume contains ejected fragments of the fiber compound and smoke. Furthermore, the resin matrix is vaporized or decomposed due to the laser absorption. The continuous heating by the laser ionizes the combustion products, leading to a partially ionized matter with a temperature in the range of several thousand Kelvin, as described by Ma et al. [40]. In similar experiments conducted by Borchert et al. [12] on glass–fiber-reinforced-polymers (GFRP), temperature evolution was measured using a four-channel infrared detector system to overcome limitations of conventional pyrometers. Their results showed a temperature plateau between 2100 K and 2500 K at later time delays from the flame emission. Herr et al. [13] utilized high-speed thermal imagery and spectral analysis to characterize the plume generated in front of laser-irradiated CFRP plates, revealing a complex composition of organic products such as hydrocarbon gases and particles.

The CFRP samples were perforated after an irradiation time of 0.4–0.5 s for both materials. Figure 3 shows images of the damage zones obtained after the laser exposure. Distinct differences between the front and back surfaces of the tested samples are noticeable. First, the area of the ablated fibers on the front is roughly comparable to the applied laser beam diameter of 20 mm, while the perforated area on the back is only a few mm in size. Furthermore, the matrix surrounding the exposed area on the front side shows a heat affected zone (HAZ) with signs of vaporization beyond the direct impact area. The matrix around the perforation hole on the back, however, shows no visible signs of any thermal effects from the laser. The HAZ seems to decrease from the front to the back side of the sample. Another notable observation is that the damage zones often exhibit a conical shape, indicating a change in material removal behavior with increasing laser power. Anisotropic properties of CFRP as well as differences in thermal diffusion of the CFRP components contribute to both the formation of a conical shape and the extended HAZ. Specifically, the heat conductivity of graphite is 50 W/(m·K), compared to only 0.2 W/(m·K) for the polymer matrix, and vaporization occurs at 3300 °C for the fibers versus 350–500 °C for the matrix [26,35]. Hence, heat conduction occurs primarily along fibers, leading to vaporization of the matrix material outside of the laser impact zone, resulting in an extended HAZ with increasing irradiation times. For lower laser intensities, heat conduction in the lower fiber layers causes the matrix to evaporate, while for higher laser intensities, the heat cannot be dissipated fast enough, resulting in evaporation of fibers and matrix within the HAZ. Remaining fibers act as a shield for underlying layers. Consequently, lower layers absorb a smaller area of the laser beam, which in turn results in a more pronounced conical shape.

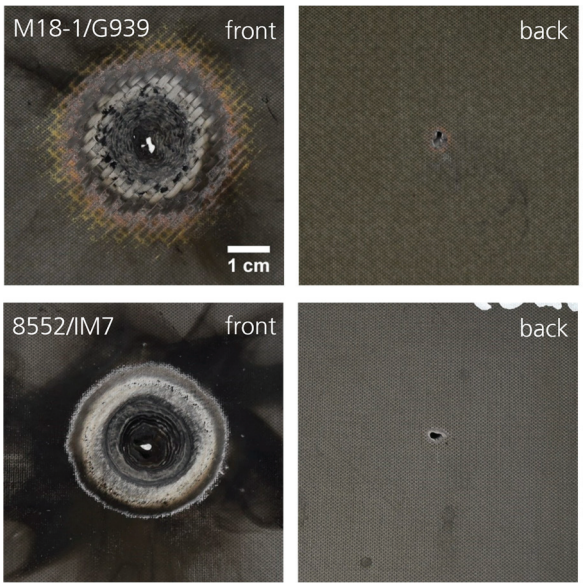

Figure 3. Damage zones of irradiated CFRP samples of two tested materials (P = 120 kW, Ø = 20 mm, d = 4 mm). The heat affected zone (HAZ) extends to areas outside the applied laser spot.

For this study, we define the failure threshold of CFRP as the laser power level and irradiation time at which complete perforation consistently occurs, correlating directly with the observed perforation times. This threshold is characterized by irreversible thermal and mechanical degradation, manifesting as delamination and structural breakdown in the material. When increasing the laser power, a decrease in perforation times can be observed, as shown in Figure 4, which shows the results of using a double-logarithmic representation. The dependence of perforation time on laser power holds true for all tested beam diameters and can be described by a power law:

$$t = m \cdot P^a \Leftrightarrow log(t) = a \cdot log(P) + log(m) \tag{2}$$

which is represented as a fit in Figure 4. The slopes of the fits varied between values of $a = -1.13$ and -1.06. The slopes determined for smaller and larger beam diameters are slightly higher ($a = -1.33$ to -1.17 for Ø = 30 mm) and lower ($a = -1.08$ to -0.93 for Ø = 10 mm), respectively. These values correspond to the exponents for the power functions when choosing a double logarithmic representation of the data. In particular, the 8552/IM7 material showed increased resistance to laser irradiation. One possible reason for the higher resistance may be the slightly higher fiber content. In addition, the homogeneous distribution of the epoxy matrix in 8552/IM7 contributes to its overall resilience, whereas the layered structure of PEI in M18-1 influences the thermal and mechanical inhomogeneity of the plastic component. This may lead to localized thermal responses that increase susceptibility to laser damage. This emphasizes the influence of material composition on the failure threshold and resilience of CFRP.

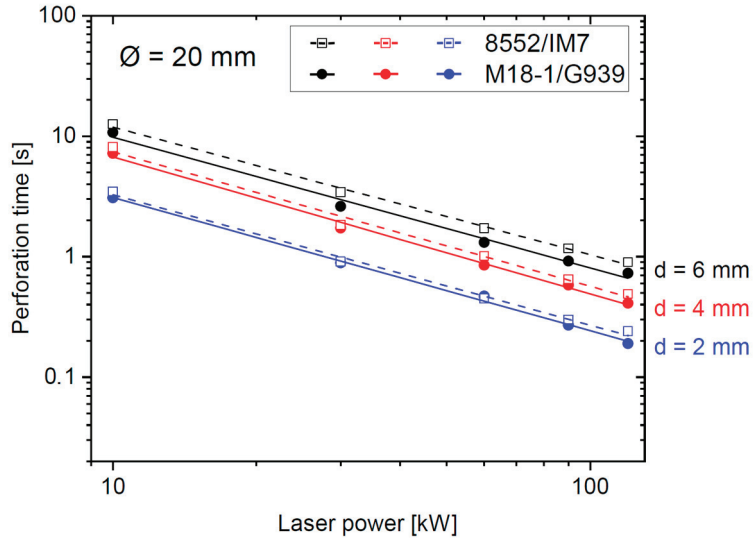

Figure 4. Perforation times as a function of laser power in a double-logarithmic representation for a beam diameter of 20 mm and different sample thicknesses d. In this diagram, a linear decrease of the logarithm of the perforation time with increase of the logarithm of the laser power can be observed, represented by the solid and dashed lines.

In [8], scaling laws are shown for the burn-through-times of CFRP samples for laser powers up to 10 kW. With the increase of laser power by one order of magnitude in this study, this scaling law is again confirmed. This indicates that an extrapolation beyond and interpolation between the investigated laser powers seems to be valid. Based on the confirmed correlation of perforation time and laser power via a power law, an empirical model can be derived. The model can be used to predict the failure behavior of CFRP samples across a wide range of laser power levels.

Furthermore, the results of the parameter study are used to establish a correlation between the perforation time and the expected material removal due to laser irradiation. The volume damage was quantitatively assessed using a simplified model, approximating

the ablated volume at perforation time V_{perf} as a cylindrical shape. In this model, the diameter of the cylinder corresponds to the laser spot diameter $D_{4\sigma}$, and the depth is defined by the thickness d of the sample, thus:

$$V_{perf} = d \cdot \pi \cdot (D_{4\sigma}/2)^2 \tag{3}$$

Based on this approximation, a linear relationship can be determined between the logarithm of the damaged volume and the logarithm of the perforation time for each laser power, as shown in Figure 5 for the tested material M18-1/G939.

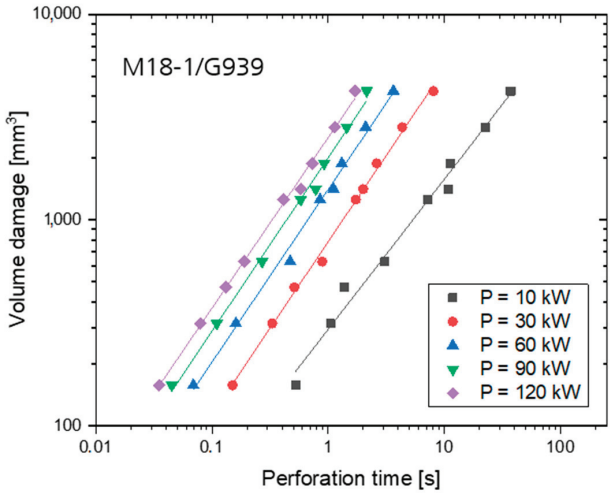

Figure 5. Volume damage as a function of perforation time in a double-logarithmic representation for various laser powers.

While some individual values for a laser power of 10 kW show a slight deviation, the values for higher laser powers can be properly described by the linear fit in Figure 5, which represents a power law when plotted linearly. A possible explanation for the higher variance of the values at a low power level is the effect of carbonization of the CFRP surface and upper matrix layers before sublimation, especially in experiments with large beam diameters. These carbonized layers act as a shield and prevent the subjacent fibers from being exposed to the incident laser light. Allheily et al. conducted experiments using a 10-kW fiber laser and observed that the delamination of CFRP plies, caused by rapid ablation of the matrix and bending of the fibers, decreases the thermal conductivity resulting in a decreased energy deposition in the underlying material [9]. This aspect is of particular importance in the context of resistance against laser irradiated damage.

To explore the relationship between laser power and the rate of volume damage r_{vol} we calculated the volume removal rate, defined as the volume of material ablated per unit time. This is again based on the assumption of a cylindrical hole with the same diameter as the laser spot, which yields the approximation:

$$r_{vol} = V_{perf}/t_{perf} \tag{4}$$

This analysis provides a direct measure showing how the efficiency of material removal scales with increasing laser power.

The values for the volume removal rate calculated from experimental data and Equation (4) are shown by the symbols in Figure 6. As laser power increases, the volume removal rate also increases, indicating that higher energy inputs significantly enhance the efficiency of ablation. The sold lines represent a linear fit indicating that the relation between volume removal rate and laser power is well described by a linear relation. Consequently, within certain limits, the perforation time for arbitrary laser spot diameters $D_{4\sigma}$ and sample thickness can be calculated directly from linear fit shown in Figure 6.

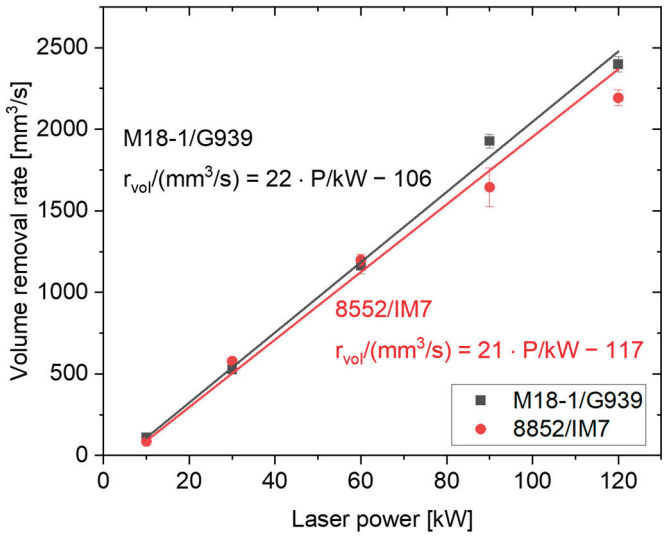

Figure 6. Volume removal rate as a function of laser power. Symbols: r_{vol} determined from experimental data and Equation (4). Lines: linear fit.

Additionally, when considering the broader context of a high-energy laser (HEL) weapon, it becomes evident that managing laser power is vital in controlling the extent of damage and the efficiency of material removal. These results emphasize the importance of parameter optimization in laser processing of CFRP, providing a foundation for further experimental design and technological advancements in laser processing technologies.

The developed empirical models for volume damage and volume removal rate offer significant implications for understanding the structural integrity and vulnerability of CFRP materials in scenarios involving intense laser exposures, thereby enhancing predictive capabilities for both industrial applications and defense strategies against high-energy laser threats.

µCT-scans were utilized to visualize and analyze the damage morphology of CFRP samples, providing a comprehensive understanding of the extent of laser-induced damage. Figure 7 displays cross-sections of CT images of CFRP panels irradiated with different laser powers and beam diameters. The effect of laser spot size is evident: with a smaller spot size of 10 mm, rapid perforation leads to localized damage confined closely to the irradiated area, indicating minimal lateral heat transfer. Conversely, larger spot sizes at the same power levels result in extensive vaporization of the epoxy matrix around the beam impact area, leading to delamination and potential structural failure as the matrix vaporizes and leaves the fibers unsupported. Hence, the HAZ is much larger. At lower powers (30 kW), a large HAZ with significant material degradation is observed. The matrix material seems to be decomposed or removed while the carbon fibers remain partially intact. This indicated an incomplete ablation. By contrast, at the maximum laser power of 120 kW, nearly all fibers within the area of the laser spot size were completely decomposed, suggesting a threshold of energy input above which total fiber decomposition occurs. The scans reveal that, depending on the applied laser intensity, laser penetration can occur so rapidly that the heat does not significantly dissipate beyond the irradiated area. This observation matches the previously described damage analysis of irradiated samples, shown in Figure 3.

As already described, the conical shape of the ablated volume can be attributed to varying absorption and thermal conductivity characteristics between the composite's constituents. As noted in studies by Herr et al. [13] and Allheily et al. [9], the thermal gradients created by laser irradiation result in differential rates of heat dissipation within the material, promoting a conical ablation profile. The delamination process allows the heat to propagate more extensively along the direction of the fiber compared to propagation into the depth of the samples. This further enhanced the appearance of the conical shaped holes.

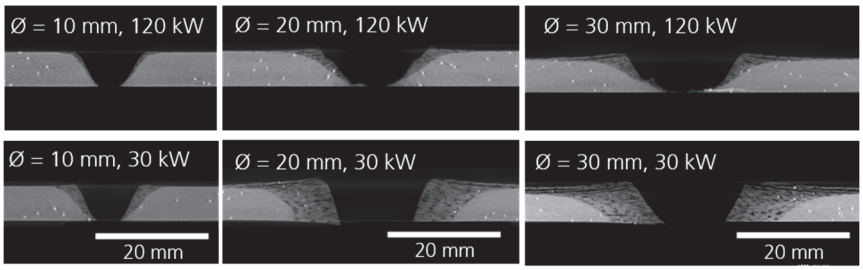

Figure 7. µCT-scan cross-sections of irradiated CFRP samples reveal details of the heat affected zone and the delamination of fibers. The holes created have a conical shape (M18-1/G939, d = 6 mm).

Similarly, Herzog et al. found that laser cutting of CFRP can maintain precise kerf sizes up to a certain depth, beyond which shadowing effects impede further penetration [23].

The conical ablation zone geometry was found to vary depending on the sample thickness. Specifically, the conical shape was confirmed for thicker samples (6 mm), in particular; while thinner samples (2 and 4 mm) partially exhibited a more cylindrical ablation pattern. This variation in ablation geometry can be attributed to differences in thermal diffusion and heat accumulation effects, which vary with sample thickness. A conical approximation was also tested to calculate the volume removal. However, it introduced significant fluctuations in the estimated volume removal rates compared to the previously presented cylindrical model. As a result, we decided to use a simpler cylindrical model for calculating the volume removal and ablation rate. While not fully capturing the conical characteristics seen in thicker samples, the cylindrical model provided a more consistent and reliable approximation for the empirical analysis.

When examining the total ablated and delaminated volumes, it is apparent that the extent of material removal remains consistent across both lower and higher power settings. This observation highlights the efficiency of the laser ablation process, where increased power does not necessarily result in greater material removal, but rather a broader spread of thermal effects, as also discussed by Sobri et al. in the context of laser machining dynamics [41].

The results shown in Figure 8 indicate that the residual strength primarily depends on the volume of the material ablated, particularly the matrix. Thicker samples, such as the 6 mm panels, exhibit higher performance across various spot sizes, indicating that thicker samples are more resistant to damage and retain more residual strength. In general, larger laser spot sizes are associated with a reduction in compressive strength.

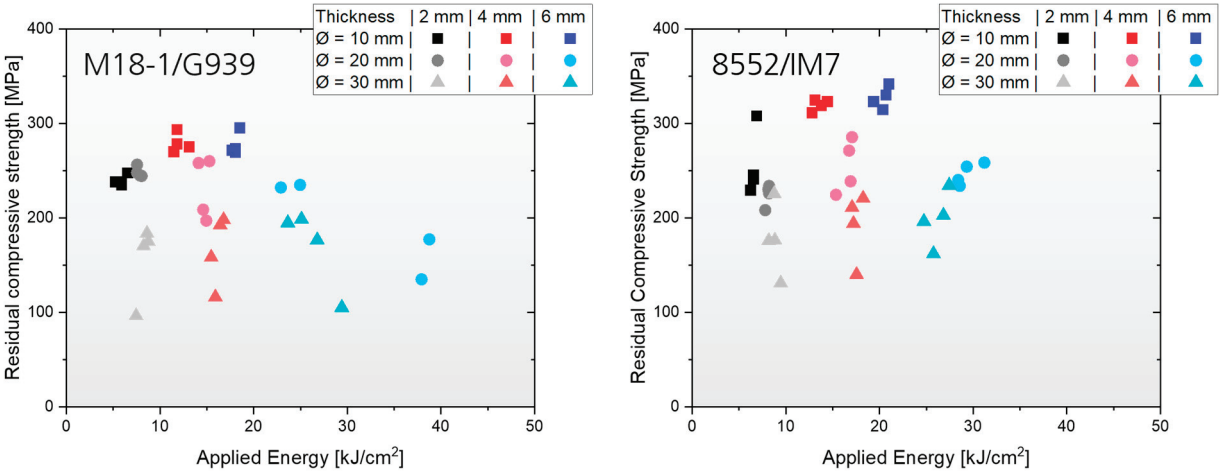

Figure 8. Residual compressive strength of laser irradiated CFRP samples determined in accordance with the compression after impact procedure.

An important aspect to consider is the observed delamination, which is more prominent with larger beam diameters and lower laser powers. Delaminated fibers, although still physically present, no longer contribute significantly to the structural integrity of the material. Their mechanical connection to the composite has been compromised, reducing their ability to carry loads and, consequently, decreasing the residual strength of the composite.

Regarding the different applied laser powers, a decline in residual strength can be noted with increasing energy input from the laser. However, there is no clear correlation to the test parameters set, indicating a complex interplay of factors. The parameters, specifically laser power and spot size, are part of a multidimensional space that affects the damage characteristics and, subsequently, the mechanical properties of CFRP. The impact of laser irradiation on CFRP is influenced by a variety of factors including thermal conductivity of the fibers and matrix. Based on the CT images and damage patterns shown, variations of the laser parameters can result in varied heterogeneous damage regions within the material. The lack of clear correlation observed in the test results underscores the nuanced interactions within this parameter space.

The residual strength behavior observed in our laser ablation study can be compared to that of composite structures subjected to extreme conditions, such as ballistic impact or lightning strikes. For instance, Wang et al. conducted ballistic impact tests on CFRP materials, reporting significant reductions in residual strength after impact [42]. In their study, ballistic damage resulted in delamination and core damage contributing to significant reduction in strength. The laser generated HAZ and the conical ablation shape observed in our experiments resembles the localized damage effects seen in ballistic impact studies. This shape is indicative of anisotropic heat diffusion within the composite structure. The implications of conical ablation are critical for practical settings, particularly in precision cutting and controlled material removal. Additionally, the broader impact of HAZ behavior on residual strength can be linked to the findings of Wang et al., where the residual compressive strengths of composites after ballistic impact were significantly lower than those of pristine samples [42]. Wang et al. conducted a detailed investigation of honeycomb sandwich composites subjected to lightning strike damage, examining the impact on residual compressive strength [43]. Their study showed that lightning-induced damage, which included extensive delamination and thermal degradation, significantly reduced the compressive strength of the specimens compared to pristine conditions.

4. Conclusions

This study contributes to the advancement of understanding CFRP under CW laser exposures up to 120 kW. The research fills a gap in the existing literature by comprehensively exploring the interaction between intense laser radiation and CFRP structures in the range of 10 kW to 120 kW. Through a parameter study that incorporates variations in material, laser power, spot size, and sample thickness, this research provides valuable insights into the reaction of the material to extreme energy exposure.

Building upon the foundational work of Wolfrum et al. [8], which developed initial empirical models for CFRP failure under laser irradiation up to 10 kW, this study expands the experiments up to 120 kW. Furthermore, an automated sample exchange system was introduced. This advancement enhances safety and efficiency while enabling systematic studies of the material's response to high-power laser exposure. The results from this series of tests have provided insights into the failure threshold of CFRP by measuring perforation times across various laser intensities. The perforation times showed a clear dependence on laser power, which could be described by power-law relationships with exponent values between -1.13 and -1.06—see Equation (2). There are clear trends for the correlation between volume damage and perforation times, which could be extrapolated for even higher power classes. Based on this relationship, volume removal rates were derived for which a linear dependence on the applied laser power could be shown. In summary, it can be stated that the empirical models have been further developed on the

basis of the determined perforation times and, in particular, the scalability for much higher laser powers was verified.

Our study also examined the responses of two different types of CFRP materials (M18-1/G939 and 8552/IM7) to laser exposure, emphasizing how variations in fiber type and matrix composition may contribute to the observed differences in laser resistance. The degradation of fibers was observed through damage pattern assessment and μCT-scans. The evaporation of the matrix and delamination of fibers are particularly critical aspects, especially in applications where material integrity is crucial. The ability to predict and mitigate such damage is essential for ensuring the reliability and safety of CFRP components in demanding applications. The residual strength of the CFRP samples, evaluated by tests in accordance with CAI procedures, was predominantly influenced by the volume of material ablated, particularly the matrix. Delamination, especially with larger beam diameters, significantly impaired the structural integrity of the composite and contributed to a reduction in compressive strength. The findings enhance the understanding of the dynamics between laser energy and material properties, enabling more effective control of the laser process and potentially leading to significant technological advancements.

The results of this study are highly relevant for industries where CFRP components are subjected to high-stress conditions, such as aerospace, automotive, and defense. Our findings suggest that optimizing laser parameters, including power density and exposure time, can help control material degradation and improve precision in laser-based processing. Additionally, selecting CFRP with higher fiber volume fractions or a homogeneous and therefore thermally stable matrix may enhance resistance to laser damage.

Future studies could explore variations in fiber content within CFRP samples to investigate how material composition influences damage thresholds and vulnerability. Such studies would further refine the understanding of material behavior under high-energy laser impacts, ensuring the continued reliability and safety of CFRP components in demanding applications. In addition, future research could explore the potential of hybrid materials or multilayered composites, which may provide enhanced resistance to high-energy laser exposure through improved thermal management and mechanical robustness. Investigating various fiber orientations, resin compositions, and reinforcement structures could lead to the development of CFRP materials optimized for high-energy environments, further expanding the applicability of these materials in advanced defense and aerospace technologies.

Author Contributions: Conceptualization, S.S.; Formal analysis, S.S., S.R., J.W., M.L. and J.O.; Funding acquisition, M.L. and J.O.; Investigation, S.S., D.H., S.R. and J.W.; Methodology, S.S. and D.H.; Project administration, M.L.; Resources, J.W.; Supervision, M.L. and J.O.; Validation, S.S., S.R., M.L. and J.O.; Visualization, S.S.; Writing—original draft preparation, S.S.; writing—review and editing, S.S., S.R., J.W. and J.O. All authors have read and agreed to the published version of the manuscript.

Funding: We acknowledge financial support by the Bundesamt für Ausrüstung, Informationstechnik und Nutzung der Bundeswehr (BAAINBw), Koblenz, Germany.

Data Availability Statement: The original contributions presented in the study are included in the article, further inquiries can be directed to the corresponding author/s.

Conflicts of Interest: The authors declare no conflicts of interest.

References

1. Belforte, D.A. The Global Market for Industrial Laser Processing. *Photonics Views* **2020**, *17*, 35–37. [CrossRef]
2. Shcherbakov, E.A.; Fomin, V.V.; Abramov, A.A.; Ferin, A.A.; Mochalov, D.V.; Gapontsev, V.P. Industrial grade 100 kW power CW fiber laser. In Proceedings of the Advanced Solid-State Lasers Congress, Virtual, 27 October–1 November 2013. [CrossRef]
3. Nissenbaum, A.; Armon, N.; Shekel, E. Dynamic beam lasers based on coherent beam combining. In Proceedings of the Fiber Lasers XIX: Technology and Systems, San Francisco, CA, USA, 22 January–28 February 2022; SPIE Photonics Europe: Strasbourg, France, 2022. [CrossRef]

4. Jung, M.; Riesbeck, T.; Schmitz, J.; Baumgärtel, T.; Ludewigt, K.; Graf, A. High energy laser demonstrators for defense applications. In Proceedings of the XXI International Symposium on High Power Laser Systems and Applications, Gmunden, Austria, 5–9 September 2016. [CrossRef]
5. Lyubomir, L.; Edmunds, T.; Risham, S.G. Applications of Laser Technology in the Army. *J. Def. Manag.* **2021**, *11*, 210.
6. Karr, T.; Trebes, J. The new laser weapons. *Phys. Today* **2024**, *77*, 32–38. [CrossRef]
7. Bibinger, J.; Eibl, S.; Gudladt, H.-J. Ply-Resolved Quantification of Thermal Degradation in Carbon Fibre-reinforced Polymers. *J. Compos. Mater.* **2023**, *57*, 1057–1072. [CrossRef]
8. Wolfrum, J.; Eibl, S.; Oeltjen, E.; Osterholz, J.; Wickert, M. High-energy laser effects on carbon fiber reinforced polymer composites with a focus on perforation time. *J. Compos. Mater.* **2021**, *55*, 2249–2262. [CrossRef]
9. Allheily, V.; Lacroix, F.; Eichhorn, A.; Merlat, L.; L'Hostis, G.; Durand, B. An experimental method to assess the thermo-mechanical damage of CFRP subjected to a highly energetic 1.07 µm-wavelength laser irradiation. *Compos. Part B Eng.* **2016**, *92*, 326–331. [CrossRef]
10. Eibl, S. Observing Inhomogeneity of Plastic Components in Carbon Fiber Reinforced Polymer Materials by ATR-FTIR Spectroscopy in the Micrometer Scale. *J. Compos. Mater.* **2008**, *42*, 1231–1246. [CrossRef]
11. HexPly® Prepregs M18-1/8552 Product Data Sheets, Hexcel Inc. Available online: https://www.hexcel.com (accessed on 20 April 2024).
12. Borchert, H.; Allheily, V.; Merlat, L.; Schmitt, R. Time resolved spectroscopic temperature measurement techniques during CW-laser matter interaction of glass–fiber-reinforced-polymers (GFRP). In Proceedings of the High Power Lasers: Technology and Systems, Platforms, Effects III, Strasbourg, France, 9–12 September 2019; p. 111620M. [CrossRef]
13. Herr, N.C.; Gonzales, A.E.; Perram, G.P. Kinetics, evolving thermal properties, and surface ignition of carbon fiber reinforced epoxy composite during laser-induced decomposition. *Polym. Degrad. Stab.* **2018**, *152*, 147–161. [CrossRef]
14. Smith, F.G.; Accetta, J.S.; Shumaker, D.L. *The Infrared & Electro-Optical Systems Handbook, Vol. 2: Atmospheric Propagation of Radiation*; Infrared Information Analysis Center, SPIE Optical Engineering Press: Ann Arbor, MI, USA; Bellingham, WA, USA, 1993.
15. Sprangle, P.; Hafizi, B. High-power, high-intensity laser propagation and interactions. *Phys. Plasmas* **2014**, *21*, 055402. [CrossRef]
16. Fante, R.L. Electromagnetic beam propagation in turbulent media: An update. *Proc. IEEE* **1980**, *68*, 1424–1443. [CrossRef]
17. Krichel, T.; Olschok, S.; Reisgen, U. Extension of the process limits for laser beam welding in vacuum of thick-walled steel sheets. *Procedia CIRP* **2022**, *111*, 453–456. [CrossRef]
18. Katayama, S.; Mizutani, M.; Kawahito, Y.; Sumimori, S.I.D. Fundamental research of 100 kW fiber laser welding technology. In Proceedings of the Lasers in Manufacturing Conference (LiM), Munich, Germany, 22–25 June 2015.
19. Pricking, A.; Kaiser, E.; Papastathopoulos, E.; Stambke, M.; Bruestle, R.; Broghammer, G.; Tillkorn, C.; Gottwald, T.; Metzger, B.; Schad, S.-S.; et al. Welding with ultra-high-power cw lasers. In Proceedings of the 12th CIRP Conference on Photonic Technologies (LANE 2022), Furth, Germany, 4–8 September 2022.
20. Reich, S.; Goesmann, M.; Heunoske, D.; Schäffer, S.; Lueck, M.; Wickert, M.; Osterholz, J. Change of dominant material properties in laser perforation process with high-energy lasers up to 120 kilowatt. *Sci. Rep.* **2023**, *13*, 21611. [CrossRef] [PubMed]
21. Kawahito, Y.; Wang, H.; Katayama, S.; Sumimori, D. Ultra high power (100 kW) fiber laser welding of steel. *Opt. Lett.* **2018**, *43*, 4667–4670. [CrossRef]
22. Herzog, D.; Schmidt-Lehr, M.; Oberlander, M.; Canisius, M.; Radek, M.; Emmelmann, C. Laser cutting of carbon fibre reinforced plastics of high thickness. *Mater. Des.* **2016**, *92*, 742–749. [CrossRef]
23. Herzog, D.; Schmidt-Lehr, M.; Canisius, M.; Oberlander, M.; Tasche, J.-P.; Emmelmann, C. Laser cutting of carbon fiber reinforced plastic using a 30 kW fiber laser. *J. Laser Appl.* **2015**, *27*, 3275. [CrossRef]
24. Tranchard, P.; Duquesne, S.; Samyn, F.; Estèbe, B.; Bourbigot, S. Kinetic analysis of the thermal decomposition of a carbon fibre-reinforced epoxy resin laminate. *J. Anal. Appl. Pyrolysis* **2017**, *126*, 14–21. [CrossRef]
25. Bibinger, J.; Eibl, S.; Gudladt, H.-J. Influence of Low and Extreme Heat Fluxes on Thermal Degradation of Carbon Fibre-reinforced Polymers. *Appl. Compos. Mater.* **2022**, *29*, 1817–1840. [CrossRef]
26. Wu, C.-W.; Wu, X.-Q.; Huang, C.-G. Ablation behaviors of carbon reinforced polymer composites by laser of different operation modes. *Opt. Laser Technol.* **2015**, *73*, 23–28. [CrossRef]
27. Zhang, Y.X.; Zhu, Z.; Joseph, R.; Shihan, I.J. Damage to aircraft composite structures caused by directed energy system: A literature review. *Def. Technol.* **2021**, *17*, 1269–1288. [CrossRef]
28. Negarestani, R.; Sundar, M.; Sheikh, M.A.; Mativenga, P.; Li, L.; Li, Z.L.; Chu, P.L.; Khin, C.C.; Zheng, H.Y.; Lim, G.C. Numerical simulation of laser machining of carbon-fibre-reinforced composites. *Proc. Inst. Mech. Eng. Part B J. Eng. Manuf.* **2010**, *224*, 1017–1027. [CrossRef]
29. Xu, H.; Hu, J. Modeling of the material removal and heat affected zone formation in CFRP short pulsed laser processing. *Appl. Math. Model.* **2017**, *46*, 354–364. [CrossRef]
30. Chippendale, R.D.; Golosnoy, I.O.; Lewin, P.L. Numerical modelling of thermal decomposition processes and associated damage in carbon fibre composites. *J. Phys. D Appl. Phys.* **2014**, *47*, 385301. [CrossRef]
31. Tresansky, A.C.; Joyce, P.; Radice, J.; Watkins, J. Numerical modeling of high-energy laser effects in polymer and composite materials. *J. Dir. Energy* **2014**, *5*, 137–158.

32. Nan, P.; Shen, Z.; Han, B.; Ni, X. The influences of laminated structure on the ablation characteristics of carbon fiber composites under CW laser irradiation. *Opt. Laser Technol.* **2019**, *116*, 224–231. [CrossRef]
33. Ohkubo, T.; Tsukamoto, M.; Sato, Y. Numerical Simulation of Laser Beam Cutting of Carbon Fiber Reinforced Plastics. *Phys. Procedia* **2014**, *56*, 1165–1170. [CrossRef]
34. Schmitt, R.; Allheily, V. Modelling the heating process of CFRP by cw-laser radiation with special focus on the heat transfer by thermal radiation between the carbon fibers. *Procedia CIRP* **2018**, *74*, 562–567. [CrossRef]
35. El-Hofy, M.H.; El-Hofy, H. Laser beam machining of carbon fiber reinforced composites: A review. *Int. J. Adv. Manuf. Technol.* **2019**, *101*, 2965–2975. [CrossRef]
36. Huang, S.; Fu, Z.; Liu, C.; Wang, C. Interactional relations between ablation and heat affected zone (HAZ) in laser cutting of glass fiber reinforced polymer (GFRP) composite by fiber laser. *Opt. Laser Technol.* **2023**, *158*, 108796. [CrossRef]
37. Leone, C.; Mingione, E.; Genna, S. Laser cutting of CFRP by Quasi-Continuous Wave (QCW) fibre laser: Effect of process parameters and analysis of the HAZ index. *Compos. Part B Eng.* **2021**, *224*, 109–146. [CrossRef]
38. Wang, Z.; Ma, Y.; Yuan, B.; Wu, C.; Li, C.; Sun, S. Development of Laser Processing Carbon-Fiber-Reinforced Plastic. *Sensors* **2023**, *23*, 3659. [CrossRef]
39. Szatkiewicz, T.; Perec, A.; Radomska-Zalas, A.; Banaszek, K.; Balasz, B. Preliminary Studies into Cutting of a Novel Two Component 3D-Printed Stainless Steel-Polymer Composite Material by Abrasive Water Jet. *Materials* **2023**, *16*, 1170. [CrossRef] [PubMed]
40. Ma, Y.; Xin, C.; Zhang, W.; Jin, G. Experimental Study of Plasma Plume Analysis of Long Pulse Laser Irradiates CFRP and GFRP Composite Materials. *Crystals*, 2021; 11, 545. [CrossRef]
41. Sobri, S.A.; Heinemann, R.; Whitehead, D.; Amini, M.H.M.; Mohamed, M. Damage to Carbon Fiber Reinforced Polymer Composites (CFRP) by Laser Machining: An Overview. In *Machining and Machinability of Fiber Reinforced Polymer Composites; Composites Science and Technology*; Springer: Singapore, 2021; Volume 3, pp. 281–297.
42. Wang, J.; Callinan, R. Residual strengths of composite structures subjected to ballistic impact. *Compos. Struct.* **2014**, *117*, 423–432. [CrossRef]
43. Wang, Y.; Zhou, D.; Yan, G.; Wang, Z. Experimental and Numerical Study on Residual Strength of Honeycomb Sandwich Composite Structure after Lightning Strike. *Aerospace* **2022**, *9*, 158. [CrossRef]

Journal of
Composites Science

MDPI

Article

Investigation on the Mechanical and Thermal Properties of Jute/Carbon Fiber Hybrid Composites with the Inclusion of Crab Shell Powder

Ravi Prakash Babu Kocharla [1], Raghu Kumar Bandlamudi [1], Abdul Ahad Mirza [1], Murahari Kolli [2], Ragavanantham Shanmugam [3] and Muralimohan Cheepu [4,*]

[1] Department of Mechanical Engineering, Prasad V. Potluri Siddhartha Institute of Technology, Kanuru, Vijayawada 520007, India; rpkocharla@gmail.com (R.P.B.K.); braghu5051@gmail.com (R.K.B.); ahadmirza1814@gmail.com (A.A.M.)
[2] Department of Mechanical Engineering, Lakireddy Bali Reddy College of Engineering, Mylavaram, Vijayawada 521230, India; kmhari.nitw@gmail.com
[3] Department of Engineering Technology, College of Science and Technology, Fairmont State University, Fairmont, WV 26554, USA; ragavanantham.shanmugam@fairmontstate.edu
[4] Department of Materials System Engineering, Pukyong National University, Busan 48547, Republic of Korea
* Correspondence: muralicheepu@gmail.com; Tel.: +82-10-2714-3774

Abstract: In recent years, natural fiber-reinforced hybrid composites have been utilized in many applications because of their lower cost, biodegradability, and low density. The aim of this research is to convert crab shell waste into an effective reinforcement in jute/carbon fiber hybrid composites. Various weight percentages of crab shell powder (0%, 1%, 3%, 5%, and 7%) were used to prepare crab shell powder hybrid composites. The performance of the crab shell powder hybrid composites was evaluated by preparing the specimens to conduct tensile, flexural, impact, and hardness tests as per ASTM standards. The results show that the inclusion of 5% crab shell powder displayed a better enhancement in the properties of the hybrid composite compared to other weight percentages. The tensile, flexural, and impact strengths of the 5% crab shell powder hybrid composite increased by 21%, 52%, and 50%, respectively. Also, the hardness of the hybrid composite was enhanced by 33%. Scanning electron microscopy (SEM) tests were conducted on the tensile-fractured specimen surfaces, and their morphology and structure confirmed the presence of a well-bonded interface between the fiber and matrix. Differential Scanning Calorimetry (DSC) and Thermogravimetry (TG) analysis have shown that the crystallization behavior and thermal stability of the composite were enhanced with the inclusion of crab shell powder. The presence of crab shell powder in the hybrid composite was identified using SEM with Energy-Dispersive X-ray Spectroscopy (EDS).

Keywords: crab shell powder; jute/carbon fiber; hybrid composites; mechanical properties; thermal properties; SEM with EDS

1. Introduction

Every year, huge quantities of seafood waste are created, which mainly consist of fish scales, crab shells, lobsters, etc., and are dumped on wastelands. These wastes create pollution in the environment and have harmful effects on society. Furthermore, their proper disposal involves significant investment. Instead, if these wastes are recycled and collected, they can be used in the development of biodegradable materials, which will help in the sustainable growth of the economy.

Global urbanization produces 7–10 billion tons of waste residues every year, and there is a need for recycling [1,2]. Oladele and Isola [3] have developed goat bone-reinforced epoxy composites for biomedical applications. The EDX data of the goat bone reinforcement showed calcium and phosphorus as the main elements. The epoxy composite with 16% goat bone reinforcement has improved mechanical properties such as tensile strength, flexural

strength, and hardness. In agriculture-based countries like India, cows have become part of people's lives. Therefore, researchers have focused on the usage of cow dung in medical, agricultural, and industrial applications [4,5]. Olabisi [6,7] developed composites using cocoa bean shell and agro-waste residue to enhance the mechanical properties of aluminum. Palm kernel shell was another agro-waste residue produced globally that was reinforced with aluminum alloys to prepare a composite with enhanced performance characteristics [8–10]. Petrovic et al. [11] have developed a composite using walnut-shell ash as a reinforcement to improve the strength and hardness of Al_2O_3. Tile et al. [12] have investigated the effect of the inclusion of groundnut shell particulates on the hardness, yield strength, and ultimate tensile strength of Al-Mg-Si composites. The results showed an enhancement in properties with an increase in the weight percentage of groundnut shell particulates up to 10%. Eggshell waste particles, consisting of 95% $CaCO_3$ ceramic particles, have also proved to be desirable reinforcements for the composites [13,14].

The poultry, fishery, meat, and leather industries are major sources of animal waste. Especially seafood wastes discarded at sea generate toxic gasses, resulting in the pollution of water, air, and soil [15–18]. Arulvel et al. [19] have investigated the role of crab shell wastes in coating applications by examining their thermal stability, surface properties, and stability. Ahmed et al. [20] have conducted studies to enhance the mechanical and thermal properties of chitosan-based nanocomposite films used as food packaging materials. The blend of crab shell chitosan and graphene oxide nanosheets has improved the tensile properties and transition temperature of the composite films due to the more compact network structure between crab shell and graphene oxide. This was ascertained from the FTIR and SEM analyses of the composite films. Subaer et al. [21] examined the effect of chitosan on the mechanical, thermal, and anti-bacterial properties of geopolymer pastes used in the manufacturing of hybrid composites. The Differential Scanning Calorimetry (DSC) and bending test results of the composites showed high thermal resistance and better flexural strength. Also, the addition of 1.5 wt. % of chitosan powder reduced the growth of the bacteria, as observed from Total Count Plate (TCP) tests. Singaravelu et al. [22] compared the thermal stability, fade rate, and recovery rate of brake pads developed using chemically treated crab shell powder and thermally processed crab shell powder. Thermogravimetric analysis results showed better thermal stability for the thermally processed crab shell powder-based brake pads, whereas the fade rate and recovery rate were better for the chemically treated crab shell powder-based brake pads when tested using the Chase test following IS2742 Part 4 [23]. Gadgey and Bahekar [24] have investigated the mechanical behavior of the crab shell in different forms. The stress–strain curves obtained for crab cuticle exhibited low strain discontinuity, indicating brittle failure. For the crab exoskeleton, tensile tests were conducted in longitudinal and normal directions on wet and dry samples. The results showed the anisotropic nature of mechanical properties along the longitudinal direction, i.e., no permanent deformation, whereas deformation exists in the normal orientation. Also, the hardness of the outer layer is twice that of the inner layer of the crab shell. Kumaran et al. [25] have developed jute fiber epoxy composites reinforced with treated and untreated Portunus sanguinolentus shell powder. The mechanical characterization of these composites was compared with that of neat jute fiber epoxy composites for their hardness, tensile strength, flexural strength, impact, compression strength, and thermal stability. Soundhar et al. [26] investigated the fatigue behavior and damage progress of chitosan/sisal/glass fiber (CS/SF/GF)-reinforced epoxy composites under cyclic stress. The fatigue behavior of the composite was evaluated based on the fatigue endurance limit of the composite. Also, XRD, FTIR, and SEM-EDS analyses were carried out to determine the ability of the composite to form a new apatite layer on the surface. Ismail et al. [27] compared the crystal phase, crystal weight percentage, crystal size, crystal system, and elemental composition of calcium carbonate extracted from green mussel and crab shells with commercially available calcium carbonate. It was observed that green mussel $CaCO_3$ is nearly identical to commercial $CaCO_3$, whereas crab shell $CaCO_3$ contains a number of components other than Ca, C, and O. Joseph et al. [28] developed PLA-reinforced fish

scale powder filament for 3D printing. The test specimens were printed based on fused deposition modeling with three different combinations (10%, 20%, and 30%) of fish scale powder with PLA. Mechanical characterizations of the 3D-printed specimens exhibited the best performance in tensile and flexural strengths with a 20% fish scale powder composite. Cheng et al. [29] contributed to providing insights for future research to bridge the gaps between advanced process and continuous fiber-reinforced composite lightweight structures (CFRSs) multi-level design and fully explored the potentials of 3D-printed CFRSs for a wide range of applications. In the past, many researchers have reported the inclusion of carbon nanoparticles as filler materials in polymer composites, which has improved their mechanical and thermal properties. In recent years, researchers have attempted to study the behavior of polymer composites when they are added to natural filler materials like plant, animal, and sea waste. One such naturally available filler material is crab shell. The present research aims to study the mechanical and thermal properties of a jute/carbon fiber epoxy composite reinforced with crab shell powder for lightweight applications. The composite laminates were fabricated and tested for mechanical loading to determine the influence of crab shell powder on the tensile, flexural, and impact strengths, as well as the hardness of the composite. DSC and TGA tests were performed, and thermal properties were extracted and analyzed. The morphology of the fractured surface of tensile test specimens was studied using the SEM technique. The optimal weight percentage of crab shell powder was estimated, for which the performance of the hybrid composite was enhanced in terms of mechanical and thermal properties.

2. Materials and Methods

2.1. Materials

The hybrid composites used in this study consist of jute and carbon fibers as the reinforcement, along with a matrix comprising epoxy resin mixed with crab shell powder and hardener. The physical properties of the jute and carbon fibers are listed in Table 1. The epoxy resin and hardener were mixed in a weight ratio of 10:1. The crab shells procured from the local market were properly cleansed for the removal of meat and appendages left in the shells. Figure 1a shows the crab shells after cleaning. The shells were then dried and ground into coarse particles, as shown in Figure 1b. The particles were then processed in a ball mill to make them into a fine powder, as shown in Figure 1c.

Table 1. Specifications of jute and carbon fiber.

Property	Jute Fiber	Carbon Fiber
Strength	380 g/m^2	300 g/m^2
Thickness	0.6 mm	0.4 mm
Density	1.5 g/cm^3	1.8 g/cm^3

(**a**) (**b**) (**c**)

Figure 1. (**a**) Cleaned crab shells; (**b**) coarse particles of crab shells; (**c**) crab shell powder.

2.2. Fabrication of Crab Shell Powder Hybrid Composites

A hybrid composite is a combination of synthetic and natural fibers and is developed for the improved mechanical behavior of two reinforcements. In this study, carbon and jute fibers were chosen as the synthetic and natural reinforcements of the hybrid composite, respectively, along with crab shell powder as the natural filler material.

The fabrication of the hybrid composite was given in the form of a flowchart, as shown in Figure 2. The jute and carbon fibers were placed in alternate layers during the manufacturing of the hybrid composite in a weight ratio of 67:33, and the weight proportion of reinforcement to the matrix was 54:46. The fine powder of crab shell was mixed into epoxy resin in different weight percentages, as given in Table 2. Figure 3 shows the composite laminates fabricated using the hand lay-up process. The specimens for tensile, flexural, and impact tests were cut from the composite laminates as per the dimensions of ASTM standards, shown in Figure 4.

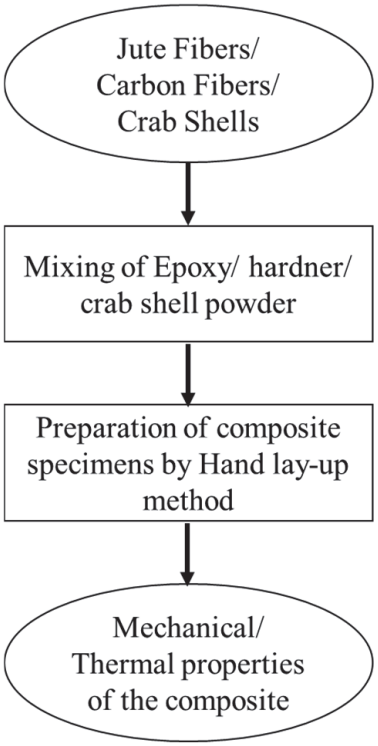

Figure 2. Flowchart for the composite preparation.

Table 2. Designation and composition of the developed composites.

Designation	Composite Composition
Pure epoxy	100% Epoxy
1%	1% Crab shell powder + 99% Epoxy
3%	3% Crab shell powder + 97% Epoxy
5%	5% Crab shell powder + 95% Epoxy
7%	7% Crab shell powder + 93% Epoxy

Figure 3. Fabricated crab shell powder hybrid composites.

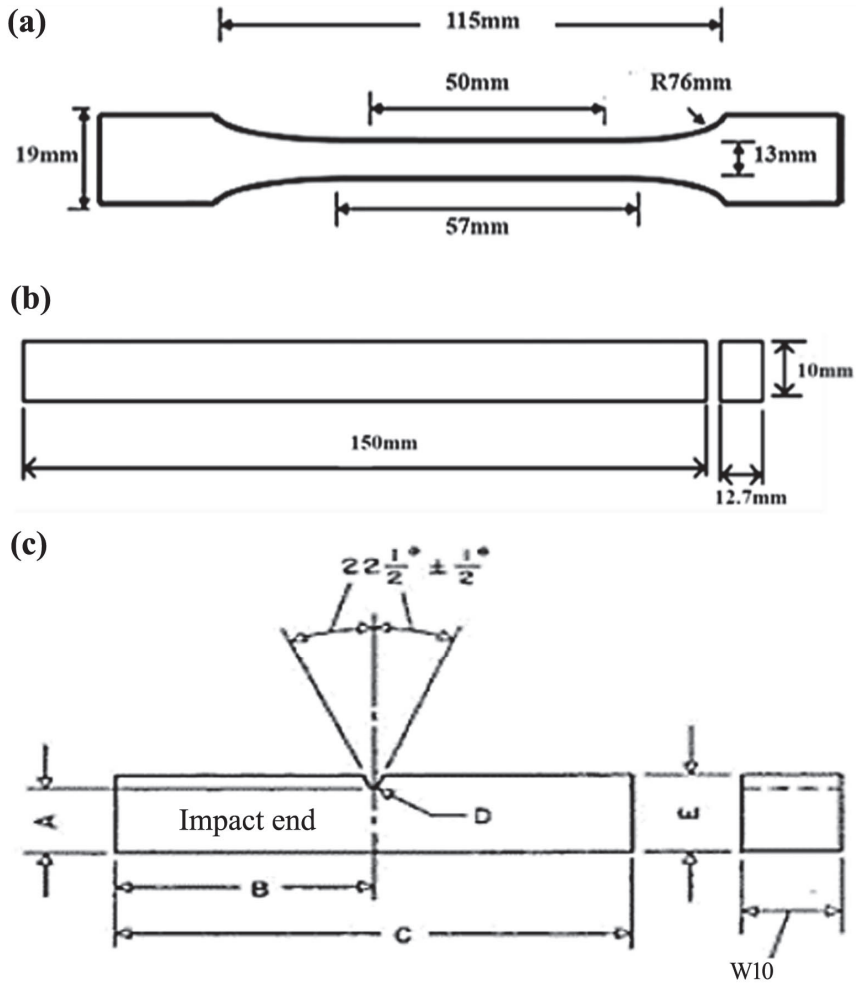

Figure 4. Schematic diagrams of specimens for (**a**) tensile, (**b**) flexural, and (**c**) impact tests.

2.3. Mechanical Testing

The hybrid composites were produced with varying weight percentages of crab shell powder and tested for mechanical properties such as tensile strength, flexural strength, impact strength, and hardness. The tension test was conducted using a 5-ton (Fuel Instruments and engineers make) ultimate tensile machine at a crosshead speed of 4 mm/min. The average of three values of the tensile test was considered for the same weight percentage of crab shell powder in order to confirm the tensile strength results. Ultimate tensile strength and elongation were determined from the tension test. A three-point bend test was conducted to determine the flexural strength of the composites. The specimen bends and breaks when the load is applied at its center. An Izod impact test was conducted using an XJJU-5.5 model impact test rig made in China, on which a specimen was mounted and a ram was allowed to swing and break the specimen. The energy needed to fracture the specimen was determined using the impact test. A Micro Vickers hardness tester from HDNS-Kelly Instruments made in China was utilized for finding the hardness value, where the loading range was 10 g to 1 kg. Scanning electron microscopy, a Carl Zeiss instrument made in Germany, was used to record the fractured surface of the tested specimens in order to analyze the morphology and structure of the crab shell powder and the matrix.

2.4. Thermal Testing

The thermal properties of the composite material were analyzed using the Differential Scanning Calorimetry (DSC) technique. DSC analysis was performed using the Themys One+ apparatus made in France, which has the capacity to heat up to 1600 °C at a rate ranging from 0.01 to 100 °C/min. The amount of heat absorbed or released by the composite sample was estimated in this analysis. The thermal stability of the polymer composites will depend on their heat resistance and thermal oxidation capability. Heat resistance measures the material's ability to remain unaffected by heat, whereas thermal oxidation capability is used to evaluate its resistance to degradation. A Thermogravimetric analyzer (TGA) was utilized to investigate the heat resistance and thermal degradation of the composites. In this analysis, the thermal stability of the composite sample was determined when it was subjected to high thermal loading.

2.5. Characterization Testing

SEM with EDS was employed to identify the major elements available in the composites. Similarly, the atomic percentage of the elements was also estimated to understand the mapping analysis of the content and the performance.

3. Results and Discussion

3.1. Tensile Behavior of the Crab Shell Powder Hybrid Composites

The tensile properties of the crab shell powder hybrid composites were used to analyze the effect of crab shell powder on the tensile behavior of the hybrid composites. Figure 5 shows the load–deflection curves obtained from the tension tests for hybrid composites with varying weight percentages of crab shell powder. It clearly shows that the tension test specimens of the hybrid composites exhibited failure due to their brittle nature. For the pure epoxy composite, the fracture occurred at a load of 3355 N with an elongation of 1.25 mm. Similarly, for the crab shell powder hybrid composites with 1%, 3%, 5%, and 7%, fracture occurs at 3428 N, 3640 N, 4118 N, and 3844 N, with elongations of 2.32 mm, 2.7 mm, 2.64 mm, and 2.53 mm, respectively, as shown in Figure 6. Therefore, it was confirmed that the load-carrying capacity of the crab shell powder hybrid composite was enhanced with the addition of crab shell powder.

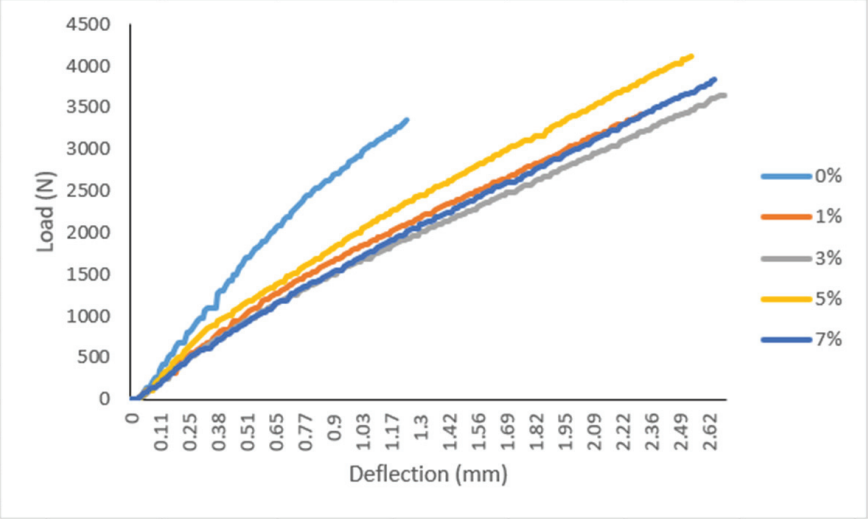

Figure 5. Load vs. deflection curve for the crab shell powder hybrid composites.

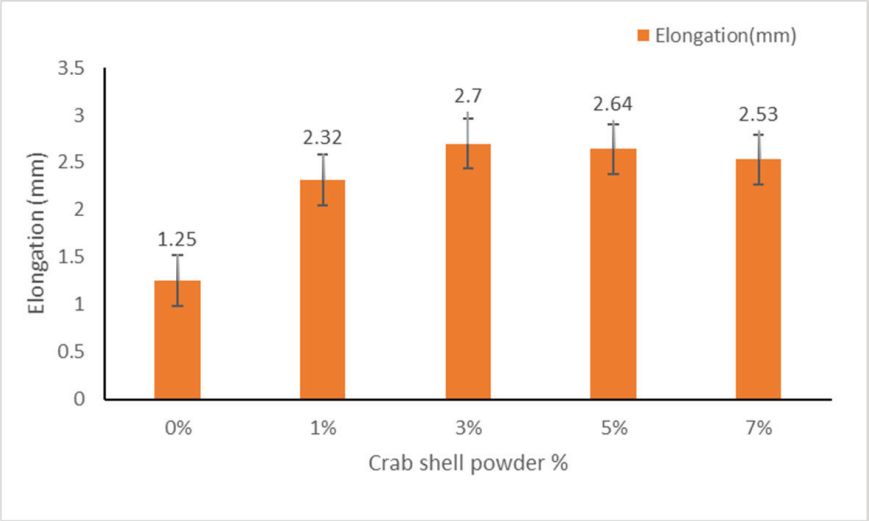

Figure 6. Elongation of the crab shell powder hybrid composites.

The stress–strain curves obtained for the crab shell powder hybrid composites are shown in Figure 7, and information about the tensile strength of the crab shell powder hybrid composites is represented in a bar chart, as shown in Figure 8. It shows an upward trend in the tensile strength of the composite up to a 5% weight of the crab shell powder, and further increases in the crab shell powder weight percentage showed a decline in tensile strength. When compared with all the other weight percentages of the crab shell powder hybrid composites, maximum tensile strength was observed at the 5% weight of crab shell powder. The reason for increased tensile strength in the 5% crab shell powder hybrid composite was strong bonding between the matrix and reinforcement fibers. Beyond this point, the tensile strength decreases due to the agglomeration of crab shell powder in the epoxy resin. The tensile strengths for the 1%, 3%, 5%, and 7% crab shell powder hybrid composites are 7.8%, 14.5%, 20.9%, and 5.5%, respectively, compared to the pure epoxy hybrid composites. From the results, it can be confirmed that the tensile strength of jute/carbon fiber hybrid composites was enhanced with the addition of crab shell powder.

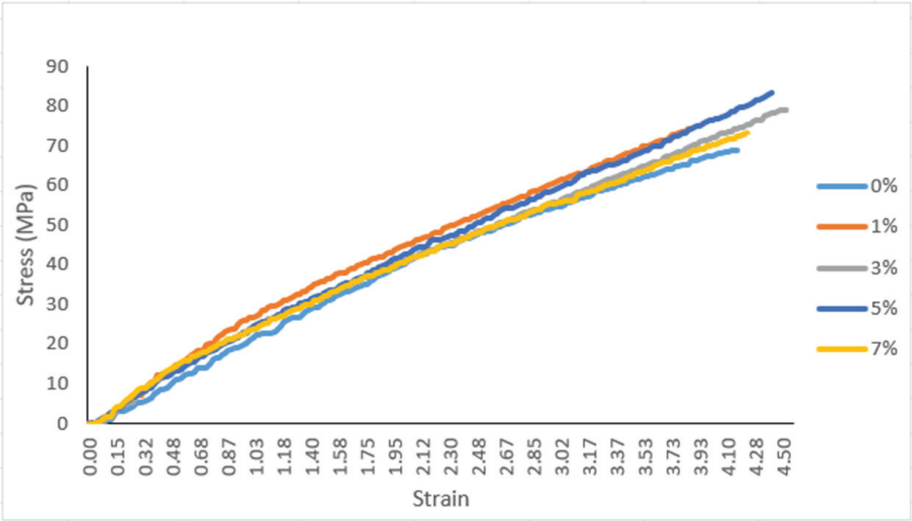

Figure 7. Stress vs. strain curve for the crab shell powder hybrid composites.

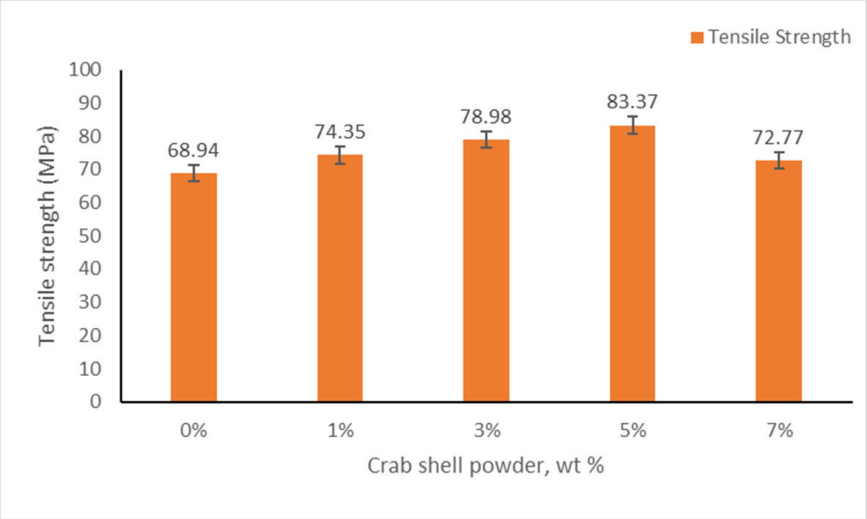

Figure 8. Ultimate tensile strength of the crab shell powder hybrid composites.

3.2. Flexural Behavior of the Crab Shell Powder Hybrid Composites

The flexural behavior of the crab shell powder hybrid composites was analyzed by conducting a series of three-point bending tests on 1%, 3%, 5%, and 7% crab shell powder hybrid composite specimens, and the test results are shown in Figure 9. It shows an upward trend in the flexural strength of the hybrid composites as the amount of crab shell powder is increased. This enhancement in flexural strength is mainly due to the good bonding between the epoxy and crab shell powder. Also, during the flexural test, the outer layer of the fiber experiences tensile load, while the inner layer experiences compressive load, which acts as the carriers of the load and helps in the uniform distribution of stress within the matrix.

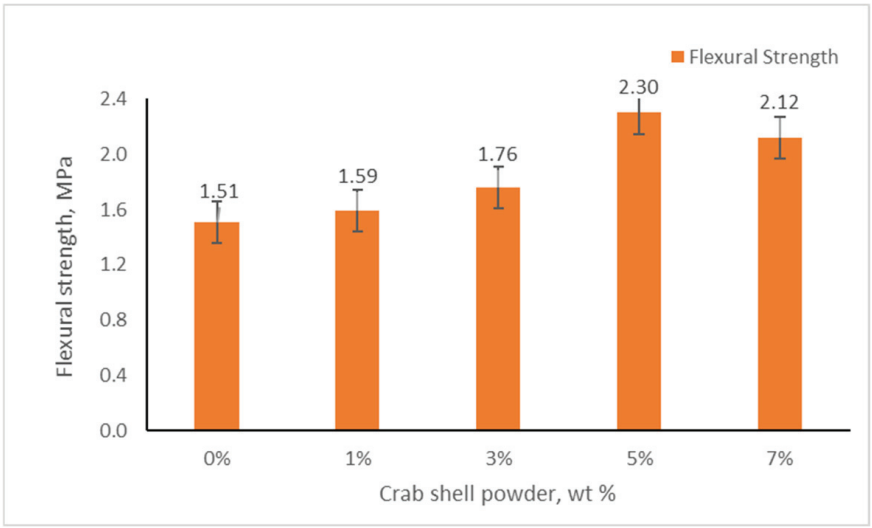

Figure 9. Flexural strength of the crab shell powder hybrid composites.

3.3. Impact Strength of the Crab Shell Powder Hybrid Composites

The capability of the material to resist fractures due to suddenly applied loads is termed impact strength. The impact behavior was studied in terms of energy absorbed during fracture caused by suddenly applied loads. Figure 10 shows the effect of crab shell powder on the impact strength of the hybrid composite. As the weight percentage of the crab shell powder increases up to 5%, the impact strength of the hybrid composite also increases, but further increases in crab shell powder decrease the impact strength.

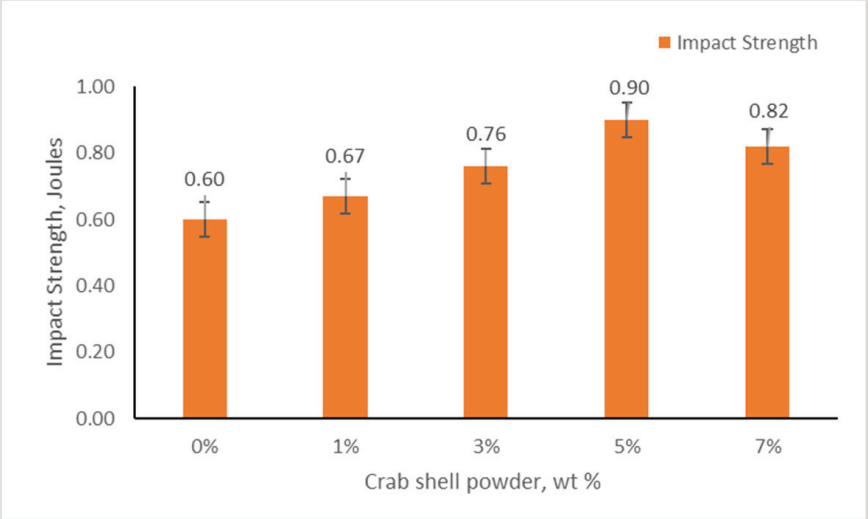

Figure 10. Impact strength of the crab shell powder hybrid composites.

3.4. Hardness of the Crab Shell Powder Hybrid Composites

The shore D hardness values for the crab shell powder hybrid composites are presented in Figure 11. The inclusion of crab shell powder in the hybrid composite improved the hardness value from 71.5 to 94.9, with the maximum hardness value obtained at 5% crab shell powder. The main reason for the improved hardness was that fewer internal pores developed in the composite due to the inclusion of carbon shell powder.

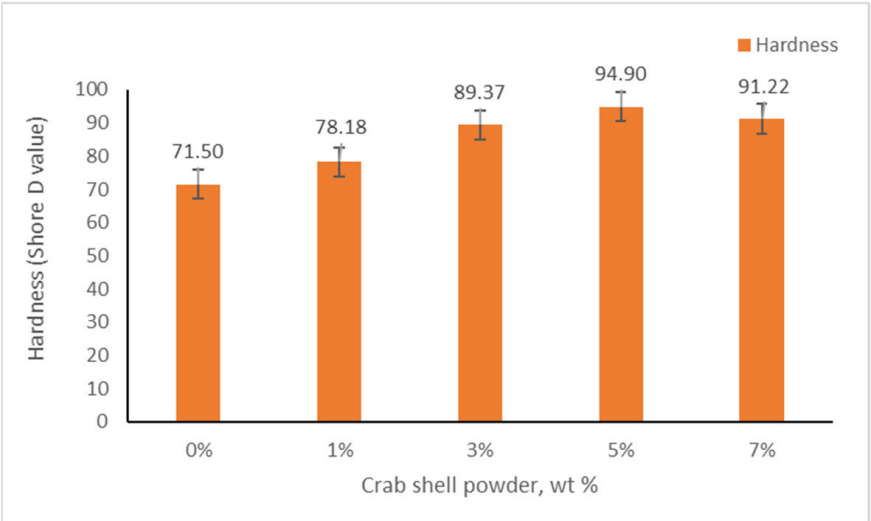

Figure 11. Hardness of the crab shell powder hybrid composites.

3.5. Tensile Fractured Surface Morphology

The tensile-fractured samples were analyzed to understand the fracture mechanisms of the composites using SEM micrographs. Figure 12 shows the fractured surfaces of the crab shell powder hybrid composites under tensile load. For the pure epoxy hybrid composites, the nature of fracture exhibited in the tension test was brittle. This is due to the matrix damage in the epoxy resin, as shown in Figure 12a. In the case of the 1% crab shell powder hybrid composites, the tensile-fractured samples displayed poor adhesion between the fiber and matrix, accompanied by matrix damage, as shown in Figure 12b. Figure 12c shows the tensile-fractured samples of the 3% weight crab shell powder hybrid composites, in which the fracture was due to both fiber bundle and matrix damages [30]. Figure 12d shows the fracture sample of the 5% crab shell powder hybrid composites,

which displayed good interfacial bonding between the fiber and matrix. Also, the crab shell powder eliminated matrix damage and enhanced the mechanical properties of the hybrid composites. Similar kinds of bonding can be seen for the 7% crab shell powder hybrid composites, except for fiber pullouts, as shown in Figure 12e. The SEM image showing the dispersion of crab shell powder within the epoxy matrix is shown in Figure 12f, and the crab shell powder size obtained was found to be 260 µm. It was confirmed that crab shell powder at weights below 5% have poor fiber matrix interfacial bonding and poor load-carrying capacity in the composites.

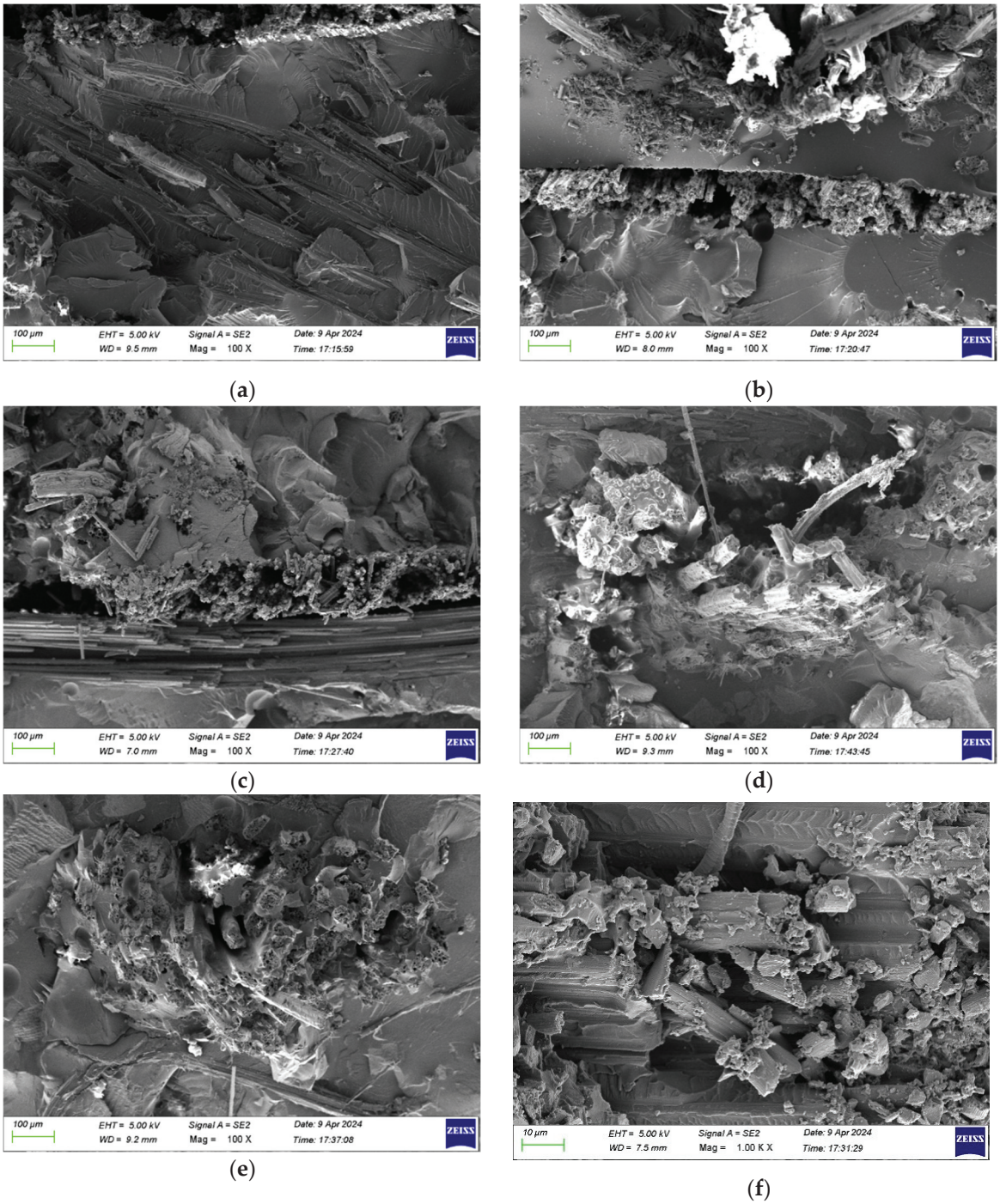

Figure 12. SEM images of the hybrid composites with (**a**) pure epoxy; (**b**) 1% crab shell powder; (**c**) 3% crab shell powder; (**d**) 5% crab shell powder; (**e**) 7% crab shell powder; and (**f**) Dispersion of crab shell powder within the epoxy matrix.

3.6. Differential Scanning Calorimetry (DSC) Analysis

To investigate the effect of crab shell powder on the crystallinity and melting point temperature of the hybrid composites, DSC analysis was conducted. A sample of 30 mg was collected from each specimen and placed on a pan made of Alumina (Al_2O_3). The samples were characterized under an inert gas atmosphere during heating to a temperature range of 0 to 400 °C. Figure 13a explains that the pure epoxy hybrid composite displayed a melting point temperature of 212.03 °C. Figure 13b,c displayed the changes in the peak temperatures of crystallization for the hybrid composites with 3% and 5% crab shell powder. The rate of heat flow was observed closely when the temperature reached the melting point of the hybrid composites.

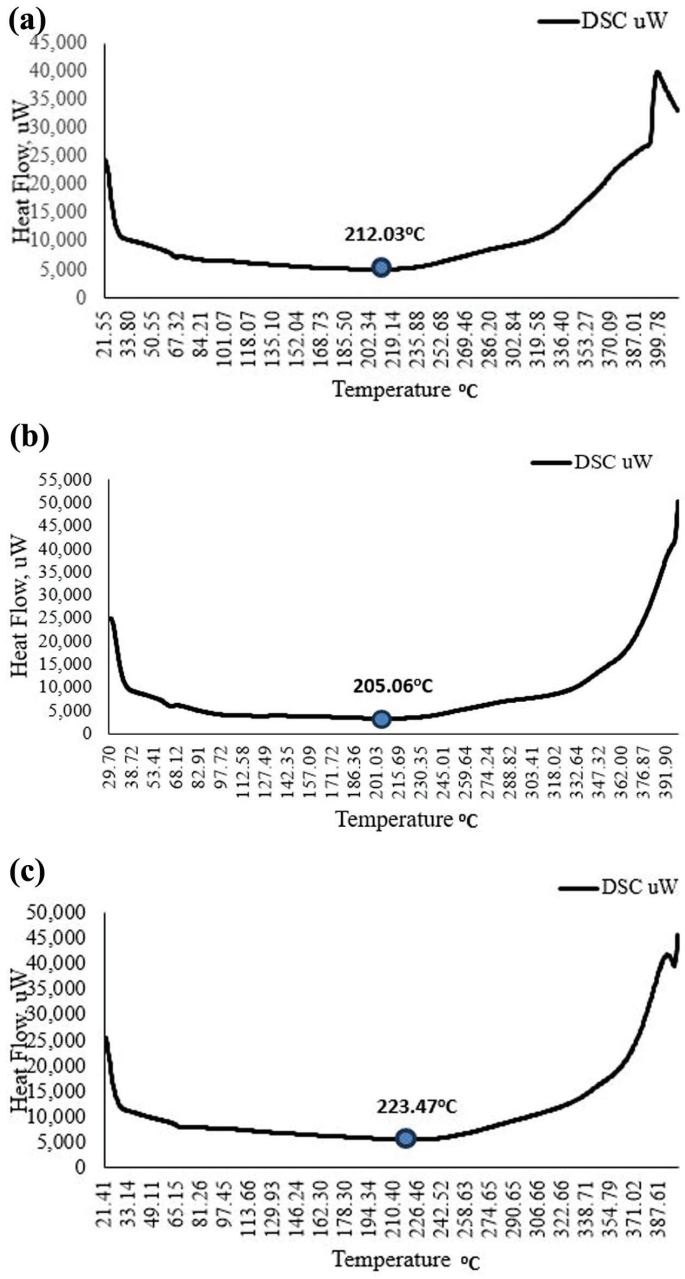

Figure 13. (**a**) DSC plot for the pure epoxy hybrid composites; (**b**) DSC plot for the 3% crab shell powder hybrid composites; (**c**) DSC plot for the 5% crab shell powder hybrid composites.

The crystallization temperatures measured for the hybrid composite with varying weight percentages of crab shell powder exhibited an interesting development. At lower

proportions of crab shell powder, as concentration increases, the crystallization temperature of the composite increases. However, after a certain limit of crab shell powder weight percentage, the crystallization temperatures began to decrease. For example, the crystallization temperature of the pure epoxy hybrid composite lowers from 212.03 to 223.47 °C with the addition of 5% crab shell powder. This outcome shows that with the inclusion of crab shell powder, the crystallization behavior of the hybrid composite changes, starting with an increase in crystallization temperature for the low weight percentages of crab shell powder and ending with a decrease in crystallization temperature for the high weight percentages of crab shell powder.

It was also observed that the jute/carbon fiber hybrid composite showed a maximum heat flow of 5094 mW (Figure 13a), but with the reinforcement of a 5% weight fraction of crab shell powder, the hybrid composite showed a maximum heat flow of 5532 mW (Figure 13c). Hence, it can be concluded that the heat flow capacity of the hybrid composite increased by 8.6% upon reinforcement with crab shell powder.

3.7. Thermogravimetry Analysis (TGA)

To evaluate the effect of crab shell powder on the thermal stability of the hybrid composite, thermogravimetric analysis was performed. The samples were characterized under an inert atmosphere during heating to a predetermined temperature of 820 °C. Figure 14a shows the breakdown curve for the pure epoxy hybrid composite, and Figure 14b,c show the breakdown curves for hybrid composites with 5% and 7% crab shell powder. It can be observed that the thermal stability has improved prominently due to the inclusion of crab shell powder as reinforcement in the hybrid composites.

The initial temperature for thermal stability of the pure epoxy hybrid composite was found to be 395.07 °C. However, the inclusion of crab shell powder in the hybrid composite led to an enhancement in thermal stability. For example, the starting temperature of the hybrid composite with 5% crab shell powder was found to be 419.57 °C, compared to 395.07 °C of the pure epoxy hybrid composite, signifying an improvement in thermal stability. This improvement in thermal stability was observed for crab shell powder weight percentages up to 5%, followed by a slight decrease at the 7% crab shell powder weight percentage. It was also demonstrated from the experiments that the temperature rise occurred in the crab shell powder hybrid composites, where the highest breakdown rate occurred. This behavior of crab shell powder hybrid composites led to good thermal characteristics and high thermal stability.

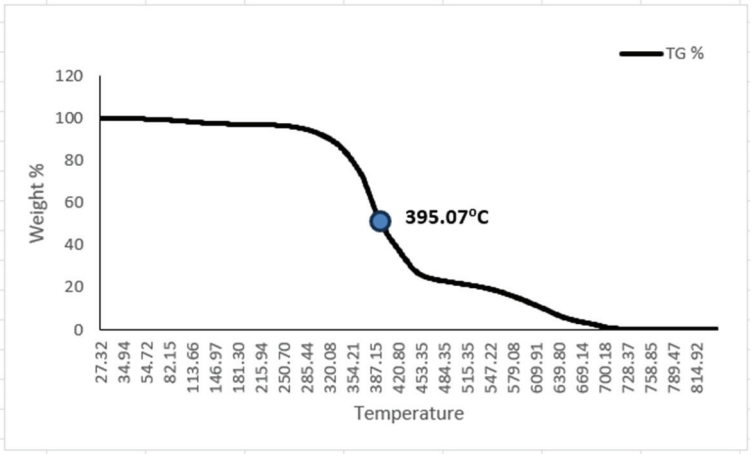

(**a**)

Figure 14. *Cont.*

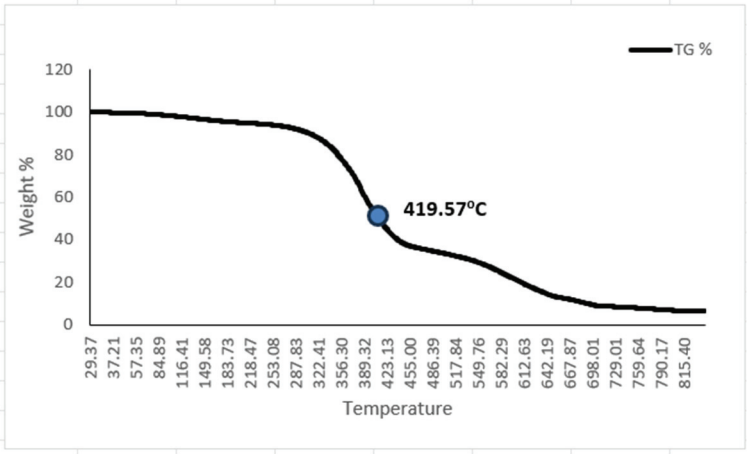

(**b**)

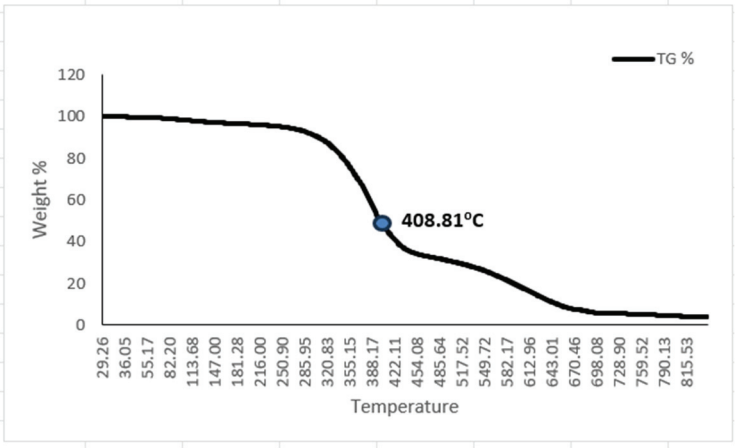

(**c**)

Figure 14. (**a**) TGA curve for the pure epoxy hybrid composites; (**b**) TGA curve for the 5% crab shell powder hybrid composites; (**c**) TGA curve for the 7% crab shell powder hybrid composites.

It is also possible to verify from the TGA curves of crab shell powder hybrid composites, in comparison to the pure epoxy hybrid composite, that the initial and maximum decomposition temperatures of crab shell powder hybrid composites were improved. This enhancement in thermal stability may indicate better interface adhesion between the crab shell powder and epoxy matrix.

3.8. Characterization of the Composites Using SEM with EDS Data

The variation in the chemical composition caused by the inclusion of crab shell powder was studied using EDS. Figure 15a–c display the SEM images and EDS of pure epoxy and crab shell powder (3% and 5%) hybrid composites. The presence of $CaCO_3$ was confirmed from the EDS data of the crab shell powder hybrid composites, and its atomic percentage increased with the increase in weight percentage of the crab shell powder. The Ca content of the crab shells was determined to be 0.8 wt% and 1.02 wt% for 3% and 5% crab shell powder hybrid composites, as shown in Figures 15b and 15c, respectively.

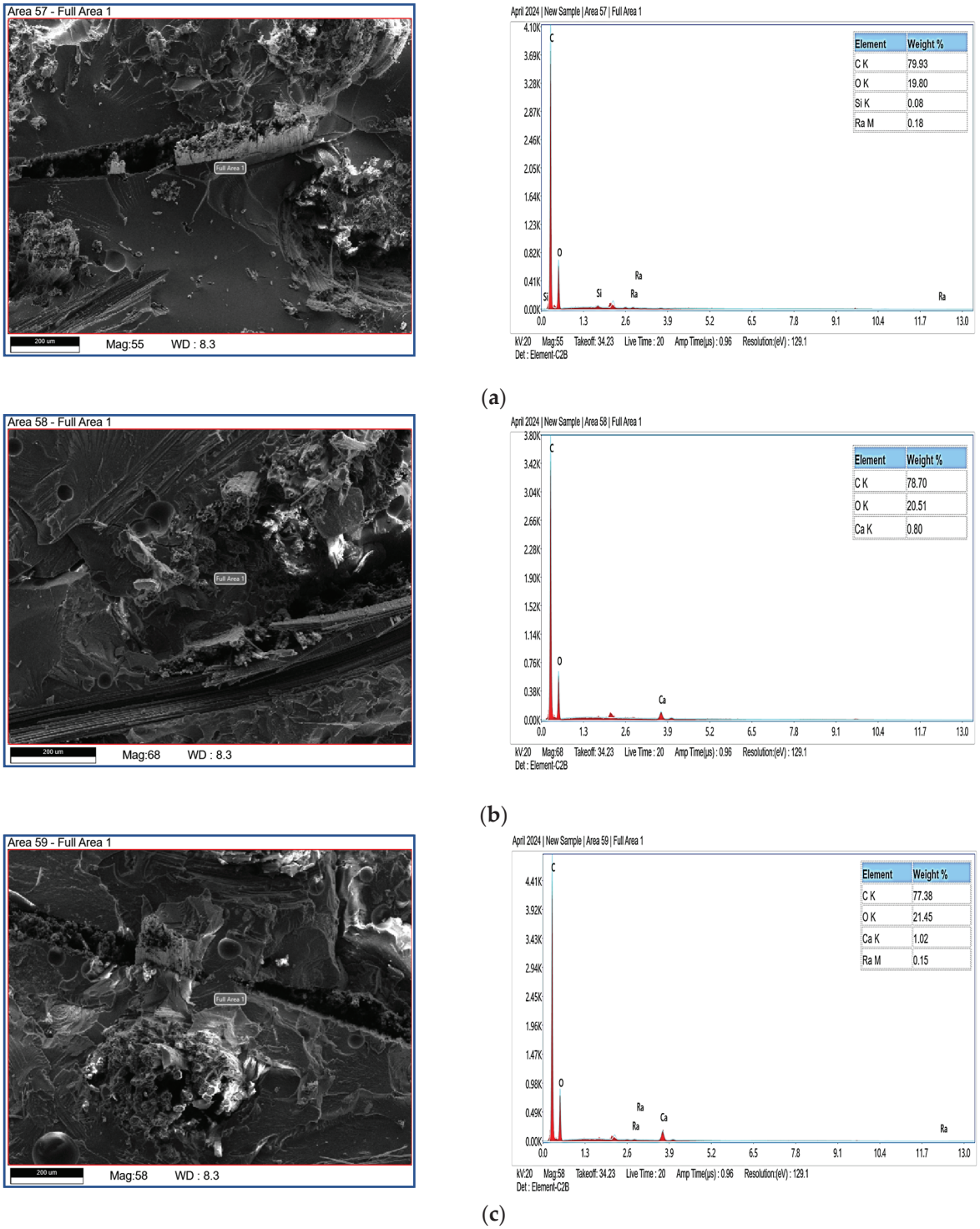

Figure 15. (**a**) SEM-EDS evaluation of pure epoxy hybrid composites; (**b**) SEM-EDS evaluation of 3% crab shell powder hybrid composites; (**c**) SEM-EDS evaluation of 5% crab shell powder hybrid composites.

4. Conclusions

In summary, the jute/carbon fiber composites were fabricated using the hand-layup method with the reinforcement of crab shell powder. The effect of crab shell powder on the tensile, flexural, and impact loadings, along with the hardness, was determined for the composite. The composites were characterized by DSC and TG to assess their heat flow

capacity and thermal stability. SEM analysis was carried out to study the morphology of the tensile fracture surface. The following are the conclusions drawn from this research:

1. The 5% crab shell powder hybrid composite showed enhancements in tensile, flexural and impact strength by 21%, 52%, and 50%, respectively, compared to other weight percentages.
2. The inclusion of 5% crab shell powder enhanced the hardness of the hybrid composite by 33%.
3. The heat flow capacity of the 5% crab shell powder hybrid composite was improved by 8.6%.
4. The thermal stability of the hybrid composite was improved as the initial decomposition temperature was raised from 395.06 °C to 419.57 °C with the inclusion of 5% crab shell powder.
5. SEM images of the crab shell powder hybrid composites showed good interfacial bonding between the fiber and matrix.
6. The SEM with EDS data showed the presence of crab shell powder in the hybrid composites.

Author Contributions: Conceptualization, R.P.B.K., M.K. and M.C.; methodology, R.P.B.K., M.K., R.K.B., A.A.M. and R.S.; software, R.P.B.K. and M.K.; validation, R.P.B.K., M.K., R.K.B., A.A.M., R.S. and M.C.; formal analysis, R.P.B.K., M.K. and M.C.; investigation, R.P.B.K., M.K., R.K.B., A.A.M., R.S. and M.C.; resources, R.P.B.K., M.K., R.K.B., A.A.M. and R.S.; data curation, R.P.B.K., M.K., R.K.B., A.A.M. and R.S.; writing—original draft preparation, R.P.B.K., M.K., R.K.B., A.A.M., R.S. and M.C. writing—review and editing, R.P.B.K., M.K., R.K.B., A.A.M., R.S. and M.C.; visualization, R.P.B.K., M.K., R.K.B., A.A.M., R.S. and M.C.; supervision, R.P.B.K., M.K. and M.C.; project administration, R.P.B.K., M.K. and M.C. All authors have read and agreed to the published version of the manuscript.

Funding: This research received no external funding.

Data Availability Statement: The original contributions presented in the study are included in the article, further inquiries can be directed to the corresponding author.

Conflicts of Interest: The authors declare no conflicts of interest.

References

1. Bahrami, A.; Soltani, N.; Pech-Canul, M.I.; Gutiérrez, C.A. Development of metal-matrix composites from industrial/agricultural waste materials and their derivatives. *Crit. Rev. Environ. Sci. Technol.* **2016**, *46*, 143–208. [CrossRef]
2. Das, O.; Babu, K.; Shanmugam, V.; Sykam, K.; Tebyetekerwa, M.; Neisiany, R.E.; Försth, M.; Sas, G.; Gonzalez-Libreros, J.; Capezza, A.J.; et al. Natural and industrial wastes for sustainable and renewable polymer composites. *Renew. Sustain. Energy Rev.* **2022**, *158*, 112054. [CrossRef]
3. Oladele, I.O.; Isola, B.A. Development of bone particulate reinforced epoxy composite for biomedical application. *J. Appl. Biotechnol. Bioeng.* **2016**, *1*, 35–40.
4. Ma, Y.; Wu, S.; Zhuang, J.; Tong, J.; Qi, H. Tribological and physio-mechanical characterization of cow dung fibers reinforced friction composites: An effective utilization of cow dung waste. *Tribol. Int.* **2019**, *131*, 200–211. [CrossRef]
5. Bose, S.; Pandey, A.; Mondal, A.; Mondal, P. A novel approach in developing aluminum hybrid green metal matrix composite material using waste eggshells, cow dung ash, snail shell ash and boron carbide as reinforcements. In *Advances in Industrial and Production Engineering*; Springer: Singapore, 2019; pp. 551–562.
6. Olabisi, A.I.; Adam, A.N.; Okechukwu, O.M. Development and assessment of composite brake pad using pulverized cocoa beans shells filler. *Int. J. Mater. Sci. Appl.* **2016**, *5*, 66–78.
7. Olabisi, A.I.; Boye, T.E.; Eyere, E. Evaluation of pure aluminium inoculated with varying grain sizes of an agro-waste based inoculant. *Adv. Sci. Technol. Eng. Syst. J.* **2017**, *2*, 14–25. [CrossRef]
8. Fono-Tamo, R.S.; Koya, O.A. Characterisation of Pulverised Palm Kernel Shell for Sustainable Waste Diversification. *Int. J. Sci. Eng. Res.* **2013**, *4*, 6–10.
9. Aigbodion, S.; Ezema, I.C. Multifunctional A356 alloy/PKSAnp composites: Microstructure and mechanical properties. *Def. Technol.* **2019**, *16*, 731–736. [CrossRef]
10. Oladele, I.O.; Okoro, A.M. The effect of palm kernel shell ash on the mechanical properties of as-cast aluminium alloy matrix composites. *Leonardo J. Sci.* **2016**, *28*, 15–30.
11. Petrović, J.; Mladenović, S.; Marković, I.; Dimitrijević, S. Characterization of Hybrid Aluminum Composites Reinforced with Al_2O_3 Particles and Walnut-Shell Ash. *Mater. Technol.* **2022**, *56*, 115–122. [CrossRef]

12. Tile, J.M.; Nyior, G.B.; Sidi, M.S. Mechanical properties of Al-Mg-Si/Groundnut shell particulate composite produced by stir casting method. *Am. J. Eng. Res.* **2018**, *7*, 247–252.
13. Kumar, S.; Dwivedi, S.; Dwivedi, V.K. Synthesis and characterization of ball-milled eggshell and Al_2O_3 reinforced hybrid green composite material. *J. Met. Mater. Miner.* **2020**, *30*, 67–75. [CrossRef]
14. Dwivedi, S.P.; Saxena, A.; Sharma, S.; Srivastava, A.K.; Maurya, N.K. Influence of SAC and eggshell addition in the physical, mechanical and thermal behaviour of Cr reinforced aluminium based composite. *Int. J. Cast Met. Res.* **2021**, *34*, 43–55. [CrossRef]
15. Sinkiewicz, I.; Śliwińska, A.; Staroszczyk, H.; Kołodziejska, I. Alternative methods of preparation of soluble keratin from chicken feathers. *Waste Biomass Valoriz.* **2017**, *8*, 1043–1048. [CrossRef]
16. Govindharaj, M.; Roopavath, U.K.; Rath, S.N. Valorization of discarded Marine Eel fish skin for collagen extraction as a 3D printable blue biomaterial for tissue engineering. *J. Clean. Prod.* **2019**, *230*, 412–419. [CrossRef]
17. Eddya, M.; Tbib, B.; Khalil, E.H. A comparison of chitosan properties after extraction from shrimp shells by diluted and concentrated acids. *Heliyon* **2020**, *6*, e03486. [CrossRef] [PubMed]
18. Boughriba, S.; Souissi, N.; Jridi, M.; Li, S.; Nasri, M. Thermal, mechanical and microstructural characterization and antioxidant potential of Rhinobatoscemiculusgelatin films supplemented by titanium dioxide doped silver nanoparticles. *Food Hydrocoll.* **2020**, *103*, 105695. [CrossRef]
19. Arulvel, S.; Elayaperumal, A.; Jagatheeshwaran, M.S. Discussion on the feasibility of using proteinized/deproteinized crab shell particles for coating applications: Synthesis and characterization. *J. Environ. Chem. Eng.* **2016**, *4*, 3891–3899.
20. Ahmed, J.; Mehrajfatema, M.; Arfat, Y.A.; Thai, T.L.A. Mechanical, thermal, structural and barrier properties of crab shell chitosan/graphene oxide composite films. *Food Hydrocoll.* **2017**, *71*, 141–148. [CrossRef]
21. Subaer Kusumawati, Y.; Akhlus, S.; Akifah, N.; Fansuri, H. Thermo-Mechanical Properties of An Anti-Bacteria Coating Material Based on A Hybrid Composite Geopolymer-Chitosan. *Ceram. Silikáty* **2019**, *63*, 223–231. [CrossRef]
22. Singaravelu, D.L.; Ragh, M.R.; Vijay, R.; Manoharan, S.; Kchaou, M. Development and Performance Evaluation of Eco-Friendly Crab Shell Powder Based Brake Pads for Automotive Applications. *Int. J. Automot. Mech. Eng.* **2019**, *16*, 6502–6523. [CrossRef]
23. *IS 2742-4*; Automotive vehicles—Brake linings, Part 4: Co-efficient of friction—Method of test. Bureau of Indian Standards: New Delhi, India, 1994.
24. Gadgey, K.K.; Bahekar, A. Investigation of Mechanical Properties of Crab Shell: A Review. *Int. J. Latest Trends Eng. Technol.* **2019**, *8*, 268–281.
25. Kumaran, P.; Mohanamurugan, S.; Madhu, S.; Vijay, R.; Singaravelu, D.L.; Vinod, A.; Sanjay, M.R.; Siengchin, S. Investigation on thermo-mechanical characteristics of treated/untreated Portunus sanguinolentus shell powder-based jute fabrics reinforced epoxy composites. *J. Ind. Text.* **2020**, *50*, 427–459. [CrossRef]
26. Soundhar, A.; Jayakrishna, K.; Sultan, M.; Shah, M.; Safri, S.N.A. Investigations on fatigue analysis and biomimetic mineralization of glass fiber/sisal fiber/chitosan reinforced hybrid polymer sandwich composites. *J. Mater. Res. Technol.* **2021**, *10*, 512–525.
27. Ismail, R.; Cionita, T.; Shing, W.L.; Fitriyana, D.F.; Siregar, J.P.; Bayuseno, A.P.; Nugraha, F.W.; Muhamadin, R.C.; Junid, R.; Endot, N.A. Synthesis and Characterization of Calcium Carbonate Obtained from Green Mussel and Crab Shells as a Biomaterials Candidate. *Materials* **2022**, *15*, 5712. [CrossRef] [PubMed]
28. Arockiam, A.J.; Rajesh, S.; Karthikeyan, S.; Thiagamani, S.M.K.; Padmanabhan, R.G.; Hashem, M.; Fouad, H.; Ansari, A. Mechanical and thermal characterization of additive manufactured fish scale powder reinforced PLA biocomposites. *Mater. Res. Express* **2023**, *10*, 075504.
29. Cheng, P.; Peng, Y.; Li, S.; Rao, Y.; Duigou, A.L.; Wang, K.; Ahzi, S. 3D printed continuous fiber reinforced composite lightweight structures: A review and outlook. *Compos. Part B* **2023**, *250*, 110450. [CrossRef]
30. Pranavi, U.; Reddy, P.V.; Venukumar, S.; Cheepu, M. Evaluation of mechanical and wear properties of Al 5059/B_4C/Al_2O_3 hybrid metal matrix composites. *J. Compos. Sci.* **2022**, *6*, 86. [CrossRef]

Journal of
Composites Science

MDPI

Article

Electrochemical Jet Machining of Surface Texture: Improving the Strength of Hot-Pressure-Welded AA6061-CF/PA66 Joints

Weidong Liu [1,*], Yan Luo [1], Yonghua Zhao [2], Haipeng Zhou [3], Sansan Ao [3] and Yang Li [3,*]

[1] College of Aeronautical Engineering, Civil Aviation University of China, Tianjin 300300, China; 2022012177@cauc.edu.cn
[2] Department of Mechanical and Energy Engineering, Southern University of Science and Technology, Shenzhen 518055, China; zhaoyh@sustech.edu.cn
[3] School of Materials Science and Engineering, Tianjin University, Tianjin 300354, China; zhp_3868@tju.edu.cn (H.Z.); ao33@tju.edu.cn (S.A.)
* Correspondence: wdliu@cauc.edu.cn (W.L.); liyang86@tju.edu.cn (Y.L.)

Abstract: Diverse industries are witnessing an increase in demand for hybrid structures of metals and carbon-fiber-reinforced thermoplastic composites (CFRTPs). Welding is an essential technique in the manufacture of metal–CFRTP hybrid structures. However, achieving high-strength metal–CFRTP welded joints faces serious challenges due to the considerable disparities in material characteristics. As an effective method to strengthen metal–CFRTP joints, surface texturing on metal is gaining significant attention. This study introduces an emerging surface texturing approach, electrochemical jet machining (EJM) using a film electrolyte jet, for enhancing the performance of AA6061-CF/PA66 hot-pressure-welded (HPW) joints. Parametric effects on surface morphology and roughness in the EJM of AA6061 are investigated. The results show that a rough surface with multiscale pores can be generated on AA6061 by EJM, and that surface morphology can be modulated by adjusting the applied current density and jet translational speed. Subsequently, the effects of different EJM-textured surface morphologies on the performance of HPW joints are examined. Surface textures created by EJM are demonstrated to significantly enhance the mechanical interlocking effect at the bonding interface between AA6061 and CF/PA66, resulting in a substantial increase in joint strength. The maximum joint strength attained in the present work with EJM texturing is raised by 45.29% compared to the joints without surface texturing. Additionally, the joint strength slightly improves as the roughness of EJM-textured surfaces rises, with the exception of rough surfaces that are textured with a combination of low current density and rapid translational speed. Overall, these findings suggest that EJM texturing using a film jet prior to welding is a potential approach for the manufacture of high-performance metal–CFRTP hybrid structures.

Keywords: electrochemical jet machining; surface texturing; metal–CFRTP welding

1. Introduction

Carbon-fiber-reinforced thermoplastic composites (CFRTPs) feature the advantages of low density, high strength, superior fatigue performance, excellent impact properties, and outstanding vibration resistance, making them a type of attractive material for a wide range of applications [1,2]. Meanwhile, with the development of optimized lightweight design via the usage of multi-materials, metal–CFRTP hybrid structures are emerging in various fields, such as the aerospace and automotive industries. For example, they are used in components such as engine cowlings, fairing and fixed trailing edges, wing panels, etc., in aircraft [3–6]. Due to the fact that welding is the major technique used to deal with the issue of joining metals and CFRTPs, its significance in the manufacture of metal–CFRTP hybrid structures continues to grow [6,7].

To date, various welding approaches have been developed for joining CFRTP with metal, including laser welding [8,9], friction welding [10,11], ultrasonic welding [12,13],

hot pressure welding [14,15], and so on. In comparison to other approaches, hot pressure welding (HPW) has demonstrated significant promise for widespread application owing to its benefits such as simple equipment design, environmental sustainability, and ease of operation [5,16]. However, due to the substantial differences in the chemical and physical properties of metals and CFRTPs, achieving high-strength metal–CFRTP dissimilar joints encounters immense challenges [3]. When welding CFRTPs to metals, the bonding mechanism and the joint strength rely primarily on the interfacial mechanical interlock phenomena generated by heating, melting, and penetrating the CFRTP into the microscale scratches and craters on the metal surface. Additionally, chemical bonding may also form at the interface, further enhancing the joint strength. Accordingly, an effective method to improve the strength of metal–CFRTP HPW joints is creating surface textures on metals before welding to provide a more robust mechanical interlock effect [17]. Liu et al. employed laser texturing to create grooves with a width of several hundred micrometers on the surface of an AZ31B magnesium alloy to improve the HPW joint strength of AZ31B-CFRTP [18]. Abe et al. demonstrated that the strength of HPW joints of aluminum–CFRTP can be increased using nanoscale spike-like surface features prepared by two-cycle electrochemical anodizing and etching [19]. Iwata et al. enhanced A5052-CFRTP hot pressure weldability using laser additively manufactured particle-shaped protrusions with an average height and width of about 20 μm and 120 μm on the metal surface [20]. In addition, a number of studies on other metal–CFRTP welding methods have also confirmed the effectiveness of surface texturing approaches like micro-arc oxidation (MAO), sandblasting, and grinding to promote interfacial mechanical interlock. Xia et al. created tiny pores with an average diameter of a few micrometers on a TC4 titanium alloy surface via MAO and found that these tiny pores contribute to the strength enhancement of TC4-CFRTP laser-welded joints [21]. Dong et al. enhanced the strength of AA5052-CFRTP joints by sandblasting rough surfaces with cavities on aluminum alloy surfaces [22]. Nagatsuka et al. demonstrated the improving effect of metal surface grinding prior to friction lap welding on the strength of aluminum alloy–CFRTP joints [10]. Overall, these studies highlight the need for developing appropriate surface texture morphologies and corresponding manufacturing processes to facilitate the HPW of metals and CFRTPs.

Electrochemical jet machining (EJM) is an important and emergent variation of electrochemical machining [23]. EJM achieves targeted material removal by using an unsubmerged "free" electrolyte jet to restrict the electrochemical anodic dissolution in the jet-impinged area on metal workpiece surfaces [24,25]. This jet-based electrochemical process enables EJM to excel in the manufacture of microstructures and surface textures. Particularly, large-area surface textures with electrochemical-etched features can be selectively created on workpieces with high efficiency by applying a film-shaped jet and appropriate parameters. For example, Kunieda et al. demonstrated that EJM with a film jet can produce a grid-patterned texture on nickel surfaces [26]. Lyu et al. showed that surfaces textured by the film-jet EJM process enhance the AA5052–polymer joints created by injection molded direct joining [27]. For the purpose of creating antibacterial surfaces, Lutey et al. utilized the film-jet EJM process to create complicated porous structures on stainless steels, varying in size from a few to hundreds of micrometers [28,29]. Considering its technical traits, the film-jet EJM process is a potential surface texture preparation method for improving the strength of metal–CFRTP HPW joints.

This study, taking 6061 aluminum alloy and a carbon-fiber-reinforced nylon 66 composite material (CF/PA66) as the typical materials, aims to examine the feasibility of increasing metal–CFRTP HPW joint strength by generating surface textures via EJM using a film jet. For this, the parametric effects on surface texture morphology in the film-jet EJM process of AA6061 are investigated. HPW experiments with different surface texture morphologies created by EJM are conducted to investigate their impact on joint performance.

2. Materials and Methods

2.1. Materials

This study utilized 6061 aluminum alloy (AA6061) and carbon-fiber-reinforced PA66 (CF/PA66) as the experimental materials. The dimensions of the AA6061 sheets and CF/PA66 sheets were 100 × 40 × 1.5 mm^3 and 100 × 40 × 3 mm^3, respectively. The used CF/PA66 sheets (Grivory® GCL-4H, EMS-CHEMIE (China) Ltd., Suzhou, China) were injection-molded and comprised 40 wt.% carbon fibers with a diameter of 7 µm and a length of approximately 10 mm. The main physical properties of AA6061 and CF/PA66 are listed in Table 1.

Table 1. Main physical properties of AA6061 and CF/PA66.

Material	Elongation	Melting Point	Solid-Phase Line Temperature	Liquid-Phase Line Temperature	Elasticity Modulus	Tensile Strength
AA6061	12.5%	-	582 °C	650 °C	68.7 GPa	311 MPa
CF/PA66	1.4%	260 °C	-	-	29.5 GPa	355 MPa

2.2. EJM of Textured Surfaces Using a Film Jet

Figure 1 depicts the principle of the EJM process using a film jet. The film-shaped electrolyte jet is ejected from a cathodic slit nozzle onto an anodic workpiece. After the film jet impinges the workpiece, the electrolyte changes the flow direction and flows rapidly to the surrounding region, creating a thin electrolyte layer around the jet. Further away from the jet, the thickness of this electrolyte layer suddenly increases due to the hydraulic jump phenomenon. The "free" jet surface and the surrounding thin electrolyte layer restrict the dispersion of the electrical field, making the electrochemical dissolution take place only in the jet-impinged region [23]. Generally, the current density distribution on the anodic surface exhibits a Gaussian-like profile [24]. As a result, the workpiece surface beneath the slit nozzle can be textured with electrochemical-etched features under suitable machining conditions [28,29]. Further, with the designed translating path of the nozzle, large-area surface textures can be selectively created on the workpiece surface.

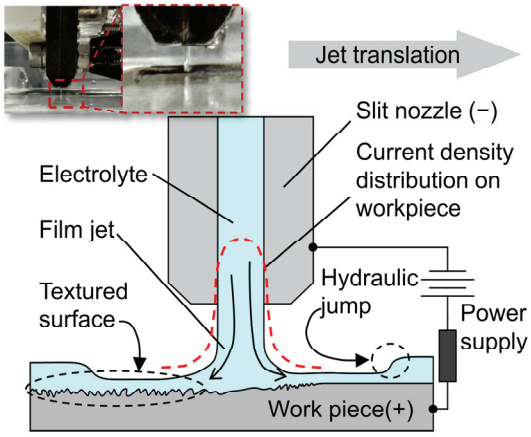

Figure 1. Principle of surface texturing by EJM using a film jet.

In this study, a home-made EJM prototype, illustrated in Figure 2, was employed for texturing AA6061 surfaces. The EJM apparatus comprised a direct current power supply, a numerically controlled positioning platform, and an electrolyte circulation system. Table 2 lists the machining parameters in the EJM experiments. A commonly used ECM electrolyte, an aqueous solution of 20 wt.% NaCl, was chosen as the electrolyte. The cross-sectional width of the slit nozzle was 0.1 mm to produce a thin-film electrolyte jet. A constant flow velocity of 4.28 m/s was used to ensure the stable configuration of the "free" film jet, surrounding thin fluid layer, and hydraulic jump phenomenon. In order to

investigate the influence of current density and jet translational speed on the surface texture morphologies created by EJM, areal current densities ranging from 20 to 300 A/cm^2 and translational speeds ranging from 0.25 to 5 mm/s were employed. To maintain consistent material removal for surfaces textured under various conditions, the imposed electric charge per unit area was kept constant by applying corresponding texturing times in all EJM experiments. The textured surfaces on AA6061 used for subsequent HPW had an area of 38 × 18 mm^2. To facilitate the characterization of surface textures, small EJM-textured surface areas of 10 × 10 mm^2 on AA6061 were created using a nozzle of the corresponding dimension for SEM examination. Note that, when parameters (i.e., current density, jet translational speed, etc.) are maintained identically, the textured surface roughness and morphology are not affected by the nozzle size employed [26].

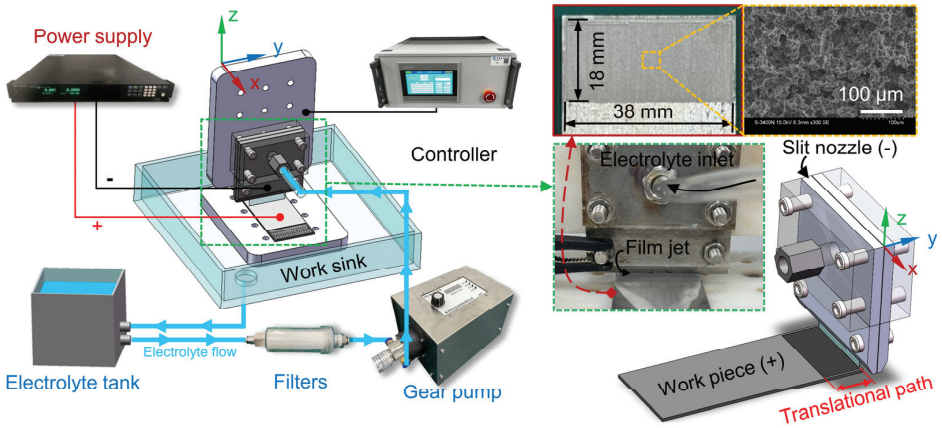

Figure 2. Schematic of the EJM apparatus.

Table 2. Experimental parameters for surface texturing by EJM.

Parameters	Value
Electrolyte	20 wt.% aq. NaCl
Slit nozzle length (l)	38 (mm)
Slit nozzle width (b)	0.1 (mm)
Flow velocity (f)	4.28 (m/s)
Electric charge (Q)	240 (C/cm^2)
Current density (i)	20, 50, 80, 120, 200, 300 (A/cm^2)
Jet translational speed (v)	0.25, 0.75, 1.25, 1.75, 3.5, 5 (mm/s)

2.3. HPW of Textured AA6061 and CF/PA66

A HPW machine (NC-RY20, NICLE, Beijing, China), as shown in Figure 3, was utilized for the welding of the EJM-textured AA6061 sheets and CF/PA66 sheets. Before the welding process, a pre-welding drying treatment was carried out at 80 °C for 4 h to ensure the drying of CF/PA66. The overlap region of the AA6061 and CF/PA66 sheets in the HPW had an area of 40 × 20 mm^2. Optimized parameters (i.e., welding temperature of 360 °C, welding pressure of 0.3 MPa, welding time of 12 s, and cooling time of 16 s) for the HPW of the same materials, as demonstrated in the literature [5], were applied in this study.

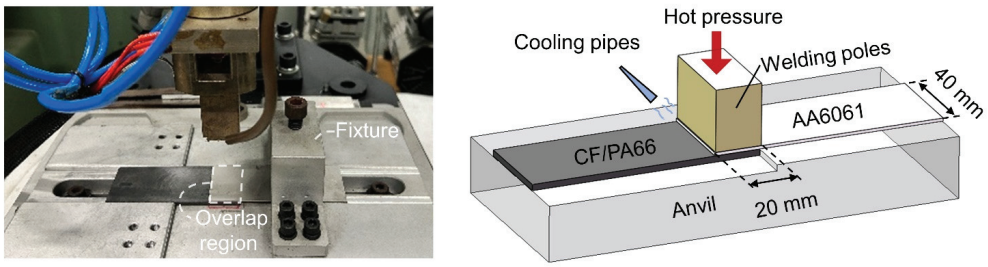

Figure 3. Schematic of HPW of textured AA6061 and CF/PA66.

2.4. Characterization

A laser scanning confocal microscope (LEXT OLS4100, Olympus, Tokyo, Japan) was used for the morphological characterization and roughness measurement of EJM-textured AA6061 surfaces. Before the characterization of surface morphologies and roughness measurements, textured surfaces were ultrasonically cleaned with alcohol and then dried with high-pressure gas. As for roughness measurements, a typical area of 640 × 640 μm^2 on the EJM-textured surface was selected as the test region. Measurements of roughness were conducted along 10 lines with an equal interval in the test region. The same measurement procedure was repeated twice on two textured surfaces generated with the same EJM parameters. The 20 measured roughness values were averaged to determine the roughness of the textured surface. Field-emission scanning electron microscopy (Sigma 300, ZEISS, Oberkochen, Germany) was utilized for the observation of surface texture morphologies. Tensile–shear tests were conducted using a universal testing machine (TSEOM-202203A, WANCE, Shenzhen, China) with a test speed of 2 mm/min to evaluate the AA6061-CF/PA66 joint performance. Each type of joint was subjected to four repeated tensile–shear tests. An optical microscope (AXIOCAM 208 COLOR, ZEISS, Oberkochen, Germany) was used to observe and analyze the microstructure of the joints. The interfaces of typical joints were characterized by Thermo Escalab 250Xi X-ray photoelectron spectroscopy (XPS) (Thermo Fisher Scientific, Waltham, MA, USA).

3. Results and Discussion

3.1. Parametric Effects on Surface Texture Generated by EJM

3.1.1. Effect of Current Density on Surface Roughness and Morphology

Figure 4 shows the correlation between the current density and roughness of the AA6061 surfaces textured by EJM. A smaller current density leads to increased surface roughness, irrespective of the jet translational speed employed. Surface morphologies at different current densities, with a translation speed of 0.5 mm/s, are shown in Figure 5. When a current density of 20 A/cm^2 is applied, the surface is quite rough and exhibits lots of pores ranging in size from a few micrometers to one hundred micrometers. In addition, these multiscale pores distribute densely, causing a knife-like sharp edge of pores. As the current density increases to 50 A/cm^2, the surface becomes relatively even. Multiscale pores still develop on the surface, but there are less large pores of a size of about one hundred micrometers. Increasing the current density further to 120 A/cm^2 causes a smooth surface with only a few shallow large dimples. This relationship between current density and surface roughness, as well as morphology, in EJM can be explained by the change in dissolution kinetics with the increased current density [30]. At a small current density, the anodic workpiece surface stays in a fresh electrochemical environment due to the slow dissolution and rapid electrolyte flushing, causing the workpiece to dissolve in an active state. As such, the workpiece surface is non-homogeneously etched because of the different electrochemical characteristics of material microstructures and sub-microstructures. However, when the current density rises, a so-called supersaturated film forms on the workpiece surface since dissolved ions are generated massively and cannot be effectively removed. The anode kinetics in this scenario are mainly governed by mass transport rather than electrochemical charge transfer, which leads to a similar dissolving rate for different microstructures and generates a reasonably smooth machined surface. From the perspective of metal–CFRTP welding, the densely distributed multiscale pores with sharp edges created by EJM with low current densities are considered to be favorable for the mechanical interlocking effect at the joint interface.

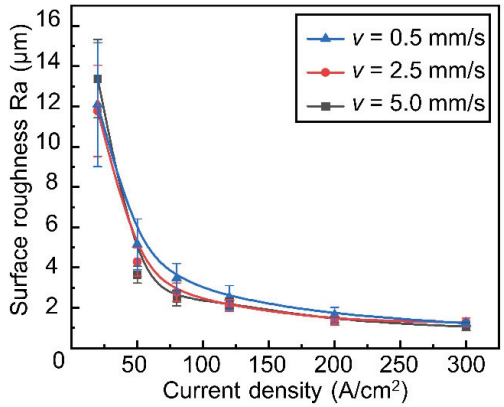

Figure 4. Relationship between current density and AA6061 surface roughness in EJM.

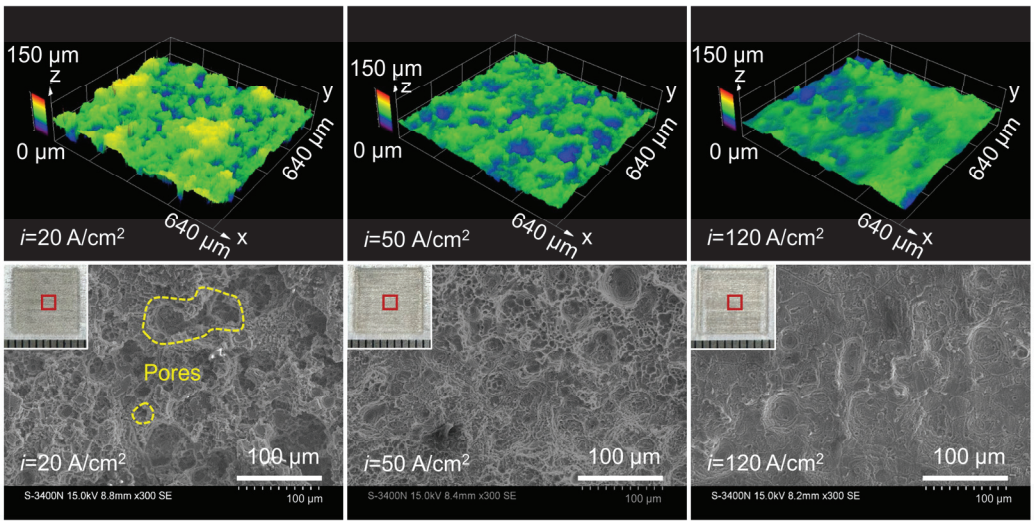

Figure 5. Typical morphologies of AA6061 surfaces textured by EJM at different current densities with a jet translation speed of 0.5 mm/s. The regions marked by red boxes on textured surfaces are for SEM examination.

3.1.2. Effect of Jet Translational Speed on Surface Roughness and Morphology

The correlation between jet translational speed and the roughness of EJM-textured surfaces is depicted in Figure 6. At a current density of 50 A/cm^2, as the translation speed rises, the roughness of textured surfaces decreases and eventually converges to a constant value of roughness. Figure 7a shows the typical surface morphologies at different jet translational speeds with a current density of 50 A/cm^2. It is obvious that at a low translational speed of 0.25 mm/s, the surface is notably rough and features numerous pores at a width and depth of tens of micrometers, in addition to densely distributed pores a few micrometers in size. With the increase in translational speed, the number of pores in the tens of micrometers range reduces, resulting in a relatively even surface. This observed relationship between jet translational speed and surface roughness is attributed to the varied dwelling duration of the low current density surrounding the jet [30–32]. A Gaussian-type distribution of current density is created on the workpiece surface impinged by the jet in EJM. Hence, each given spot of the workpiece surface always eventually gets affected by a low current density when the jet translates. The faster translation of the jet leads to a shorter dwelling time of low current density, which, therefore, helps in weakening the material-microstructure-dependent etching induced by low current density. Meanwhile, at a higher current density of 300 A/cm^2, the roughness is low and remains relatively constant irrespective of translational speed. This can be explained by considering that an excessively high machining current causes a significant increase in current density even at

the periphery of the jet, thereby limiting the effect of material-microstructure-dependent etching even at a low jet translational speed.

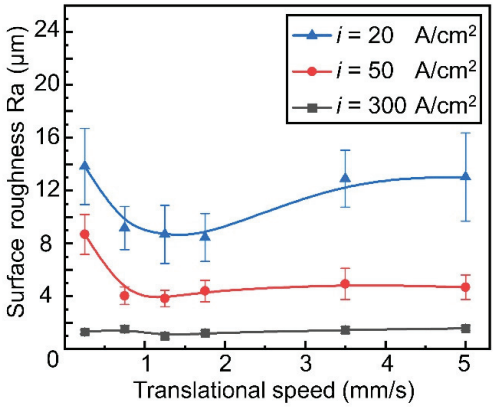

Figure 6. Relationship between jet translational speed and AA6061 surface roughness in EJM.

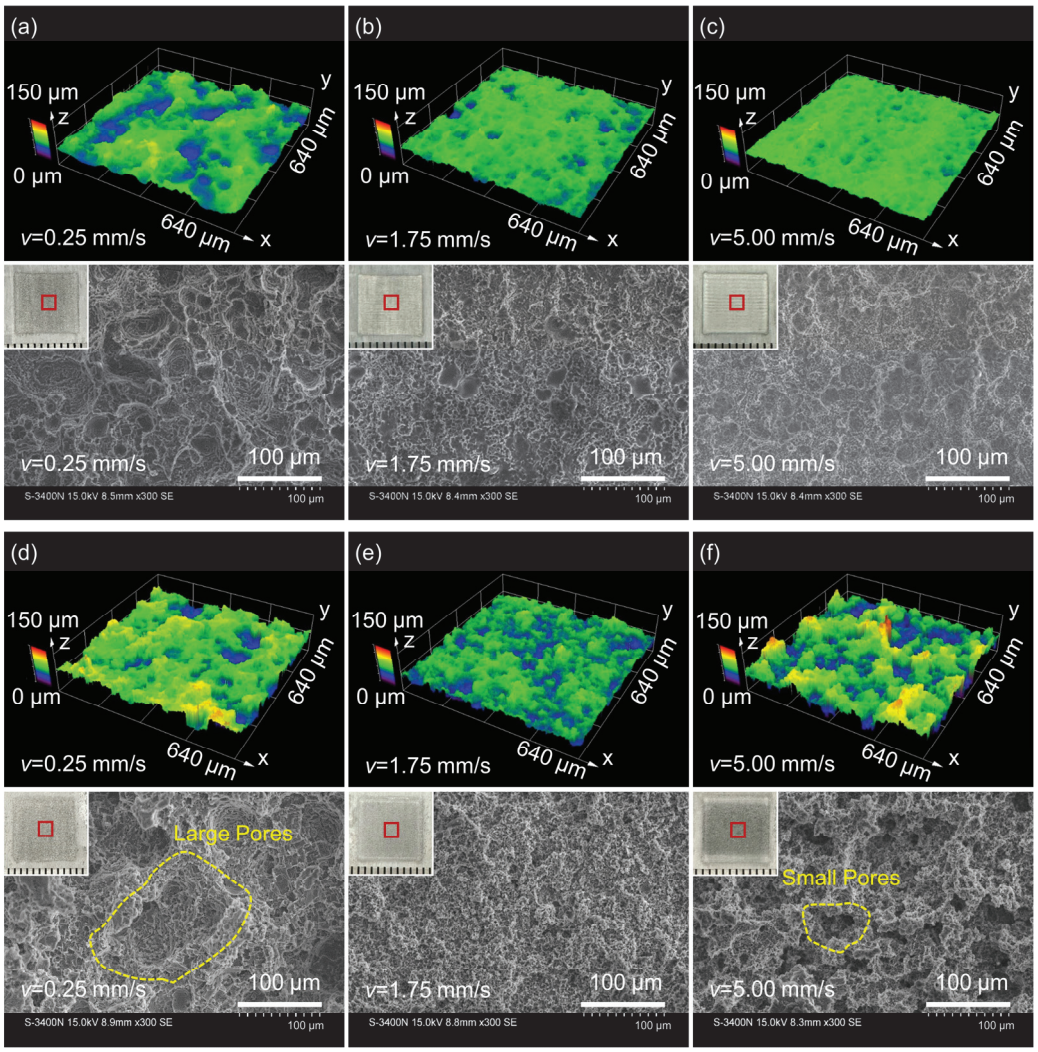

Figure 7. Typical morphologies of AA6061 surfaces textured by EJM at different translational speeds with current densities of 50 A/cm^2 and 20 A/cm^2. (**a**) i = 50 A/cm^2, v = 0.25 mm/s; (**b**) i = 50 A/cm^2, v = 1.75 mm/s; (**c**) i = 50 A/cm^2, v = 5 mm/s; (**d**) i = 20 A/cm^2, v = 0.25 mm/s; (**e**) i = 20 A/cm^2, v = 0.25 mm/s; (**f**) i = 20 A/cm^2, v = 0.25 mm/s. The regions marked by red boxes on textured surfaces are for SEM examination.

Note that the roughness–speed curve at a current density of 20 A/cm^2 exhibits a different tendency within the range of high jet translational speed from the abovementioned current densities. When the translational speed exceeds 1.75 mm/s, the surface roughness begins to noticeably increase and finally reaches a roughness comparable to that at a low translational speed. The reason for this behavior may be associated with the inhomogeneous breakdown of the oxide layer of a valve metal in EJM when using small current densities combined with a fast translational speed [32]. In each translation of the jet, the complete breaking down of the oxide layer requires sufficient imposed electric charge. At a fast translational speed, combined with a small current density, the oxide layer on AA6061 cannot be completely removed, and the remaining local oxide layer hinders the dissolution while other regions dissolve, which, thus, results in a considerably rough surface. As shown in Figure 7b, the surface roughness at a high translational speed of 5 mm/s is similar to that at a low one (0.25 mm/s), but the surface morphologies are different. This evidence also suggests a different etching behavior at fast translational speeds paired with small current densities. The surface at 5 mm/s contains numerous pores with a comparable depth to that at 0.25 mm/s, while the width of pores generated at 5 mm/s is smaller than that at 0.25 mm/s. Therefore, it is reasonable to anticipate that EJM-textured surfaces at 0.25 mm/s and 5 mm/s may have a distinct influence on the metal–CFRTP joint performance, even though they have a similar roughness.

Further, for the subsequent selection of typical textured surfaces for the HPW process, it is necessary to obtain the roughness of all textured surfaces generated by EJM, employing current densities from 20 to 300 A/cm^2 and jet translational speeds from 0.25 to 5 mm/s. For this, additional EJM experiments are conducted to determine the comprehensive effects of current density and jet translational speed on the roughness of textured surfaces, as shown in Figure 8. As can be seen, three typical levels of roughness can be created on AA6061 by EJM.

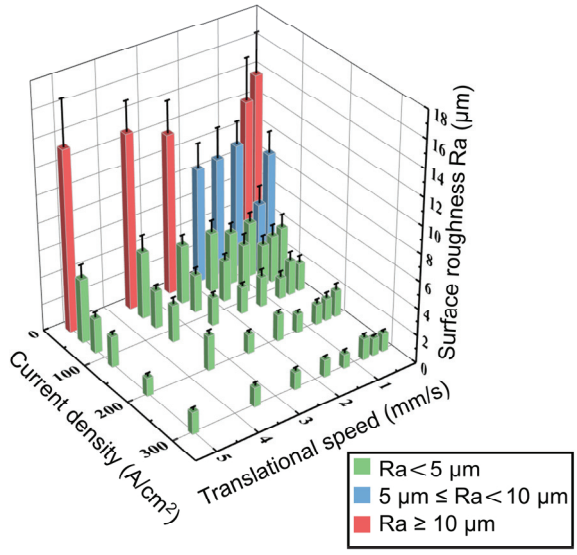

Figure 8. Dependence of AA6061 surface roughness textured by EJM on current density and jet translational speed.

3.2. Effect of Surface Texture Generated by EJM on AA6061-CF/PA66 HPW Joints

Based on the experimental results in Section 3.1, surface textures with various roughnesses and morphologies can be generated on AA6061 by EJM. For the welding of metal–CFRTP, higher roughness on metal surfaces generally leads to improved joint performance due to strong mechanical interlocking [33]. Accordingly, to investigate the impact of surface textures created by EJM on the performance of HPW AA6061/CFRTP joints, four typical surface textures with varying surface roughnesses and morphologies (designated as groups A_S, A_F, B, and C in Table 3) were prepared prior to the welding process. Note that the A_S

and A_F groups have the same level of roughness but different morphologies of surface textures, as discussed in Section 3.1.2. Additionally, non-treated surfaces, labeled as group D, were also arranged in the HPW experiments for comparison.

Table 3. EJM-textured AA6061 surfaces for HPW experiments.

Groups	EJM Parameters	Surface Roughness Ra	Surface Morphology
A_S	i = 20 A/cm^2; v = 0.25 mm/s	13 µm	Shown in Figure 7d
A_F	i = 20 A/cm^2; v = 5 mm/s	13 µm	Shown in Figure 7f
B	i = 50 A/cm^2; v = 0.25 mm/s	8 µm	Shown in Figure 7a
C	i = 80 A/cm^2; v = 3.5 mm/s	4 µm	Shown in Figure 9
D	No treatment	1 µm	—

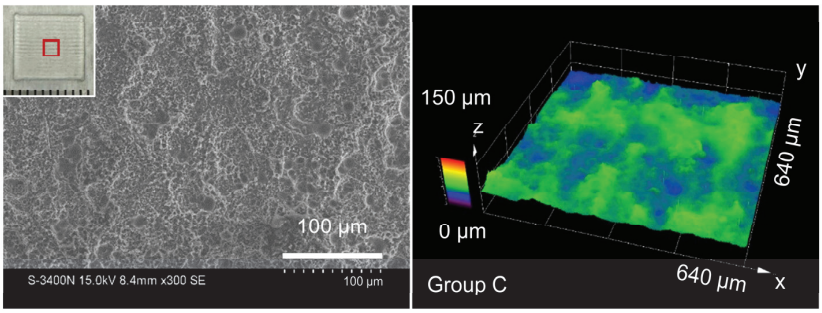

Figure 9. Morphologies of AA6061 surfaces textured by EJM with a translational speed of 3.5 mm/s and a current density of 80 A/cm^2. The regions marked by red boxes on textured surfaces are for SEM examination.

3.2.1. Mechanical Properties

Figure 10 displays the tensile–shear peak loads of the HPW joints with different AA6061 surface textures and non-treated AA6061 surfaces. In comparison to the joints with non-treated surfaces, the joint strength increases significantly with the EJM-textured surfaces on AA6061. Further, while comparing the joint strength of groups A_S, B, and C, it is observed that the joint strength slightly increases with an increase in surface roughness. This may be explained by considering the interfacial area between the CFRTP and the metal, which is also an important factor affecting the joint strength in addition to the surface roughness [5,34]. Surfaces with large roughness have loosely distributed large pores, whereas surfaces with small roughness have densely distributed small pores. As a result, although groups A_S, B, and C have different surface roughnesses, the interfacial area between the metal and CFRTP may be comparable. Hence, the shear strength may not differ much. Interestingly, the joints of group A_F employ textured surfaces with an elevated level of roughness, but they have a comparatively lower strength. This might be associated with the different texture morphologies resulting from distinct etching mechanisms with a low current density and a fast translational speed, as explained in Section 3.1.2.

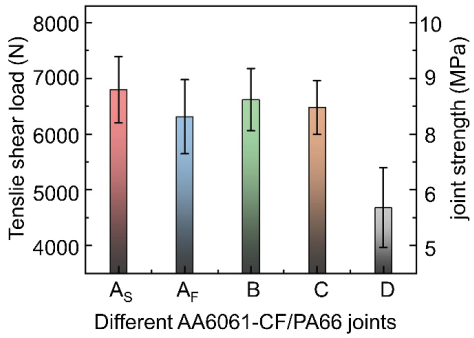

Figure 10. Joint strength with different surface textures and non-treated surface.

3.2.2. Interfacial Microstructure

The interfacial cross-sections of AA6061-CF/PA66 joints with varying surface treatments are shown in Figure 11. More apparent mechanical interlocking is found with EJM-textured surfaces compared to group D, which utilizes non-treated AA6061 surfaces. The resin fills the pores with sharp edges on the EJM-textured AA6061 surfaces, which allows the joints of groups A_S, A_F, B, and C to withstand greater shear force. Furthermore, in comparison with groups A_S, B, and C, voids are observed at the joint interface of group A_F. A probable reason for this is that the relatively small, deep pores on A_F surfaces inhibit the effective infiltration of molten resin into these pores during the welding process. These voids cause a reduced bonding area and high stress concentration, leading to a comparably weak joint as a result. Among groups A_S, B, and C, as the surface roughness rises, the increase in both the depth and width of pores on EJM-textured surfaces permits greater resin filling and enhanced mechanical interlocking.

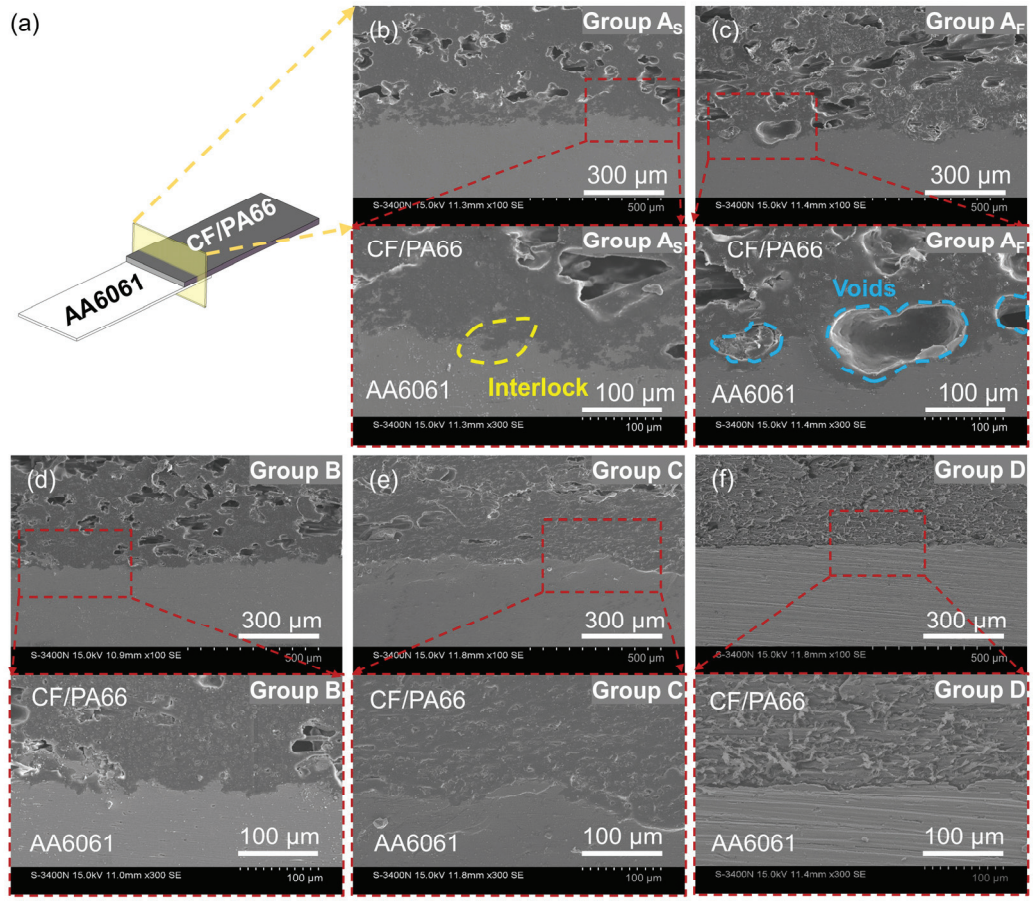

Figure 11. SEM images of interfacial cross-sections of different joints. (**a**) Schematic of interfacial cross-sections of joints; (**b**) group A_S; (**c**) group A_F; (**d**) group B; (**e**) group C; (**f**) group D.

3.2.3. Fracture Morphology

Figure 12 depicts the typical morphologies of AA6061 surfaces after joint failure. Residual resin and carbon fibers are observed on the surfaces of AA6061 under all conditions. Nevertheless, group D exhibits a bare AA6061 surface in some locations, whereas the EJM-textured surfaces in groups A_S, A_F, B, and C are almost entirely covered with residual CF/PA66. Generally, the characteristics of the fracture morphology, as well as resin and carbon remaining on the metal surface, suggest a cohesive failure mode with a greater bonding strength between the metal and the CFRTP than the shear strength of the polymer matrix. In contrast, the bare metal surface indicates an adhesive failure mode, i.e., interfacial bond failure between the metal and the CFRTP. Hence, EJM texturing helps

in enlarging the area of joints experiencing cohesive failure and considerably improves strength. Moreover, as shown in Figure 12b,d,e, the amount of carbon fibers remaining on the surfaces of groups A_S, B, and C progressively diminishes in a sequential manner. When the carbon fibers are mechanically interlocked with the metal surface, they are peeled from the CFRTP matrix and remain on the metal surface after the joint failure. Accordingly, the mechanical interlocking effect and joint strength are reduced in the order of groups A_S, B, and C. Additionally, in comparison with groups A_S, B, and C, the residual CF/PA66 on the AA6061 surface of group A_F exhibits numerous holes and minimal carbon fibers (Figure 12c). This further indicates that the molten resin and carbon fibers are not effectively filled into the textured-surface pores of group A_F during the HPW process, and voids form at the joint interface, which, consequently, leads to poor mechanical interlocking and low joint strength, specifically measured at 7.8 MPa.

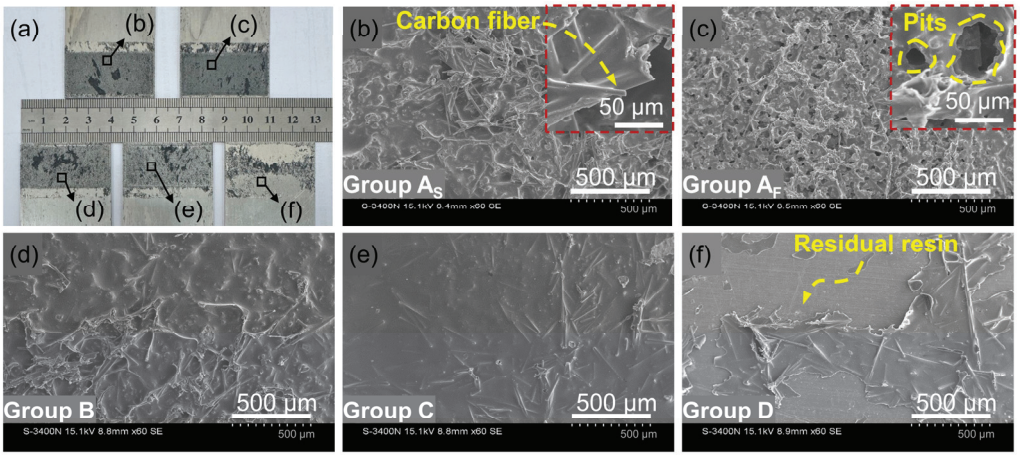

Figure 12. AA6061 surface morphologies of different joints after failure. (**a**) Macroscopic view; (**b**) group A_S; (**c**) group A_F; (**d**) group B; (**e**) group C; (**f**) group D. The regions for SEM examination are marked by black boxes.

3.2.4. Interfacial Composition

Numerous studies have demonstrated that element diffusion occurs at the interface of metal–CFRTP joints, which is commonly regarded as evidence of chemical bonding [14]. For this reason, EDS line scanning is performed on the interface of different AA6061-CF/PA66 joints. Figure 13 demonstrates that, in all joints, the concentration of the C element decreases progressively from the CF/PA66 side to the AA6061 side, while the concentration of the Al element grows gradually. This indicates the existence of interfacial diffusion layers. Thus, chemical interactions, such as the formation of chemical bonds, may take place at the interface of CF/PA66 and AA6061 in addition to the mechanical interlock. Furthermore, it can be seen from Figure 13ab that there are clearly fluctuating concentration distributions at the interface. The reason for this phenomenon could be related to the complicatedly porous EJM-textured AA6061 surfaces of groups A_S and A_F. A partial sidewall of deep pores might appear above the base AA6061 at cross-sections, causing a rise in the Al element and a corresponding reduction in the C element at some locations of the interface. Therefore, the wide interface regions with fluctuating concentration distributions in groups A_S and A_F seem to be unrelated to enhanced chemical bonding, but demonstrate strong local mechanical interlocking.

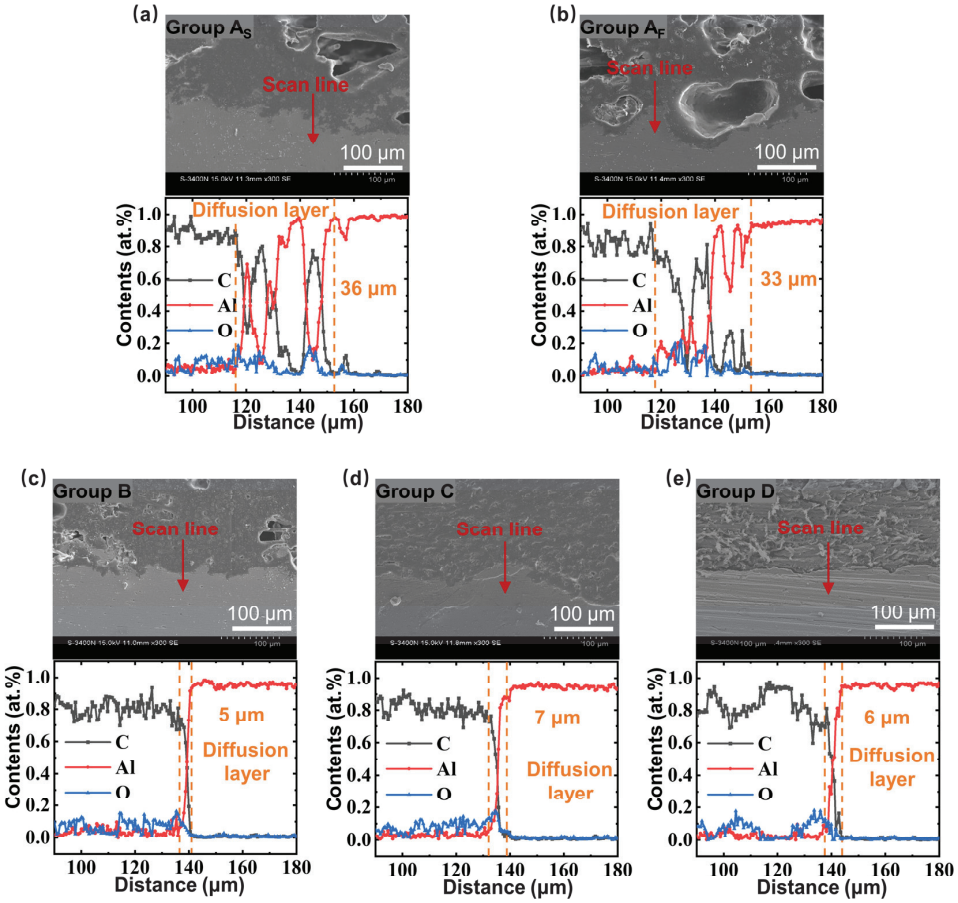

Figure 13. EDS line scanning results at the interfaces of different joints. (**a**) Group A_S; (**b**) group A_F; (**c**) group B; (**d**) group C; (**e**) group D.

For the further examination of the chemical bonds at the interface of the metal–CFRTP joints, a typical group of joints, A_S, is analyzed by XPS. The XPS survey spectra are shown in Figure 14a. Al, C, O, and N elements are detected. In order to determine the bonding state of the C elements at the interface, high-resolution spectra of C1s are analyzed, as shown in Figure 14b. The Al-C and Al-O-C bonds are detected at binding energies of 283 eV and 284 eV, respectively. According to the literature [35], these bonds are developed at the interface of AA6061 and CF/PA66 during the welding process, providing support for the joining mechanism of chemical bonding.

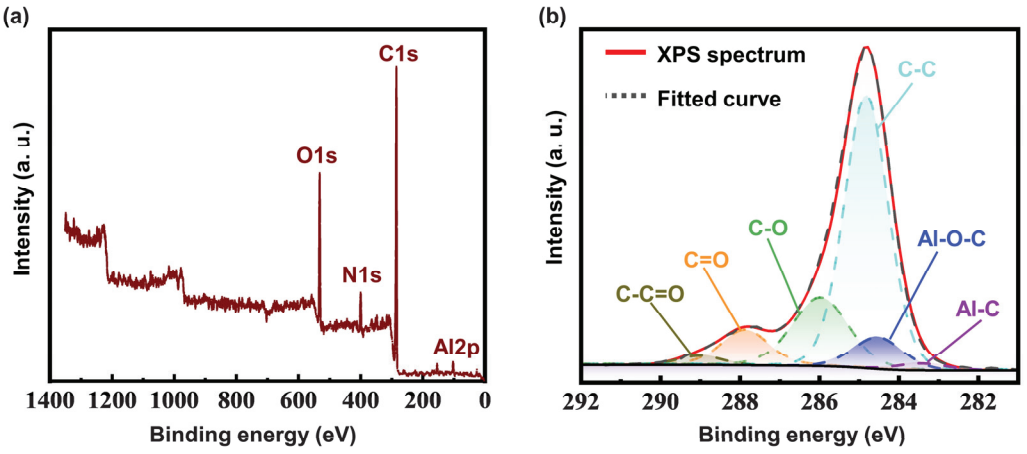

Figure 14. XPS results for the joint interface of group A_S. (**a**) Survey spectrum; (**b**) high-resolution spectra of C1s.

4. Discussion

In this study, EJM is employed to generate surface texture to enhance the performance of AA6061-CF/PA66 HPW joints. The effects of the main parameters on the roughness and morphology of textured AA6061 surfaces in the EJM process are identified. In addition, the effects of EJM-textured surfaces on the strength of AA6061-CF/PA66 HPW joints are investigated. The following conclusions can be drawn from the present study.

(1) The EJM experimental results demonstrate that complex porous textures can be generated on AA6061 surfaces. The pores on the textured surfaces under suitable EJM conditions feature multiscale sizes ranging from a few micrometers to one hundred micrometers, and sharp edges.

(2) The investigation of EJM parametric effects shows that at a constant jet translational speed, decreasing the applied current density leads to an increase in both the size and number of pores produced on the textured AA6061 surfaces, resulting in a higher roughness. When a relatively high current density is employed, reducing the jet translational speed has a similar effect. However, at a relatively low current density (such as 20 A/cm^2 in the present study), combined with a fast translational speed (such as >1.75 mm/s in the present study), further increasing the translational speed leads to the formation of deep pores and a significant increase in surface roughness.

(3) The results of the HPW experiments confirm that the strength of AA6061-CF/PA66 joints is significantly enhanced by EJM-textured AA6061 surfaces. Specifically, with suitable EJM parameters (such as a current density of 20 A/cm^2 and a jet translational speed of 0.25 mm/s in the present work), the joint strength is increased by approximately 45.29%. The highest shear strength of the joint enhanced by EJM texturing reaches 8.49 MPa, while the joints without texturing have a shear strength of 5.84 MPa. The joint strength moderately improves as the roughness of EJM-textured AA6061 surfaces increases, with the exception of surfaces that are textured utilizing a combination of low current density and rapid translational speed.

(4) An improvement in the interfacial mechanical interlocking effect induced by EJM texturing is identified, contributing to the enhancement of joint strength. Furthermore, an observable diffusion layer, indicating the potential occurrence of chemical bonding, exists at the interface between AA6061 and CF/PA66.

Author Contributions: Conceptualization, W.L. and Y.L. (Yang Li); methodology, W.L.; validation, W.L. and Y.L. (Yan Luo); formal analysis, W.L. and Y.L. (Yan Luo); investigation, Y.L. (Yan Luo); resources, Y.L. (Yan Luo) and H.Z.; data curation, Y.L. (Yan Luo); writing—original draft preparation, W.L. and Y.L. (Yan Luo); writing—review and editing, W.L., Y.L. (Yang Li), Y.Z. and S.A.; visualization, Y.L. (Yan Luo); supervision, W.L. and Y.L. (Yang Li); project administration, W.L. and Y.L. (Yang Li); funding acquisition, W.L. All authors have read and agreed to the published version of the manuscript.

Funding: This research was funded by the Scientific Research Project of Tianjin Municipal Education Commission, grant number 2021KJ040.

Data Availability Statement: The data presented in this study are available on request.

Conflicts of Interest: The authors declare no conflicts of interest.

References

1. Lambiase, F.; Scipioni, S.I.; Lee, C.J.; Ko, D.C.; Liu, F. A State-of-the-Art Review on Advanced Joining Processes for Metal-Composite and Metal-Polymer Hybrid Structures. *Materials* **2021**, *14*, 1890. [CrossRef] [PubMed]
2. Almushaikeh, A.; Alaswad, S.; Alsuhybani, M. Manufacturing of carbon fiber reinforced thermoplastics and its recovery of carbon fiber: A review. *Polym. Test.* **2023**, *122*, 108029. [CrossRef]
3. Liu, Z.G.; Li, Y.; Liu, Z.W.; Yang, Y.; Li, Y.; Luo, Z. Ultrasonic welding of metal to fiber-reinforced thermoplastic composites: A review. *J. Manuf. Process.* **2023**, *85*, 702–712. [CrossRef]
4. Liu, Z.G.; Li, Y.; Liu, W.D.; Zhou, H.P.; Ao, S.S.; Luo, Z. Enhancing the ultrasonic plastic welding strength of Al/CFRTP joint via coated metal surface and structured composite surface. *J. Manuf. Process.* **2023**, *108*, 227–237. [CrossRef]
5. Zhou, H.P.; Li, Y.; Liu, W.D.; Luo, Y.; Ao, S.S.; Luo, Z. Effect of Process Parameters on Joint Performance in Hot Pressure Welding of 6061 Aluminum Alloy to CF/PA66. *Materials* **2024**, *17*, 329. [CrossRef] [PubMed]

6. Zhang, D.W.; Zhang, Q.; Fan, X.G.; Zhao, S.D. Review on Joining Process of Carbon Fiber-Reinforced Polymer and Metal: Methods and Joining Process. *Rare Met. Mater. Eng.* **2018**, *47*, 3689–3696.
7. Faes, K.; Vermeersch, J.; Silva, R. Joining of Metal-Plastic Composites with Advanced Welding Processes. In Proceedings of the ASME 2021 16th International Manufacturing Science and Engineering Conference, Virtual, Online, 21–25 June 2021; V002T06A010; pp. 1–9.
8. Li, Y.; Bu, H.C.; Yang, H.Y.; Liu, G.; Yao, J.A.; Zhan, X.H. Effect of laser heat input on the interface morphology during laser joining of CFRTP and 6061 aluminum alloy. *J. Manuf. Process.* **2020**, *50*, 366–379. [CrossRef]
9. Jiao, J.; Xu, J.; Jing, C.; Cheng, X.; Wu, D.; Ru, H.; Zeng, K.; Sheng, L. Effect of Laser Micro-Texturing on Laser Joining of Carbon Fiber Reinforced Thermosetting Composites to TC4 Alloy. *Materials* **2022**, *16*, 270. [CrossRef] [PubMed]
10. Nagatsuka, K.; Yoshida, S.; Tsuchiya, A.; Nakata, K. Direct joining of carbon-fiber-reinforced plastic to an aluminum alloy using friction lap joining. *Compos. Part B Eng.* **2015**, *73*, 82–88. [CrossRef]
11. Guo, Y.; Zhao, H.B.; Ai, C.J.; Zhao, J.J.; Su, H.; Chen, J.; Zhao, G.Q. Parameter optimization of friction stir spot welded Al 6061 and CFRTP PA6 with surface treatment and interfacial adhesion. *Thin-Walled Struct.* **2024**, *197*, 111585. [CrossRef]
12. Lionetto, F.; Mele, C.; Leo, P.; D'Ostuni, S.; Balle, F.; Maffezzoli, A. Ultrasonic spot welding of carbon fiber reinforced epoxy composites to aluminum: Mechanical and electrochemical characterization. *Compos. Part B Eng.* **2018**, *144*, 134–142. [CrossRef]
13. Feistauer, E.E.; Santos, D.; Amancio, F. An investigation of the ultrasonic joining process parameters effect on the mechanical properties of metal-composite hybrid joints. *Weld. World* **2020**, *64*, 1481–1495. [CrossRef]
14. Liu, Y.; Su, J.; Tan, C.W.; Feng, Z.; Zhang, H.; Wu, L.; Chen, B.; Song, X. Effect of laser texturing on mechanical strength and microstructural properties of hot-pressing joining of carbon fiber reinforced plastic to Ti6Al4V. *J. Manuf. Process.* **2021**, *65*, 30–41. [CrossRef]
15. Li, W.; Geng, P.; Ma, N.; Chen, C. Effect of thermal-mechanical conditions on strength of silanized Al alloy/CFRTP hybrid joint made by thinning-controlled hot pressing. *Mater. Today Commun.* **2024**, *38*, 108507. [CrossRef]
16. Zhang, X.Y.; Su, J.H.; Feng, Z.W.; Liu, H.R.; Xia, H.B.; Zhang, Z.Q.; Tan, C.W.; Chen, B.; Song, X.G. Effect of laser textured patterns on the interfacial characteristics and mechanical properties of 6061Al/GFRTP joints via hot-pressing. *Thin-Walled Struct.* **2023**, *189*, 110916. [CrossRef]
17. Sandeep, R.; Natarajan, A. Advances in joining technologies for the innovation of 21st century lightweight aluminium-CFRP hybrid structures. *Proc. Inst. Mech. Eng. Part E J. Process Mech. Eng.* **2022**, *236*, 1239–1255. [CrossRef]
18. Liu, Y.F.; Su, J.H.; Ma, G.L.; Han, X.H.; Tan, C.; Wu, L.J.; Chen, B.; Song, X.G. Effect of the laser texturing width on hot-pressing joining of AZ31B and CFRTP. *Opt. Laser Technol.* **2021**, *143*, 107350. [CrossRef]
19. Abe, H.; Chung, J.C.; Mori, T.; Hosoi, A.; Jespersen, K.M.; Kawada, H. The effect of nanospike structures on direct bonding strength properties between aluminum and carbon fiber reinforced thermoplastics. *Compos. Part B Eng.* **2019**, *172*, 26–32. [CrossRef]
20. Iwata, K.; Suzuki, A.; Kim, S.G.; Takata, N.; Kobashi, M. Enhancing the solid-state joinability of A5052 and CFRTP via an additively manufactured micro-structure. *J. Mater. Process. Technol.* **2022**, *306*, 117629. [CrossRef]
21. Xia, H.B.; Yang, B.Y.; Su, J.H.; Liu, Y.F.; Su, X.; Wang, C.; Qiang, X.; Wu, T.; Tan, C.W. Improvement of laser welded TC4/CFRTP joint strength by combination of surface modification of MAO and laser texturing. *Thin-Walled Struct.* **2024**, *196*, 111409.
22. Dong, H.G.; Tang, Z.Y.; Li, P.; Wu, B.S.; Hao, X.H.; Ma, C.Q. Friction stir spot welding of 5052 aluminum alloy to carbon fiber reinforced polyether ether ketone composites. *Mater. Des.* **2021**, *201*, 109495. [CrossRef]
23. Speidel, A.; Bisterov, I.; Saxena, K.K.; Zubayr, M.; Reynaerts, D.; Natsu, W.; Clare, A.T. Electrochemical jet manufacturing technology: From fundamentals to application. *Int. J. Mach. Tools Manuf.* **2022**, *180*, 103931. [CrossRef]
24. Yoneda, K.; Kunieda, M. Numerical analysis of cross sectional shape of micro-indents formed by the electrochemical jet machining. *J. Jpn. Soc. Electr. Mach. Eng.* **1995**, *29*, 1–8.
25. Hackert-Oschätzchen, M.; Paul, R.; Martin, A.; Meichsner, G.; Lehnert, N.; Schubert, A. Study on the dynamic generation of the jet shape in jet electrochemical machining. *J. Mater. Process. Technol.* **2015**, *223*, 240–251. [CrossRef]
26. Kunieda, M.; Mizugai, K.; Watanabe, S.; Shibuya, N.; Iwamoto, N. Electrochemical micromachining using flat electrolyte jet. *CIRP Ann.* **2011**, *60*, 251–254. [CrossRef]
27. Lyu, X.; Kimura, F.; Zhao, Y.; Kunieda, M.; Kajihara, Y. Metal-polymer injection molded direct joining using electrolyte jet machining. In Proceedings of the 7th International Conference of Asian Society for Precision Engineering and Nanotechnology (ASPEN), Seoul, Republic of Korea, 14–17 November 2017. MFT–O–01.
28. Lutey, A.H.A.; Jing, H.Y.; Romoli, L.; Kunieda, M. Electrolyte Jet Machining (EJM) of antibacterial surfaces. *Precis. Eng.* **2021**, *70*, 145–154. [CrossRef]
29. Lutey, A.H.A.; Romoli, L.; Lee, J.; Kunieda, M. Tailoring microbial response to stainless steel surfaces via electrolyte jet machining and electrodeposition. *J. Adv. Manuf. Technol.* **2023**, *129*, 727–738. [CrossRef]
30. Kawanaka, T.; Kunieda, M. Mirror-like finishing by electrolyte jet machining. *CIRP Ann.* **2015**, *64*, 237–240. [CrossRef]
31. Kong, H.H.; Qu, N.S. Flat jet electrochemical milling of TC4 alloy with tailoring backward parallel flow. *Chin. J. Aeronaut.* **2023**, *23*, 574–592. [CrossRef]
32. Liu, W.D.; Ao, S.S.; Li, Y.; Liu, Z.M.; Zhang, H.; Manladan, S.M.; Luo, Z.; Wang, Z.P. Effect of Anodic Behavior on Electrochemical Machining of TB6 Titanium Alloy. *Electrochim. Acta* **2017**, *233*, 190–200. [CrossRef]

33. Feng, Z.W.; Zhao, H.Y.; Tan, C.W.; Zhang, X.Y.; Chen, B.; Song, X.G. Nanosecond laser ablation for improving the strength of CFRTP and aluminum alloy adhesively bonded joints. *Compos. Struct.* **2021**, *274*, 114369. [CrossRef]
34. Yang, G.X.; Yang, T.; Yuan, W.H.; Du, Y. The influence of surface treatment on the tensile properties of carbon fiber-reinforced epoxy composites-bonded joints. *Compos. Part B Eng.* **2019**, *160*, 446–456. [CrossRef]
35. Liu, F.C.; Dong, P.; Lu, W.; Sun, K. On formation of Al-O-C bonds at aluminum/polyamide joint interface. *Appl. Surf. Sci.* **2019**, *466*, 202–209. [CrossRef]

Journal of
Composites Science

MDPI

Article

A Finite Element Analysis Study of Influence of Femoral Stem Material in Stress Shielding in a Model of Uncemented Total Hip Arthroplasty: Ti-6Al-4V versus Carbon Fibre-Reinforced PEEK Composite

Mario Ceddia [1,*], Giuseppe Solarino [2], Giorgio Giannini [2], Giuseppe De Giosa [2], Maria Tucci [2] and Bartolomeo Trentadue [1]

[1] Department of Mechanics, Mathematics and Management, Polytechnic of Bari, 70125 Bari, Italy; bartolomeo.trentadue@poliba.it
[2] Department of Translational Biomedicine and Neuroscience, University of Bari "Aldo Moro", Policlinic Piazza G. Cesare, 11, 70124 Bari, Italy; giuseppe.solarino@uniba.it (G.S.); giorgiogiannini1993@tiscali.it (G.G.); degiosa.giuseppe@libero.it (G.D.G.); tuccim.199@gmail.com (M.T.)
* Correspondence: marioceddia1998@gmail.com

Abstract: Total hip arthroplasty is one of the most common and successful orthopaedic operations. Occasionally, periprosthetic osteolysis associated with stress shielding occurs, resulting in a reduction of bone density where the femur is not properly loaded and the formation of denser bone where stresses are confined. To enhance proximal load transfer and reduce stress shielding, approaches, including decreasing the stiffness of femoral stems, such as carbon fibre-reinforced polymer composites (CFRPCs), have been explored through novel modular prostheses. The purpose of the present study was to analyse, by the finite element analysis (FEA) method, the effect that the variation of material for the distal part of the femoral stem has on stress transmission between a modulable prosthesis and the adjacent bone. **Methods**: Through three-dimensional modelling and the use of commercially available FEA software Ansys R2023, the mechanical behaviour of the distal part of the femoral stem made of CFRPC or Ti-6Al-4V was obtained. A load was applied to the head of the femoral stem that simulates a complete walking cycle. **Results**: The results showed that the use of a material with mechanical characteristics close to the bone, like CFRPC, allowed for optimisation of the transmitted loads, promoting a better distribution of stress from the proximal to the distal part of the femur. This observation was also found in some clinical studies in literature, which reported not only an improved load transfer with the use of CFRPC but also a higher cell attachment than Ti-6Al-4V. **Conclusions**: The use of a material that has mechanical properties that are close to bone promotes load transfer from the proximal to the distal area. In particular, the use of CFRPC allows the material to be designed based on the patient's actual bone characteristics. This provides a customised design with a lower risk of prosthesis loss due to stress shielding.

Keywords: hip replacement arthroplasty; modular femoral stem; stress shielding; finite element analysis; carbon fibre-reinforced polymer composites (CFRPC)

1. Introduction

The hip joint, also called the coxofemoral joint, plays a key function in providing dynamic support for the body's weight and transmitting loads that are distributed from the skeletal axis to the lower limbs [1–3]. However, the hip joint is exposed to various risks and damage that can lead to pathological conditions [4–8]. In some cases where the joint is severely compromised by diseases such as osteoarthritis or complex fractures of the femoral head or bone tumours, it may be necessary to surgically replace the joint with a prosthetic device [9–15]. This surgery can be a total hip joint replacement (total hip

arthroplasty, THA), which involves removing both the femoral head and the acetabulum of the patient, or a partial replacement (hemi-replacement) in which only part of the joint is replaced [16]. Generally, titanium alloys, such as Ti-6Al-4V, are used for the femoral stems due to their lightweight, corrosion resistance and biocompatibility [17,18]. These alloys offer good dynamic mechanical strength and show high success rates [19]. The prosthesis, when inserted, transfers the load from the femoral head and acetabular cavity at the hip to the prosthesis itself [20–24]. This can affect the biomechanics of the joint and the surrounding bone. In particular, the stress applied to the bone may promote its physiological remodelling [25–29]. In fact, when a prosthesis is introduced into the bone, the distribution of loads is altered, causing atrophic bone to form in unloaded areas and denser bone in overloaded areas. This is due to the different stiffnesses between the bone and the prosthetic materials, with metals having a higher stiffness [29]. For example, cortical bone has a modulus of elasticity of about 16 GPa, while common materials used for prostheses, such as stainless steel, have a modulus of elasticity of about 200 GPa [30]. This considerable difference causes what is called stress shielding. To mitigate the effects of stress shielding, it is important to design prostheses that better mimic the biomechanical properties of natural bone and allow for a more even distribution of mechanical load on the surrounding bone. In this respect, the development of modular prostheses has made it possible to adjust implant stiffness or to select components that reduce stress shielding, allowing a better distribution of load on the surrounding bone [31]. In addition, the choice of modular part materials with properties like natural bone can help reduce the risk of stress shielding. In a study of 118 patients undergoing femur reconstruction using a modular femoral stem system, it was found that distal bone fixation was achieved in 100% of patients, the offset was corrected in 66%, leg length discrepancy was corrected in 78%, and stability was achieved in 97% of cases [32]. The suggested solution to this complication is to use a less rigid material with mechanical properties close to the properties of bone, for example, using porous structures of the femoral stems. In a study conducted by Hou et al. [33] where, using a porous honeycomb structure of the femoral stem in Ti-6Al-4V, stress shielding was reduced by adaptation of Young's modulus. In another study by Thomas et al. [34], the use of 3D-printed Ti6Al4V additive manufacturing lattice structures provided an elastic modulus of 15.7 GPa and yield strength of 296 MPa, values very similar to bone. This resulted in improved stress transfer between bone and femoral stem and reduced stress shielding. Krishna et al. [35] introduced a porous titanium implant with reduced stiffness (2–45 GPa) by a laser-assisted lattice structure. A reduction in stress shielding was observed with this technique. The use of materials with mechanical properties like bone, such as composites, could solve the stress shielding problem. For example, the use of (CF/PEEK) has an elastic modulus that can vary depending on processing and be very close to the values of the femoral bone. Finite Element Analysis (FEA) can be used to evaluate how stress is distributed in the bone and prosthesis, identify potential areas of stress shielding, and optimise the design of the prosthesis to reduce them [36,37]. However, nowadays, there are many studies on the optimisation of stress shielding for Ti-6Al-4V femoral stems, but few have evaluated the effect of stress shielding using composite materials such as CFRP combined with metallic materials such as Ti-6Al-4V through modularity [38,39]. Therefore, in this study, the effect of stress shielding with a femoral stem with a distal section made of carbon fibre-reinforced polymer composites CFRPC was analysed using finite element analysis, and the results were compared with a femoral stem made of Ti6Al4V. CFRP was chosen as the composite material because it is known for its high strength and stiffness while being lightweight. It also offers the possibility of designing femoral stems with complex shapes and geometries, allowing more accurate customisation and adaptation to the anatomical needs of the patient, helping to reduce the phenomenon of stress shielding, as its modulus of elasticity can be designed to be close to that of the surrounding bone. The null hypothesis was that the use of a CFRPC would produce a more homogeneous stress distribution on the bone from the proximal end to the distal end than when Ti-6Al-4V is used.

2. Materials and Methods

The 3D model of the femoral prosthesis was constructed using Autodesk Inventor 3D 2024 software. Figure 1 shows the main dimensions of the model and the two configurations using an interchangeable distal part with a circular cross-section.

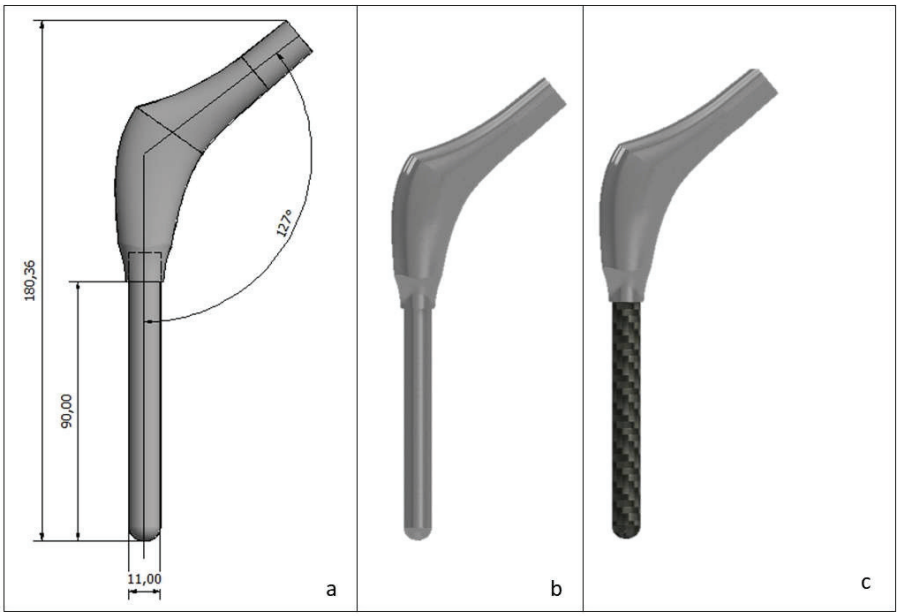

Figure 1. 3D model of the femoral prosthesis: (**a**) main dimensions, (**b**) model with distal part in Ti6Al4V, (**c**) model with distal part in CFRPC.

The three-dimensional (3D) geometric model of the healthy femur and the femur with prosthesis is shown in Figure 2a,b, which corresponds to a two-dimensional cut through the entire femur in the mid-frontal plane for both in the case of a healthy femur (HF) and a femur with prosthesis (FP). Subsequently, cortical and trabecular tissue thicknesses were obtained from previous studies [40,41] and compared with standard anatomical femur dimensions (Figure 2a) [41]. After that, the simplified model of the femur was constructed using Autodesk Inventor 3D 2024 software, and through the Boolean operation, the cavity inside the femur was created to reflect the external geometry of the prosthesis. Then, with the assembly operation, the prosthesis was inserted inside the modular canal Figure 2b,c.

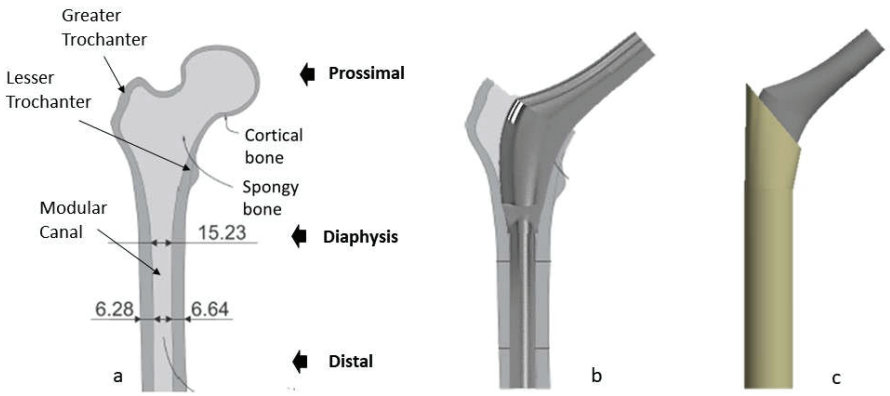

Figure 2. Healthy femur (HF) and the femur with prosthesis (FP): (**a**) sectional model of the healthy femur, (**b**) sectional model of the femur with prosthesis, (**c**) simplified 3D model of the femur with prosthesis.

The model was then saved in stp format and transferred into the FEA software Ansys R2023 (ANSYS Workbench). Ti-6Al-4V alloy, cortical bone, and cancellous bone were each considered to have linearly isotropic and homogeneous elastic properties (Table 1) [42–45].

Table 1. Modulus of elasticity and Poisson's ratio of Ti-6Al-4V alloy and bones [43–46].

Material	Modulus of Elasticity E (GPa)	Poisson's Ratio ν
Cortical bone	16.7	0.3
Trabecular bone	0.155	0.3
Ti-6Al-4V	110	0.3

For the CFRPC, the mechanical properties are influenced by the mechanical characteristics of the fibre but also by the orientation of the fibres between the individual layers. In this study, configuration I was chosen in which the fibres are oriented at 0, +45, −45 and 90 degrees, which allows an optimal distribution of the applied load and a homogeneous mechanical behaviour in the system (Figure 3). This type of fibre orientation helps to distribute the applied load and to transfer it to the bone. Furthermore, with this configuration, the mechanical behaviour is transversely isotropic [45]. In addition, a fibre volume fraction of approximately 60% was chosen. This percentage represents the critical volume below in which the mechanical properties of the composite would be lower than that of the matrix.

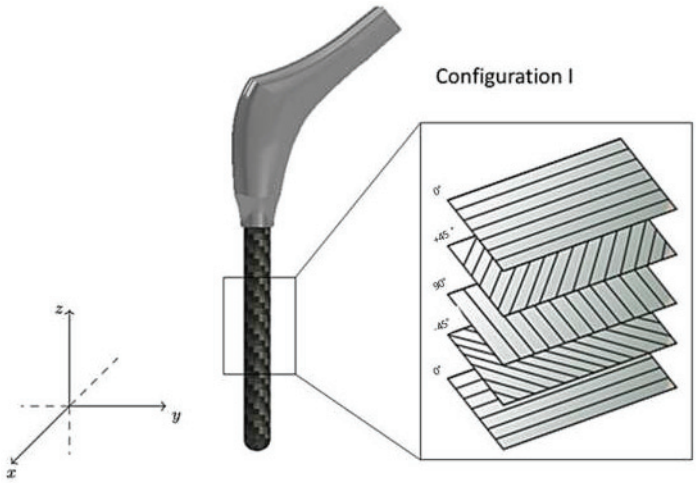

Figure 3. Configuration 1 CFRPC layers.

The relevant mechanical properties of the configuration of the CFRPC are given in Table 2 [45].

Table 2. Modulus of elasticity and Poisson's ratio of configuration I of CFRPC [45].

Plane	Elastic Modulus E (GPa)	Shear Modulus G (GPa)	Poisson's Ratio ν
xx	4		-
yy	9.8		-
zz	9.8		-
xy	-	3.5	0.3
yz	-	3	0.3
xz	-	3.5	0.3

2.1. Meshing

The model was constructed with 516,752 quadratic tetrahedral elements Figure 4, adopting an average element size of 0.5 mm, as reported in [43]. Based on the chosen mesh, a convergence test was carried out to test the reliability of the results based on the number of elements with which the 3D model was discretised (Figure 5).

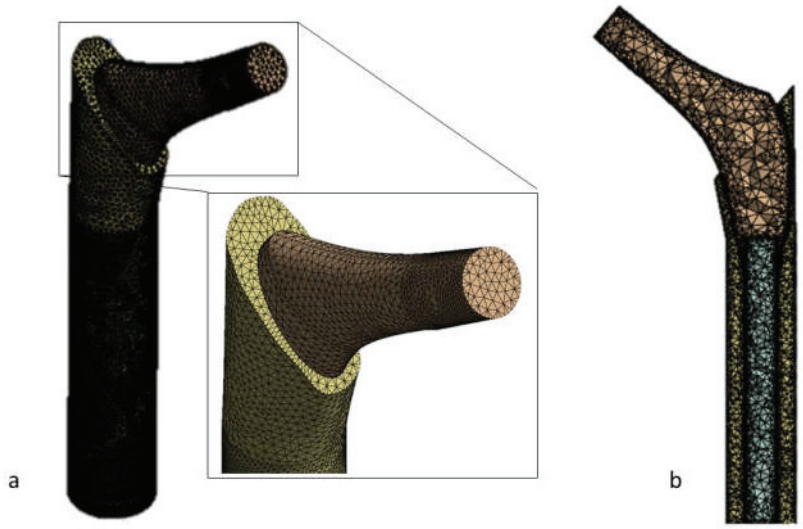

Figure 4. 3D mesh model: (**a**) three-dimensional view (**b**) sectional view.

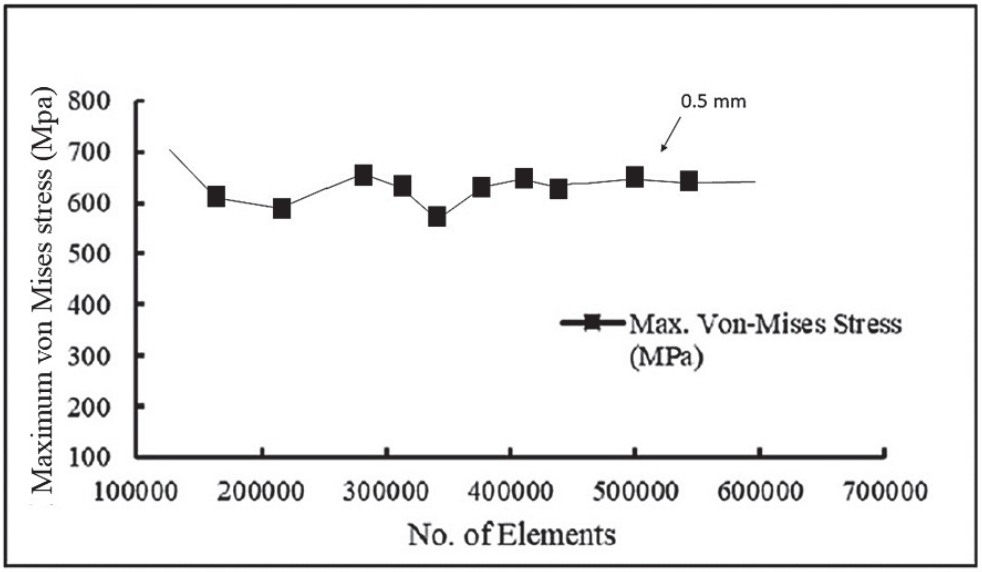

Figure 5. Mesh convergence analysis carried out on the implant neck.

In the convergence test conducted in Figure 5, the von Mises stress error with a mesh of 0.5 mm is 0.2% compared to a 0.4 mm mesh.

2.2. Loads and Boundary Conditions

The loading condition was considered as a gait cycle on a plane with an average speed of 1.1 m/s [45], which consisted of the loads on the femoral head [4.5 times body weight with force components (x, y, z) (1492, 915, 2925) N] [46]. Consequently, the lower surface of the femur was constrained in all directions (x, y, z) Figure 6 [46]. In addition, to simulate the contact conditions between bone and femoral stem after insertion, a fixed contact interface between bone and femoral stem was defined. For this purpose, surface-to-surface contact elements were used, which do not allow separation and sliding from the proximal

zone to the distal zone of the femoral stem. All solutions were processed with ANSYS WORKBENCH R 2023 (ANSYS Inc., Canonsburg, PA, USA).

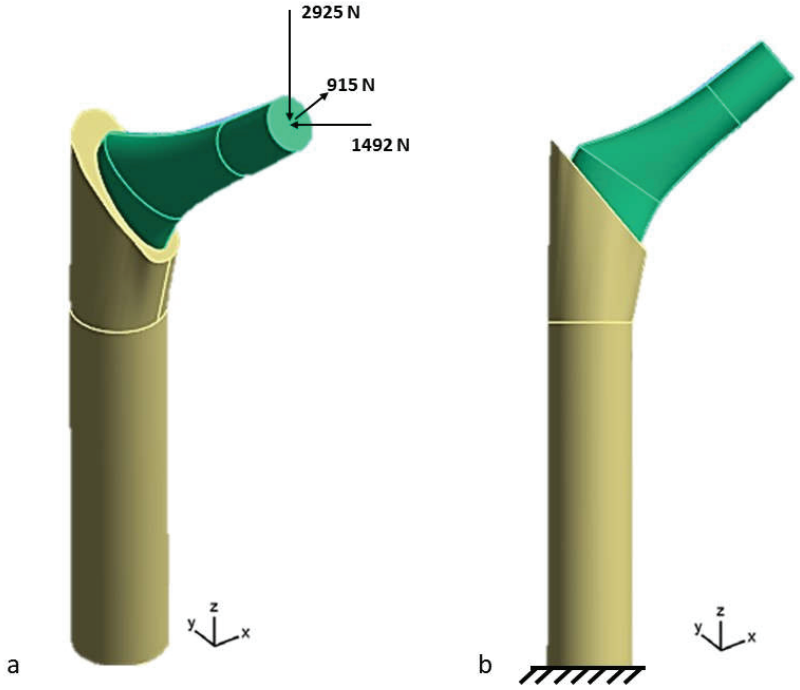

Figure 6. Loading conditions (**a**) and constraint conditions (**b**) in the 3D model consisting of the prosthesis and the femur.

Calculation of Stress Shielding

The insertion of the prosthesis into the femur generates a reduction in stress in the proximal area because most of the load bypasses this area and is directly transmitted from the femoral stem to the distal portion of the femur. Weinans et al. [47] defined stress shielding may be expressed as a function of stress in the proximal zone of the femur. The finite element method can be used to identify the design solution that best limits the stress shielding phenomenon. In this study, in the absence of an accurate model of the real femoral bone, the effect of stress shielding was evaluated by comparing the two materials for the femoral stem. Specifically, the stress on the bone is evaluated using a prosthesis made of Ti-6Al-4V and one with a distal part made of CFRPC. In addition, muscle insertion forces were not considered in this study because the analysis mainly focuses on the forces exchanged between the femoral stem and bone in the distal and proximal areas. In a future study, the effect of the stress shield will be evaluated using a real femoral bone as a model, including muscle insertion forces.

3. Results

The analysis of the results was carried out considering the von Mises equivalent stress criterion. The von Mises criterion is used in the FEA analysis of a femoral stem because it provides an accurate and reliable assessment of the failure behaviour of ductile materials under complex loads, thus helping to ensure the safety and effectiveness of the prosthetic implant. Figure 7 shows the von Mises stress results of the 3D model consisting of the femoral stem with the two configurations of the distal part in CFRPC and Ti6-Al-4V inserted inside the femur.

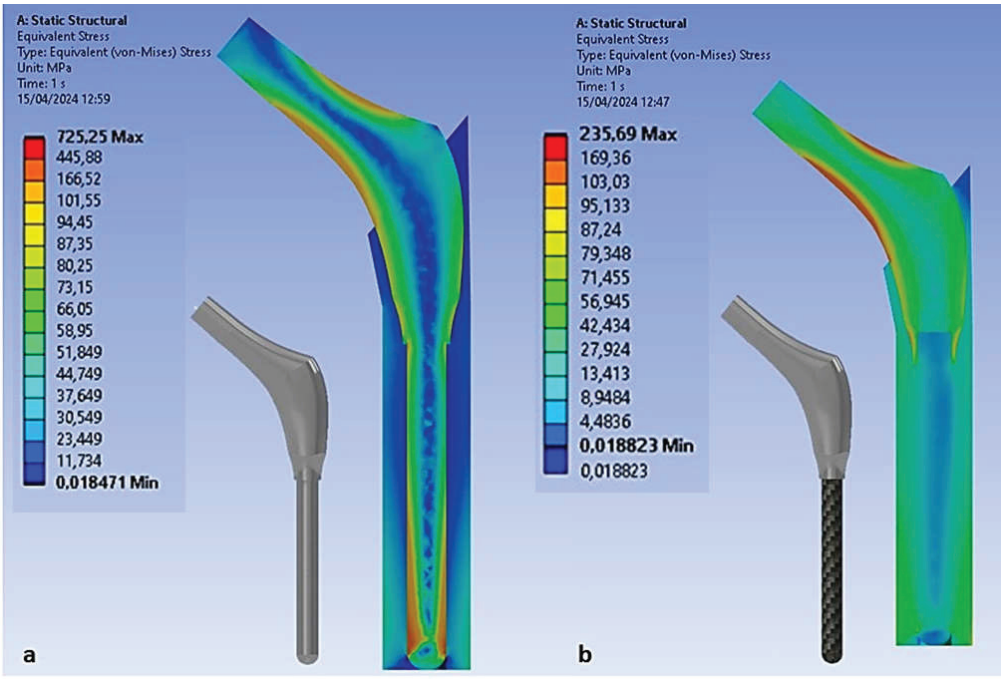

Figure 7. Von Mises stress results: (**a**) distal part in Ti6Al4V, (**b**) distal part in CFRPC.

Figure 7 shows that the von Mises stress is higher when a modular prosthesis is used, with the proximal and distal parts made of the same material (Ti-6Al-4V) Figure 7a. Specifically, the maximum stress obtained at the implant is 725.25 MPa in the first case and 235.69 MPa in the case where the material of the distal component is CFRPC Figure 7b. In case (a), the stress distribution is mainly absorbed by the prosthesis; in fact, a first analysis shows that the bone in contact with the prosthesis in the proximal zone does not seem to be adequately stimulated. Moreover, in case (a), the distal zone of the femur is subjected to a greater load than the proximal zone. This makes it clear that the phenomenon of stress shielding is greater in the first case than in the second, using a distal part of the CFRPC prosthesis, where a more even distribution of stresses is observed between the femoral stem and the adjacent bone (Figure 7b).

Figure 8 shows the distribution of von Mises stresses calculated along a path (red line) of the femur section. In the case where the distal part of the implant is made of Ti-6Al-4V (Figure 8a), the stress in the proximal zone of the bone is 6.21 MPa, but in the central zone, there is an increase in stress. For example, at 70 mm from the distal zone, the stress is 37.25 MPa. However, in the distal zone, the stress increases, reaching 78.5 MPa. On the other hand, the distribution and trend of the von Mises stress in the case where a distal component of the implant made of CFRPC is used shows significant differences compared to the previous case. In fact, it is observed that the stress in the proximal zone may be 17 MPa compared to 6.21 MPa. Considering 70 mm from the distal zone, the stress is 26.75 MPa. While in the distal zone, stress values of approximately 67.25 MPa are reached compared to 78.5 MPa. This shows how the use of a distal CFRPC component, which has a stiffness similar to that of bone, allows a more even distribution of stress from the proximal to the distal zone.

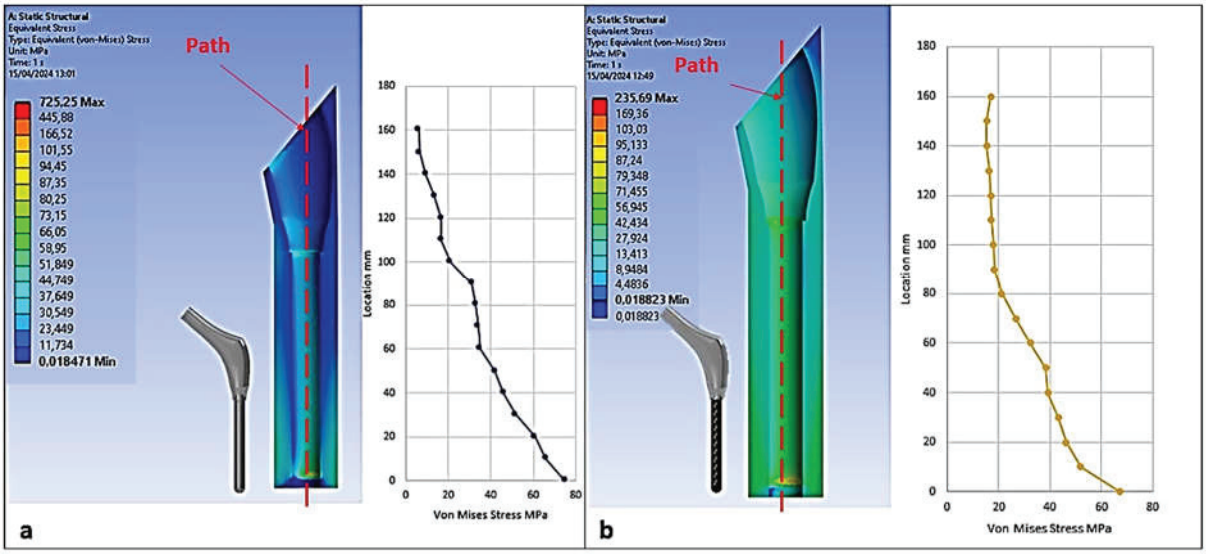

Figure 8. Von Mises stress trend in the femur: (**a**) prosthesis with titanium distal part, (**b**) prosthesis with CFRPC distal part.

Stress Shielding Evaluation

In this study, Gruen's seven periprosthetic zones were considered for stress shielding analysis, in which the tip of the lesser trochanter defines the distal boundary of zones 1 and 7. The midpoint between the lesser trochanter and the bottom tip of the femoral stem defines the limit between zone 2 and zones 3, 5 and 6. Zone 4 represents the total bone area located 20 mm distal to the tip of the femoral stem. Vertically, the central axis of the femur divides the medial and lateral zones (Figure 9).

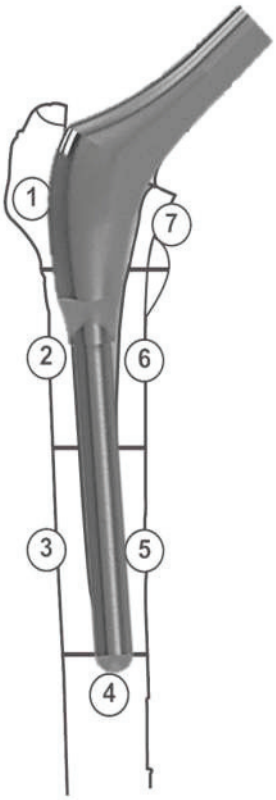

Figure 9. Gruen's seven zones: a model for evaluating the stress between the femoral stem and femoral bone.

At a specified Gruen zone, the stress shielding factor was defined as the ratio of the von Mises stress at the zone when the distal part of the femoral stem was made of CFRPC to von Mises stress at the zone when the distal part of the femoral stem was made of Ti-6Al-4V. Thus, it is desirable for the factor to be >1 in the proximal region (Gruen zones 1 and 7) and <1 in the distal region (Gruen zone 4). The present results (Table 3) demonstrate this.

Table 3. Evaluation of the effect of Stress shielding factors in the 7 Gruen zones.

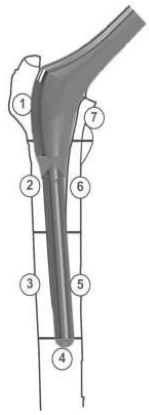

Gruen Zone	Prosthesis with CFRPC Distal Part: Von Mises Stress (MPa)	Prosthesis with Ti-6Al-4V Distal Part: Von Mises Stress (MPa)	Stress Shielding Factor
1	4.32	3.21	1.34
2	25.14	31.41	0.80
3	38.31	45.21	0.84
4	67.25	78.25	0.85
5	42.31	48.32	0.87
6	26.75	73.25	0.36
7	17.15	12.52	1.36

From Table 3, using a distal CFRPC part for a femoral stem, the shielding stress factor is 1.34 in the proximal zone (Gruen zone 1). While in the distal zone (Gruen zone 4), the stress shielding factor is 0.85. This analysis, therefore, showed that the use of a distal part of the femoral stem in CFRPC improved the stress distribution by promoting greater stress in the proximal zone (Gruen zones 1 and 7).

4. Discussion

The use of carbon fibre-reinforced polymer composites CFRPC allows mechanical properties comparable to those of bone in terms of stiffness, contributing to the reduction of the stress shielding phenomenon [48]. The mechanical properties of these materials depend on the orientation and amount of carbon fibres in the composite matrix, with strength ranging from 70 to 1900 MPa and stiffness from 10 to 100 GPa. In addition, CFRPC composites have demonstrated excellent biocompatibility, environmental stability, and chemical resistance [49–51]. Nakahara et al. [51] studied the results of uncemented and cemented CFRPC hip prostheses in sheep femoral bone, observing the strength at different loading levels without significant stress shielding effect. Hacking et al. [52] evaluated the tissue response to a hydroxy-apatite-coated composite femoral implant, showing positive bone apposition and no adverse reactions. Scotchford et al. [53] demonstrated good biocompatibility of carbon fibre-based composites through cell attachment and proliferation studies. However, few studies have been conducted using the finite element method, which allows quantitative evaluation of stress transmission on bone tissue and then analyses the effect of stress shielding for different material configurations, shapes and structures of femoral stems. Specifically, a numerical finite element analysis (FEA) performed by Ayham Darwich et al. [54] evaluated the effect of stress shielding on hip prosthesis stems coated with composite (carbon/PEEK) and polymer (PEEK) materials. The results of the study showed that the use of coating materials such as PEEK on a CFRPC femoral stem can reduce the effect of stress shielding. In a numerical study conducted by Akay et al. [55] analysing the stress distribution in a Ti-6Al-4V and CFRPC cemented prosthesis, the authors showed that in the case of CFRPC, the transfer occurred over a larger surface area, thus potentially reducing local stress. In another finite element analysis (FEA) study, Caouette et al. [56] evaluated the performance of a biomimetic hip stem made of a hydroxyapatite-coated carbon fibre composite. Compared to the Ti-6Al-4V stem, the CFRPC femoral stem allowed reduced stress shielding. However, early failure of a CFRPC implant due to inadequate

fixation and fracture of the femoral stem was observed in a study by Allcock et al. [57] inadequate fixation is due to the inability of the CFRPC stem to provide surfaces for bone growth and allow adequate osseointegration. Nowadays, modularity between prosthetic components, such as the proximal and distal part of the femoral stem, is used to provide greater versatility in the choice of sizes, lengths and angles of prosthetic components, allowing for better anatomical adaptability and more precise joint alignment in procedures such as total hip or total knee arthroplasty [58,59]. However, it is important to note that excessive modularity can lead to additional risks, such as the potential for component damage, accelerated wear, and the possibility of fractures or other complications related to the interface between different modular components [60]. The idea of modularity was explored in this study using numerical finite element analysis to evaluate the effect of stress shielding on a full Ti-6Al-4V femoral stem and a femoral stem with an interchangeable CFRPC distal section. Only one in vitro study by Bennett et al. [61] was found in the literature, which showed that the femoral stem with a CFRP distal part provided an increase in proximal bone density and a reduction in distal bone density, with promising results at 10 years of follow-up and clinical outcomes like those of an all-metal stem. Therefore, in this study, from a stress point of view, an improvement in stress shielding reduction was obtained by using a distal part of the femoral stem made of CFRPC. In fact, the results showed that with this configuration, the stress shielding factor was 1.34 in the proximal zone and 0.85 in the distal zone of the prosthesis. This finding proves that the stress distribution was more concentrated in the proximal area, thus promoting bone remodelling. From a clinical point of view, the results presented in this work allow the perfect combination of the constituent materials of the femoral stem through modularity. Promoting better stress distribution and reducing the problem of stress shielding. However, the distal part of the femoral stem can be anatomically adapted to the shape of the femur, improving stability and connection with the surrounding bone. The current study is limited by the use of isotropic mechanical properties for the bone model, which may not fully capture the anisotropic nature of bone. Future research should consider the real anisotropic properties for more accurate modelling. In addition, modularity can increase the risk of corrosion between prosthetic components due to the increased complexity of the interface and stresses that can cause micro-fretting, leading to loss of connection between components [62,63]. However, in this study, the contact between the modular parts of the femoral stem was fixed, as the study focused on evaluating stress in the surrounding bony tissues. In addition, another limitation of this study is the application of a static load to the femoral stem. Further studies should consider the effect of variable loading during the gait cycle and the influence of different materials in the modularity of the connection with other components of the femoral stem. Finally, based on the results obtained in this FEA analysis, an evaluation by in vitro tests will be necessary to validate the modelling performed in this study.

5. Conclusions

The Finite Element Method (FEM) was developed and applied for stress analysis and stress shielding evaluation of a modular femoral stem with a distal part made of Ti-6Al-4V or CFRPC. Using the concept of modularity, the distal part of the femoral stem can be designed with innovative materials such as CFRPC to adapt the mechanical properties of the prosthesis to the bone by reducing the risk of stress shielding. The results obtained from this study show that using a distal part made of CFRPC contributes to an increase in stress in the proximal part of the femur with a stress shielding factor of 1.34 and 0.85 in the distal part. In addition, the maximum stresses obtained are lower than those obtained using a femoral stem made entirely of Ti-6Al-4V. These results provide a basis for appropriate validation through in vitro testing.

Author Contributions: Conceptualisation, M.C. and B.T.; methodology, M.C.; software, M.C.; validation, B.T. and G.S. formal analysis, M.C. and B.T.; investigation, M.C.; resources, M.C. and B.T.; data curation, M.C.; writing—original draft preparation, M.C. and B.T.; writing—review and editing, M.C., B.T., G.S. and G.D.G.; visualisation, B.T., G.S., G.G., G.D.G. and M.T.; supervision, G.S. and B.T.; project administration, G.S. and B.T. All authors have read and agreed to the published version of the manuscript.

Funding: This research received no external funding.

Data Availability Statement: All experimental data to support the findings of this study are available by contacting the corresponding author upon request.

Conflicts of Interest: The authors declare no conflicts of interest.

References

1. Knight, S.R.; Aujla, R.; Biswas, S.P. Total Hip Arthroplasty—Over 100 years of operative history. *Orthop. Rev.* **2011**, *3*, 16.
2. Ridzwan, M.I.Z.; Shuib, S.; Hassan, A.Y.; Shokri, A.A.; Mohamad Ibrahim, M.N. Problem of Stress-shielding and Improvement to the Hip Implant Designs: A Review. *J. Med. Sci.* **2007**, *7*, 460–467. [CrossRef]
3. Babaei, N.; Hannani, N.; Dabanloo, N.J.; Bahadori, S. A systematic review of the use of commercial wearable activity trackers for monitoring recovery in individuals undergoing total hip replacement surgery. *Cyborg Bionic Syst.* **2022**, *2022*, 9794641. [CrossRef]
4. Duffy, S.; Gelfer, Y.; Trompeter, A.; Clarke, A.; Monsell, F. The clinical features, management options and complications of paediatric femoral fractures. *Eur. J. Orthop. Surg. Traumatol.* **2021**, *31*, 883–892. [CrossRef] [PubMed]
5. Zhang, B.; Liu, S.; Liu, Z.; Liu, B.; Huo, J.; Li, M.; Han, Y. Clinical and radiologic outcomes in patients undergoing primary total hip arthroplasty with Collum Femoris Preserving stems: A comparison between the direct anterior approach and the posterior approach. *BMC Musculoskelet. Disord.* **2022**, *23*, 77. [CrossRef]
6. Rodrigues, L.; Cornelis, F.H.; Chevret, S. Hip Fracture Prevention in Osteoporotic Elderly and Cancer Patients: An On-Line French Survey Evaluating Current Needs. *Medicina* **2020**, *56*, 397. [CrossRef] [PubMed]
7. Rozell, J.C.; Donegan, D.J. Periprosthetic Femur Fractures Around a Loose Femoral Stem. *J. Orthop. Trauma.* **2019**, *33*, S10–S13. [CrossRef] [PubMed]
8. Ransohoff, C.B.; Wanner, R.; Solinger, T.; Gautier, E.; Eijer, H.; Wahl, P. The different failure modes of the connecting elements of the modular hip arthroplasty revision stem Revitan. *J. Mech. Behav. Biomed. Mater.* **2021**, *123*, 104778.
9. Bischoff, P.; Kramer, T.S.; Schröder, C.; Behnke, M.; Schwab, F.; Geffers, C.; Aghdassi, S.J.S. Age as a risk factor for surgical site infections: German surveillance data on total hip replacement and total knee replacement procedures 2009 to 2018. *Eurosurveillance* **2023**, *28*, 2200535. [CrossRef]
10. Goodman, S.M.; Mehta, B.Y.; Mandl, L.A.; Szymonifka, J.D.; Finik, J.; Figgie, M.P.; Singh, J.A. Validation of the hip disability and osteoarthritis outcome score and knee injury and osteoarthritis outcome score pain and function subscales for use in total hip replacement and total knee replacement clinical trials. *J. Arthroplast.* **2020**, *35*, 1200–1207. [CrossRef]
11. Perticarini, L.; Rossi, S.M.; Benazzo, F. Unstable total hip replacement: Why? Clinical and radiological aspects. *Hip Int.* **2020**, *30*, 37–41. [CrossRef] [PubMed]
12. Ray, G.S.; Ekelund, P.; Nemes, S.; Rolfson, O.; Mohaddes, M. Changes in health-related quality of life are associated with patient satisfaction following total hip replacement: An analysis of 69,083 patients in the Swedish Hip Arthroplasty Register. *Acta Orthop.* **2020**, *91*, 48–52. [CrossRef] [PubMed]
13. Kim, J.S.; Moon, N.H.; Do, M.U.; Jung, S.W.; Suh, K.T.; Shin, W.C. The use of dual mobility acetabular cups in total hip replacement reduces dislocation rates in hip dysplasia patients. *Sci. Rep.* **2023**, *13*, 22404. [CrossRef] [PubMed]
14. Hao, Y.; Wang, L.; Jiang, W.; Wu, W.; Ai, S.; Shen, L.; Dai, K. 3D printing hip prostheses offer accurate reconstruction, stable fixation, and functional recovery for revision total hip arthroplasty with complex acetabular bone defect. *Engineering* **2020**, *6*, 1285–1290. [CrossRef]
15. Hevesi, M.; Wyles, C.C.; Rouzrokh, P.; Erickson, B.J.; Maradit-Kremers, H.; Lewallen, D.G.; Berry, D.J. Redefining the 3D topography of the acetabular safe zone: A multivariable study evaluating prosthetic hip stability. *JBJS* **2022**, *104*, 239–245. [CrossRef] [PubMed]
16. Lakstein, D.; Eliaz, N.; Levi, O.; Backstein, D.; Kosashvili, Y.; Safir, O.; Gross, A.E. Fracture of cementless femoral stems at the mid-stem junction in modular revision hip arthroplasty systems. *J. Bone Jt. Surg.* **2011**, *93*, 57–65. [CrossRef] [PubMed]
17. Cassar-Gheiti, A.J.; McColgan, R.; Kelly, M.; Cassar-Gheiti, T.M.; Kenny, P.; Murphy, C.G. Current concepts and outcomes in cemented femoral stem design and cementation techniques: The argument for a new classification system. *EFORT Open Rev.* **2020**, *5*, 241–252. [CrossRef]
18. Al Zoubi, N.F.; Tarlochan, F.; Mehboob, H.; Jarrar, F. Design of titanium alloy femoral stem cellular structure for stress shielding and stem stability: Computational analysis. *Appl. Sci.* **2022**, *12*, 1548. [CrossRef]
19. Zajc, J.; Moličnik, A.; Fokter, S.K. Dual modular titanium alloy femoral stem failure mechanisms and suggested clinical approaches. *Materials* **2021**, *14*, 3078. [CrossRef]

20. Mavčič, B.; Antolič, V. Cementless femoral stem fixation and leg-length discrepancy after total hip arthroplasty in different proximal femoral morphological types. *Int. Orthop.* **2021**, *45*, 891–896. [CrossRef]
21. Radaelli, M.; Buchalter, D.B.; Mont, M.A.; Schwarzkopf, R.; Hepinstall, M.S. A new classification system for cementless femoral stems in total hip arthroplasty. *J. Arthroplast.* **2023**, *38*, 502–510. [CrossRef] [PubMed]
22. Springer, B.D.; Hubble, M.J.; Howell, J.R.; Moskal, J.T. Cemented femoral stem fixation: Back to the future. *J. Arthroplast.* **2023**, *38*, S38–S44. [CrossRef] [PubMed]
23. Buks, Y.; Wendelburg, K.L.; Stover, S.M.; Garcia-Nolen, T.C. The effects of interlocking a universal hip cementless stem on implant subsidence and mechanical properties of cadaveric canine femora. *Vet. Surg.* **2016**, *45*, 155–164. [CrossRef] [PubMed]
24. Toci, G.R.; Magnuson, J.A.; DeSimone, C.A.; Stambough, J.B.; Star, A.M.; Saxena, A. A systematic review and meta-analysis of non-database comparative studies on cemented versus uncemented femoral stems in primary elective total hip arthroplasty. *J. Arthroplast.* **2022**, *37*, 1888–1894. [CrossRef] [PubMed]
25. Jafari Chashmi, M.; Fathi, A.; Shirzad, M.; Jafari-Talookolaei, R.A.; Bodaghi, M.; Rabiee, S.M. Design and analysis of porous functionally graded femoral prostheses with improved stress shielding. *Designs* **2020**, *4*, 12. [CrossRef]
26. López-Subías, J.; Panisello, J.J.; Mateo-Agudo, J.; Lillo-Adán, M.; Bejarano, C.; Rodríguez-Chacón, L.; Martín-Hernández, C. Bone remodelling, around an anatomical hip stem: A one year prospective study using DEXA. *Rev. Española Cirugía Ortopédica y Traumatol. (Engl. Ed.)* **2021**, *65*, 31–40. [CrossRef]
27. Wolff, J. The Classic: On the Inner Architecture of Bones and its Importance for Bone Growth:(Ueber die innere Architectur der Knochen und ihre Bedeutung für die Frage vom Knochenwachsthum). *Clin. Orthop. Relat. Res.* **2010**, *468*, 1056–1065. [CrossRef]
28. Frost Harold, M. Wolff's Law and bone's structural adaptations to mechanical usage: An overview for clinicians. *Angle Orthod.* **1994**, *64*, 175–188.
29. Nabudda, K.; Suriyawanakul, J.; Tangchaichit, K.; Pholdee, N.; Kosuwon, W.; Wisanuyotin, T.; Sukhonthamarn, K. Identification of Flexural Modulus and Poisson's Ratio of Fresh Femoral Bone Based on a Finite Element Model. *Int. J. Online Biomed. Eng.* **2022**, *16*. [CrossRef]
30. Barui, S.; Chatterjee, S.; Mandal, S.; Kumar, A.; Basu, B. Microstructure and compression properties of 3D powder printed Ti-6Al-4V scaffolds with designed porosity: Experimental and computational analysis. *Mater. Sci. Engineering. C Mater. Biol. Appl.* **2017**, *70*, 812–823. [CrossRef]
31. Valtanen, R.S.; Hwang, K.L.; Amanatullah, D.F.; Huddleston, J.I., III; Maloney, W.J.; Goodman, S.B. Revision hip arthroplasty using a modular, cementless femoral stem: Long-term follow-up. *J. Arthroplast.* **2023**, *38*, 903–908. [CrossRef] [PubMed]
32. Restrepo, C.; Mashadi, M.; Parvizi, J.; Austin, M.S.; Hozack, W.J. Modular femoral stems for revision total hip arthroplasty. *Clin. Orthop. Relat. Res.* **2011**, *469*, 476–482. [CrossRef] [PubMed]
33. Hou, C.; Sinico, M.; Vrancken, B.; Denis, K. Investigation of the laser powder bed fusion manufacturing process and quasi-static behaviour of Ti6Al4V Voronoi structures. *J. Mater. Process. Technol.* **2024**, *328*, 118410. [CrossRef]
34. Thomas, J.; Alsaleh, N.A.; Ahmadein, M.; Elfar, A.A.; Farouk, H.A.; Essa, K. Graded cellular structures for enhanced performance of additively manufactured orthopaedic implants. *Int. J. Adv. Manuf. Technol.* **2024**, *130*, 1887–1900. [CrossRef]
35. Krishna, B.V.; Bose, S.; Bandyopadhyay, A. Low Stiffness Porous Ti Structures for Load–Bearing Implants. *Acta Biomater.* **2007**, *3*, 997–1006. [CrossRef] [PubMed]
36. Bougherara, H.; Zdero, R.; Dubov, A.; Shah, S.; Khurshid, S.; Schemitsch, E.H. A preliminary biomechanical study of a novel carbon–fibre hip implant versus standard metallic hip implants. *Med. Eng. Phys.* **2011**, *33*, 121–128. [CrossRef]
37. Gok, M.G. Static, fatigue and stress-shielding analysis of the use of different PEEK based materials as hip stem implants. *Int. Polym. Process.* **2022**, *37*, 152–163. [CrossRef]
38. Ortega, P.C.; Medeiros, W.B., Jr.; Moré, A.D.O.; Vasconcelos, R.F.; da Rosa, E.; Roesler, C.R.M. Failure analysis of a modular revision total HIP arthroplasty femoral stem fractured in vivo. *Eng. Fail. Anal.* **2020**, *114*, 104591. [CrossRef]
39. Chethan, K.N.; Bhat, N.S.; Zuber, M.; Shenoy, B.S. Finite element analysis of hip implant with varying in taper neck lengths under static loading conditions. *Comput. Methods Programs Biomed.* **2021**, *208*, 106273. [CrossRef]
40. Alfonzo-González, M.A.; Cerrolaza, M. Simulación y análisis computacional del conducto medular del fémur en presencia de una prótesis de cadera. *Rev. Fac. Ing. Univ. Cent. Venez.* **2013**, *28*, 25–34.
41. Morgan, E.F.; Unnikrisnan, G.U.; Hussein, A.I. Bone Mechanical Properties in Healthy and Diseased States. *Annu. Rev. Biomed. Eng.* **2018**, *20*, 119–143. [CrossRef] [PubMed]
42. Osterhoff, G.; Morgan, E.F.; Shefelbine, S.J.; Karim, L.; McNamara, L.M.; Augat, P. Bone mechanical properties and changes with osteoporosis. *Injury* **2016**, *47*, 11–20. [CrossRef] [PubMed]
43. Ceddia, M.; Trentadue, B. Evaluation of Rotational Stability and Stress Shielding of a Stem Optimized for Hip Replacements—A Finite Element Study. *Prosthesis* **2023**, *5*, 678–693. [CrossRef]
44. Xe, G. Mechanical properties of cortical bone and cancellous bone tissue. *Bone Mech. Handb.* **2001**, *10*, 1–23.
45. Darwich, A.; Nazha, H.; Daoud, M. Effect of coating materials on the fatigue behavior of hip implants: A three-dimensional finite element analysis. *J. Appl. Comput. Mech.* **2020**, *6*, 284–295.
46. Chen, W.-C.; Lai, Y.-S.; Cheng, C.-K.; Chang, T.-K. A cementless, proximally fixed anatomic femoral stem induces high micromotion with nontraumatic femoral avascular necrosis: A finite element study. *J. Orthop. Transl.* **2014**, *2*, 149–156. [CrossRef]
47. Weinans, H.; Sumner, D.R.; Igloria, R.; Natarajan, R.N. Sensitivity of periprosthetic stress-shielding to load and the bone density–modulus relationship in subject-specific finite element models. *J. Biomech.* **2000**, *33*, 809–817. [CrossRef] [PubMed]

48. Ceddia, M.; Trentadue, B.; De Giosa, G.; Solarino, G. Topology optimization of a femoral stem in titanium and carbon to reduce stress shielding with the FEM method. *J. Compos. Sci.* **2023**, *7*, 298. [CrossRef]
49. Stratton-Powell, A.A.; Pasko, K.M.; Brockett, C.L.; Tipper, J.L. The biologic response 423 to polyetheretherketone (PEEK) wear particles in total joint replacement: A systematic review. *Clin. Orthop. Relat. Res.* **2016**, *474*, 2394–2404. [CrossRef]
50. Chua, C.Y.; Liu, H.C.; Di Trani, N.; Susnjar, A.; Ho, J.; Scorrano, G.; Rhudy, J.; Sizovs, A.; Lolli, G.; Hernandez, N.; et al. Carbon fiber reinforced polymers for implantable medical 426 devices. *Biomaterials* **2021**, *271*, 120719. [CrossRef]
51. Nakahara, I.; Takao, M.; Bandoh, S.; Bertollo, N.; Walsh, W.R.; Sugano, N. In vivo implant fixation of carbon fiber-reinforced PEEK hip prostheses in an ovine model. *J. Orthop. Res.* **2013**, *31*, 485–492. [CrossRef] [PubMed]
52. Hacking, S.A.; Pauyo, T.; Lim, L.; Legoux, J.G.; Bureau, M.N. Tissue response to the components of a hydroxyapatite coated composite femoral implant. *J. Biomed. Mater. Res.* **2010**, *94*, 953–960. [CrossRef] [PubMed]
53. Scotchford, C.A.; Garle, M.J.; Batchelor, J.; Bradley, J.; Grant, D.M. Use of a novel carbon fibre composite material for the femoral stem component of a THR system: In vitro biological assessment. *Biomaterials* **2003**, *24*, 4871–4879. [PubMed]
54. Darwich, A.; Nazha, H.; Abbas, W. Numerical study of stress shielding evaluation of hip implant stems coated with composite (carbon/PEEK) and polymeric (PEEK) coating materials. *Biomed. Res.* **2019**, *30*, 169–174. [CrossRef]
55. Akay, M.; Aslan, N. Numerical and experimental stress analysis of a polymeric composite hip joint prosthesis. *J. Biomed. Mater. Res. Off. J. Soc. Biomater. Jpn. Soc. Biomater.* **1996**, *31*, 167–182. [CrossRef]
56. Caouette, C.; Yahia, L.; Bureau, M. Reduced stress shielding with limited micromotions using a carbon fibre composite biomimetic hip stem: A finite element model. *Proc. Inst. Mech. Eng. H* **2011**, *225*, 907–919. [CrossRef] [PubMed]
57. Allcock, S.; Ali, M.A. Early failure of a carbon-fiber composite femoral component. *J. Arthroplast.* **1997**, *12*, 356–358. [CrossRef]
58. Palmisano, A.C.; Nathani, A.; Weber, A.E.; Blaha, J.D. Femoral Neck Modularity: A Bridge Too Far-Affirms. *Semin. Arthroplast.* **2014**, *25*, 93–98. [CrossRef]
59. Blakey, C.M.; Eswaramoorthy, V.K.; Hamilton, L.C.; Biant, L.C.; Field, R.E. Mid-Term Results of the Modular ANCA-Fit Femoral Component in Total Hip Replacement. *J. Bone Jt. Surg. Ser. B* **2009**, *91*, 1561–1565. [CrossRef]
60. Atwood, S.A.; Patten, E.W.; Bozic, K.J.; Pruitt, L.A.; Ries, M.D. Corrosion-Induced Fracture of a Double-Modular Hip Prosthesis: A Case Report. *J. Bone Jt. Surg. Ser. A* **2010**, *92*, 1522–1525. [CrossRef]
61. Bennett, D.B.; Hill, J.C.; Dennison, J.; O'Brien, S.; Mantel, J.L.; Isaac, G.H.; Beverland, D.E. Metal-carbon fiber composite femoral stems in hip replacements: A randomized controlled parallel-group study with mean ten-year follow-up. *JBJS* **2014**, *96*, 2062–2069. [CrossRef]
62. Gilbert, J.L.; Mali, S.; Urban, R.M.; Silverton, C.D.; Jacobs, J.J. In Vivo Oxide-Induced Stress Corrosion Cracking of Ti-6Al-4V in a Neck-Stem Modular Taper: Emergent Behavior in a New Mechanism of in Vivo Corrosion. *J. Biomed. Mater. Res. Part. B Appl. Biomater.* **2012**, *100B*, 584–594. [CrossRef]
63. Lanzutti, A.; Andreatta, F.; Rossi, L.; Di Benedetto, P.; Causero, A.; Magnan, M.; Fedrizzi, L. Corrosion Fatigue Failure of a High Carbon CoCrMo Modular Hip Prosthesis: Failure Analysis and Electrochemical Study. *Eng. Fail. Anal.* **2019**, *105*, 856–868. [CrossRef]

Journal of
Composites Science

MDPI

Article

Processing and Mechanics of Aromatic Vitrimeric Composites at Elevated Temperatures and Healing Performance

Tanaya Mandal [1], Unal Ozten [2], Louis Vaught [3], Jacob L. Meyer [4], Ahmad Amiri [5,6], Andreas Polycarpou [3,5] and Mohammad Naraghi [2,*]

[1] Department of Materials Science & Engineering, Texas A&M University, College Station, TX 77843, USA; tmandal90@tamu.edu
[2] Department of Aerospace Engineering, Texas A&M University, College Station, TX 77843, USA; uozten@tamu.edu
[3] J. Mike Walker '66 Mechanical Engineering Department, Texas A&M University, College Station, TX 77843, USA; lovaught@tamu.edu (L.V.); andreas-polycarpou@utulsa.edu (A.P.)
[4] ATSP Innovations, Houston, TX 77055, USA; jacob.l.meyer@atspinnovations.com
[5] Russell School of Chemical Engineering, The University of Tulsa, Tulsa, OK 74104, USA; ahmad-amiri@utulsa.edu
[6] Department of Mechanical Engineering, The University of Tulsa, Tulsa, Oklahoma 74104, USA
* Correspondence: naraghi@tamu.edu

Abstract: Carbon fiber reinforced polymer (CFRP) composites are renowned for their exceptional mechanical properties, with applications in industries such as automotive, aerospace, medical, civil, and beyond. Despite these merits, a significant challenge in CFRPs lies in their repairability and maintenance. This study, for the first time, delves into the processing and self-healing capability of aromatic thermosetting co-polyester vitrimer-based carbon fiber composites through mechanical testing. Vitrimers are an emerging class of thermosetting polymers, which, owing to their exchangeable covalent bonds, enable the re-formation of bonds across cracks. The specific vitrimer chosen for this study is an aromatic thermosetting co-polyester (ATSP). The mechanical properties of samples were analyzed initially through three-point bending (3PB) testing at room temperature before and after healing (by curing samples for 2 h at 280 °C). Samples were also 3PB tested at 100 °C to analyze their mechanical properties at an elevated temperature for comparison to the samples tested at room temperature. To investigate the fracture properties, optical microscopy images of samples were taken after 3PB tests, which were analyzed to observe crack initiation and crack growth behavior. Through load–displacement curves from double cantilever beam (DCB) mechanical testing, the Mode I crack initiation fracture toughness values of self-healed composites and control composites were calculated to evaluate healing efficiency in ATSP CFRP composites cured at 280 °C for 2 h. Scanning electron microscopy (SEM) showed a similar surface morphology of cracks before and after self-healing. Micro-computed tomography (CT) X-ray imaging confirmed that the healed samples closely resembled the as-fabricated ones, with the exception of some manufacturing voids, caused by outgassing in the initial healing cycle. This research demonstrated the ability for the in situ repair of ATSP CFRPs by restoring the fracture toughness to values comparable to the pristine composite (~289 J/m^2).

Keywords: carbon fibers; polymer matrix composites; aromatic thermosetting co-polyester; vitrimers; self-healing

1. Introduction

Carbon fiber reinforced polymers (CFRPs) are highly desired in many fields including automotive, aerospace, and medical industries due to their exceptional mechanical properties, such as high elastic modulus and mechanical strength (as high as 1200–2410 MPa). These properties often exceed those of traditional engineering materials such as steel and aluminum, while offering the advantages of lower mass density and remarkable corrosion resistance [1–7]. In

a polymer-based composite, the matrix is a thermoset or thermoplastic [8–10]. Thermoset matrices contain polymer chains connected by strong covalent bonds, forming a network structure post-curing, offering enhanced thermal stability and strength [7,11–14]. Therefore, thermosets are extensively used in various sectors, including aerospace and wind energy [7,11–13].

Although thermoset composites have desirable properties, a main challenge is maintenance and repair, which is required upon the formation of microcracks, for instance, due to cyclic loading and fatigue damage, especially in aerospace epoxies [14–17]. In contrast, cracks in thermoplastics can heal by means of chain reconfiguration with heat, allowing dispersive bond reformation when crack faces are brought together above their glass transition temperature (T_g) [14,18].

Numerous studies have achieved self-healing in thermoset composites via incorporating microcapsules or microvascular networks to deliver healing agents into cracks after ruptured as well as self-healing intrinsic reactions in composites [19–28]. Microcapsule-based strategies include utilizing encapsulated healing agents such as ruthenium-based catalysts (Grubb's catalyst, G3) with 5-ethylidenenorbornene/dicyclopentadiene (ENB/DCPD) microcapsules [24–31], which demonstrated a 50% healing efficiency [24]. Although self-healing occurs through these microcapsule strategies, challenges persist such as monitoring the full use of healing agents and addressing insufficient microcapsule integration, resulting in partial self-healing. To combat this issue, Dry et al. developed a self-healing strategy involving microvascular networks, which embed liquid healing agents in hollow fiber or tubes. These methods increased the content of liquid healing agent that is injected into the samples' crack planes [32–35]. Some approaches use larger channels filled with resin, while others use smaller glass fibers filled with a cyanoacrylate resin to both heal and support the structure [36–38]. These techniques can restore ~97% of a material's flexural strength [23,38–44]. However, microvascular networks have disadvantages such as the need for low-viscosity resin to facilitate fiber infiltration and thermal strains in the composite due to thermal expansion coefficient mismatches. Moreover, given the much wider diameter of the microvascular tubes, the presence of the tubes required the removal of a large number of fibers, thereby diminishing the performance of the as-fabricated composites.

To address these challenges, it is desired for the thermoset matrix to exhibit reversible interchain bonding capability. This property enables damage repair similar to thermoplastics. To integrate these features, reformable covalent bonds are incorporated into the matrix, allowing thermoset network reconfiguration. In the 1990s, Economy's research group pioneered thermoset polymers with plasticity and adhesive bond formation across interfaces from bond exchange reactions [45,46]. From epoxy resins containing polyester bonds, Leibler et al. drew an analogy to glass by naming thermosets possessing exchangeable bonds as vitrimers [14,47]. Vitrimers' network structures can be reversible at/above certain temperatures depending on chemical composition [14,46]. Prior to crosslink formation, vitrimers exhibit viscous properties ~T_g according to Arrhenius' law [48,49]. At around the so-called freezing transition temperature (Tv), reversible reactions occur at labile sites, enabling self-healing and thermoplastic-like behavior [50–53].

Vitrimers, which can be utilized as a matrix material in CFRPs, should also demonstrate enhanced mechanical strength and retain bond exchange capability through covalent adaptable networks such as transesterification [53–55]. Transesterification exchanges bonds between beta-hydroxyls and esters cause epoxy precursor reactions with acids or anhydrides. Transesterification can be accelerated by metal-containing compound catalysts, such as zinc catalysts, which modulate epoxy resin reactivity through ligand exchange, causing anhydride ring-opening β-hydroxyl ester chain formation, resulting in monoester and carboxylic acid production [4]. In one study, diglycidyl ether (DGEBA) epoxy resin was treated with glutaric anhydride treatment. These samples underwent two different cure cycles: 180 °C for 4 h and 200 °C for 4 h. After DCB testing and healing, samples cured at 200 °C exhibited higher healing efficiency (~80%), compared to ~65% for samples cured at 180 °C [55]. In another study, a vitrimeric epoxy system was synthesized using

DGEBA and AV5 (1:1 epoxy/acyl ratio with 5% zinc acetate catalyst). DCB tests showed a decrease in G_{IC} for AV5 samples compared to epoxy resin A samples. Furthermore, lap shear tests on AV5 samples heated to ~200 °C revealed an ~84% healing efficiency [54]. These vitrimeric composites are desirable due to their recyclability, repairability, and reprocessability. Challenges include depolymerization and repolymerization as a self-healing mechanism to maintain composite integrity, especially at high temperatures >300 °C. Vitrimers withstanding high temperatures and maintaining integrity are sought to address these challenges.

One particularly high-performing vitrimer, which contains an effective combination of thermoset and thermoplastic properties, is known as aromatic thermosetting co-polyester (ATSP) [56]. ATSP contains crosslinked aromatic polyester oligomers, which have two oligomer types: those with acetoxy end groups (A-type) and those with carboxylic end groups (C-type). The oligomer combinations can include CB2AB2 and C1A1, derived from oligomer types such as C1, CB, A1, and AB, where B is derived from bisphenol diacetate. The ATSP family of vitrimers has notable properties such as self-healing, high T_g (174–310 °C), and resistance to high temperatures (>300 °C) [57,58]. The self-healing mechanism in ATSP is activated by interchain transesterification reactions when ATSP reaches temperatures > T_g [15,57–60]. These curing reactions involve covalent bond exchange between two thermoset ATSP sheets by reversible bonding through acidolysis and esterolysis with acetic acid by-products [57,61]. Uniquely, among published vitrimeric materials, ATSP resins are all fully aromatic thermosets—giving them very high T_g values among vitrimers. Additionally, their potential for strong liquid crystalline character, as introduced by their aromatic polyester repeat units, introduces characteristics, advantages, and challenges not typically seen in vitrimers [6].

Previous experimentation demonstrated that ATSP has minimal moisture absorption, similar to epoxy resins, and enhanced thermal stability, which is comparable to high-performing thermoset polyimides [62–64]. ATSPs have easier repairability than both polyimide and epoxy materials. ATSP is stable in air at 350 °C and also surpasses the decomposition thresholds temperature of most thermally stable epoxies in air (~170–190 °C) [65,66]. ATSPs have increased durability from physical aging since the moisture pickup of ATSP is low (0.3 wt%) compared to polyimides (2.6%) and epoxy (2.3%) [64–66]. These ATSP properties are desirable for high-temperature applications such as tribology, aerospace, oil and gas, and automotive industries [59,67,68].

In the present study, CB2AB2 ATSP was used as the matrix material to create CFRP composites to evaluate ATSP's self-healing properties on pre-notched samples and bending coupons. The CB2AB2 resin was chosen from the studied ATSP-type resins due to its lowest T_g within the family (174 °C) and because it was previously studied for its effective reversible bonding performance on metallic adherends. These characteristics suggest that it would perform well as the CFRP's matrix phase [58,61]. For the pre-notched samples, CFRPs were DCB-tested before and after self-healing to evaluate healing efficiency after a cure cycle. Based on load–displacement curves from DCB testing, the Mode I crack initiation fracture toughness (G_{IC}) and healing efficiency of ATSP CFRPs were calculated. Morphological analysis from SEM imaging and micro–CT X-ray imaging of the crack surfaces for both the as-fabricated ATSP CFRP samples and self-healed samples show evidence of similar surface morphology. In addition, 3PB testing of CFRPs was conducted to analyze mechanical properties at room temperature before and after self-healing at 280 °C for 2 h based on fracture mechanism behavior. The ATSP CFRP samples exhibited reduced fiber failure due to fiber sliding in 3PB testing conducted at room temperature before and after healing.

2. Experimental Section

2.1. Materials

The vitrimer used in this study was CB2AB2 ATSP, which was supplied by ATSP Innovations (Houston, TX, USA). N-methyl-2-pyrrolidone (NMP) was purchased from Millipore

Sigma (Burlington, MA, USA). Unidirectional carbon fiber sheets (12K unidirectional carbon fiber fabric, 95% carbon; Fiber Glast, Brookville, OH, USA) were used for composite fabrication.

2.2. ATSP CFRP Composite Processing

Composites were fabricated by first coating unidirectional carbon fiber sheets (12K unidirectional carbon fiber fabric, 95% carbon; Fiber Glast, Brookville, OH, USA) with ATSP and NMP, using a convection oven and a hot press. Eight 254 mm × 254 mm carbon fiber sheets were coated with a mixture of ATSP (CB2AB2) and NMP. The ATSP (density: 1.32 g/cm^3) and NMP were stirred via magnetic stir bar for 24 h at 400 rpm at room temperature. This mixture was then sonicated for 30 min and then magnetically stirred at 900 rpm at 90 °C for 24 h. The ATSP/NMP mixture was applied to each carbon fiber sheet with a roller and spreader. Sixteen sheets were placed in an oven to evaporate the NMP at 60 °C for 12 h. These sheets were then partially cured in the oven at 230 °C for 1 h followed by 260 °C for 1 more hour. After the partial cure to form the thermoset network from ATSP in the carbon fiber sheets, the sheets were cut into thirty-two 127 mm × 254 mm sheets. In preparation of hot pressing these sheets, an aluminum plate was prepared with a release layer of aluminum foil sheet, and sixteen carbon fiber sheets were placed on top. Six 63.5 mm aluminum foil sheets (three sheets at each end for DCB sample preparation) were placed between the two middle plies to maintain the pre-crack regions of the composite panel. The pre-crack dimensions were selected as per ASTM 5528 standards. The remaining sixteen carbon fiber sheets were then positioned, followed by the placement of another aluminum plate on top, and underwent hot pressing at 330 °C for 1 h under 5 MPa. This completed the composite laminate configuration of $[0]_{16s}$. The samples were removed from the hot press to cool, demolded, and cut into fourteen pieces via computer numerical control (CNC) (Mega V Router; Mill Right CNC, Leesburg, GA, USA) and a band saw. T-shaped sample grip fixtures were made from aluminum and fitted with aluminum rods. The grips were designed and cut from an aluminum plate. To prepare the samples for DCB testing, grip fixtures were fitted with resin glue on the pre-cracked end of the samples. ATSP CFRP samples with attached grip fixtures were fitted in the sample grip fixtures for DCB testing. A schematic of the procedure to construct ATSP CFRP samples is illustrated in Figure 1.

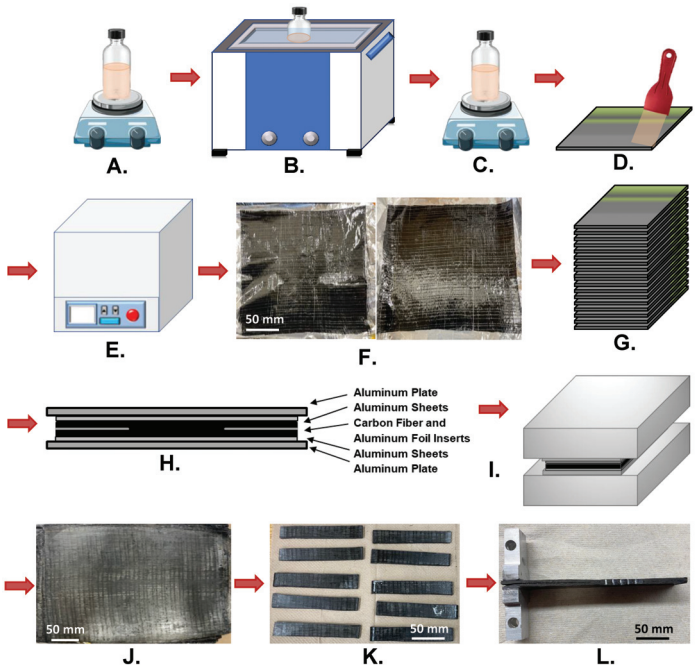

Figure 1. Schematic of ATSP CFRP composite processing is shown. (**A**–**C**). NMP-ATSP solution was obtained through a series of magnetic stirring and sonication. (**D**). The solution was spread onto

carbon fiber sheets. (**E**). Coated carbon sheets were cured in the oven. (**F**). ATSP-coated cured sheets were taken out of the oven. (**G**). Coated cured sheets were laid up. (**H**). The carbon fiber sheets, aluminum foil sheets, aluminum foil inserts, and aluminum plates were laid up for hot pressing. (**I**). The sample was hot-pressed. (**J**). The completed ATSP CFRP panel was removed from the hot press. (**K**). The panel was cut into fourteen samples. (**L**). Grip fixtures were glued to samples for DCB testing.

2.3. Sample Preparation and Mechanical Characterization of the Composites

For the three-point bending (3PB) tests, the composite panel was cut into samples for three-point bend (3PB) testing with dimensions of ~63 mm × 12.50 mm × 2.5 mm. The 3PB testing was performed at 1 mm/min using the ASTM 7264 standard with a gauge length of ~48 mm in two different temperature conditions: room temperature and 100 °C. A minimum of three tests were performed per case. To evaluate the ability of the material to recover from plastic deformations, the 3PB tests were carried out in a displacement-controlled mode, and the displacement was continued beyond the peak load, followed by unloading. The mechanical properties of the samples, namely the flexural strength and modulus, was compared between the samples tested at room temperature and elevated temperature to evaluate the effect of thermally induced softening and the viscoelastic behavior of the matrix on the overall mechanical properties of the composites.

Next, we utilized the exchangeable bonds in the matrix to recover the initial unbent shape of the 3PB tested samples. To this end, the plastically bent samples were heated in the oven at 280 °C for 2 h by clamping them between two aluminum plates under ~0.03 MPa. This temperature was selected to be considerably above the vitrification temperature to accelerate the healing of the samples. These samples were then retested at room temperature to compare and evaluate the extent to which the mechanical properties of the unbent samples were recovered. The room temperature samples underwent two healing cycles and retested for 3PB testing at room temperature. Flexural strength, modulus, and maximum strain were calculated after 3PB testing.

The flexural strength (σ) was calculated by using Equation (1), where P is applied force (N), L is gauge length (mm), b is width (mm), and h is thickness (mm):

$$\sigma = \frac{3PL}{2bh^2} \tag{1}$$

The flexural secant modulus of elasticity (E_f^{secant}) was calculated by using Equation (2), where m is the slope of the secant of the force–displacement curve.

$$E_f^{secant} = \frac{L^3 m}{4bh^3} \tag{2}$$

Moreover, the maximum strain experienced by the sample at the peak load (ε_{max}) during the 3PB test was calculated by Equation (3)

$$\varepsilon_{max} = \frac{6\delta h}{L^2} \tag{3}$$

2.4. Double Cantilever Beam Testing (DCB) and Self-Healing Cure Cycles

The DCB test was performed on ATSP CFRPs following the ASTM 5528 standards at a strain rate of 5 mm/min with a 2.5 kN load cell (MTS Systems Corporation, Eden Prairie, MN, USA) on the MTS Insight electromechanical tester machine (MTS Systems Corporation, Eden Prairie, MN, USA). The dimensions of each sample were 127 mm × 20.27 mm × 2.78 mm. The samples were secured by using pneumatic grips powered by compressed air on the sample grips holding the grip fixtures. During DCB testing, crack growth was measured optically by video recording the crack propagation so that data retrieval and video were concurrent. Crack length, a, was measured as the horizontal distance from the T bars to the end of the pre-crack region (Figure 2).

The DCB tests were run on each sample before and after healing (cure) cycles. Based on the test and healing procedure, the four samples were DCB-tested initially and then samples were cured at 280 °C for 2 h and cooled for 1 h. For the cure cycle, the samples with propagated cracks were placed between two aluminum plates wrapped in aluminum foil and secured by a clamp. Each sample was then self-healed in a Vulcan oven at 280 °C for 2 h and cooled for 1 h by clamping a sample between two aluminum plates under ~0.03 MPa. Following the cure cycles, the samples were tested again. Load–displacement data were recorded during the DCB tests to extract fracture toughness. The DCB experimental setup is shown in Figure 2.

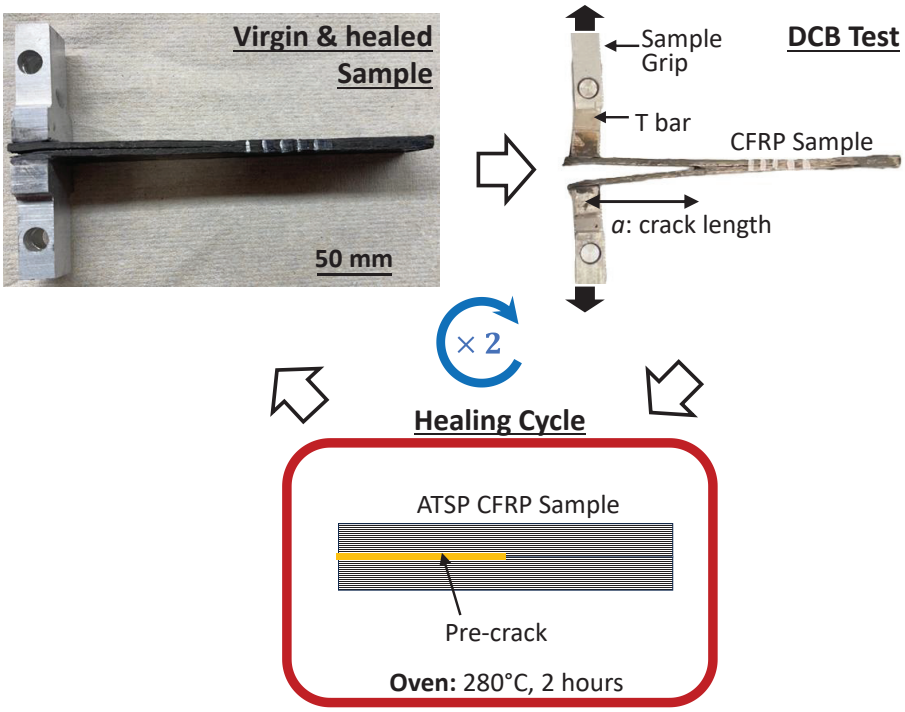

Figure 2. The virgin composite is first subjected to DCB test, followed by self-healing cycle and a subsequent DCB test to characterize the performance of the healed sample relative to the virgin material.

2.5. Measurement of Mode I Fracture Toughness and Healing Efficiency

The load–displacement data were then used to calculate Mode I interlaminar fracture toughness, G_{IC} (J/m^2), by using Equation (4), where ΔU is change in internal work (N mm), b is width (mm), a is crack length (mm), P is the load at crosshead displacement (N), δ is the displacement (mm), w is width (mm), and a is crack length (mm):

$$G_{IC} = \frac{1\Delta U}{b\Delta a} \text{ where } \Delta U = \int_0^{\delta} Pd\delta|_{\Delta a'} \quad (4)$$

where P and δ were obtained from the DCB testing, and b was measured for each sample [69]. a was acquired optically from the video of the crack growth. The G_{1C} was calculated for all samples before healing (virgin sample) and after self-healing (healed sample) and denoted as $G_{IC\text{-}v}$ and $G_{IC\text{-}h}$, respectively. The healing efficiency (H) of the ATSP CFRP samples was assessed by dividing the G_{IC} value before self-healing ($G_{IC\text{-}v}$) by the G_{IC} of the sample after self-healing ($G_{IC\text{-}h}$), as presented in Equation (5) [24]:

$$H(\%) = \frac{G_{IC-h}}{G_{IC-v}} \times 100 \quad (5)$$

The "area" approach laid out in Equation (4) to calculate the fracture toughness from DCB tests, unlike other methods, such as the "compliance" method, does not require compliance corrections based on the "true" value of the crack length [70]. Therefore, even

though it cannot be used to obtain an R-curve by calculating values of G_{IC} at different crack lengths, it is commonly used in the self-healing literature [71].

2.6. Material Characterization

A V2 Teledyne Lumenera INFINITY Optical Microscope was used to image the crack and fracture surface morphology of the 3PB samples before and after each healing cycle. An FEI Quanta 600 Field Emission Scanning Electron Microscope was used to image the surface morphology of the cracked surface of the samples before and after self-healing. Micro-CT X-ray imaging, utilizing the North Star Imaging (NSI) X50 X-ray/CT, was used to examine the internal structural morphology of ATSP CFRP samples before and after self-healing.

3. Results and Discussion

3.1. Identification of the Vitrification Temperature

To determine the temperature conducive to the healing process, we initially assessed the vitrification temperature of the polymer. The vitrification temperature, T_v, represents the lower temperature threshold at which healing may take place, with the option of employing higher temperatures to expedite the healing process. Traditionally, the vitrification temperature for self-healing thermosets is analyzed via either a fixed-displacement stress relaxation analysis or a fixed-load creep study. These methods determine the temperature at which the material begins to undergo plastic flow, representing a macroscale response that corresponds to molecular bond exchange behavior. For both the CB2AB2 material and ATSP copolyester vitrimers, analysis via these methods is obfuscated by significant viscoelastic response. Previous studies into the wear performance of materials within this family have shown significant elastic recovery via indentation testing [72–74]. As such, to confidently demonstrate the presence of self-healing behavior within the material, a cyclic creep test methodology was developed using a 30 min on–off loading cycle at 20 °C temperature increments and a loaded stress of 100 kPa. This procedure follows a prior study, which used a similar methodology to demonstrate self-healing but not to precisely determine the vitrification temperature [74]. Testing was performed using a PerkinElmer DMA 8000 in tensile mode, with a grip spacing of 10 mm; the raw test data are shown in Figure 3A and can be interpreted directly by noting trends in residual displacement after the material is relaxed. Under this testing regime, the material exhibited residual deformation until 140 °C, followed by recovery to an amount of permanent deformation that falls within the measurement error of the machine by 180 °C, indicating T_v = ~160–180°C, highlighted in Figure 3B.

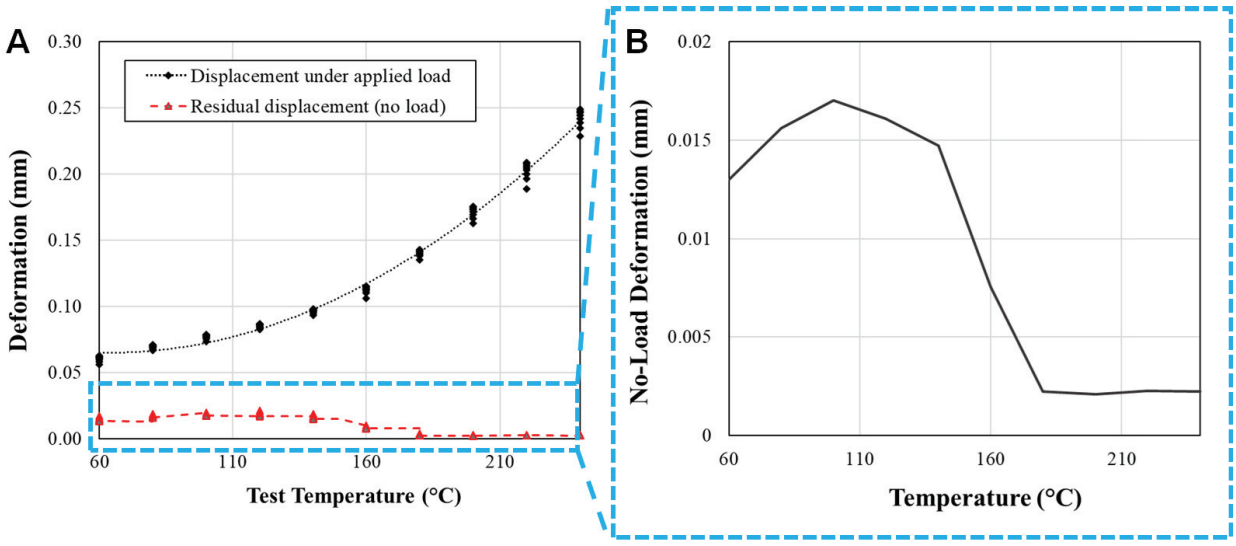

Figure 3. Vitrification temperature analysis showing (**A**) raw data from cyclic creep loading tests and (**B**) residual deformation in unloaded test sample as temperature is increased.

3.2. Mechanics of Vitrimeric Composites at Room and Elevated Temperatures

Advanced polymer-based composites are often exposed to temperatures above room temperature during their lifetime. A limiting factor at such temperatures includes various molecular relaxation mechanisms, such as polymer chain segmental mobility, as well as thermal degradation. To evaluate the mechanical behavior of vitrimeric composites, their mechanical properties such as flexural strength and modulus were measured via three-point bending (3PB) testing at two different temperatures: room temperature and 100 °C. This temperature range was chosen such that the dependence of the mechanical properties of the vitrimeric composites on temperature can be compared and contrasted with the corresponding changes in conventional epoxy composites in the literature [75,76]. The 3PB tests were displacement controlled, and the load applied to the midspan of the sample was monotonically increased until a peak in the load was achieved followed by ~3 mm of extra deflection (corresponding to a maximum tensile strain of ~1.2–1.4%). The applied deflections beyond the peak load were primarily intended to induce damage and plastic deformation in the sample and to subsequently explore the utility of the bond exchanges to recover the initial shape via thermo-mechanical processing.

In the samples that were mechanically loaded at room temperature, the load dropped suddenly when the peak load was reached, due to fiber rupture on the tensile side (Figure 4A). The damage, which mainly occurred during the ~3 mm deflections past the peak load, were studied via optical microscopy. Samples experienced material failure and structural damage (buckling) on the tensile and compressive sides of the sample, respectively, during 3PB testing, as seen from optical images in Figure 4C. On the tensile side (the face that is away from the loading fixture), the surfaces experienced fiber–matrix separation, with some fibers being fractured by the application of high tensile forces. Additionally, matrix cracks were observed on that surface. Conversely, on the compressive side, fibers exhibited breakage, often accompanied by sharp-edged matrix fractures resulting from buckling and fiber deformation away from their straight axis, rather than fiber–matrix separation. However, in the samples that were 3PB-tested at 100 °C, upon reaching the peak load, a gradual decline in the load with displacement was observed, indicative of the sliding between fibers (Figure 4A). The optical images support these findings, as seen in Figure 4C. Comparing initial 3PB tests conducted at room temperature and at elevated temperature, 3PB test analysis reveals that no significant fiber breakage occurred at elevated temperature, since fibers were able to slide during loading.

The flexural strength and modulus of the samples tested at RT and elevated temperature were then estimated from the 3PB load–displacement curves, as presented in Figure 4D,E. The measured strength and modulus of the samples at RT are 888.6 $\pm$ 109.2 MPa and 86.03 $\pm$ 10.2 GPa, respectively, which is comparable to the properties of advanced composites made with conventional epoxy resins [77,78]. Moreover, the strength and modulus of the samples at RT are ~59% and ~58% higher than the high temperature values, respectively, reflecting the molecular relaxation mechanisms in the matrix at the elevated temperatures. The drop in strength and modulus in our vitrimer composites at elevated temperatures is comparable to those obtained from continuous carbon fiber composites with conventional epoxy matrix [79]. Given the permanent nature of covalent bonds in the conventional epoxy matrix and the dynamic nature of those bonds in ATSP, this favorable comparison reveals the robustness of the exchangeable bonds in our matrix material.

Next, in the plastically deformed three-point bent samples, we studied the utility of the bond exchanges to recover their initial flat shape. For this investigation, the plastically bent samples were subsequently placed in an oven at 280 °C for 2 h at ~0.03 MPa of pressure. As a result of the application of the applied pressure and temperature, the initial shape of the samples (straight bars with no bent) was fully recovered, indicating the significance of bond exchanges in recovering the initial shape of the bars. The images of samples before and after 3PB testing in different temperature conditions as well as the healing setup are seen in Figure 4B. To quantify the extent of the recovery in mechanical properties, the

plastically deformed and subsequently straightened samples were subjected to 3PB tests. Flexural strength and modulus were calculated for these samples before and after healing, as shown in Figure 4D,E.

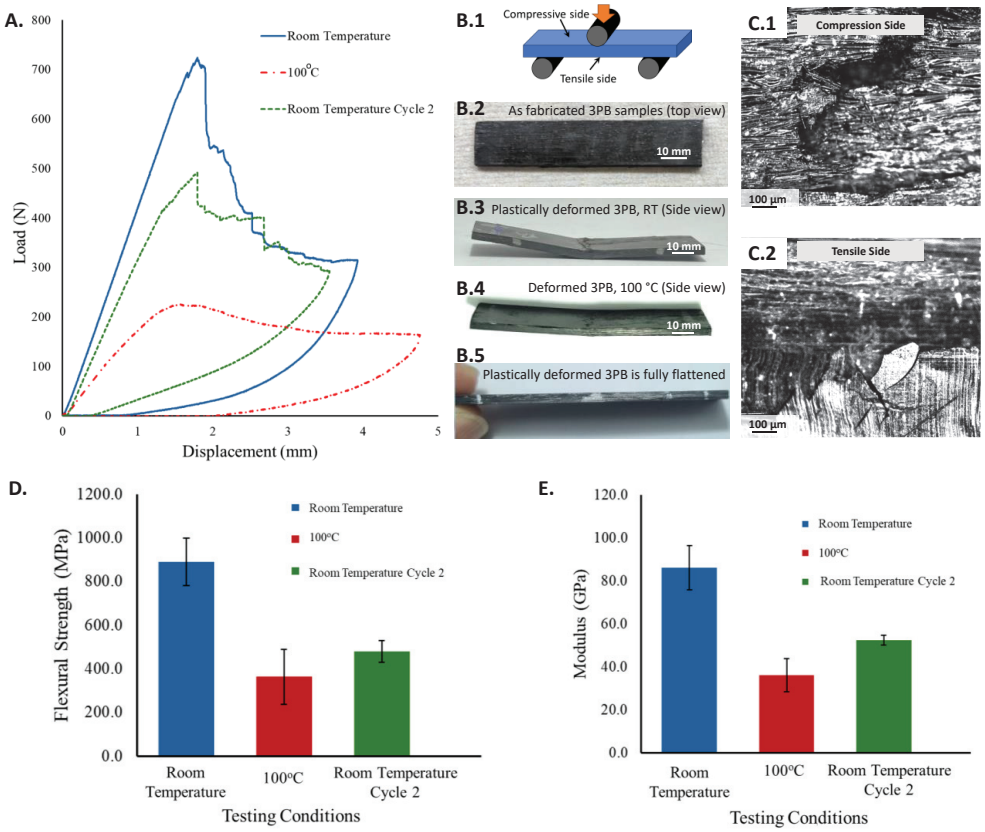

Figure 4. (**A**) Representative load–displacement curves are seen for samples 3PB tested at room temperature, 100 °C, and after one cycle of healing for the room temperature samples. (**B**) (Top) Schematic of 3PB sample is shown. (**B.1**) Schematic of 3PB test, (**B.2**) top view of the as-fabricated sample, (**B.3**) side view of the 3PB sample tested at room temperature, (**B.4**) side view of the 3PB sample tested at 100 °C temperature, (**B.5**) the plastically deformed samples flattened out to their initial shape. (**C**) Digital images of samples before and after 3PB testing and healing with healing set up for room temperature samples shown. (**D**) A graph comparing average flexural strength of 3PB-tested samples is shown. (**E**) A graph comparing average modulus of 3PB-tested samples is shown.

As seen from Figure 4, the strength and modulus of the hot-pressed samples is nearly 50% of the as-fabricated samples. While the full recovery of the initial flat shape is indicative of the role of bond exchange at elevated temperatures that allows for sliding between fibers, the recovery in mechanical properties is only partial, mainly due to nonreversible damages accumulated on the sample, such as fiber failure.

3.3. Mode I Fracture Toughness of Virgin and Healed Vitrimeric Composites

DCB test was conducted on composite samples, and foe each sample it yielded a load vs. displacement curve in a displacement-controlled loading. In this curve, the force initially increased with displacement. Throughout this phase, the crack mouth opened without any apparent crack growth. Following this initial rise, the load rapidly decreased. When synchronizing the data with a video of the DCB testing, this decrease was associated with crack growth as well as a resounding crack noise. After this load drop, the load–displacement curve showed a saw-tooth behavior, corresponding to instances of crack growth and crack arrest [80]. The sample was fully unloaded when the crack grew by ~20 mm from the initial crack length (a_0) of ~54 mm at a rate comperable to the loading

rate. As expected, the accumulated damage on the sample led to a reduced stiffness, such that the zero load corresponds to nearly zero displacement. A representative example of a load–displacement curve with a change in crack length (Δa) for an ATSP CFRP sample is shown in Figure 5.

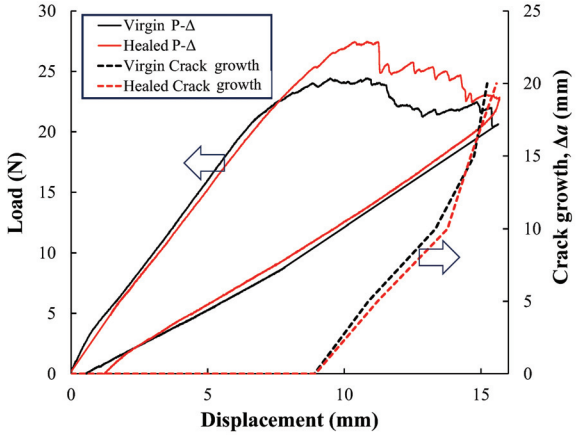

Figure 5. DCB results used for calculating G_{IC} from load vs. displacement and change in crack length of DCB testing before and after a sample was self-healed at 280 °C for 2 h.

After the crack growth, the sample was unmounted, the two faces of the crack were pressed against one another via a grip, and the sample was placed inside an oven at 280 °C for 2 h to complete the healing, at a pressure of ~0.03 MPa. This temperature was chosen as it was above the T_v (~160 °C) after vitrification temperature analysis, as seen in Section 3.1, which is required to trigger the bond exchange and reformation of the crosslinks (Figure 5). The fixtures were mounted onto the healed samples, and the DCB tests were repeated to measure $G_{IC\text{-}h}$.

The fracture toughness of the virgin and healed samples, $G_{IC\text{-}v}$ and $G_{IC\text{-}h}$, respectively, were calculated as discussed in Section 2.5 and compared in Figure 6. Healing efficiency, as the ratio of $G_{IC\text{-}h}$ to $G_{IC\text{-}v}$, was estimated for all samples, as reported in Table S1 (109.48 ± 7.92). Even though the average value of healing efficiency is slightly more than one, the values of $G_{IC\text{-}v}$ and $G_{IC\text{-}h}$ were statistically the same as verified by a *t*-test with a significance level (α) of 0.05. Here, the *t*-test null hypothesis is defined as foillows: there is no significant difference between the average $G_{IC\text{-}v}$ and $G_{IC\text{-}h}$. The *p*-values were calculated by $p = 2 \times (1 - t_{dist}(|t|, df))$ to be ~0.394, where t is the *t*-statistic, t_{dist} is the cumulative distructation of the *t*-distribution, and df is degrees of freedom. Therefore, the *p*-value is much more than 0.05, and the null hypothesis stands. The mechanisms which may lead to slightly higher than unity healing efficiency are explained in Section 3.5.

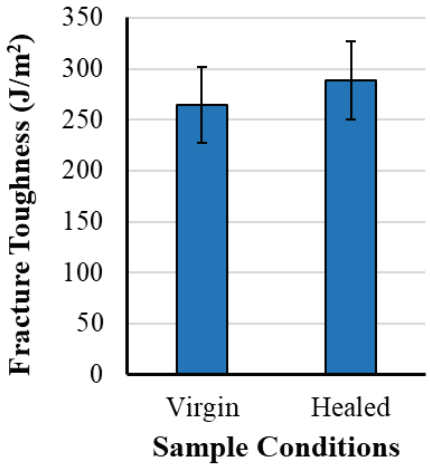

Figure 6. $G_{IC\text{-}v}$ and $G_{IC\text{-}h}$ comparison is shown in the graph.

3.4. Fracture Surface Morphology of DCB Samples

More insight into the healing mechanisms in DCB samples was obtained via investigating the morphology of the samples. To study the fracture surface of ATSP CFRP samples (both the as-fabricated samples and the virgin and self-healed samples), the sample was loaded in the DCB test until the two parts of a sample debonded. The fracture surface was then imaged in SEM. The fractured crack surfaces of the as-fabricated and healed samples were SEM-imaged in the vicinity of the initial crack tip, as shown in the schematic in Figure 7A. The crack path is prominent in the ATSP CFRP samples after DCB testing before self-healing (Figure 7B). Prominent longitudinal intralaminar crack growth is seen in the direction of the carbon fibers in the ATSP CFRP sample. A similar crack path is seen along the direction of the longitudinal crack in the ATSP CFRP sample after DCB testing after self-healing (Figure 7C). After self-healing, the crack path surface and carbon fiber structure are similar to the surface morphology on the as-fabricated ATSP CFRP sample. In both samples, there are observable similar appearances of surface ATSP resin residue and carbon fibers. These surface morphological findings support the effectiveness of the self-healing behavior of ATSP to maintain the integrity of the CFRP sample.

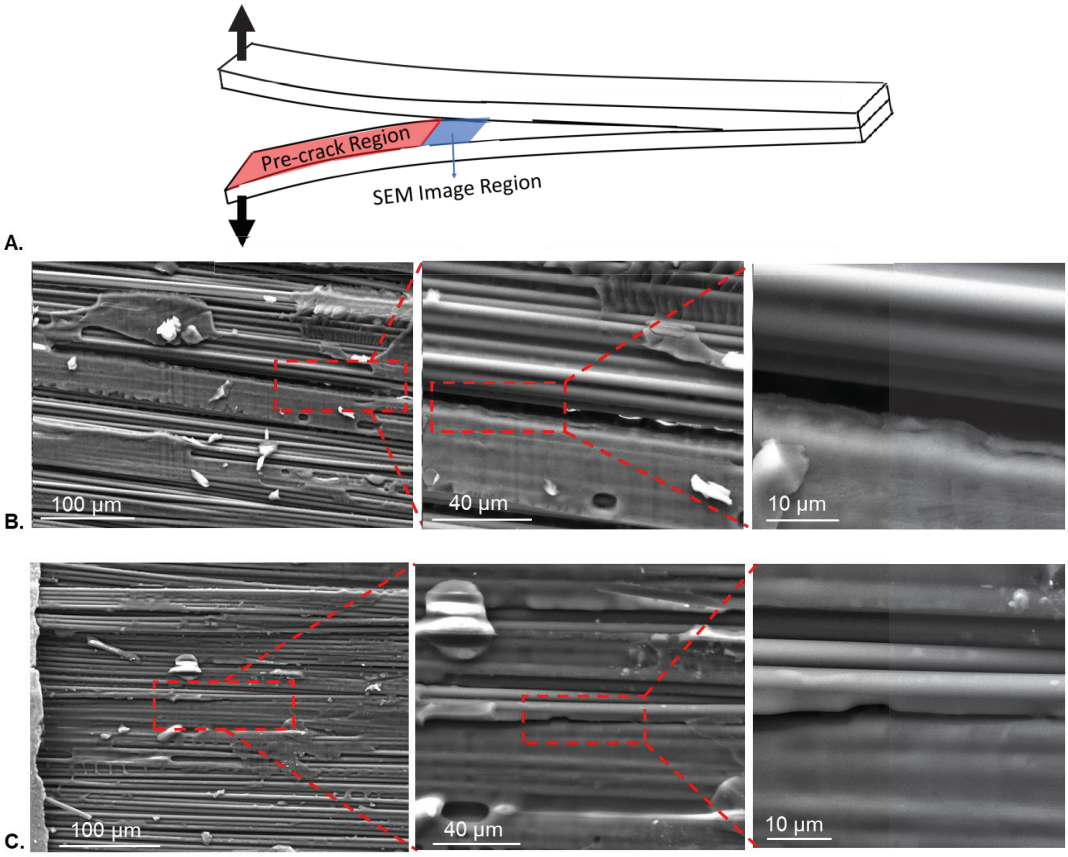

Figure 7. Cross-section SEM images of the fracture surface of ATSP CFRP sample seen in the (**A**) schematic of the fracture surface location (**B**) before self-healing and (**C**) and after self-healing are shown.

3.5. Internal Structure Morphology of DCB Samples

For a more comprehensive understanding of the healing capabilities of ATSP composites, we employed micro-CT X-ray imaging to capture the as-fabricated and self-healed conditions in various planes and locations. The schematics above the micro-CT X-ray images presented in Figure 8A,B provide a visual reference. In the XZ plane (side-view) of both the as-fabricated and self-healed samples comparable pre-crack regions are observed. In the magnified view of the crack tip region in the as-fabricated sample, some voids and gaps are observed in the composite structure, whereas there are fewer voids and gaps in

the healed sample after 280 °C at 2 h (Figure 8A). This finding is very much in line with the slightly higher-than-unity healing efficiency, as discussed in Section 3.1. The presence of voids in the as-fabricated samples may reflect the outgassing from the cure reaction's release of acetic acid from the processing of the virgin samples, which act as a barrier to bonding between composite plies [57]. During DCB testing, the crack mostly grew along the mid-plane of the sample, while the presence of pores may favor slight deviations in crack path, leading to crack growth along the trapped pores. Such crack growth will release volatile species that are trapped in the sample, facilitating the formation of interfacial bonds during subsequent healing. During the healing phase the voids become filled by the self-healing mechanism of ATSP from increased trans-esterification reactions activated by the cure cycle. Thus, the previously weakest available crack surface of the samples is now stronger due to fewer pores for the cracks to propagate along with. It is conceivable to eliminate the manufacturing voids, for instance, by applying higher pressure or longer duration of curing to allow for the volatile species to leave the sample, which is a subject of future studies.

In the front view plane (YZ plane) of the as-fabricated sample, the aluminum foil maintaining the pre-crack area of the sample is observed along with voids and gaps, and the initial compact structure of the composite is seen in the after pre-crack area (Figure 8B). As seen in Figure 8A,B, the cracked area completely healed up to the edge of the pre-crack area in both XZ and YZ planes. The micro-CT X-ray images of as-fabricated and self-healed samples show that the overall structural integrity of the ATSP CFRP samples is restored after self-healing.

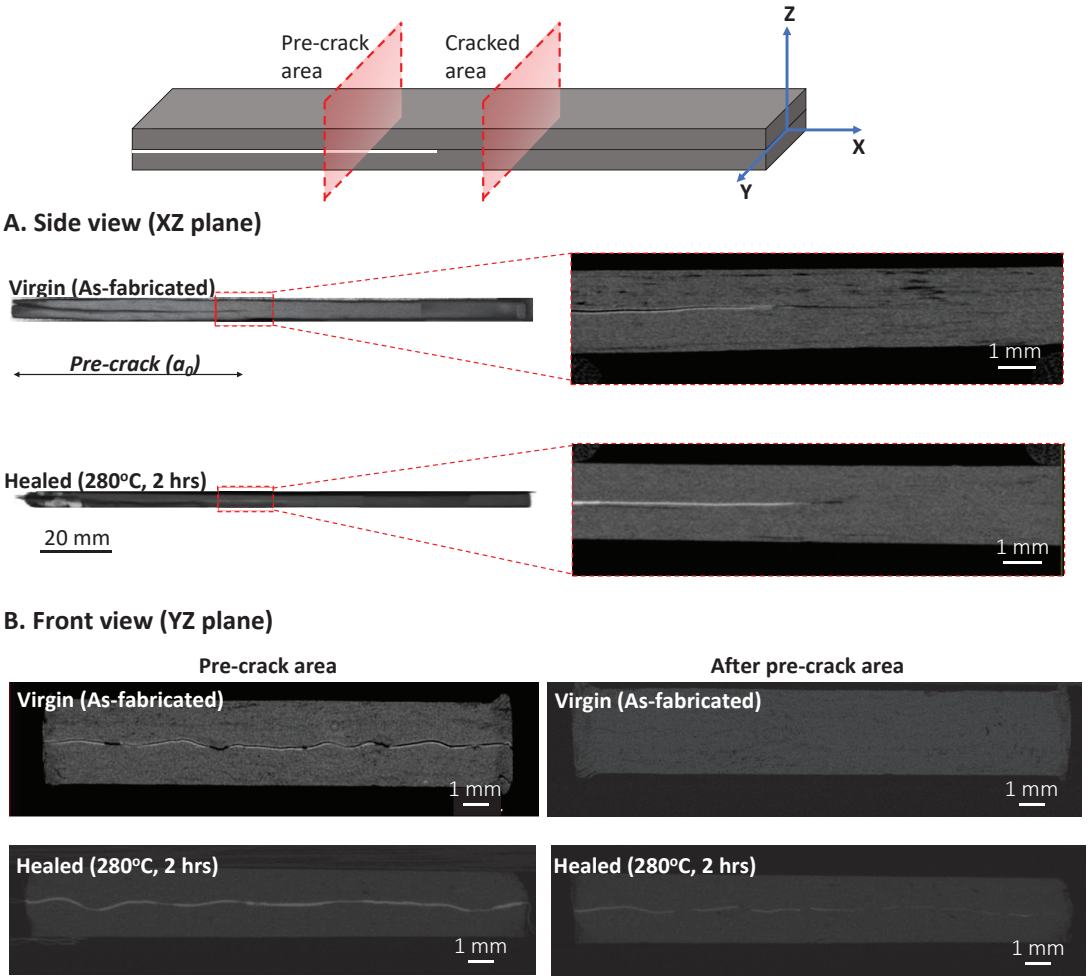

Figure 8. Micro-CT X-ray images of the (**A**) side view (XZ plane) and (**B**) crack plane (YZ plane) are shown of ATSP CFRP samples as fabricated and after self-healing at 280 °C for 2 h.

4. Conclusions

The self-healing mechanical behaviors of ATSP vitrimer composites were studied in both three-point bending and double cantilever beam tests. The healing cycle was composed of heating at 280 °C for 2 h. In all 3PB samples that were plastically deformed, the flat shape of the sample was fully recovered via thermomechanical treatment. After each healing cycle, a reduction in flexural strength and modulus was observed, mainly due to the breakage of the fiber. The restoration of mechanical properties was more successful for samples with less broken fibers for 3PB testing after the second healing cycle. Testing at elevated temperatures reveals that the maximum load did not exceed the breaking limits of the fibers. This is attributed to the sliding mechanism of the fibers within the relatively flexible/softer state of the matrix material (vitrimer), leading to reduced flexural strength compared to testing at ambient temperature.

DCB testing before and after the self-healing of the ATSP CFRP samples demonstrates elevated healing efficiency, which shows the effectiveness of ATSP's self-healing properties. SEM imaging confirms that there is a similar surface morphology of ATSP CFRP samples before and after self-healing. Micro-CT X-ray imaging substantiates the self-healing behavior of ATSP in the samples, since the internal structural morphologies of gaps and voids are decreased after ATSP CFRPs are self-healed. The healing efficiency of all samples was very close to 100%. In some samples, the healing efficiency was barely above 100%. From micro-CT imaging, this was attributed to the removal of the voids in the virgin sample during healing. Despite that, the comparable properties of the healed and virgin fracture toughness suggest that the impacts of voids on the measured properties is very minimal. The presence of the voids was attributed to the outgassing of the ATSP during the curing process. The propagation of cracks enables volatile species to escape from the sample, thereby promoting improved bonding between plies during the healing process. As seen from the results, ATSP has proven to be exceptional by offering self-healing properties that can be used for material repair with various applications in aerospace, medicine, oil and gas, and automotive industries.

Supplementary Materials: The following supporting information can be downloaded at: https://www.mdpi.com/article/10.3390/jcs8070252/s1, Table S1: Average Mode I Fracture Toughness and Average Healing Efficiency.

Author Contributions: The manuscript was written through contributions of all authors. All authors have given approval to the final version of the manuscript. T.M. led the processing and characterization of composites, as well as data analysis, and prepared the first draft of the article; U.O. helped in conducting and analyzing mechanical tests; L.V. characterized the vitrimer; A.A., J.L.M. and A.P. contributed to the discussions of the paper; and M.N. contributed to developing the outline of the work and data analysis. All authors have read and agreed to the published version of the manuscript.

Funding: The authors acknowledge the support from the Air Force Office of Scientific Research (AFOSR) under the award number FA9550-22-1-0496.

Data Availability Statement: The data presented in this study are available upon request to the authors.

Acknowledgments: The authors would like to acknowledge the Texas A&M Microscopy and Imaging Center (MIC), the Micro-CT X-ray Imaging Center at the Texas A&M University Cardiovascular Pathology Laboratory, and the Department of Aerospace Engineering for infrastructural support.

Conflicts of Interest: Author Dr. Jacob L. Meyer was employed by the company ATSP innovations. The remaining authors declare that the research was conducted in the absence of any commercial or financial relationships that could be construed as a potential conflict of interest.

References

1. Yao, S.-S.; Jin, F.-L.; Rhee, K.Y.; Hui, D.; Park, S.-J. Recent advances in carbon-fiber-reinforced thermoplastic composites: A review. *Compos. Part B Eng.* **2018**, *142*, 241–250. [CrossRef]
2. You, J.; Jee, S.M.; Lee, Y.M.; Lee, S.-S.; Park, M.; Kim, T.A.; Park, J.H. Carbon fiber-reinforced polyamide composites with efficient stress transfer via plasma-assisted mechanochemistry. *Compos. Part C Open Access* **2021**, *6*, 100209. [CrossRef]
3. Ozkan, D.; Gok, M.S.; Karaoglanli, A.C. Carbon fiber reinforced polymer (CFRP) composite materials, their characteristic properties, industrial application areas and their machinability. In *Engineering Design Applications III*; Springer: Berlin/Heidelberg, Germany, 2020; pp. 235–253.
4. Kuppusamy, R.R.P.; Rout, S.; Kumar, K. Advanced manufacturing techniques for composite structures used in aerospace industries. In *Modern Manufacturing Processes*; Elsevier: Amsterdam, The Netherlands, 2020; pp. 3–12.
5. Skirbutis, G.; Dzingutė, A.; Masiliūnaitė, V.; Šulcaitė, G.; Žilinskas, J.J. A review of PEEK polymer's properties and its use in prosthodontics. *Stomatologija* **2017**, *19*, 19–23. [PubMed]
6. Chung, D.D. *Composite Materials: Science and Applications*; Springer Science & Business Media: Berlin, Germany, 2010.
7. Mallick, P.K. *Fiber-Reinforced Composites: Materials, Manufacturing, and Design*; CRC Press: Boca Raton, FL, USA, 2007.
8. Jin, F.-L.; Park, S.-J. Preparation and characterization of carbon fiber-reinforced thermosetting composites: A review. *Carbon Lett.* **2015**, *16*, 67–77. [CrossRef]
9. Ozturk, F. Thermoplastic Composite Materials for the Aerospace Industry. *Res. Dev. Mater. Sci.* **2021**, *15*, 1745–1748. [CrossRef]
10. Xu, Y.; Zehnder, A.T. Pressure, hydrolytic degradation and plasticization drive high temperature blistering failure in moisture saturated polyimides. *Extrem. Mech. Lett.* **2017**, *16*, 49–55. [CrossRef]
11. Barbero, E.J. *Introduction to Composite Materials Design*; CRC Press: Boca Raton, FL, USA, 2010.
12. Rao, P.S.; Hardiman, M.; O'Dowd, N.P.; Sebaey, T.A. Comparison of progressive damage between thermoset and thermoplastic CFRP composites under in-situ tensile loading. *J. Compos. Mater.* **2020**, *55*, 1473–1484. [CrossRef]
13. Ivanov, S.G.; Beyens, D.; Gorbatikh, L.; Lomov, S.V. Damage development in woven carbon fibre thermoplastic laminates with PPS and PEEK matrices: A comparative study. *J. Compos. Mater.* **2016**, *51*, 637–647. [CrossRef]
14. Kamble, M.; Vashisth, A.; Yang, H.; Pranompont, S.; Picu, C.R.; Wang, D.; Koratkar, N. Reversing fatigue in carbon-fiber reinforced vitrimer composites. *Carbon* **2022**, *187*, 108–114. [CrossRef]
15. Yang, Y.; Ding, X.; Urban, M.W. Chemical and physical aspects of self-healing materials. *Prog. Polym. Sci.* **2015**, *49*, 34–59. [CrossRef]
16. Yang, Y.; Urban, M.W. Self-healing polymeric materials. *Chem. Soc. Rev.* **2013**, *42*, 7446–7467. [CrossRef] [PubMed]
17. Garcia, S.J. Effect of polymer architecture on the intrinsic self-healing character of polymers. *Eur. Polym. J.* **2014**, *53*, 118–125. [CrossRef]
18. Jud, K.; Kausch, H.; Williams, J. Fracture mechanics studies of crack healing and welding of polymers. *J. Mater. Sci.* **1981**, *16*, 204–210. [CrossRef]
19. Lu, L.; Fan, J.; Li, G.J.P. Intrinsic healable and recyclable thermoset epoxy based on shape memory effect and transesterification reaction. *Polymer* **2016**, *105*, 10–18. [CrossRef]
20. Hornat, C.C.; Urban, M.W. Shape memory effects in self-healing polymers. *Prog. Polym. Sci.* **2020**, *102*, 101208. [CrossRef]
21. Abend, M.; Zechel, S.; Schubert, U.S.; Hager, M.D. Detailed Analysis of the Influencing Parameters on the Self-Healing Behavior of Dynamic Urea-Crosslinked Poly (methacrylate) s. *Molecules* **2019**, *24*, 3597. [CrossRef] [PubMed]
22. Sumerlin, B.S. Next-generation self-healing materials. *Science* **2018**, *362*, 150–151. [CrossRef] [PubMed]
23. Williams, G.; Trask, R.; Bond, I. A self-healing carbon fibre reinforced polymer for aerospace applications. *Compos. Part A Appl. Sci. Manuf.* **2007**, *38*, 1525–1532. [CrossRef]
24. Kontiza, A.; Semitekolos, D.; Milickovic, T.K.; Pappas, P.; Koutroumanis, N.; Galiotis, C.; Charitidis, C.A. Double cantilever beam test and micro-computed tomography as evaluation tools for self-healing of CFRPs loaded with DCPD microcapsules. *Compos. Struct.* **2022**, *279*, 114780. [CrossRef]
25. Lemmens, R.J.; Dai, Q.; Meng, D.D.; Mechanics, A.F. Side-groove influenced parameters for determining fracture toughness of self-healing composites using a tapered double cantilever beam specimen. *Theor. Appl. Fract. Mech.* **2014**, *74*, 23–29. [CrossRef]
26. Benazzo, F.; Rigamonti, D.; Sala, G.; Grande, A.M. A critical appraisal of fracture mechanics methods for self-healing and healable composites characterization. *Compos. Part A Appl. Sci. Manuf.* **2023**, *167*, 107450. [CrossRef]
27. Cho, S.H.; Andersson, H.M.; White, S.R.; Sottos, N.R.; Braun, P.V. Polydimethylsiloxane-based self-healing materials. *Adv. Mater.* **2006**, *18*, 997–1000. [CrossRef]
28. Romero-Sabat, G.; Gago-Benedí, E.; Roa Rovira, J.J.; González-Gálvez, D.; Mateo, A.; Medel, S.; Tolentino Chivite, A. Development of a highly efficient extrinsic and autonomous self-healing polymeric system at low and ultra-low temperatures for high-performance applications. *Compos. Part A Appl. Sci. Manuf.* **2021**, *145*, 106335. [CrossRef]
29. Thies, C. *Microencapsulation*; Wiley: Hoboken, NJ, USA, 2005. [CrossRef]
30. Jones, A.S.; Rule, J.D.; Moore, J.S.; White, S.R.; Sottos, N.R. Catalyst morphology and dissolution kinetics of self-healing polymers. *Chem. Mater.* **2006**, *18*, 1312–1317. [CrossRef]
31. Shansky, E. *Synthesis and Characterization of Microcapsules for Self-Healing Materials*; Department of Chemistry Indiana University: Bloomington, IN, USA, 2005.
32. Dry, C. Procedures developed for self-repair of polymer matrix composite materials. *Compos. Struct.* **1996**, *35*, 263–269. [CrossRef]

33. Dry, C.M. Adhesive liquid core optical fibers for crack detection and repairs in polymer and concrete matrices. *Smart Struct. Mater. 1995 Smart Sens. Process. Instrum.* **1995**, *2444*, 410–413.
34. Dry, C.M.; McMillan, W. Crack and damage assessment in concrete and polymer matrices using liquids released internally from hollow optical fibers. *Smart Struct. Mater. 1996 Smart Sens. Process. Instrum.* **1996**, *2718*, 448–451.
35. Dry, C.M.; Sottos, N.R. Passive smart self-repair in polymer matrix composite materials. *Smart Struct. Mater. 1993 Smart Mater.* **1993**, *1916*, 438–444.
36. Motuku, M.; Vaidya, U.; Janowski, G. Parametric studies on self-repairing approaches for resin infused composites subjected to low velocity impact. *Smart Mater. Struct.* **1999**, *8*, 623. [CrossRef]
37. Bleay, S.M.; Loader, C.B.; Hawyes, V.; Humberstone, L.; Curtis, P. A smart repair system for polymer matrix composites. *Compos. Part A Appl. Sci. Manuf.* **2001**, *32*, 1767–1776. [CrossRef]
38. Hucker, M.; Bond, I.; Foreman, A.; Hudd, J. Optimisation of hollow glass fibres and their composites. *Adv. Compos. Lett.* **1999**, *8*, 096369359900800406. [CrossRef]
39. Trask, R.; Bond, I. Biomimetic self-healing of advanced composite structures using hollow glass fibres. *Smart Mater. Struct.* **2006**, *15*, 704. [CrossRef]
40. Pang, J.; Bond, I. 'Bleeding composites'—Damage detection and self-repair using a biomimetic approach. *Compos. Part A Appl. Sci. Manuf.* **2005**, *36*, 183–188. [CrossRef]
41. Pang, J.W.; Bond, I.P. A hollow fibre reinforced polymer composite encompassing self-healing and enhanced damage visibility. *Compos. Sci. Technol.* **2005**, *65*, 1791–1799. [CrossRef]
42. Williams, H.R.; Trask, R.S.; Bond, I.P. Self-healing composite sandwich structures. *Smart Mater. Struct.* **2007**, *16*, 1198. [CrossRef]
43. Sanada, K.; Yasuda, I.; Shindo, Y. Transverse tensile strengh of unidirectional fiber-reinforced polymers and self-healing of interfacial debonding. *Plast. Rubber Compos.* **2006**, *35*, 67–72. [CrossRef]
44. Zhang, M.Q.; Rong, M.Z. *Extrinsic and Intrinsic Approaches to Self-Healing Polymers and Polymer Composites*; John Wiley & Sons: Hoboken, NJ, USA, 2022.
45. Frich, D.; Goranov, K.; Schneggenburger, L.; Economy, J. Novel high-temperature aromatic copolyester thermosets: Synthesis, characterization, and physical properties. *Macromolecules* **1996**, *29*, 7734–7739. [CrossRef]
46. Frich, D.; Economy, J.; Goranov, K. Aromatic copolyester thermosets: High temperature adhesive properties. *Polym. Eng. Sci.* **1997**, *37*, 541–548. [CrossRef]
47. Montarnal, D.; Capelot, M.; Tournilhac, F.; Leibler, L. Silica-like malleable materials from permanent organic networks. *Science* **2011**, *334*, 965–968. [CrossRef]
48. Yang, Y.; Xu, Y.; Ji, Y.; Wei, Y.J. Functional epoxy vitrimers and composites. *Prog. Mater. Sci.* **2021**, *120*, 100710. [CrossRef]
49. Zheng, J.; Png, Z.M.; Ng, S.H.; Tham, G.X.; Ye, E.; Goh, S.S.; Loh, X.J.; Li, Z.J. Vitrimers: Current research trends and their emerging applications. *Mater. Today* **2021**, *51*, 586–625. [CrossRef]
50. Shi, Q.; Yu, K.; Kuang, X.; Mu, X.; Dunn, C.; Dunn, M.; Wang, T.; Qi, H. Recyclable 3D Printing of Vitrimer Epoxy. *Mater. Horiz.* **2017**, *4*, 598–607. [CrossRef]
51. Zheng, N.; Xu, Y.; Zhao, Q.; Xie, T. Dynamic Covalent Polymer Networks: A Molecular Platform for Designing Functions beyond Chemical Recycling and Self-Healing. *Chem. Rev.* **2021**, *121*, 1716–1745. [CrossRef] [PubMed]
52. Hubbard, A.M.; Ren, Y.; Konkolewicz, D.; Sarvestani, A.; Picu, C.R.; Kedziora, G.S.; Roy, A.; Varshney, V.; Nepal, D. Vitrimer Transition Temperature Identification: Coupling Various Thermomechanical Methodologies. *ACS Appl. Polym. Mater.* **2021**, *3*, 1756–1766. [CrossRef]
53. Sharma, H.; Rana, S.; Singh, P.; Hayashi, M.; Binder, W.H.; Rossegger, E.; Kumar, A.; Schlögl, S. Self-healable fiber-reinforced vitrimer composites: Overview and future prospects. *RSC Adv.* **2022**, *12*, 32569–32582. [CrossRef] [PubMed]
54. Palmieri, B.; Cilento, F.; Amendola, E.; Valente, T.; Dello Iacono, S.; Giordano, M.; Martone, A. An Investigation of the Healing Efficiency of Epoxy Vitrimer Composites Based on Zn^{2+} Catalyst. *Polymers* **2023**, *15*, 3611. [CrossRef] [PubMed]
55. Zhao, Y.; Zhao, M.; Wang, A.; Chang, Z.; Wang, Z.; Zhang, K. Experimental study on the mode I interlaminar properties of self-healable vitrimeric CFRP with various interfaces. *Compos. Part B Eng.* **2023**, *261*, 110806. [CrossRef]
56. Bakir, M.; Elhebeary, M.; Meyer, J.L.; Sutrisno, A.; Economy, J.; Jasiuk, I.J. Interfacial liquid crystalline mesophase domain on carbon nanofillers in aromatic thermosetting copolyester matrix. *J. Appl. Polym. Sci.* **2018**, *135*, 46584. [CrossRef]
57. Vaezian, B.; Meyer, J.L.; Economy, J. Processing of aromatic thermosetting copolyesters into foams and bulk parts: Characterization and mechanical properties. *Polym. Adv. Technol.* **2016**, *27*, 1006–1013. [CrossRef]
58. Meyer, J.L.; Lan, P.; Bakir, M.; Jasiuk, I.; Economy, J. Wide Area Reversible Adhesive for In-Space Assembly. *Macromol. Mater. Eng.* **2020**, *305*, 2000006. [CrossRef]
59. Bashandeh, K.; Lan, P.; Meyer, J.L.; Polycarpou, A.A. Tribological Performance of Graphene and PTFE Solid Lubricants for Polymer Coatings at Elevated Temperatures. *Tribol. Lett.* **2019**, *67*, 99. [CrossRef]
60. Frich, D.; Hall, A.; Economy, J.J. Nature of adhesive bonding via interchain transesterification reactions (ITR). *Macromol. Chem. Phys.* **1998**, *199*, 913–921. [CrossRef]
61. Meyer, J.L.; Bakir, M.; Lan, P.; Economy, J.; Jasiuk, I.; Bonhomme, G.; Polycarpou, A.A. Reversible Bonding of Aromatic Thermosetting Copolyesters for In-Space Assembly. *Macromol. Mater. Eng.* **2019**, *304*, 1800647. [CrossRef]
62. Taynton, P.; Zhu, C.; Loob, S.; Shoemaker, R.; Pritchard, J.; Jin, Y.; Zhang, W. Re-healable polyimine thermosets: Polymer composition and moisture sensitivity. *Polym. Chem.* **2016**, *7*, 7052–7056. [CrossRef]

63. Chao, A.; Negulescu, I.; Zhang, D. Dynamic covalent polymer networks based on degenerative imine bond exchange: Tuning the malleability and self-healing properties by solvent. *Macromolecules* **2016**, *49*, 6277–6284. [CrossRef]
64. Boutelle, R.C.; Northrop, B.H. Substituent effects on the reversibility of furan–maleimide cycloadditions. *J. Org. Chem.* **2011**, *76*, 7994–8002. [CrossRef] [PubMed]
65. Schneggenburger, L.; Osenar, P.; Economy, J. Direct evidence for sequence ordering of random semicrystalline copolyesters during high-temperature annealing. *Macromolecules* **1997**, *30*, 3754–3758. [CrossRef]
66. Stevens, M.P. *Polymer Chemistry: An Introduction*; Oxford University Press: Oxford, UK, 1999.
67. Mangalgiri, P.J. Polymer-matrix composites for high-temperature applications. *Def. Sci. J.* **2005**, *55*, 175. [CrossRef]
68. Bashandeh, K.; Lan, P.; Polycarpou, A.A. Tribology of self-lubricating high performance ATSP, PI, and PEEK-based polymer composites up to 300 °C. *Friction* **2023**, *11*, 141–153. [CrossRef]
69. Krull, B.; Patrick, J.; Hart, K.; White, S.; Sottos, N. Automatic optical crack tracking for double cantilever beam specimens. *Exp. Tech.* **2016**, *40*, 937–945. [CrossRef]
70. Hashemi, S.M.K.; Kinloch, A.J.; Williams, J.G. Corrections needed in double-cantilever beam tests for assessing the interlaminar failure of fibre-composites. *J. Mater. Sci. Lett.* **1989**, *8*, 125–129. [CrossRef]
71. Snyder, A.; Phillips, Z.; Turicek, J.; Diesendruck, C.; Nakshatrala, K.; Patrick, J. Prolonged in situ self-healing in structural composites via thermo-reversible entanglement. *Nat. Commun.* **2022**, *13*, 6511. [CrossRef] [PubMed]
72. Lan, P.; Polychronopoulou, K.; Zhang, Y.; Polycarpou, A.A. Three-body abrasive wear by (silica) sand of advanced polymeric coatings for tilting pad bearings. *Wear* **2017**, *382*, 40–50. [CrossRef]
73. Lan, P.; Zhang, Y.; Dai, W.; Polycarpou, A.A. A phenomenological elevated temperature friction model for viscoelastic polymer coatings based on nanoindentation. *Tribol. Int.* **2018**, *119*, 299–307. [CrossRef]
74. Lei, Y.; Wang, Y.; Yuan, A.; Zhao, S.; Chen, Y.; Xiao, Y.; Jiang, L.; Lei, J. Solving the difficult recyclability of conventional thermosetting polyurea elastomers based on commercial raw materials in a facile way. *J. Mater. Chem. A* **2022**, *10*, 6713–6723. [CrossRef]
75. Mulqueen, D.W.; Sattar, S.; Kravchenko, O.G. Mechanical and thermal properties of carbon fiber epoxy composite with interlaminar graphene at elevated temperature. *Compos. Part B Eng.* **2023**, *255*, 110609. [CrossRef]
76. Mani, D.; Vu, M.C.; Jeong, T.-H.; Kim, J.-B.; Lim, C.-S.; Lim, J.-H.; Kim, K.-M.; Kim, S.-R. 3D structured graphene fluoride-based epoxy composites with high thermal conductivity and electrical insulation. *Compos. Part A Appl. Sci. Manuf.* **2021**, *149*, 106585. [CrossRef]
77. Kim, S.G.; Heo, S.J.; Kim, S.; Kim, J.; Kim, S.O.; Lee, D.; Lee, S.; Kim, J.; You, N.-H.; Kim, M.; et al. Ultrahigh strength and modulus of polyimide-carbon nanotube based carbon and graphitic fibers with superior electrical and thermal conductivities for advanced composite applications. *Compos. Part B Eng.* **2022**, *247*, 110342. [CrossRef]
78. Chae, H.G.; Newcomb, B.A.; Gulgunje, P.V.; Liu, Y.; Gupta, K.K.; Kamath, M.G.; Lyons, K.M.; Ghoshal, S.; Pramanik, C.; Giannuzzi, L. High strength and high modulus carbon fibers. *Carbon* **2015**, *93*, 81–87. [CrossRef]
79. Wen, J.; Wu, Y.; Hou, X.; Yan, M.; Xiao, Y. Effect of high temperature on mechanical properties and porosity of carbon fiber/epoxy composites. *J. Reinf. Plast. Compos.* **2022**, *42*, 990–1005. [CrossRef]
80. Carlsson, L.A.; Adams, D.F.; Pipes, R.B. *Experimental Characterization of Advanced Composite Materials*; CRC Press: Boca Raton, FL, USA, 2014.

Journal of
Composites Science

MDPI

Article

An Experimental Study Incorporating Carbon Fiber Composite Bars and Wraps for Concrete Performance and Failure Insight

Ali Akbarpour, Jeffery Volz and Shreya Vemuganti *

School of Civil Engineering and Environmental Science, University of Oklahoma, 202 W. Boyd St., Room 334, Norman, OK 73019, USA; ali.akbarpour@ou.edu (A.A.); volz@ou.edu (J.V.)
* Correspondence: svemugan@ou.edu

Abstract: Corrosion of conventional steel reinforcement is responsible for numerous structurally deficient bridges, which is a multi-billion-dollar challenge that creates a vicious cycle of maintenance, repair, and replacement of infrastructure. Repair of existing structures with fiber-reinforced polymer (FRP) has become widespread due to multiple advantages. Carbon FRP's superior tensile strength and stiffness make it particularly effective in shear and flexural strengthening of reinforced concrete (RC) beams. This experimental study incorporates carbon fiber polymer composite bars and wraps to study and report on the flexural behavior of RC beams. By employing a combination of CFRP bar and wrap for strengthening RC beams, this study observed an approximate 95% improvement in flexural load capacity relative to control RC beams without strengthening. This substantial enhancement highlights the effectiveness of integrating CFRP in structural applications. Nevertheless, the key observation is the failure mode due to this combination providing significant insights into the changes facilitated by this combination approach.

Keywords: near-surface mounting (NSM); U-wrap; fiber-reinforced polymer (FRP); carbon fiber-reinforced polymer (CFRP); strengthening; reinforced concrete

1. Introduction

The American Society of Civil Engineers (ASCE) 2021 report card for infrastructure scored a C-, which indicates a mediocre condition with signs of deterioration and deficiencies in condition and functionality. Reinforced and prestressed concrete infrastructure built in the 60s and 70s is now observing severe deterioration, and action is needed to ensure the structural performance is adequate for the demands imposed. Infrastructure from the 60s–70s is now reaching the end of its service life, with marked deterioration becoming increasingly evident. Quantitative studies reveal that up to 60% of bridges constructed in temperate climates during this era exhibit significant structural decline, primarily due to corrosion of steel reinforcement, with most showing severe deterioration after surpassing the 50 year mark. This widespread degradation underlines the urgency for rehabilitation methods that can extend the lifespan of these critical structures [1]. Corrosion of conventional steel reinforcement is responsible for numerous structurally deficient bridges, which is a multi-billion-dollar challenge that creates a vicious cycle of maintenance, repair, and replacement of infrastructure. This presents a higher risk for future closure or weight restrictions and requires substantial investment. Repair and strengthening techniques can provide a cost-effective means to extend the service lives of bridges efficiently and safely. This is necessary to accommodate rising traffic volumes and to comply with contemporary design standards [2,3].

In recent years, fiber-reinforced polymers (FRPs) have garnered considerable interest from the engineering community, resulting in the widespread adoption of composite structures by the construction industry [4]. FRPs have been adopted for the repair and strengthening of infrastructure. Its usage spans a range of geographic regions from the

harsh climates of Northern Europe and North America to the tropical environments of Southeast Asia, illustrating its versatility and reliability in diverse conditions. Economically, despite higher initial costs compared to traditional materials, FRP offers significant long-term benefits through reduced maintenance and repair costs, supporting its cost-effectiveness and extensive use in both developed and developing economies [5]. The progress in FRP composites, particularly in aerospace applications, has underscored their potential for civil engineering uses [6]. FRP's resistance to corrosion contributes significantly to enhancing strength and durability in various applications [7]. FRP's corrosion-resistant properties are critical in its role in prolonging the structural integrity of retrofitted steel columns, making it an invaluable material in the rehabilitation of aging infrastructure plagued by corrosion-related deterioration [8]. FRP is composed of a polymer matrix with different types of fibers. The specific type of FRP is defined based on the kind of fiber employed [5]. Diverse fibers such as glass, carbon, aramid, and basalt are utilized in FRP due to their high strength, stiffness, and low-density characteristics [9]. In the field of construction, carbon-fiber-reinforced polymers (CFRP) and glass-fiber-reinforced polymers (GFRP) are widely used due to their robust properties [10,11]. Yet their application is limited in environments requiring high fire resistance standards due to the vulnerability of CFRP composites to degradation at elevated temperatures. Compared to steel, CFRP can offer five times the strength of steel. Although CFRP's initial costs are higher than those of steel, its maintenance-free properties and lighter weight provide significant long-term economic and structural benefits, making it a valuable alternative depending on project-specific demands. CFRP and GFRP are both used for structural strengthening but differ significantly in their mechanical properties. CFRP exhibits tensile strengths of 3500 to 6000 MPa and an elastic modulus of 230,000 to 250,000 MPa, making it ideal for high-stress applications. In contrast, GFRP has tensile strengths of 1500 to 2500 MPa and an elastic modulus of 70,000 to 90,000 MPa [12]. This enables CFRP to be more effective in reducing deformations in reinforced concrete (RC) structures [13]. CFRP's superior tensile strength and stiffness make it particularly effective in shear and flexural strengthening of RC beams, offering improved ability of RC beams to resist mechanical stresses and maintain structural integrity under increased loads [14].

In flexural strengthening of RC beams with the usage of FRP, two approaches are suggested by the American Concrete Institute (ACI) 440-2R [15]: near-surface-mounted (NSM) FRP and externally bonded (EB) FRP [16,17]. EB-FRP involves attaching an FRP laminate to the beam's tension side using epoxy, allowing the laminate to serve as extra reinforcement and boost the beam's flexural strength [16]. NSM-FRP entails creating a groove on the beam's tension side, partially filling it with epoxy, inserting an FRP bar or strips, and then completely sealing it with epoxy [17]. The primary benefit of the NSM-FRP method is its bonding efficiency with the concrete [18]. The bonding efficacy is crucial for NSM-FRP's performance, as demonstrated in Figure 1.

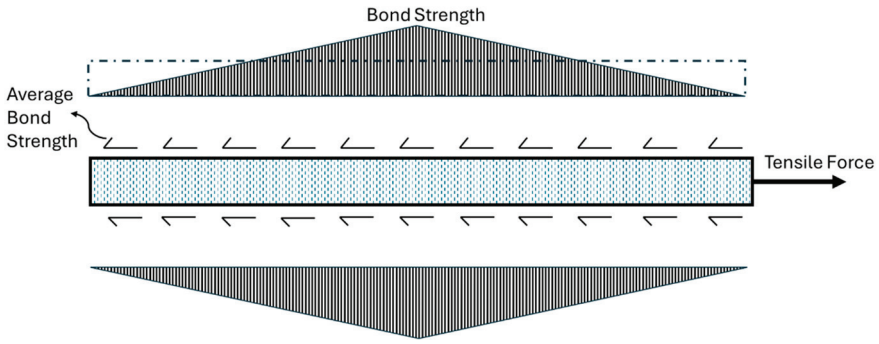

Figure 1. Transfer of forces in a NSM FRP bar (developed from ACI 440-2R).

For flexural strengthening using NSM-FRP for RC beams, CFRP is often preferred over GFRP. CFRP is often the material of choice due to its superior axial stiffness and tensile

strength [19]. This allows for a reduction in the necessary concrete cover area for NSM-FRP, optimizing the use of space and materials in construction projects [20]. The failure modes for RC beams incorporating the NSM-FRP technique typically include FRP rupture or debonding post tension steel yield [21]. Research by Hassan and Rizkalla [5] suggests that FRP rupture is unlikely in NSM-FRP with an adequate length of NSM-FRP bars. This is because the FRP bar generally only reaches about 60–70% of its maximum tensile capacity, indicating a lower risk of rupture under normal conditions. Therefore, in the context of NSM-FRP-strengthened RC beams, debonding is often the primary mode of failure. Often, U-wrap shear strengthening is performed on RC beams in combination with NSM flexural strengthening to meet both demands. The U-wrapping method, utilizing wet layup, involves saturating FRP fabric in epoxy and adhering it to concrete surfaces in the direction of shear reinforcement [22]. This method has been implemented in various configurations, including complete U-wraps, three-sided U-wraps, and two-sided U-wraps [23]. Extensive research has examined the impact of different wrapping schemes on the efficiency of shear strengthening in beams and columns [24–26]. The application of externally bonded systems employing an inorganic matrix, such as fabric-reinforced cementitious matrix (FRCM) composites, has been recognized for its enhanced thermal resistance and structural integrity in elevated temperature environments [27]. Studies have shown that combining U-wrap FRP with NSM steel significantly enhances flexural load capacity, effectively preventing premature failures in RC beams reinforced solely with NSM steel [28].

The primary focus of this study was to comprehensively evaluate the flexural response of 20 laboratory scale RC beams strengthened with NSM-CFRP and U-wrap CFRP individually and as a combination. The load displacement behaviors of each beam were carefully recorded in addition to data from strain gauges at multiple locations in the beam. Visual inspection of failure modes was performed. Emphasis was also placed on optimizing surface preparation techniques for both methods to enhance the efficacy of the strengthening systems. The findings aim to provide insightful recommendations for the application of CFRP systems for strengthening RC beams, potentially informing future updates to design codes and engineering practices.

2. Materials and Methods

2.1. Materials

This study utilized 20 RC beams divided into five groups to evaluate the impact of different FRP strengthening systems: control group ('C'), U-wrap group ('U'), NSM group ('N'), NSM and U-wrap group ('NU') and NSM and shear zone U-wrap group ('NSU'). C beams were used to establish a baseline performance. To isolate the effects of U-wrap and NSM, U and NU groups were used. For the combination of NSM and U-wrap, full U-wrap and shear zone U-wrap were considered to obtain two types of confinement effects.

The concrete employed featured a maximum nominal aggregate size of 12.7 mm, with an observed slump measuring 10 ± 1.2 cm. The slump test was performed using the ASTM C143 [29]. The chosen maximum nominal aggregate size of 12.7 mm improves the concrete mix by enhancing workability, reducing shrinkage, and optimizing mechanical strength. Larger aggregates help achieve a better void ratio, decrease cement paste use, and consequently enhance the structural and economic efficiency of the concrete. To assess the mechanical characteristics of the selected mix design, three distinct experimental tests were conducted. The unconfined compression tests were carried out in accordance with ASTM C39 [30] on samples after 7 and 28 days of curing. Furthermore, for a comparative analysis, the compressive strength of samples subjected to heat curing was evaluated at the age of 7 days. Also, the split tensile strength of specimens was evaluated at the age of 28 days based on ASTM C496 [31]. Moreover, the elastic modulus of the specimens was assessed following the ASTM 469 [32]. At 28 days, the average compressive strength of the concrete was 53.09 MPa with a standard deviation of 1.78 MPa. The split tensile strength recorded was 3.49 MPa with a standard deviation of 0.16 MPa. Additionally, the elastic modulus was determined to be 27,636 MPa. Each test result is a mean value of three tested specimens.

No. 3 (10 mm) NSM bars were acquired from RenewWrap®, as shown in Figure 2. The NSM strengthening systems involved using a specialized 2 part epoxy resin NSM gel, produced by the RenewWrap®. The guaranteed tensile strength provided by the manufacturer was 2171.85 MPa, and the tensile modulus of elasticity was 124.11 GPa with 1.75% ultimate strain. The U-wrap strengthening system technique was carried out using a unidirectional CFRP fabric, which was 1 mm thick, applied via a wet-layup method. Both the epoxy and the CFRP fabric used in this method were supplied by FyfeFRP, LLC. Specifically, unidirectional carbon fabric with the Tyfo S-330 epoxy was used in this study, as shown in Figure 2a. After 3 days of curing, the epoxy material properties as listed by the manufacturer had a tensile strength of 72.39 MPa, a tensile modulus of 3178 MPa, elongation of 5% and a minimum adhesion strength to concrete of 2.76 MPa. The composite's gross laminate properties as provided by the manufacturer included an ultimate tensile strength of 965.27 MPa, a tensile modulus of 93.08 GPa and elongation at break of 1%.

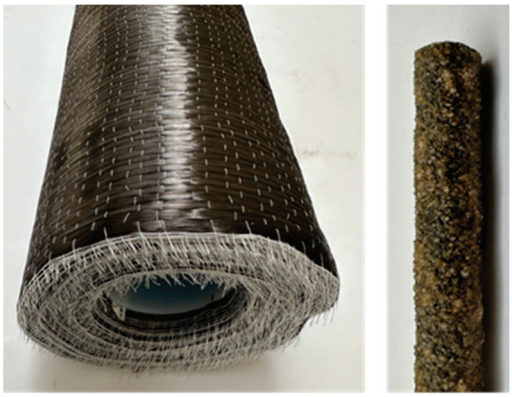

Figure 2. (**a**) Tyfo unidirectional CFRP fabric (**b**) No. 3 RenewWrap CFRP bar.

2.2. Methods

The beam groups were subjected to a displacement controlled static four-point bending test (2 loading points and 2 supports) until failure at a rate of 1 mm/min. The test was conducted using an MTS 810 with a 55 kip load cell and a data acquisition system. The load cell captured the resistance from the beams and machine displacement was recorded. Failure was defined when the load was reduced to more than 30% of the peak load. The loading points were spaced 152.4 mm apart and 660.4 mm between supports. In this study, flexural load capacity reported is defined as the maximum load a beam can support before failure when subjected to bending. The beams had a square cross-section, each with a depth of 152.4 mm. The beams were reinforced with four No. 3 (10 mm diameter) steel bars. Within these, two bars were allocated for compression reinforcement while the remaining two were used for tension reinforcement. The top cover was maintained at 29.5 mm and the bottom cover at 25.4 mm. This configuration was integral to the structural setup of each beam. For shear reinforcement, No. 3 stirrups, also 10 mm in nominal diameter, were spaced at intervals of 76 mm. After the concrete beams were cast, they were placed in heat curing for 7 days.

To facilitate strain readings, strain gauges were attached in four locations: concrete compression surface, steel compression surface, steel tension surface, and CFRP bar surface. To ensure the strain gauges were well attached, steps were adopted sequentially (1). Surface preparation: Initially, the surface underwent grinding using various grinders, selected based on the material. Subsequently, the surface was thoroughly cleaned, rendering it prepared for the subsequent steps. (2). Surface cleaning: to eliminate any dust and oily residues from the specimens' surfaces, a combination of three cleaning agents—acetone, a water-based acidic surface cleaner, and a water-based alkaline surface cleaner—was employed. (3). Strain gauge attachment: following the meticulous cleaning and preparation

of the material surfaces, strain gauges were affixed using either super glue or epoxy. (4). Surface finishing: To safeguard the strain gauges during the concrete casting process and subsequent phases, a protective surface finishing was implemented. Super 88 Scotch tape was applied to shield the wires, Silicone RTV adhesive sealant was utilized to guard against water exposure, and Nashua 367-17 foil mastic sealant was employed for protection against aggregates. Figure 3 shows the strain gauges attached to different materials.

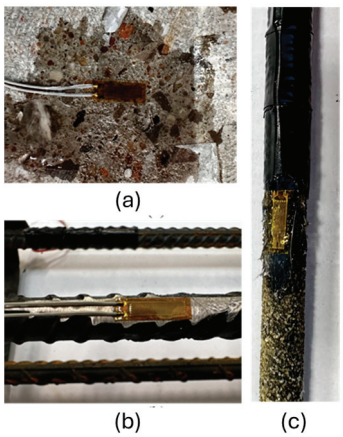

Figure 3. Strain gauge on (**a**) on concrete (**b**) steel (**c**) NSM CFRP.

2.2.1. U-Wrap Shear Strengthening (U Type)

Three side U-wrapping is a technique employed for shear strengthening of concrete beams. Beams U, NU and NSU were strengthened using this CFRP wrapping technique. The concrete surface was prepared to a minimum concrete surface profile as defined by the CFRP fabric manufacturer's guidelines, ACI 440-2R and ICRI surface profile. Abrasive grinding was performed on flat concrete surfaces and for wrapping around edges using a 1.2 cm radius rounded grinder. The prepared surface was cleaned using a water jet and compressed air. The beams were allowed to air dry for twenty-four hours to remove moisture on the surface of the beams. Surface preparation is shown in Figure 4.

Part A and Part B mixed resin was initially applied as a prime coat on the concrete surface using a soft roller. Mix ratio of Tyfo S-330 according to the manufacturer was 100A:34.5B by weight. For U and NU beams, the CFRP fabric was cut to specified dimensions: 406 mm along the two sides and the bottom of the beam in the direction of the fibers, and a length of 660 mm opposite to the fiber direction, equal to the length between the two supports for the beam. For the NSU beams, the U-wrap was only applied in the shear area. After cutting the fabric, the CFRP fabric was saturated in epoxy. Saturated fabric was wrapped around the beam and a hard roller was employed to eliminate any trapped air and ensure even layup as illustrated in the figures below. Wrapped beams were allowed to cure for 14 days at room temperature to enable complete hardening of the wrapping and have composite action with the beams. Figures 4–7 show the steps of U-wrapping technique.

2.2.2. NSM Flexural Strengthening (N Type)

In the beam series labeled 'N', 'NU', and 'NSU', which underwent NSM-CFRP flexural reinforcement, each was constructed with an integrated groove on the tension face. To facilitate the creation of the groove on the tension side of the beam, a plastic piece, measuring 25.4 mm in width and depth, was affixed to the concrete form using a double-sided adhesive tape. Twenty-four hours after casting, specimens were demolded and the plastic piece was removed, and they were subjected to heat curing for a period of 7 days. Following a 7 day heat curing process, the surface underwent a grinding process using a wire brush, followed by cleaning with a water jet, as shown in Figure 8. The prepared surface was then left to air dry for a day to eliminate any lingering moisture from the surface of the groove. To ensure the NSM groove was devoid of dust and unwanted materials, compressed air was used to remove any remaining particles. These meticulous steps were taken to guarantee

the cleanliness of the NSM groove, free from dust, moisture, and unwanted substances. Special attention was given to surface preparation to achieve a rough surface, ensuring a strong mechanical bond between the NSM gel and the concrete, thereby preventing any potential failure between the two materials.

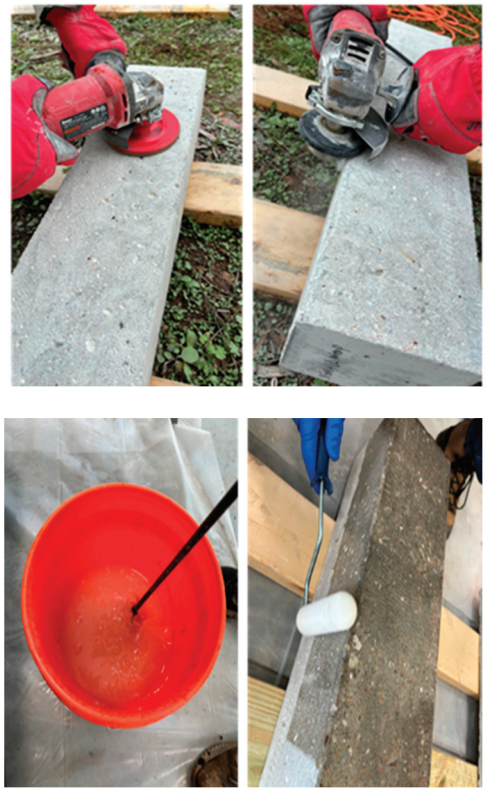

Figure 4. Surface preparation for U-wrap to ensure adequate bond through surface and edge grinding. Part A and Part B mixing for prime coat application on beam prior to U-wrap.

Figure 5. (**a**) Carbon fiber fabric wetting process for U-wrap. (**b**) Rolling wet fabric onto plastic pipe for layup on beam.

Figure 6. Rolling wet fabric onto pre-marked beam covering three sides for U-wrap.

Figure 7. Wet layup process (**a**). Layup with soft roller (**b**). Layup with hard roller (**c**). Finished beam after U-wrap.

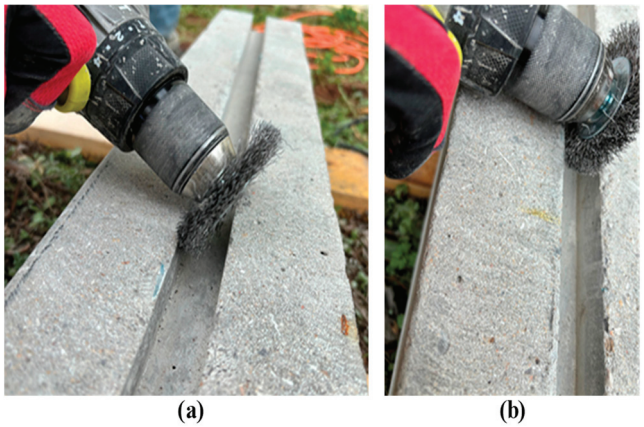

Figure 8. Grinding process for the NSM groove to ensure adequate bond between resin and concrete. (**a**) Use of wire brush for grinding inside the groove. (**b**) Closer look at grind surface.

NSM-CFRP flexural strengthening was performed utilizing carbon CFRP No. 3 bars with a nominal diameter of 10 mm and NSM gel. Figure 9 illustrates the different steps of flexural strengthening of the beams using the NSM-CFRP technique.

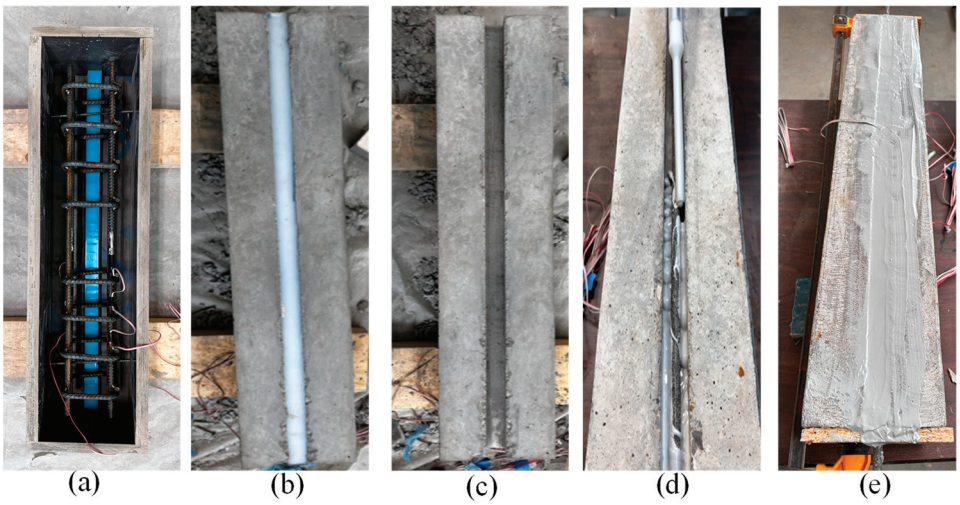

Figure 9. Steps of NSM-CFRP strengthening: (**a**) plastic form used at the bottom of the beam to create groove before casting, (**b**) beam after fabrication and hardening, (**c**) beam after removing plastic form, (**d**) dispensing NSM gel in the groove, (**e**) beam after performing surface preparation and NSM-CFRP flexural strengthening.

2.2.3. Combination of Shear and Flexural Strengthening Methods (NU and NSU Type)

NSM-strengthened beams for NU and NSU types were allowed to cure for 3 days for hardening of epoxy gel. The process described for U-wrap was adopted for the NSM-strengthened beams for NU and NSU types. Wrapped beams were allowed to cure for 14 days at room temperature to enable complete hardening of wrapping and composite action with the beams. Therefore, combination beams were cured after strengthening for a total of 17 days before testing. Figures 10 and 11 show the process of U-wrapping for NU and NSU beams.

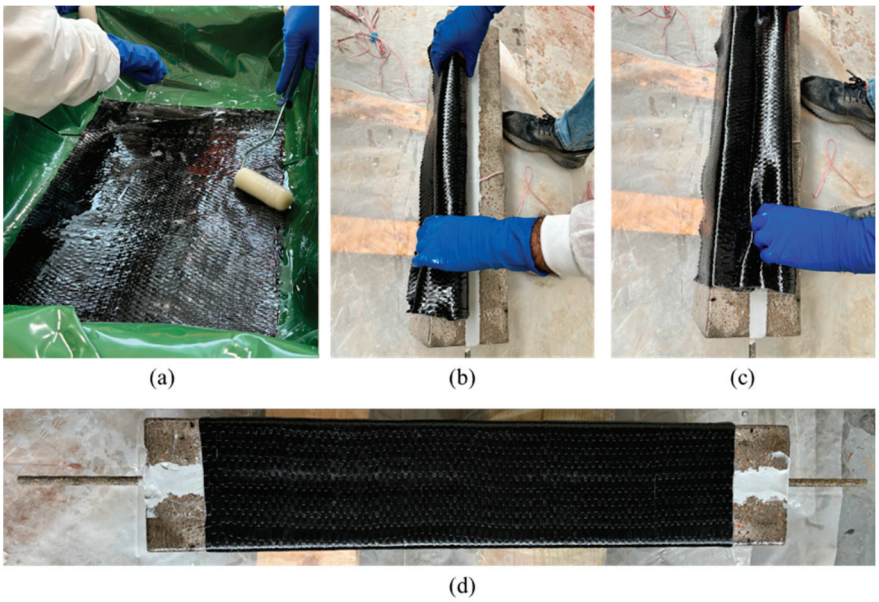

Figure 10. Combination strengthening NSM + complete U-wrap. (**a**) Wetting process of carbon fiber fabric, (**b**,**c**) wet-layup on NSM strengthened beams, (**d**) completed U-wrap strengthening on NSM-strengthened beam.

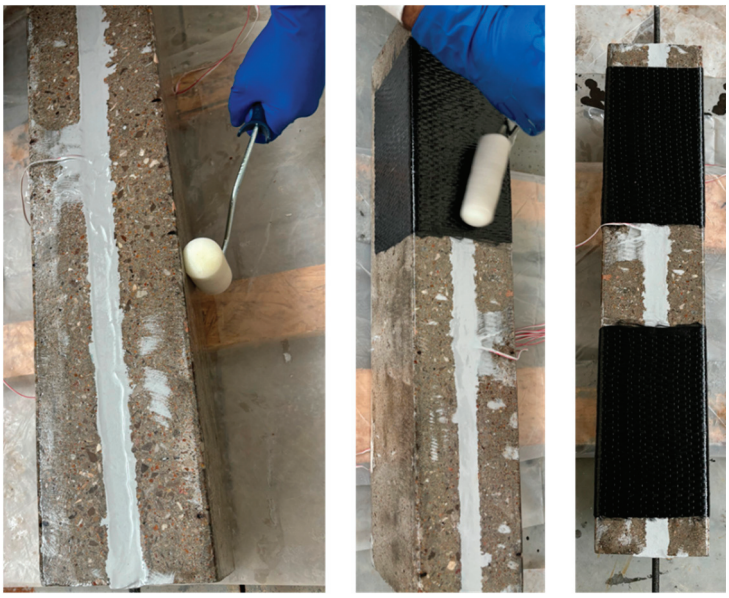

Figure 11. Combination strengthening NSM + shear only U-wrap (**a**) prime coat on NSM-strengthened beams for wet layup, (**b**) wet layup in shear only zones, (**c**) finished wet layup for U-wrap strengthening in shear-only zones for NSM-strengthened beams.

3. Results and Discussion

The comprehensive experimental findings for all types of the beams are systematically detailed in Table 1. The load-deflection data for a representative beam from each group is depicted in Figure 12. For the control group of RC beams, labeled C1 to C4, the average peak load at failure was found to be 79.19 kN, with a standard deviation of 2.99 kN. The mean deflection associated with this load was 8.70 mm, with a standard deviation of 8.70 mm. The load–deflection pattern of these beams exhibited typical RC beam characteristics, with linear elastic behavior observed up to approximately 50.5 kN, beyond which nonlinear behavior was noted up to the point of failure. For RC beams U1 to U4, reinforced with a CFRP U-wrap, the average peak load at failure was recorded as 94.42 kN, with a standard deviation of 7.19. The mean deflection measured for these beams was 9.73 mm, with a variation of ±0.84 mm. The "U" series beams showed a conventional RC beam load–deflection profile, exhibiting linear elasticity up to an average load of 57.1 kN, after which nonlinear behavior was demonstrated up to the failure load. The RC beams N1 to N4, reinforced with NSM-FRP, showed an average ultimate load at failure of 144.60 kN, with a standard deviation of 18.39 kN. The corresponding average deflection was 9.60 mm, with a variation of ±0.91 mm. The load–deflection characteristics of these "N" series beams differed notably from both the control "C" beams and the "U" series beams. In the "N" series beams reinforced with NSM-FRP, the load–deflection diagram exhibits linear elasticity up to an average load of 110 kN. Beyond this point, a slope change is noted, maintaining relatively linear behavior up to the maximum load. Nonlinearity then becomes obvious, and the load gradually decreases as the CFRP begins to slip, continuing until failure occurs. The RC beams designated as NU1 to NU4, which were reinforced with both NSM-FRP bars and U-wrap shear strengthening along their entire span, exhibited an average peak load at failure of 157.95 kN, with a standard deviation of 4.57 kN. The average deflection for these beams was measured at 12.86 mm, with a variation of ±2.01 mm. Their load–deflection behavior maintains a linear behavior up the peak load. Beyond the linear elastic portion, NU-type beams demonstrated a slight change in slope in the load displacement behavior but continued to be linear until the first load drop, demonstrating a bilinear behavior.

Table 1. Load and deflection results upon test completion.

Beam Type	Load (kN)	Deflection (mm)	Failure Mode	Increase (%)
Control	79.19 ± 2.99	8.70 ± 0.46	CC	
U-wrap only	94.42 ± 7.19	9.73 ± 0.84	CC	19
NSM only	144.60 ± 18.39	9.60 ± 0.91	DB	83
NSM + U-wrap	157.95 ± 4.57	12.86 ± 2.01	R	99
NSM + shear U-wrap	162.17 ± 6.65	14.28 ± 2.23	R/SE	105

Notes: SE is splitting of epoxy cover, R is strength rupture of CFRP bar, DB is debonding of NSM-FRP bar with surrounding epoxy, and CC is concrete crushing after yielding of steel.

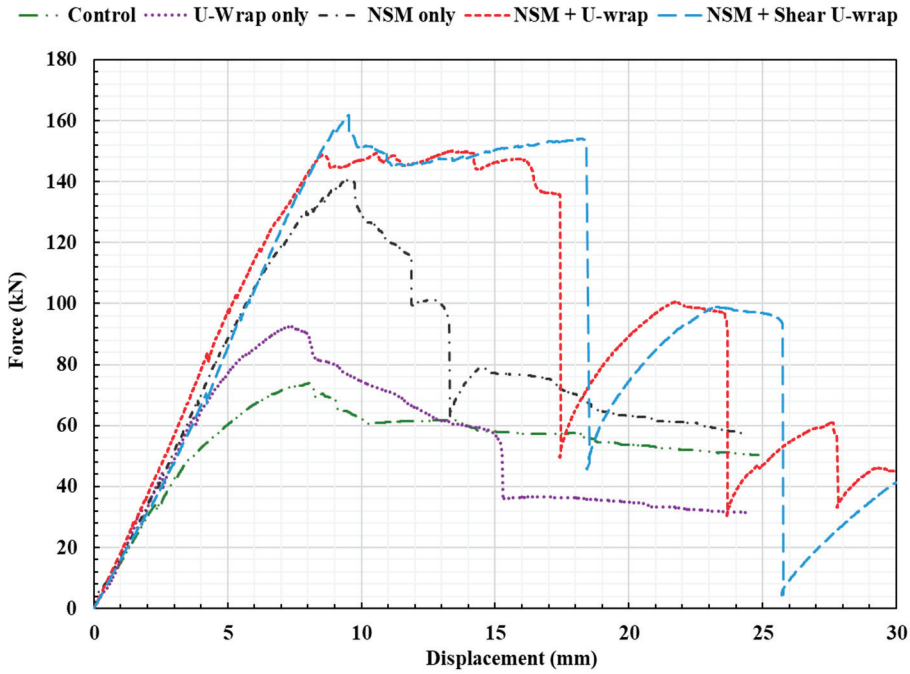

Figure 12. Load–displacement behavior of median of all tested beams.

From observation of the load displacement graphs, large load drops are evident after some ductile behavior. Almost all beams had a large load drop of around 18 mm displacement with a load drop rate of 78 kN/mm. There is a noticeable stiffness change between beams, which could be attributed to the change in effect of confinement due to the wrapping or also due to the change in bond developed between the NSM bar and the surrounding epoxy. Beyond the load drop, the beams continued to support the load and observed a decrease in load of more than 50% of the peak. At this point, the test was stopped as the test setup would not allow for any more beam deflection. The "NSU" series beams, incorporating U-wrap in the shear span and NSM-FRP for flexural strengthening, displayed an average ultimate load at failure of 162.17 with a variation of ±6.65 kN. The mean deflection was 14.28 mm, with a standard deviation of 2.23 mm. Their load–deflection pattern was largely akin to that observed in the "NU" series, but in some of the specimens, the failure mode was different. Two of the beams experienced a sudden failure due to the tension rupture of the CFRP. In contrast, the other two showed a progressive failure characterized by continuous CFRP slipping and epoxy splitting until eventual failure occurred. Two of the beams had a large load drop around an 18 mm displacement with a load drop rate of 90 kN/mm. Large drops were not observed in the other two beams where a gradual load decrease was seen. There was a noticeable stiffness change between one of the beams and the rest, which could be attributed to the change in effect of confinement due to the wrapping or also due to the change in bond developed between the NSM bar and the surrounding epoxy.

The data in Figure 13 clearly show that combining U-wrap shear and NSM-FRP flexural strengthening significantly alters beam behavior. It is evident that the control beams have the lowest peak load when compared to the N, U, NU and NSU types. It is evident from this comparison that incorporating NSM flexural strengthening for the control RC beams improves their flexural strength. It can be clearly observed that the NSM-FRP has a significant strength increase in the control specimens as also observed in previous studies [13,17]. The flexural strength is even more dominant because of the high-strength materials, such as the CFRP, which was used to strengthen these beams. Also, it is worth mentioning that the change in slope beyond the linear elastic portion is marginal for N, NU and NSU beam types, which continue in a linear fashion when compared to the C- and U-type beams. This is attributed to the NSM CFRP bar that is highly linear to failure. None of the beams except the combination types (NU and NSU) had significant load drops in the load displacement graphs. Figure 13 provides a summary of these variations in load carrying capacity across the five beam groups. Performing an analysis to compare peak load of control beams to other types of beams, it was observed that there was a 19% increase for U-type beams compared to the control beams. This increase in flexural performance for U-wrap beams can be attributed to the confinement effect. An 83% increase in N-type beams, a 99% increase in NU-type beams and a 105% increase in NSU-type beams was observed, indicating that the incorporation of the CFRP bar as NSM improves flexural strength and even more so in combined beams. This marks a drastic increase in flexural performance in the NSM only and combination-strengthened beams compared to control beams. The combination-strengthened beams were 9% and 12% higher in flexural performance compared to N-type beams, indicating that confining the NSM only beams with the U-wrap improves confinement and bond, thus increasing the flexural strength. In previous work [22], using GFRP NSM, the improvement in flexural performance compared to RC beams was 47%, which is less than the improvement seen in this study as the type of NSM used was CFRP.

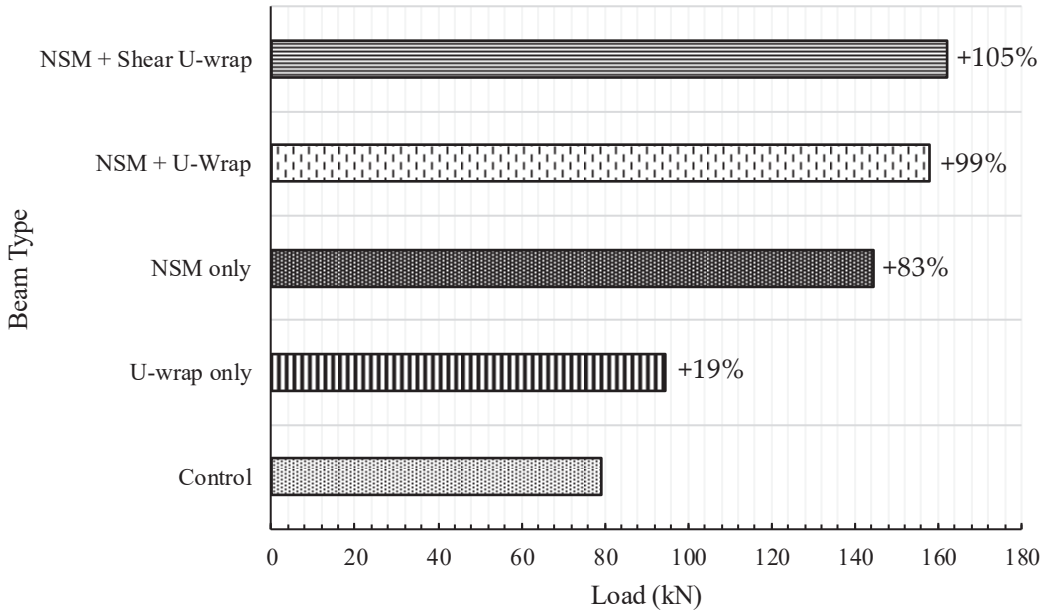

Figure 13. Mean flexural load capacity of tested beams. Percentage increase compared to control beams shown on each bar.

Figure 14 illustrates the failure modes for each group of beams. It shows significant debonding in NSM-FRP beams and abrupt CFRP rupture in beams where NSM-FRP is used alongside U-wrap shear reinforcement. The control groups, "C" and "U", mirrored typical RC beam behavior, failing due to concrete crushing following steel yield. The "N" group experienced CFRP bar and epoxy debonding from the concrete. The "NU" group, showing

improved bond strength, failed due to CFRP bar rupture. The "NSU" group exhibited two failure patterns: either sudden epoxy cover splitting or CFRP bar rupture, depending on the epoxy cover's efficacy in strain transfer. In cases where the epoxy effectively transferred strain, CFRP bar rupture occurred. Otherwise, the failure was marked by epoxy cover splitting. The CFRP bars in "NU" and "NSU" reached strains up to near their ultimate capacity before failure, indicating that U-wrap confinement helps prevent debonding and allows the bars to achieve higher strain levels. In the experimental findings, it was noted that in the "N" group, the CFRP bar and epoxy started to slip at maximum load due to debonding from the surrounding concrete. Nonetheless, this slippage was not observed in the "NU" group, where CFRP U-wrap was applied along the entire span.

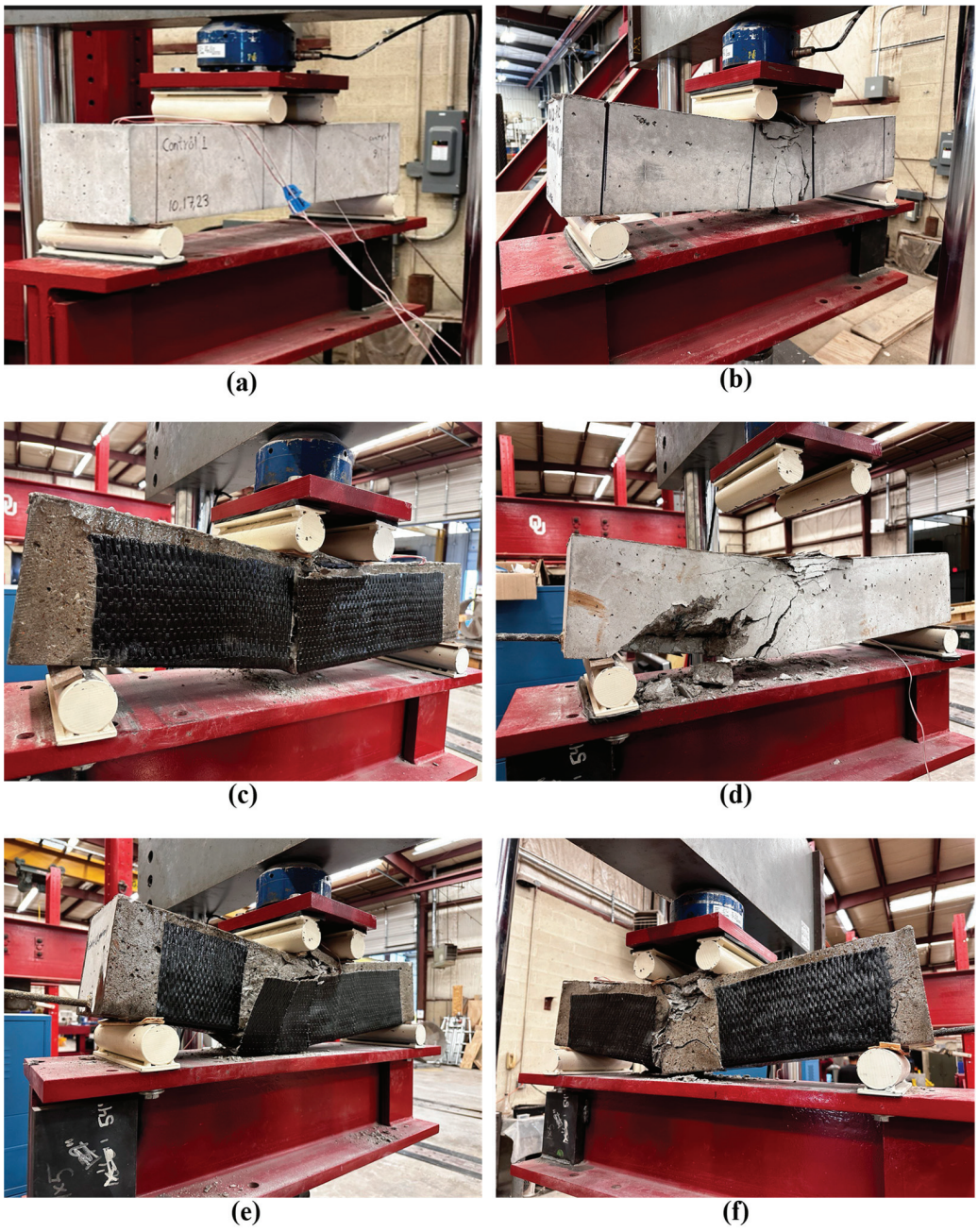

Figure 14. Different failure modes of the tested beams. (**a**) Control beam before performing the test, (**b**) control beam after performing the test, (**c**) only U-wrap beam, (**d**) NSM only beam, (**e**) NSM + full U-wrap beam, (**f**) NSM + shear U-wrap beam.

For the "C" control beam group, specifically beam C3, the tension steel reached a yield strain of 0.0021 at a load of 49.3 kN, with a midspan deflection of 4.1 mm. The strain gauge readings ceased at a strain of 0.0052, corresponding to a load of 56.9 kN. Simultaneously, the strain in the top compression fibers of the beam reached 0.003. At this level of strain, the beam experienced failure due to crushing of the concrete. The load at the 0.003 strain level was 74.05 kN, with a midspan deflection of 8.11 mm. In the "N" beam group, for the beam N3, the tension steel reached a strain of 0.0021, while the corresponding CFRP bar strain was 0.0055 at a load of 102.8 kN and a midspan deflection of 5.45 mm. The highest strain recorded in the tension steel was 0.0026 at 149.88 kN load. The CFRP bar's maximum strain recorded was 0.013 at a load of 153.14 kN, and after that, the beam ultimately failed at a load of 165.51 kN. In the "NU" beam group, specifically at beam NU2, the strain in the tension steel reached 0.0021, with the CFRP bar strain at 0.0025 under a load of 80.94 kN and a midspan deflection of 5.45 mm. The maximum strain in tension steel was 0.004 at a 91.19 kN load. The beam ultimately failed at 150 kN. The failure was abrupt due to CFRP bar rupture, with the bar's maximum strain reaching 0.0125, which is 70% of the bar's ultimate tensile strain. In the "NSU" beam group, specifically for NSU4, the tension steel reached a strain of 0.0021, with the CFRP bar strain at 0.0032 under a load of 79.3 kN and a midspan deflection of 5.14 mm. The maximum strain in the tension steel was 0.0044 at a 162.22 kN load, and the beam failed at 163.68 kN. The highest recorded concrete compression strain was 0.00386 at 161.59 kN. Also, the peak strain in the CFRP bar was 0.0119. It is noteworthy that in the "NSU" group of beams, two out of the four experienced failures due to CFRP bar rupture. The strain distribution of type N, NU, and NSU beams is depicted in Figure 15.

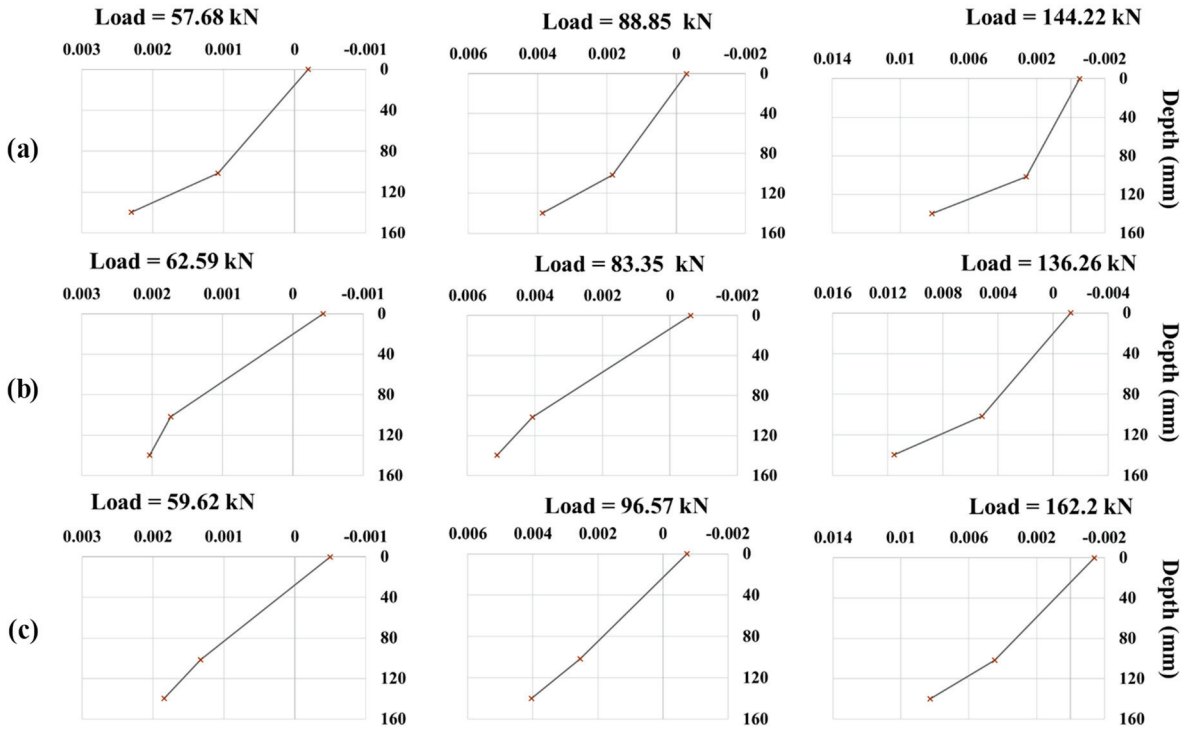

Figure 15. Strain distribution diagrams at various loads for type (**a**) N, (**b**) NU, (**c**) NSU beams.

The failure mode of each beam group is shown in Figure 16. As noted in previous research [17], the integration of NSM-FRP flexural strengthening with U-wrap shear strengthening not only enhances the bonding in RC beams but also maintains their deformability up to the point of failure. This combination effectively improves the overall structural performance without compromising the beam's ability to deform under load. However, it should be noted that the failure mode for beams strengthened with both U-wrap and

NSM-FRP can be quite sudden and abrupt. This highlights a critical aspect to consider in the combined application of these strengthening techniques. The investigation reveals that combining NSM-FRP and U-wrap shear strengthening in RC beams enhances their load bearing capacity. However, this comes with a trade-off: the strengthened beams are prone to sudden and abrupt failures, along with a rapid loss in capacity, primarily due to the tension rupture of the FRP. As mentioned earlier, 50% of tested NSU beams did not experience sudden failure. So, the investigation interestingly suggests that using U-wrap in the shear span leads to an improved bond in FRP, which effectively enhances the beam's strength. This method manages to increase the bond without the associated risk of sudden failure, a notable benefit in structural engineering applications.

Figure 16. Various failure modes of RC beams strengthened with NSM-CFRP, (**a**) type NU beams, failed by the CFRP bar rupture, (**b**) type NSU beams, failed by the CFRP bar rupture, (**c**) type NSU beams, failed by sudden spilling of the epoxy cover.

4. Key Discussion

Based on the strain data of the NSM-CFRP bar, a 33.3% increase was observed for the NU beam series over N beam seriesshowing the improvement in bond between the NSM-FRP bar and surrounding epoxy as a result of U-wraps. However, they were accompanied by bar rupture. U-wrap FRP provides significant external confinement to the concrete, which helps in uniformly distributing the stresses across the concrete section. This confinement effect is particularly beneficial in regions susceptible to high shear stresses and where bending moments induce tensile stresses at the concrete surface. By doing so,

U-wrap effectively delays the initiation and propagation of cracks. From this study, it is evident that special care should be taken in designing RC strengthening combining NSM and U-wrap FRP strengthening.

5. Conclusions

In this study, a total of 20 RC beams were organized into five groups. These beams were all subjected to static load testing. The aim of this study was to assess the effects of employing NSM-CFRP for flexural strengthening along with U-wrap CFRP for shear strengthening in concrete structures. This evaluation sought to understand how these methods affect the structural performance concrete beams. Here are some significant conclusions.

1. The obtained results indicated that RC beams reinforced with NSM-FRP exhibited a significant increase in flexural strength, showing an 82% enhancement compared to the control beams. The primary mode of failure observed in these beams was the debonding of the FRP bar and epoxy from the surrounding concrete.
2. The research demonstrated that integrating NSM-FRP for flexural enhancement with full-span U-wrap in RC beams led to an increase in flexural load capacity by approximately 9% compared to beams reinforced only with NSM-FRP. The U-wrap effectively prevented crack growth in the epoxy, improving the bond between NSM-FRP and concrete. This combination altered the failure mode from debonding of the CFRP bar to its rupture at peak tensile strength.
3. The research revealed that applying U-wrap shear strengthening in combination with NSM-FRP flexural strengthening solely in the shear area led to a 12.1% increase in flexural load capacity, compared to beams with NSM-FRP. Among the four beams tested, two failed due to CFRP bar rupture, while the other two experienced sudden epoxy cover splitting. Despite these varying failure modes, strain measurements confirmed that the CFRP bars reached their full tensile capacity, indicating improved bond performance. Both observed failure modes (CFRP rupture and epoxy splitting) were abrupt, impacting the beams' ductility.
4. The integration of U-wrap shear strengthening with NSM-FRP flexural strengthening has shown a marked enhancement in bond performance, increasing the overall flexural load capacity of RC beams. Nevertheless, this combination also led to a shift in failure modes. While NSM-FRP flexural-strengthened beams alone exhibited relatively ductile failure, the addition of full U-wraps, which enhances bond performance through confinement, resulted in more sudden and less ductile failure modes, primarily through bar rupture.
5. The structural design of components is based on a 'fail-safe' concept, necessitatingelements to give a warning prior to failure to prevent catastrophes. In infrastructure applications, nonlinear behavior of structural components is important to avoid brittle (catastrophic) failure, which is required by most design codes worldwide. From this study, it is evident that special care should be taken in designing RC strengthening combining NSM and U-wrap FRP strengthening.
6. Future work can be performed with a larger matrix and large-scale beams for further understanding. Positioning LVDTs for the NSM bars can provide information on slippage during testing.

Author Contributions: A.A. fabricated and tested specimens, performed analysis of results and contributed towards the paper draft. S.V. curated, supervised the work and contributed towards the paper draft. J.V. supervised the work and contributed towards review of the paper draft. All authors have read and agreed to the published version of the manuscript.

Funding: This research was funded by Oklahoma Department of Transportation 2160-23-04 and partially by the University of Oklahoma.

Data Availability Statement: The datasets generated during and/or analyzed during the current study are available from the corresponding author on reasonable request.

Acknowledgments: The authors would also like to acknowledge the contribution of John Bullock, Royce Floyd, William Jordan and Trent Rogers. The authors would like to thank Rahulreddy Chennareddy for his consulting help.

Conflicts of Interest: The contents of this report reflect the views of the author(s) who are responsible for the facts and the accuracy of the data presented herein. The contents do not necessarily reflect the views of the Oklahoma Department of Transportation or the Federal Highway Administration. This report does not constitute a standard, specification, or regulation. While trade names may be used in this report, it is not intended as an endorsement of any machine, contractor, process, or product.

References

1. Gucunski, N.; Pailes, B.; Kim, J.; Azari, H.; Dinh, K. Capture and Quantification of Deterioration Progression in Concrete Bridge Decks through Periodical NDE Surveys. *J. Infrastruct. Syst.* **2017**, *23*, B4016005. [CrossRef]
2. Wang, X.; Cheng, L. Bond characteristics and modeling of near-surface mounted CFRP in concrete. *Compos. Struct.* **2021**, *255*, 113011. [CrossRef]
3. Sharaky, I.A.; Baena, M.; Barris, C.; Sallam, H.E.M.; Torres, L. Effect of axial stiffness of NSM FRP reinforcement and concrete cover confinement on flexural behaviour of strengthened RC beams: Experimental and numerical study. *Eng. Struct.* **2018**, *173*, 987–1001. [CrossRef]
4. Vedernikov, A.; Tucci, F.; Carlone, P.; Gusev, S.; Konev, S.; Firsov, D.; Akhatov, I.; Safonov, A. Effects of pulling speed on structural performance of L-shaped pultruded profiles. *Compos. Struct.* **2021**, *255*, 112967. [CrossRef]
5. Bakis, C.E.; Bank, L.C.; Brown, V.L.; Cosenza, E.; Davalos, J.F.; Lesko, J.J.; Machida, A.; Rizkalla, S.H.; Triantafillou, T.C. Fiber-Reinforced Polymer Composites for Construction—State-of-the-Art Review. *Perspect. Civ. Eng. Commem. 150th Anniv. Am. Soc. Civ. Eng.* **2003**, *6*, 369–383. [CrossRef]
6. Van Den Einde, L.; Zhao, L.; Seible, F. Use of FRP composites in civil structural applications. *Constr. Build. Mater.* **2003**, *17*, 389–403. [CrossRef]
7. Tharmarajah, G.; Taylor, S.E.; Cleland, D.J.; Robinson, D. Corrosion-resistant FRP reinforcement for bridge deck slabs. *Proc. Inst. Civ. Eng.-Bridg. Eng.* **2015**, *168*, 208–217. [CrossRef]
8. Liu, X.; Nanni, A.; Silva, P.F. Rehabilitation of compression steel members using FRP pipes filled with non-expansive and expansive light-weight concrete. *Adv. Struct. Eng.* **2005**, *8*, 129–141. [CrossRef]
9. Bizindavyi, L.; Neale, K.W.; Erki, M.A. Experimental Investigation of Bonded Fiber Reinforced Polymer-Concrete Joints under Cyclic Loading. *J. Compos. Constr.* **2003**, *7*, 127–134. [CrossRef]
10. Sokairge, H.; Elgabbas, F.; Elshafie, H. Structural behavior of RC beams strengthened with prestressed near surface mounted technique using basalt FRP bars. *Eng. Struct.* **2022**, *250*, 113489. [CrossRef]
11. Kadhim, M.M.A.; Jawdhari, A.; Altaee, M.M.; Majdi, A.; Fam, A. Parametric investigation of continuous beams strengthened with near surface mounted FRP bars. *Eng. Struct.* **2023**, *293*, 116619. [CrossRef]
12. Kabashi, N.; Avdyli, B.; Krasniqi, E.; Këpuska, A. Comparative approach to flexural behavior of reinforced beams with GFRP, CFRP, and steel bars. *Civ. Eng. J.* **2020**, *6*, 50–59. [CrossRef]
13. Sbahieh, S.; Mckay, G.; Al-Ghamdi, S.G. A comparative life cycle assessment of fiber-reinforced polymers as a sustainable reinforcement option in concrete beams. *Front. Built Environ.* **2023**, *9*, 1194121. [CrossRef]
14. Zhang, S.S.; Yu, T.; Chen, G.M. Reinforced concrete beams strengthened in flexure with near-surface mounted (NSM) CFRP strips: Current status and research needs. *Compos. Part B Eng.* **2017**, *131*, 30–42. [CrossRef]
15. Guide for the Design and Construction of Externally Bonded FRP Systems for Strengthening Concrete Structures. 2017. Available online: www.concrete.org (accessed on 6 February 2024).
16. Saadatmanesh, H.; Ehsani, M.R. Fiber composite plates can strengthen beams. *Concr. Int.* **1990**, *12*, 65–71. Available online: https://www.concrete.org/publications/internationalconcreteabstractsportal/m/details/id/2060 (accessed on 29 December 2023).
17. Nanni, A.; Alkhrdaji, T.; Chen, G.; Barker, M.; Xinbao, Y.; Mayo, R. Overview of testing to failure program of a highway bridge strengthened with FRP composites. In Proceedings of the 4th International Symposium on FRP for Reinforcement of Concrete Structures (FRPRCS4), Baltimore, MD, USA; 1999; pp. 69–80. Available online: https://www.researchgate.net/profile/Antonio-Nanni-3/publication/241138044_OVERVIEW_OF_TESTING_TO_FAILURE_PROGRAM_OF_A_HIGHWAY_BRIDGE_STRENGTHENED_WITH_FRP_COMPOSITES/links/004635321cdb15c373000000/OVERVIEW-OF-TESTING-TO-FAILURE-PROGRAM-OF-A-HIGHWAY-BRIDG (accessed on 29 December 2023).
18. De Lorenzis, L.; Teng, J.G. Near-surface mounted FRP reinforcement: An emerging technique for strengthening structures. *Compos. Part B Eng.* **2007**, *38*, 119–143. [CrossRef]
19. Van Cao, V.; Pham, S.Q. Comparison of CFRP and GFRP Wraps on Reducing Seismic Damage of Deficient Reinforced Concrete Structures. *Int. J. Civ. Eng.* **2019**, *17*, 1667–1681. [CrossRef]
20. Zhang, S.S.; Teng, J.G.; Yu, T. Bond Strength Model for CFRP Strips Near-Surface Mounted to Concrete. *J. Compos. Constr.* **2014**, *18*, A4014003. [CrossRef]
21. Chennareddy, R.; Taha, M.M.R. Effect of Combining Near-Surface-Mounted and U-Wrap Fiber-Reinforced Polymer Strengthening Techniques on Behavior of Reinforced Concrete Beams. *ACI Struct. J.* **2017**, *114*, 721–730. [CrossRef]

22. ChennaReddy, R. Significance of U-Wrap FRP Shear Strengthening on Flexural Behavior of RC Beams Strengthened Using Near Surface Mounted FRP Bars (700 mm Beam). 2016. Available online: http://search.ebscohost.com/login.aspx?direct=true&db=ddu&AN=EC93B2989CA19E9C&site=ehost-live (accessed on 1 February 2016).
23. Murad, Y.; Abu-AlHaj, T. Flexural strengthening and repairing of heat damaged RC beams using continuous near-surface mounted CFRP ropes. *Structures* **2021**, *33*, 451–462. [CrossRef]
24. Kachlakev, D.; McCurry, D.D. Behavior of full-scale reinforced concrete beams retrofitted for shear and flexural with FRP laminates. *Compos. Part B Eng.* **2000**, *31*, 445–452. [CrossRef]
25. Chajes, M.J.; Januszka, T.F.; Mertz, D.R.; Thomson, T.A.; Finch, W.W. Shear strengthening of reinforced concrete beams using externally applied composite fabrics. *ACI Struct. J.* **1995**, *92*, 295–303. [CrossRef] [PubMed]
26. Taerwe, L. Rehabilitation of navy pier beams with composite sheets. In *Non-Metallic (FRP) Reinforcement for Concrete Structures*; Chapman & Hall: London, UK, 2020; pp. 551–558. [CrossRef]
27. Ombres, L.; Mazzuca, P. Residual Flexural Behavior of PBO FRCM-Strengthened Reinforced Concrete Beams after Exposure to Elevated Temperatures. *J. Compos. Constr.* **2024**, *28*, 04023063. [CrossRef]
28. Wuertz, A.F. Strengthening Rectangular Beams with NSM Steel Bars and Externally Bonded GFRP. 2013. Available online: https://krex.k-state.edu/bitstream/handle/2097/15624/AugustineWuertz2013.pdf?sequence=3 (accessed on 9 January 2024).
29. *ASTM/C143M-15a*; Standard Test Method for Slump of Hydraulic Cement Concrete (C 143). ASTM International: West Conshohocken, PA, USA, 2009; Volume 27, pp. 99–101. Available online: https://www.astm.org/c0143_c0143m-00.html (accessed on 5 February 2022).
30. *ASTM C39*; Standard Test Method for Compressive Strength of Cylindrical Concrete Specimens. ASTM International: West Conshohocken, PA, USA, 2001.
31. *ASTM C496-96*; Standard Test Method for Splitting Tensile Strength of Cylindrical Concrete Specimens. Annual Book of ASTM Standards: West Conshohocken, PA, USA, 2022; Volume i, pp. 1–5. [CrossRef]
32. *ASTM C469/C469M-14*; Standard Test Method for Static Modulus of Elasticity and Poisson's Ratio of Concrete in Compression. Annual Book of ASTM Standards: West Conshohocken, PA, USA, 2014; pp. 1–5. [CrossRef]

Journal of
Composites Science

MDPI

Article

Effect of Chitin Nanocrystal Deacetylation on a Nature-Mimicking Interface in Carbon Fiber Composites

Abdellatif M. Abdel-Mohsen [1], Rasha M. Abdel-Rahman [1], Lukáš Kalina [2], Vishakha Vishakha [3], Ludmila Kaprálková [1], Pavel Němeček [1], Josef Jančář [2,3] and Ivan Kelnar [1,*]

[1] Institute of Macromolecular Chemistry, Czech Academy of Sciences, Heyrovského nám. 2, 162 00 Praha, Czech Republic; abdellatif@imc.cas.cz (A.M.A.-M.); radwan@imc.cas.cz (R.M.A.-R.); kapralkova@imc.cas.cz (L.K.); nemecek@imc.cas.cz (P.N.)
[2] Materials Research Center, Faculty of Chemistry, Brno University of Technology, Purkyňova 464/118, 612 00 Brno, Czech Republic; kalina@fch.vut.cz (L.K.); jancar@fch.vut.cz (J.J.)
[3] CEITEC-Central European Institute of Technology, Brno University of Technology, Purkyňova 656/123, 612 00 Brno, Czech Republic; vishakhavishakha2322@gmail.com
* Correspondence: kelnar@imc.cas.cz

Abstract: The formation of a rigid, tough interface based on a nacre-like structure in carbon fiber (CF) composites is a promising way to eliminate low delamination resistance. An effective method of coating CFs is electrophoretic deposition (EPD), which, in the case of dissimilar components like graphene oxide (GO) and polymeric glue, usually requires chemical bonding/strong interactions. In this work, we focus on chitin nanocrystals (ChNCs), leading to an excellent mechanical performance of artificial nacre, where favorable interactions and bonding with GO are controlled by degrees of deacetylation (5, 15, and 30%). We prepared coatings based on GO/ChNC adducts with 95/5, 90/10, 50/50, and 25/75 ratios using optimized EPD conditions (pH, concentration, voltage, and time). The prepared materials were characterized using FTIR, TEM, XPS, SEM, DLS, and XRD. SEM evaluation indicates the formation of a homogeneous interlayer, which has a fair potential for chemical bonding with the epoxy matrix. Short-beam testing of epoxy matrix composites indicates that the coating does not decrease stiffness and has a relatively low dependence on composition. Therefore, all coatings are promising for a detailed study of delamination resistance using laminate samples. Moreover, facile EPD from the water solution/suspension has a fair potential for industrial applications.

Keywords: graphene oxide; chitin nanocrystals; delamination resistance; tough interface; electrophoresis; carbon fiber composite

1. Introduction

It is now well accepted that combinations of carbon nanoplatelets (CN) with small amounts of various polymers [1–3] and polysaccharides [4] may form nature-mimicking materials with unique compact structures and impressive mechanical parameters, which can exceed those of nacre, that is, the natural 'gold standard' of strong, tough material [5,6].

It was recently demonstrated that analogous materials with unique performance (deformation mechanism) can be obtained by combining CN with suitable organic anisotropic nanoparticles, mostly nanofibrils/whiskers. An example is a system containing reduced graphene oxide (GO) and covalently linked cellulose nanofibrils (CNC) [7] with a typical composition for nacres (80–97% GO), some other nanoplatelet/CNC combinations [7–12] or the nanofibrillated cellulose/CN/diblock protein system [13]. Other high-performance nature-mimicking materials are based on different silk fibroin/GO combinations [14,15].

So far, only one study has reported the application of chitin nanocrystals (ChNCs) in a system combining silk nanofibril, hydroxyapatite nanocrystals, and ChNCs [16]. These results are consistent with the fact that nacre is a ternary composite consisting of aragonite

platelets, nanofibrillar chitin, and protein [5]. In this respect, considering the prime importance of interactions/linking between components [7,10], we can consider the promising potential of nanosized polar amino-functionalized ChNCs with a favorable aspect ratio (AR) to form GO-based nacre analogs. Furthermore, ChNC preparation is easier than nanofibrillated cellulose, with further benefits in using waste material [17,18].

ChNCs, mostly prepared from chitin, is a rigid crystalline nanofiber with Young's modulus at 40–80 GPa. It comprises repeating units of glucosamine and *N*-acetylglucosamine that contain reactive groups, i.e., amines. Thus, chitin has more significant potential for chemical modifications than cellulose. Chitin nanocrystals can be produced in a relatively wide range of lengths, diameters, charge densities, types of charge, and crystallinity through various top-down procedures [17–20].

In the area of fibrous composites, different nanoparticles, mainly CN and CNT, are applied to modify the interface as a single coating. This includes electrophoretic deposition (EPD) [21,22] and carbon vapor deposition [23], components of sizing [24], or even direct linking to CF to form hierarchical hairy fibers [25–27].

In the case of cellulose nanocrystals (CNC) and microfibrils [28–30] or silane-modified CNC [30], various dip coatings of glass fibers and carbon fibers (CFs) are reported, while aramid fibers were coated with aramid microfibers by EPD [30,31] or by the dip coating of the aramid microfibers/graphene combination [32]. This modification of the fiber surface provides the benefit of enhanced roughness, increasing frictional adhesion components, and higher interphase modulus. At the same time, an important deficiency of composites with low resistance against impact-delamination [33] (interlaminar cracking) can be eliminated by a tough, usually low-modulus interface [34] due to an increase in impact energy release. However, this leads to a significant reduction in stiffness [35].

Fair mechanical properties, including increased interlaminar shear strength (ILSS), were found with a more rigid coating by CNC [28,29]. At the same time, the solution by various methods that improve the toughness of the matrix brings processing limitations and a reduction in resistance against fiber buckling [36]. On the basis of the above facts, we consider the important role of the tough, rigid interfaces using nature-mimicking nacre-like structures. So far, rigid-soft structures based on carbon nanotubes (CNTs) modified with the poly(ethylene glycol)methylether [37] and CNT/polyetherimide combination [37] have been reported. However, unlike the comparable effect on a single coating using neat GO or CNT [38] to enhance interfacial properties, the ability of tubular nanoelements to form effective complex structures with polymers and excellent mechanical properties is limited. In the case of 2D platelets, the potential to create effective ordered nacre-mimicking "brick and mortar" structures and, thus, a rigid, tough interface is more marked [5,38].

So far, only some layer-by-layer deposition of alternating polymer/nanoparticle (NP) layers has been reported. Examples are layers of polydopamine (PDA)/GO [39,40], PDA/polyhedral silsesquioxane (POSS) [41], or PDA/NiOH platelets [42]. The grafting of nanoparticles to the deposited polymeric layer [43] has also been reported.

Recently, we prepared CF coatings using nacre-like interlayers by EPD of PDA-coated GO or some polymer-grafted GO combinations, showing an excellent ability to enhance ILSS without loss of stiffness [37]. To control the composition of EPD coatings in the two-component system, the grafting of an aminated polymer to GO or borate-mediated interactions/bonding of hydroxyl-containing poly(vinylalcohol) and carboxymethylcellulose was necessary. Therefore, this study is aimed at highlighting the potential of alternative nacre-like coatings of carbon fibers based on GO with attached chitin nanocrystals (GO/ChNC adducts) to upgrade epoxy/fiber composites together with a thorough study of the effect of ChNCs parameters and adduct composition on the electrophoretic deposition of the multiscale rigid tough hierarchical interphase.

2. Experimental Part

2.1. Materials

Epoxy resin LG700 based on diglycidyl ether of bisphenol A (DGEBA) + hardener HG737 (GRM Systems, s.r.o.). Chitin flakes, 1-ethyl-3-(3-dimethylaminopropyl) carbodiimide hydrochloride (EDC), and N-hydroxysuccinimide (NHS) were purchased from Sigma Aldrich (Praha, Czech Republic); graphite flakes were from (Graphite Týn, Týn nad, Vltavou, Czech Republic); and the carbon fiber (CF) roving yarn filament Torayca T700SC 12 k was from GRM Systems, s.r.o. (Olomouc, Czech Republic).

2.2. Preparation of Graphene Oxide (GO)

The modified Hummer's method [44] was used; briefly, 95 mL of concentrated sulfuric acid and 2 g of $NaNO_3$ were added to 4 g of graphite flakes in an ice bath. In total, 12 g of $KMnO_4$ was slowly added, and the mixture was stored at 35 °C for 100 min. Then, 184 mL of water was added while the temperature increased to ~95 °C. After 15 min, 420 mL of water with 5 mL of 30% H_2O_2 was added. The residue was washed with a mixture of water, 35% HCl, and ethanol by centrifugation. The oxygen content was ~40%, as evaluated using elemental analysis. The final ~2% water suspension was delaminated using a Bandelin 200 W sonicator with 30% amplitude for 15 min.

2.3. Preparation of Chitin Nanocrystals (ChNCs)

Chitin nanocrystals (ChNC) with different degrees of deacetylation (DDA) were prepared according to our previous works [18,45]. Briefly, chitin nanocrystals were synthesized by an acid hydrolysis process using HCl (5 M) for 6 h at 90 °C, and the solid-to-medium-solution ratio was approximately (1/100). The nanocrystals were obtained after centrifugation at 7500 rpm for 30 min at room temperature. ChNCs were dialyzed using a cellulose membrane cut (12–14 KDa) for one week at room temperature using deionized water, which changed every 12 h until the pH reached 4.5. ChNCs were stored at 4 °C in a refrigerator until further use. The DDA of ChNCs was 5, 15, and 30% DDA from ^{13}C-CP/MAS NMR [18], respectively. The degree of deacetylation was also confirmed by FTIR spectroscopy in combination with XRD [45]; see Figure S1a,b.

2.4. GO/ChNC Adduct Synthesis

A certain amount (0.5%) of GO was dispersed in deionized water. Then, 50/25 mM of EDC/NHS was added to the GO while stirring for 2 h at room temperature to activate the carboxylic and epoxide groups of the GO. ChNCs with different degrees of deacetylation (5, 15, 30% DDA) were added to the GO suspension drop by drop with stirring for 5 h at room temperature to obtain the GO/ChNC adduct. The prepared materials were coded according to DDA (GO/$ChNCs_5$, GO/$ChNCs_{15}$, and GO/$ChNCs_{30}$ adducts). The materials obtained were dialyzed for 3 days at rt using deionized water.

2.5. Electrophoretic Coating

Oxidized carbon fibers (OCFs), prepared with nitric acid at 22 °C for 120 h according to our previous work [46], were fixed between two stainless steel electrodes with a distance of ~10 mm. Electrophoretic deposition (EPD) proceeded according to the details in Table 1, also showing the composition of the respective adducts. The applied voltage was 5, 10, and 20 V, respectively, and three concentrations of GO/ChNC adducts (5, 10, and 15 mg/mL) were applied. Moreover, coating was performed at various pHs (3.5, 7.5, and 11) and times of 10 and 20 min. After washing and drying, the composite bar was prepared (see Section 2.5). According to the literature, surface oxidation of CF has a negligible effect on the mechanical parameters of CF [47].

Table 1. Composition of GO/ChNC adducts used for CF coating.

Number	GO (% wt)	ChNCs (% wt)	DDA of ChNCs * (%)	Abbreviation
1	95	5	5	GO/$ChNCs_5$ adduct
2	90	10	5	GO/$ChNCs_5$ adduct
3	80	20	5	GO/$ChNCs_5$ adduct
4	50	50	5	GO/$ChNCs_5$ adduct
5	95	5	15	GO/$ChNCs_{15}$ adduct
6	90	10	15	GO/$ChNCs_{15}$ adduct
7	80	20	15	GO/$ChNCs_{15}$ adduct
8	50	50	15	GO/$ChNCs_{15}$ adduct
9	95	5	30	GO/$ChNCs_{30}$ adduct
10	90	10	30	GO/$ChNCs_{30}$ adduct
11	80	20	30	GO/$ChNCs_{30}$ adduct
12	50	50	30	GO/$ChNCs_{30}$ adduct

* degree of ChNCs deacetylation.

2.6. Characterization of OCF Coated with a GO/CHNC Adduct

Attenuated total reflectance Fourier transform infrared spectroscopy (ATR-FTIR) was carried out using a Bruker Vertex V70 FTIR spectrometer and a Bruker Platinum ATR accessory (Bruker GmbH, Ettlingen, Germany) with a single reflection diamond crystal mount (Bruker Optik GmbH, Ettlingen, Germany). Samples were clamped directly against the diamond crystal using the platinum ATR sample clamp mechanism, ensuring consistent pressure per sample. Spectra were collected in the wavenumber region 3900–650 cm^{-1}. Four data sets per sample were recorded, adding 128 interferograms per set. Spectra were measured at a resolution of 4.0 cm^{-1}, and 128 background scans per sample were collected. The averaged spectra per sample were generated using the Bruker OPUS version 7.2 software, where all spectra were corrected for ATR.

Short-beam strength (SBS), also called interlaminar shear strength (ILSS), if applied to laminate samples, was determined according to ASTM D2344/D2344M using beam samples 3 × 6 × 18 mm. These samples were cut from unidirectional composites prepared by the manual impregnation/mixing of a bundle of a weighed amount of CF (0.52 g) with epoxy in a silicone mold. The dimension of mold was 3 × 6 × 60 mm; the length of CF was ~60 mm. The three-point short-beam bending test (span length 12 mm, span length to thickness ratio of 4) was performed with Instron 5800 apparatus using 1 mm/min crosshead speed. The morphology of native GO, ChNC, and GO/ChNC adduct with different DDA (%) was visualized by transmission electron microscopy (TEM). The experiment was carried out with a Tecnai G2 spirit 12 electron microscope (FEI, Brno, Czech Republic). The surface of the fibers and fracture surfaces was observed using a scanning electron microscope (SEM) using a, Maia apparatus(FEI, Brno, Czech Republic) at 3 kV.

The rheological characterization of water suspensions (5 mg/mL) of native GO, ChNCs, and the GO/ChNC adduct was conducted at room temperature using the ARES G2 Rheometer (TA Instruments, New Castle, IN, USA). Parallel plates with cone/plate geometry (cone angle of 2°, diameter of 40 mm) were used. Frequency sweep measurements were made in the range from 0.05 to 100 rad/s at a 1% strain amplitude.

The X-ray photoelectron spectroscopy (XPS) of oxidized CF (OCF), neat ChNW, GO, and coated OCF was carried out with the Kratos Analytical Axis Ultra DLD system (Kratos Analytical, Manchester UK) using a monochromatic Al Kα (hν = 1486.7 eV) operating at 75 W (5 mA, 15 kV). Spectra were obtained using an analysis area of ~300 × 700 μm. The Kratos charge neutralizer system was used for all analyses. The high-resolution spectra were measured with 0.1 eV step size and 20 eV pass energy. The instrument base pressure was 2·10–8 Pa. Spectra were analyzed using the CasaXPS software (version 2.3.15) by applying a Gaussian–Lawrence line shape for fitting and the ORIGIN 2016 software.

X-ray diffraction patterns were collected using a D-8 Advance diffractometer (Bruker AXS, Karlsruhe Germany) with a Bragg–Brentano (θ-θ) goniometer (radius 217.5 mm)

equipped with a secondary beam curved graphite monochromator and Na (Tl) I scintillation detector. The generator was operated at 40 kV and 30 mA.

3. Results and Discussions

3.1. Effect of DDA on GO/ChNC Adduct Formation

The degree of deacetylation (%) affected the morphology of the ChNCs, as is clear from (Figure 1a–c), showing the STEM of the ChNCs with different DDAs. At a lower DDA %, ChNCs show high aggregation with short crystal length (Figure 1a,f); when increasing the DDA from 15 to 30%, the nanocrystals are slightly longer compared to 5 DDA (Figure 1b,c,f). Figure 1d shows the FTIR of ChNCs with different DDAs. The peak intensity ratio between the amino-to-acetamide groups increased with an increase in the amino group content from 5 to 30 DDA. Figure 1e shows the XRD of native chitin and ChNC within different DDAs (5, 15, 30%). From XRD, all the pristine chitin and ChNCs with different DDAs exhibited six diffraction peaks at 2θ = 9.5°, 12.8°, 19.2°, 20.71°, 23.4° and 26.4°, indexed as (020), (021), (110), (120), (130) and (013), respectively (Figure 1e), suggesting the crystalline structure of the α-chitin [18,48,49]. From Figure 1e, DDA did not significantly affect the crystallization of the ChNCs.

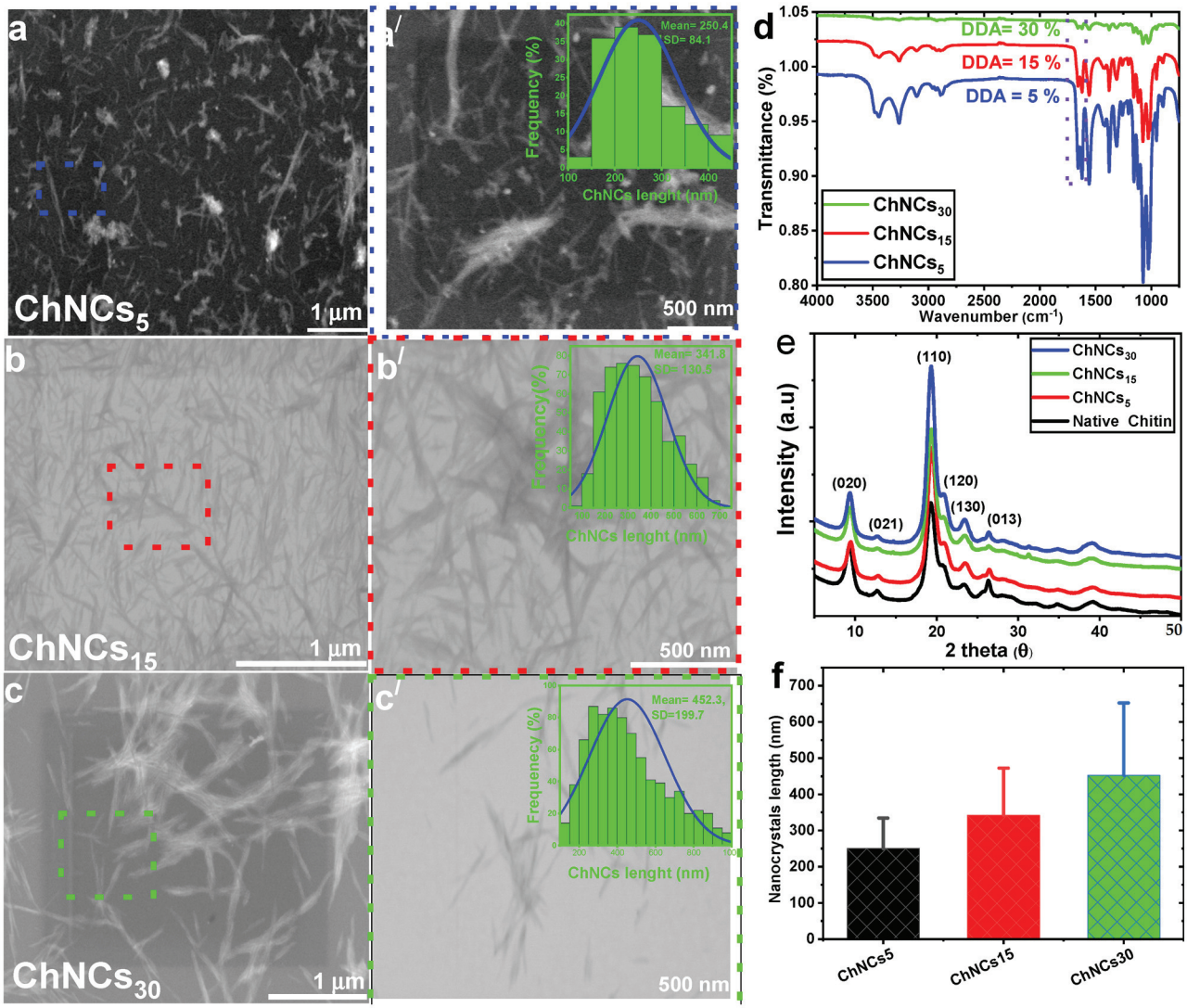

Figure 1. Representative STEM ((**a**–**c**,**a′**–**c′**)), FTIR (**d**), XRD (**e**), and his-tograms (**f**) of ChNCs (see subfigures inside (**a′**–**c′**) with different DDAs (5, 15, 30%). The dashed areas are magnified in (**a′**–**c′**).

Our preliminary results indicate that different charge densities and mobility/dimensions of both GO and ChNCs practically exclude the control of electrophoretic deposition (EPD) of these two-component systems, similar to other GO/polymer combinations [46]. Therefore, mutual bonding between components, using their functionality enabled by EDC/NHS, was applied to prepare the GO/ChNC adduct. When optimizing the EDC/GO/ChNCs/NHS ratio, amide and ester bonds between GO and ChNCs were created (Scheme 1a).

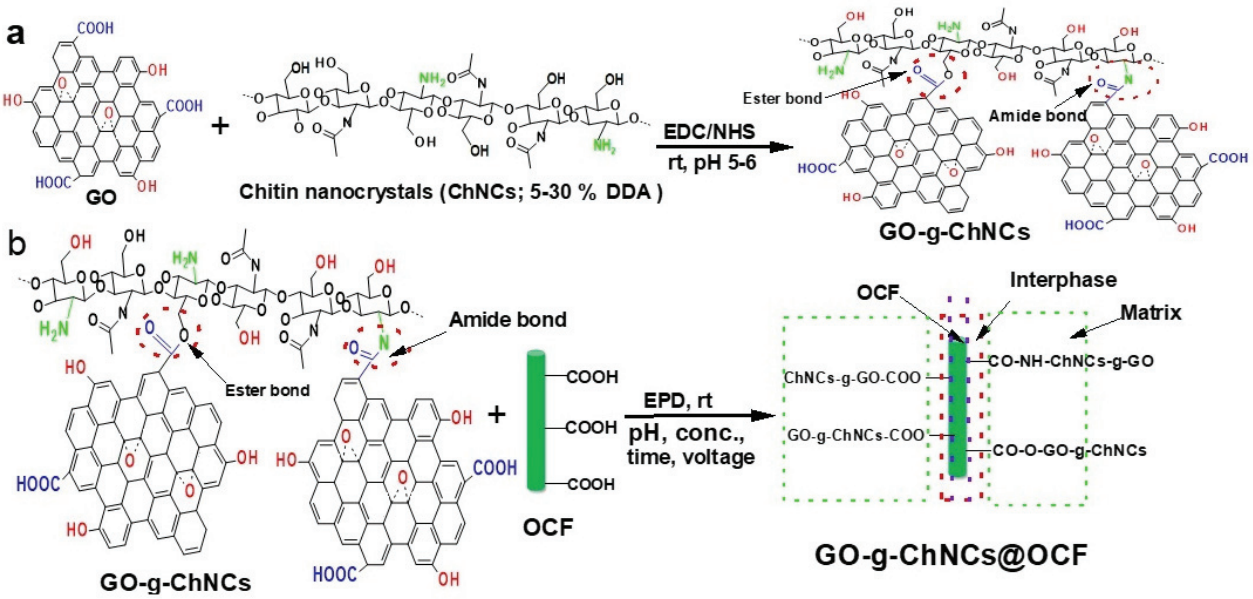

Scheme 1. Proposed chemical bonding and interaction between GO and the ChNC and the coating of OCF using the GO/ChNC adduct. (**a**) Linking GO with ChNCs using EDC/NHS as the crosslinker and catalyst, respectively; (**b**) the coating of OCF using the GO/ChNC adduct (GO/ChNC adduct@OCF).

From Figure 2, it follows that the formation of a GO/ChNC polyelectrolyte complex and crosslinking reduced absorption for the OH and NH/NH_2 stretching vibration peaks. Furthermore, a new peak in the 1718 cm^{-1} region showed the esterification reaction between the –COOH of graphene oxide (GO) and –OH of ChNCs. The band in the spectrum of native GO at 1729 cm^{-1} was naturally broad due to the presence of various types of "carbonyls" and was sharper after the ester bond formed after grafting with $ChNCs_{30}$ (Figure 2a). The strong ionic interaction between carboxylic/epoxide GO and amino/hydroxyl ChNCs in the presence of an EDC/NHS crosslinker agent (Figure 2a) caused the peak intensity of the free amino groups at 1553 cm^{-1} to weaken.

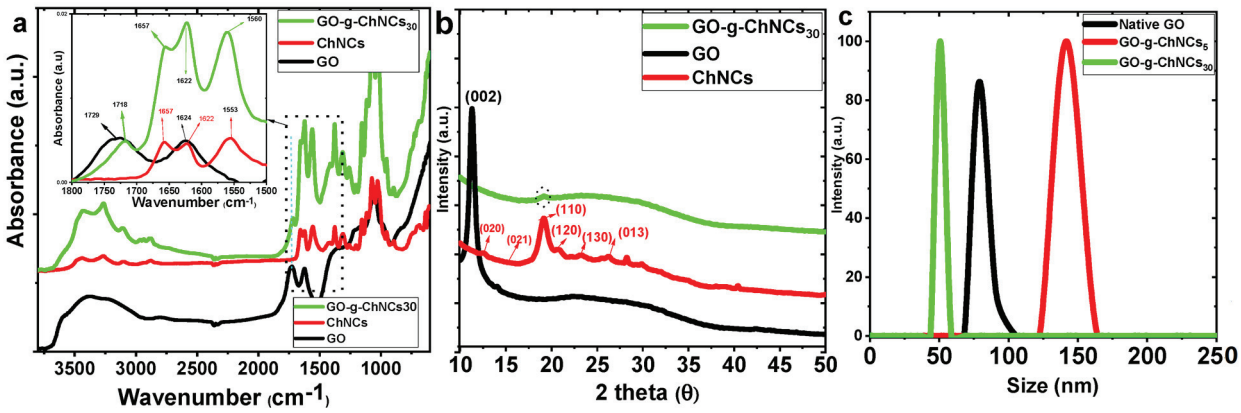

Figure 2. FTIR (**a**), XRD (**b**), and DLS (**c**) of native components and their adducts.

Figure 2b shows the XRD patterns of the GO, $ChNCs_{30}$, and GO/ChNC $adduct_{30}$. The diffraction peak of GO appeared at 2θ = 11.5°, which was associated with the characteristic peak (001 plane) of the interlayer structure of the GO nanosheets [50–52]. The $ChNCs_{30}$ diffraction peaks exhibited six diffraction peaks at 2θ = 9.5°, 12.8°, 19.2°, 20.71°, 23.4° and 26.4°, indexed as (020), (021), (110), (120), (130) and (013), respectively. GO grafted with $ChNCs_{30}$ showed only broader diffraction peaks at 2θ = 20–30°, attributed to the presence of GO and ChNCs. Chitin nanocrystals are considered to be intercalated in the layered GO nanosheets.

Figure 2c shows the DLS of the native GO, GO/$ChNCs_5$ adduct, and GO/$ChNCs_{30}$ adduct. The size distribution of the native GO was about 90 nm, whereas, for the GO/ChNCs5 adduct, it decreased to 55 nm. At higher DDAs, the size distribution of the adduct was about 150 nm. This corresponds to the size of the ChNCs increasing with increased DDA from 5 to 30% (Figure 1).

Interestingly, the rheological characterization of water suspensions (Figure S2a) indicates substantially improved viscosity for adducts compared to both constituents, with the highest value for adducts containing 75% ChNC. This indicates the important effect of the adduct composition on its size, shape, and interactions.

Figure 3 shows fine ChNCs (Figure 3a,b) and a very thin layer of GO with a smooth surface (Figure 3c,d). The GO/ChNC adduct showed a layered structure with a larger thickness against GO, indicating adduct formation (Figure 3e,f).

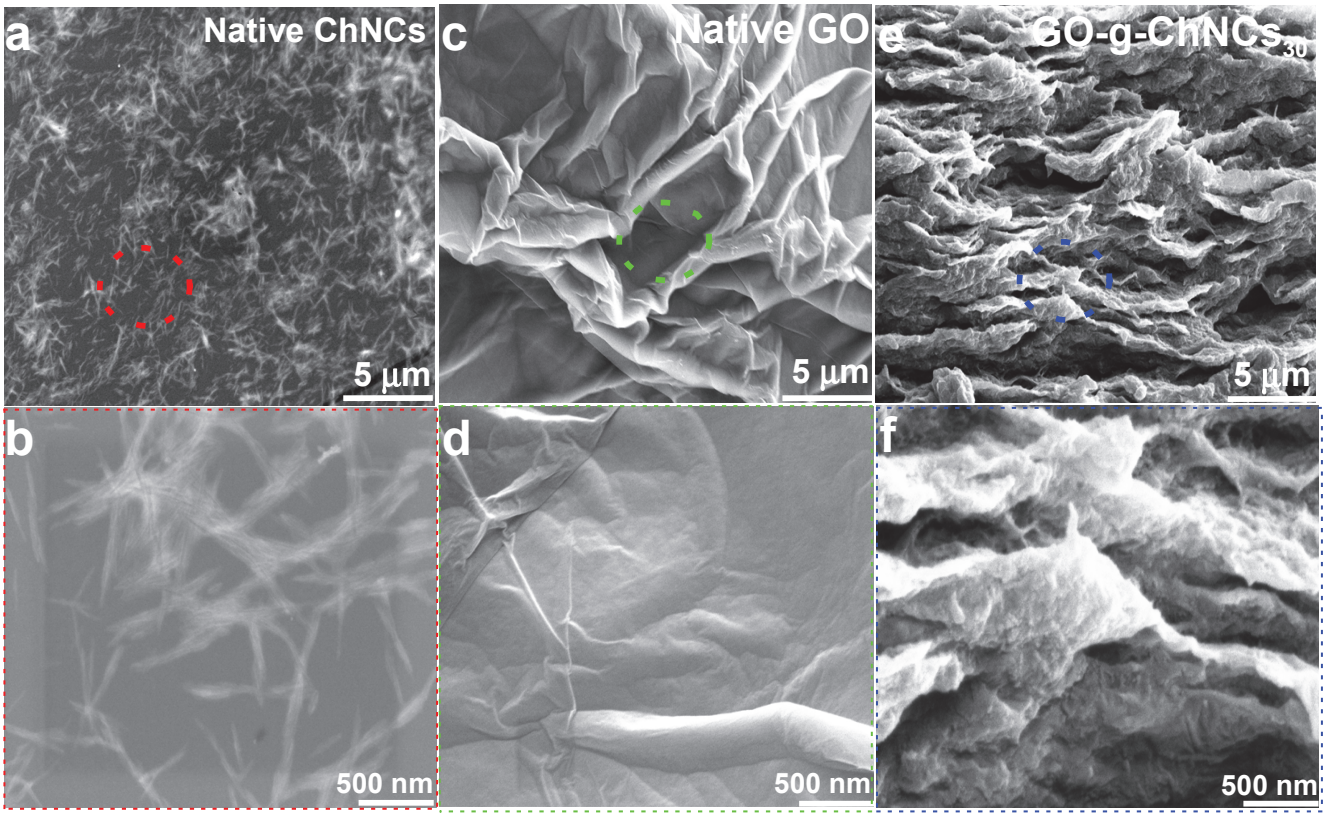

Figure 3. Representative SEM images of native ChNCs (**a**), the GO (**c**) and GO/$ChNCs_{30}$ (**e**) adduct after freeze-drying. Dashed areas are magnified in figures below (**b**,**d**,**f**).

From the XPS analysis of the adduct composition (Figure 4), it follows that only C, O, and N were detected from the broad spectra of oxidized carbon fibers (OCF). OCF C 1 showed different binding energies of –C=C, –C–C, –C–OH, –C–O, –COO, at 284.26 284.96, 286.03, 286.9 and 288.2. Ev. From the C 1s and O 1s data, we can confirm that due to the nitric acid used to oxidize the carbon fiber, a partial nitration reaction was observed in N 1 (Figure 4). The broad XPS spectrum of native ChNCs showed expected signals for

C, O, and N. The C 1s of native ChNCs showed that the binding energy of 289.33 and 290.62 belongs to the carbonate region. The C 1s spectrum showed the bonds of carbon with nitrogen. The binding energies of 289.33 and 290.62 belong to the region of carbonyl groups coordinated with water molecules. The binding energy at 288.18 relates to amide bonds, and 286.32 is connected to C–N bonds (primary amino groups). The O 1s of native ChNCs were observed only at 532.9 and 531.5 eV in relation to the –C–O and –C=O groups in the chemical structure. Partially deacetylated ChNCs show two binding energies at 400.01 and 402.14 that correspond to amide (N–C=O) and positively charged nitrogen (Figure 4).

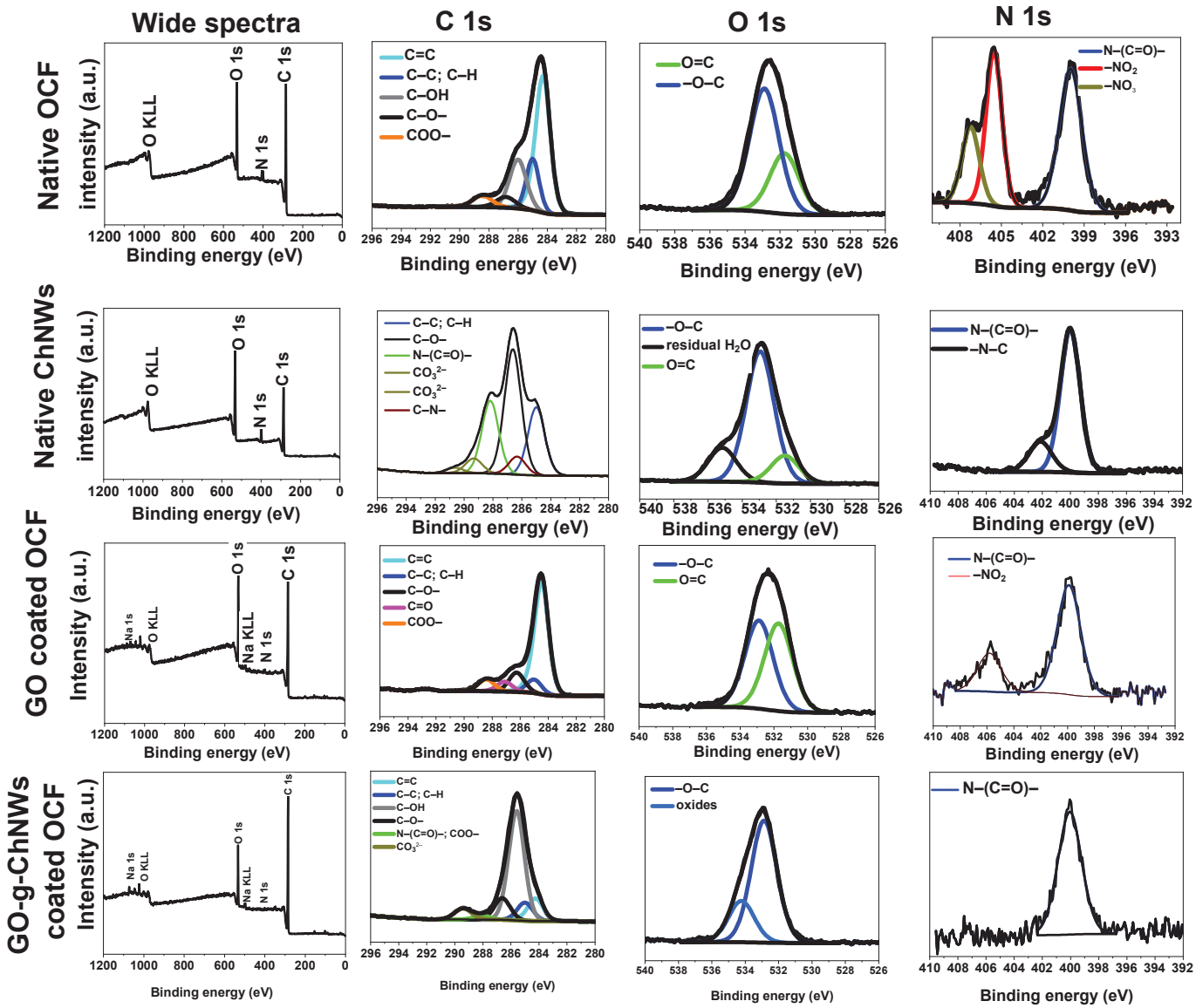

Figure 4. XPS of OCF, ChNCs, and OCF coated by the GO and GO/ChNCs$_{30}$ adduct The EPD conditions were as follows: adduct concentration at 5 mg/mL, time of 10 min, voltage at 5 V, pH 3.5 and temperature at 23 °C.

From the wide spectrum of native graphene oxide, as shown in the figure above, only O and C are observed. C 1s of GO@OCF show carbon in the hybridization state sp3 (285 eV) and sp2 (284.5 eV). The peak of carbon in the sp2 state indicates a strong asymmetry, as expected, with a high proportion of C–O bonds. The different binding energies at 284.5, 286.67, 288.24, and 285 eV correspond to C=C, C–O, COOH, and C–C/C–H, respectively.

Oxidized carbon fibers coated with native graphene oxide (GO@OCF) are shown in Figure 4. As expected from the wide-spectrum data, C, O, and Na peaks were observed. The presence of a sodium hydroxide peak was due to the neutralization of OCF with NaOH after the oxidation step, which resulted in a salt form (–COONa). The C 1s spectrum shows carbon in two hybridization states as in the native GO spectrum. However, the contribution of C–O bonds decreases in comparison to that of pure GO. The spectrum contains the bonds C=O and ester groups. A new ester group appeared in the C 1s spectrum of GO@OCF at 288.42 eV, belonging to carbon in the ester groups, due to the esterification reaction between GO and OCF. The intensity of C-O groups of GO@OCF was decreased compared to native GO due to the interaction between OCF and GO.

From the wide spectrum of GO/ChNC adduct@OCF, only C, O, and N peaks appeared, and these peaks were peaks for Na as well. C 1s of GO/ChNC adduct@OCF show different binding energies at 284.24, 285, 285.6, 286.62, 288.07, 289.41 corresponding to C=C, C–C/CH, C–OH, C–O–, N–C=O–/COO– and carbon binding with water molecules. From the C 1s spectrum, we could conclude that an esterification/amidation reaction could occur between the functional group of the GO/ChNC adduct and groups of OCF. From the N 1s spectrum of the GO/ChNC adduct@OCF, only the N–C=O peak appeared, and no C–N peak appeared for free amino groups of partially deacetylated ChNCs. From both C 1 and O 1 of GO/ChNC adduct@OCF, both esterification and amidation reactions could occur between the GO/ChNC adduct and OCF (Figure 4). Unfortunately, the high complexity of the whole system [46] did not allow for the precise calculation of the GO/ChNC ratio. To conclude, both XPS and FTIR indicated interactions/bonding between components in the GO/ChNC adduct.

3.2. Effect of the GO/ChNC Adduct Composition and EPD Variations on the Structure of the Coating

The systematic evaluation of the degree of ChNC/GO interactions/bonding on the OCF coating was combined with variations in the EPD conditions to obtain complete information about this process, which, up to now, has not been studied. Figures 5, S3 and S4 follow the marked effect of pH, voltage, and GO/ChNC adduct concentration on the homogeneity and thickness of the coating. Figure 5 shows the important effect of pH; at a lower pH, the OCF was coated with compact homogeneous layers using adducts of all DDAs (Figure 5a–c). At neutral pH, the compact layer of the adducts showed a small aggregation on the OCF surface, which was different for respective DDAs (Figure 5d–f). At pH 11, the thickness of the coating was small compared to pH 3.4, with high aggregation on the OCF surface, mainly for 5 and 30% DDA (Figure 5g–i).

The most homogeneous coating for the GO/$ChNC_{15}$ adduct at all pHs (Figure 5b,e,h) confirmed the effect of DDA on the structure of the adduct. This fact was also indirectly indicated by the rheology of the water suspensions as well; the differences in G' of the adducts with different DDAs can be observed (5, 30%, Figure S2b).

Due to the relatively large size of the adducts and the expected high charge density together with the related slower assembly/ordering, unlike the GO-g-polymer chain or polydopamine-coated GO, the best deposition occurred at a lower voltage [46]. As we can see, the lower applied voltage (5 V) led to more homogeneous and compact layers of the GO/ChNC adduct (Figure S3) compared to the highly applied voltage (20 V). Figure S4 shows the effect of adduct concentration on the homogeneity of the OCF coating. As we can see, at lower concentrations, the coating had a heterogeneous distribution on the fiber surface up to (1 mg/mL). A more compact and homogeneous layer was obtained on the OCF surface at higher adduct concentrations.

From Figure 6, it follows that the effect of DDA and, thus, the structure, size, and charge density of the adduct strongly influenced the thickness of the EPD layer; its growing tendency with DDA can be observed, marking its most considerable thickness for 30% DDA with about 120–160 nm.

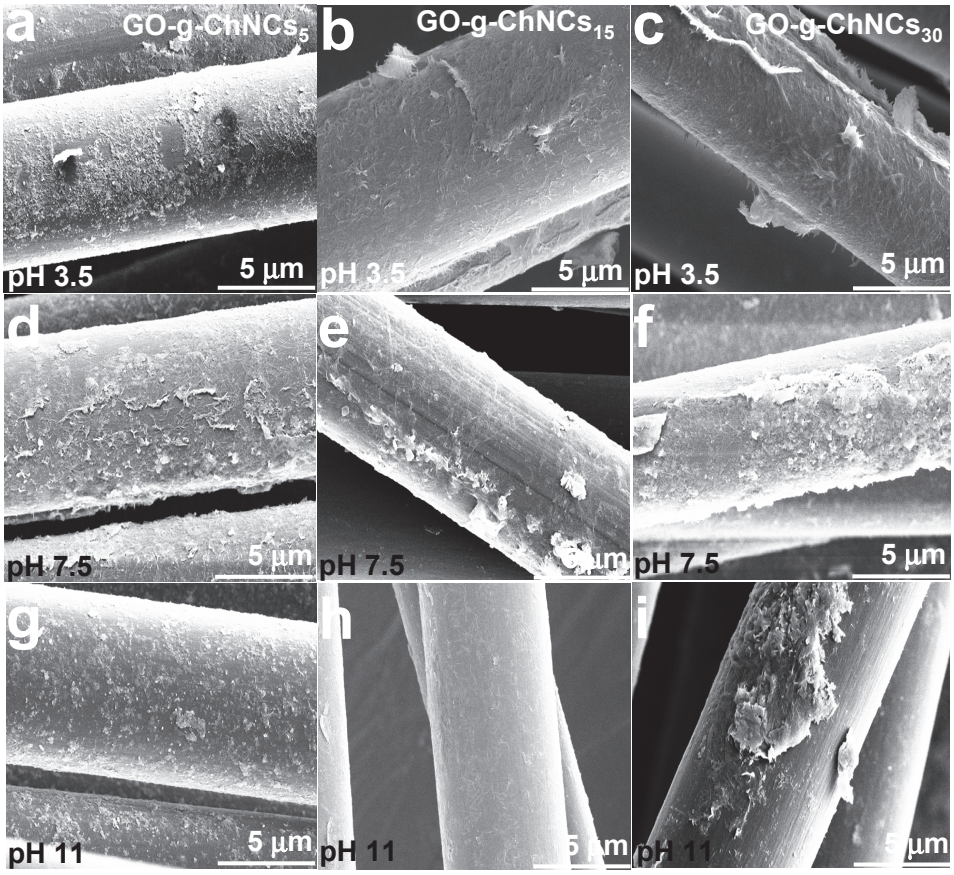

Figure 5. SEM images showing the effects of pH and DDA percentages on the OCF coating efficiency using the GO/ChNC adduct. EPD proceeded at 23 °C with voltage at 5 V; the adduct concentration was 5 mg/mL, and coating time was 20 min.

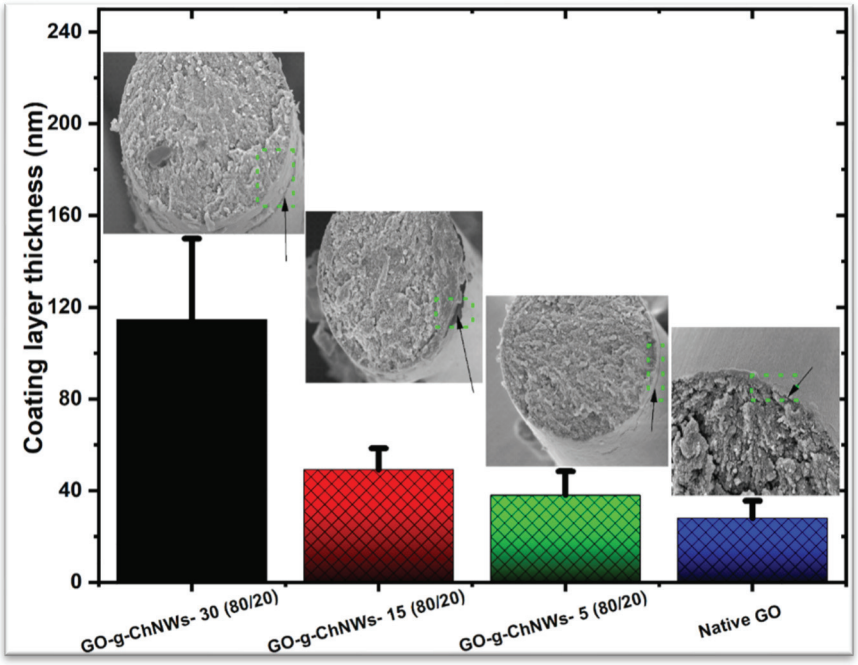

Figure 6. Effects of the DDA of ChNCs on the coating thickness of the GO/ChNC adduct with an 80/20 composition. The EPD conditions were an adduct concentration of 5 mg/mL, time of 10 min, voltage of 5 V, pH 3.5, and temperature of 23 °C.

3.3. Short-Beam Testing (SBS)

Based on the systematic evaluation of EPD conditions on the homogeneity and composition of the coating (see above), we used fibers with the most 'compact' coating, i.e., prepared using the GO/ChNC adduct with a concentration of 5 mg/mL, pH ~3.5, voltage of 5 V, and coating time of 10 min for the preparation of the composite short-beam samples. The GO/ChNC ratios were 95/5, 90/10, 80/20, and 50/50, which were used with different DDAs of ChNCs (5, 15, 30%), respectively. The thickness of the coating ranged between 40 and 120 nm (Figure 6); due to the very low effect of the coating thickness in this range on composite parameters, indicated both experimentally and by FEA modeling in our previous paper [46], we did not focus on achieving an identical coating size for the respective adducts in this study. Here, it is important to note that the testing of beam samples made from a 'bundle' of fibers, unlike those from plies (laminate samples), has low relevancy to interlaminar shear strength (ILSS). The main purpose of this test was to evaluate the possible unfavorable effect of the coating on basic mechanical properties, which is a limiting factor in most existing solutions using tough coatings [34,53]. At the same time, the first results of a laminate plate made from 30 layers of carbon cloth with an interlayer based on the EPD of (relatively rigid) polydopamine PDA-coated GO indicate a positive effect on delamination resistance. Therefore, we can expect a similar performance for the system studied.

Figure 7 and Table 2 show the results of the SBS testing following the relatively marked effect of DDA of ChNC on the modulus with a strong dependence on the GO/ChNCs ratio, which is reflected in various trends for each composition. In the case of nacre-like composition, that is, 95/5 and 90/10 GO/ChNCs ratios, we can see the most marked modulus increase against the samples with GO-coated fibers. Therefore, with all DDAs, we can undoubtedly expect the formation of favorable brick-and-mortar structures, as reported by others in the case of planar samples (films) [1,3,4,6]. Interestingly, in the case of the 95/5 composition, the modulus decreased with DDA, whereas with the 90/10 ratio, it slightly increased.

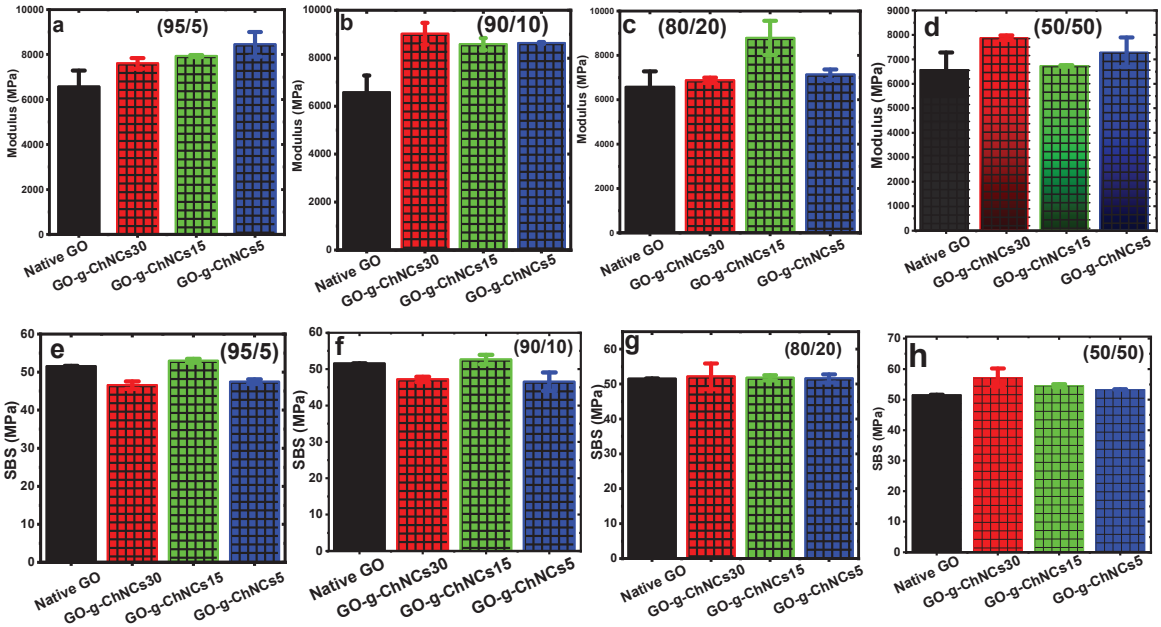

Figure 7. Three-point short-beam bending test of composite samples. (**a**–**d**) Show the effect of CF coating with GO-g-ChNCs with different GO/ChNC ratios on the modulus, (**e**–**h**) show the analogous effect on SBS (numbers in brackets inside of charts indicate the GO/ChNCs ratio in the GO-g-ChNCs-based coating of CF). Coating conditions: pH ~3.5, voltage 5 V, time 10 min, adduct content of 5 mg/mL.

Table 2. Effect of coating composition on modulus and SBS strength of composite bars. Coating conditions: pH ~3.5, voltage 5 V, time 10 min, adduct content of of 5 mg/mL.

Adduct	GO (% wt)	ChNCs (% wt)	DDA * (%)	Modulus (MPa)	SBS (MPa)
GO	100	-	-	6640 ± 950	51.8 ± 1.1
GO/ChNCs$_5$	95	5	5	8460 ± 450	47.8 ± 1.5
GO/ChNCs$_{15}$	95	5	15	8000 ± 50	52.2 ± 1.5
GO/ChNCs$_{30}$	95	5	30	7750 ± 250	47.4 ± 2.0
GO/ChNCs$_5$	90	10	5	8490 ± 120	46.7 ± 4.0
GO/ChNCs$_{15}$	90	10	15	8400 ± 240	52.4 ± 2.5
GO/ChNCs$_{30}$	90	10	30	9100 ± 460	47.5 ± 1.5
GO/ChNCs$_5$	80	20	5	7100 ± 150	51.8 ± 1.5
GO/ChNCs$_{15}$	80	20	15	8930 ± 850	51.9 ± 1.0
GO/ChNCs$_{30}$	80	20	30	6900 ± 100	52.1 ± 4.5
GO/ChNCs$_5$	50	50	5	7250 ± 550	53.2 ± 1.0
GO/ChNCs$_{15}$	50	50	15	6750 ± 100	54.9 ± 1.0
GO/ChNCs$_{30}$	50	50	30	7890 ± 120	57.2 ± 3.0

* degree of ChNCs deacetylation.

For 80/20 and 50/50 GO/ChNC ratios, we can see more marked modulus variations with DDA, that is, the maximal value (exceeding GO) at 15% DDA and 30% DDA, respectively. Especially in the case of 50/50 adducts, the relatively higher content of ChNC amines at the interface with a higher potential for bonding with the matrix may be of importance. This is confirmed by the most marked matrix layer attached to the OCF, which is also coated with the GO/ChNCs$_{30}$ 90/10 adduct (Figure 8). At the same time, the effect of DDA on the short-beam strength (SBS) was less pronounced, with values comparable to those of the GO coating. Slightly higher values against GO were found for 95/5 and 90/10 interlayers containing ChNCs with 15% DDA. This also indicates a similar brick-and-mortar structure. Figure 6 further follows practically no effect of DDA for an 80/20 ratio, while a slight enhancement with 30% DDA for a 50/50 ratio may correspond to the highest potential for bonding with the epoxy matrix (Figure 7). The short-beam testing results indicate that all coating types do not cause an unbearable decrease in composite parameters, so they can be used for further research focused on revealing their effect on delamination resistance using planar multilayered laminates.

Finally, from the observation of fracture surfaces of composites with OCF coated with GO and GO/ChNC 90/10 adducts (Figure 8), there follows practically no matrix presented on the surface of GO-coated OCF whereas the relatively marked matrix layer on GO/ChNC adducts with coated OCF indicate the expected bonding of ChNW amines to the epoxy matrix. An increase in the size and thickness of the attached matrix fragments with ChNC with higher DDAs and, thus, the content of primary amines corresponds to the higher reactivity of primary amines with epoxy groups of the epoxy resin in comparison to secondary amines [54]. At the same time, practically no correspondence of this bonding to SBS strength indicated that the effect of the EPD coating on strength dominated.

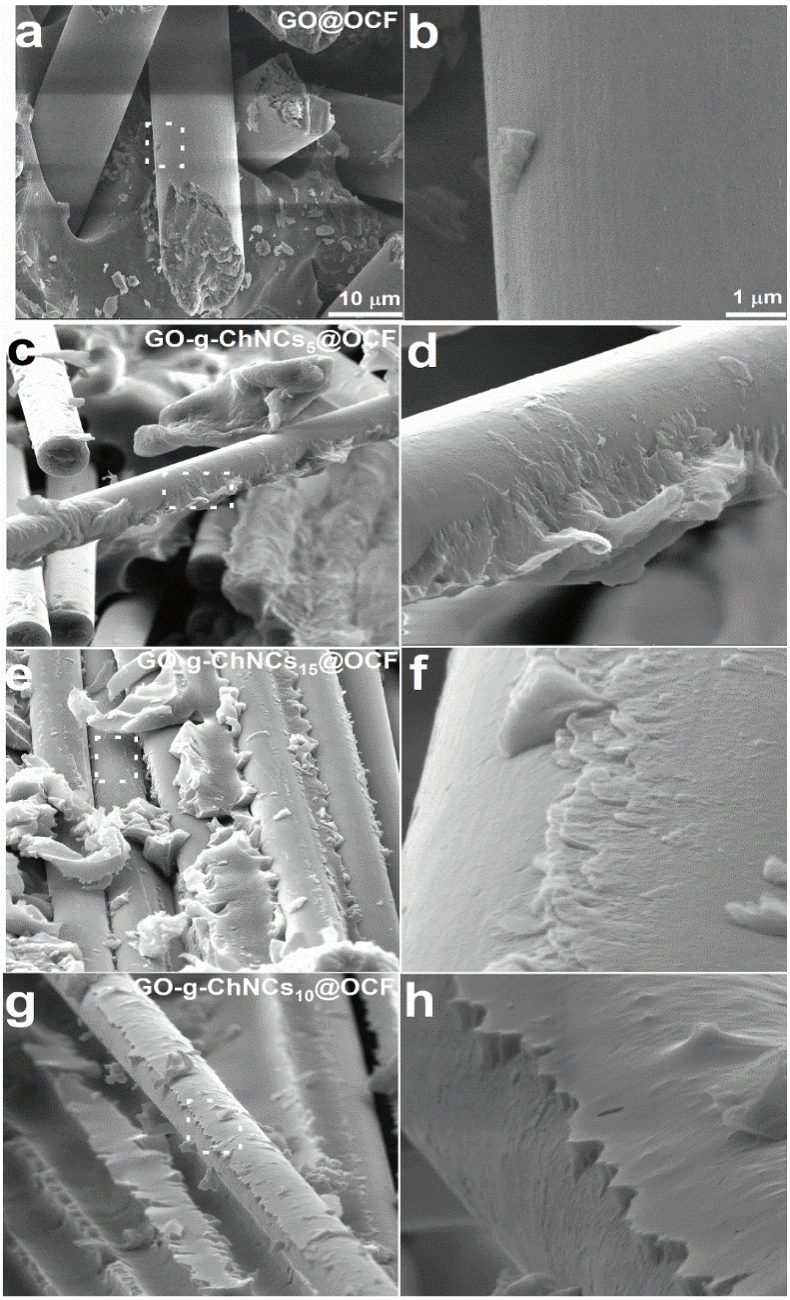

Figure 8. SEM of fractured composite with OCF coated with native GO (**a**,**b**); the GO/ChNCs$_5$ adduct (**c**,**d**); GO/ChNCs$_{15}$ adduct (**e**,**f**) and GO/ChNCs$_{30}$ adduct (**g**,**h**). GO-ChNCs$_{30}$ (90/10 GO/ChNC ratio in all cases). The dashed areas are magnified in the figures in right.

4. Conclusions

Chitin nanocrystals (ChNCs) with different DDAs were prepared and used for the preparation of adducts with graphene oxide (GO) at different GO/ChNCs ratios. Their structure was confirmed using different techniques, such as FTIR, XRD, XPS, and DLS. The results indicate that the formation of the GO/ChNC adduct enables an effective electrophoretic coating of the OCFs to form a rigid, tough interface. We have revealed crucial parameters controlling the EPD and homogeneity of the coatings (pH, concentration, voltage) with comparable mechanical parameters, which were also confirmed by the negligible effect of such an interface on the SBS and the modulus of composites. We expect that especially coating with a nacre-like composition, i.e., using the GO/ChNC adduct with a 95/5 and 90/10 ratio, can provide a rigid, tough interface with fair potential to increase

delamination resistance; moreover, the low effect of coating composition on mechanical properties of the composite allows its optimization in the case of laminates.

Supplementary Materials: The following supporting information can be downloaded at: https://www.mdpi.com/article/10.3390/jcs8050163/s1, Figure S1: (a) FTIR and (b) XRD of ChNCs with different degree of deacetylation; Figure S2: Rheological characterization of water suspensions (5 mg/mL) of single components and adducts; Figure S3: Effects of voltage and DDA percentages on OCF coating efficiency Conditions: 10 min; 5 mg; pH 3.5, rt.; Figure S4: Effect of concentration of GO/$ChNCs_{30}$ adduct suspension on OCF coating structure Conditions: 10 min, 5 V, DDA 30%, pH 3.5, different concentration of GO-g-ChNCs (0.01 to 15 mg/mL)., rt.

Author Contributions: Conceptualization, I.K.; Formal analysis, A.M.A.-M. and L.K. (Ludmila Kaprálková); Investigation, A.M.A.-M., R.M.A.-R., L.K. (Lukáš Kalina), V.V., L.K. (Ludmila Kaprálková) and P.N.; Writing—original draft, I.K. and J.J.; Supervision, J.J.; Funding acquisition, I.K. All authors have read and agreed to the published version of the manuscript.

Funding: This work was funded by the Ministry of Education Youth and Sports of the Czech Republic (Grant LUAUS 23004).

Data Availability Statement: The data presented in this study are available in this article.

Conflicts of Interest: The authors declare no conflict of interest.

References

1. Zhang, Y.; Gong, S.; Zhang, Q.; Ming, P.; Wan, S.; Peng, J.; Jiang, L.; Cheng, Q. Graphene-based artificial nacre nanocomposites. *Chem. Soc. Rev.* **2016**, *45*, 2378–2395. [CrossRef] [PubMed]
2. Bonderer, L.J.; Studart, A.R.; Gauckler, L.J. Bioinspired Design and Assembly of Platelet Reinforced Polymer Films. *Science* **2008**, *319*, 1069–1073. [CrossRef]
3. Wegst, U.G.K.; Bai, H.; Saiz, E.; Tomsia, A.P.; Ritchie, R.O. Bioinspired structural materials. *Nat. Mater.* **2015**, *14*, 23–36. [CrossRef] [PubMed]
4. Wan, S.; Peng, J.; Li, Y.; Hu, H.; Jiang, L.; Cheng, Q. Use of Synergistic Interactions to Fabricate Strong, Tough, and Conductive Artificial Nacre Based on Graphene Oxide and Chitosan. *ACS Nano* **2015**, *9*, 9830–9836. [CrossRef]
5. Wang, R.Z.; Suo, Z.; Evans, A.G.; Yao, N.; Aksay, I.A. Deformation mechanisms in nacre. *J. Mater. Res.* **2001**, *16*, 2485–2493. [CrossRef]
6. Chen, K.; Tang, X.; Yue, Y.; Zhao, H.; Guo, L. Strong and Tough Layered Nanocomposites with Buried Interfaces. *ACS Nano* **2016**, *10*, 4816–4827. [CrossRef] [PubMed]
7. Duan, J.; Gong, S.; Gao, Y.; Xie, X.; Jiang, L.; Cheng, Q. Bioinspired Ternary Artificial Nacre Nanocomposites Based on Reduced Graphene Oxide and Nanofibrillar Cellulose. *ACS Appl. Mater. Interfaces* **2016**, *8*, 10545–10550. [CrossRef]
8. Yao, K.; Huang, S.; Tang, H.; Xu, Y.; Buntkowsky, G.; Berglund, L.A.; Zhou, Q. Bioinspired Interface Engineering for Moisture Resistance in Nacre-Mimetic Cellulose Nanofibrils/Clay Nanocomposites. *ACS Appl. Mater. Interfaces* **2017**, *9*, 20169–20178. [CrossRef]
9. Li, M.; Wang, X.; Zhao, R.; Miao, Y.; Liu, Z. A novel graphene-based micro/nano architecture with high strength and conductivity inspired by multiple creatures. *Sci. Rep.* **2021**, *11*, 1387. [CrossRef]
10. Xiong, R.; Kim, H.S.; Zhang, L.; Korolovych, V.F.; Zhang, S.; Yingling, Y.G.; Tsukruk, V.V. Wrapping Nanocellulose Nets around Graphene Oxide Sheets. *Angew. Chem. Int. Ed.* **2018**, *57*, 8508–8513. [CrossRef]
11. Liu, Y.; Yu, S.-H.; Bergström, L. Transparent and Flexible Nacre-Like Hybrid Films of Aminoclays and Carboxylated Cellulose Nanofibrils. *Adv. Funct. Mater.* **2018**, *28*, 1703277. [CrossRef]
12. Xu, D.; Wang, S.; Berglund, L.A.; Zhou, Q. Surface Charges Control the Structure and Properties of Layered Nanocomposite of Cellulose Nanofibrils and Clay Platelets. *ACS Appl. Mater. Interfaces* **2021**, *13*, 4463–4472. [CrossRef] [PubMed]
13. Laaksonen, P.; Walther, A.; Malho, J.-M.; Kainlauri, M.; Ikkala, O.; Linder, M.B. Genetic Engineering of Biomimetic Nanocomposites: Diblock Proteins, Graphene, and Nanofibrillated Cellulose. *Angew. Chem. Int. Ed.* **2011**, *50*, 8688–8691. [CrossRef] [PubMed]
14. Huang, L.; Li, C.; Yuan, W.; Shi, G. Strong composite films with layered structures prepared by casting silk fibroin–graphene oxide hydrogels. *Nanoscale* **2013**, *5*, 3780–3786. [CrossRef] [PubMed]
15. Li, M.; Xiong, P.; Mo, M.; Cheng, Y.; Zheng, Y. Electrophoretic-deposited novel ternary silk fibroin/graphene oxide/hydroxyapatite nanocomposite coatings on titanium substrate for orthopedic applications. *Front. Mater. Sci.* **2016**, *10*, 270–280. [CrossRef]
16. Zhang, W.; Zheng, K.; Ren, J.; Fan, Y.; Ling, S. Strong, ductile and lightweight bionanocomposites constructed by bioinspired hierarchical assembly. *Compos. Commun.* **2020**, *17*, 97–103. [CrossRef]

17. Tran, T.H.; Nguyen, H.-L.; Hwang, D.S.; Lee, J.Y.; Cha, H.G.; Koo, J.M.; Hwang, S.Y.; Park, J.; Oh, D.X. Five different chitin nanomaterials from identical source with different advantageous functions and performances. *Carbohydr. Polym.* **2019**, *205*, 392–400. [CrossRef] [PubMed]
18. Abdelrahman, R.; Abdel-Mohsen, A.; Zboncak, M.; Frankova, J.; Lepcio, P.; Kobera, L.; Steinhart, M.; Pavlinak, D.; Spotaz, Z.; Sklenářévá, R.; et al. Hyaluronan biofilms reinforced with partially deacetylated chitin nanowhiskers: Extraction, fabrication, in-vitro and antibacterial properties of advanced nanocomposites. *Carbohydr. Polym.* **2020**, *235*, 115951. [CrossRef] [PubMed]
19. Kelnar, I.; Kovářová, J.; Tishchenko, G.; Kaprálková, L.; Pavlová, E.; Carezzi, F.; Morganti, P. Chitosan/Chitin nanowhiskers composites: Effect of plasticisers on the mechanical behaviour. *J. Polym. Res.* **2015**, *22*, 5. [CrossRef]
20. Uddin, A.J.; Fujie, M.; Sembo, S.; Gotoh, Y. Outstanding reinforcing effect of highly oriented chitin whiskers in PVA nanocomposites. *Carbohydr. Polym.* **2012**, *87*, 799–805. [CrossRef]
21. Wang, C.; Li, J.; Sun, S.; Li, X.; Zhao, F.; Jiang, B.; Huang, Y. Electrophoretic deposition of graphene oxide on continuous carbon fibers for reinforcement of both tensile and interfacial strength. *Compos. Sci. Technol.* **2016**, *135*, 46–53. [CrossRef]
22. Jiang, J.; Yao, X.; Xu, C.; Su, Y.; Zhou, L.; Deng, C. Influence of electrochemical oxidation of carbon fiber on the mechanical properties of carbon fiber/graphene oxide/epoxy composites. *Compos. Part A Appl. Sci. Manuf.* **2017**, *95*, 248–256. [CrossRef]
23. Wang, C.; Li, Y.; Tong, L.; Song, Q.; Li, K.; Li, J.; Peng, Q.; He, X.; Wang, R.; Jiao, W.; et al. The role of grafting force and surface wettability in interfacial enhancement of carbon nanotube/carbon fiber hierarchical composites. *Carbon* **2014**, *69*, 239–246. [CrossRef]
24. Zhang, Q.; Jiang, D.; Liu, L.; Huang, Y.; Long, J.; Wu, G.; Wu, Z.; Umar, A.; Guo, J.; Zhang, X.; et al. Effects of Graphene Oxide Modified Sizing Agents on Interfacial Properties of Carbon Fibers/Epoxy Composites. *J. Nanosci. Nanotechnol.* **2015**, *15*, 9807–9811. [CrossRef] [PubMed]
25. Zhang, R.L.; Gao, B.; Ma, Q.H.; Zhang, J.; Cui, H.Z.; Liu, L. Directly grafting graphene oxide onto carbon fiber and the effect on the mechanical properties of carbon fiber composites. *Mater. Des.* **2016**, *93*, 364–369. [CrossRef]
26. Qian, H.; Greenhalgh, E.S.; Shaffer, M.S.P.; Bismarck, A. Carbon nanotube-based hierarchical composites: A review. *J. Mater. Chem.* **2010**, *20*, 4751–4762. [CrossRef]
27. Li, Y.; Peng, Q.; He, X.; Hu, P.; Wang, C.; Shang, Y.; Wang, R.; Jiao, W.; Lv, H. Synthesis and characterization of a new hierarchical reinforcement by chemically grafting graphene oxide onto carbon fibers. *J. Mater. Chem.* **2012**, *22*, 18748–18752. [CrossRef]
28. Asadi, A.; Miller, M.; Moon, R.J.; Kalaitzidou, K. Improving the interfacial and mechanical properties of short glass fiber/epoxy composites by coating the glass fibers with cellulose nanocrystals. *Express Polym. Lett.* **2016**, *10*, 587–597. [CrossRef]
29. Uribe, B.E.B.; Chiromito, E.M.S.; Carvalho, A.J.F.; Tarpani, J.R. Low-cost, environmentally friendly route for producing CFRP laminates with microfibrillated cellulose interphase. *Express Polym. Lett.* **2017**, *11*, 47–59. [CrossRef]
30. Reale Batista, M.D.; Drzal, L.T. Carbon fiber/epoxy matrix composite interphases modified with cellulose nanocrystals. *Compos. Sci. Technol.* **2018**, *164*, 274–281. [CrossRef]
31. Lee, J.U.; Park, B.; Kim, B.-S.; Bae, D.-R.; Lee, W. Electrophoretic deposition of aramid nanofibers on carbon fibers for highly enhanced interfacial adhesion at low content. *Compos. Part A Appl. Sci. Manuf.* **2016**, *84*, 482–489. [CrossRef]
32. Zhang, B.; Lian, T.; Shao, X.; Tian, M.; Ning, N.; Zhang, L.; Wang, W. Surface Coating of Aramid Fiber by a Graphene/Aramid Nanofiber Hybrid Material to Enhance Interfacial Adhesion with Rubber Matrix. *Ind. Eng. Chem. Res.* **2021**, *60*, 2472–2480. [CrossRef]
33. Wisnom, M.R. The role of delamination in failure of fibre-reinforced composites. *Philos. Trans. R. Soc. A Math. Phys. Eng. Sci.* **2012**, *370*, 1850–1870. [CrossRef] [PubMed]
34. Gerard, J.-F. Characterization and role of an elastomeric interphase on carbon fibers reinforcing an epoxy matrix. *Polym. Eng. Sci.* **1988**, *28*, 568–577. [CrossRef]
35. Agarwal, B.D.; Bansal, R.K. Effect of an interfacial layer on the properties of fibrous composites: A theoretical analysis. *J. Fiber Sci. Technol.* **1979**, *12*, 149–158. [CrossRef]
36. Lee, S.; Ryu, S. Theoretical study of the effective modulus of a composite considering the orientation distribution of the fillers and the weakened interface. *Eur. J. Mech. A/Solids* **2018**, *72*, 79–89. [CrossRef]
37. Kausar, A.; Siddiq, M. Epoxy composites reinforced with multi-walled carbon nanotube/poly(ethylene glycol)methylether-coated aramid fiber. *J. Polym. Eng.* **2016**, *36*, 465–471. [CrossRef]
38. Yao, X.; Gao, X.; Jiang, J.; Xu, C.; Deng, C.; Wang, J. Comparison of carbon nanotubes and graphene oxide coated carbon fiber for improving the interfacial properties of carbon fiber/epoxy composites. *Compos. B Eng.* **2018**, *132*, 170–177. [CrossRef]
39. Wang, P.; Yang, J.; Liu, W.; Tang, X.-Z.; Zhao, K.; Lu, X.; Xu, S. Tunable crack propagation behavior in carbon fiber reinforced plastic laminates with polydopamine and graphene oxide treated fibers. *Mater. Des.* **2017**, *113*, 68–75. [CrossRef]
40. De Luca, F.; Sernicola, G.; Shaffer, M.S.P.; Bismarck, A. "Brick-and-Mortar" Nanostructured Interphase for Glass-Fiber-Reinforced Polymer Composites. *ACS Appl. Mater. Interfaces* **2018**, *10*, 7352–7361. [CrossRef]
41. Yang, X.; Du, H.; Li, S.; Wang, Z.; Shao, L. Codepositing Mussel-Inspired Nanohybrids onto One-Dimensional Fibers under "Green" Conditions for Significantly Enhanced Surface/Interfacial Properties. *ACS Sustain. Chem. Eng.* **2018**, *6*, 4412–4420. [CrossRef]
42. Jin, L.; Zhang, M.; Shang, L.; Liu, L.; Li, M.; Ao, Y. A nature-inspired interface design strategy of carbon fiber composites by growing brick-and-mortar structure on carbon fiber. *Compos. Sci. Technol.* **2020**, *200*, 108382. [CrossRef]

43. Wang, J.; Zhou, S.; Huang, J.; Zhao, G.; Liu, Y. Interfacial modification of basalt fiber filling composites with graphene oxide and polydopamine for enhanced mechanical and tribological properties. *RSC Adv.* **2018**, *8*, 12222–12231. [CrossRef]
44. Marcano, D.C.; Kosynkin, D.V.; Berlin, J.M.; Sinitskii, A.; Sun, Z.; Slesarev, A.; Alemany, L.B.; Lu, W.; Tour, J.M. Improved Synthesis of Graphene Oxide. *ACS Nano* **2010**, *4*, 4806–4814. [CrossRef]
45. Kelnar, I.; Kaprálková, L.; Němeček, P.; Dybal, J.; Abdel-Rahman, R.M.; Vyroubalová, M.; Nevoralová, M.; Abdel-Mohsen, A.M. The Effects of the Deacetylation of Chitin Nanowhiskers on the Performance of PCL/PLA Bio-Nanocomposites. *Polymers* **2023**, *15*, 3071. [CrossRef]
46. Kelnar, I.; Kaprálková, L.; Němeček, P.; Janata, M.; Dybal, J.; Svoboda, J.; Padovec, Z.; Abdel-Mohsen, A. Nature-mimicking rigid tough interface in fibrous composites: Effect of polymer/GO combination. *Mater. Today Commun.* **2022**, *33*, 104883. [CrossRef]
47. Wu, Q.; Yang, X.; Ye, Z.; Deng, H.; Zhu, J. Dopamine-dependent graphene oxide modification and its effects on interfacial adhesion of carbon fiber composites. *Surf. Interfaces* **2022**, *31*, 102086. [CrossRef]
48. Abdel-Mohsen, A.; Abdel-Rahman, R.; Kubena, I.; Kobera, L.; Spotz, Z.; Zboncak, M.; Prikryl, R.; Brus, J.; Jancar, J. Chitosan-glucan complex hollow fibers reinforced collagen wound dressing embedded with aloe vera. Part I: Preparation and characterization. *Carbohydr. Polym.* **2020**, *230*, 115708. [CrossRef]
49. Aly, A.S.; Abdel-Mohsen, A.M.; Hrdina, R.; Abou-Okeil, A. Preparation and Characterization of Polyethylene Glycol/Dimethyl Siloxane Adduct and Its Utilization as Finishing Agent for Cotton Fabric. *J. Nat. Fibers* **2011**, *8*, 176–188. [CrossRef]
50. Lin, Z.; Ma, Y.; Hu, C.; Zhang, Q. Molecular intercalated graphene oxide with finely controllable interlayer spacing for fast dye separation, Colloids Surf. A: Physicochem. *Eng. Asp.* **2023**, *677*, 132437. [CrossRef]
51. Dong, S.; Wang, B.; Liu, D.; He, M.; Chen, M.; Zhao, J.; Jin, W. Tailoring the interlayer channel structure of graphene oxide membrane with conjugated cationic dyes for butanol dehydration. *Sep. Purif. Technol.* **2023**, *325*, 124728. [CrossRef]
52. Xu, W.L.; Fang, C.; Zhou, F.; Song, Z.; Liu, Q.; Qiao, R.; Yu, M. Self-Assembly: A Facile Way of Forming Ultrathin, High-Performance Graphene Oxide Membranes for Water Purification. *Nano Lett.* **2017**, *17*, 2928–2933. [CrossRef]
53. Zheng, N.; Huang, Y.; Liu, H.-Y.; Gao, J.; Mai, Y.-W. Improvement of interlaminar fracture toughness in carbon fiber/epoxy composites with carbon nanotubes/polysulfone interleaves. *Compos. Sci. Technol.* **2017**, *140*, 8–15. [CrossRef]
54. Riccardi, C.C.; Adabbo, H.E.; Williams, R.J.J. Curing reaction of epoxy resins with diamines. *J. Appl. Polym. Sci.* **1984**, *29*, 2481–2492. [CrossRef]

Journal of
Composites Science

MDPI

Article

Determination of the In-Plane Shear Behavior of and Process Influence on Uncured Unidirectional CF/Epoxy Prepreg Using Digital Image Correlation Analysis

Hongfu Li [1,*,†], Haoxuan Zhang [2,†], Guangquan Yue [2], Boyu Guo [3] and Ying Wu [1,*]

[1] School of Materials Science and Engineering, University of Science and Technology Beijing, Beijing 100083, China
[2] Shanghai Collaborative Innovation Center of High Performance Fibers and Composites (Province-Ministry Joint), Center for Civil Aviation Composites, Donghua University, Shanghai 201620, China; zhx_dhu_2535@163.com (H.Z.); yueguangquan@dhu.edu.cn (G.Y.)
[3] Faculty of Engineering, Hong Kong Polytechnic University, Hong Kong, China; boyu08.guo@connect.polyu.hk
* Correspondence: lihongfu@ustb.edu.cn (H.L.); wuying@ustb.edu.cn (Y.W.)
† These authors contribute equally to this work.

Abstract: The investigation of the in-plane shear behavior of prepreg is crucial for understanding the generation of wrinkles of preforms in advanced composite manufacturing processes, such as automated fiber placement and thermoforming. Despite this significance, there is currently no standardized test method for characterizing uncured unidirectional (UD) prepreg. This paper introduces a ±45° off-axis tensile test designed to assess the in-plane shear behavior of UD carbon fiber-reinforced epoxy prepreg (CF/epoxy). Digital image correlation (DIC) was employed to quantitatively track the strains in three dimensions and the shear angle evolution during the stretching process. The influences of the temperature and stretching rate on the in-plane shear behavior of the prepreg were further investigated. The results reveal that four shear characteristic zones and wrinkling behaviors are clearly distinguished. The actual in-plane shear angle is significantly lower than the theoretical value due to fiber constraints from both the in-plane and out-of-plane aspects. When the off-axis tensile displacement (d) is less than 15.6 mm, the ±45° specimens primarily exhibit macroscale in-plane shear behavior, induced by interlaminar interface shear between the +45° ply and −45° ply at the mesoscale. The shear angle increases linearly with the d. However, when d > 15.6 mm, fiber squeezing and wrinkling begin to occur. When d > 29 mm, the in-plane shear disappears in the completely sheared zone (A). The reduction in the resin viscosity of the CF/epoxy prepreg caused by increased temperature is identified as the primary factor in lowering the in-plane shear force resistance, followed by the effect of the increasing resin curing degree. Higher shear rates can lead to a substantial increase in shear forces, eventually causing cracking failure in the prepreg. The findings demonstrate the feasibility of the test method for predicting and extracting uncured prepreg in-plane shear behaviors and the strain-rate and temperature dependency of the material response.

Keywords: thermoset composite; prepreg; in-plane shear; buckling and wrinkling; temperature; shear rate

1. Introduction

Prepreg has found extensive applications in advanced composite manufacturing processes, notably in the aerospace industry, including automated fiber placement (AFP) and thermoforming [1,2]. The quality of the prepreg layup in the preforms directly impacts the molding quality and performance of the final composite product [3,4]. However, a practical challenge that arises during the layup process is that the prepreg is typically forced to deform from a flat-sheet form into a three-dimensional shape with a complex structure.

To adapt to this transformation, prepreg undergoes significant in-plane shear, bending, twisting, yarn slippage, fiber redistribution, and deformations, resulting in changes in the microstructure of the preform in regions experiencing substantial shear deformations, such as R corners. Noticeable defects like wrinkles and buckling may even occur [3]. These factors directly determine the molding quality, performance, and delivery of the final composite components [5]. Overcoming these process defects is traditionally addressed through expensive and time-consuming trial-and-error experimental programs, significantly impacting the economics. Approximately 70% of the cost of manufacturing a composite part is typically incurred before producing a single defect-free part [6]. Therefore, predicting and evaluating the in-plane shear behavior of prepreg and the mechanisms of wrinkle formation are crucial for controlling the layup molding quality of the composite components.

For dry-fiber fabrics, woven prepreg, and cured composite materials, various in-plane shear testing and wrinkle formation prediction methods have been developed [7–16]. For instance, Mei et al. [17] analyzed the shear performance of fabric strips at 30°, 45°, and 60° tensile angles, demonstrating that a 45° off-axis tensile test accurately characterizes the in-plane shear performance of unidirectional fabric strips. Schirmaier et al. [18] investigated the spatial distribution of the in-plane strain components in non-crimp fabrics (NCFs) subjected to multi-axial deformation. Boisse and Harrison [19,20] modeled the mechanics of forming and wrinkling, as well as the mechanical behavior of engineering fabrics and textile composite reinforcements, utilizing the standard continuum mechanics principles of Cauchy.

However, these methods are not suitable for unidirectional (UD) prepregs. It is challenging to design a testing procedure that ensures a pure deformation mode, prevents samples from buckling out-of-plane, and maintains the integrity until the advanced deformation stages. Various attempts have been made to address the challenge, yet there is still no standardized test method for characterizing uncured UD prepregs under pure in-plane shear loading. The currently reported performance testing methods suitable for UD prepregs include off-axis tensile testing and torsion bar testing [21]. Scobbo [22] and Stanley [23] proposed fixtures comprising three parallel plates, in which the top and bottom plates were fixed, and the central plate could be dynamically pulled out. Consolidated unidirectional laminates were placed against both sides of the central plate, and dynamic shear deformation was induced by oscillating translational motion or by pulling out the plate at a constant velocity to achieve steady-state shear deformation. The test revealed certain material behavior trends, but the contribution of inter-ply sliding to the deformation mechanism was inconclusive. Larberg et al. [24] performed bias extension tests on various cross-plied UD prepregs at ± 45 degrees, showing that in-plane shear dominates only at small deformations. Wang et al. [21] developed a 10° off-axis tensile test, demonstrating its suitability for two commonly used aerospace-grade thermoset epoxy prepreg systems. Larberg et al. [25] verified that, in small deformations, in-plane shear plays a dominant role. Determining the cross-ply sequence and sample size is crucial for accurately characterizing the in-plane shear properties of prepregs. Groves [26,27] introduced a test setup with UD thermoplastic laminates between two parallel rheometer platens, later adapted by Hormann [28], for testing thermoset prepregs. In this test, shear deformation resulted from rotating one of the plates, and laminates, either off-center UD or cross-ply layups, were sheared under low-frequency oscillatory motion. Haanappel and Akkerman [29] proposed a torsion bar test using a rheometer and a standard torsion fixture. Thick unidirectional prismatic specimens from 80 plies of carbon fiber-reinforced polyetheretherketone (PEEK) thermoplastic prepreg were twisted by oscillating rotations in a controlled environment. The kinematics of the test were analytically derived to separate the shear and axial contributions to the applied load. Dörr et al. [30] later adopted the test for the intra-ply shear characterization of UD prepreg made from carbon fiber-reinforced polyamide 6 (PA6). It is evident that there remains a challenge in quantitatively analyzing the in-plane shear behavior, particularly for uncured thermoset prepregs.

Additionally, the inherent misalignment of fibers within UD prepreg, which directly induces fiber waviness during the shearing process, is further influenced by processing parameters such as the temperature, shear rate, and fiber tension during the composite preform molding process [31–33]. Shah et al. [34] studied the influence of temperature on the off-axis tensile shear performance of epoxy resin composites after curing. Yao et al. [35] examined the effect of temperature on the fatigue delamination behavior of fiber bridging in composite materials, discovering that higher temperatures weaken the interfacial adhesion, leading to faster fatigue delamination growth. Zhang et al. [36] experimentally investigated the impact of the processing parameters, including various shear rates and fiber tensions, on the shear behavior of two different CF/epoxy prepreg tapes. Pheysey [37] and colleagues studied the correlation between the strain rate and temperature in CF/PEEK composite materials, finding that the resin matrix exhibits significant temperature dependence during compression, with increased strain as the temperature rises. From the above, it is evident that characterizing the process-related parameters of uncured CF/epoxy prepreg and analyzing their impacts on the shear behavior is necessary.

In the characterization of in-plane shear deformation, it is essential to consider the adoption of reliable and effective methods. To compensate for the unidirectionality of the fibers in UD prepregs, the in-plane shear performance often requires cross-ply layups, introducing the influence of interlaminar shear [38]. Traditional methods involve attaching strain gauges to the prepregs, where the adhesive part can affect fiber slippage and deformation, leading to less precise characterizations of the in-plane shear deformation in the prepregs. Digital image correlation (DIC) technology is an image recognition technique used for qualitative and quantitative analyses of the surface deformation strain on objects. It does not introduce additional loads to the specimen and offers high accuracy; thus, it is being increasingly applied in strain measurements for composite materials [39]. Zhang et al. [36] utilized DIC to obtain full-field strains of specimens, investigating fiber realignment during shearing. Yu et al. [40] used DIC to analyze the impact of heat treatment on the strain distribution under bending loads in laminated panels. Wang et al. [21] employed DIC technology for measuring out-of-plane displacements in thin-film structures. Lan et al. [41] utilized DIC to study the shape recovery capability of shape-memory materials.

In this paper, addressing the in-plane shear and wrinkle prediction issues of uncured UD CF/epoxy resin prepreg, the $\pm 45^{\circ}$ off-axis tensile method and DIC strain characterization technology were employed to investigate the in-plane shear behaviors. Combining quantitative image analysis calculations, the evolution trend of the actual shear angle compared to the theoretical shear angle during the in-plane shear process was assessed. Simultaneously, the influence of the temperature and shear rate on the in-plane shear performance of the prepreg was examined. Through this comprehensive study, process recommendations are provided for the manufacturing and shaping of preforms, such as those used in the AFP and thermoforming processes of composite materials.

2. Materials and Methods

2.1. Materials

Unidirectional carbon fiber/epoxy resin prepreg, brand PD230211, with T300-grade carbon fibers and a resin mass fraction of 35% (areal density: 400 g/m^2), was procured from Avic Composites Co., LTD, Beijing, China. The prepreg was stored at -20 °C and required thawing for 12 h at 25 °C before use. Test specimens were cut using a cutting machine (model DCS-2506-24, purchased from Gerber Company) with a fiber angle of 45°. During cutting, strict measures were taken to ensure the accuracy of the prepreg fiber angle, minimizing its impact on the test results. The cutting method, dimensions, and physical appearance of the specimens are shown in Figure 1.

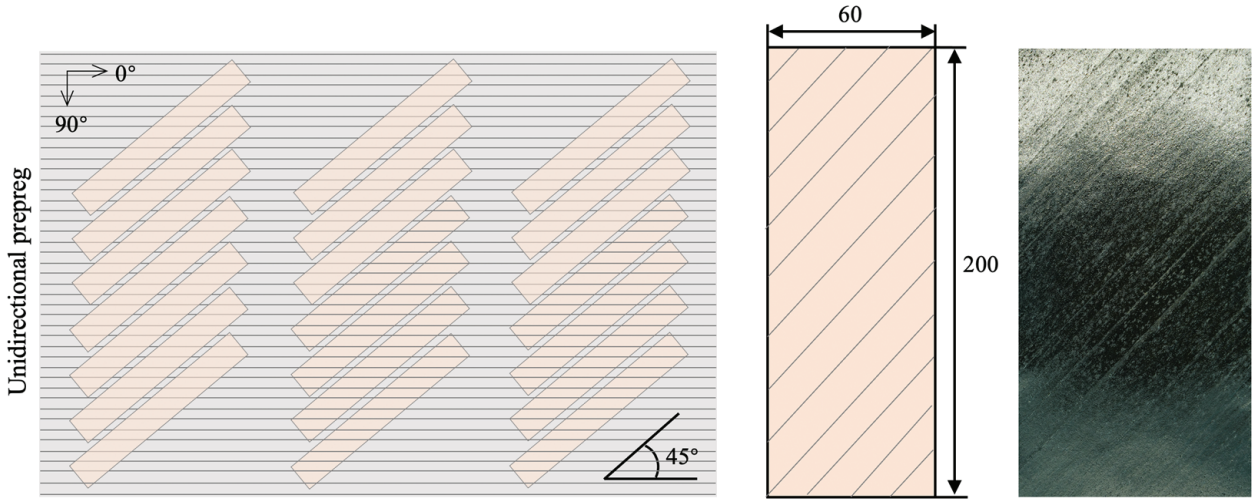

Figure 1. Unidirectional CF/epoxy prepreg used for in-plane interlaminar shear performance testing.

2.2. In-Plane Shear Testing of Prepreg

Sample preparation: The layering arrangement for the in-plane shear performance testing specimens of the prepreg was [45/−45/45/−45]. After layering, the specimens were placed in a vacuum bag and pre-pressed at 1 bar pressure. Subsequently, as shown in Figure 2a, the specimens were marked with lines using a 45° angle method and characterized into four zones (*A*, *B*, *C*, and *D*), with the identified feature points *H*1, *H*2, *W*1, and *W*2. The backsides of the specimens were marked with white marker lines along the fiber direction so that changes in the fiber angle during the tensile process could be recognized. The angle change of the 45° line passing through point *W*1 or *W*2 is often used for quantitatively evaluating the extent of the in-plane interlaminar shear behavior in prepreg. This angle change value is referred to as the shear angle (γ), and its relationship with the displacement (d) near the upper-grip end point ($H1$) is expressed by Formula (1):

$$\gamma = \frac{\pi}{2} - 2\arccos\left(\frac{\sqrt{2}}{2} + \frac{d}{\sqrt{2}(H-W)}\right) \quad (1)$$

where γ is the shear angle of the prepreg in zone A (i.e., the angle between the direction of the fiber deformation and the initial fiber direction); d is the displacement at point $H1$ or the beam displacement, which is the length of the specimen being stretched; H is the initial length of the specimen; and W is the initial width of the specimen.

In-plane shear test: We used the ±45° off-axis tensile test to characterize the macroscale in-plane shear behaviors of uncured UD prepreg specimens. During the off-axis tensile testing of the samples, a fixture consisting of two upper and two lower plates (Figure 2b) was first secured on a universal testing machine (ETM204C, Shenzhen WANCE Testing Equipment Co., Ltd., Shenzhen, China). The effective test gauge length of the test specimen was adjusted to 120 mm, ensuring that specimens within the same group had identical clamping forces. Next, thermocouples for temperature collection were installed on the off-axis tensile fixture near the ends of the prepreg, specifically at points *H*1 and *H*2. The environmental chamber (model FPYD-41AJW) was then used to provide four different test temperatures for the specimen: 30 °C, 80 °C, 120 °C, and 150 °C. After maintaining thermal equilibrium for 15 min and ensuring that the temperature difference between the two thermocouples was less than 1 °C (Figure 2c), the tensile test was initiated. The test was stopped when the tensile distance reached 35 mm. Simultaneously, the in-plane interlaminar shear behavior of the prepreg was compared under four different stretching rates: 1 mm/min, 2 mm/min, 10 mm/min, and 100 mm/min. Each group consisted of three repeated tests. Throughout the tensile testing process, a DIC system (FETECH 3200, Shenzhen Fetech Technology Co., Ltd., Shenzhen, China) was employed to capture the

deformation data of the standard specimen feature points in the width (V), length (U), and thickness (W) directions, producing two-dimensional strain maps.

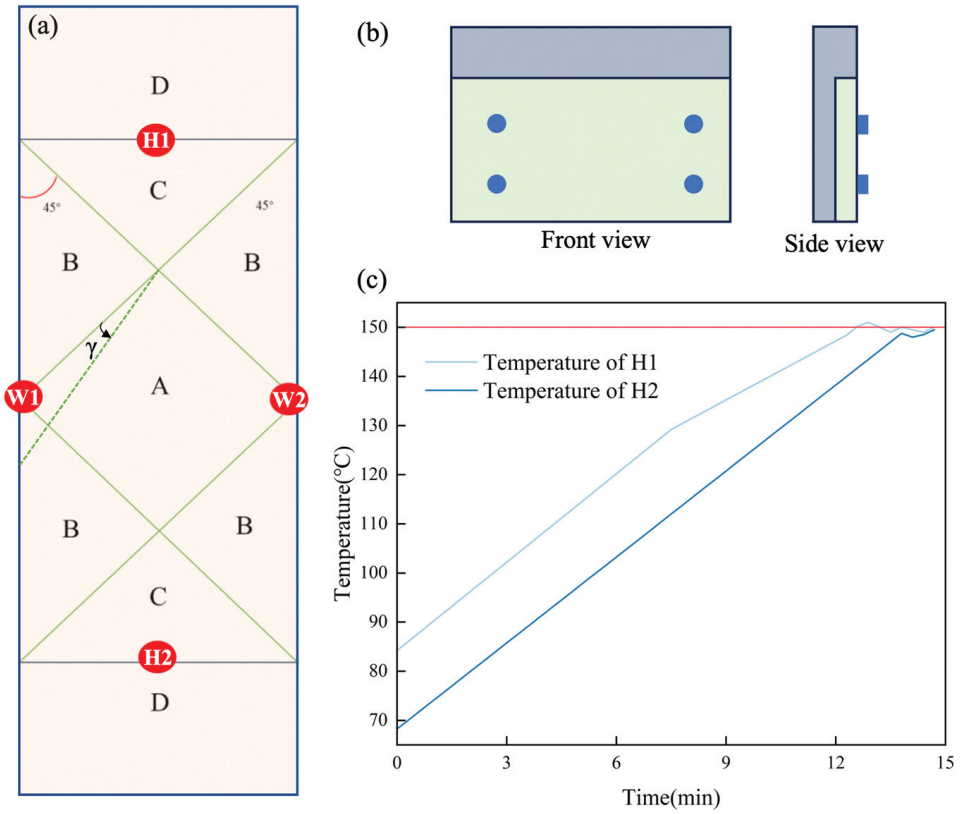

Figure 2. In-plane shear testing of unidirectional CF/epoxy prepreg: (**a**) concept of four shear characteristic zones and shear angle (γ); (**b**) fixture configuration; and (**c**) representative temperature collection curves of thermocouples at points $H1$ and $H2$, where the red line represents 150 °C.

Figure 3 illustrates the concepts of the in-plane shear and interlaminar shear in a ±45° off-axis tensile specimen of UD tape at both the macroscale and mesoscale. For a single unidirectional (UD) prepreg ply, constrained by the unidirectional orientation of the fibers, when subjected to off-axis tensile stress, it only generates shear forces in a single direction and lacks the ability to generate the theoretically defined "in-plane shear force couple" that can be observed in fabric forms. However, in practical composite simulations or manufacturing evaluations, it is essential to assess the in-plane shear performance of UD prepreg to evaluate its shear resistance capability. Therefore, to determine this parameter, it is often necessary to design off-axis tensile specimens with ±45° layups (as per international testing standard ASTM D3518), in which the different fiber orientations in the upper and lower layers produce distinct responses to the off-axis tension, thereby inducing interlaminar shear behaviors through the effects of friction and resin shear lag, which, in turn, cause in-plane shear deformation in the single-layer prepreg. In conclusion, in UD prepregs, the in-plane shear behavior is essentially a macroscale concept rather than a strictly mesoscale one. In this study, we focus on the in-plane shear behavior at the macroscale.

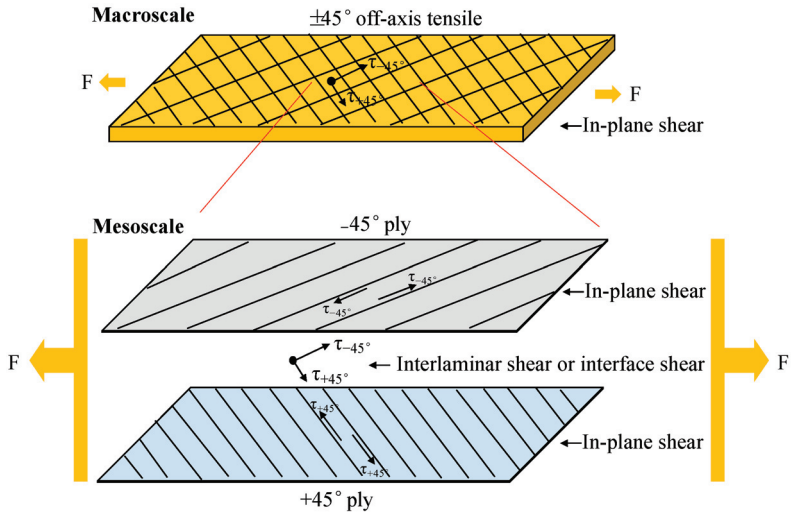

Figure 3. Diagram of in-plane shear and interlaminar shear in ±45° off-axis tensile specimen of UD tape at both the macroscale and mesoscale.

2.3. Rheological Behavior Testing of Prepreg

Unlike unidirectional non-crimped dry-fiber fabrics in off-axis tensile tests, composite material prepregs contain resin. Changes in the resin viscosity and flow properties induced by temperatures or resin curing during testing can affect the shear behavior of prepregs, consequently influencing changes in the shear angles [42]. Therefore, accurately testing the variation in the prepreg viscosity with temperature and time is crucial for a precise quantitative analysis of the prepreg shear behavior.

Viscosity testing of prepregs was conducted using a rotational rheometer (TA DHR-2). Samples, in the form of small circular discs with diameters of 25 mm, were layered and pre-pressed in the same stacking sequence, [45/−45/45/−45], as in the in-plane shear testing. The samples were then placed between the upper and lower rotors of the rheometer, with the material's bottom adhered to the lower rotor using polyimide adhesive tape to prevent slipping during testing [43,44]. (a) For the viscosity–temperature relationship test, the strain was set to 0.1%, the frequency was set to 1 Hz, and a normal force of 5 N was applied after reaching the set temperature of 30 °C. After allowing the instrument ambient temperature to reach the designated temperature and maintaining it for 5 min to ensure thorough temperature equilibration in all regions of the material, the test was initiated with a heating rate of 3 °C/min. The test was stopped when the temperature reached 180 °C, obtaining the viscosity–temperature curve for the prepreg. (b) For the viscosity–time relationship test, the testing temperature was set to 150 °C, and the scanning time was 1800 s. The frequency and pressure conditions were consistent with the settings mentioned above.

2.4. Curing Kinetics

The curing kinetics of the prepreg under the same time as that of the in-plane shear test process were analyzed by differential scanning calorimetry (DSC) (Netzsch, DSC 214, Selb, Germany), which was used to analyze the relationships between the curing degree, viscosity, and shear behaviors. Specifically, a 10 mg prepreg sample was weighed and placed into a crucible, followed by heating from 20 °C to 80 °C, 120 °C, and 150 °C at a rate of 5 °C/min. After being held for 30 min, corresponding to the shear preheating time and shear testing time, it was then cooled to 20 °C at a rate of 5 °C/min. For comparison, the complete cured curve was also tested according to the curing process provided by the prepreg supplier (i.e., curing at 180 °C for 2 h, with the other parameters set the same as mentioned above).

3. Results and Discussion

3.1. In-Plane Shear Characteristic Zones

The tensile in-plane shear behavior of the uncured CF/epoxy prepreg with a ±45° layup is illustrated in Figure 4. With increasing displacement, the prepreg gradually elongates in the length direction, while uneven contraction occurs in the width direction. At high tensile displacements, noticeable fiber squeezing and wrinkles start to appear (red lines), accompanied by distinct dark and light zones on the specimen surface, corresponding precisely to the *A*, *B*, and *C* zones in Figure 2a. The deformation data (purple area) in the *W* direction distinctly reveal the evolution of zone *A*, transitioning from no initial shear behavior to gradually increasing shear behavior at $d = 5.6$ mm, which eventually disappears at $d > 29$ mm. The *U*-directional DIC map identifies symmetrical contraction in the two *B* zones, persisting until the end, while zone *C* shows no significant deformation in the width direction, maintaining a constant area. The *V*-directional map indicates that zone *B* undergoes no apparent deformation in the length direction, while the deformation in zone *C* is induced by tensile displacement, with no significant change in the area observed.

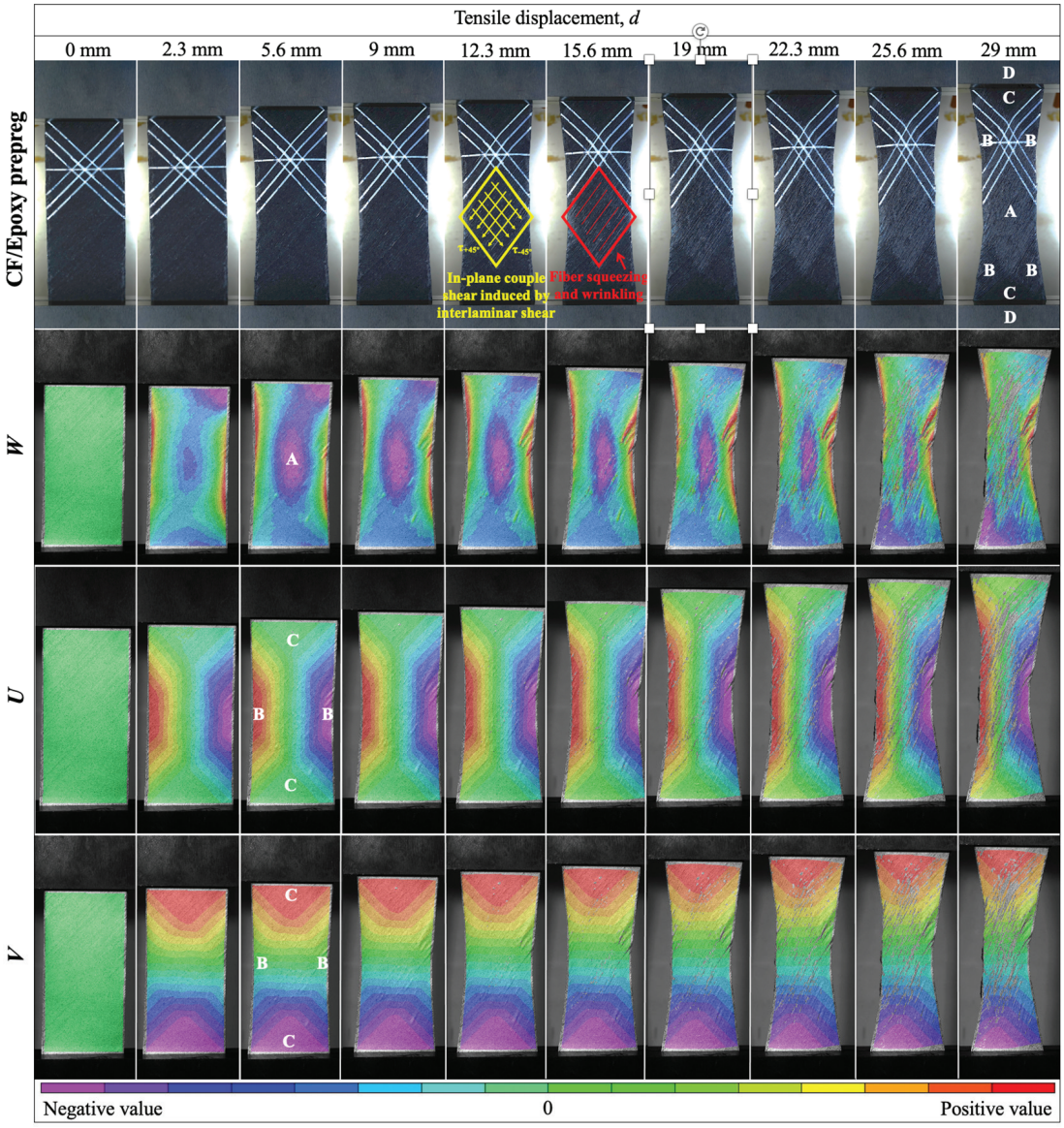

Figure 4. The ±45° off-axis tensile testing process and DIC strain maps of CF/epoxy prepreg depicting in-plane shear deformations in the thickness (*W*), width (*U*), and length (*V*) directions.

Thus, under the tensile constraints imposed by the clamps at both ends, the in-plane shear deformation of the prepreg can be divided into four characteristic zones with the following features: zone *A* is the completely sheared zone; zone *B* is the semi-sheared deformation zone; zone *C* is the zone influenced by the clamp constraints, experiencing no shear deformation; zone *D* is the clamped zone, experiencing no shear deformation.

According to the definitions provided above and Figures 3 and 4, when the off-axis tensile displacement (*d*) is less than 15.6 mm, the ±45° specimens primarily exhibit macroscale in-plane shear behavior (yellow lines in Figure 4), induced by the interlaminar interface shear between the +45° ply and −45° ply at the mesoscale (Figure 3). However, when $d > 15.6$ mm, fiber squeezing and wrinkling began to occur (red lines in Figure 4), induced by the interlaminar interface shear between the +45° ply and −45° ply at the mesoscale, as well as by the in-plane shear between parallel fiber yarns squeezing at the mesoscale. When $d > 29$ mm, the in-plane shear disappears in the completely sheared zone (*A*), as indicated by the purple strain variation along the *W* direction in Figure 4.

3.2. Quantitative Analysis of In-Plane Shear

The displacement changes of the four characteristic points, *H*1, *H*2, *W*1, and *W*2, during the tensile process are depicted in Figure 5a. It can be observed that the strain at point *H*1 linearly increases with the elongation of the prepreg during tensile loading. In contrast, the strain at *H*2 remains consistently zero due to the fixed constraints of the lower clamp, directly confirming that zone *C* experienced no shear deformation. However, the strain trends at points *W*1 and *W*2 are similar, with a temporary opposite deviation midway, indicating asymmetric shear deformation on both sides of the prepreg in zone *B*, caused by the non-uniform shear deformation in zone *A*, as seen in Figure 4. Theoretically, the complete shearing of the yarns in zone *A* induces the slipping of the yarns in zone *B*, while the yarns in zone *C* hold and fix the yarns in zone *B*. The combined effect of the yarns in zones *A* and *C* on zone *B* leads to the occurrence of semi-shear deformation in zone *B*. However, in reality, due to the difficulty of achieving an ideal uniformly distributed state of yarns at the microscopic scale during the manufacturing process, the deformation of the yarns in zone *A* is uneven in experiments. This unevenness results in the asymmetry of the deformation in zone *B* on both sides. Moreover, this asymmetrical difference gradually increases as the tensile loading progresses, as observed at $d = 29$ mm in Figure 4.

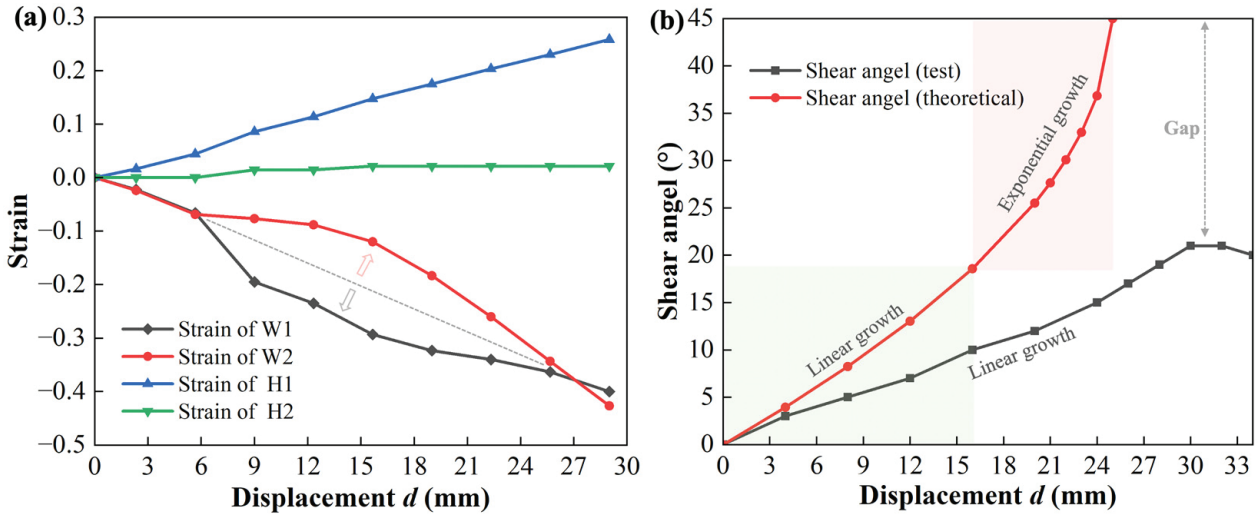

Figure 5. (**a**) Strain–displacement curves of characteristic points *H*1, *H*2, *W*1, and *W*2 during in-plane shear testing process; (**b**) variation in theoretical and actual shear angles in zone *A* of the prepreg with tensile displacement.

For the relationship between the shear angle (γ) and tensile displacement (d), combined with Equation 1 and Figure 5b, we can deduce through theoretical calculations that, under the assumption that the fibers can freely rotate, as the tensile displacement gradually increases from d = 0 mm to d = 24 mm, the shear angle changes from 0° to 45°, indicating that the fibers are tending toward a vertical distribution. Specifically, when the d is less than 15.6 mm, the increase in the in-plane shear angle of the prepreg approaches linearity. This is because, at small angles, the shear deformation is primarily controlled by the rotation of the fibers. However, as the angle continues to increase, the fibers start to squeeze each other, reducing the gap, and wrinkles begin to form, increasing the impact on the fiber shear deformation. This is consistent with the red-marked diamond frame in Figure 4 that shows that, during the tensile process, when d > 12.3 mm, the fibers in the shear region (A) begin to squeeze each other. When d = 15.6 mm, the compression of the fibers gradually becomes severe, resulting in the appearance of obvious wrinkles. At this point, the shear angle increases rapidly at an exponential rate until d = 24 mm, when the shear angle reaches 45°. However, in actual shear tests on prepreg with a [45/−45/45/−45] layup, the fiber rotation is constrained by both the in-plane and out-of-plane resin, as well as by the compression of the in-plane fibers and the obstruction from the out-of-plane perpendicular fibers. This results in the actual maximum rotated shear angle of the fibers (black line in Figure 5b) being far from the theoretical 45°. Instead, it maintains a relatively slow linear increase and reaches a plateau when d > 29 mm, with no further increase. Further increasing the displacement causes mutual compression between the fibers, leading to the onset of significant inter-ply sliding or wrinkling. This is consistent with the experimental observation in Figure 4, in which the purple region representing the shear behavior in the A zone gradually disappears after d > 29 mm, and significant wrinkles appear in zone B.

3.3. Temperature Influence

The molding temperature is a crucial factor affecting the resin flow, curing rate, deformability of the prepreg, and quality of the composite components during the molding process of thermoset composites [45]. Digital images of the in-plane shear testing at different temperatures are shown in Figure 6, and the corresponding force resistances to the in-plane shear deformations are collected in Figure 7a. With the increase in the test environment temperature, a noticeable change in the specimen appearance is observed, accompanied by a significant decrease in the shear deformation force resistance. At 30 °C, the force resistance to the in-plane shear deformation is significantly higher than those at other temperatures. The lowest shear force resistance is observed at 120 °C and 150 °C, where the curves almost overlap. The main reason for the observed changes in the appearance and force resistance is the variation in the resin viscosity caused by the temperature increase. At this time, two competing behaviors affecting the change in viscosity occur: temperature increase promotes molecular movement, which helps to reduce the viscosity, and it promotes epoxy curing, increasing the viscosity. This is evidenced by Figures 7b,c and 8. As shown in Figure 7b, the viscosity–temperature curve of the prepreg indicates a rapid decrease in viscosity with the temperature increase from 30 °C to 150 °C, with the viscosity at 120 °C being similar to that at 150 °C. This is consistent with the trend of the almost overlapped force resistance to the in-plane shear deformation with the temperature change. However, the viscosity starts to increase after the temperature exceeds 150 °C due to the occurrence of curing. Further insights from the viscosity–time curve in Figure 7c also reveal that under in-plane shear tensile testing conditions at 150 °C for nearly 30 min, the viscosity approximately doubles from 9721 Pa·s to 17,116 Pa·s due to the resin curing. However, even with this increase, the viscosity remains significantly lower than that of 32,305 Pa·s at 80 °C (i.e., the magnitude of the viscosity increase due to curing is much lower than the magnitude of the viscosity reduction caused by the temperature rise). Therefore, it can be concluded that the decrease in the resin viscosity caused by the temperature is a direct factor influencing the in-plane shear force behavior of the prepreg within 30 min.

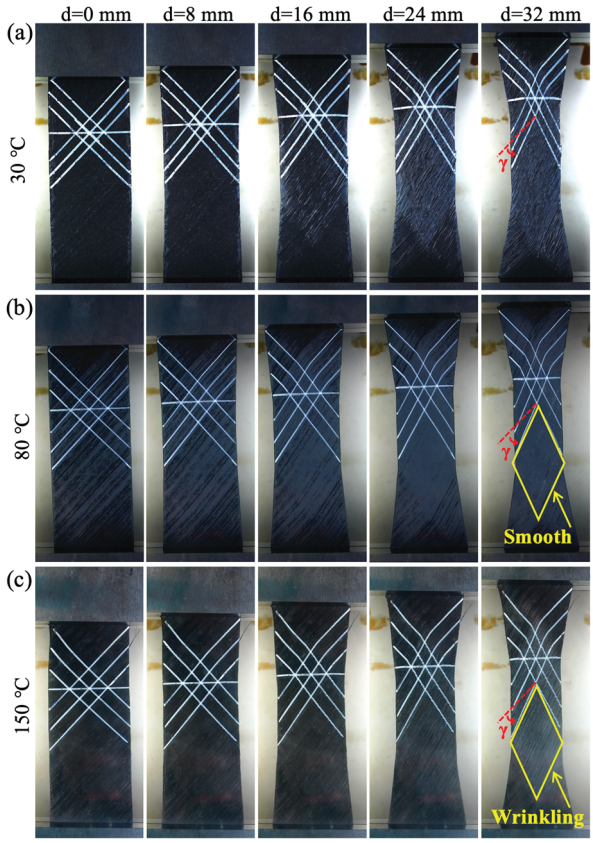

Figure 6. Digital images of in-plane shear testing of the CF/epoxy prepreg at different temperatures: (**a**) 30 °C, (**b**) 80 °C, and (**c**) 150 °C.

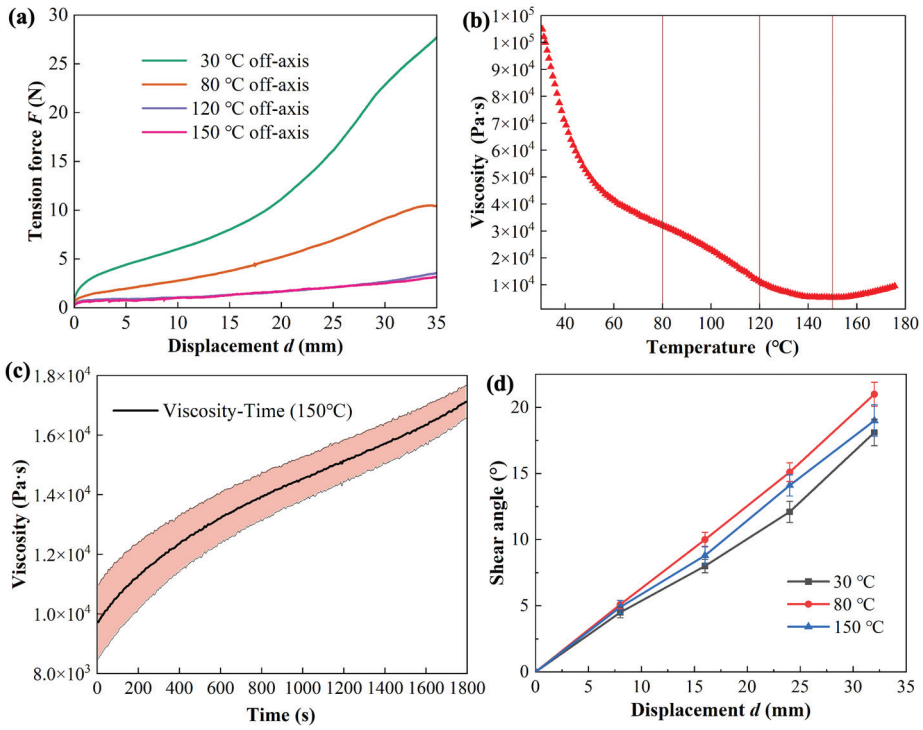

Figure 7. Impact of temperature on in-plane shear behaviors of the CF/epoxy prepreg: (**a**) deformation resistance forces of the prepreg; (**b**) viscosity–temperature curve of the prepreg; (**c**) viscosity–time curve of the prepreg at 150 °C; (**d**) variations in shear angles in specimens at different temperatures.

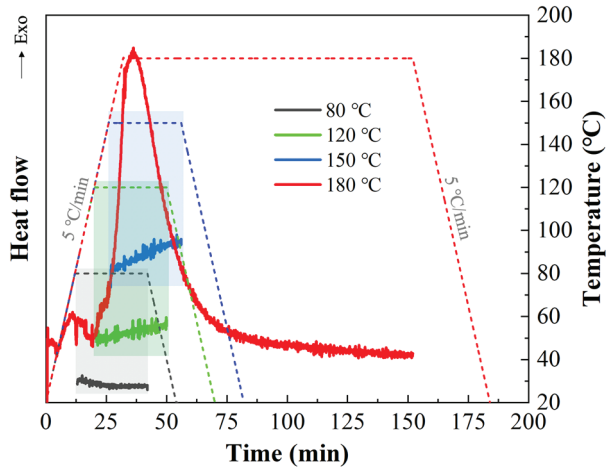

Figure 8. The curing kinetic curves of the prepreg analyzed by DSC. Note: For the incomplete-curing DSC curves at 80 °C, 120 °C, and 150 °C, due to significant temperature fluctuations in the transient states from heating to constant temperature and from constant temperature to cooling, which affect the analysis of the curing behavior during the constant-temperature stage, we have omitted the curve data for the heating and cooling processes here.

However, it is worth noting that, although the temperature increase is beneficial in reducing the resin viscosity and shear force, there is no significant difference in the shear angles (Figure 7d). Instead, the shear angle values at the higher temperature of 150 °C are slightly lower than those at 80 °C. This is mainly because after slight curing at 150 °C, although the increase in viscosity has little effect on the tensile force of the sample, it has a significant impact on the movement of the fibers in the local shear area (*A*). At this point, the movement of the fibers is hindered by the shear resistance from the fibers and cured resins in the in-plane and out-of-plane perpendicular directions, resulting in a decrease in the shear angle, but producing more pronounced mutual squeezing and wrinkling (Figure 6b,c).

The evidence for the increase in viscosity and curing degree at different temperatures during shear testing is revealed in Figure 8. It can be seen that, under the curing temperature of 180 °C (red curve) recommended by the supplier, the CF/epoxy sample started to release heat during the heating stage, and it completed the entire curing process approximately 40 min after reaching 180 °C. In contrast, during the entire testing time, including heating to 80 °C, 120 °C, and 150 °C, and maintaining these temperatures for 30 min, no complete curing exothermic peaks were observed. However, through subtle observation and comparison of the slope of the heat flow curve, it can still be observed that the slopes increase with the increasing temperature, indicating the occurrence of slight curing, and the curing rate increases with the increasing temperature. However, within our limited testing time, corresponding to the time scale of in-plane shear testing, the overall degree of curing remains at a relatively low level. The above phenomenon well explains why the viscosity starts to increase after the temperature exceeds 150 °C in Figure 7b,c, and why the shear angle at 150 °C in Figure 7d is lower than that at 80 °C.

In summary, in the actual manufacturing process of composite materials, appropriately raising the temperature of the CF/epoxy prepreg can effectively reduce the molding resistance, decrease the frictional resistance and wear between the mold and fibers, improve the molding efficiency, and enhance the product quality without significantly affecting the predetermined orientation of the fibers.

3.4. Shear Rate Influence

Figure 9 illustrates the influence of the tensile rate on the in-plane shear behavior of the prepreg. It is evident that the shear deformation resistance force of the prepreg is positively correlated with the tensile rate. Higher tensile rates result in greater shear

deformation resistance. Notably, at a rate of 100 mm/min, the prepreg experiences direct tensile failure around d = 15 mm. This corresponds to the rapid increase in the mid-shear angle and resistance force, as shown in Figures 5b and 7a. This is primarily attributed to the substantial viscous resistance of the resin at room temperature, wherein its high relaxation time hinders the epoxy resin from responding promptly under a high tensile rate, consequently leading to the in-plane shear failure of the prepreg. Therefore, in practical manufacturing processes of composite materials, it is essential to choose an appropriate laying rate to enhance the molding quality or elevate the temperature of the CF/epoxy prepreg to reduce the resin viscosity and improve the shear response speed, thereby achieving the enhanced manufacturing efficiency of the preform.

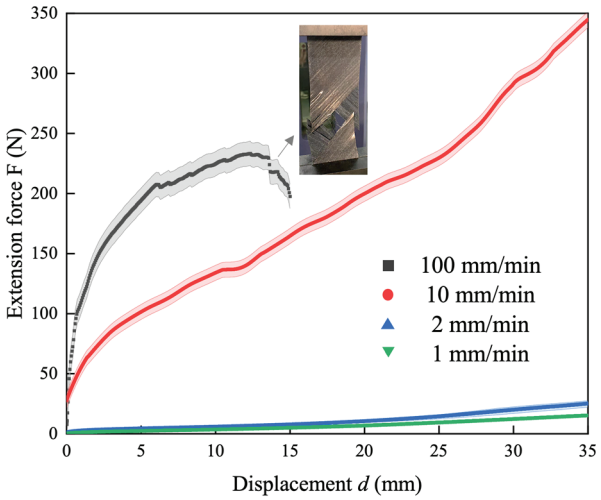

Figure 9. Impact of shear rate on in-plane shear behavior of CF/epoxy prepregs.

4. Conclusions

Based on the shear deformation and wrinkling issues faced by unidirectional thermoset prepregs in the AFP process of preform manufacturing, this study, including the ±45° off-axis tension determination, DIC triaxial strain characterization, and shear angle prediction, establishes a quantitative characterization method for in-plane shear issues in prepregs. It successfully reveals four shear characteristic zones and conducts dynamic quantitative evaluations of the deformation in the thickness, width, and length dimensions, as well as of the shear angles. The results indicate that the actual shear angle is significantly lower than the theoretical shear angle due to the constraints imposed by the fibers from both the in-plane and out-of-plane directions. When the off-axis tensile displacement (d) is less than 15.6 mm, the ±45° specimens primarily exhibit macroscale in-plane shear behavior, induced by interlaminar interface shear between the +45° ply and −45° ply at the mesoscale. The shear angle increases linearly with the d. However, when d > 15.6 mm, fiber squeezing and wrinkling begin to occur. When d > 29 mm, the completely sheared behavior in the A zone gradually disappears, and further increases in the shear displacement lead to mutual fiber squeezing, resulting in significant interlayer slip or wrinkling. The resin viscosity is a direct factor influencing the in-plane shear resistance of CF/epoxy prepreg, but it has no obvious effect on the shear angle. The impact of the resin viscosity increase induced by the curing on the shear deformation is much smaller than that of the temperature-induced viscosity reduction. At higher shear rates, the in-plane deformation resistance of the prepreg increases, leading to interlayer cracking failure. Therefore, during the manufacturing process of CF/epoxy preform, it is necessary to appropriately increase the temperature to simultaneously improve the forming efficiency and preform quality. These findings provide a theoretical reference for quantitatively analyzing the in-plane shear deformation capability and for predicting defects in composite processing, highlighting the ±45° UD prepreg layups in AFP manufacturing.

Author Contributions: Conceptualization, H.Z. and G.Y.; methodology, H.L. and H.Z.; software, H.L. and H.Z.; validation, G.Y., H.Z., and B.G.; formal analysis, H.L. and G.Y.; investigation, H.L. and H.Z.; resources, G.Y. and Y.W.; data curation, H.L. and G.Y.; writing—original draft preparation, H.L. and H.Z.; writing—review and editing, H.L. and Y.W.; visualization, H.L., G.Y., and B.G.; supervision, G.Y. and Y.W.; project administration, G.Y.; funding acquisition, G.Y. All authors have read and agreed to the published version of the manuscript.

Funding: This research was funded by the National Key R&D Program of China, grant number 2022YFB3704503.

Data Availability Statement: Data are contained within the article.

Conflicts of Interest: The authors declare no conflicts of interest.

References

1. Van Barschot, J. Airbus en Boeing vliegen met TenCate. *NRC Handelsblad, Rotterdam*, 5 January 2005; Volume 17.
2. Rodríguez-García, V.; Gómez, J.; Cristiano, F.; Gude, M.R. Industrial manufacturing and characterization of multiscale CFRP laminates made from prepregs containing graphene-related materials. *Mater. Res. Express* **2020**, *7*, 075601. [CrossRef]
3. Zhang, S.; Tang, H.; Tang, D.; Liu, T.; Liao, W. Effect of fabrication process on the microstructure and mechanical performance of carbon fiber reinforced PEEK composites via selective laser sintering. *Compos. Sci. Technol.* **2024**, *246*, 110396. [CrossRef]
4. Frossard, G.; Cugnoni, J.; Gmür, T.; Botsis, J. Ply thickness dependence of the intralaminar fracture in thin-ply carbon-epoxy laminates. *Compos. Part A-Appl. Sci.* **2018**, *109*, 95–104. [CrossRef]
5. Dirk, H.J.L.; Ward, C.; Potter, K.D. The engineering aspects of automated prepreg layup: History, present and future. *Compos. Part B-Eng.* **2012**, *43*, 997–1009.
6. Poursatip, A. Transitioning composites manufacturing simulation into industrial practice: Challenges and opportunities. In Proceedings of the ICMAC 2015-International Conference on Manufacturing Advanced Composites, Bristol, UK, 24–25 June 2015.
7. Harrison, P.; Abdiwi, F.; Guo, Z.; Potluri, P.; Yu, W. Characterising the shear–tension coupling and wrinkling behaviour of woven engineering fabrics. *Compos. Part A-Appl. Sci.* **2012**, *43*, 903–914. [CrossRef]
8. Potter, K. Bias extension measurements on cross-plied unidirectional prepreg. *Compos. Part A-Appl. Sci.* **2002**, *33*, 63–73. [CrossRef]
9. Boisse, P.; Hamila, N.; Guzman-Maldonado, E.; Madeo, A.; Hivet, G.; Dell'Isola, F. The bias-extension test for the analysis of in-plane shear properties of textile composite reinforcements and prepregs: A review. *Int. J. Mater. Form.* **2017**, *10*, 473–492. [CrossRef]
10. Harrison, P.; Clifford, M.J.; Long, A. Shear characterisation of viscous woven textile composites: A comparison between picture frame and bias extension experiments. *Compos. Sci. Technol.* **2004**, *64*, 1453–1465. [CrossRef]
11. McGuinness, G.; ÓBrádaigh, C. Characterisation of thermoplastic composite melts in rhombus-shear: The picture-frame experiment. *Compos. Part A-Appl. Sci.* **1998**, *29*, 115–132. [CrossRef]
12. Trejo, E.A.; Ghazimoradi, M.; Butcher, C.; Montesano, J. Assessing strain fields in unbalanced unidirectional non-crimp fabrics. *Compos. Part A-Appl. Sci.* **2020**, *130*, 105758. [CrossRef]
13. Haanappel, S.; ten Thije, R.H.; Sachs, U.; Rietman, B.; Akkerman, R. Formability analyses of uni-directional and textile reinforced thermoplastics. *Compos. Part A-Appl. Sci.* **2014**, *56*, 80–92. [CrossRef]
14. Li, H.; Wei, Y.; Wang, L. A general model for predicting the off-axis performance of fiber reinforced composite materials. In *Structures*; Elsevier: Amsterdam, The Netherlands, 2021; Volume 34, pp. 2087–2097.
15. Zhu, B.; Yu, T.; Tao, X. An experimental study of in-plane large shear deformation of woven fabric composite. *Compos. Sci. Technol.* **2007**, *67*, 252–261. [CrossRef]
16. Hautefeuille, A.; Comas-Cardona, S.; Binetruy, C. Mechanical signature and full-field measurement of flow-induced large in-plane deformation of fibrous reinforcements in composite processing. *Compos. Part A-Appl. Sci.* **2019**, *118*, 213–222. [CrossRef]
17. Mei, M.; Huang, J.; Yu, S.; Zeng, T.; He, Y.; Wei, K. Shear deformation characterization and normalized method of tricot-stitched unidirectional non-crimp fabric. *Compos. Sci. Technol.* **2024**, *246*, 110391. [CrossRef]
18. Schirmaier, F.J.; Dörr, D.; Henning, F.; Kärger, L. A macroscopic approach to simulate the forming behaviour of stitched unidirectional non-crimp fabrics (UD-NCF). *Compos. Part A-Appl. Sci.* **2017**, *102*, 322–335. [CrossRef]
19. Boisse, P.; Hamila, N.; Madeo, A. The difficulties in modeling the mechanical behavior of textile composite reinforcements with standard continuum mechanics of Cauchy. Some possible remedies. *Int. J. Solids Struct.* **2018**, *154*, 55–65. [CrossRef]
20. Harrison, P.; Alvarez, M.F.; Anderson, D. Towards comprehensive characterisation and modelling of the forming and wrinkling mechanics of engineering fabrics. *Int. J. Solids Struct.* **2018**, *154*, 2–18. [CrossRef]
21. Wang, Y.; Chea, M.K.; Belnoue, J.P.-H.; Kratz, J.; Ivanov, D.S.; Hallett, S.R. Experimental characterisation of the in-plane shear behaviour of UD thermoset prepregs under processing conditions. *Compos. Part A-Appl. Sci.* **2020**, *133*, 105865. [CrossRef]
22. Scobbo, J., Jr.; Nakajima, N. Modification of the mechanical energy resolver for high temperature and rigid material applications. *Polym. Test.* **1990**, *9*, 245–255. [CrossRef]
23. Stanley, W.; Mallon, P. Intraply shear characterisation of a fibre reinforced thermoplastic composite. *Compos. Part A-Appl. Sci.* **2006**, *37*, 939–948. [CrossRef]

24. Larberg, Y.R.; Åkermo, M.; Norrby, M. On the in-plane deformability of cross-plied unidirectional prepreg. *J. Compos. Mater.* **2012**, *46*, 929–939. [CrossRef]
25. Larberg, Y.; Åkermo, M. In-plane deformation of multi-layered unidirectional thermoset prepreg–modelling and experimental verification. *Compos. Part A-Appl. Sci.* **2014**, *56*, 203–212. [CrossRef]
26. Groves, D.; Bellamy, A.; Stocks, D. Anisotropic rheology of continuous fibre thermoplastic composites. *Composites* **1992**, *23*, 75–80. [CrossRef]
27. Groves, D. A characterization of shear flow in continuous fibre thermoplastic laminates. *Composites* **1989**, *20*, 28–32. [CrossRef]
28. Hörmann, P.M. Thermoset Automated Fibre Placement–on Steering Effects and Their Prediction. Ph.D. Thesis, Technische Universität München, München, Germany, 2015.
29. Haanappel, S.; Akkerman, R. Shear characterisation of uni-directional fibre reinforced thermoplastic melts by means of torsion. *Compos. Part A-Appl. Sci.* **2014**, *56*, 8–26. [CrossRef]
30. Dörr, D.; Henning, F.; Kärger, L. Nonlinear hyperviscoelastic modelling of intra-ply deformation behaviour in finite element forming simulation of continuously fibre-reinforced thermoplastics. *Compos. Part A-Appl. Sci.* **2018**, *109*, 585–596. [CrossRef]
31. Gao, M.; Wang, C.; Yang, D.; Fu, Y.; Li, B.; Guan, R. Effect of stress concentration and deformation temperature on the tensile property and damage behavior of a B4Cp/Al composite. *J. Mater. Res. Technol.* **2021**, *15*, 2601–2610. [CrossRef]
32. Aghdam, M.; Morsali, S.; Hosseini, S.; Sadighi, M. Mechanical behavior of unidirectional SiC/Ti composites subjected to off-axis loading at elevated temperatures. *Mater. Sci. Eng. A* **2017**, *688*, 244–249. [CrossRef]
33. Zhai, Z.; Jiang, B.; Drummer, D. Temperature-dependent response of quasi-unidirectional E-glass fabric reinforced polypropylene composites under off-axis tensile loading. *Compos. Part B-Eng.* **2018**, *148*, 180–187. [CrossRef]
34. Shah, S.; Megat-Yusoff, P.; Sharif, T.; Hussain, S.Z.; Choudhry, R. Off-axis tensile performance of notched resin-infused thermoplastic 3D fibre-reinforced composites. *Mech. Mater.* **2022**, *175*, 104478. [CrossRef]
35. Yao, L.; Chuai, M.; Li, H.; Chen, X.; Quan, D.; Alderliesten, R.; Beyens, M. Temperature effects on fatigue delamination behavior in thermoset composite laminates. *Eng. Fract. Mech.* **2024**, *295*, 109799. [CrossRef]
36. Zhang, B.; Kim, B.C. Experimental characterisation of large in-plane shear behaviour of unidirectional carbon fibre/epoxy prepreg tapes for continuous tow shearing (CTS) process. *Compos. Part A-Appl. Sci.* **2022**, *162*, 107168. [CrossRef]
37. Pheysey, J.; De Cola, F.; Pellegrino, A.; Martinez-Hergueta, F. Strain rate and temperature dependence of short/unidirectional carbon fibre PEEK hybrid composites. *Compos. Part B-Eng.* **2024**, *268*, 111080. [CrossRef]
38. Rashidi, A.; Montazerian, H.; Yesilcimen, K.; Milani, A. Experimental characterization of the inter-ply shear behavior of dry and prepreg woven fabrics: Significance of mixed lubrication mode during thermoset composites processing. *Compos. Part A-Appl. Sci.* **2020**, *129*, 105725. [CrossRef]
39. Jiang, L.; Wang, J.; Xiao, S.; Li, Y.; Yang, L. Dynamic tensile properties of carbon/glass hybrid fibre composites under intermediate strain rates via DIC and SEM technology. *Thin-Walled Struct.* **2023**, *190*, 110986. [CrossRef]
40. Hsu, F.Y.; Hung, K.C.; Xu, J.W.; Liu, J.W.; Wu, Y.H.; Chang, W.S.; Wu, J.H. Analyzing the impact of veneer layup direction and heat treatment on plywood strain distribution during bending load by digital image correlation (DIC) technique. *J. Mater. Res. Technol.* **2023**, *27*, 5257–5265. [CrossRef]
41. Liu, Z.; Mu, T.; Lan, X.; Liu, L.; Bian, W.; Liu, Y.; Leng, J. Damage behavior analysis of unidirectional fiber reinforced shape memory polymer composites. *Compos. Struct.* **2023**, *304*, 116392. [CrossRef]
42. Gu, Q.; Quan, Z.; Shen, M.; Xie, Y.; Yu, J. Fabrication and braiding angle effect on the improved interlaminar shear performances of 3D braided sandwich hybrid composites. *J. Mater. Res. Technol.* **2023**, *25*, 5795–5806. [CrossRef]
43. Robles, J.B.; Dubé, M.; Hubert, P.; Yousefpour, A. Healing study of poly (ether-imide) and poly ether ether ketone using resin films and a parallel plate rheometer. *Compos. Part A-Appl. Sci.* **2023**, *174*, 107736. [CrossRef]
44. Das, A.; Choong, G.Y.; Dillard, D.A.; De Focatiis, D.S.; Bortner, M.J. Characterizing friction for fiber reinforced composites manufacturing: Method development and effect of process parameters. *Compos. Part B-Eng.* **2022**, *236*, 109777. [CrossRef]
45. Obande, W.; O'Rourke, K.; Stankovic, D.; Lykkeberg, A.; Garden, J.A.; Brádaigh, C.Ó.; Ray, D. Multi-stage, in-situ polymerisation for low-exotherm, liquid resin infusion of thick thermoplastic laminates at room temperature. *Compos. Commun.* **2024**, *45*, 101788. [CrossRef]

Journal of
Composites Science

MDPI

Article

Surface Quality Related to Face Milling Parameters in 3D Printed Carbon Fiber-Reinforced PETG

Mohamad El Mehtedi, Pasquale Buonadonna, Gabriela Loi , Rayane El Mohtadi, Mauro Carta * and Francesco Aymerich *

Department of Mechanical, Chemical and Materials Engineering, University of Cagliari, Via Marengo 2, 09123 Cagliari, Italy; m.elmehtedi@unica.it (M.E.M.); pasquale.buonadonna@unica.it (P.B.); gabriela.loi@unica.it (G.L.); rayane.elmohtadi@unica.it (R.E.M.)
* Correspondence: mauro.carta94@unica.it (M.C.); francesco.aymerich@unica.it (F.A.)

Abstract: Three-dimensional printing technology holds significant potential for enhancing the flexibility and cost-efficiency of producing carbon fiber-reinforced polymer composites (CFRPs). However, it faces limitations such as challenges in achieving high surface qualityand precise dimensional accuracy and managing the distinctive anisotropic mechanical properties that it demonstrates. This study aims to explore the machinability of 3D printed PETG infused with 20% short carbon fiber and to assess the resulting surface roughness and burr formation. Employing a Design of Experiments (DoE) approach, three factors were considered: rotational speed, feed rate, and depth of cut. These factors were tested at varying levels—rotational speeds of 3000, 5500, and 8000 rpm; feed rates of 400, 600, and 800 mm/min; and depth of cut values of 0.2, 0.4, 0.6, and 0.8 mm. The evaluation of machinability relied on two key response parameters: surface roughness (Sa) determined from the milled surface and burr height measured on both sides using a roughness meter. The findings revealed a significant influence of milling parameters on both roughness and burr formation. However, the ideal conditions for minimizing roughness and reducing burr formation did not align. Furthermore, a comparative analysis was conducted between these results and the machinability of PETG under similar conditions.

Keywords: 3D printing; PETG; carbon fiber; milling; surface quality; burr

1. Introduction

Additive Manufacturing (AM), also known as 3D printing, is a well-established technology gaining an ever-rising interest in several industrial branches ranging from automotive to aerospace, civil, and biomedical engineering [1–3]. Compared to conventional manufacturing processes, AM is able to produce intricately shaped parts at a cost-effective rate, facilitate swift processes, allow rapid prototyping, and diminish scrap production [4]. Therefore, several AM techniques, differing in both the methodology and the material employed for manufacturing, have been proposed, including Fused Deposition Modeling (FDM), Direct Metal Deposition (DRM), Selective Laser Sintering (SLS), Ink Jet Modeling (IJM), and stereo-lithography (SLA).

Nowadays, Polylactic Acid (PLA) and Acrylonitrile Butadiene Styrene (ABS) are among the most widely employed thermoplastic materials for 3D printing, although polyethylene terephthalate glycol (PETG) is receiving increasing attention. Synthesized from the co-polymerization of PolyEthylene Terephthalate (PET) with cyclohexane-dimethanol, PETG provides relatively high machinability and impact resistance, a higher toughness and ductility than conventional thermoplastics, which result in an increased tensile modulus and strength [5]. Moreover, PETG exhibits high transparency [6] and resistance to crystallization when exposed to high heat levels [7], good hydrophobic properties and hygrothermal aging resistance [8,9], high photostability, and a high glass transition temperature [10], making it a viable material for a wide range of industrial applications, especially biomedical and clinical

applications. Kim et al. studied the fatigue behavior of 3D printed PETG, developing a theoretical method for predicting residual fatigue life [11].

Among the proposed 3D printing technologies, Fused Deposition Modeling (FDM), also named Fused Filament Fabrication (FFF), consists of melting a thermoplastic filament, which is subsequently extruded and selectively layered to create a three-dimensional object. However, due to the layer-by-layer printing process, the bonding between layers (interlayer bonding) tends to be inherently weaker than that within the material itself. The resulting material anisotropy may significantly limit the application of 3D printed components in critical applications. Hence, extensive research has been devoted to characterizing the mechanical properties of FDM 3D printed components and structures [12–15], which highly depend on the employed process variables. In this regard, Durgashyam et al. [16] evaluated the influence of several printing parameters, i.e., infill density, feed rate, and layer thickness, on the tensile and flexural strength of 3D printed PETG samples. The authors found that higher flexural performance was achieved when the layer thickness and the feed rate were set at the minimum level. Furthermore, improved tensile properties were achieved by combining a high percentile of infill density with a low layer thickness and feed rate. Similarly, Kumar and co-workers [8] investigated the effect of three process parameters, namely, print speed, layer height, and infill density, on the tensile and flexural strength of PETG samples. The experimental results showed that layer height and infill density predominantly affect the flexural strength, while the print speed and infill density most affect the hardness and the tensile strength of 3D printed samples.

Besides the mechanical properties, printing parameters were also found to significantly influence surface quality [17–19]. Barrios and Romero [20] investigated the influence of several printing parameters on the surface quality of 3D printed PETG samples, highlighting the significant impact of flow rate and print acceleration. Later on, Vidakis and co-workers [19] employed a variance analysis and a reduced quadratic regression model to further assess the influence of six printing parameters, i.e., raster deposition angle, infill density, nozzle temperature, bed temperature, printing speed, and layer thickness, on three critical quality indicators (i.e., surface roughness, dimensional deviation, and porosity) and provide predictive models to optimize the desired response parameter.

These findings point out the limitations of FDM technology, which, while enabling intricate designs, often falls short in terms of surface finish, dimensional tolerance, mechanical properties, and machinability. The surface quality of FDM is inferior when compared to that of other 3D printing processes [21]. In a study by Kadhum et al., the influence of infill patterns on roughness was investigated, with the best condition identified as a quarter cubic pattern, yielding an Ra value of 4.8 μm [22]. Mat et al. [23] explored the impact of layer thickness and infill design on PETG samples. They discovered that the lowest roughness (4.2 μm) was achieved at the highest infill density and lowest layer thickness. Adding 15% carbon fiber to PETG improved its surface properties by 32.7%, reducing roughness from 6.34 to 4.01 μm, according to the study by Hadeeyah et al. [24]. Some authors studied the effects of process parameters on the dimensional accuracy of FDM 3D printed samples using various materials, showing acceptable dimensional accuracy [25–28].

In order to address these issues, several post-printing solutions have been proposed, such as applying post-processing heat treatment [29], hot cutter, milling, and acetone vapor bath [1,21,30–32]. Among them, the potential of CNC milling to refine 3D printed samples has been widely exploited, especially in 3D printed carbon fiber-reinforced polymer (CFRP) composites [33]. Table 1 shows the main milling parameters on 3D printed samples of different materials that are available in the literature. In this regard, Cococcetta et al. [34] investigated the surface finish, burr formation, and tool wear during the machining of 3D printed CFRP composites to take advantage of the chance to vary the fill geometry, fill density, and fiber orientation. The authors observed that post-process milling increased the surface quality of the inspected samples. In particular, a lower feed rate allowed part of the workpiece to adhere to the tool, causing tool wear and burr formation, which may be minimized through minimum quantity lubrication. Meanwhile, Guo et al. [35] performed

an investigation on the dry milling of the exterior stepped surfaces of amorphous PEEK and CF/PEEK components, highlighting the influence of factors like raster angle on surface quality and demonstrating the co-dependency between the milling parameters (e.g., the raster angle and the layer thickness) and 3D-printing parameters (e.g., the depth of cut, the spindle speed, and the feed rate per tooth).

Table 1. Comparison of the main milling parameter ranges for 3D printed samples, as available in the literature.

Authors	3D Printed Materials	n	V_f
Lalelgani et al. [21]	PLA	3283–10,504 rpm	1000 mm/min
Pamarac et al. [30]	ABS	3500 rpm	35–840 mm/min
Pamarac et al. [30]	PLA	3500 rpm	35–1880 mm/min
EL Mehtedi et al. [1]	PLA	3500–8000 rpm	400–800 mm/min
Guo et al. [35]	PEEK and CF-PEEK	3000–12,500 rpm	0.02–0.1 mm/teeth
Cococcetta et al. [34]	Onyx and CF-Onyx	6000 rpm	600–1200 mm/min
Vallejo et al. [36]	PETG and CF-PETG	3500 rpm	800 mm/min

Despite the numerous studies on PLA and ABS components, only a few attempts have been made to assess whether a post-printing milling process is a viable solution to enhance the surface quality of 3D printed PETG and CF-PETG samples. Vallejo et al. [36] investigated CF-PETG machinability, finding that the layer thickness was mostly insignificant, except for in peripheral milling, while a higher layer thickness negatively impacted geometric properties.

This study focuses on the machinability of CF-PETG components and assesses the effects of milling parameters, i.e., rotational speed, feed rate, and depth of cut, on surface roughness and burr formation. In order to comprehensively capture their impact, different parameter configurations are considered. An Analysis of Variance (ANOVA) is performed to pinpoint the most influential parameter in the machining process. Additionally, the mechanical properties of the 3D printed components are assessed across three printing directions. Furthermore, a comparison is made between the achieved results and those obtained under similar conditions for unreinforced PETG. This comparative analysis highlights the performance and characteristics of both PETG and carbon fiber-reinforced PETG components, enriching the understanding of their distinctions.

2. Materials and Methods

This study compares the mechanical properties and machinability of two PETG filaments: a PETG infused with 20% short carbon fiber, referred to as CF-PETG, and an unreinforced PETG. Both materials were manufactured by *Soitech* (Bernin, France).

Samples were printed following the manufacturer's guidelines, employing a *Tronxy 5SA FDM* printer equipped with a 0.4 mm extruder. Thus, while the extrusion temperature was set at 250 °C, the temperature of the printer bed, treated with a lacquer spray to enhance adhesion, was set at 70 °C. The project's mesh and G-code files were generated using the open-source software *FreeCAD* (v. 0.17).

In order to evaluate the mechanical properties of the printed samples, room-temperature tensile tests were performed on a *Galdabini Sun500* servo-electric machine equipped with a 5 kN load cell. Sample geometry and printing directions, shown in Figure 1, were defined in accordance with the UNE 116005:2012 standard [37], as the results achieved following its guidelines show superior repeatability to those achieved following alternative standards [38]. During testing, an *HBM DD1* displacement transducer was mounted on the sample to measure its strain across a 50 mm gauge length. Each printing direction underwent three replications to ensure the robustness and reliability of the results.

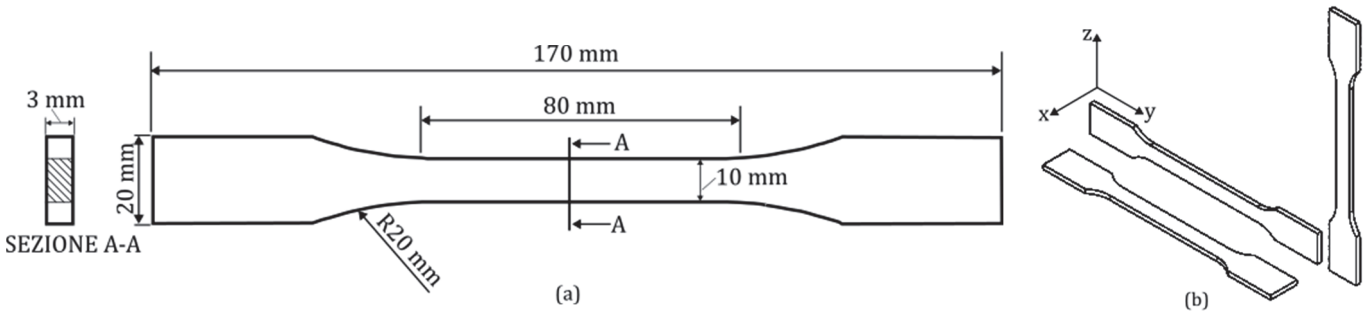

Figure 1. Geometry of the dog-bone samples used for the tensile strength tests (**a**) and printing direction used for tensile samples (**b**).

Figure 2 shows the specimen designed for the machinability tests. In order to maximize the efficiency of the milling experiments, a Design of Experiments (DoE) approach incorporating a full factorial design that accounts for the three selected parameters was applied. The selected factors, i.e., rotational speed (n), feed rate (V_f), and depth of cut (a_p), are detailed in Table 2, for a total of 36 different conditions. These parameters were chosen after a thorough study of the available literature to determine a feasible range that could suit PETG material, despite the limited existing research on the milling of 3D printed PETG and CF-PETG (Table 1). Milling trials were conducted on a *CNC3018* milling machine equipped with a commercial tool (*Master 660C*). The experiment was conducted in a random order to minimize the effects of uncontrolled external variables. *Vectric Aspire* software V11.5 was used as CAD-CAM software, and the *GRBL control* open-source controller was employed to perform the milling process. Throughout the milling process, experiments were conducted in MQL using mineral oil in water emulsion. One replicant was used for each milling condition.

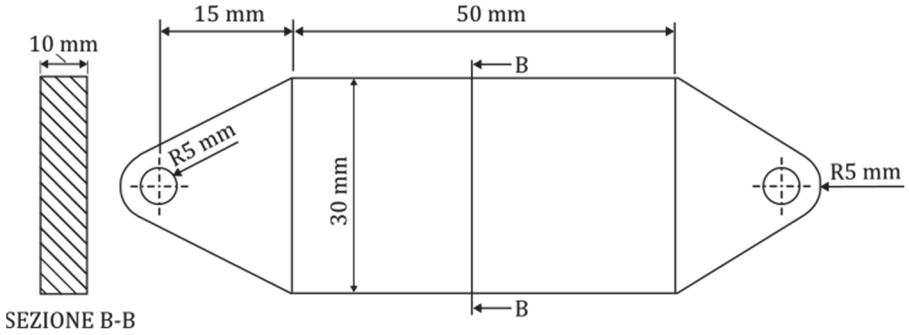

Figure 2. Geometry of the samples used for CNC milling.

Table 2. Summary of Design of Experiments factors.

Factors				Levels			
Name	**Type**	**Units**	**Symbols**	**1**	**2**	**3**	**4**
Rotational speed (n)	Numeric	[rpm]	A	3000	5500	8000	-
Feed rate (V_f)	Numeric	[mm/min]	B	400	600	800	-
Depth of cut (a_p)	Numeric	[mm]	C	0.2	0.4	0.6	0.8

Surface roughness was assessed by measuring a 3×4 mm^2 area (shown in Figure 3a) at the center of the milled surface for each milling condition, using the *Taylor Hobson Ultra 2* roughness tester, equipped with a 50 mm stylus. Subsequently, the gathered surface data underwent processing through *Talymap Silver* software (V4.1). The S_a parameter, defined by Equation (1), was employed to characterize the surface quality (Figure 3b).

$$S_a = \frac{1}{A}\iint_A |S(x,y)|dxdy \quad (1)$$

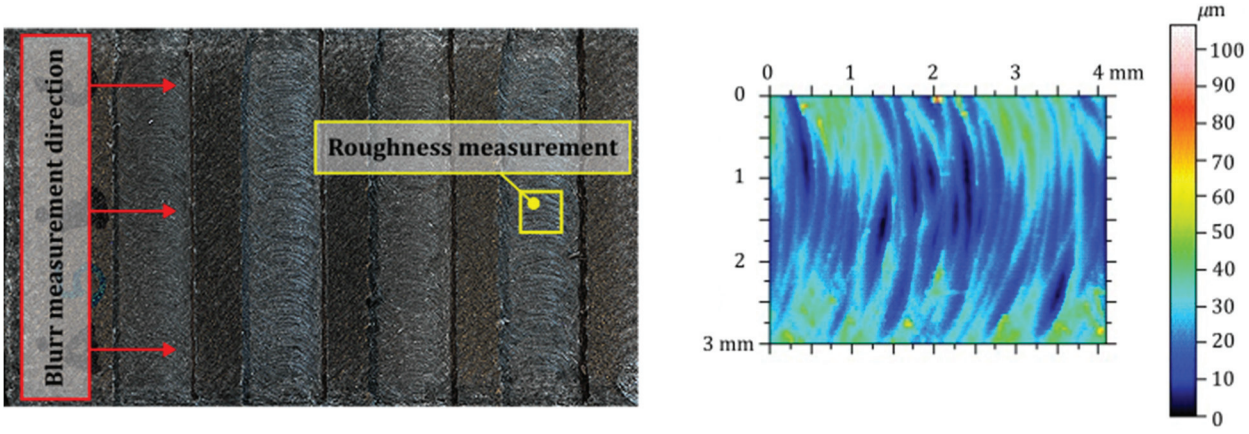

(**a**) (**b**)

Figure 3. (**a**) Machined sample showing the three measured burr directions, (**b**) example measurement of surface roughness Sa (in µm).

To measure the burr height on both sides of each milled surface, three profile measurements were taken perpendicular to the milling direction, evenly spaced at 10 mm intervals, as shown in Figure 3a. The burr height measurements were processed in *Matlab* (version R2024a) using the least-squares method to establish a zero line, providing a reference level for precise evaluation, with the methodology described in [1]. Each measurement was divided into five zones: the non-milled surface zones were utilized to determine a regression line based on points lacking a burr, and the burr's height was calculated by subtracting the coordinate of the highest point on the burr from the corresponding coordinate on the regression line.

3. Results

3.1. Mechanical Properties

Figure 4 displays the nominal stress–strain curves for the examined CF-PETG samples and unreinforced PETG. Using the recorded applied load and measured strain data, Young's modulus (E), Ultimate Tensile Strength (UTS), and Elongation at Break ($A\%$) were determined. These computed values are detailed in Table 3 alongside those for the unreinforced PETG for comparability.

Table 3. Mechanical properties of 3D printed PETG and CF-PETG under different printing orientations.

	Young's Modulus [MPa]		Ultimate Strength [MPa]		Elongation [%]	
	PETG	**CF-PETG**	**PETG**	**CF-PETG**	**PETG**	**CF-PETG**
X	1661.1 ± 30.4	4784.5 ± 37.2	41.9 ± 0.6	46.1 ± 0.7	5.1 ± 1.0	2.4 ± 0.35
Y	1560.8 ± 34.1	5816.8 ± 197.9	38.5 ± 1.2	49.3 ± 1.6	5.3 ± 1.6	2.1 ± 0.31
Z	1233.4 ± 126.2	1186.2 ± 133.7	15.0 ± 1.8	13.2 ± 1.0	1.3 ± 0.1	1.3 ± 0.34

The tensile test results for CF-PETG indicate varied mechanical properties across different printing directions. Among the examined orientations, the Y printing direction notably showed the highest mechanical properties. The X direction demonstrated mechanical properties similar to those of the Y direction, indicating its suitability for achieving desirable mechanical strength. Conversely, the Z direction exhibited inferior mechanical properties in comparison to both the X and Y directions. This disparity can be attributed to

the inherent challenges associated with establishing robust interlayer bonding vertically. In FDM technology, building layers vertically poses difficulties in ensuring adequate adhesion and bonding, leading to the *Z* direction's diminished mechanical attributes, including reduced strength, stiffness, and elongation at break. These findings align with those of prior research by other authors [39], validating the reliability of these conclusions across different studies.

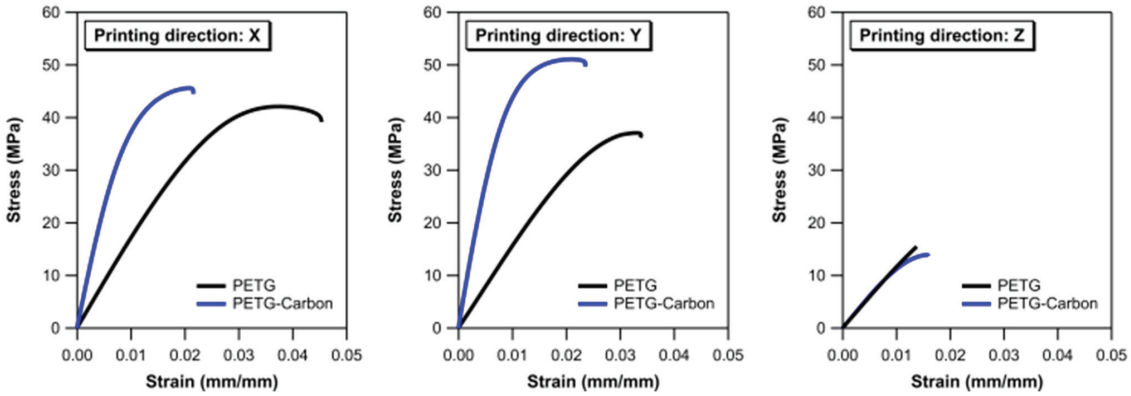

Figure 4. Stress vs. engineering strain for CF-PETG test samples.

Figure 5 presents three bar graphs comparing the mechanical properties of the 3D printed PETG and carbon fiber-reinforced PETG (PETG-Carbon) across three printing directions: *X*, *Y*, and *Z*. Figure 5a illustrates the Young's modulus for both materials in each printing direction. CF-PETG consistently shows a higher Young's Modulus than the unreinforced PETG, with the most significant difference observed in the Y direction. Conversely, PETG exhibits better performance in the *X* direction, while CF-PETG shows better mechanical properties in the *Y* direction. The results in the *Z* direction are similar for both materials. The second graph, presented in Figure 5b, displays the ultimate strength (MPa). Like the Young's Modulus, CF-PETG has a higher ultimate strength in the *X* and *Y* directions, with the Y direction showing the greatest difference. The *Z* direction results are comparable for both materials. Figure 5c depicts elongation (%). In this case, the differences between the two materials are quite evident, with PETG exhibiting higher ductility in the *X* and *Y* directions. The *Z* direction shows the lowest elongation for both materials, a typical outcome due to the layer-by-layer printing process, which often leads to weaker interlayer bonding. This evidence may be linked to the microstructure of the sample printed in the *Z* direction, shown in Figure 6. It can be seen that the short carbon fibers lie within the filament in a plane orthogonal to the applied load. Thus, as they are not aligned with the load direction, fibers do not significantly contribute to the sample's load-bearing capability.

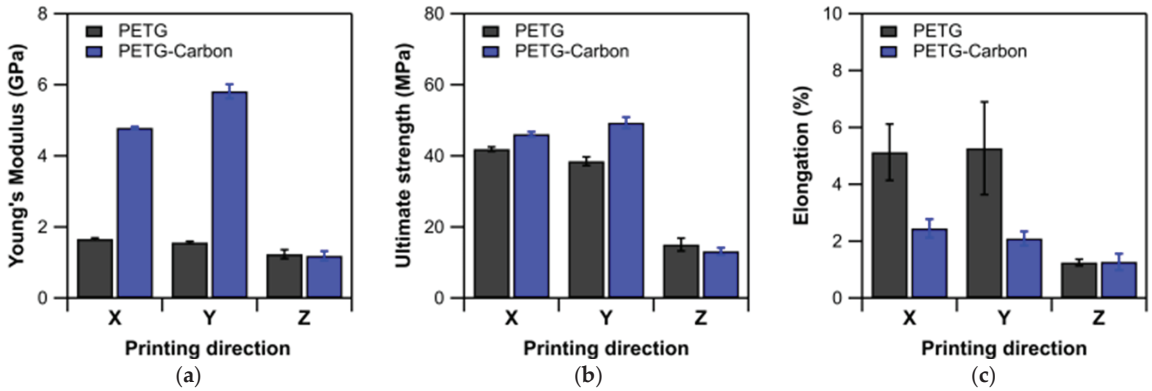

Figure 5. Comparison between the mechanical properties of PETG and CF-PETG among different printing orientations: Young's modulus (**a**), ultimate tensile strength (**b**), elongation (**c**).

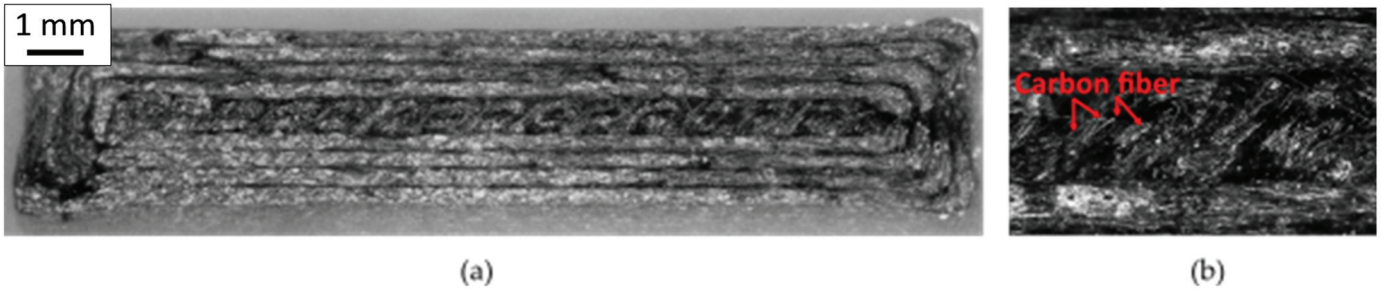

Figure 6. Microstructure of the 3D printed sample in *Z* direction: cross-section (**a**) and detail (**b**).

3.2. ANOVA Analysis of S_a

The CF-PETG and PETG milled surface data, processed with *Talymap Silver* software, allowed us to obtain the S_a parameter for each condition, as indicated above. The S_a values for CF-PETG ranged from 3.04 µm to 7.65 µm, recorded under the conditions of 8000 rpm at a feed rate of 800 mm/min with a 0.2 mm depth of cut and 3000 rpm at a feed rate of 600 mm/min with a 0.6 mm depth of cut, respectively. In the study of the PETG data, surface roughness (S_a) variability was observed within a range of 3.46 µm to 8.79 µm under the conditions of 5500 rpm, 400 mm/min, and 0.2 mm, and 5500 rpm, 800 mm/min, and 0.4 mm. These values were analyzed using *Minitab software* (v. 19) to assess the significance of the effect of each factor on surface quality, using a preset *p*-value threshold of 0.05 to determine statistical relevance. The Pareto plots of the Standardized Effects for the unreinforced PETG (Figure 7a) rank the parameters by their statistical significance. The plot reveals that rotational speed (*A*), feed rate (*B*), and depth of cut (*C*), along with their interactions, significantly affect the surface roughness, except for the combination of rotational speed and depth of cut (*AC*). Among these factors, the feed rate was found to have the most significant influence on the milling process. The chart in Figure 7b ranks the parameters by their statistical significance for CF-PETG, indicating that the rotational speed (*A*), feed rate (*B*), and depth of cut (*C*), along with their interaction (*AC*), significantly influence the response. Among these, the rotational speed was identified as having the most substantial impact on the process.

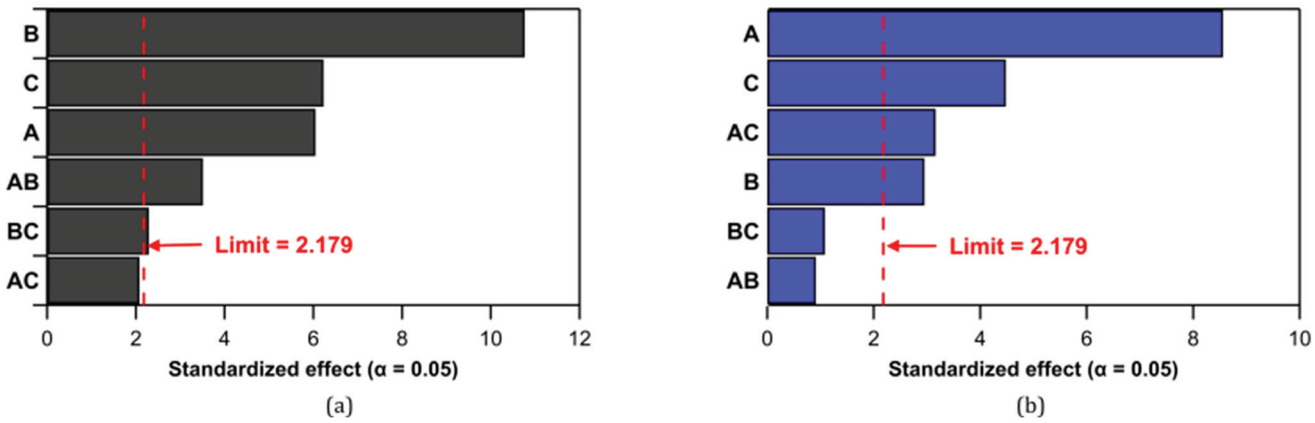

Figure 7. Pareto chart of the Standardized Effects for surface quality (S_a): PETG (**a**) and CF-PETG (**b**).

Figure 8a presents the main effect plot for surface roughness (S_a), delineating the impact of various factors on the milled surface roughness of both PETG and CF-PETG. For PETG, the graph indicates that an increase in rotational speed results in decreased roughness, whereas an increased feed rate and depth of cut contribute to greater roughness. In the case of CF-PETG, the plot distinctly shows a decrease in roughness with higher rotational speeds, achieving the lowest roughness at a medium level. However, a rise in

feed rate and depth of cut correlates with an increase in surface roughness, exhibiting a more linear relationship than for PETG.

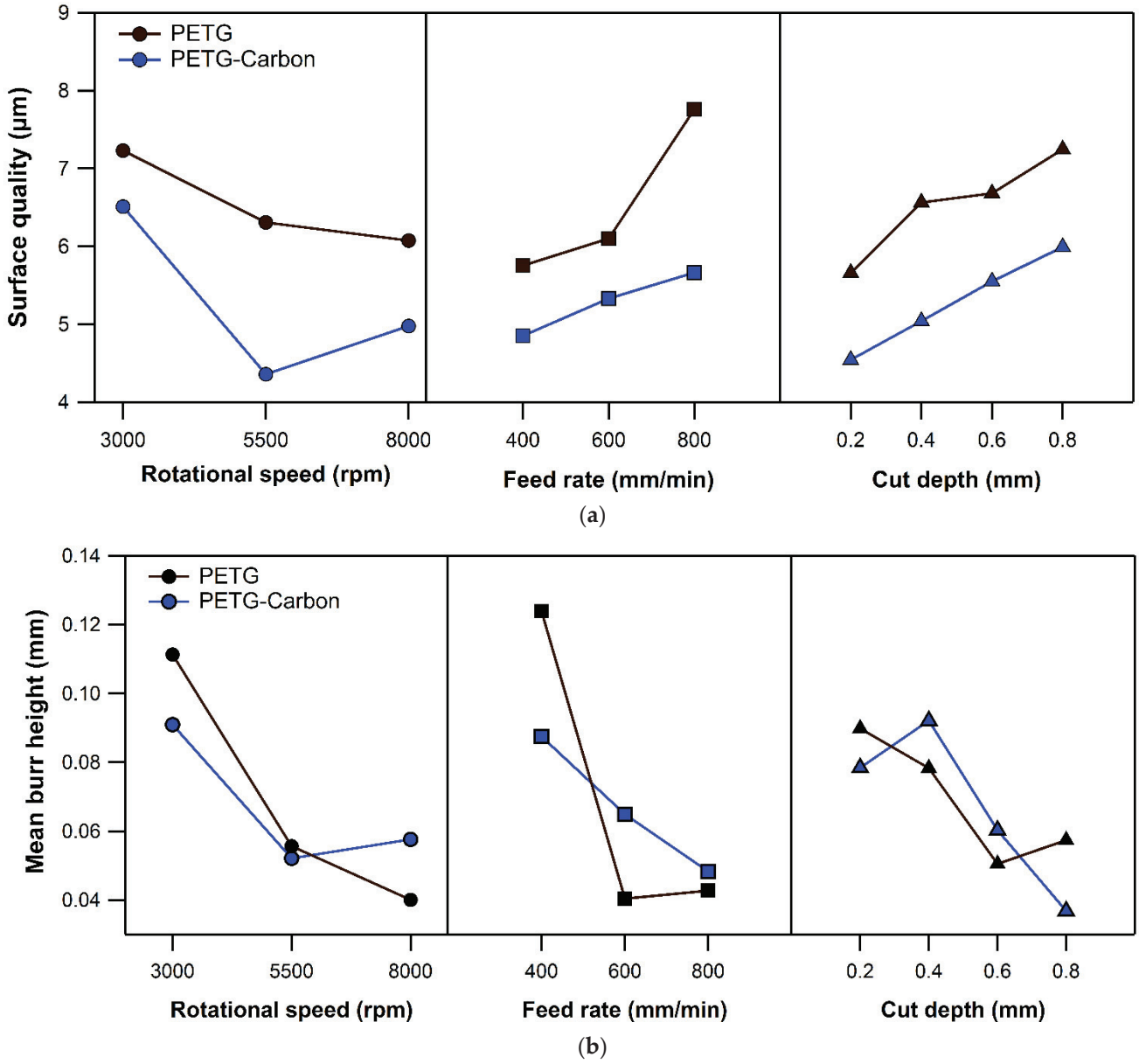

Figure 8. Comparison of roughness (**a**) and burr height (**b**) main effect plots for PETG (black solid line) and CF-PETG (blue solid line). Different markers indicate the effect of each considered process parameters: circles for the rotational speed, squares for feed rate, and tringles for depth of cut.

3.3. Burr Height Response

Burr formation was evaluated on both sides of the milled surface, with each condition undergoing three measurements. The burr height response was analyzed using an ANOVA test, which took into account the mean values from both sides and included three replicates for accuracy. The outcomes of burr height are depicted in Figure 9.

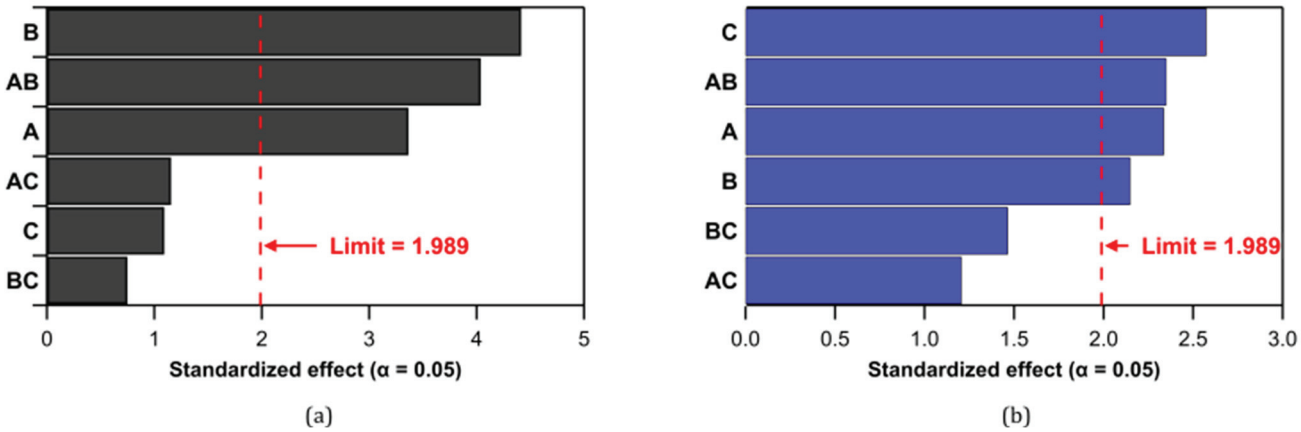

Figure 9. Pareto chart of the Standardized Effects for burr height: PETG (**a**) and CF-PETG (**b**).

The Pareto diagrams of the Standardized Effects depicted in Figure 9a show the results for the unreinforced PETG. It indicates that only three parameters have a statistically significant influence on the process. They are ranked in order of impact as follows: feed rate (B), the combination of feed rate and rotational speed (AB), and rotational speed (A).

In Figure 9b, the Pareto chart of the Standardized Effects shows the results for CF-PETG; four parameters are identified as having a statistically significant impact on the process, listed in order of their effect as follows: depth of cut (C), the interaction between feed rate and rotational speed (AB), rotational speed (A), and feed rate (B). Figure 8b, however, shows the main effect plot for burr height, illustrating the relationship between the process parameters and the range of burr heights observed. The plot reveals that, in the case of PETG, increasing all process parameters typically leads to a decrease in burr height. However, it is important to note that, at elevated feed rates and depths of cut, there is a slight increase in burr height. Similarly, for CF-PETG, an overall increase in the process parameters typically leads to a reduction in burr height. However, it is notable that, at the medium level of rotational speed, the minimum burr height is achieved, and at the second level of depth of cut, there is a slight increase in burr height.

In summary, within the studied range, reducing burr formation for CF-PETG necessitates operating at higher levels for each parameter, except for rotational speed, for which the minimum burr height is achieved at a medium level. Conversely, achieving a smoother surface involves milling at lower feed rates and depths of cut, coupled with medium rotational speeds. Hence, the optimal settings for minimizing burrs and refining surface roughness distinctly differ and exhibit an inverse relationship, except for the rotational speed. While diminishing burr formation calls for working at elevated parameter levels within the range studied, obtaining a smoother surface requires lower feed rates and depths of cut. Thus, striking a balance among these parameters is crucial to achieving desired outcomes for both burr formation and surface roughness in the machining process. For instance, aiming to enhance the surface quality of a 3D printed part necessitates lower feed rates and depths of cut. However, it is important to note that this condition tends to yield higher burr formation, potentially requiring an additional process to eliminate the burrs. This implication affects the overall process time, as lower V_f and a_p also mean reduced material removal per unit time, along with added time to remove burrs post-milling.

4. Discussion and Conclusions

The results indicate a pronounced impact of the milling parameters on the responses, with the optimal settings for minimizing surface roughness not coinciding with those for mitigating burr formation. A comparative evaluation of the machinability of standard PETG under analogous conditions further underscored the differential effects of carbon fibers on machining outcomes. This study on 3D printed PETG and CF-PETG yields several key findings, summarized as follows:

- Mechanical properties: CF-PETG consistently exhibited a higher Young's modulus in the *X* and *Y* printing directions compared to the unreinforced PETG and a comparable value in the *Z* direction. Among the CF-PETG samples, the most significant difference was observed in the samples printed along the *Y* direction, indicating superior stiffness in this orientation for CF-PETG. In contrast, PETG showed a higher E modulus in the *X* direction, suggesting directional variability in material properties. Similar to the Young's Modulus, CF-PETG demonstrated a higher ultimate strength in the *X* and *Y* directions, with the *Y* direction showing the most notable disparity when compared with PETG. This finding implies that CF-PETG is mechanically stronger in these two directions. For both materials, the results in the *Z* direction were comparable, highlighting the uniformity in strength across the layering axis. The elongation data revealed pronounced differences between the two materials. PETG showed higher ductility in the *X* and *Y* directions. However, both materials exhibited the lowest elongation in the *Z* direction. This outcome is typical for layer-by-layer printed objects and is attributed to weaker interlayer bonding, which restricts elongation in this direction. The data suggest that the addition of carbon fibers to PETG significantly enhances its mechanical properties in terms of stiffness and strength, particularly in the *X* and *Y* directions. This enhancement makes CF-PETG a suitable material for applications where high structural rigidity and load-bearing capacity are required. However, for applications where a higher degree of deformation is necessary before failure, unreinforced PETG might be the preferable choice due to its higher ductility. These results are consistent with the findings reported in the existing literature by other researchers [40].
- Roughness: Figure 8a presents a comparison of the machinability between PETG and CF-PETG in terms of surface roughness. The main effect plot in Figure 8a shows that incorporating carbon fibers into PETG consistently yields a lower surface roughness across all tested conditions. Notably, as the rotational speed increases from 3000 to 8000 rpm, CF-PETG exhibits decreased surface roughness, with the lowest roughness at the medium level. PETG, however, shows reduced roughness at the highest rotational speed. Roughness increases for both materials as the feed rate increases, but CF-PETG maintains a lower roughness at all feed rates, suggesting better performance under increased feed rates in terms of maintaining a smoother surface. Both materials experience increased surface roughness with a greater depth of cut; however, CF-PETG's roughness remains lower at each depth of cut level. Nonetheless, CF-PETG consistently maintains a lower roughness compared to PETG in all the studied conditions, highlighting its ability to retain a smoother surface even at higher material removal rates. Overall, the main effect plot suggests that CF-PETG offers a machining advantage over PETG, with better surface finishes achievable under a broader range of machining conditions. This could be attributed to the enhanced material properties provided by the carbon fiber reinforcement, such as increased rigidity and thermal stability, which contribute to a more consistent cutting action and less material deformation during the machining process.
- Burr height: Figure 8b illustrates the mean burr height of the 3D printed PETG and PETG reinforced with short carbon fibers (CF-PETG). Burr height, a critical quality attribute in machining and finishing, affects the fit and function of parts and, if necessary, must be removed with additional processing. Both materials show decreased burr height with increased rotational speed, but CF-PETG demonstrates a minimum burr height at a medium level and a consistently lower burr height compared to PETG, except for at the highest rotational speed. A higher feed rate generally leads to reduced burr height for both materials, with PETG showing a more pronounced decrease between lower and medium levels before stabilizing, and CF-PETG presenting a gradual, linear reduction. This behavior could result from the carbon fibers' reinforcing effect, which might offer more cutting stability. Concerning depth of cut, burr height generally decreases for both materials but with distinct

patterns. PETG's burr height diminishes until 0.6 mm and then slightly rises, while CF-PETG experiences an initial increase in burr height from 0.2 to 0.4 mm before linearly decreasing with greater depths of cut. Overall, the data suggest that both PETG and CF-PETG exhibit similar tendencies in burr formation across the range of machining parameters. This indicates that the addition of carbon fibers to PETG does not significantly alter the material's propensity for burr formation.

- Optimal milling parameters and implications for manufacturing: The lower roughness of CF-PETG might be attributed to the carbon fibers reinforcing the material, promoting a smoother surface by providing uniformity and reducing deformation during milling. These fibers could also enhance the material's structural stability, resisting surface irregularities during machining. Such data are invaluable for applications where surface finish is paramount, suggesting CF-PETG as the preferable material for achieving a finer surface quality. In terms of rotational speed, CF-PETG is optimal at 5500 rpm, showing reduced roughness and burr height, indicative of a cleaner cut and superior finishing surface. For PETG, a higher rotational speed is advisable to minimize both burr and roughness. CF-PETG is less sensitive to feed rate variations, maintaining lower roughness levels compared to PETG while showing comparable burr heights, albeit with inverse trends. Overall, CF-PETG exhibits preferable machining characteristics across all the studied parameters. It consistently achieves a lower surface roughness while also maintaining a burr formation comparable to that of PETG. This advantage enables the production of parts with superior quality, considering not only the improved surface finish but also the enhanced mechanical properties, and it represents an essential benefit for industries where both attributes are critical. Consequently, opting for 3D printed CF-PETG and then milling operations could be a strategic choice for manufacturers aiming to enhance both the quality and the efficiency of their production processes.

Achieving an optimal balance among rotational speed, feed rate, and depth of cut is crucial for the machining of 3D printed parts to optimize surface roughness and burr height. Lower feeds and shallower cuts can improve surface finish but may increase burr formation, requiring additional deburring processes. Such adjustments, while enhancing surface quality, could lower the material removal rate and prolong the total processing time due to the extra deburring step after machining. These conclusions highlight the potential of CF-PETG in enhancing the quality and efficiency of 3D printing applications, especially where surface finish and mechanical properties are critical.

These study results help find the optimal conditions for milling parameters to achieve not only the desired surface quality but also dimensional accuracy. Milling allows for precise material removal, which can correct dimensional inaccuracies introduced during the printing process. This is especially important for parts with tight tolerances. Milling can help remove excess material and layers from the surface of a 3D printed part, effectively smoothing rough surfaces caused by layering in FDM printing. This combination of processes holds promise across various industrial sectors such as the aerospace and automotive. It offers a cost-effective solution for producing functional prototypes or customized components. Furthermore, in sectors where timely repair and maintenance are crucial, this approach can facilitate the on-demand manufacturing of replacement parts, thereby minimizing downtime and inventory expenses.

Author Contributions: Conceptualization, M.E.M., M.C. and P.B.; investigation, G.L., P.B., R.E.M., M.C., M.E.M. and F.A.; writing—original draft preparation, G.L., P.B., R.E.M., M.C., M.E.M. and F.A.; writing—review and editing, G.L., M.C. and M.E.M. All authors have read and agreed to the published version of the manuscript.

Funding: This work was developed within the framework of the project eINS—Ecosystem of Innovation for Next Generation Sardinia (cod. ECS 00000038)—funded by the Italian Ministry for Research and Education (MUR) under the National Recovery and Resilience Plan (PNRR)-MISSION

4 COMPONENT 2, "From research to business" INVESTMENT 1.5, "Creation and strengthening of Ecosystems of innovation" and construction of "Territorial R&D Leaders".

Data Availability Statement: The data presented in the paper are available upon request.

Conflicts of Interest: The authors declare no conflicts of interest.

References

1. El Mehtedi, M.; Buonadonna, P.; Carta, M.; El Mohtadi, R.; Marongiu, G.; Loi, G.; Aymerich, F. Effects of milling parameters on roughness and burr formation in 3D-Printed PLA Components. *Procedia Comput. Sci.* **2023**, *217*, 1560–1569. [CrossRef]
2. Boparai, K.S.; Singh, R.; Singh, H. Development of rapid tooling using Fused Deposition Modeling: A review. *Rapid Prototyp. J.* **2016**, *22*, 281–299. [CrossRef]
3. Clini, P.; El Mehtedi, M.; Nespeca, R.; Ruggeri, L.; Raffaelli, E. A Digital Reconstruction Procedure from Laser Scanner Survey to 3d Printing: The Theoretical Model of the Arch of Trajan (Ancona). *SCIRES-IT-Sci. Res. Inf. Technol.* **2018**, *7*, 1–12. [CrossRef]
4. Wang, X.; Jiang, M.; Zhou, Z.; Gou, J.; Hui, D. 3D Printing of Polymer Matrix Composites: A Review and Prospective. *Compos. Part B Eng.* **2017**, *110*, 442–458. [CrossRef]
5. Guessasma, S.; Belhabib, S.; Nouri, H. Printability and Tensile Performance of 3D Printed Polyethylene Terephthalate Glycol Using Fused Deposition Modelling. *Polymers* **2019**, *11*, 1220. [CrossRef] [PubMed]
6. Petrov, P.; Agzamova, D.; Pustovalov, V.; Zhikhareva, E.; Saprykin, B.; Chmutin, I.; Shmakova, N. Research into the Effect of the 3D-Printing Mode on Changing the Properties of PETG Transparent Plastic. In Proceedings of the ESAFORM 2021 24th International Conference on Material Forming, Liege, Belgium, 14–16 April 2021. [CrossRef]
7. Tsai, H.-H.; Wu, S.-J.; Wu, Y.-D.; Hong, W.-Z. Feasibility Study on the Fused Filaments of Injection-Molding-Grade Poly(Ethylene Terephthalate) for 3D Printing. *Polymers* **2022**, *14*, 2276. [CrossRef] [PubMed]
8. Moreno Nieto, D.; Alonso-García, M.; Pardo-Vicente, M.-A.; Rodríguez-Parada, L. Product Design by Additive Manufacturing for Water Environments: Study of Degradation and Absorption Behavior of PLA and PETG. *Polymers* **2021**, *13*, 1036. [CrossRef] [PubMed]
9. Li, W.; Zhao, X.; Liu, Y.; Ouyang, Y.; Li, W.; Chen, D.; Ye, D. Hygrothermal aging Behavior and Flexural Property of Carbon Fiber-Reinforced Polyethylene Terephthalate Glycol Composites. *Text. Res. J.* **2023**, *93*, 1005–1018. [CrossRef]
10. Brydson, J.A. *Plastics Materials*; Elsevier: Amsterdam, The Netherlands, 1999; ISBN 978-0-08-051408-6.
11. Kim, H.S.; Huang, S. S-N Curve Characterisation for Composite Materials and Prediction of Remaining Fatigue Life Using Damage Function. *J. Compos. Sci.* **2021**, *5*, 76. [CrossRef]
12. Mansour, M.; Tsongas, K.; Tzetzis, D.; Antoniadis, A. Mechanical and Dynamic Behavior of Fused Filament Fabrication 3D Printed Polyethylene Terephthalate Glycol Reinforced with Carbon Fibers. *Polym.-Plast. Technol. Eng.* **2018**, *57*, 1715–1725. [CrossRef]
13. Rodríguez-Panes, A.; Claver, J.; Camacho, A. The Influence of Manufacturing Parameters on the Mechanical Behaviour of PLA and ABS Pieces Manufactured by FDM: A Comparative Analysis. *Materials* **2018**, *11*, 1333. [CrossRef] [PubMed]
14. Vinyas, M.; Athul, S.J.; Harursampath, D.; Nguyen Thoi, T. Mechanical Characterization of the Poly Lactic Acid (PLA) Composites Prepared through the Fused Deposition Modelling Process. *Mater. Res. Express* **2019**, *6*, 105359. [CrossRef]
15. Selvam, A.; Mayilswamy, S.; Whenish, R.; Velu, R.; Subramanian, B. Preparation and Evaluation of the Tensile Characteristics of Carbon Fiber Rod Reinforced 3D Printed Thermoplastic Composites. *J. Compos. Sci.* **2021**, *5*, 8. [CrossRef]
16. Durgashyam, K.; Indra Reddy, M.; Balakrishna, A.; Satyanarayana, K. Experimental Investigation on Mechanical Properties of PETG Material Processed by Fused Deposition Modeling Method. *Mater. Today Proc.* **2019**, *18*, 2052–2059. [CrossRef]
17. Kovan, V.; Tezel, T.; Topal, E.S.; Camurlu, H.E. Printing Parameters Effect on Surface Characteristics of 3D Printed PLA Materials. *Mach. Technol. Mater.* **2018**, *12*, 266–269.
18. Vasudevarao, B.; Natarajan, D.P.; Henderson, M.; Razdan, A. Sensitivity of RP Surface Finish to Process Parameter Variation 251. 2000. Available online: https://repositories.lib.utexas.edu/items/649c6e91-1b20-4a36-8cb2-5350cda868be (accessed on 27 December 2023).
19. Vidakis, N.; David, C.; Petousis, M.; Sagris, D.; Mountakis, N.; Moutsopoulou, A. The Effect of Six Key Process Control parameters on the Surface Roughness, Dimensional Accuracy, and Porosity in Material Extrusion 3D Printing of Polylactic Acid: Prediction Models and Optimization Supported by Robust Design Analysis. *Adv. Ind. Manuf. Eng.* **2022**, *5*, 100104. [CrossRef]
20. Barrios, J.M.; Romero, P.E. Improvement of Surface Roughness and Hydrophobicity in PETG Parts Manufactured via Fused Deposition Modeling (FDM): An Application in 3D Printed Self–Cleaning Parts. *Materials* **2019**, *12*, 2499. [CrossRef] [PubMed]
21. Lalegani Dezaki, M.; Mohd Ariffin, M.K.A.; Ismail, M.I.S. Effects of CNC Machining on Surface Roughness in Fused Deposition Modelling (FDM) Products. *Materials* **2020**, *13*, 2608. [CrossRef] [PubMed]
22. Kadhum, A.H.; Al-Zubaidi, S.; Abdulkareem, S.S. Effect of the Infill Patterns on the Mechanical and Surface Characteristics of 3D Printing of PLA, PLA+ and PETG Materials. *ChemEngineering* **2023**, *7*, 46. [CrossRef]
23. Mat, M.A.C.; Ramli, F.R.; Alkahari, M.R.; Sudin, M.N.; Abdollah, M.F.B.; Mat, S. Influence of Layer Thickness and Infill Design on the Surface Roughness of PLA, PETG and Metal Copper Materials. *Proc. Mech. Eng. Res. Day* **2020**, *7*, 64–66.
24. Hadeeyah, A.; Jamhour, H.; Emhemed, I.; Alhadar, F.; Masmoudi, N.; Wali, M. The Impact Of Carbon Fiber on the Surface Properties of the 3D Printed PEGT Product. *J. Pure Appl. Sci.* **2023**, *22*, 23–27. [CrossRef]
25. Tunçel, O. The Influence of the Raster Angle on the Dimensional Accuracy of FDM-Printed PLA, PETG, and ABS TENSILE specimens. *Eur. Mech. Sci.* **2024**, *8*, 11–18. [CrossRef]

26. Bolat, Ç.; Ergene, B. An Investigation on Dimensional Accuracy of 3D Printed PLA, PET-G and ABS Samples with Different Layer Heights. *Çukurova Üniversitesi Mühendislik Fakültesi Derg.* **2022**, *37*, 449–458. [CrossRef]
27. Alexopoulou, V.E.; Christodoulou, I.T.; Markopoulos, A.P. Effect of Printing Speed and Layer Height on Geometrical Accuracy of FDM-Printed Resolution Holes of PETG Artifacts. *Eng. Proc.* **2022**, *24*, 11. [CrossRef]
28. Santana, L.; Lino Alves, J.; Da Costa Sabino Netto, A. Dimensional analysis of pla and petg parts built by open source extrusion-based 3d printing. In Proceedings of the 10° Congresso Brasileiro de Engenharia de Fabricação, São Carlos, SP, Brazil, 5–7 August 2019.
29. Bhandari, S.; Lopez-Anido, R.A.; Gardner, D.J. Enhancing the Interlayer Tensile Strength of 3D Printed Short Carbon Fiber Reinforced PETG and PLA Composites via Annealing. *Addit. Manuf.* **2019**, *30*, 100922. [CrossRef]
30. Pămărac, R.G.; Petruse, R.E. Study Regarding the Optimal Milling Parameters for Finishing 3D Printed Parts from ABS and PLA Materials. *ACTA Univ. Cibiniensis* **2018**, *70*, 66–72. [CrossRef]
31. Pandey, P.M.; Reddy, N.V.; Dhande, S.G. Improvement of Surface Finish by Staircase Machining in Fused Deposition Modeling. *J. Mater. Process. Technol.* **2003**, *132*, 323–331. [CrossRef]
32. Lalehpour, A.; Barari, A. Post processing for Fused Deposition Modeling Parts with Acetone Vapour Bath. *IFAC-PapersOnLine* **2016**, *49*, 42–48. [CrossRef]
33. Altin Karataş, M.; Gökkaya, H. A Review on Machinability of Carbon Fiber Reinforced Polymer (CFRP) and Glass Fiber Reinforced Polymer (GFRP) Composite Materials. *Def. Technol.* **2018**, *14*, 318–326. [CrossRef]
34. Cococcetta, N.M.; Pearl, D.; Jahan, M.P.; Ma, J. Investigating Surface Finish, Burr Formation, and Tool Wear during Machining of 3D Printed Carbon Fiber Reinforced Polymer Composite. *J. Manuf. Process.* **2020**, *56*, 1304–1316. [CrossRef]
35. Guo, C.; Liu, X.; Liu, G. Surface Finishing of FDM-Fabricated Amorphous Polyetheretherketone and Its Carbon-Fiber-Reinforced Composite by Dry Milling. *Polymers* **2021**, *13*, 2175. [CrossRef] [PubMed]
36. Vallejo, J.; García-Plaza, E.; Núñez, P.J.; Chacón, J.M.; Caminero, M.A.; Romero, A. Machinability Analysis of Carbon Fibre Reinforced PET-Glycol Composites Processed by Additive Manufacturing. *Compos. Part A Appl. Sci. Manuf.* **2023**, *172*, 107561. [CrossRef]
37. Fabricación por Adición de Capas en Materiales Plásticos. Fabricación Aditiva. Preparación de Probetas. 2012. Available online: https://www.en-standard.eu/une-116005-2012-manufacturing-by-additive-of-caps-on-plastics-additive-manufacturing-preparation-of-test-pieces/ (accessed on 1 March 2024).
38. García-Domínguez, A.; Claver, J.; Camacho, A.M.; Sebastián, M.A. Considerations on the Applicability of Test Methods for Mechanical Characterization of Materials Manufactured by FDM. *Materials* **2020**, *13*, 28. [CrossRef] [PubMed]
39. Mahesh, V.; Joseph, A.S.; Mahesh, V.; Harursampath, D.; Vn, C. Investigation on the Mechanical Properties of Additively Manufactured PETG Composites Reinforced with OMMT Nanoclay and Carbon Fibers. *Polym. Compos.* **2021**, *42*, 2380–2395. [CrossRef]
40. Kannan, S.; Ramamoorthy, M.; Sudhagar, P.E.; Gunji, B. Mechanical Characterization and Vibrational Analysis of 3D Printed PETG and PETG Reinforced with Short Carbon Fiber. In *AIP Conference Proceedings*; AIP Publishing: Melville, NY, USA, 2020; Volume 2270.

Journal of
Composites Science

MDPI

Article

Innovative Wedge Anchorage for CFRP Plates: Development and Testing

Mustafa Alhusain [1,2,*] and Adil Al-Mayah [2,3]

[1] Department of Mechanical Engineering, King Faisal University, Al-Ahsa 31982, Saudi Arabia
[2] Department of Mechanical & Mechatronics Engineering, University of Waterloo, Waterloo, ON N2L 3G1, Canada
[3] Department of Civil and Environmental Engineering, University of Waterloo, Waterloo, ON N2L 3G1, Canada; aalmayah@uwaterloo.ca
* Correspondence: malhusain@kfu.edu.sa

Abstract: Gripping prestressed carbon fiber-reinforced polymers (CFRPs) in structural strengthening applications is challenging due to CFRPs' susceptibility to lateral loading. This paper presents a reliable and reusable wedge anchorage for gripping CFRP plates that are 50 mm wide and 1.2 mm thick. The cylindrical anchorage, which is 75 mm long and 76.2 mm in diameter, consists of an external steel barrel, two internal steel wedges, and two soft copper sleeves. The barrel-wedge interface is designed using an innovative arc–linear configuration, through which the desired stress distribution is attained, preventing stress concentration and the premature failure of the CFRP plate. The wedge anchorage was experimentally tested by applying a displacement-controlled tensile load of 0.6 mm/min until the complete fracture of the CFRP plate. The anchorage's performance was examined under distinct installation conditions by applying different presetting levels: high (40–120 kN) and low (hammering) presetting. It was observed that the anchorage successfully prevented CFRP premature failure in all tests by achieving an average tensile loading of 172.3 (±5.7) kN, exceeding its reported tensile strength of 168 kN (2800 MPa). Minor CFRP displacements of 6.26 (±0.75) mm and 3.33 (±0.16) mm were recorded under low and high presetting levels, respectively. Similarly, the CFRP slippage relative to the wedges for the low and high presetting tests was only 1.18 (±0.75) mm and 0.33 (±0.15) mm, respectively. Also, only minor scratches were observed in the wedge–barrel interface, indicating the absence of extensive plastic deformation.

Keywords: carbon fiber-reinforced polymer (CFRP) plate; CFRP fracture; concrete damage; concrete repair; prestressing; post-tensioning; wedge anchorage

1. Introduction

Numerous concrete structures require strengthening and repair due to the growing applied loads and reinforcement corrosion [1,2]. According to the American Society of Civil Engineering (ASCE) report (2017), infrastructure repair is anticipated to cost the United States about USD 2 trillion by 2025 [3]. The total replacement of the degraded concrete structures is not practical due to the associated costs and time; hence, the efficient strengthening of concrete structures with durable and corrosion-resistant retrofitting materials, such as carbon fiber-reinforced polymers (CFRPs), is essential. In addition to its high corrosion resistance, CFRPs have lightweight, superior tensile strength and exceptional fatigue properties, making them an excellent material for retrofitting concrete structures [4,5].

The overall performance of concrete structures can be enhanced by mounting CFRPs to its surface through adhesive bonding [6] or mechanical linkage [7]. While adhesive bonding is easy to apply, it is prone to CFRP delamination, particularly in hot environments [8]. On the other hand, properly designed mechanical linkages, such as anchorages, can effectively grip CFRP reinforcement, preventing delamination [9]. As reported by Al-Mahaidi and Kalfat (2010), using FRP anchorages increased the bond strength between FRP and concrete

from about 5 MPa to 11.3 MPa, improving the delamination resistance and enabling higher prestressing levels [10]. Also, utilizing the high tensile strength of CFRP through prestressing can enhance the load-carrying capacity of concrete structures [11–14]. Hong and Park (2017) observed that increasing CFRPs' prestressing level from 20% to 60% improved the flexural concrete-cracking load from 33.5 kN to 54.1 kN [11]. Similarly, Peng et al. (2016) reported that subjecting the CFRP reinforcement to pre-tension stress of 1000 MPa increased the concrete-cracking load from 18 kN to 60 kN [14]. However, prestressing CFRPs without causing premature failure is challenging due to their vulnerability to lateral loads [15–17]. Thus, several anchorage systems have been developed to grip CFRP elements effectively, including resin-potted [18–22], clamp [23,24], and wedge anchorages [25–27].

Resin-potted anchorage is a bond-based system consisting mainly of a steel sleeve and a resin that is made of an adhesive material or an expansive cement [18,19]. Zhang and Benmokrane (2004) reported that resin-potted anchorage can effectively grip CFRP elements without causing premature failure when a bonding anchorage length of 250 mm is provided [21]. Nonetheless, an adequate bond length is needed to reach CFRPs' full strength without experiencing bond failure. As observed by Puigvert et al. (2014), increasing the bond length from 200 mm to 460 mm enhanced the tensile failure load from 58.7 kN to 110.7 kN [22]. In addition to its bond length requirement, an adequate curing time must be provided to attain its full gripping strength [28].

The clamp anchorage is another system utilized for gripping CFRP plates. It is generally composed of two steel clamps and a number of bolts. As reported by Bengar and Shahmansouri (2020), gripping CFRP plates using clamp anchorages instead of adhesive bonding improved the flexural strength of concrete, increasing its failure load from 206 kN to 255.3 kN [29]. Unlike the resin-potted anchorage, the clamp anchorage is a friction-based system that requires no curing time, making the installation process much faster. However, the clamp anchorage normally produces a uniform CFRP confinement (i.e., lateral stress) due to the even fastening of its bolts, resulting in stress concentration and premature CFRP failure [30]. Although it is possible to fasten the bolts to different degrees to minimize the stress concentration, a precise and adequate clamping force is essential to maintain the performance of the anchorage.

Similarly, the wedge anchorage is a friction-based system made of an external steel barrel, internal wedges, and soft sleeves. The wedge anchorage can produce a variable (non-uniform) CFRP confinement through the interference between its barrel and wedges, preventing stress concentration and premature CFRP failure [31]. As reported by Al-Mayah et al. (2001) and Han et al. (2017), wedge anchorages can utilize CFRPs' full tensile strength without causing premature CFRP failure [26]. Also, the onsite prestressing of CFRP reinforcements using wedge anchorages is relatively fast due to its self-seating mechanism. During the prestressing process, the CFRP plate is pre-tensioned using a hydraulic jack until the required prestressing level is attained, after which the wedge anchorage is assembled through hammering [32]. As the applied tensile load is gradually released, the CFRP plate drives the wedges further into the barrel, resulting in a firm CFRP grip through the anchorage's self-seating mechanism with a slight prestress loss. In addition to being reliable for gripping CFRP reinforcement, the wedge anchorage is reusable, compact in size, and easy to install, making it an excellent candidate for further research.

Most currently developed wedge anchorages were designed to grip circular FRP tendons. Little attention has been paid to developing wedge anchorages for CFRP plates. Therefore, the main objective of this paper is to present an innovative, compact, and reusable wedge anchorage for CFRP plates. Also, the performance of the developed anchorage system was experimentally tested under different presenting levels to demonstrate its reliability, reusability, and cost-effectiveness in field applications.

2. Test Elements

2.1. CFRP Plate

Unidirectional CFRP plates that are 1000 mm long, 50 mm wide, and 1.2 mm thick were tested. The plate has a high tensile strength of 2800 MPa, an excellent tensile strength-to-weight ratio of 1867 kN·m/kg, and a shear strength of 100 MPa. However, it has low lateral tensile and compressive strengths of 62 MPa and 350 MPa, respectively, making it vulnerable to transverse stress.

2.2. Copper Sleeves

Two soft copper sleeves that are 75 mm long, 50 mm wide, and 0.81 mm thick were placed between the two wedges and the CFRP plate to maximize the actual contact area, improve gripping, minimize stress concentration, and prevent the premature failure of CFRP [30,33]. Soft copper sleeves have been proven to enhance CFRP gripping [34], attributed to their role in filling surface asperities, resulting in better gripping at the CFRP-sleeve and wedge-sleeve interfaces. Hence, the copper sleeves were heat-treated at a temperature of 500 °C for an hour and then air-cooled before testing. A new set of disposable copper sleeves was used in each test to maintain the anchorage's performance, as the sleeves are expected to experience considerable plastic deformation. This, however, has little impact on the anchorage's installation cost, given the availability of the sleeve material with the required dimensions at a low cost.

2.3. Wedge Anchorages

Two wedge anchorages were used, namely the developed and dead-end systems. Both anchorages are generally similar; however, the dead-end is larger in length and diameter than the developed anchorage. The developed wedge anchorage consists of two identical wedges and one barrel. The novelty of the developed wedge anchorage is its unique arc–linear interface between the barrel and the wedges. The new configuration comprises two segments: an arc segment near the loading end (Edge 1) and a linear segment close to the presetting end (Edge 2), as illustrated in Figure 1. The arc segment of the interface is used to gradually increase the interference between the wedges and the barrel, creating a stronger grip of the CFRP plate. On the other hand, the linear segment is utilized to maintain the interference within the desired range to mitigate high stress and prevent plastic deformation of the elements. Also, it was observed through finite element (FE) modeling that using identical linear segments (e.g., identical slope) improved the anchorage performance [35]; thus, the wedges and the barrel were designed with identical linear segments.

The developed wedge anchorage is 70 mm in length and 76.2 in diameter. The radius for the arc-segment of 1750 mm was determined as appropriate for improving the performance after conducting an extensive numerical investigation using a verified finite element model [35]. Also, the linear segments of the wedges and the barrel were designed with identical linear segments with the same suitable slope that was determined using FE modeling. The best-performing dimensions of the developed anchorage are presented in Figure 1.

It is recommended to manufacture the anchorage from 440C stainless steel for field usage since it has high yield and tensile strengths and excellent corrosion resistance [36]. However, in this paper, the wedges and barrel were manufactured from heat-treated 4140 steel, which has comparable yield and tensile strengths of 1896 MPa and 1965 MPa, respectively. Also, the wedges and the barrel were made of the same material to minimize surface ploughing [37].

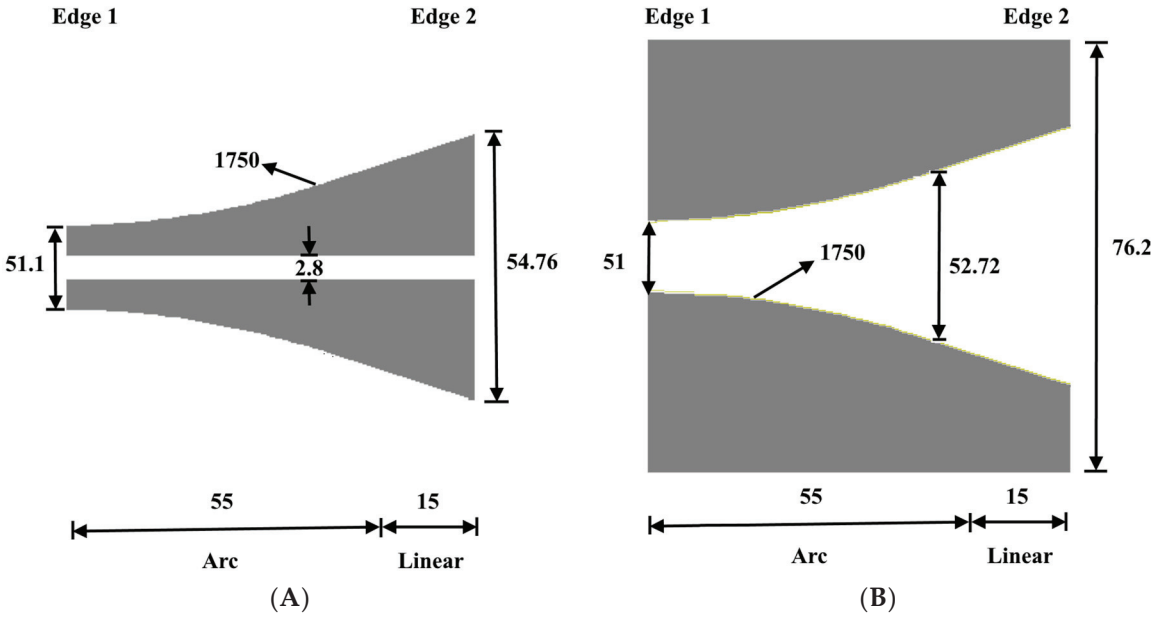

Figure 1. Dimensions of the anchorage's (**A**) wedges and (**B**) barrel in mm.

3. Test Procedures and Instrumentations

3.1. Part Assembly

The CFRP plate, the copper sleeves, the dead-end anchorage, and the developed wedge anchorage were carefully cleaned using acetone before assembly to remove any undesired particles, such as debris and lubrication from the previous test. The CFRP plate, sleeves, and wedges were carefully assembled and gripped using a C-clamp, as shown in Figure 2, before applying a high-pressure lubricant to the wedge-barrel interface to facilitate the movement of the core elements (CFRP plate, sleeves, and wedges) into the barrel. The wedges were then carefully hammered to insert the core elements into the barrel, as illustrated in Figure 3. It is worth noting that misassembling the elements, such as uneven insertion of the wedges, can alter the stress distribution within the CFRP plate and may affect anchorage performance. Thus, a digital vernier caliper was used to confirm the even placement of the wedges into the barrel.

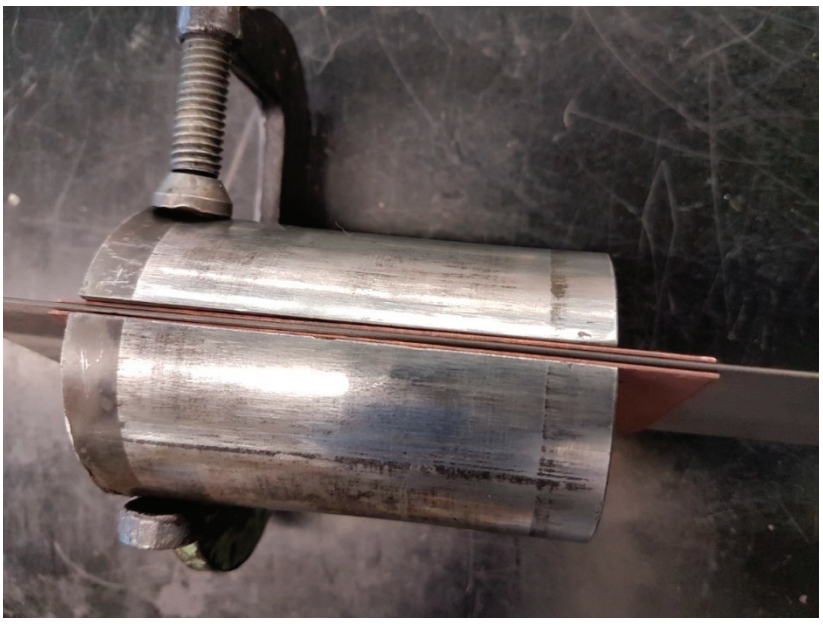

Figure 2. Assembled CFRP plate, sleeves, and wedges before lubrication.

Figure 3. Assembled wedge anchorage (**left**), dead-end anchorage (**right**), and CFRP plate.

3.2. Anchorage Presetting

After assembly, the wedges were pushed further into the barrel using two different presetting levels: high presetting using the hydraulic jack, shown in Figure 4, and low presetting by manual hammering. Two identical steel rods of the same dimensions were employed to evenly push the wedges into the barrel without damaging the CFRP plate, after which a digital vernier caliper was used to ensure even the presetting of the wedges.

(**A**) (**B**)

Figure 4. Anchorage presetting: (**A**) hydraulic press apparatus and (**B**) presetting setup. Reproduced from Alhusain and Al-Mayah (2022) [38] with permission from Springer Nature.

Three presetting loads of 40 kN, 80 kN, and 120 kN were applied in the high presetting tests to investigate the presetting effect on the anchorage's performance. The other three low-presetting tests were preset using manual hammering to examine the effectiveness of the anchorage's self-seating mechanism.

3.3. CFRP Tensile Loading

The anchorage performance was examined by applying a slow uniaxial displacement-controlled tensile load of 0.6 mm/min to the CFRP plate until the CFRPs' full fracture. The tensile load was applied using the rig, shown in Figure 5A, operated by a servo-hydraulic material testing system (MTS). The displacements of the wedges and the CFRP plate were measured using two linear variable differential transducers (LVDTs) mounted to the steel where the wedge anchorage was seated, as shown in Figure 5B. The tip of one LVDT

was placed on the wedge to measure its displacement. The other LVDT was employed to measure the CFRPs' displacement by positioning its probe tip on a metallic plate fixed to the CFRP plate. The CFRP slippage, which is the relative displacement of the CFRP plate with respect to the wedges, was determined by computing the difference between the readings of the two LVDTs, as shown in Figure 6.

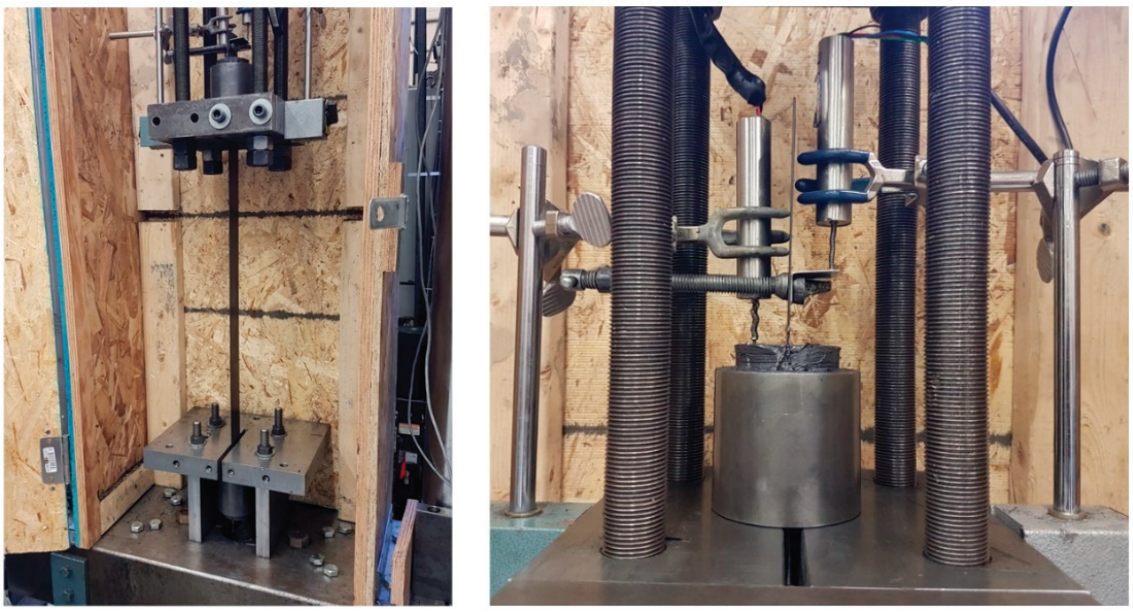

(**A**) (**B**)

Figure 5. Tensile loading: (**A**) test rig with assembled CFRP plate, two anchorages, and two LVDTs and (**B**) the setup of two LVDTs. Reproduced from Alhusain and Al-Mayah (2022) [38] with permission from Springer Nature.

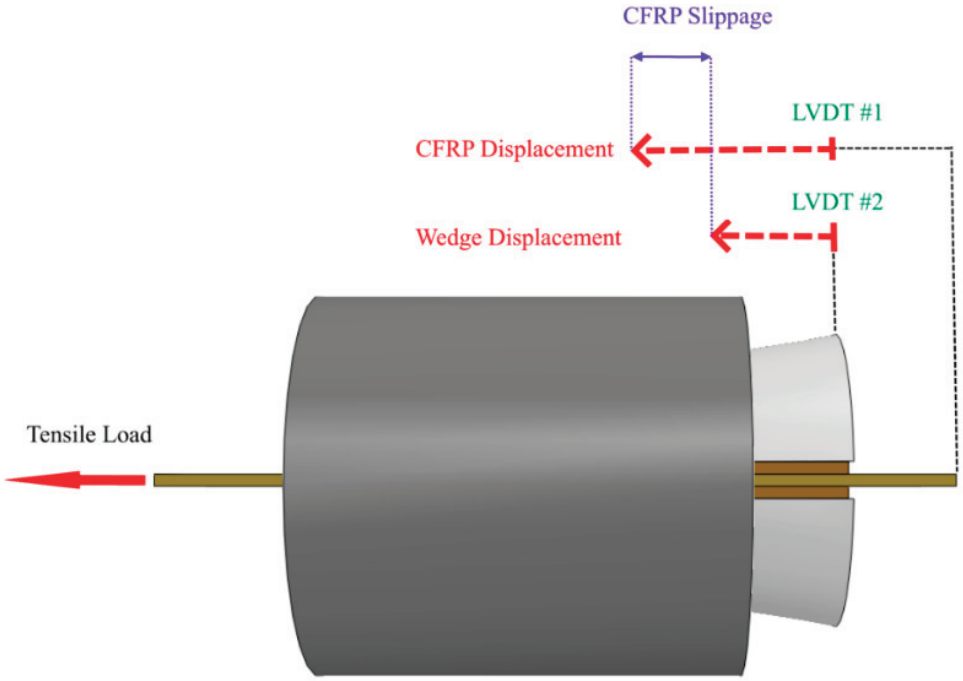

Figure 6. Recorded wedge, CFRP displacements, and CFRP slippage.

4. Results and Discussion

4.1. General

Six tensile tests were conducted under high and low presetting levels. Three tests were performed using high presetting levels of 40 kN, 80 kN, and 120 kN to examine the presetting effect on the anchorage's performance. The other three tests were conducted with low presetting levels using manual hammering to investigate the effectiveness of the anchorage's self-seating mechanism. A displacement-controlled tensile loading of 0.6 mm/min was applied until CFRP failure. The CFRPs' fracture mode, shown in Figure 7, was observed in all tests outside the anchorage, indicating effective CFRP gripping. This was achieved by eliminating stress concentration and extensive CFRP plate slippage. The anchorage's high performance was illustrated by the average recorded CFRP failure load of 172.3 (±5.7) kN, which surpassed the reported CFRP tensile strength of 168 kN (2800 MPa). As a comparison, the mechanical anchorage developed by Ye et al. (2018) successfully gripped a CFRP plate that was 25 mm wide and 1.5 mm thick with a tensile strength of 1950 MPa; however, the anchorage was somewhat large in size with a length of 150 mm, a width of 120 mm, and a thickness of 40 mm [24]. On the other hand, the developed wedge anchorage has a length of 70 mm and a diameter of 76.2 mm, and it was capable of gripping a wider CFRP plate with a higher tensile strength of 2800 MPa, illustrating its high performance despite its small size.

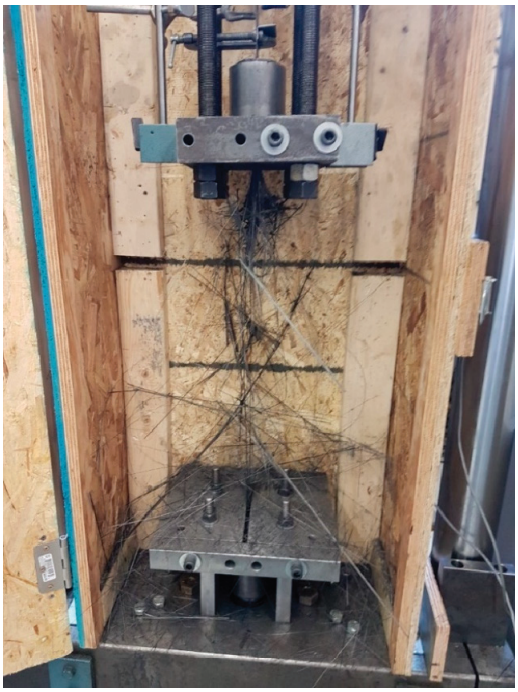

Figure 7. Fracture mode of CFRP plate outside the anchorage. Reproduced from Alhusain and Al-Mayah (2022) [38] with permission from Springer Nature.

As stated earlier, the disposable soft copper sleeves were expected to experience substantial plastic deformation, as shown in Figure 8; hence, new sets of sleeves were used per test to maintain the anchorage's performance. It is worth mentioning that the soft copper sleeves were 5 mm longer than the wedges for easier assembly. However, that extra length was not subjected to wedge confinement, which resulted in deformation at the sleeves' ends.

The effect of the presetting level on the anchorage's performance was assessed. It was observed that the presetting level had a minor effect on the CFRPs' failure load, as indicated by the average fracture loads of 171.3 (±2.5) kN and 173.3 (±7.5) kN under high and low presetting levels, respectively. On the other hand, the CFRP displacement and slippage

were substantially impacted by the presetting level. It was observed that the average CFRP displacement and slippage under low presetting were 6.04 (±0.27) mm and 1.18 (±0.75) mm, whereas the CFRP displacement and slippage were only 3.57 (±0.66) mm and 0.34 (±0.15) mm, respectively, in the case of high presetting. In other words, applying high presetting resulted in 41% and 71% reductions in the CFPR displacement and slippage, respectively. Based on these results, the wedge anchorage demonstrated an excellent performance under both low and high presetting levels.

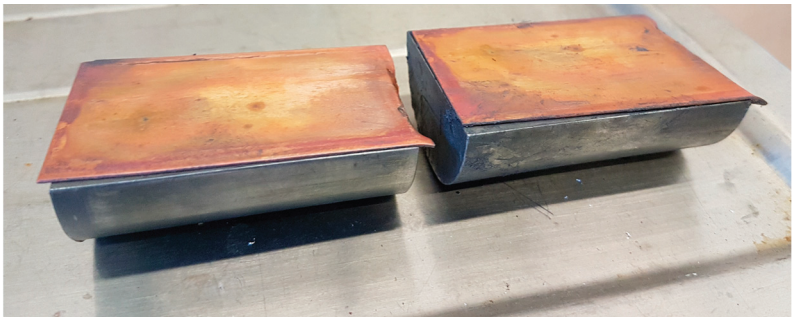

Figure 8. Deformed copper sleeves after testing.

The fracture mode of the CFRP plate was inspected, and the plastic deformation within the wedges and barrel was investigated after conducting the six tensile tests. It was observed that while the CFRP's loaded end (Edge 1) fragmented, its anchored segment was still intact, illustrating the effective gripping of the anchorage. Also, it was found that the wedges and barrel experienced only minor plastic deformation, mainly at the loading (Edge 1) and presetting (Edge 2) ends, indicating that the anchorage can withstand further testing.

4.2. CFRP Failure Load

The performance of the wedge anchorage was investigated by analyzing the fracture load of the CFRP plate under high and low presetting levels. The recorded CFRP failure loads of the high presetting tests 1–3 are 174 kN, 172 kN, and 168 kN, respectively, with an average of 171.3 (±2.5) kN, which exceeded the reported CFRP tensile strength of 168 kN (2800 MPa), as illustrated in Figure 9A. It is noteworthy that applying a higher presetting level was not required to reach the CFRPs' tensile strength. In fact, increasing the presetting load slightly reduced the CFRPs' failure load. Increasing the presetting load from 40 kN (Test 1) to 120 kN (Test 3) decreased the CFRP failure load by 6 kN, attributed to the CFRPs' preloading damage caused by excessive confinement.

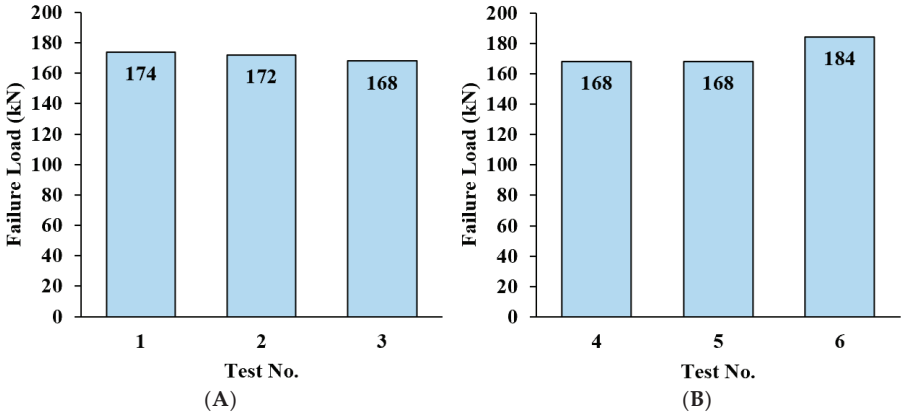

Figure 9. CFRPs' failure load under (**A**) high and (**B**) low presetting levels.

On the other hand, the fracture loads of the low presetting tests 4–6 are 168 kN, 168 kN, and 184 kN, respectively, with an average of 173.3 (±7.5) kN, as shown in Figure 9B. Based on the results, the wedge anchorage successfully achieved the full reported tensile strength of the CFRP plates in all tests under both high and low presetting conditions, illustrating its excellent performance.

4.3. CFRP Displacement

The excessive displacement of the CFRP plate during the tensioning process is not desired in field applications since it causes a considerable loss of CFRP prestressing. Thus, the wedge anchorage was evaluated based on the resulting CFRP displacement, as shown in Figure 10. The general plot of the recorded load–displacement data consisted of vertical and inclined linear segments, which correlated well with previously reported findings [39]. It was observed that applying a higher presetting load produced a higher displacement-initiation load, represented by the vertical segment, and a lower CFRP displacement, attributed to the increased confinement. The presetting level had a minor effect on the resistance of wedge insertion into the barrel, represented by the inclined segment's slope because it is primarily a function of the barrel's thickness and the interference of the wedge–barrel interface. In other words, the presetting level had a significant impact on the CFRP displacement.

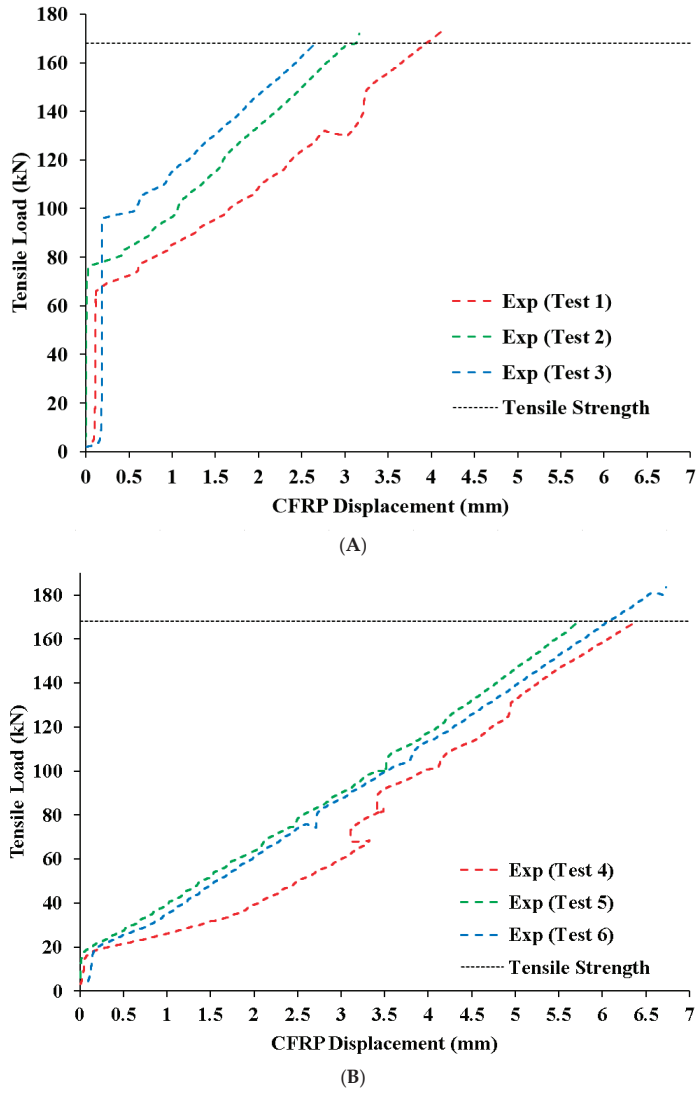

Figure 10. Tensile load vs. CFRP displacement for (**A**) high-presetting, and (**B**) low-presetting tests.

As illustrated in Figure 10A, increasing the presetting load from 40 kN (Test 1) to 120 kN (Test 3) reduced the CFRPs' displacement, at a tensile load of 168 kN, from 3.91 mm to 2.65 mm, improving the prestressing effectiveness. Consequently, applying low presetting through manual hammering produced higher CFRP displacement with an average of 6.04 (±0.27) mm, as shown in Figure 10B. However, it is clear from the results that the wedge anchorage allowed only minor CFRP displacement ranging from 2.65 mm to 6.35 mm, demonstrating its ability to preserve the CFRP prestressing. It is worth noting that the CFRP plate of Test 4 experienced noticeable displacement as the tensile loading was increased from 15 kN to 38 kN, possibly due to the uneven hammering of the two wedges. Nonetheless, the wedge anchorage was still capable of gripping the CFRP plate effectively.

4.4. CFRP Slippage

Investigating the CFRP slippage, which is the displacement with respect to the wedges, is crucial since CFRP is vulnerable to abrasion damage that can lead to premature fracture. Therefore, the CFRP slippage was recorded and analyzed, as illustrated in Figure 11. It was observed that the maximum recorded CFRP slippages of the high presetting tests 1–3 were 0.55 mm, 0.25 mm, and 0.2 mm, respectively, with an average of 0.33 (±0.15) mm. Increasing the presetting level generally decreased the CFRP slippage. Hence, increasing the presetting load from 40 kN (Test 1) to 80 kN (Test 2) and 120 kN (Test 3) reduced the CFRP slippage by 55% and 64%, respectively.

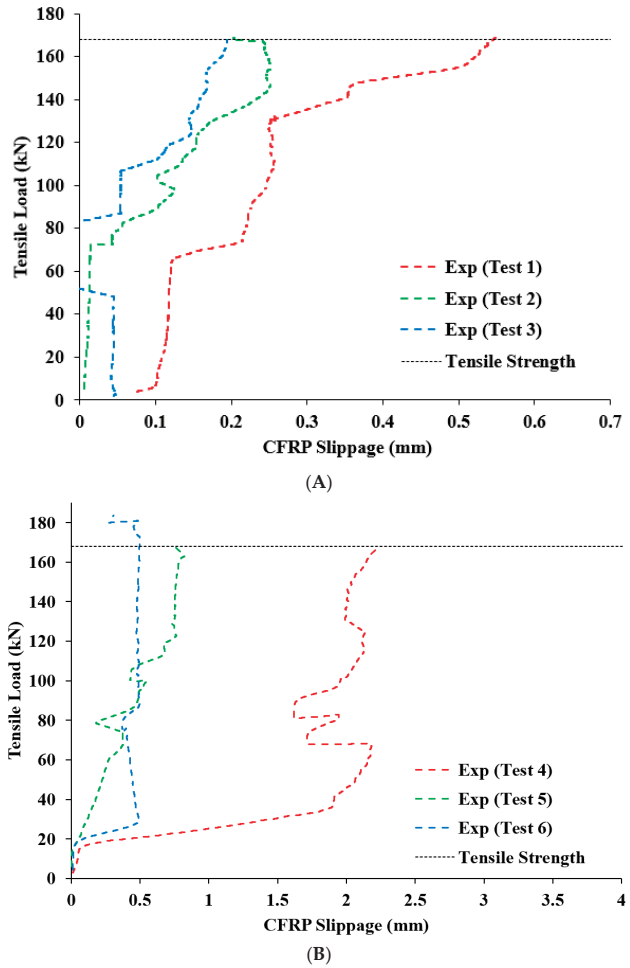

Figure 11. Tensile load vs. CFRP slippage for (**A**) high-presetting and (**B**) low-presetting tests.

As a result, higher CFRP slippage occurred in the low presetting tests. The maximum recorded CFRP slippage of the low presetting tests 4–6 was 2.2 mm, 0.82 mm, and 0.5 mm,

respectively, with an average of 1.18 (±0.75) mm. The CFRP plate of Test 4 experienced almost 85% of its slippage as the tensile loading was increased from 15 kN to 38 kN, likely because of uneven presetting of the wedges. On the contrary, the CFRP slippage of Test 6 was only 0.5 mm despite being manually hammered, illustrating the anchorage's excellent performance even under low presetting. Based on the results, the wedge anchorage minimized the CFRP displacement with respect to the wedges and, consequently, mitigated the abrasion damage, preventing the premature failure of the CFRP plate.

4.5. CFRP Fracture and Anchorage Damage Analysis

A fragmented CFRP plate failure, shown in Figure 12, was observed after reaching the ultimate load in every test. As illustrated, while the CFRPs' loaded end experienced full rupture, the anchored segment of the CFRPs remained intact. This is evidence that the wedge anchorage successfully gripped the CFRP plate and prevented fracture propagation into the anchored portion of the CFRP plate inside the anchorage. Advanced monitoring technologies (e.g., high-speed camera) can be employed to gain a better understanding of the CFRPs' failure process.

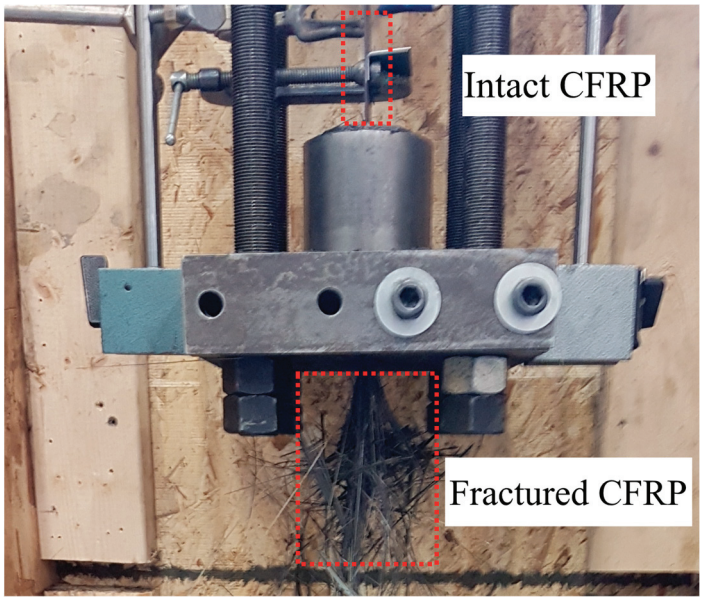

Figure 12. Intact and fractured CFRP parts of CFRP plate.

The wedge anchorage was visually inspected after conducting the tensile tests. Minor plastic deformation was observed mainly at the loading (Edge 1) and presetting (Edge 2) ends of the wedges and barrel, as highlighted in Figure 13. Different underlying factors were involved in producing plastic deformation at each edge. While plastic deformation near the loading end was mostly caused by elevated shear stress between the barrel and the wedges, plastic deformation around the presetting end was induced by a combination of high shear and contact (interference) stresses. The partial removal of lubrication at the loading end by the moving wedges and the low barrel thickness at the presetting end could have contributed to the plastic deformation within the anchorage. It is worth noting that the machining pattern on the surface is still visible, illustrating the absence of significant plastic deformation. Therefore, the anchorage maintained its excellent performance throughout the repeated tests, proving that its performance was not affected by the minor plastic deformation.

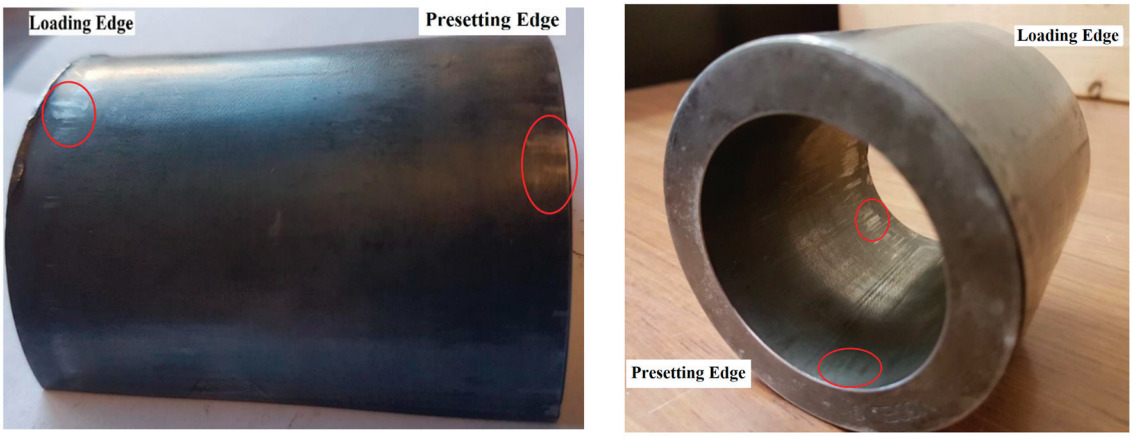

(**A**) (**B**)

Figure 13. Plastically deformed (**A**) wedge and (**B**) barrel.

5. Conclusions

A compact, reliable, and reusable wedge anchorage for CFRP plates was developed using the innovative configuration that utilized an arc-linear profile in the wedge-barrel interface. The performance of the wedge anchorage was tested repeatedly under high and low presetting levels. The CFRP failure load, displacement, slippage, and fracture mode were analyzed. Based on the experimental results, the following points were concluded.

- The wedge anchorage effectively gripped the CFRP plate under both high and low presetting conditions until its full reported tensile strength was reached by preventing stress concentration within the CFRP plate.
- Only minor CFRP displacement ranging from 2.65 mm to 6.35 mm was recorded, indicating that the wedge anchorage is capable of preserving CFRP prestressing.
- The CFRP plate experienced low slippage of only 0.2–2.2 mm, mitigating abrasion damage.
- Applying a higher presetting level had a minor effect on the failure load of the CFRP plate, but it substantially reduced the CFRPs' displacement and slippage.
- Post-experimental visual inspection revealed that the anchored segment of the CFRP plate remained intact even after the full fracture of its loading end.
- The wedge anchorage maintained its excellent performance throughout the repeated tests while enduring only minor surface scratches at the loading and presetting ends of its wedges and barrel.

Author Contributions: Conceptualization, M.A. and A.A.-M.; methodology, M.A. and A.A.-M.; validation, M.A. and A.A.-M.; formal analysis, M.A. and A.A.-M.; investigation, M.A. and A.A.-M.; writing—original draft preparation, M.A.; writing—review and editing, A.A.-M.; visualization, M.A. and A.A.-M.; supervision, A.A.-M., funding acquisition, M.A. All authors have read and agreed to the published version of the manuscript.

Funding: This work was supported by the Deanship of Scientific Research, Vice Presidency for Graduate Studies and Scientific Research, King Faisal University, Saudi Arabia [Grant No. KFU241830]. It was also supported by the Saudi Arabian Cultural Bureau (SACB), Ottawa, Canada.

Data Availability Statement: The research-related data is illustrated in the figures.

Conflicts of Interest: The authors declare no conflict of interest.

References

1. Wardhana, K.; Hadipriono, F. Analysis of Recent Bridge Failures in the United States. *J. Perform. Constr. Facil.* **2003**, *17*, 144–150. [CrossRef]
2. Petrović, Z.C. Catastrophes caused by corrosion. *Vojnoteh. Glas.* **2016**, *64*, 1048–1064. [CrossRef]
3. *ASCE Infrastructure Report Card*; American Society of Civil Engineers (ASCE): Reston, VA, USA, 2017.

4. Al-Mahaidi, R.; Kalfat, R. Investigation into CFRP plate end anchorage utilising uni-directional fabric wrap. *Compos. Struct.* **2011**, *93*, 821–830. [CrossRef]
5. Meier, U. Carbon fiber-reinforced polymers: Modern materials in bridge engineering. *Struct. Eng. Int.* **1992**, *2*, 7–12. [CrossRef]
6. Hassan, S.A.; Gholami, M.; Ismail, Y.S.; Sam, A.R.M. Characteristics of concrete/CFRP bonding system under natural tropical climate. *Constr. Build. Mater.* **2015**, *77*, 297–306. [CrossRef]
7. Zheng, Y.; Zhou, Y.; Zhou, Y.; Pan, T.; Zhang, Q.; Liu, D. Cracking behavior of reinforced concrete beams strengthened with CFRP anchorage system under cyclic and monotonic loading. *Eng. Struct.* **2020**, *207*, 110222. [CrossRef]
8. Al-Safy, R.; Al-Mahaidi, R.; Simon, G.P.; Habsuda, J. Experimental investigation on the thermal and mechanical properties of nanoclay-modified adhesives used for bonding CFRP to concrete substrates. *Constr. Build. Mater.* **2012**, *28*, 769–778. [CrossRef]
9. Al-Rousan, R.Z. Impact of elevated temperature and anchored grooves on the shear behavior of reinforced concrete beams strengthened with CFRP composites. *Case Stud. Constr. Mater.* **2021**, *14*, e00487. [CrossRef]
10. Kalfat, R.; Al-Mahaidi, R. Investigation into bond behaviour of a new CFRP anchorage system for concrete utilising a mechanically strengthened substrate. *Compos. Struct.* **2010**, *92*, 2738–2746. [CrossRef]
11. Hong, S.; Park, S.-K. Concrete beams strengthened with prestressed unbonded carbon-fiber-reinforced polymer plates: An experimental study. *Polym. Compos.* **2017**, *38*, 2459–2471. [CrossRef]
12. Hong, S.; Park, S.-K. Effect of prestress and transverse grooves on reinforced concrete beams prestressed with near-surface-mounted carbon fiber-reinforced polymer plates. *Compos. Part B Eng.* **2016**, *91*, 640–650. [CrossRef]
13. Peng, H.; Zhang, J.; Cai, C.S.; Liu, Y. An experimental study on reinforced concrete beams strengthened with prestressed near surface mounted CFRP strips. *Eng. Struct.* **2014**, *79*, 222–233. [CrossRef]
14. Peng, H.; Zhang, J.; Shang, S.; Liu, Y.; Cai, C.S. Experimental study of flexural fatigue performance of reinforced concrete beams strengthened with prestressed CFRP plates. *Eng. Struct.* **2016**, *127*, 62–72. [CrossRef]
15. Benmokrane, B.; Xu, H.; Nishizaki, I. Aramid and carbon fibre-reinforced plastic prestressed ground anchors and their field applications. *Can. J. Civ. Eng.* **1997**, *24*, 968–985. [CrossRef]
16. Kim, H.-J.; Sim, J. Mechanical properties of GFRP slip-form for in-situ application. *KSCE J. Civ. Eng.* **2016**, *20*, 1842–1851. [CrossRef]
17. Zhao, X.-L. *FRP-Strengthened Metallic Structures*; CRC Press: Boca Raton, FL, USA, 2014; ISBN 978-0-203-89521-4.
18. Lees, J.M.; Gruffydd-Jones, B.; Burgoyne, C.J. Expansive cement couplers: A means of pre-tensioning fibre-reinforced plastic tendons. *Constr. Build. Mater.* **1995**, *9*, 413–423. [CrossRef]
19. Meier, U.; Farshad, M. Connecting high-performance carbon-fiber-reinforced polymer cables of suspension and cable-stayed bridges through the use of gradient materials. *J. Comput.-Aided Mater. Des.* **1996**, *3*, 379–384. [CrossRef]
20. Taerwe, L. *Non-Metallic (FRP) Reinforcement for Concrete Structures: Proceedings of the Second International RILEM Symposium*; CRC Press: Boca Raton, FL, USA, 1995; ISBN 978-0-419-20540-1.
21. Zhang, B.; Benmokrane, B. Design and evaluation of a new bond-type anchorage system for fiber reinforced polymer tendons. *Can. J. Civ. Eng.* **2004**, *31*, 14–26. [CrossRef]
22. Puigvert, F.; Crocombe, A.D.; Gil, L. Static analysis of adhesively bonded anchorages for CFRP tendons. *Constr. Build. Mater.* **2014**, *61*, 206–215. [CrossRef]
23. Schmidt, J.W.; Bennitz, A.; Taljsten, B.; Pedersen, H. Development of Mechanical Anchor for CFRP Tendons Using Integrated Sleeve. *J. Compos. Constr.* **2010**, *14*, 397–405. [CrossRef]
24. Ye, H.; Liu, C.; Hou, S.; Wang, T.; Li, X. Design and experimental analysis of a novel wedge anchor for prestressed CFRP plates using pre-tensioned bolts. *Compos. Struct.* **2018**, *206*, 313–325. [CrossRef]
25. Burtscher, S. Wedge Anchorage for CFRP Strips. *J. Compos. Constr.* **2008**, *12*, 446–453. [CrossRef]
26. Han, Q.; Wang, L.; Xu, J. Test and numerical simulation of large angle wedge type of anchorage using transverse enhanced CFRP tendons for beam string structure. *Constr. Build. Mater.* **2017**, *144*, 225–237. [CrossRef]
27. Sayed-Ahmed, E.Y.; Shrive, N.G. A new steel anchorage system for post-tensioning applications using carbon fibre reinforced plastic tendons. *Can. J. Civ. Eng.* **1998**, *25*, 113–127. [CrossRef]
28. Czaderski, C.; Martinelli, E.; Michels, J.; Motavalli, M. Effect of curing conditions on strength development in an epoxy resin for structural strengthening. *Compos. Part B* **2011**, *43*, 398–410. [CrossRef]
29. Akbarzadeh Bengar, H.; Shahmansouri, A.A. A new anchorage system for CFRP strips in externally strengthened RC continuous beams. *J. Build. Eng.* **2020**, *30*, 101230. [CrossRef]
30. Schmidt, J.W.; Bennitz, A.; Täljsten, B.; Goltermann, P.; Pedersen, H. Mechanical anchorage of FRP tendons—A literature review. *Constr. Build. Mater.* **2012**, *32*, 110–121. [CrossRef]
31. Al-Mayah, A.; Soudki, K.; Plumtree, A. Simplified Anchor System for CFRP Rods. *J. Compos. Constr.* **2013**, *17*, 584–590. [CrossRef]
32. Li, X.; Deng, J.; Wang, Y.; Xie, Y.; Liu, T.; Rashid, K. RC beams strengthened by prestressed CFRP plate subjected to sustained loading and continuous wetting condition: Time-dependent prestress loss. *Constr. Build. Mater.* **2021**, *275*, 122187. [CrossRef]
33. Feng, P.; Zhang, P.; Meng, X.; Ye, L. Mechanical Analysis of Stress Distribution in a Carbon Fiber-Reinforced Polymer Rod Bonding Anchor. *Polymers* **2014**, *6*, 1129–1143. [CrossRef]
34. Al-Mayah, A.; Soudki, K.; Plumtree, A. Effect of sleeve material on interfacial contact behavior of CFRP-metal couples. *J. Mater. Civ. Eng.* **2006**, *18*, 825–830. [CrossRef]

35. Alhusain, M. Development, Optimization and Testing of an Innovative Wedge Anchorage for CFRP Plates. Master's Thesis, University of Waterloo, Waterloo, ON, Canada, 2018.
36. American Iron and Steel Institute. *Design Guidelines for the Selection and Use of Stainless Steel*; American Iron and Steel Institute: Washington, DC, USA, 1993.
37. Shaji, S.; Radhakrishnan, V. An investigation on solid lubricant moulded grinding wheels. *Int. J. Mach. Tools Manuf.* **2003**, *43*, 965–972. [CrossRef]
38. Alhusain, M.; Al-Mayah, A. Novel Wedge Anchorage for CFRP Plates. In Proceedings of the 10th International Conference on FRP Composites in Civil Engineering, İstanbul, Turkey, 8–10 December 2021; Ilki, A., Ispir, M., Inci, P., Eds.; Springer International Publishing: Cham, Switzerland, 2022; pp. 2197–2208.
39. Al-Mayah, A.; Soudki, K.; Plumtree, A. Experimental and analytical investigation of a stainless steel anchorage for CFRP prestressing tendons. *PCI J.* **2001**, *46*, 88–99. [CrossRef]

Journal of
Composites Science

MDPI

Article

Stiffness Retention in Cyclic-Loaded CFRP Composites Produced via Novel Automatic Tape Laying

Ashley Blythe [1], Bronwyn Fox [2,*], Mostafa Nikzad [1], Boris Eisenbart [1] and Boon Xian Chai [1]

[1] Faculty of Science, Engineering and Technology, Swinburne University of Technology, Hawthorn, VIC 3122, Australia; ablythe@swin.edu.au (A.B.); mnikzad@swin.edu.au (M.N.); beisenbart@swin.edu.au (B.E.); bchai@swin.edu.au (B.X.C.)
[2] CSIRO, Clayton, VIC 3168, Australia
* Correspondence: bronwyn@csiro.au

Abstract: Sixteen-head automatic tape laying of non-crimped carbon-fibre-reinforced plastic is performed, and the fibre alignment is compared with that produced via hand laying. The effect of fibre alignment is tested via quasi-static and cyclic three-point bending tests. Using the Fill Multilayer (a 16-head tape-laying machine), precision fibre laying of unidirectional fabrics is performed with deliberate misalignment to examine the effect of fibre orientation and investigate the random effect on longitudinal misalignment. The automatic tape-layered coupons are compared with hand-layered carbon fibre tapes to investigate the relationship between the fibre alignment and the flexural strength. A 52% reduction in the fibre alignment scatter is achieved via the Fill Multilayer. Fibre orientation increases lead to a higher flexural strength of 16.08% for Fill Multilayer-made coupons compared with hand-layered samples. An investigation of the correlation between fibre alignment and flexural strength shows that shear-based failure increases exponentially as the alignment decreases. Fill Multilayer-made coupons have a higher void concentration due to ultrasonic welding, but also the highest modulus and flexural strength, as fibre misalignment is reduced to 1.68°, with a modulus degradation of 1.4%.

Keywords: crack initiation; crack propagation; delamination; damage mechanisms

1. Introduction

Composites such as carbon-fibre-reinforced plastic (CFRP) have the potential to reduce automotive components by 60–80% [1–4]. CFRP is also frequently adopted in other fields and applications, such as for the structural reinforcement of buildings [5,6]. However, CFRP is produced slowly by hand laying, which lowers reproducibility [7–10]. The introduction of automated tape laying (ATL) has accelerated composite part manufacturing in the automotive industry, helping composites to become a more attractive alternative to reduce the weight of structural components. ATL has the advantages of increased efficiency, reproducibility and laying accuracy over traditional hand stacking or raw material strips [11–13]. Recent developments in multiheaded construction have enabled the parallel laying of multiple tapes, allowing for even faster composite part manufacturing to keep up with automotive demand. A key issue with CFRP is reproducibility; due to the multifibre nature of CFRP, the alignment of individual tows within the laminate can cause major deviations in mechanical performance.

The ATL system used here is the Fill Multilayer machine [14]. In this machine, a combination of thermoset and thermoplastic prepregs can be used in the machine heads and dry fabrics. Using typical prepregs in the Fill Multilayer causes issues with adhesion in the rollers; this is mitigated with zero-tack prepregs. In comparison with previous ATL machines (e.g., those described in [15,16]), ultrasonic welding of the prepregs or dry fabrics is used to prevent tow shifting. Ultrasonic welding is employed to adhere plies together in a novel approach using the Fill Multilayer to adhere zero-tack resin prepregs. The effect of

ultrasonic welding is optimised regarding stack welding penetration and adhesion between plies without causing significant defects in the final laminate during consolidation [17,18].

Automatic tape-laying systems require both a low tack and dynamic stiffness in order for prepreg fibres to be spooled and unspooled without resin adhering to the roll [19]. The random scattering of the fibres produced using the Fill Multilayer is compared with that of handmade CFRP coupons to investigate fibre alignment in different laying methods. The preform is held together with ultrasonic weld dots to prevent the preform from shifting during curing. Fibre alignment is a critical issue, with the numerous defects introduced during composite manufacturing leading to random fibre alignment, as outlined in the reviews by Oromiehie et al. [12] and Falk et al. [11]. Oromiehie et al. indicated that many defects in pre-impregnated fibres during resin (prepreg) manufacturing occur before tape placement due to fibre spooling and unspooling, which causes misalignment due to resin adhesion. Tape defects such as splitting can cause gaps. Croft et al. [20] showed that gaps in the tape are caused by either fibre shifting or tape defects, leading to a decrease in the compression strength by 3 to 12%. Minimising the alignment defects introduced after placement is critical for maximising part performance. As Jeppesen et al. [21] showed, the manufacturing approach is the main contributor to fibre misalignment and the waviness of the produced composite.

Analyses of the fibre angle have shown that a high degree of misalignment is correlated with data scattering in fatigue testing [13,22,23]. To further research the randomness in fabrics, this investigation will use different fibre angles in ATL. Previous alignment studies show a linear correlation between the fibre alignment and the flexural strength [15,24]. Manufacturing defects, leading to fibre misalignment, are highlighted by Alam et al. [25] as being the primary cause of data scattering in CFRP. Random fibre alignment is a crucial aspect affecting a composite's permeability during the filling stage of liquid composite moulding processes [26–29].

In this paper, the fibre alignment of composites layered using either Fill Multilayer or hand laying is investigated to determine the relationship between fibre alignment and flexural strength. Alignments of less than 5° are used to determine whether the alignment contributes to the mechanical performance of the composite laminate. The Fill Multilayer uses a zero-tack UD prepreg; this is compared with the same prepreg produced via hand layering and a UD CFRP. The UD CFRP contains cross stitching to prevent ply splitting; however, the stitching adds waviness. This waviness, which leads to longitudinal misalignment, is investigated and is compared with random misalignment due to stitching during hand laying. To test the precision of the Fill Multilayer, the UD CFRP fabric is deliberately misaligned by 5° and 90° to investigate the alignment effect on the flexural behaviour. An angle of 5° is chosen as it is difficult to accurately hand lay tape with a 5° offset, and 90° is chosen because it can be cut from the UD plates. In the Fill Multilayer, a prepreg of unidirectional (UD) CFRP is used, interlayered by hand, to determine the static and cyclic loading characteristics via three-point bending tests. The flexural characteristics of the composites produced using the Fill Multilayer are determined and compared against those of composites fabricated via hand laying. The alignment of the manufactured carbon-fibre-reinforced plastic coupons is compared with those manufactured via hand laying.

2. Methodology

2.1. Material Characteristics and Resin Curing

The CFRPs used were the intermediate modulus epoxy prepregs shown in Table 1. The first material contained a cross stitch, which induced waviness in the fabric. The other material was an intermediate modulus epoxy zero-tack prepreg. The zero-tack additive prevented the prepreg from adhering during unravelling. Curing was conducted in a press at 18 MPa compression; the mould was coated in mould release wax to enable part removal. Curing was carried out as per the manufacturer's recommendations (FILL). The Fill Multilayer-produced non-crimped fabric was isothermally cured at 150 °C for 5 min, and the crimped fabric without zero-tack resin was cured at 130 °C for 5 min. An increase

in temperature was required to ensure curing due to the tackifiers in the zero-tack resin additive. The hot plates were then released from the mould and cooled at room temperature overnight. The fibres were displaced during pressing, causing mould edge misalignment. However, the edge misalignment error was minimal as the edges were discarded. The 200 mm^2 coupons were layered with a 50 mm overhang and manually cut to fill the mould.

Table 1. Material characteristics for tensile strength and modulus.

Material Type	Tensile Strength (MPa)	Tensile Modulus (GPa)
Crimped CFRP	1235	126.6
Non-crimped CFRP	2137	135

Cutting the material led to an additional potential error in the hand-placed laminates. Instead of using a machined length and tapes to control the width, as was the case in the Fill Multilayer, during hand laying, the material was cut to size, creating a uniform edge distribution. For this reason, coupons were cut away from the edge to prevent waviness, which caused scatter in the alignment data. Each plate was manufactured with 10 plies of CFRP and compressed to a 2 mm thickness; for off-the-shelf CFRP, 6 plies were used and pressed to a thickness of 2 mm. Maintaining a constant coupon geometry ensured a reproducible result during testing, as both fabrics consisted of carbon fibres with comparable intermediate tensile moduli.

2.2. Fill Multilayer Tape Laying

This article investigates the Fill Multilayer (shown in Figure 1) and the performance of its products in both static and dynamic scenarios. Automatic tape laying was performed and the resulting fibre orientation and mechanical bending were studied and further compared with those resulting from hand laying. A cross-section micrograph of the surface was used to determine fibre orientation changes between stackings. The development of high-stiffness light materials required a higher tolerance between samples. This tolerance was the deviation between samples from different composite laminates. The comparison between defects and mechanical stiffness under static and dynamic bending would be the basis of the measurements.

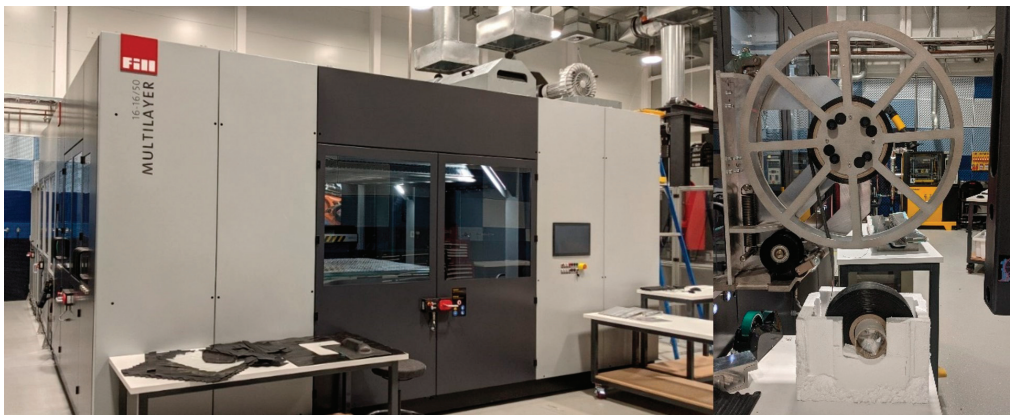

Figure 1. Reference photo of the Fill Multilayer during tape-laying operations and CFRP winding from a roll to a cassette.

There were several issues when stacking UD fabrics in the Fill Multilayer that needed to be addressed. Firstly, the fabrication of a 200 mm^2 CFRP plate required the tapes to be stacked on top of one another. However, ultrasonic welding was performed in the centre of the tape, as shown in Figure 2. This central placement of ultrasonic weld marks for UD fabrics led to no adhesion to the adjacent fibre stack; thus, overlapped fibre layers were required to achieve a fully adhered stack that could be transported without separating. In

contrast, in offset fabrics, the change in fibre direction meant multiple fibres could adhere with one weld mark.

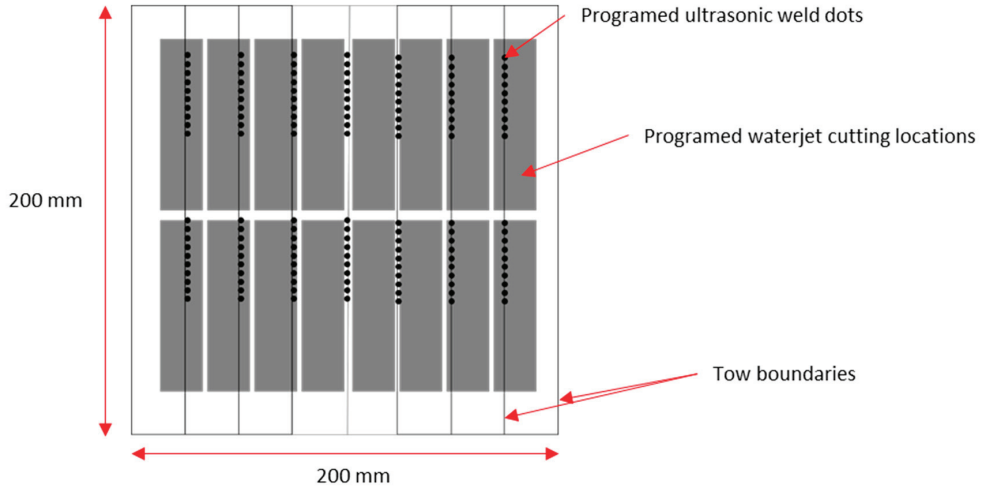

Figure 2. CFRP layered using the Fill Multilayer (10 layers) for $(0°)^{10}$ UD fabric. Each increment on the side is 50 mm, for a total internal machine diameter of 2250 mm^2. Black lines represent the probable weld mark locations and black dots represent the programmed areas where ultrasonic weld dots occur during laying.

Uni-directional non-crimp 200 GSM zero-tack intermediate modulus carbon fibre and ten plies of CFRP were used in the Fill Multilayer. The fabric was layered and cut with the Fill Multilayer machine head; after cutting, a welding horn was used to make an ultrasonic weld mark at 20 kHz. Ultrasonic welding can produce a shear strength of up to 50 MPa, as ply only needs to adhere to the layer below. This weld strength can be reduced to prevent defects from welding. For this reason, the weld time was 1 s rather than using a high-strength weld joint. With long adhesion times, multiple prepreg plies can adhere. Compared with hand laying, fibre cutting using a machine is more consistent, as the machine holds the tape under tension, whilst cutting and guillotine cutting by hand is less consistent. To mitigate tow splitting on the cutting edge, a 10 mm boundary was cut for the coupons.

2.3. Tape-Laying Optimisation and Ultrasonic Welding Defect Mitigation

The welding of tape layers prevented fibre movement during laying, allowing the composites to toughen in one stage rather than having to replace the tape cassettes, leading to the rapid laying of both prepreg and dry fibre tapes. Additional defects introduced by the Fill Multilayer were weld spots (as shown in Figure 3), causing an indent in the fabric.

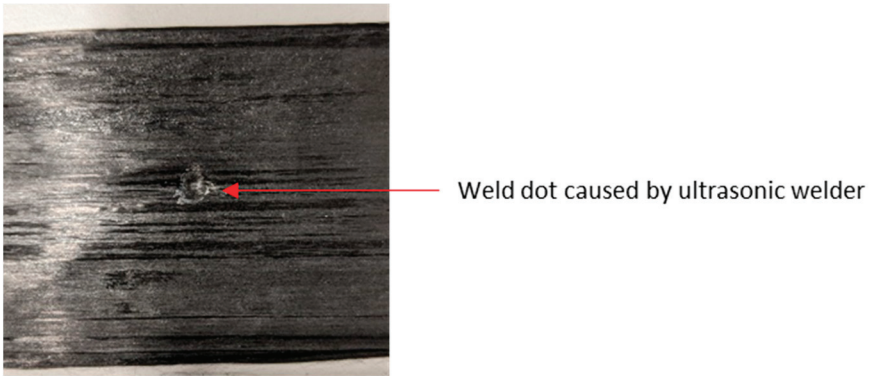

Figure 3. Ultrasonic weld spot on two layers of uncured CFRP welded at ten joules for one second.

To avoid ultrasonic weld marks and prevent fibre shifting, thermoplastic interlaying was employed. However, during laying with the Fill Multilayer, only ultrasonic welding was performed to prevent lateral movement rather than increasing the mechanical strength. Ultrasonic CFRP welding leads to heating and deformation of the welded layers in thermoplastic matrices [30]. The mitigation of thermosetting polymer degradation during welding has been investigated by Villegas and Rubio [31], who concluded that a higher force and a short heating duration prevent the thermal degradation of epoxy. Tsianhou et al. [32] showed that CF/epoxy composites have good adhesion with an interphase thermoplastic coupling layer to thermoplastic PEEK. Initial testing using GF-PP prepregs showed that using thermoplastic avoided ultrasonic weld damage to the fibres. However, CFRP PP and thermoplastic binders have modulus values inappropriate for most CFRP applications [33]. Using interlayered or interleaved thermoplastic as a tackifier leads to improved load-bearing capabilities [34]. Thermoplastic films, tubes and nanofibres are alternatives that can be used to improve the mechanical performance and as tackifiers for prepregs [35,36]. Typically, these interlayering materials are added to dry fibre and used to improve Mode I and II fracture toughness [37,38] and reduce the delamination area [39,40].

2.4. Optical Investigation of Fibre Alignment and Void Content of CFRP

To analyse random fibre defects due to the tape and fibre misalignment, the Fill Multilayer and hand-laying methods were used to induce a common fibre misalignment across the data set for each type. A BX61 Olympus microscope and Zeiss Supra 40VP SEM micrographs of polished coupons were used to determine the alignment, waviness and defects associated with the hand-laying and Fill Multilayer processes. Figure 4 shows the average fibre misalignment that was used in this research.

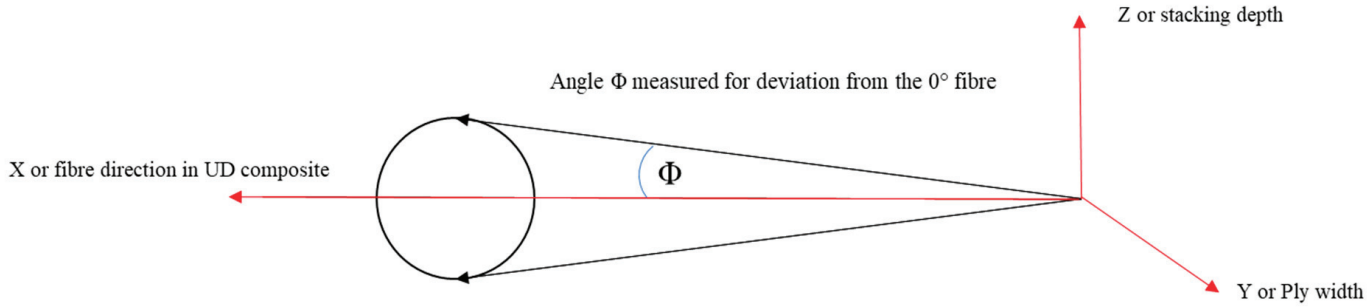

Figure 4. Diagram of fibre measurements in the x direction. Angle Φ measured for deviation from a 0° fibre.

Determining the radial sum of the fibre in ImageJ (v.1.54h) gives a grey intensity for the fibre direction for each tow shown in Figure 5 in order to determine the average distribution. To convert the fibres into a binary image, the intensity was selected based on prior void research [41,42]; the grey intensity of fibres was well-defined against the resin and void content, allowing for image skeletonisation to show just the fibres.

Comparing the radial sum of the fibre ply (V) with the individual fibre tow direction (IV) gave the average longitudinal fibre direction and alignment. Using the radial sum of the entire composite gave an accurate estimate of the fibre's waviness in one direction; the waviness and fibre misalignment were considered to be the same as those of the crimped laminate. In contrast to crimped fabrics, the waviness and alignment of fibres and the fabric may be above 5°. An individual ply radial sum analysis showed the fibre alignment and the waviness (instead of analysing the entire composite, which was the case when using a radial sum analysis, leading to error). The error was due to the circular nature of the radial sum analysis, where the fibre angle was relative to the centre of a circle. Fibres on the edge of the analysis were perpendicular to the centre, thus creating a peak at 90° to the fibre.

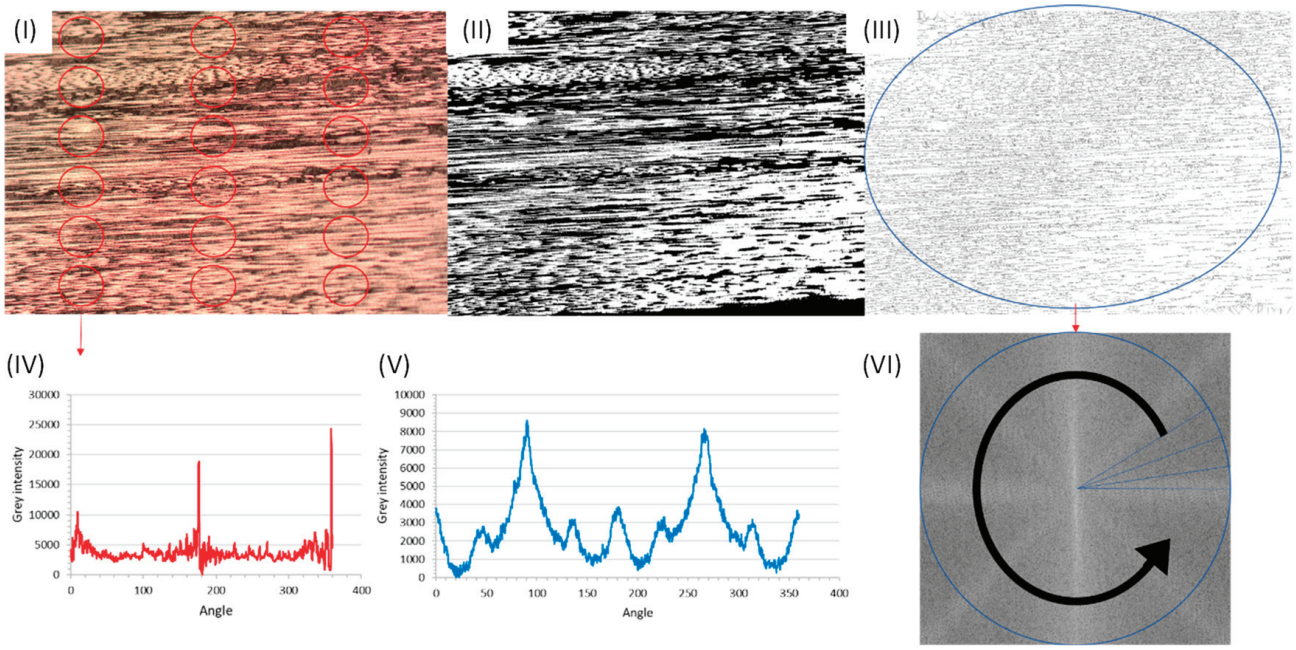

Figure 5. Method used for ImageJ analysis of the fibre waviness and misalignment during testing. (**I**) Cut through of CFRP Fill mounted in optical resin; (**II**) 2D image made binary; (**III**) 2D image skeletonised so only the edges are visible; (**IV**) radial sum analysis of the localised red circles to fibre alignment; (**V**) global fibre alignment given with radial sum analysis and (**VI**) image depicting global radial sum analysis of the blue circle.

The radial sum of each ply was taken from different points to create an average across the composite. The direction of the individual plies and the fibre waviness were determined. The average was taken across the press plate by taking coupons from the centre and edges. Using the same coupons, defects, including ultrasonic weld spots and voids, were analysed using ImageJ™, as shown in Figure 6. The threshold of the void grey intensity has been previously used to accurately measure the void content [43].

Using micro-CT, the void content and fibre alignment of the (45°, 40°, 35°, 30°, 25°, 20°, 15°, 10°, 5°, 0) offset samples were determined. The deliberate offset meant that the fibre angle was unable to be determined in ImageJ, as the fibre was required to be in the 2D plane rather than the quasi-isotropic alignment of the (45°, 40°, 35°, 30°, 25°, 20°, 15°, 10°, 5°, 0) samples. After 3D stacking of the micro-CT images, the void content and fibre alignment could be determined as per the previous method.

The void content was measured using micro-CT and determined through optical images, as shown in Figure 7. The void content measured via micro-CT was 2.017 ± 1.61% on average across the entire coupon, which was lower with a high deviation than that determined via optical imaging due to the higher sample size in micro-CT. There were two regions where this was an issue. Firstly, in the centre of the coupon, weld spots were likely here, increasing the likelihood of artificial defects. Secondly, in the second cut-through on the edge of the coupon, cutting and machining defects associated with tooling were likely to be present in the optical images. Several samples contained tooling defects on the edges of the samples, as determined via micro-CT, which occurred during waterjet cutting. The void concentration was determined to be inter-tow rather than inter-laminar, as the pressing process led to the centre of the tow being the location with the lowest permeability, with resin flows filling the mould cavity and leaving voids in the inter-tow region.

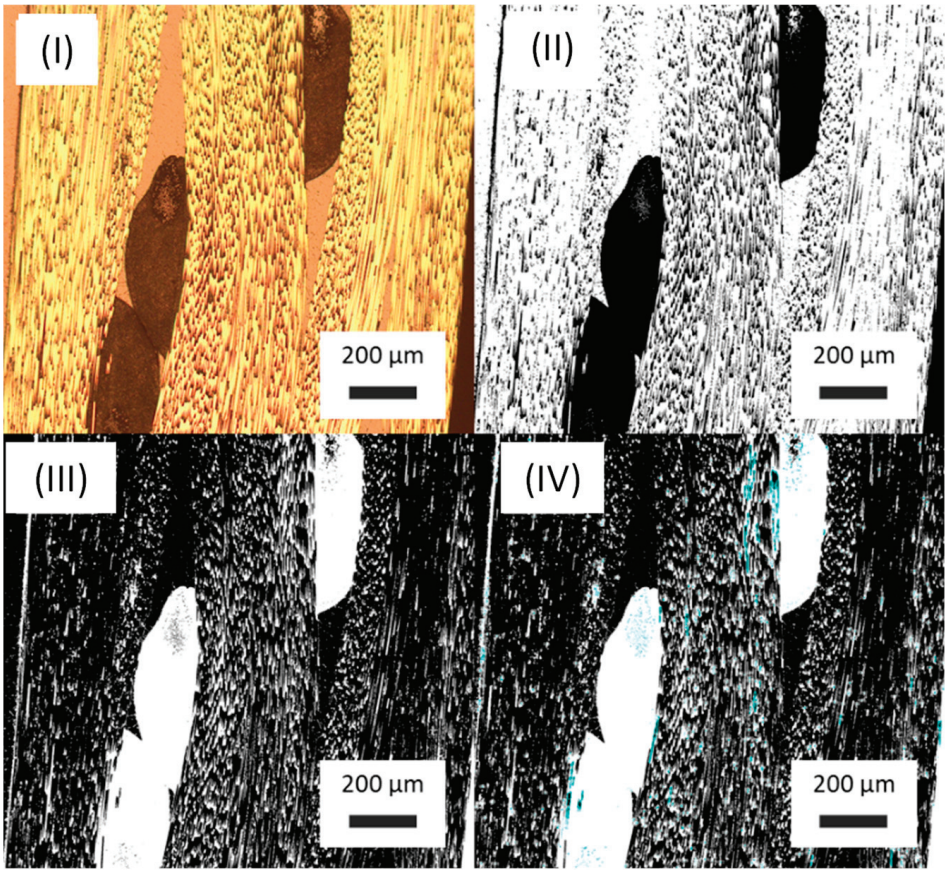

Figure 6. CFRP optical images in ImageJ: (**I**) optical cross section for alignment of CFRP fibres after compression moulding. The image in (**I**) was made binary (**II**) and the image threshold was reduced to a 0–40 grey level to detect voids in each sample over fibre ends as per Santulli et al. [43] (**III**). (**IV**) CFRP with voids marked in blue.

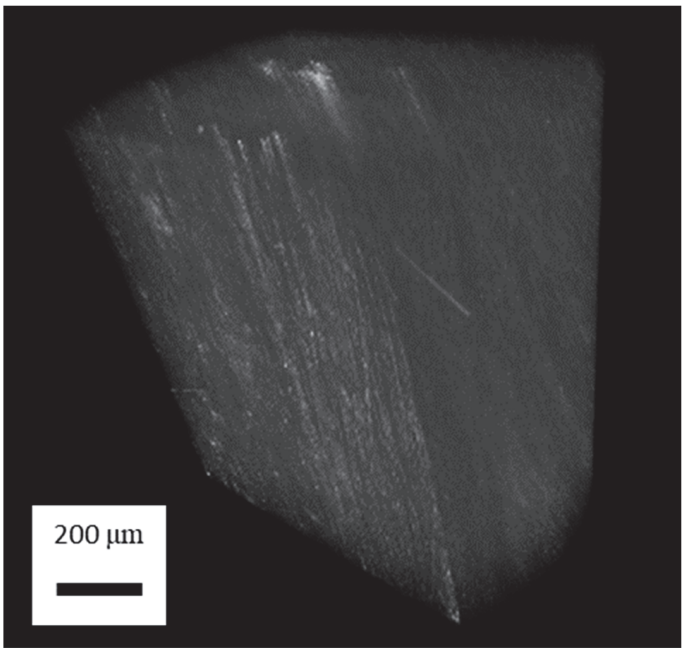

Figure 7. Three-dimensional image created from micro-CT images of CFRP-(45°, 40°, 35°, 30°, 25°, 20°, 15°, 10°, 5°, 0). Deliberate offsets of 5° were used to determine the fibre alignment accuracy of the Fill Multilayer at low-angle reinforcement.

2.5. Three-Point Bending in Cyclic and Quasi-Static Bending Setup

Flexural three-point bending tests with quasi-static cyclic loading were in accordance with ASTM D7264/D7264M–15 [44]. The use of cyclic loading allowed us to investigate the inter-fibre failure (IFF) under fatigue loading, which was the initial stage of fatigue failure [45,46], during which microcracking occurred in the matrix and a drop in the modulus was noted [46].

In the three-point bending tests, a rate of 1 mm/min was used using the Zwick UTM with a 10 kN load cell for quasi-static testing of the flexural modulus using an FLAB-3-11-3LJC-F strain gauge. For cyclic loading, a similar setup was used in an Instron UTM 100 kN load cell, as depicted in Figure 8. The test setup used 10 mm grips on a 40 mm span, satisfying the 1:20 ratio in the ASTM.

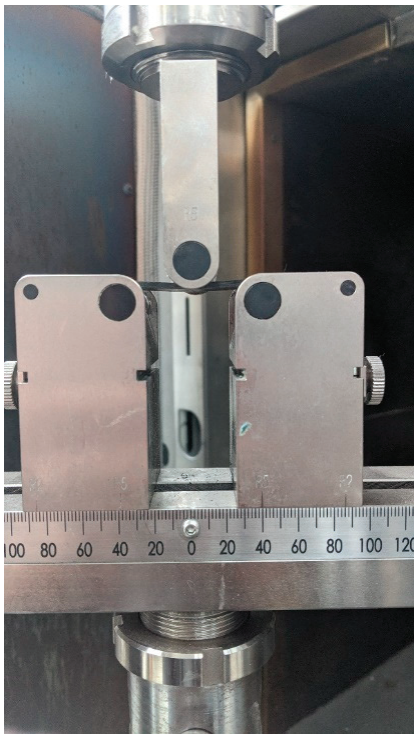

Figure 8. Three-point bending diagram for both quasi-static and cyclic three-point bending.

2.6. Testing Parameters for Fatigue Loading

To determine the stiffness degradation of the CFRP made in the Fill Multilayer, the CFRP was subjected to 70% of its maximum flexural strength for 4000 three-point bending cycles at 1 Hz. Fatigue testing of composites with minor fabric alignments can create variations in material behaviour, as previously determined by Alam et al. [25]. Blythe et al. [40] showed that matrix cracking occurred within 4000 cycles, after which, the next significant modulus decrease was due to fibre failure. The unidirectional composites were tested with a load of 700 N, while the testing load for the deliberately offset samples was 300 N. The loading was set to 700 N, which was converted from the value in MPa that was determined during quasi-static testing. The preloading condition for both scenarios was 100 N to prevent sample movement during cyclic loading. A constant load of 700 N was chosen to simulate the fixed force experienced by load-bearing structures.

3. Results and Discussion

3.1. Waviness Effect of CFRP in Hand-Layered Composites

As a basis for comparison, in this section, off-the-shelf CFRP prepregs and the effect of crimping on alignment and waviness are investigated. Crimped CFRP was deliberately wavy and illustrated the mechanical performance with slight angular defects, as shown in

Figure 9. The maximum outliers shown in Figure 9I,II, highlight that the fibre alignment was affected by cross stitching, which is depicted in (IV), showing a misalignment of up to 6.89° measured at Φ.

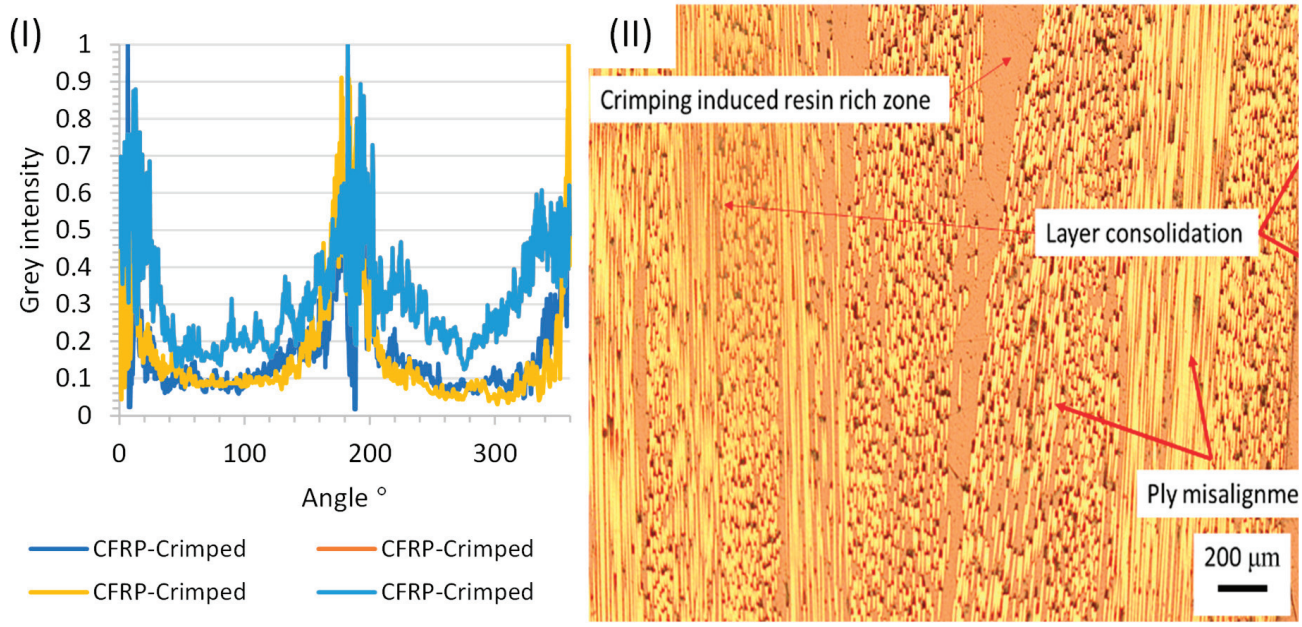

Figure 9. Crimped fabric to illustrate the effect of waviness on both the fibre alignment and the mechanical strength: (**I**) crimped CFRP fibre alignment as determined via a radial sum analysis in ImageJ and (**II**) fibre consolidation and misalignment in crimped CFRP.

The resin-rich zones created in crimped CFRP created a wavy pattern. The fibres were then prevented from fully consolidating into a laminate. Instead, a solid crimped fabric existed, which caused a defect zone within the composite laminate, as shown in Figure 9I. There were many different fibre angles present in one localised area due to crimping; this created a random distribution. As other layers were not aligned with the previous layer, the randomness further increased. Machine tooling ensured that the crimping could be distributed evenly across the laminate. However, with hand laying, it was difficult to evenly spread the crimping throughout the laminate. As a result, the fibre angle was ±5.04° and ±5.02° for the crimped fabric. Partial consolidation was achieved between the fibre bundles during pressing; however, resin rich zones were present, as depicted in Figure 10II.

3.2. *Alignment of CFRP Fibres Created by Hand Laying and the Fill Multilayer*

To analyse the Fill Multilayer's performance, a comparative study of both static and dynamic three-point bending was conducted. To determine the effect of alignment on the fabric's mechanical properties, both modulus and flexural strength destructive evaluations of the untested samples were performed. The alignment was measured using radial sum analysis in ImageJ, as shown in Figure 10. Four samples were taken from the outer edges of the plate, and an additional four were taken from the internal plate structure. This was to investigate differences occurring due to edge alignment between the mould and the CFRP plate.

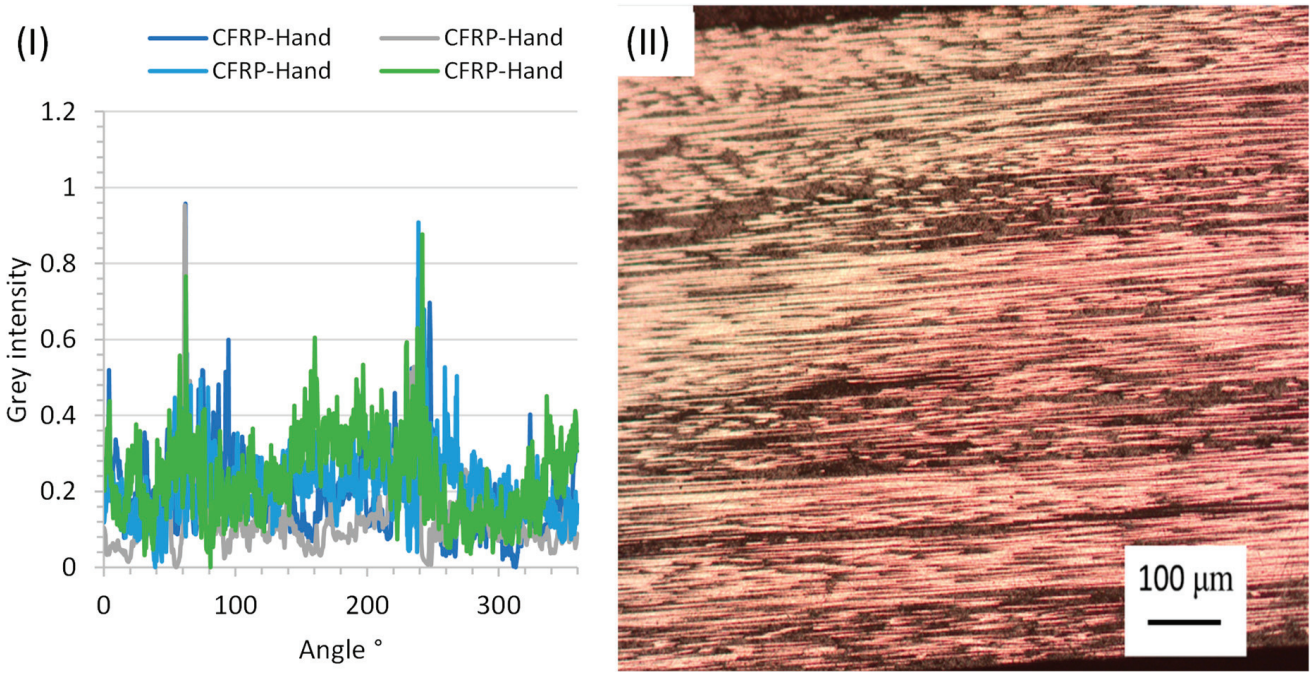

Figure 10. Analysis of the orientation of CFRP fibres produced by hand laying: (**I**) fibre alignment graph of a row from sample 1 taken from the centre of the test plate; (**II**) ten CFRP layers from the edge. Images were taken after cutting though an untested sample; fibre orientation images were analysed using ImageJ.

The radial sum analysis showed that the fabric was more aligned in non-crimped fabric compared with crimped fabric. Crimping induced waviness, with an average fibre alignment of over 5°, and that of the hand-layered samples of only 3.45°. The main cause of misalignment was determined to be ply rotation rather than individual fibre misalignment. One artefact noticeable in the radial sum analysis was the split peak on the ninety-degree side; in Figure 10, the fibres were aligned such that cutting through the fabric removed the fibre ends. In this figure, there are several layers that appear to be aligned in contrast with the other fabric. This was visible in the radial sum analysis, and although it was difficult to quantify the degree of misalignment, the grey intensity was different due to the lack of fibres. Use of the Fill Multilayer led to an expected improvement in the fibre alignment compared with the hand-layered counterpart, with a decrease in the fibre dispersion from 3.45° to 1.68°.

After examining the helix structure, it was determined that a minor fibre scattering of only 1.68° occurred during CFRP-F pressing; thus, the misalignment for a multidirectional composite should have a <2° margin for error. This result shows that the coupons produced in the Fill Multilayer were better aligned and had a greater mechanical strength. As there was greater fibre misalignment between CFRP-Hand, as shown in Figure 10, and CFRP-Fill, as shown in Figure 11, the next step was to analyse the difference in the defects present in these samples. The void concentration was shown to increase after ultrasonic welding, with the average void content increasing by 9.24% from 3.46 $\pm$ 0.55% to 3.78 $\pm$ 0.58% for CFRP-Hand and CFRP-Fill, respectively. This similarity in the void content suggests that the CFRP-Fill sample was minorly impacted by ultrasonic welding. However, mechanical tests showed that that this was not detrimental to the laminate's quality. It was anticipated that cross stitching would lead to a larger resin-rich zone for void formation; however, there was no additional void content in this area. From the micro-CT data, it was shown that there were several instances of void formation during ultrasonic welding in the helix structure. Using Image-J, the void content of the thousand image slice was taken to accurately determine the void content for the centre of the structure.

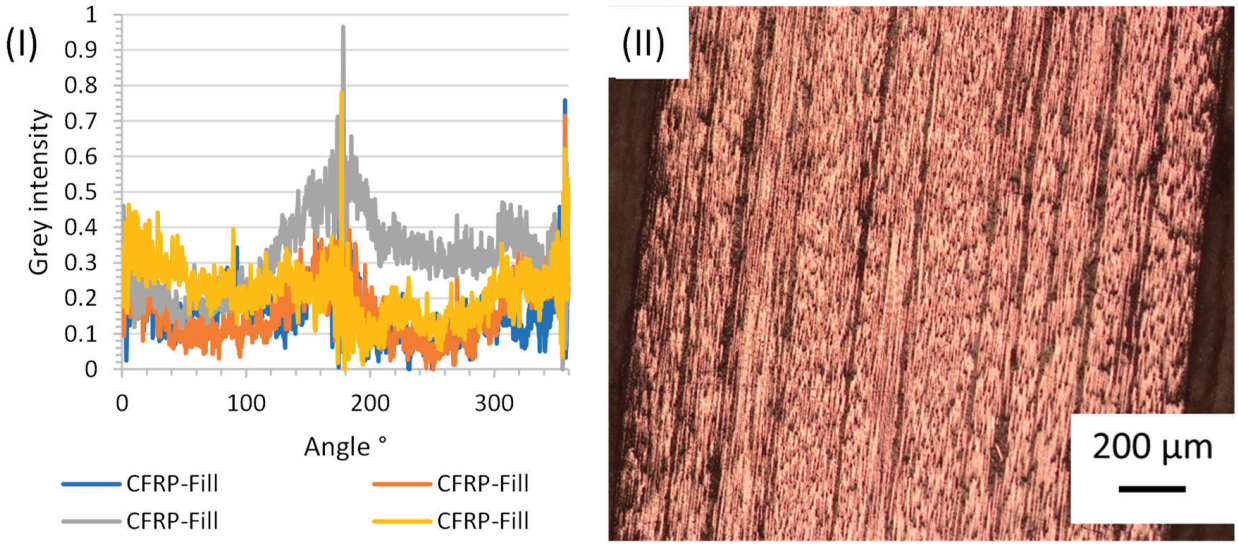

Figure 11. (**I**) Fibre alignment graph of CFRP-Fill test samples taken from the centre of the test plate; (**II**) fibre alignment graph of CFRP-Fill test samples taken from the outer edge of the test plate.

3.3. Alignment of Fibre Stacks at Different Layup Orientations

To test the alignment performance of the Fill Multilayer, a bioinspired helicoidal structure was created with a tape offset of 5°. This helicoidal structure, based on Bouligand structures, has been shown to have an improved impact resistance [47–50] and would serve to showcase the Fill Multilayer's laying accuracy. The improved impact resistance could be attributed to the coupled effects of the fibre offset (1° to 25°) and spiral stacking sequence, which resulted in a longer crack propagation path. A helicoidal structure can be developed via automatic tape laying at a 5° offset. The structure's behaviour was tested alongside the accuracy of the machine's placement. There was a problem with low-angle fibre offsets, as the fibre tolerance needed to be high to stop gaps from occurring within the fibre stacks.

Assuming that the Fill Multilayer had a margin of error of ~1.26°, it was expected that a helix structure that was layered every 5° would result in fibre alignment of 4° to 6°. Figure 12 shows that ultrasonic welding produced a void concentration below the tape, assuming some tow splitting, which resulted in the resin being partially cured; this then created inter-tow voids during curing.

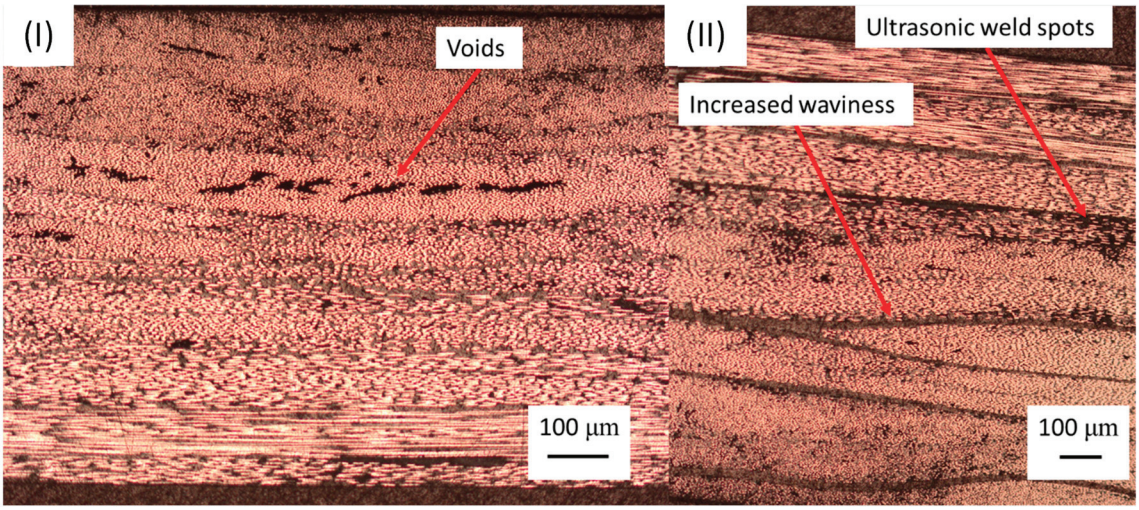

Figure 12. Analysis of the orientation of CFRP 5+ fibres created by the Fill Multilayer using ImageJ; (**I**) mid slice, (**II**) end slice, (**II**) graph of the fibre angle measured via microscopy and micro-CT.

Figure 12I shows the effect of improper consolidation on the centrepiece (the fibre contained voids). An increase in void concentration could be observed from the micro-CT results shown in Figure 13, where the fibre exhibited divots caused by compression of the fibres using an ultrasonic weld horn. The divot in the CFRP prepreg resulted in a semicircular displacement of the resin, and it was shown via CT that this displacement caused voids under the divot area. The preform was held together with resin; therefore, the only fabric characteristics affecting the fibre geometry in the Z direction were fibre nesting and ultrasonic weld spots. Ultrasonic weld spots were difficult to detect by examining cross sections; instead, micro-CT images of the entire sample were taken and are shown in Figure 13.

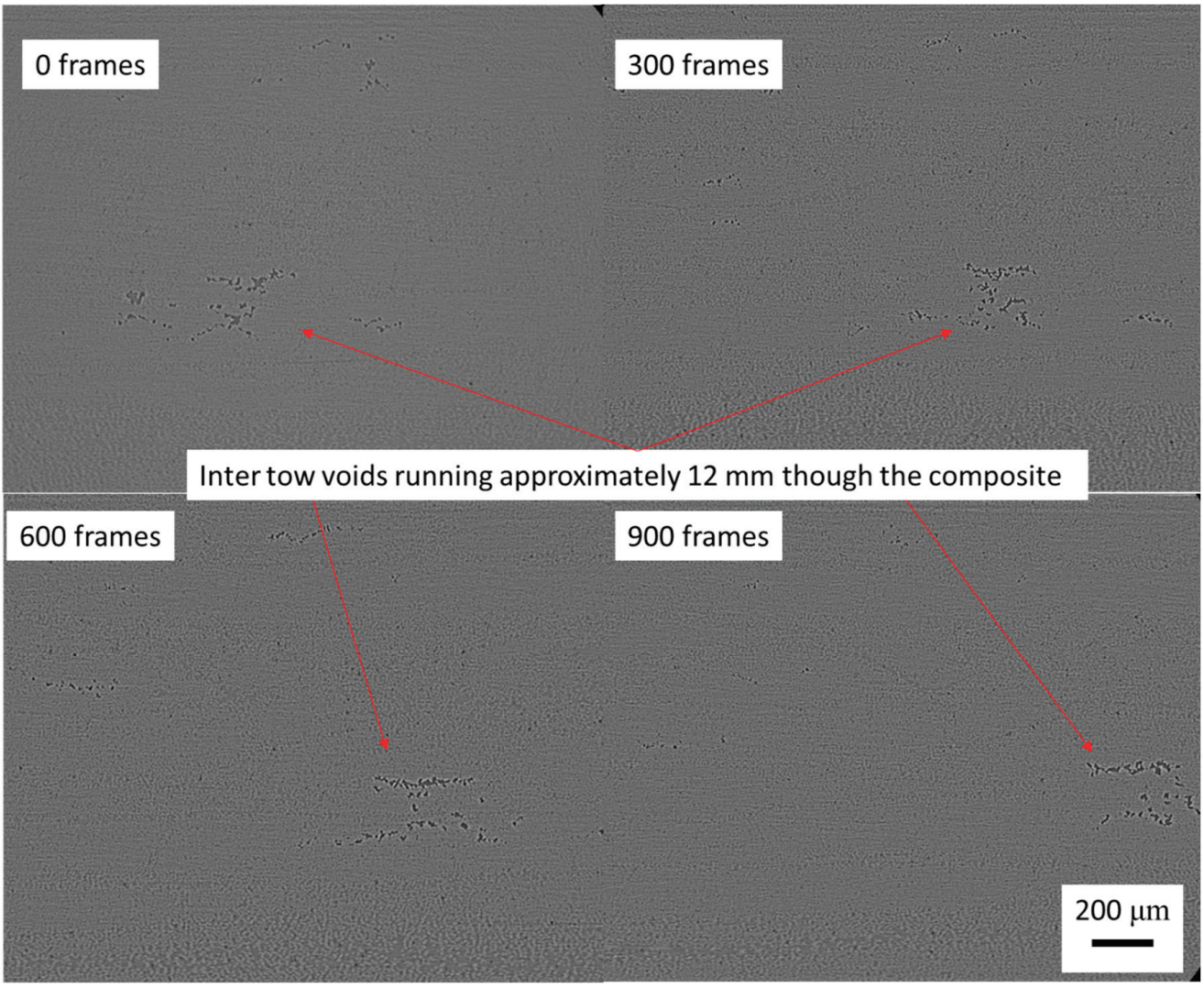

Figure 13. Micro-CT of CFRP helix structure slices 0 to 900. View of the CFRP voids within the fibre tow.

The initial micro-CT images shown in Figure 13 show that the majority of the void contents in the material were positioned between the tapes. The tape and inter-tape voids were likely a result of gaps in the tape, which were formed by compressed trapped air. The image slices were stacked in the XZ axis, as shown in Figure 14, allowing for a radial sum analysis of the (45°, 40°, 35°, 30°, 25°, 20°, 15°, 10°, 5°, 0) offsets.

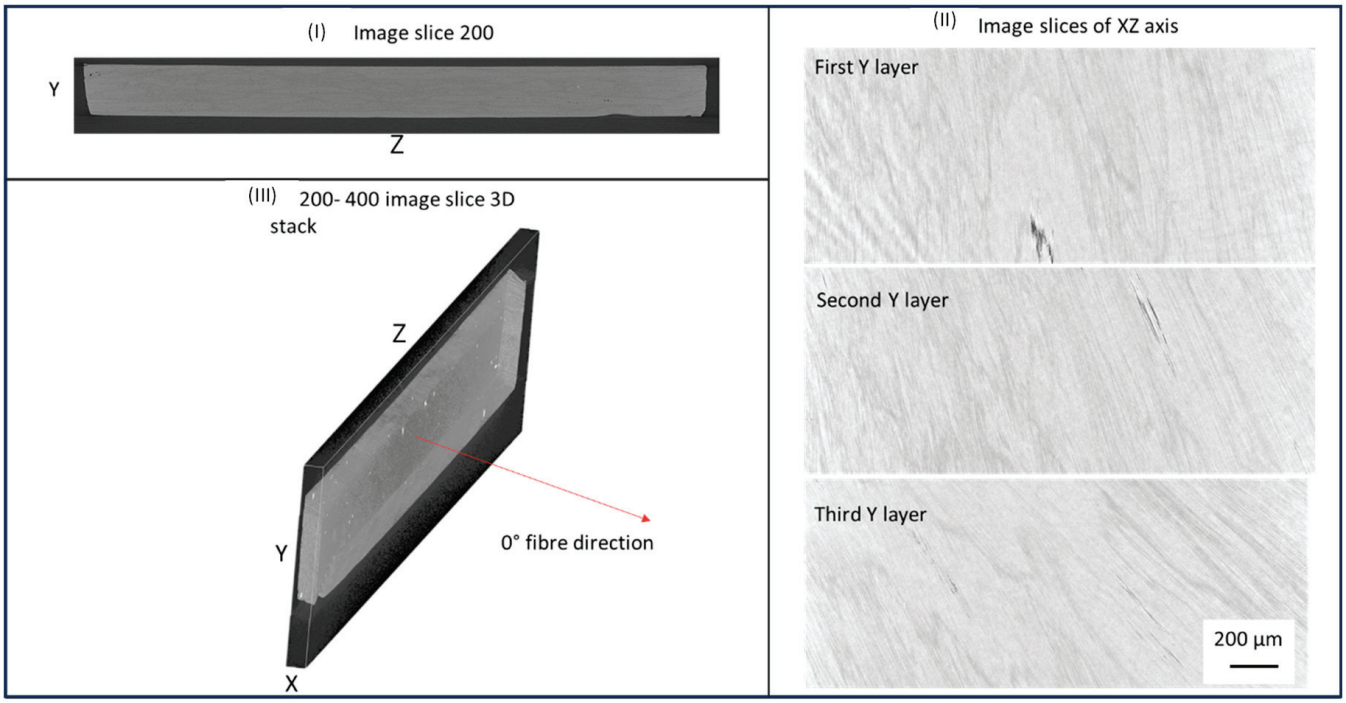

Figure 14. Micro-CT scan of top-down beam in 3D snippet of (**I**) images slices of the Y-Z axis; (**II**) image slices of the XZ axis; (**III**) 3D image stack of image slices 200–400.

From the images, it is clear that the coupon edges were minorly damaged due to the cutting process with deliberate misalignments. Several cracks ran from the voids to the edges, resulting in pre-cracked coupons. The XZ images were used to generate the radial sum plot shown in Figure 15.

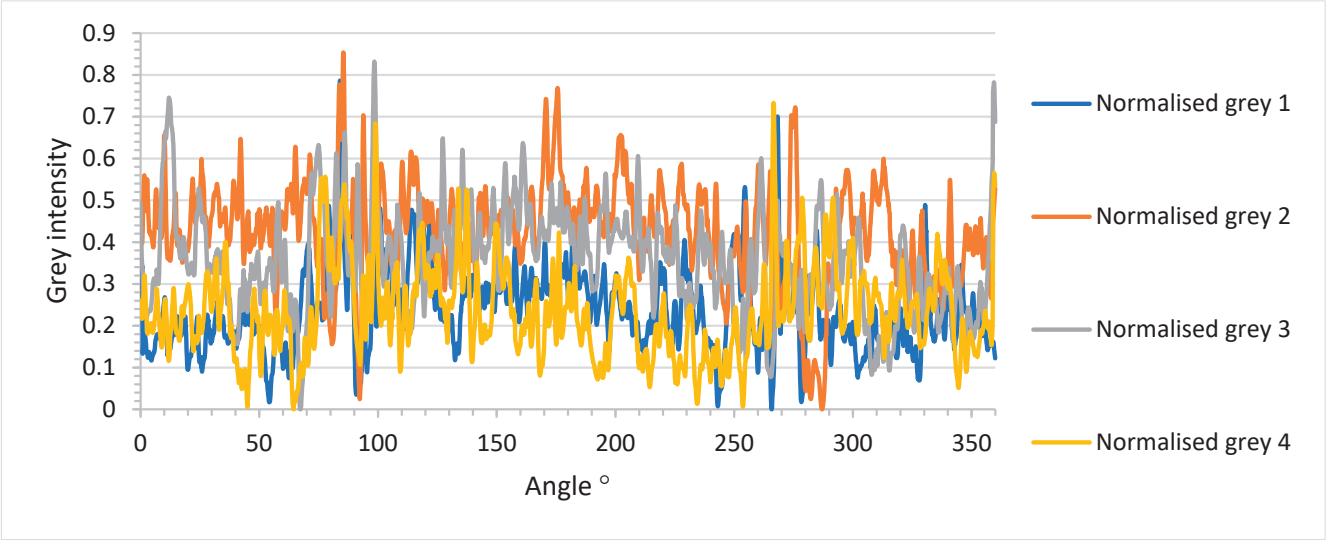

Figure 15. Fibre alignment of each layer in (45°, 40°, 35°, 30°, 25°, 20°, 15°, 10°, 5°, 0) taken from micro-CT scans.

The fibre alignment of the (45°, 40°, 35°, 30°, 25°, 20°, 15°, 10°, 5°, 0) samples was determined to be 2.21°. This increase, compared with the UD fabrics, suggests that tape misalignment increased as the fibres were pressed. This was expected as the fibres were moving over one another, becoming wavey, and the fibres were unable to nest without being bent.

3.4. Quasi-Static Three-Point Bending of CFRP-UD Fabrics

As in the hand-laying method, a sheet of CFRP prepreg and not tape was used so that no gaps or ultrasonic weld marks could form. It was expected then that these defects would not be present in samples produced via hand laying compared with those produced via the Fill Multilayer. The change in the CFRP-Hand samples was shown to be less than that of the CFRP-Fill samples.

The hand-layered CFRP-Hand samples had a similar flexural strength maximum, as shown in Figure 16. The samples produced using the Fill Multilayer exhibited a higher flexural strength than that of the hand-layered samples, with an average of 1218.57 ± 78.85 MPa compared with 1116.59 ± 82.39 MPa, taken from Figure 17. No observable difference in the failure mechanism was found between the CFRP-Hand and CFRP-Fill samples.

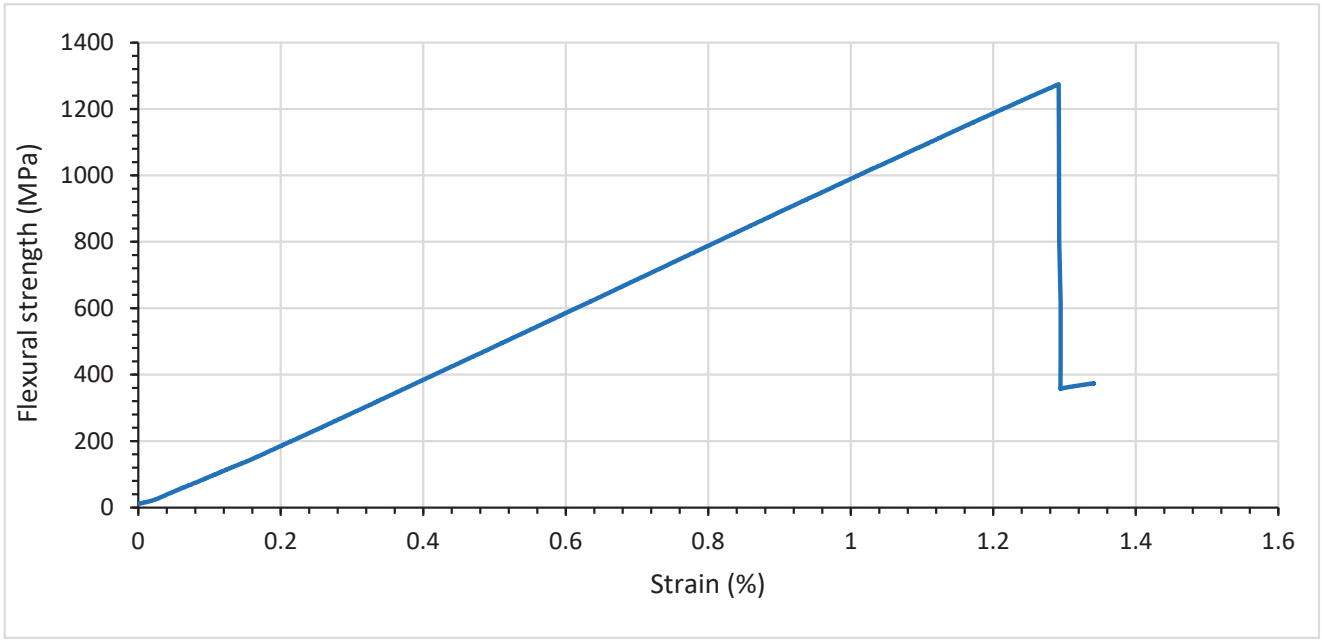

Figure 16. Hand-layered CFRP stress–strain curve after three-point bending tests.

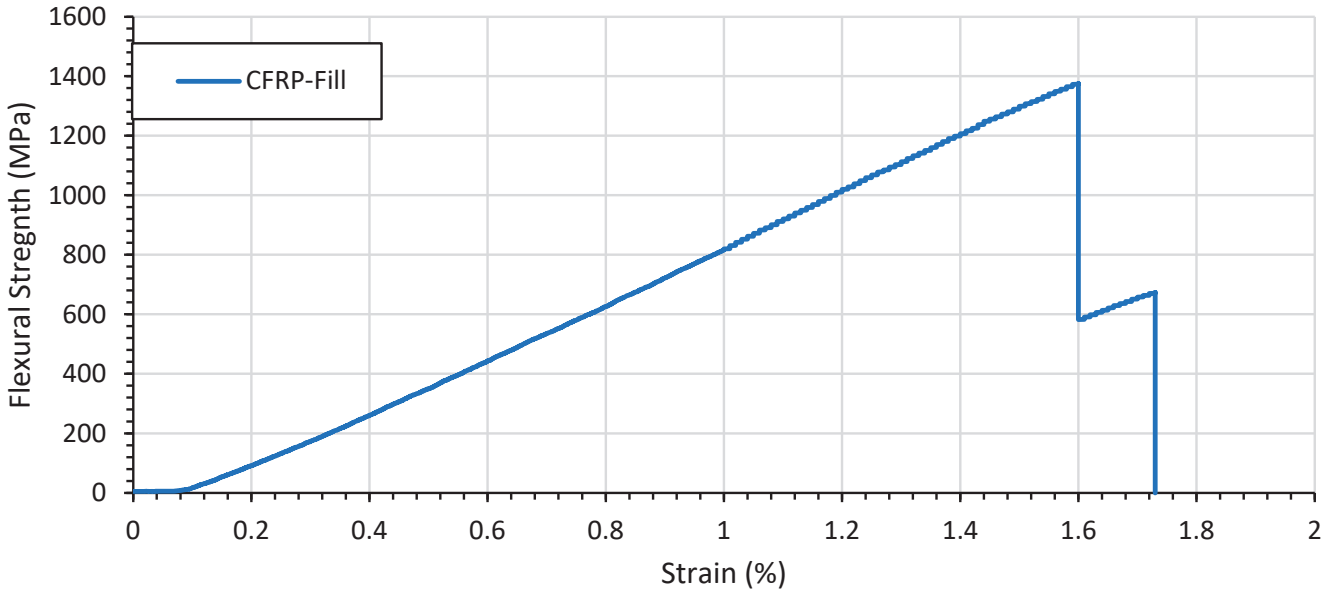

Figure 17. Flexural strength of Fill Multilayer-manufactured CFRP.

The main issue with the Fill Multilayer machine was the high deviation in the flexural strength of 78.85 MPa, which was higher than that of the hand-layered samples. This deviation was investigated to determine whether the result was due to ultrasonic welding marks occurring under the machine head (out of the cut 18 samples, 4 should be free from ultrasonic welding marks). During testing, it was shown that minor premature failure occurred in samples with ultrasonic weld spots. This sample inconsistency led to the use of a thermoplastic nanofibre inter-layer to attempt to reduce the weld defects. Additionally, this failure could be due to gaps between the tape, as alternating tapes would wither and thus a weld mark or gap would appear.

The failure mechanisms of the UD samples shown in Figure 18 showed that both Fill multiplayer samples failed due to compression failure turning into inter-laminar delamination, as expected. From microscopy performed on the Fill Multilayer samples, it was clear that the failure of both samples initiated due to buckling of the first carbon fibre layer, which then propagated into inter-laminar failure.

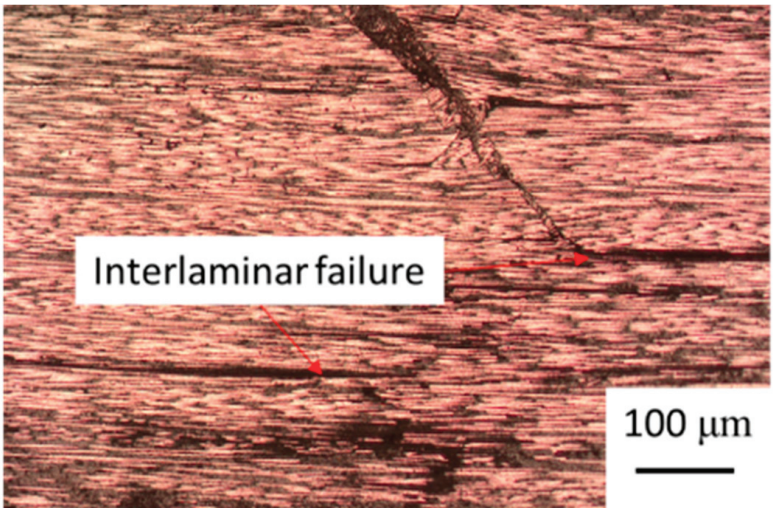

Figure 18. Failure mechanisms of Fill Multilayer-produced UD samples.

3.5. Tape-Laying Accuracy at Different Fibre Angles

In deliberately offset samples, the stress–strain response exhibited a more pseudo-ductile response than that of the brittle UD samples. Rotation around the fibre angle produced a flattened peak response in the crack propagation, as shown in Figure 18.

The response showed that the (0°, 5°, 10°, 15°, 20°, 25°, 30°, 35°, 40°, 45°) CFRP underwent catastrophic failure due to failure of the compression layer's UD fabric. In the (45°, 40°, 35°, 30°, 25°, 20°, 15°, 10°, 5°, 0) sample, the UD fabric under tension was aligned, resulting in a higher flexural strength.

This investigation into the flexural strength and angle of alignment demonstrated an exponential relationship between the fibre alignment and flexural strength. It is important to note that a unidirectional fabric was assumed in the (0°, 5°, 10°, 15°, 20°, 25°, 30°, 35°, 40°, 45°) helix sample with the characteristics of a single carbon layer under compression. The reverse sample, as depicted in Figure 18, had a significantly higher flexural strength than the 0° fibre angle sample under compression.

From Figure 18, an average flexural strength of 487.70 ± 53.23 MPa for helix-CFRP could be determined. The (45°, 40°, 35°, 30°, 25°, 20°, 15°, 10°, 5°, 0) samples had flexural strengths of 204.08 MPa and 245.62 MPa. The pseudo-ductile behaviour was examined via microscopy, and it was determined that the failure of the material was very similar to that of the helicoidal structure. As with the helicoidal structure, crack propagation was deflected by the low angle of reinforcement around the fibres. The resulting failure was delamination and inter-fibre failure, as shown in Figure 19.

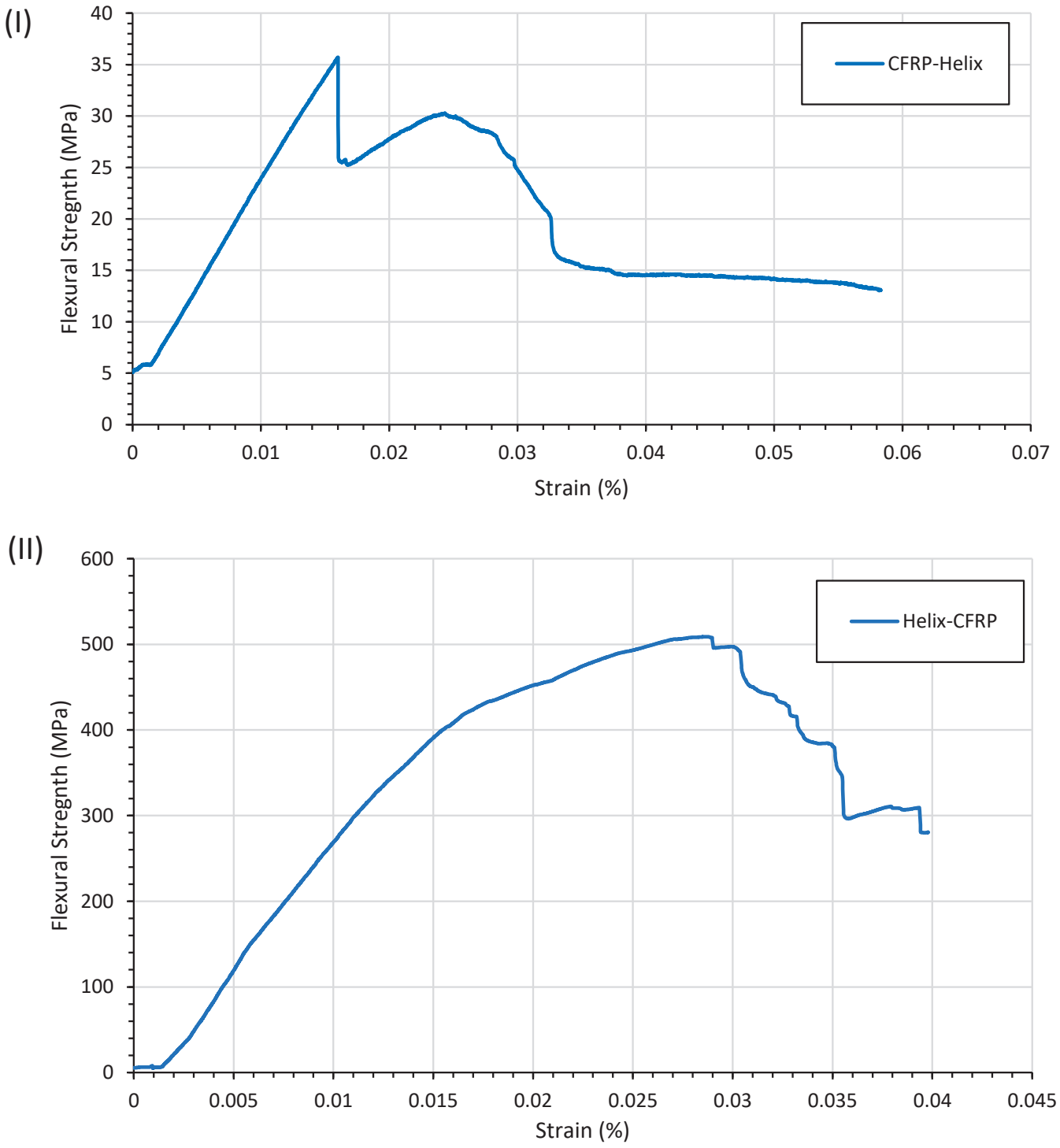

Figure 19. Flexural testing of CFRP via three-point bending tests for stacking sequences: (**I**) helix-CFRP (45°, 40°, 35°, 30°, 25°, 20°, 15°, 10°, 5°, 0) and (**II**) (0°, 5°,10°, 15°, 20°, 25°, 30°, 35°, 40°, 45°). A pseudo-ductile response to flexural loading is demonstrated.

There was little difference between the failure mechanisms of the helix-CFRP and the control samples. All samples exhibited significant fibre propagation in the inter-fibre region due to the change in fibre direction. This resulted in extensive inter-fibre delamination between fibres, as shown in Figure 20.

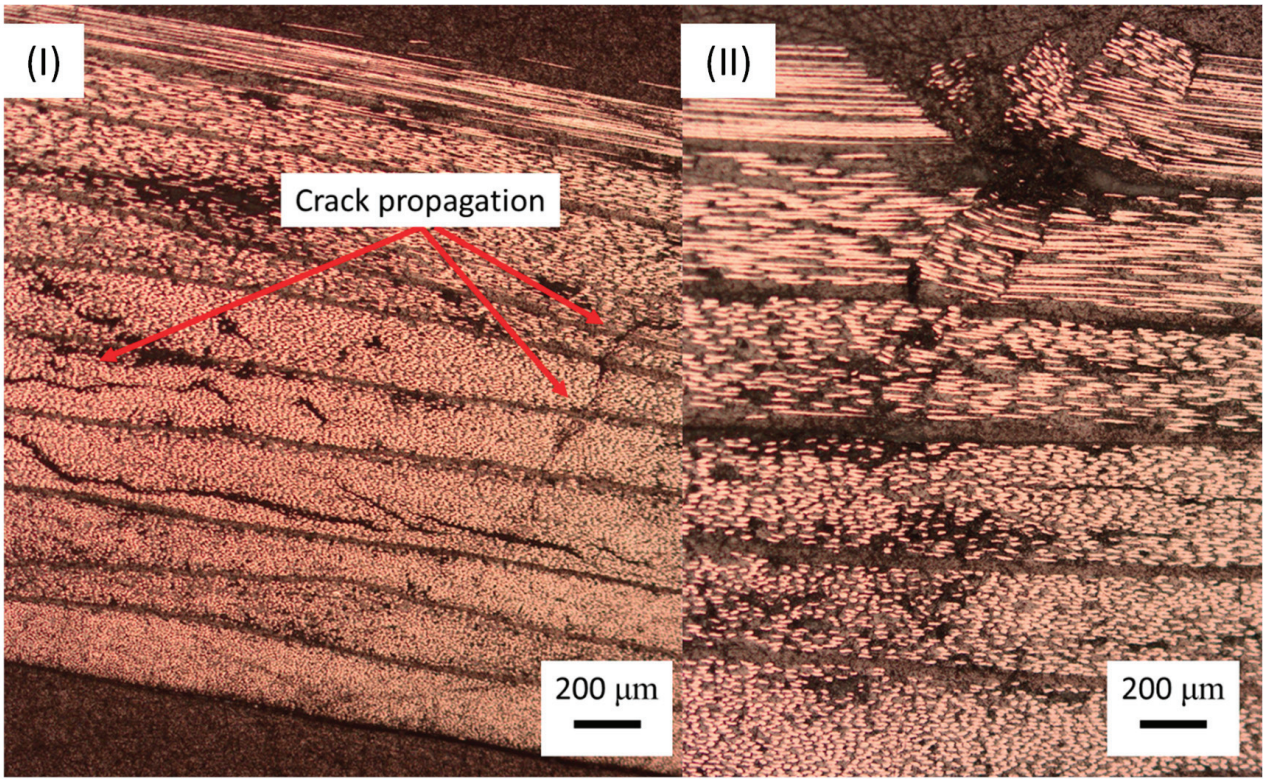

Figure 20. Helix-CFRP (0°, 5°,10°, 15°, 20°, 25°, 30°, 35°, 40°, 45°) optical images of failure mechanisms with (**I**) helix-CFRP-Fill and (**II**) control.

3.6. Examination of the Flexural Strength at Different Fibre Misalignment Angles

The resulting fibre alignment and void characteristics are shown in Table 2. The hand-layered CFRP plies exhibited a fibre misalignment of 0° ± 3.5° in the in-plane direction after curing, as shown in Table 2. A potential flaw found in the Fill Multilayer process was the ultrasonic welding step, which caused a section of epoxy to be cured and fibre waviness to occur. Initial imaging showed that the fibres were pushed out from the centre of the weld spot, causing a resin-rich centre under the welder horn. Tow splitting in the y-direction, as seen in Figure 12, was a contributing factor to misalignment in the x-direction.

Table 2. Mechanical and fibre alignment of CFRP produced by hand and by the Fill Multilayer.

Sample	Fibre Alignment	Flexural Strength MPa	Flexural Modulus GPa
CFRP-Hand	3.45 °	1049.81 ± 35.45	72.15 ± 6.85
CFRP-Fill	1.68 °	1218.57 ± 78.85	73.33 ± 4.01
(45°, 40°, 35°, 30°, 25°, 20°, 15°, 10°, 5°, 0)	2.21 °	475.128 ± 38.46	19.7 ± 0.49
(0°, 5°, 10°, 15°, 20°, 25°, 30°, 35°, 40°, 45°)	2.21 °	31.8 ± 1.92	6.57 ± 0.38
CFRP-Crimped	5.18 °	920.33 ± 39.8	60.28 ± 5.86
CFRP-Crimped-Traverse	5.04 °	326.25 ± 45.2	2.17

The alignment of the fabric differed between hand-layered CFRP and that layered by the machine. The deliberately offset fabric had a higher misalignment angle than the CFRP-Fill sample. It was anticipated that the compression process would result in fibres rotating to nest in one another, as well as waviness during compression, hence the higher angle of misalignment compared with the UD samples. During processing in the Fill Multilayer, the tape became the limiting factor, affecting random fibre alignment. There were several issues with the tape, such as splitting of the toes before spooling and prepreg sliding due to friction and pressing. To determine the effect of fibre alignment, a hand-layered sample was compared with a Fill Multilayer-manufactured sample under identical curing

conditions. As a further reference, a hand-layered crimped UD fabric was studied. The resulting average flexural strength and modulus were recorded for each sample, as shown in Table 2. The angle of fibre misalignment was measured at different flexural strengths, as shown in Figure 21, showing the exponential relationship between the fibre angle and the flexural strength.

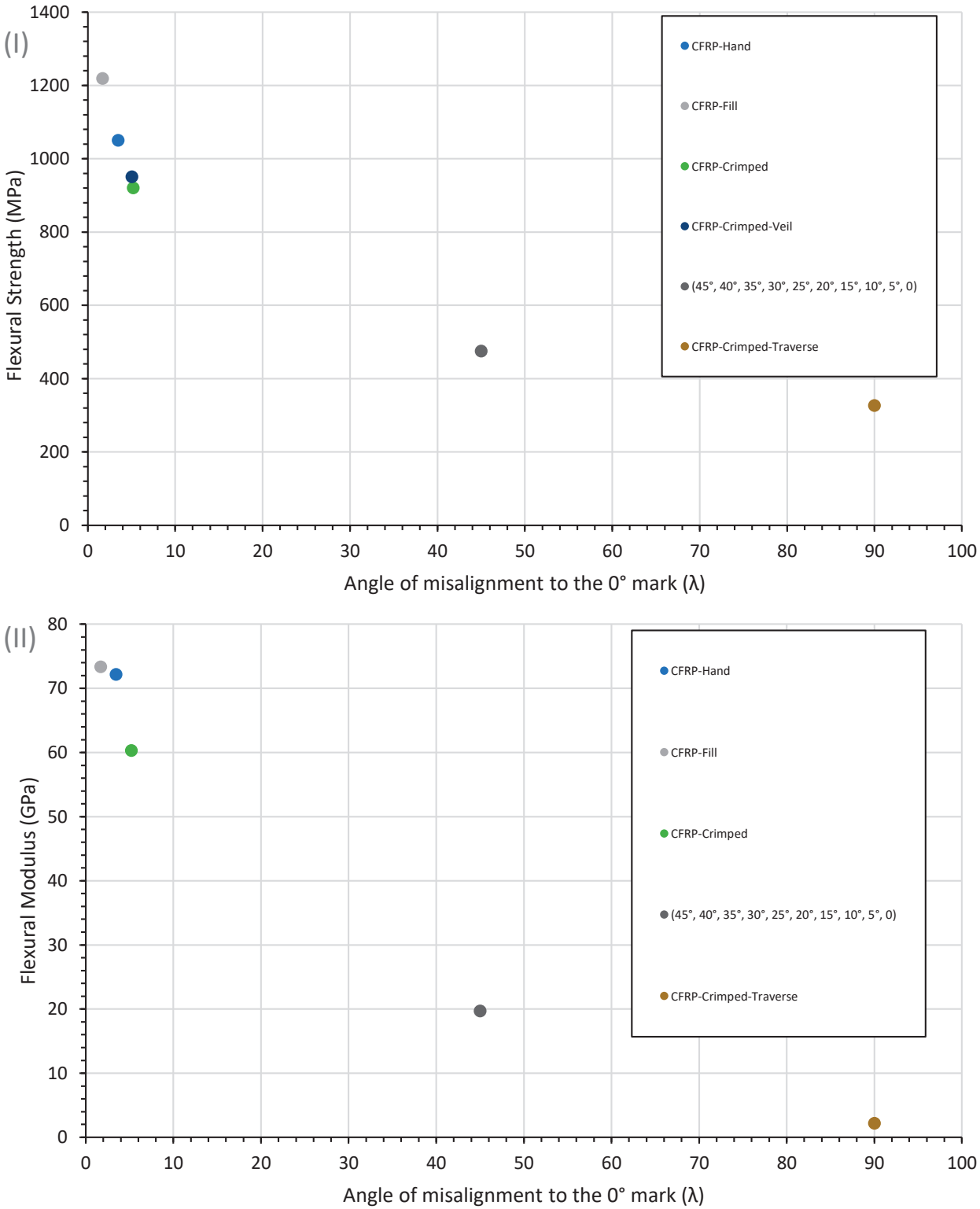

Figure 21. Plot of CFRP's flexural (**I**) strength and (**II**) modulus at different fibre orientations as a function of the average alignment of the fibre over the span of the test length.

The logarithmic relationship between the CFRP alignment and fibres shown in Figure 21 indicated that, despite the cross stitching, the material properties obtained by aligning the fibres manually could be reliably predicted. However, this relationship was not true for the (0°, 5°,10°, 15°, 20°, 25°, 30°, 35°, 40°, 45°) stacking order, only the reverse. The lower limit of the yield point perpendicular to the fibre angle was determined by the resin's flexural characteristics. The upper limit of the composite was determined by the maximum tensile strength.

3.7. Dynamic Testing of CFRP

To determine the shear stress in the presence of fibre misalignment in the matrix, which is the main cause of matrix cracking, a comparison of cross-stitched CFRP to non-crimped CFRP was performed to determine the effects of waviness on the fibre. Initial matrix cracking was visible around the cross stitches, as the matrix-rich areas were prone to crack initiation. Compared with the CFRP without stitching, a higher flexural modulus was determined via quasi-static testing. It was expected that, due to higher misalignment, the hand-layered material would have more matrix cracks and the Fill-CFRP sample would have a higher stiffness retention.

During quasi-static tests, the strain behaviour was dominated by the modulus of the CFRP-Fill and CFRP-Hand samples, with values of 73.33 GPa and 72.15 GPa, respectively. However, the stress–strain behaviour was correlated with the fibre alignment, with Fill samples having a higher strain of 0.008% compared with 0.006% for hand-layered samples. The failure mechanism that led to this nonlinear behaviour is shown in Figure 22. The majority of CFRP-H samples exhibited ply delamination in the compression layer; this also occurred in quasi-static testing.

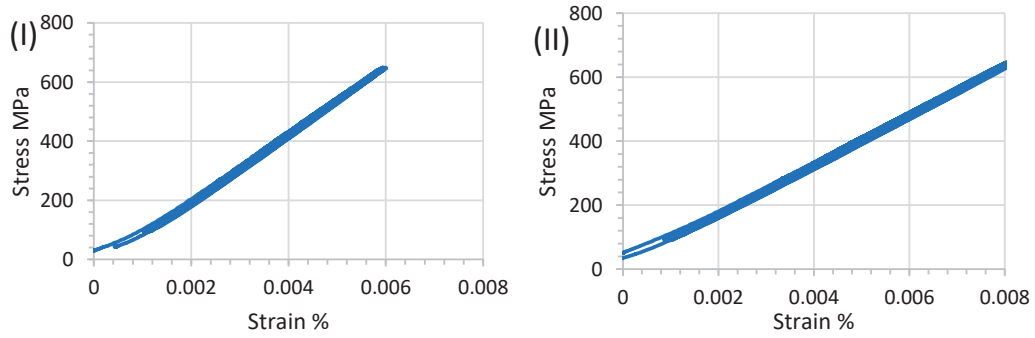

Figure 22. Stress–strain curve of CFRP manufactured via (**I**) hand laying, (**II**) the Fill Multilayer, cyclically tested using three-point bending to a maximum loading of 700 N for 4000 cycles to examine matrix cracking.

The failure of the crimped and non-crimped fabrics in both static and dynamic testing clearly indicated the difference in flexural strength. In CFRP-Crimped samples, failure occurred via block crack propagation compared with the delamination occurring between plies in CFRP-Fill and CFRP-Hand samples. Delamination caused a larger drop in the modulus compared with CFRP-Crimped. After 4000 cycles, the modulus of CFRP-Hand was 54 GPa ± 1.98 GPa.

The UD CFRP samples all exhibited little stiffness degradation after 4000 cycles at 70% of the maximum loading, with the lowest occurring for CFRP-Fill at less than 3% across the data set, as shown in Figure 23.

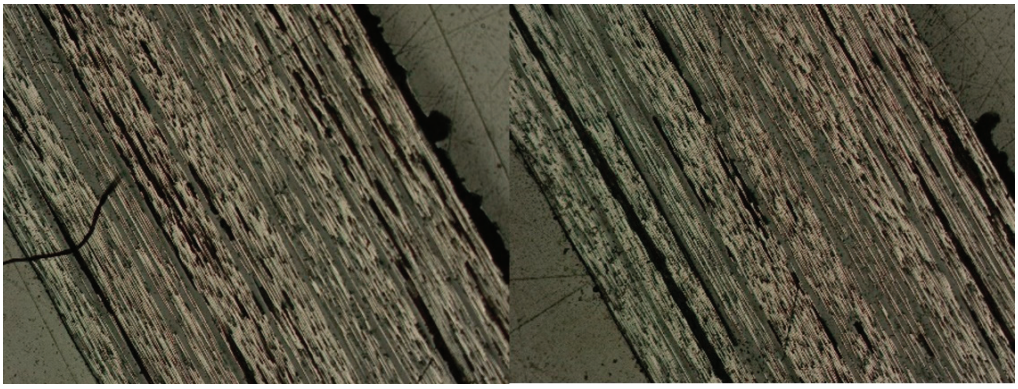

Figure 23. Microscopy of CFRP manufactured by hand laying, cyclically tested using three-point bending to a maximum loading of 700 N for 4000 cycles to examine matrix cracking.

The non-crimped fabric produced via the Fill Multilayer exhibited a smaller flexural modulus decrease compared with hand-layered samples, as shown in Figure 24. A decrease in the fibre alignment led to a greater stiffness retention in these samples compared with hand-layered samples. The reproducibility of the CFRP-Fill samples was significantly higher than the other samples, suggesting minimal manufacturing defects. The zero-tack resin used in the CFRP in the Fill Multilayer required a five-minute curing time. However, when the fibre alignment was as low as 1.68, the shear stress affected the matrix and thus large longitudinal delamination occurred. Compared with the Fill Multilayer-produced samples, the stiffness loss was minimal, with an average drop of 1.4% in the modulus after cycling.

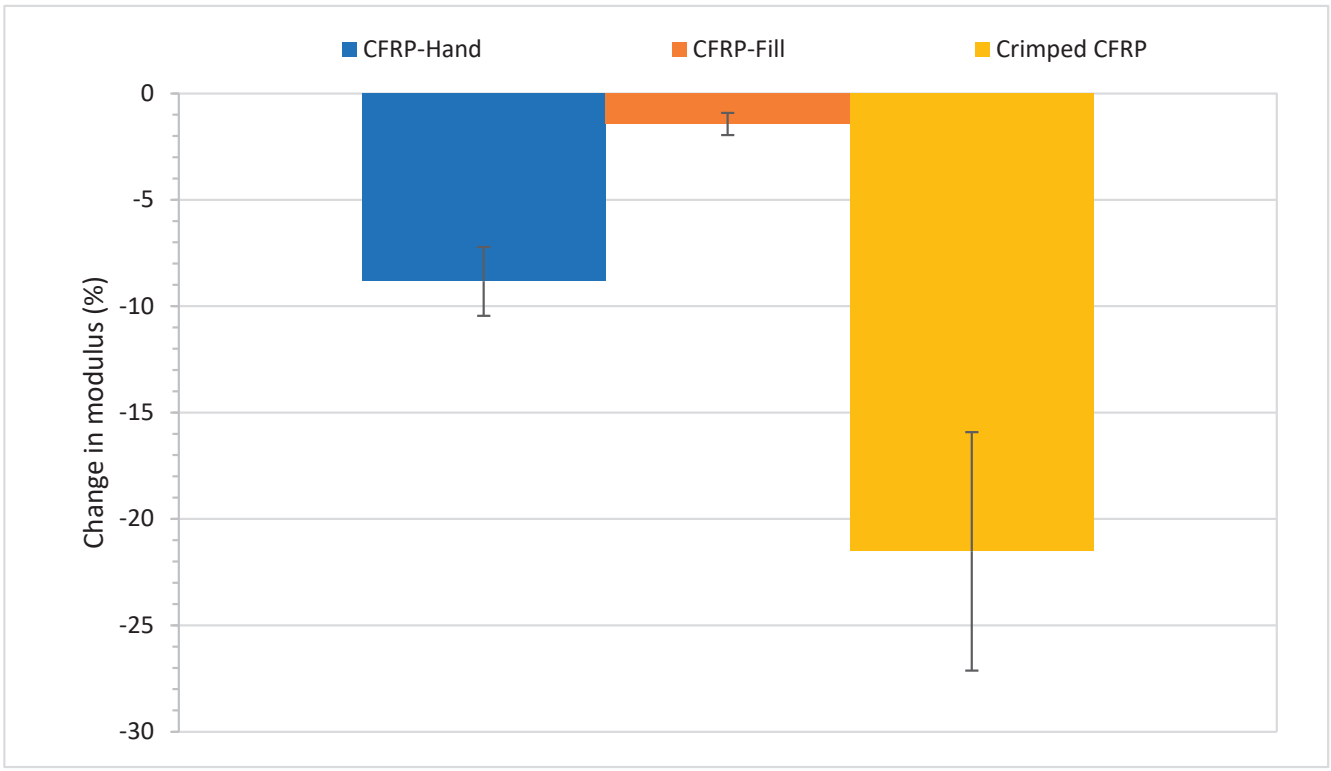

Figure 24. CFRP modulus change after 4000 cycles at 700 N loading for 4000 cycles for handmade and Fill Multilayer-manufactured CFRP.

4. Conclusions

Fibre alignment was shown as the lead cause of matrix cracking, as poor alignment led to fibre shearing. The Fill Multilayer machine produced UD composites with an alignment of $\pm 1.26^{\circ}$, lower in comparison with hand-layered composites, which had a minimum alignment of $\pm 3.45^{\circ}$. Minimal misalignment occurred due to the Fill Multilayer, leading to a higher flexural strength, with inter-laminar failure occurring on the tension side. Compression failure in the hand-layered samples resulted in significant delamination and buckling. The cracks continued to propagate after their initial formation, with significant loading retention.

The improved fibre alignment of samples manufactured by the Fill Multilayer led to significant improvements in the flexural strength. With the Fill Multilayer, an improvement in the fibre alignment compared with hand laying was observed, showing a better reproducibility. The deviation in Fill Multilayer samples was high due to several processing issues and the effects of ultrasonic welding. In the microscopy cross sections, there was a high concentration of voids within the inter-tow region of the fabrics. During ultrasonic welding, a divot occurred within fabrics with a higher alignment; this had a minimal impact on the laminate. The void content in handmade and Fill Multilayer-produced CFRP was 3.46% and 3.75% in this study. As the void content was within the standard deviation of the Fill Multilayer-produced coupons, it was concluded that ultrasonic welding had only a minor effect on the void content. The increase in void concentration was consistent with the prior literature.

The main manufacturing defects were rolling and unrolling, as the Fill Multilayer had a tape width threshold of ± 0.05 mm, which resulted in a low fibre alignment as the tooling became the limiting factor affecting the fabric alignment. Random alignment was limited by the Fill Multilayer machine, with the tolerances for the roll and tape being a limiting factor in alignment. It is therefore necessary to identify the machine tolerances when predicting fibre alignment. In addition to investigating these machine tolerances, in situ process monitoring and modelling also have great potential in future work.

Author Contributions: Methodology, A.B.; conceptualisation, A.B.; writing—original draft preparation A.B., M.N. and B.X.C.; writing—review and editing, A.B., M.N., B.E. and B.X.C.; supervision, B.F., M.N. and B.E. All authors have read and agreed to the published version of the manuscript.

Funding: This research was funded by Ford Motor Company, grant number URP2016-4010R.

Data Availability Statement: Data are available upon request.

Conflicts of Interest: The authors declare no conflicts of interest. The funders had no role in the design of the study; in the collection, analyses, or interpretation of data; in the writing of the manuscript; or in the decision to publish the results.

References

1. Blythe, A.; Fox, B.; Nikzad, M.; Eisenbart, B.; Chai, B.X.; Blanchard, P.; Dahl, J. Evaluation of the Failure Mechanism in Polyamide Nanofibre Veil Toughened Hybrid Carbon/Glass Fibre Composites. *Materials* **2022**, *15*, 8877. [CrossRef] [PubMed]
2. Chai, B.X.; Eisenbart, B.; Nikzad, M.; Fox, B.; Blythe, A.; Bwar, K.H.; Wang, J.; Du, Y.; Shevtsov, S. Application of KNN and ANN Metamodeling for RTM Filling Process Prediction. *Materials* **2023**, *16*, 6115. [CrossRef] [PubMed]
3. Chai, B.X.; Eisenbart, B.; Nikzad, M.; Fox, B.; Wang, Y.; Bwar, K.H.; Zhang, K. Review of Approaches to Minimise the Cost of Simulation-Based Optimisation for Liquid Composite Moulding Processes. *Materials* **2023**, *16*, 7580. [CrossRef] [PubMed]
4. Shevtsov, S.; Zhilyaev, I.; Chang, S.H.; Wu, J.K.; Snezhina, N. Multi-Criteria Decision Approach to Design a Vacuum Infusion Process Layout Providing the Polymeric Composite Part Quality. *Polymers* **2022**, *14*, 313. [CrossRef] [PubMed]
5. Rodrigues, H.; Arêde, A.; Furtado, A.; Rocha, P. Seismic behavior of strengthened RC columns under biaxial loading: An experimental characterization. *Constr. Build. Mater.* **2015**, *95*, 393–405. [CrossRef]
6. Rodrigues, H.; Arêde, A.; Furtado, A.; Rocha, P. Seismic Rehabilitation of RC Columns Under Biaxial Loading: An Experimental Characterization. *Structures* **2015**, *3*, 43–56. [CrossRef]
7. Zhilyaev, I.; Chang, S.-H.; Shevtsov, S.; Snezhina, N. Preform Porosity and Final Thickness Variability Prediction after Controlled Post-Infusion External Pressure Application with the FEA Model. *J. Compos. Sci.* **2022**, *6*, 361. [CrossRef]
8. Djavadifar, A.; Graham-Knight, J.B.; Körber, M.; Lasserre, P.; Najjaran, H. Automated visual detection of geometrical defects in composite manufacturing processes using deep convolutional neural networks. *J. Intell. Manuf.* **2022**, *33*, 2257–2275. [CrossRef]

9. Mehdikhani, M.; Gorbatikh, L.; Verpoest, I.; Lomov, S.V. Voids in fiber-reinforced polymer composites: A review on their formation, characteristics, and effects on mechanical performance. *J. Compos. Mater.* **2019**, *53*, 1579–1669. [CrossRef]
10. Gokce, A.; Advani, S.G. Simultaneous gate and vent location optimization in liquid composite molding processes. *Compos. Part A Appl. Sci. Manuf.* **2004**, *35*, 1419–1432. [CrossRef]
11. Falk, H.; Christian, W. Manufacturing-Induced Imperfections in Composite Parts Manufactured via Automated Fiber Placement. *J. Compos. Sci.* **2019**, *3*, 56. [CrossRef]
12. Oromiehie, E.; Prusty, B.G.; Compston, P.; Rajan, G. Automated fibre placement based composite structures: Review on the defects, impacts and inspections techniques. *Compos. Struct.* **2019**, *224*, 110987. [CrossRef]
13. Belnoue, J.P.H.; Mesogitis, T.; Nixon-Pearson, O.J.; Kratz, J.; Ivanov, D.S.; Partridge, I.K.; Potter, K.D.; Hallett, S.R. Understanding and predicting defect formation in automated fibre placement pre-preg laminates. *Compos. Part A Appl. Sci. Manuf.* **2017**, *102*, 196–206. [CrossRef]
14. FILL Multilayer. Available online: https://www.fill.co.at/en/products/multilayer (accessed on 6 November 2023).
15. Yadav, N.; Schledjewski, R. Review of in-process defect monitoring for automated tape laying. *Compos. Part A Appl. Sci. Manuf.* **2023**, *173*, 107654. [CrossRef]
16. Sacco, C.; Baz Radwan, A.; Anderson, A.; Harik, R.; Gregory, E. Machine learning in composites manufacturing: A case study of Automated Fiber Placement inspection. *Compos. Struct.* **2020**, *250*, 112514. [CrossRef]
17. Li, H.; Chen, C.; Yi, R.; Li, Y.; Wu, J. Ultrasonic welding of fiber-reinforced thermoplastic composites: A review. *Int. J. Adv. Manuf. Technol.* **2022**, *120*, 29–57. [CrossRef]
18. Boros, R.; Sibikin, I.; Ageyeva, T.; Kovács, J.G. Development and Validation of a Test Mold for Thermoplastic Resin Transfer Molding of Reactive PA-6. *Polymer* **2020**, *12*, 976. [CrossRef]
19. Crossley, R.J.; Schubel, P.J.; De Focatiis, D.S.A. Time–temperature equivalence in the tack and dynamic stiffness of polymer prepreg and its application to automated composites manufacturing. *Compos. Part A Appl. Sci. Manuf.* **2013**, *52*, 126–133. [CrossRef]
20. Croft, K.; Lessard, L.; Pasini, D.; Hojjati, M.; Chen, J.; Yousefpour, A. Experimental study of the effect of automated fiber placement induced defects on performance of composite laminates. *Compos. Part A Appl. Sci. Manuf.* **2011**, *42*, 484–491. [CrossRef]
21. Jeppesen, N.; Mikkelsen, L.P.; Dahl, A.B.; Christensen, A.N.; Dahl, V.A. Quantifying effects of manufacturing methods on fiber orientation in unidirectional composites using structure tensor analysis. *Compos. Part A Appl. Sci. Manuf.* **2021**, *149*, 106541. [CrossRef]
22. Bodaghi, M.; Vanaerschot, A.; Lomov, S.V.; Correia, N.C. On the variability of mesoscale permeability of a 2/2 twill carbon fabric induced by variability of the internal geometry. *Compos. Part A Appl. Sci. Manuf.* **2017**, *101*, 394–407. [CrossRef]
23. Bunea, M.; Bria, V.; Silva, F.S.; Birsan, I.G.; Buciumeanu, M. Influence of Fiber Orientation and Fillers on Low Velocity Impact Response of the Fabric Reinforced Epoxy Composites. *Appl. Compos. Mater.* **2021**, *28*, 1277–1290. [CrossRef]
24. Nugroho, G.; Budiyantoro, C. Optimization of Fiber Factors on Flexural Properties for Carbon Fiber Reinforced Polypropylene. *J. Compos. Sci.* **2022**, *6*, 160. [CrossRef]
25. Alam, P.; Mamalis, D.; Robert, C.; Floreani, C.; Ó Brádaigh, C.M. The fatigue of carbon fibre reinforced plastics—A review. *Compos. Part B Eng.* **2019**, *166*, 555–579. [CrossRef]
26. Chai, B.X.; Eisenbart, B.; Nikzad, M.; Fox, B.; Blythe, A.; Blanchard, P.; Dahl, J. A novel heuristic optimisation framework for radial injection configuration for the resin transfer moulding process. *Compos. Part A Appl. Sci. Manuf.* **2023**, *165*, 107352. [CrossRef]
27. Capricho, J.C.; Subhani, K.; Chai, B.X.; Bryant, G.; Salim, N.; Juodkazis, S.; Fox, B.L.; Hameed, N. Porous macroradical epoxy-based supercapacitors. *Polymer* **2022**, *259*, 125356. [CrossRef]
28. Seyednourani, M.; Yildiz, M.; Sas, H.S. A two-stage optimization methodology for gate and vent locations and distribution media layout for liquid composite molding process. *Compos. Part A Appl. Sci. Manuf.* **2021**, *149*, 106522. [CrossRef]
29. Li, J.; Zhang, C.; Liang, R.; Wang, B. Robust design of composites manufacturing processes with process simulation and optimisation methods. *Int. J. Prod. Res.* **2008**, *46*, 2087–2104. [CrossRef]
30. Wang, Y.; Rao, Z.; Liao, S.; Wang, F. Ultrasonic welding of fiber reinforced thermoplastic composites: Current understanding and challenges. *Compos. Part A Appl. Sci. Manuf.* **2021**, *149*, 106578. [CrossRef]
31. Fernandez Villegas, I.; Vizcaino Rubio, P. On avoiding thermal degradation during welding of high-performance thermoplastic composites to thermoset composites. *Compos. Part A Appl. Sci. Manuf.* **2015**, *77*, 172–180. [CrossRef]
32. Tsiangou, E.; Kupski, J.; Teixeira de Freitas, S.; Benedictus, R.; Villegas, I.F. On the sensitivity of ultrasonic welding of epoxy- to polyetheretherketone (PEEK)-based composites to the heating time during the welding process. *Compos. Part A Appl. Sci. Manuf.* **2021**, *144*, 106334. [CrossRef]
33. Terekhov, I.V.; Chistyakov, E.M. Binders used for the manufacturing of composite materials by liquid composite molding. *Polymers* **2021**, *14*, 87. [CrossRef]
34. Bhudolia, S.K.; Gohel, G.; Leong, K.F.; Joshi, S.C. Damping, impact and flexural performance of novel carbon/Elium® thermoplastic tubular composites. *Compos. Part B Eng.* **2020**, *203*, 108480. [CrossRef]
35. Dong, C. Flexural behaviour of carbon and glass reinforced hybrid composite pipes. *Compos. Part C Open Access* **2021**, *4*, 100090. [CrossRef]
36. Wang, Y.; Emerson, M.J.; Conradsen, K.; Dahl, A.B.; Dahl, V.A.; Maire, E.; Withers, P.J. Evolution of fibre deflection leading to kink-band formation in unidirectional glass fibre/epoxy composite under axial compression. *Compos. Sci. Technol.* **2021**, *213*, 108929. [CrossRef]

37. Quan, D.; Yue, D.; Ma, Y.; Zhao, G.; Alderliesten, R. On the mix-mode fracture of carbon fibre/epoxy composites interleaved with various thermoplastic veils. *Compos. Commun.* **2022**, *33*, 101230. [CrossRef]
38. Tsotsis, T.K. Interlayer toughening of composite materials. *Polym. Compos.* **2009**, *30*, 70–86. [CrossRef]
39. Cheng, C.; Zhang, C.; Zhou, J.; Jiang, M.; Sun, Z.; Zhou, S.; Liu, Y.; Chen, Z.; Xu, L.; Zhang, H.; et al. Improving the interlaminar toughness of the carbon fiber/epoxy composites via interleaved with polyethersulfone porous films. *Compos. Sci. Technol.* **2019**, *183*, 107827. [CrossRef]
40. Blythe, A.; Fox, B.; Nikzad, M.; Eisenbart, B.; Chai, B.X. Stiffness Degradation under Cyclic Loading Using Three-Point Bending of Hybridised Carbon/Glass Fibres with a Polyamide 6,6 Nanofibre Interlayer. *J. Compos. Sci.* **2022**, *6*, 270. [CrossRef]
41. Sebaey, T.A.; Bouhrara, M.; O'Dowd, N. Fibre Alignment and Void Assessment in Thermoplastic Carbon Fibre Reinforced Polymers Manufactured by Automated Tape Placement. *Polymers* **2021**, *13*, 473. [CrossRef]
42. Kratmann, K.K.; Sutcliffe, M.P.F.; Lilleheden, L.T.; Pyrz, R.; Thomsen, O.T. A novel image analysis procedure for measuring fibre misalignment in unidirectional fibre composites. *Compos. Sci. Technol.* **2009**, *69*, 228–238. [CrossRef]
43. Santulli, C.; Gil, R.G.; Long, A.C.; Clifford, M.J. Void Content Measurements in Commingled E-Glass/Polypropylene Composites Using Image Analysis from Optical Micrographs. *Sci. Eng. Compos. Mater.* **2002**, *10*, 77–90. [CrossRef]
44. *D7264/D7264M-15*; Standard Test Method for Flexural Properties of Polymer Matrix Composite Materials. ASTM International: Newark, DE, USA, 2015.
45. Brod, M.; Dean, A.; Scheffler, S.; Gerendt, C.; Rolfes, R. Numerical modeling and experimental validation of fatigue damage in Cross-Ply CFRP composites under inhomogeneous stress states. *Compos. Part B Eng.* **2020**, *200*, 108050. [CrossRef]
46. Stinchcomb, W.W.; Bakis, C.E. Chapter 4—Fatigue Behavior of Composite Laminates. In *Composite Materials Series*; Reifsnider, K.L., Ed.; Elsevier: Amsterdam, The Netherlands, 1991; Volume 4, pp. 105–180.
47. Pinto, F.; Iervolino, O.; Scarselli, G.; Ginzburg, D.; Meo, M. *Bioinspired Twisted Composites Based on Bouligand Structures*; SPIE: Bellingham, WA, USA, 2016; p. 97970E-E-13.
48. Apichattrabrut, T.; Ravi-Chandar, K. Helicoidal Composites. *Mech. Adv. Mater. Struct.* **2006**, *13*, 61–76. [CrossRef]
49. Qin, X.; Marchi, B.C.; Meng, Z.; Keten, S. Impact resistance of nanocellulose films with bioinspired Bouligand microstructures. *Nanoscale Adv.* **2019**, *1*, 1351–1361. [CrossRef] [PubMed]
50. Cheng, L.; Thomas, A.; Glancey, J.L.; Karlsson, A.M. Mechanical behavior of bio-inspired laminated composites. *Compos. Part A Appl. Sci. Manuf.* **2011**, *42*, 211–220. [CrossRef]

Journal of
Composites Science

MDPI

Article

Damage Model of Carbon-Fiber-Reinforced Concrete Based on Energy Conversion Principle

Ruiqi Zheng *, Jianyong Pang *, Jian Sun, Yongqiang Su and Guoping Xu

School of Civil Engineering and Architecture, Anhui University of Science and Technology, Huainan 232001, China; 2021200328@aust.edu.cn (J.S.)
* Correspondence: 2021200346@aust.edu.cn (R.Z.); jypang@aust.edu.cn (J.P.)

Abstract: In order to enhance the practical application of carbon-fiber-reinforced concrete (CFRC) in engineering, it is necessary to study the damage mechanism of CFRC. Experimental research on the mechanical properties of CFRC under multiple strain rates was conducted. Five different fiber contents were analyzed to study the compressive strength and tensile strength of CFRC, and the damage characteristics of CFRC under multiple strain rates were analyzed based on failure modes and energy changes. An energy-based damage constitutive model was established. The results showed the following: (1) When the carbon fiber content was 0.4%, CFRC had the best comprehensive performance, with a 15.02% increase in compressive strength and a 51.12% increase in tensile strength. With the increase in strain rate, the compressive strength of the concrete increased. (2) Under high strain rates, carbon fiber significantly enhanced the compressive strength of the concrete, and the input energy, elastic strain energy, and dissipated energy increased. The peak value of the elastic strain energy conversion rate increased, and the minimum value of the dissipated energy conversion rate decreased. (3) Under the same strain rate, the CFRC had a larger inflection point of dissipated energy corresponding to the strain compared to the reference group of concrete during the loading process. A constitutive model for CFRC was established based on damage mechanics and probability statistics. The research results will provide theoretical references for the application of carbon-fiber-reinforced concrete.

Keywords: concrete; carbon fiber; damaged model; energy; mechanical properties; strain rate

1. Introduction

Building materials are one of the key factors affecting the performance of building structures [1]. Concrete is a porous brittle material commonly used in civil engineering [2]. Its failure characteristics include quasibrittle failure; that is, once failure occurs, the load-bearing capacity is almost completely lost [3]. To ensure the safety and durability of the project, modified concrete [4] was developed. Incorporating fibers into concrete for modification can play a role in reinforcement, crack resistance, and impermeability [5–8]. Among them, carbon fiber has attracted great attention due to its excellent properties such as its high specific modulus and high specific strength [9].

Existing studies have shown that carbon fibers can significantly improve the mechanical properties and durability of concrete materials [10–13]. Studies by Kizilkanat [14] have shown that the overall performance of CFRC is best when the carbon fiber content is 0.5%. To improve the frost resistance of concrete, Kan et al. [15] added carbon fibers to the concrete. The results show that the addition of carbon fibers in concrete can reduce the mass loss of concrete in freeze–thaw experiments. These studies have shown that the research content of CFRC has engineering significance. However, most of these studies only focused on the effect of carbon fiber content on the static loading properties of CFRC. We need to further explore the damage mechanism of CFRC. Deng et al. [16] studied the mechanical properties of carbon-fiber-reinforced coral aggregate concrete and proposed

that the damage model can effectively reflect the stress–strain relationship of FRCAC. However, the damage to concrete specimens is closely related to energy dissipation, and the constitutive model parameters do not involve energy. The energy method is commonly used to represent the damage and failure characteristics of concrete materials when studying the properties of concrete materials under dynamic loads [17–19]. Based on the principle of energy dissipation, Li et al. [20] established the relationship between the energy consumption density and the fractal dimension of concrete under dynamic loading and revealed the characteristics of the microdamage and macrofracture of concrete and the law of energy dissipation. Therefore, we can try to use energy methods to study the damage mechanism of CFRC under static load.

To sum up, there has been a lot of research on concrete materials, but most of it focuses on the mechanical properties of concrete materials, and there are fewer studies based on the energy characteristics and damage constitutive models of carbon-fiber-reinforced concrete. In order to make carbon-fiber-reinforced concrete widely used in practical engineering, it is necessary to study the damage mechanism of carbon-fiber-reinforced concrete. CFRC with five kinds of fiber content (0%, 0.2%, 0.4%, 0.6%, and 0.8%) was prepared in this paper. The uniaxial compression test of CFRC under a multistrain rate was carried out to study the influence of different carbon fiber contents and different strain rates on the mechanical properties of CFRC. Based on the principle of energy conversion, combined with the failure mode of CFRC, the failure characteristics of CFRC under a multistrain rate are analyzed. Based on the principle of energy conversion, the damage model of carbon fiber concrete is proposed. The specific study process of this paper is shown in Figure 1.

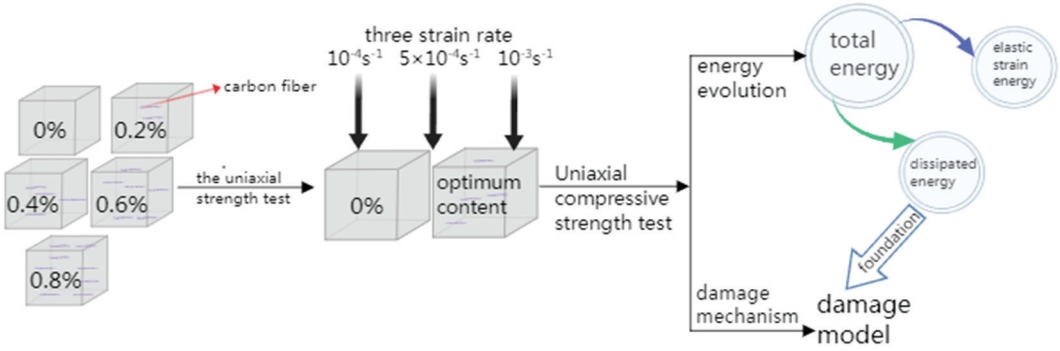

Figure 1. Study process.

2. Test Materials and Methods

2.1. Materials

The cement used is ordinary Portland cement of grade P.O. 42.5. The density of the cement is 2900 kg·m^{-3}. The carbon fiber is straight. The main performance parameters are listed in Table 1. The sand used in the test is ordinary Huaihe River sand with a silicon content of 97.89%, an apparent density of 2510 kg·m^{-3}, and a fineness modulus of 2.67. The apparent density of the coarse aggregate is 2609 kg·m^{-3}, the particle size is 5~31.5 mm continuously graded gravel, the bulk density is 1575 kg·m^{-3}, and the mud content is 1.1%. Water is normal tap water. The water-reducing agent is a PCA-I type superplasticizer, and the water reduction rate is 30%.

Table 1. Key performance parameters of carbon fiber.

Density /(kg·m^{-3})	Tensile Strength/MPa	Length /mm	Carbon Content/%	Diameter /μm	Tensile Modulus/GPa
1800	3450	3	95	7	230

2.2. Experimental Design

In this experiment, there are five groups with different mixing ratios, where the carbon fiber content is 0, 0.2%, 0.4%, 0.6%, and 0.8%, marked as C_0, $C_{0.2}$, $C_{0.4}$, $C_{0.6}$, and $C_{0.8}$ respectively. Specific mixing ratios are listed in Table 2.

Table 2. Mixing ratio of carbon fiber concrete specimens ($kg \cdot m^{-3}$).

Specimens	Cement	Fine Aggregate	Coarse Aggregate	Water	Carbon Fiber
C_0	361	650	1360	145	0
$C_{0.2}$	361	650	1360	145	3.6
$C_{0.4}$	361	650	1360	145	7.2
$C_{0.6}$	361	650	1360	145	10.8
$C_{0.8}$	361	650	1360	145	14.4

Nine 100 mm × 100 mm × 100 mm cube specimens were prepared for the cube compressive strength test of each group, and three 100 mm × 100 mm × 100 mm cube specimens were prepared for the tensile strength test of each group.

In this study, a WAW-1000 electrohydraulic servo universal testing machine was used, and the main parameters are shown in Table 3. The experimental process was operated according to the requirements of GB/T 50081-2002 [21]. First, the uniaxial strength test of the cube specimen was carried out, and the test results were analyzed to determine the optimal carbon fiber content. Then, the optimal content group and the reference group were subjected to compressive strength tests at different strain rates ($10^{-4}s^{-1}$, $5 \times 10^{-4}s^{-1}$, and $10^{-3}s^{-1}$).

Table 3. Main technical parameters of electrohydraulic servo uniaxial testing machine.

Subject	Parameter
Maximum axial test force	3000 kN
Test force accuracy	±1%
Displacement range	100 mm
Displacement accuracy	±2%
Displacement equal velocity control	0.5~50 mm/min
Power supply	4 kW/AC380V/50 Hz

2.3. Specimen Making

Add cement, gravel, and sand to the blender in turn and stir for 3 min. Then, add a small amount of fiber to the blender many times, stir the fiber completely, and then stir the superplasticizer and water evenly into the blender for 4 min. After that, it is placed in a 100 mm × 100 mm × 100 mm cube mold with prelubricated oil. Finally, put it on the shaking table to vibrate the compaction molding. The molded concrete specimen was covered with plastic film for 24 h, and then the specimen was taken out for standard curing for 28 days.

2.4. Energy Calculation Method

Essentially, the failure process of materials is an energy-driven state instability phenomenon [22]. Therefore, it is of great importance to study the energy evolution of the uniaxial compressive failure of carbon fiber concrete to investigate the failure mechanism of carbon fiber concrete. According to the first law of thermodynamics, the energy conversion of carbon-fiber-reinforced concrete under uniaxial compression [23,24] can be expressed as follows:

$$U = U^{\mathrm{e}} + U^{d} \tag{1}$$

where U is the total strain energy input per unit of working volume; U^{e} is the releasable elastic strain energy stored in the unit volume; and U^{d} is the energy dissipated per unit volume.

Figure 2 shows the relationship between U^e, U^d, and E_u in the stress failure process of CFRC specimens. The calculation of each energy can be expressed as follows:

$$U = \int_0^{\varepsilon} \sigma \mathrm{d}\varepsilon \tag{2}$$

$$U^e = \frac{1}{2}\sigma\varepsilon^e = \frac{1}{2E_u}\sigma^2 \tag{3}$$

$$U^d = U - U^e \tag{4}$$

where ε is the strain value of the specimen at a certain time; σ is the stress value of the specimen at a certain time, and the unit is MPa; and E_u is the elastic modulus of the specimen.

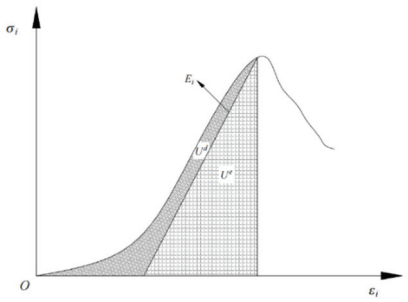

Figure 2. Energy distribution of carbon fiber concrete during uniaxial compression.

3. Compressive Test Results with Different CF Contents

3.1. Uniaxial Compressive Strength, Splitting Tensile Strength

The test results of concrete strength with different carbon fiber content are shown in Table 4. Compared to the plain concrete, the compressive strength remains on an upward trend with a carbon fiber content of 0–0.4%, but the increase is small. After that, with the increase in the carbon fiber content, the compressive strength began to decrease and was lower than the strength of the plain concrete, and the rate of decline was higher. At a carbon fiber content of 0.2%, 0.4%, 0.6%, and 0.8%, the compressive strength of the specimen is 4.93%, 15.02%, −15.02%, and −23.74% higher than that of the reference, respectively. The split tensile strength initially increases and then decreases with increasing carbon fiber content, and the overall tensile strength is higher than that of the reference group. At a carbon fiber content of 0.2%, 0.4%, 0.6%, and 0.8%, the tensile strength of the specimen is 41.32%, 51.12%, 46.26%, and 25.42% higher than that of the concrete of the reference group, respectively. This is because, with the appropriate amount of carbon fibers, the carbon fibers can be fully stirred and evenly distributed, creating a staggered network of fibers within the specimen, which acts as a bridge and stress transfer, preventing the aggregate from sinking into the specimen. The carbon fiber has excellent tensile properties. If the carbon fiber content is too high, agglomeration is easy to occur due to the poor distribution of carbon fibers, resulting in the deterioration of concrete workability and negative effects on the mechanical properties of concrete.

Table 4. Uniaxial compressive strength and splitting tensile strength of concrete specimens.

Specimens	C_0	$C_{0.2}$	$C_{0.4}$	$C_{0.6}$	$C_{0.8}$
Compressive strength/MPa	43.456	45.6	49.982	36.928	33.14
Tensile strength/MPa	4.349	6.146	6.572	6.361	5.454

3.2. Stress–Strain Relationship

The stress–strain curve of concrete with different carbon fiber contents is shown in Figure 3. The failure process of concrete with different carbon fiber contents went through the compaction phase, the elastic deformation phase, the plastic deformation phase, and the failure phase. At the initial stage of loading, the internal pores of the specimen are compacted, and the stress–strain curves of the concrete specimen with different carbon fiber contents are concave. As the stress increases, the specimen enters the stage of elastic deformation, and the stress–strain curve is approximately linear. Under sustained loading, the specimen begins to show plastic deformation and enters the plastic deformation stage. As the load increases, the load reaches the maximum load capacity of the specimen. At the failure stage, the specimen begins to fail and the load capacity decreases.

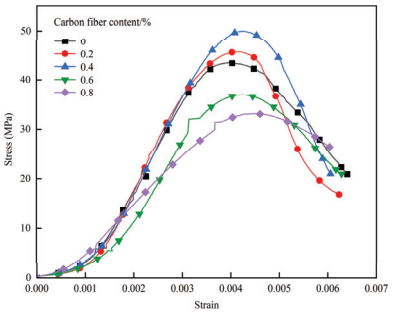

Figure 3. Stress–strain curves of concrete with different carbon fiber content.

Based on the above study, the compressive strength of CFRC (f) is as follows: $f_{0.4} > f_{0.2} > f_0 > f_{0.6} > f_{0.8}$; the tensile strength ($R_m$) is expressed as $R_{m_{0.4}} > R_{m_{0.6}} > R_{m_{0.2}} > R_{m_{0.8}} > R_{m_0}$, and the peak strain ($\varepsilon$) is expressed as $\varepsilon_{0.8} > \varepsilon_{0.4} > \varepsilon_{0.6} > \varepsilon_{0.2} > \varepsilon_0$.

3.3. Normal Strain Rate Failure Mode

Figure 4 shows the ultimate failure mode of the concrete specimens with different carbon fiber contents in compression tests. The failure of the reference concrete is brittle failure, the failure is more thorough, and the final failure mode is an hourglass type. As the fiber content increases, during the compression process, the surface spalling of the specimen becomes less. After loading, the integrity of the concrete specimen becomes higher and the overall failure mode is "cracks but not scattered", which is different from the large-scale complete spalling of the specimen after the loss of the bearing capacity.

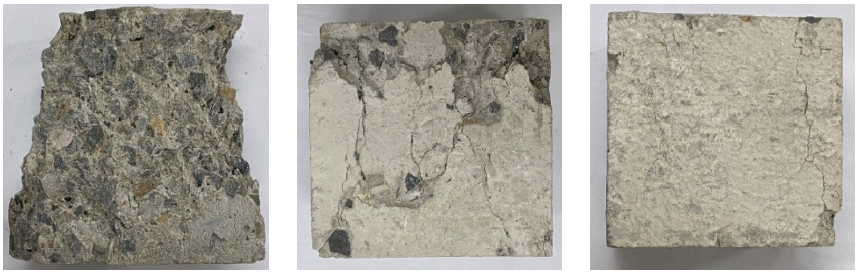

(**a**) $\omega_c = 0\%$ (**b**) $\omega_c \leq 0.5\%$ (**c**) $\omega_c > 0.5\%$

Figure 4. Failure modes of cube test blocks made of reference group concrete and carbon fiber concrete in compression tests.

Figure 5 shows the final failure mode of the tensile splitting test on the concrete specimens with different carbon fiber contents. The fracture surface of the concrete specimen of the reference group is complete under the splitting action, and the fracture surface is mainly of I type, which is close to the ideal splitting model of concrete [25]. When the fiber volume fraction is low, the fracture surface is dominated by two cracks (main cracks

and branch cracks), and the integrity of the fracture surface is not as good as that of the reference group concrete. When the fiber volume fraction is high, three obvious cracks appear on the fracture surface of the specimen, and the integrity of the fracture surface is poor.

(**a**) $\omega_c = 0\%$ (**b**) $\omega_c \leq 0.5\%$ (**c**) $\omega_c > 0.5\%$

Figure 5. Failure patterns of cube test blocks made of reference group concrete and carbon fiber concrete in the split tensile test.

3.4. Energy Characteristics at Peak Load

The variation trend of the energy properties of the concrete specimens with different carbon fiber contents at peak stress is shown in Figure 6. The change trend of the input energy, elastic strain energy, and dissipation energy of the concrete specimens with different carbon fiber contents at peak stress is basically the same. When the carbon fiber content is less than or equal to 0.4%, the input energy and elastic strain energy of the carbon fiber concrete specimen at peak stress increase with an increase in the carbon fiber content. When the carbon fiber content is more than 0.4%, the input energy and elastic strain energy of the carbon fiber concrete specimen at the peak stress decrease with increasing carbon fiber content.

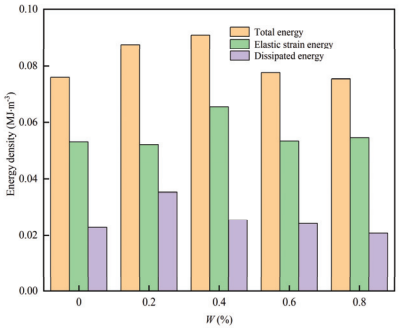

Figure 6. Energy properties of soil specimens at peak strain with different carbon fiber contents.

When the carbon fiber content is 0.4%, the input energy and elastic strain energy peak at the peak stress. The dissipated energy initially increases and then decreases as the carbon fiber content increases, and the dissipated energy at the peak voltage peaks when the carbon fiber content is 0.2%.

The compressive strength, peak strain, tensile strength, input energy, elastic strain energy, and dissipation energy at the peak strain of the concrete specimens with different carbon fiber contents were compared. The overall performance of the carbon fiber concrete was best at a carbon fiber content of 0.4%.

4. Compressive Test Results at Multiple Strain Rates

Uniaxial compression tests were carried out on the concrete of the reference group and concrete with 0.4% carbon fiber at different strain rates.

4.1. Uniaxial Compressive Strength

Figure 7 is the compressive strength histogram of the reference group concrete and 0.4% CFRC at different strain rates. At a strain rate of $10^{-4}s^{-1}$, $5 \times 10^{-4}s^{-1}$, and $10^{-3}s^{-1}$, the compressive strength of the 0.4% CFRC increases by 10.01%, 15.02%, and 18.27%, respectively, compared to the reference group concrete.

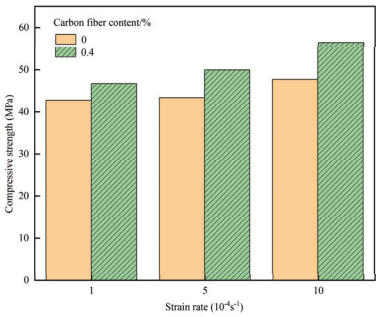

Figure 7. Compressive strength of C0 and C0.4 at different strain rates.

The compressive strength of the concrete specimens of the reference group and the 0.4% CFRC specimens increases with an increasing strain rate. With the increase in the strain rate, the compressive strength of the concrete in the reference group increased by 2.29% and 12.41%. The compressive strength of the 0.4% CFRC specimens increased by 6.95% and 20.85%. This is because the greater the strain rate, the shorter the time required to respond to the stretch and the greater the stress required for the stretch to occur. At the same strain rate, the compressive strength of the reference group concrete is lower than that of the 0.4% carbon fiber concrete, and at a high strain rate, carbon fiber can significantly improve the compressive strength of concrete.

4.2. Multi-Strain Rate Failure Modes

Figure 8 shows the failure modes of the concrete specimens at different strain rates. As the strain rate increases, the brittleness of the specimen increases and the integrity of the failure mode deteriorates. At a low strain rate, there are only cracks on the surface of the specimen, no obvious deposits and spalling, and the cracks are shallow. Under the high strain rate, when the specimen is destroyed, it is accompanied by a bursting sound, the surface of the specimen peels off obviously, and the surface crack deepens.

(**a**) $10^{-4}s^{-1}$ (**b**) $5 \times 10^{-4}s^{-1}$ (**c**) $10^{-3}s^{-1}$

Figure 8. Failure patterns of concrete test blocks at different strain rates.

This is due to the fact that under higher strain rate conditions, the applied energy is absorbed by the initial cracks on the specimen surface and there is more form. These microcracks cause the specimen to break down into smaller fragments, which is different from the damage morphology of the quasistatic state. The compression testing of specimens under high strain rate conditions is characterized by impact damage to some extent [26].

4.3. Energy Development Laws and Transformation Properties

Figure 9 shows the energy development of concrete from the plain concrete and 0.4% CFRC at different strain rates ($10^{-4}s^{-1}$, $5 \times 10^{-4}s^{-1}$, and $10^{-3}s^{-1}$). With the increase in the loading stress, the total energy, elastic strain energy, and dissipation energy of the CFRC and reference concrete are on the rise. When the stress increases to the peak stress, the total energy, elastic strain energy, and dissipation energy of the CFRC increase by 18.28%, 18.52%, and 17.70%, respectively, compared with the reference concrete at a $10^{-4}s^{-1}$ strain rate. At the strain rate of $5 \times 10^{-4}s^{-1}$, the total energy, elastic strain energy, and dissipated energy of the CFRC increased by 19.73%, 23.04%, and 12.01%, respectively. At the $10^{-3}s^{-1}$ strain rate, the total energy, elastic strain energy, and dissipation energy of the CFRC increased by 7.44%, 45.82%, and −43.32%, respectively. It can be found that the dissipation energy of the CFRC decreases at the $10^{-3}s^{-1}$ strain rate, but it can be clearly seen from Figure 9 that the corresponding peak strain increases compared with the reference concrete, which indicates that the effect of the fiber on improving the toughness of the concrete matrix is weakened at this strain rate.

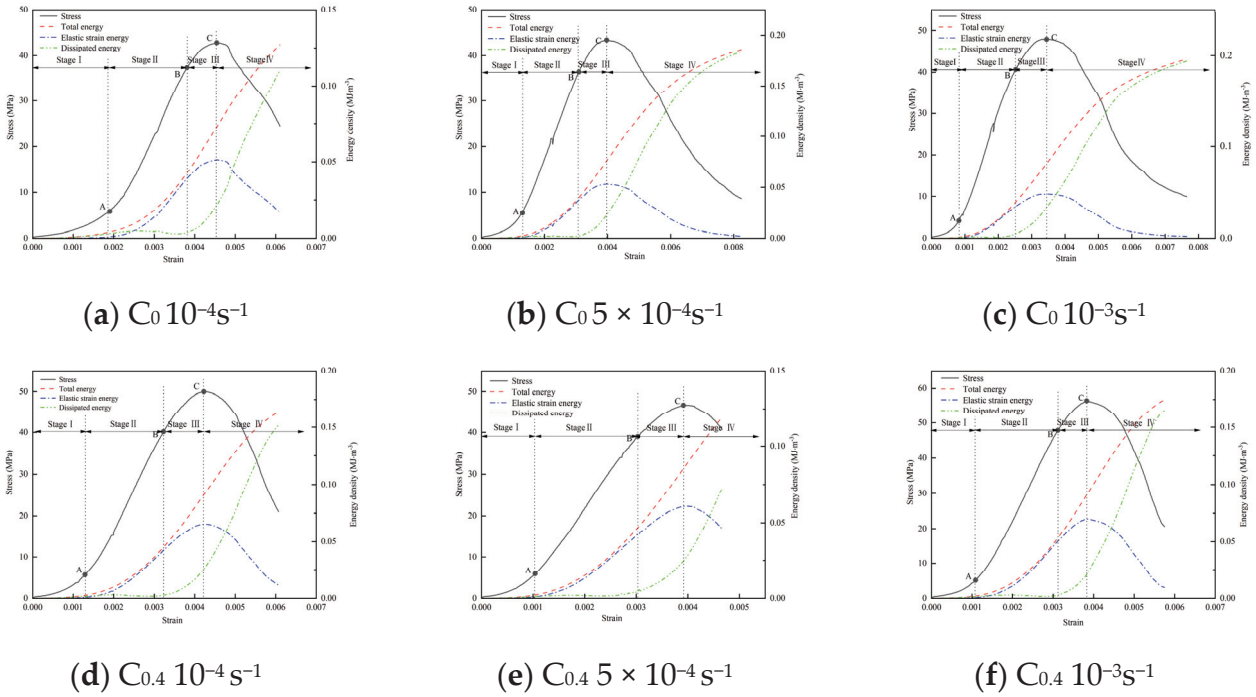

(**a**) C0 $10^{-4}s^{-1}$ (**b**) C0 $5 \times 10^{-4}s^{-1}$ (**c**) C0 $10^{-3}s^{-1}$

(**d**) C0.4 10^{-4} s^{-1} (**e**) C0.4 5×10^{-4} s^{-1} (**f**) C0.4 $10^{-3}s^{-1}$

Figure 9. Energy evolution characteristics.

The destruction of the concrete specimens can be divided into four stages: the compaction stage (I), elastic deformation stage (II), plastic deformation stage (III), and destruction stage (IV). To express the energy conversion relationship intuitively, the energy conversion rate of elastic strain $\alpha = U_e/U$ and the energy conversion rate of dissipation $\beta = U_d/U$ are introduced. Using the example of the 0.4% CFRC at a strain rate of $5 \times 10^{-4}s^{-1}$, the relationship between the stress–strain curve and the energy conversion rate is shown in Figure 10. Figure 11a–c shows the strain rate of $10^{-4}s^{-1}$, $5 \times 10^{-4}s^{-1}$, and $10^{-3}s^{-1}$; the reference group concrete; and a comparison table of the energy conversion rates of the concrete specimens with the 0.4% carbon fiber concrete.

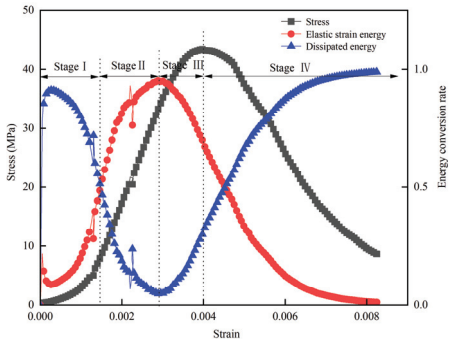

Figure 10. Relationship between energy conversion and stress–strain.

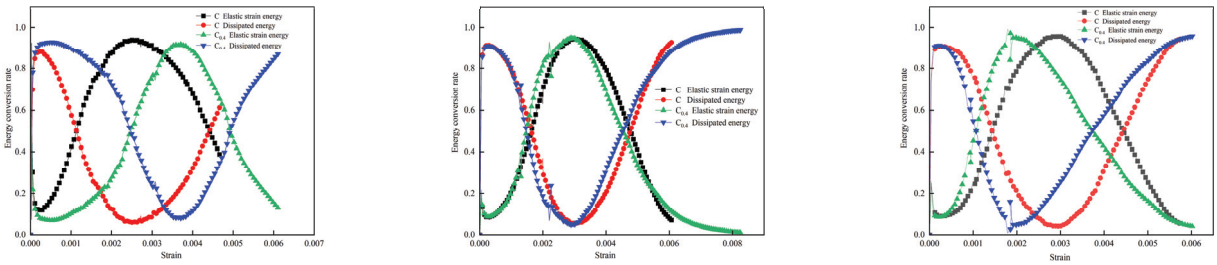

(**a**) $10^{-4}s^{-1}$ (**b**) $5 \times 10^{-4}s^{-1}$ (**c**) $10^{-3}s^{-1}$

Figure 11. Energy conversion–strain curves at different strain rates.

(1) Compression stage (I). Due to the presence of pores and microcracks in the carbon fiber concrete specimen, at this stage, the energy absorbed from the outside of the concrete specimen is essentially used to close the internal pores and microcracks of the specimen, and there is almost no input energy at this time that the elastic strain energy is converted. It can be seen from Figure 10 that the conversion rate of the elastic deformation energy gradually increases and the conversion rate of the dissipation energy gradually decreases during the densification phase.

(2) Elastic deformation stage (II). When the elastic deformation energy conversion-rate curve intersects with the dissipation energy conversion-rate curve for the first time, i.e., $\alpha = \beta$, the specimen enters the phase of elastic deformation. At this stage, the concrete specimen can be regarded as an ideal linear elastic body, and the concrete mainly undergoes reversible elastic deformation. In the elastic deformation phase, the energy conversion rate of elastic deformation gradually increases, and the conversion rate of dissipated energy gradually decreases. Comparing Figure 9a–c, the energy dissipation at the elastic deformation stage can be seen more clearly at a small strain rate. This is because at a low strain rate, the load is applied over a longer period of time, and crack sliding occurs within the specimen.

(3) Plastic deformation stage (III). With increasing strain, the energy conversion rate of elastic strain reaches the maximum value, and the conversion rate of the dissipation energy reaches the minimum value. At this point, the specimen enters the plastic deformation phase. At this stage, the concrete specimen gradually loses elasticity under the action of axial tension. The microcracks inside the specimen expand rapidly, the elastic strain energy conversion rate decreases rapidly, and the dissipative energy conversion rate increases sharply. The specimen gradually reaches the limit of its load-bearing capacity and plastic deformation occurs. As can be seen from Figure 9, with the increasing strain rate of the 0.4% carbon fiber concrete specimen, the strain corresponding to the sudden turning point of the dissipated energy is larger than that of the plain concrete. This is because the carbon fiber consumes the deformation energy through its own compression deformation before the dissipation energy reaches the abrupt inflection point, so as to retard the deformation of the

specimen. When the strain rate is small, the energy dissipation phenomenon is serious. As the strain rate increases, the proportion of dissipated energy gradually decreases.

(4) Destruction stage (IV). With the gradual increase in the axial load, the specimen reaches the peak stress and begins to damage. Numerous cracks appear on the surface of the specimen, and the input strain energy is mainly dissipated in the form of the surface energy and kinetic energy of the cracks. During the destruction phase of the specimen, as α continues to decrease and β gradually increases, a second point occurs where $\alpha = \beta$ occurs and the critical point of permanent concrete damage is reached. After that, the energy conversion rate of the elastic strain continues to decrease and the dissipation energy conversion rate continues to increase, $\alpha < \beta$; the level of elastic strain energy is low; and the specimen is unable to store the elastic strain energy, causing damage to occur.

From Figure 11a–c, it can be seen that the energy conversion rate–strain curves of the plain concrete and 0.4% CFRC have the same trend at different strain rates, but the difference between the curves is due to the influence of the strain rate, and the carbon fiber installation is not negligible. As can be seen from Figure 11, CFRC energy conversion has a significant influence on the strain rate. As the strain rate increases, the maximum value of the elastic strain energy conversion rate increases, and the minimum value of the dissipative energy conversion rate decreases. With the increase in the strain rate, the elastic strain energy fraction of the concrete in the plain concrete is less than the 0.4% CFRC, but the elastic strain energy fraction of the plain concrete is larger than that of the 0.4% CFRC. It shows that the carbon fiber incorporated into concrete can accumulate energy and slow down the energy distribution of the concrete. At higher strain rates, the strain value corresponding to the second $\alpha = \beta$ point of the energy conversion rate–strain curve of the CFRC specimen is larger than that of the plain concrete. It shows that carbon fibers have a significant impact on retarding concrete damage at higher strain rates. At a lower strain rate, the 0.4% CFRC enters the elastic deformation phase first before the plain concrete. This is because the carbon fiber fills the internal pores of the concrete, causing the concrete specimen to complete the compaction phase more quickly.

5. Ontological Modeling Based on Energy Dissipation

5.1. Establishment of the Ontological Model

Damage mechanics suggest that the main mechanism of material degradation is the reduction in the effective area due to microdefects. Let the initial damage degree of the CFRC be 0; the cross-sectional area be A; and the effective area after damage be A^*, i.e., the physical meaning of the degree of continuity ψ is the ratio of the effective load-bearing cross-sectional area to the cross-sectional area in the initial state:

$$\psi = \frac{A^*}{A} \tag{5}$$

In the formula, if $\psi = 1$, it means the ideal material without defects, and if $\psi = 0$, it means the material state of complete destruction and the loss of the bearing capacity.

For concrete materials, it is common to introduce the damage variable D [27] to describe the degree of damage, i.e.:

$$D = 1 - \psi = 1 - \frac{A^*}{A} \tag{6}$$

The theory of damage mechanics results in the following relationship between nominal and effective stresses in concrete materials:

$$\sigma = \frac{A^*}{A}\sigma^* \tag{7}$$

where σ is nominal stress and σ^* is effective stress.

From Equations (6) and (7), we obtain:

$$\sigma = (1 - D)\sigma^* \tag{8}$$

According to the strain equivalence hypothesis proposed by J. Lemaitre [28], the strain induced by the effective stress acting on the damaged material is the same as the strain induced by the nominal stress acting on the undamaged material, which can be obtained as

$$\sigma = (1 - D)E\varepsilon \tag{9}$$

where E is the elastic modulus and ε is the strain.

5.2. Calculation of Damage Sizes

Approaching the interior of concrete as an innumerable composition of microelements, the degree of damage can be expressed by the ratio of the value of microelements destroyed by damage, N, to the value of microelements destroyed by damage, M, and the value of damage-destroyed microelements is related to the energy dissipation during the damage process. Since the two-parameter WEIBULL probability distribution has been applied to the analysis of concrete volume rupture and failure data, this article assumes that the dissipation energy of CFRC follows the two-parameter WEIBULL probability density function [29]:

$$f\left(U^d\right) = \frac{\beta}{\alpha}\left(\frac{U^d}{\alpha}\right)^{\beta-1}\exp\left[-\left(\frac{U^d}{\alpha}\right)^{\beta}\right] \tag{10}$$

where U^d is the dissipated energy, α is the scale parameter, and β is the shape parameter.

$$N = M\int_0^{U^d} f(x)\mathrm{d}x = M\left\{1 - \exp\left[-\left(\frac{U^d}{\alpha}\right)^{\beta}\right]\right\} \tag{11}$$

So, the damage variable D can be expressed as:

$$D = \frac{N}{M} = 1 - \exp\left[-\left(\frac{U^d}{\alpha}\right)^{\beta}\right] \tag{12}$$

According to Formulas (9) and (12), the constitutive relationship of the uniaxial compression of CFRC based on energy dissipation is as follows:

$$\sigma = E\varepsilon\exp\left[-\left(\frac{U^d}{\alpha}\right)^{\beta}\right] \tag{13}$$

5.3. Determination of Parameters

α and β are derived in the formula, and two logarithms on both sides of the formula can be obtained at the same time:

$$\ln\left[-\ln\left(\frac{\sigma}{E\varepsilon}\right)\right] = \beta\ln\left(\frac{U^d}{\alpha}\right) \tag{14}$$

In the formula, α and β are obtained by fitting the data obtained from the experiment. Let $x = \ln U^d$, $y = \ln\left[-\ln\left(\frac{\sigma}{E\varepsilon}\right)\right]$, $b = -\beta\ln a$; that is, Equation (14) can be expressed as a linear form of $y = \beta x + b$, so this article uses the linear fitting method to estimate both parameters. The slope obtained is the shape parameter β, and then the scale parameter

α can be obtained by $b = -\beta \ln a$. The parameters of the uniaxial compression damaged model of CFRC with different carbon fiber contents are listed in Table 5.

Table 5. Parameters of the damaged model.

Carbon Fiber Content/%	α	β	R^2
0	0.1356	2.36205	0.94
0.2	0.12427	2.48615	0.92
0.4	0.14445	2.62611	0.91
0.6	0.11683	1.77243	0.90
0.8	0.13127	1.19205	0.97

5.4. Model Confirmation

From the α and β values obtained in Table 5 and the stresses, strains, and elastic moduli obtained from the tests, the stress–strain curve of the CFRC damaged model can be calculated and compared with the test curve, as shown in Figure 12.

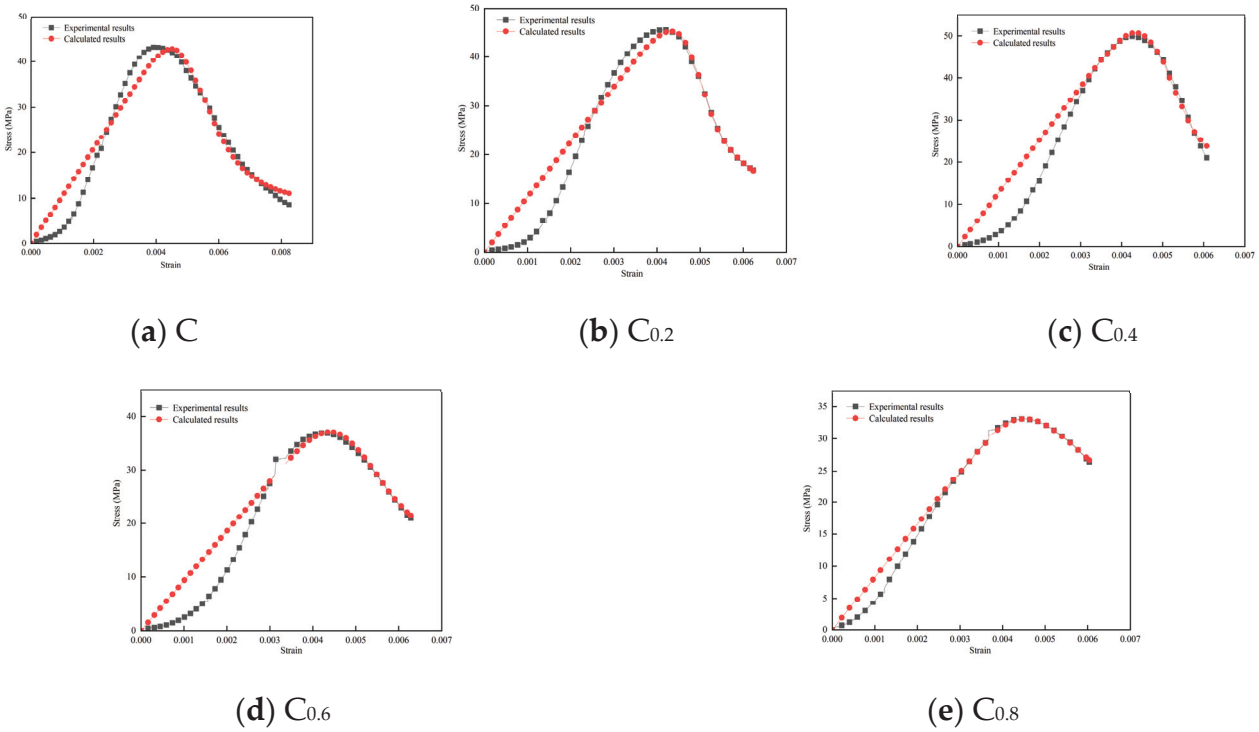

Figure 12. Comparison of stress–strain curve and test curve of CFRC constitutive model.

As can be seen from Figure 12, the calculated curves of the model fit well with the CFRC stress–strain test curves, and the calculated results of the model are higher than the test results in the elastic phase only. This is due to improper testing methods for the elastic deformation and gap compaction phases of the press during the actual test. In general, the energy-dissipation-based uniaxial compression damaged model can better represent the stress–strain relationship of CFRC.

5.5. Damage Development

The damage variable D of CFRC under different carbon fiber contents can be obtained by Formula (12), and the damage evolution law of CFRC is shown in Figure 13. It can be seen from the figure that when the ultimate elongation of the CFRC specimen is reached, with the increase in carbon fiber doping, the degree of damage decreases, and it can be found that the carbon fiber can effectively limit the damage development of CFRC and delay the deformation of the specimen.

In the process of uniaxial compression, the change trend of the damage variable D shows "S" type growth. The first gentle stage is the elastic stage of the CFRC specimen. At this point, the specimen can be regarded as an ideal linear elastic body, and the damage development is slow. After the transition from the flat stage to the rising stage, the conversion rate of the dissipated energy increases sharply due to the increasing friction between the fiber and the concrete matrix, and the specimen is in the stage of plastic deformation. After reaching the peak tension, the curvature of the specimen begins to transition from steep to gentle. This is because the bridging effect of the fiber can effectively inhibit the formation of the cracks, and the loss energy conversion rate of the CFRC specimen is reduced. At this point, the specimen is in the failure stage.

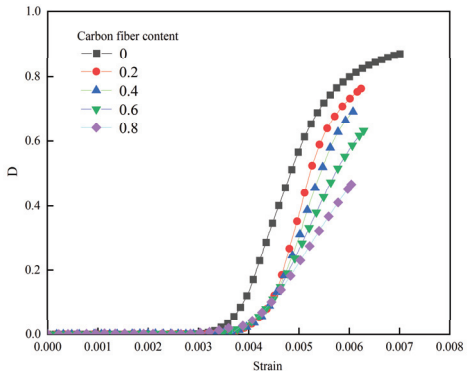

Figure 13. Damage evolution of CFRC.

6. Conclusions

In this paper, CFRC with five kinds of fiber content was prepared for a uniaxial compression test. The effects of carbon fiber contents and strain rate on the mechanical properties of CFRC were studied. Combined with the failure mode, the damage model of CFRC is established based on the principle of energy conversion. Although this paper proposes to calculate the damage model of concrete specimens by the dissipation energy of concrete specimens, it has certain limitations. The next work is to determine whether the model is suitable for other fiber-reinforced concrete or building materials and the engineering application of the model. The conclusions are as follows:

(1) When the mixing amount of carbon fiber is 0.4%, the overall performance of the carbon fiber concrete is optimal. The compressive strength of the specimen is 15.02% higher than that of the reference concrete, the splitting tensile strength is increased by 51.12%, and the total strain energy and elastic strain energy reach their peak. With the gradual increase in the carbon fiber dosage, each energy of the carbon fiber concrete specimens at the peak stress showed a trend of increasing and then decreasing, and the peak strain gradually increased. At different strain rates, the compressive strength of the optimal content group is 10.01%, 15.02%, and 18.27% higher than that of the plain concrete.

(2) The energy dissipation of the plain concrete at low strain rates is important in the compaction-density phase of the deformation damage process in CFRC; in the elastic deformation phase, the input energy is mainly converted into elastic strain energy storage, and the elastic strain energy ratio increases significantly with the increase in the strain rate. In the plastic deformation stage, the larger the strain rate. At the smaller proportion of dissipated energy and the same strain rate of the carbon fiber concrete, the dissipation energy increases significantly at the same strain rate as the plain concrete, effectively retarding the specimen deformation.

(3) As the strain rate increases, the peak value increases, followed by a decrease in the minimum value of b, indicating that the strain rate has a large influence on the energy distribution. As the strain rate increases, the elastic strain energy percentage of the base concrete increases more than that of carbon fiber concrete, but the elastic strain

energy percentage of carbon fibers is still higher than that of plain concrete, indicating that the carbon fibers have the ability to accumulate elastic strain energy and slow down the energy distribution of the concrete.

(4) The CFRC material model is based on the damage mechanics theory and the probabilistic statistical method, and the calculated curve of the model fits well with the CFRC stress–strain test curve, which reflects the effect of carbon fiber doping on the CFRC material damage.

Author Contributions: Conceptualization, R.Z.; methodology, J.P.; software, J.S. and R.Z.; validation, R.Z., J.S., Y.S. and G.X.; formal analysis, R.Z.; investigation, R.Z.; resources, J.P.; data curation, J.S.; writing—original draft preparation, R.Z.; writing—review and editing, R.Z.; visualization, J.S.; supervision, J.P. All authors have read and agreed to the published version of the manuscript.

Funding: Funding was received by the University Natural Science Research Project of Anhui Province (2023AH051219).

Data Availability Statement: All data used to support the findings of this study are available from the corresponding author upon request.

Conflicts of Interest: The authors have no relevant financial or non-financial interests to disclose.

References

1. Pontinha, A.D.R.; Mäntyneva, J.; Santos, P.; Durães, L. Thermomechanical Performance Assessment of Sustainable Buildings' Insulating Materials under Accelerated Ageing Conditions. *Gels* **2023**, *9*, 241. [CrossRef]
2. Mo, L.; Deng, M.; Tang, M.; Al-Tabbaa, A. MgO expansive cement and concrete in China: Past, present and future. *Cem. Concr. Res.* **2014**, *57*, 1–12. [CrossRef]
3. Lawler, J.S.; Wilhelm, T.; Zampini, D.; Shah, S.P. Fracture processes of hybrid fiber-reinforced mortar. *Mater. Struct.* **2003**, *36*, 197–208. [CrossRef]
4. Beeldens, A.; Van Gemert, D.; Schorn, H.; Ohama, Y.; Czarnecki, L. From microstructure to macrostructure: An integrated model of structure formation in polymer-modified concrete. *Mater. Struct.* **2005**, *38*, 601–607. [CrossRef]
5. Aydin, A.C. Self compactability of high volume hybrid fiber reinforced concrete. *Constr. Build. Mater.* **2007**, *21*, 1149–1154. [CrossRef]
6. Guo, H.; Tao, J.; Chen, Y.; Li, D.; Jia, B.; Zhai, Y. Effect of steel and polypropylene fibers on the quasi-static and dynamic splitting tensile properties of high-strength concrete. *Constr. Build. Mater.* **2019**, *224*, 504–514. [CrossRef]
7. Zheng, Y.; Zhang, Y.; Zhuo, J.; Zhang, Y.; Wan, C. A review of the mechanical properties and durability of basalt fiber-reinforced concrete. *Constr. Build. Mater.* **2022**, *359*, 129360. [CrossRef]
8. Song, P.S.; Hwang, S. Mechanical properties of high-strength steel fiber-reinforced concrete. *Constr. Build. Mater.* **2004**, *18*, 669–673. [CrossRef]
9. Muthukumarana, T.V.; Arachchi MA VH, M.; Somarathna HM, C.C.; Raman, S.N. A review on the variation of mechanical properties of carbon fiber-reinforced concrete. *Constr. Build. Mater.* **2023**, *366*, 130173. [CrossRef]
10. Chen, T.; Wang, Z.H.; Wang, A.; Bai, E.; Zhu, X. Comparative study on the static and dynamic mechanical properties and micro-mechanism of carbon fiber and carbon nanofiber reinforced concrete. *Case Stud. Constr. Mater.* **2023**, *18*, e01827. [CrossRef]
11. Patchen, A.; Young, S.; Penumadu, D. An Investigation of Mechanical Properties of Recycled Carbon Fiber Reinforced Ultra-High-Performance Concrete. *Materials* **2022**, *16*, 314. [CrossRef]
12. Wu, L.; Lu, Z.; Zhuang, C.; Chen, Y.; Hu, R. Mechanical properties of nano SiO2 and carbon fiber reinforced concrete after exposure to high temperatures. *Materials* **2019**, *12*, 3773. [CrossRef]
13. Boris, R.; Antonovich, V.; Spudulis, É.; Volochko, A.; Stonis, R. Effect of carbon fiber on medium-cement heat-resistant concrete properties. *Refract. Ind. Ceram.* **2014**, *55*, 352–355. [CrossRef]
14. Kizilkanat, A.B. Experimental evaluation of mechanical properties and fracture behavior of carbon fiber reinforced high strength concrete. *Period. Polytech. Civ. Eng.* **2016**, *60*, 289–296. [CrossRef]
15. Kan, W.; Yang, Z.; Yu, L. Study on Frost Resistance of the Carbon-Fiber-Reinforced Concrete. *Appl. Sci.* **2022**, *12*, 3823. [CrossRef]
16. Deng, Z.H.; Zhou, Y.W.; Jiang, J.S.; Huang, X.; Liu, B. Mechanical properties and uniaxial constitutive model of fiber-reinforced coral aggregate concrete. *Struct. Concr.* **2023**, *24*, 4259–4275. [CrossRef]
17. Wang, H.; Dang, F.; Ren, J.; Li, Y.; Zhu, L. Experimental Research on the Energy Evolution of Concrete under Impact Loading. *Materials* **2023**, *16*, 5140. [CrossRef]
18. Geng, K.; Chai, J.; Qin, Y.; Li, X.; Duan, M.; Liang, D. Exploring the brittleness and fractal characteristics of basalt fiber reinforced concrete under impact load based on the principle of energy dissipation. *Mater. Struct.* **2022**, *55*, 78. [CrossRef]
19. Ren, J.; Dang, F.; Wang, H.; Xue, Y.; Fang, J. Enhancement mechanism of the dynamic strength of concrete based on the energy principle. *Materials* **2018**, *11*, 1274. [CrossRef]

20. Li, Y.; Zhai, Y.; Liu, X.; Liang, W. Research on fractal characteristics and energy dissipation of concrete suffered freeze-thaw cycle action and impact loading. *Materials* **2019**, *12*, 2585. [CrossRef]
21. *GB/T50081-2002*; Standard for Test Method of Mechanical Properties on Ordinary Concrete. China Architecture and Building Press: Beijing, China, 2003. (In Chinese)
22. Zhao, Z.; Ma, W.; Fu, X.; Yuan, J. Energy theory and application of rocks. *Arab. J. Geosci.* **2019**, *12*, 1–26. [CrossRef]
23. Wang, C.; He, B.; Hou, X.; Li, J.; Liu, L. Stress–energy mechanism for rock failure evolution based on damage mechanics in hard rock. *Rock Mech. Rock Eng.* **2020**, *53*, 1021–1037. [CrossRef]
24. Meng, Q.; Zhang, M.; Han, L.; Pu, H.; Nie, T. Effects of acoustic emission and energy evolution of rock specimens under the uniaxial cyclic loading and unloading compression. *Rock Mech. Rock Eng.* **2016**, *49*, 3873–3886. [CrossRef]
25. Jin, X.C.; Hou, C.; Fan, X.L.; Lu, C.; Yang, H.; Shu, X.; Wang, Z. Quasi-static and dynamic experimental studies on the tensile strength and failure pattern of concrete and mortar discs. *Sci. Rep.* **2017**, *7*, 15305. [CrossRef] [PubMed]
26. Chen, X.; Ge, L.; Zhou, J.; Wu, S. Dynamic Brazilian test of concrete using split Hopkinson pressure bar. *Mater. Struct.* **2017**, *50*, 1–15. [CrossRef]
27. Xiao, Y.J.; Chen, Z.S.; Zhou, J.T.; Leng, Y.; Xia, R. Concrete plastic-damage factor for finite element analysis: Concept, simulation, and experiment. *Adv. Mech. Eng.* **2017**, *9*, 1687814017719642. [CrossRef]
28. Lemaitre, J. A Continuous Damage Mechanics Model for Ductile Fracture. *J. Eng. Mater. Technol.* **1985**, *107*, 83–89. [CrossRef]
29. Wang, C.; Fu, P.; Liu, Z.; Xu, Z.; Wen, T.; Zhu, Y.; Long, Y.; Jiang, J. Study of the Durability Damage of Ultrahigh Toughness Fiber Concrete Based on Grayscale Prediction and the Weibull Model. *Buildings* **2022**, *12*, 746. [CrossRef]

Journal of
Composites Science

MDPI

Article

Effects of the Injection Material and Resin Layer on the Mechanical Properties of Carbon Fiber-Reinforced Thermoplastic (CFRTP) Press and Injection Hybrid Molded Parts

Kazuto Tanaka * and Masaki Taniguchi

Department of Biomedical Engineering, Doshisha University, Kyotanabe 610-0394, Japan; ctuh0030@mail4.doshisha.ac.jp
* Correspondence: ktanaka@mail.doshisha.ac.jp

Abstract: In the press and injection hybrid molded parts of fiber-reinforced thermoplastics (FRTPs), failure at the interface between the surface material (the outer shell) and the ribs (the injection part) or that at the injection part has become an issue. Adding a resin layer to the rib roots at the same time that the ribs are molded through injection has been proposed, which may increase the mechanical properties and reduce the material cost. To prevent failure at the injection part, the use of fiber-reinforced resin as an injection material has been suggested. This approach contributes to a higher bond strength by lowering the molding shrinkage rate. In this study, the hat-shaped parts of carbon fiber-reinforced thermoplastics (CFRTPs) with fiber-reinforced and neat resin layers at the rib root were fabricated through press and injection hybrid molding, and their mechanical properties were evaluated through three-point bending tests. The effects of the resin layer at the rib root and the existence or nonexistence of fiber reinforcement on the mechanical properties, as well as the relationship between the material cost and the mechanical properties, were clarified through an experiment and FEM analysis. The bond strength was also evaluated through tensile tests that were undertaken at the rib root. Molded parts with neat PA6 and glass fiber-reinforced PA6 resin layers at the rib roots showed higher bond strength than those without resin layers. In a three-point bending test of a CFRTP hat-shaped part with a resin layer at the rib roots, the use of a 1 mm thick CFRTP laminate for the outer shell and glass fiber-reinforced PA6 resin as the injection material showed the same stiffness as a part that used a 2 mm thick CFRTP laminate for the outer shell. FEM analysis showed that the resin layer prevented the concentration of strain at the rib roots, and the model that used a 1 mm thick CFRTP laminate for the outer shell and glass fiber-reinforced PA6 resin as the injection material showed the best specific stiffness in this study. By adding a resin layer to the rib roots, the fabrication of molded parts with excellent specific stiffness was enabled at a small increase in cost.

Keywords: CFRTPs (carbon fiber-reinforced thermoplastics); press and injection hybrid molding; rib structure; resin layer; injection material; bond strength; stiffness; FEM analysis

1. Introduction

The Fit for 55 policy packages announced by the EU on 14 July 2021 will effectively prohibit the production of internal combustion engine vehicles (ICEVs) after 2035. This announcement has accelerated the spread of zero emission vehicles such as battery electric vehicles (BEVs) more than ever. This is due to the increase in carbon dioxide emission reduction targets for new vehicles, which will be raised from a 37.5% reduction to a 55% reduction from 2021 levels after 2030, with a further increase to a 100% reduction planned after 2035. BEVs need to carry many batteries to extend the required mileage, so it is important to reduce the weight of the vehicle's body [1]. To meet this demand, carbon fiber-reinforced plastics (CFRPs), which are lightweight and have both an excellent specific strength and stiffness, are expected to be used as a substitute for metal [2,3]. CFRPs can be

divided into CFRTSs (carbon fiber-reinforced thermosetting plastics) and CFRTPs (carbon fiber-reinforced thermoplastics) depending on the resin used as the matrix. The use of CFRTPs is currently limited to luxury vehicles due to the high cost of autoclave production and the high cost of the raw materials used for the thermosetting resin itself [4]. On the other hand, CFRTPs are expected to have a short molding cycle and a high level of recyclability by taking advantage of the properties of thermoplastic resin and are a candidate for use as a lightweight material [4]. Therefore, research and development are underway to apply CFRTPs to the structural parts of mass-produced vehicles [5–7]. The molding methods used for CFRTP structural parts include press molding using continuous fiber-reinforced thermoplastic laminates and injection molding using short or long fiber-reinforced thermoplastic. Although press molding using continuous fiber as a reinforcement material has excellent mechanical properties, it is difficult to mold automotive parts with complex shapes such as ribs. On the other hand, injection molding can mold complex shapes. However, the mechanical properties of injection-molded structural parts are insufficient when short fibers are used. In recent years, the press and injection hybrid molding method, which combines press molding and injection molding, has been attracting attention. In this method, a continuous fiber-reinforced thermoplastic laminate that has been preheated and melted is placed in a mold, and short fiber-reinforced resin is injected at the same time as the press molding to give the rib structures [8,9]. The press and injection hybrid molding method is suitable for molding CFRTP structural parts for mass-produced vehicles because it can significantly reduce the molding cycles and unit costs [8]. However, it has been reported that press and injection hybrid molded parts frequently fail at the interface between the surface material (the outer shell) and the ribs (the injected part) [8–11] or at the injection part. A method to prevent interfacial failure between the surface material and the ribs is one that the CFRTP laminate penetrates into the ribs. The authors have developed a method to improve bond strength by supplying either cut or slit materials of a continuous fiber prepreg that has excellent flowability at the bonding area [12,13]. However, there is concern that the end of the fiber bundle in the cut material and the cut portion in the slit material may be the starting point of failure [14]. Therefore, it is necessary to develop methods to increase bond strength in addition to the inflow of surface materials, such as continuous fibers or cut materials, into the ribs. It was reported that the failure load can be increased by designing a geometrically large bonding area between the surface material and the ribs [11]. Therefore, one candidate that can be used to increase bond strength is that of adding a resin layer to the rib roots at the same time that the ribs are molded. Furthermore, the addition of a resin layer is expected to increase the sectional secondary moment of the structural part, thereby increasing the stiffness and reducing the cost of materials. Moreover, failure at the injection part may be prevented by using fiber-reinforced resins as the injection material, which are expected to have high strength. Another advantage of using fiber-reinforced resins is that they have a lower molding shrinkage rate than neat resins. For example, in a study on bonding injection materials to metal, it was reported that fiber-reinforced resins have a higher bond strength to aluminum plates than neat ones [15]. This is because fiber reinforcement can lower the molding shrinkage rate and therefore prevent the peeling that occurs at the interface between the injection material and the aluminum plate.

Press and injection hybrid molded structural parts are now commercially available and displayed as prototypes at many exhibitions. On the other hand, academic papers are usually focused on the interfacial bond properties between the surface material and the injection material [16–18], which represent an issue in actual structural parts. Quantitatively evaluated mechanical properties (stiffness, strain distribution, etc.) of actual structural parts based on different configurations of the surface and injection materials are difficult to find in journal papers. To prepare for the optimal design of real structural parts in the future, it is necessary to experimentally evaluate the mechanical properties of press and injection hybrid molded parts and to verify the consistency of the results with the FEM model. In general, it is expected that high strength and high stiffness can be obtained by using fiber-reinforced resins [19]. On the other hand, quantitatively evaluated mechanical

properties are difficult to find in journal papers when fiber-reinforced and neat resins are applied to actual hybrid structural parts. In this study, CFRTP hat-shaped parts with fiber-reinforced or neat resin layers at the rib root were molded through press and injection hybrid molding, and their mechanical properties were evaluated using three-point bending tests. The effects of the resin layer at the rib root and the existence of fiber reinforcement in the resin on the mechanical properties, as well as the relationship between the cost and the mechanical properties, were also clarified through an experiment and FEM analysis. FEM analysis was used to evaluate the mechanical properties of parts that could not be fabricated using the existing molds. The bond strength between the surface material (the outer shell) and the ribs (the injection part) was also evaluated through tensile tests of the rib root specimens.

2. Materials and Methods

2.1. Materials and Method of Fabricating Hat-Shaped Parts

The CFRTP laminates used as the surface material of the outer shell of the hat-shaped parts were a CF/Phenoxy prepreg (CF: TR50S-15L, Vf: 50%, area weight: 264 g/m^2, KURABO INDUSTRIES Ltd., Osaka, Japan) made of unidirectional carbon fiber impregnated with phenoxy resin. Injection materials supplied to the ribs and flange of the hat-shaped parts were PA6 resin (1015B, melting point: 225 °C, tensile modulus: 2.9 GPa, Ube Industries Ltd., Tokyo, Japan) and glass fiber-reinforced PA6 resin (1015GC6, melting point: 225 °C, tensile modulus: 9.3 GPa, Vf: 15–17%, Ube Industries Ltd., Tokyo, Japan). The CFRTP laminates were laminated in a configuration of $[0°/90°/0°]_2$ and $[0°/90°/0°]_4$ to achieve a thickness of 1 mm or 2 mm and pressed at a forming temperature of 180 °C, a press pressure of 4 MPa, and a holding time of 300 s. An injection-press hybrid molding machine (STIP05-05, SATOH MACHINERY WORKS Co., Ltd., Nagoya, Japan), which combines an injection molding machine and a press molding machine, was used to mold hat-shaped parts. Figure 1 shows the molding method for hat-shaped parts. The CFRTP laminate was heated and melted (Figure 1a) in advance in a contact heater (TH-5, Leibrock, Pirmasens, Germany) set at 180 °C and placed in a mold maintained at 150 °C (Figure 1b). Next, neat PA6 resin or glass fiber-reinforced PA6 resin was injected from the bottom of the mold (Figure 1c). Finally, the mold was closed and compressed (Figure 1d) to fabricate the hat-shaped molded parts shown in Figure 2. In this study, three types of hat-shaped parts were fabricated. The composition of the surface material and resin layer is shown in Table 1, and a schematic drawing is shown in Figure 3. P0C1 and P0C1G, without a resin layer, could not be fabricated with the existing molds, so they were used only for FEM analysis, as discussed in Section 2.4. P means PA6, C means CFRTP laminate, G means glass fiber, and the number after the code indicates the thickness. P1C1 and P1C1G, which used a 1 mm thick CFRTP laminate placed on the top surface of the outer shell, had a 1 mm thick neat PA6 resin layer or glass fiber-reinforced PA6 resin layer by injection molding; P0C2 used a CFRTP laminate with 2 mm thickness for the outer shell.

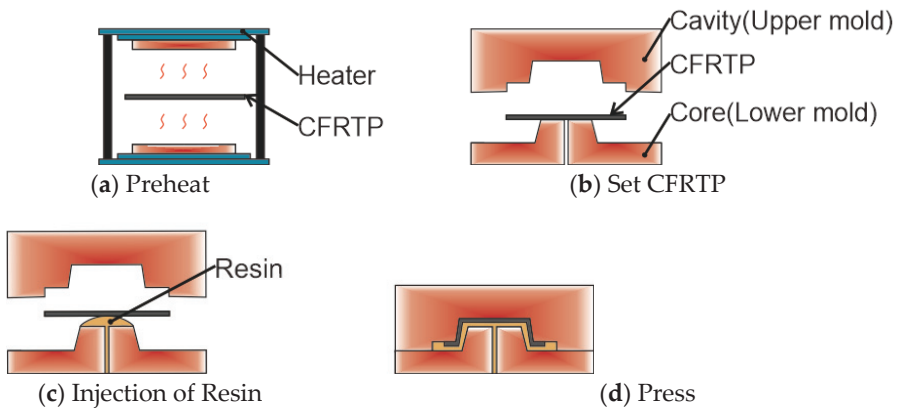

(**a**) Preheat (**b**) Set CFRTP

(**c**) Injection of Resin (**d**) Press

Figure 1. Molding process of injection-press hybrid molded part.

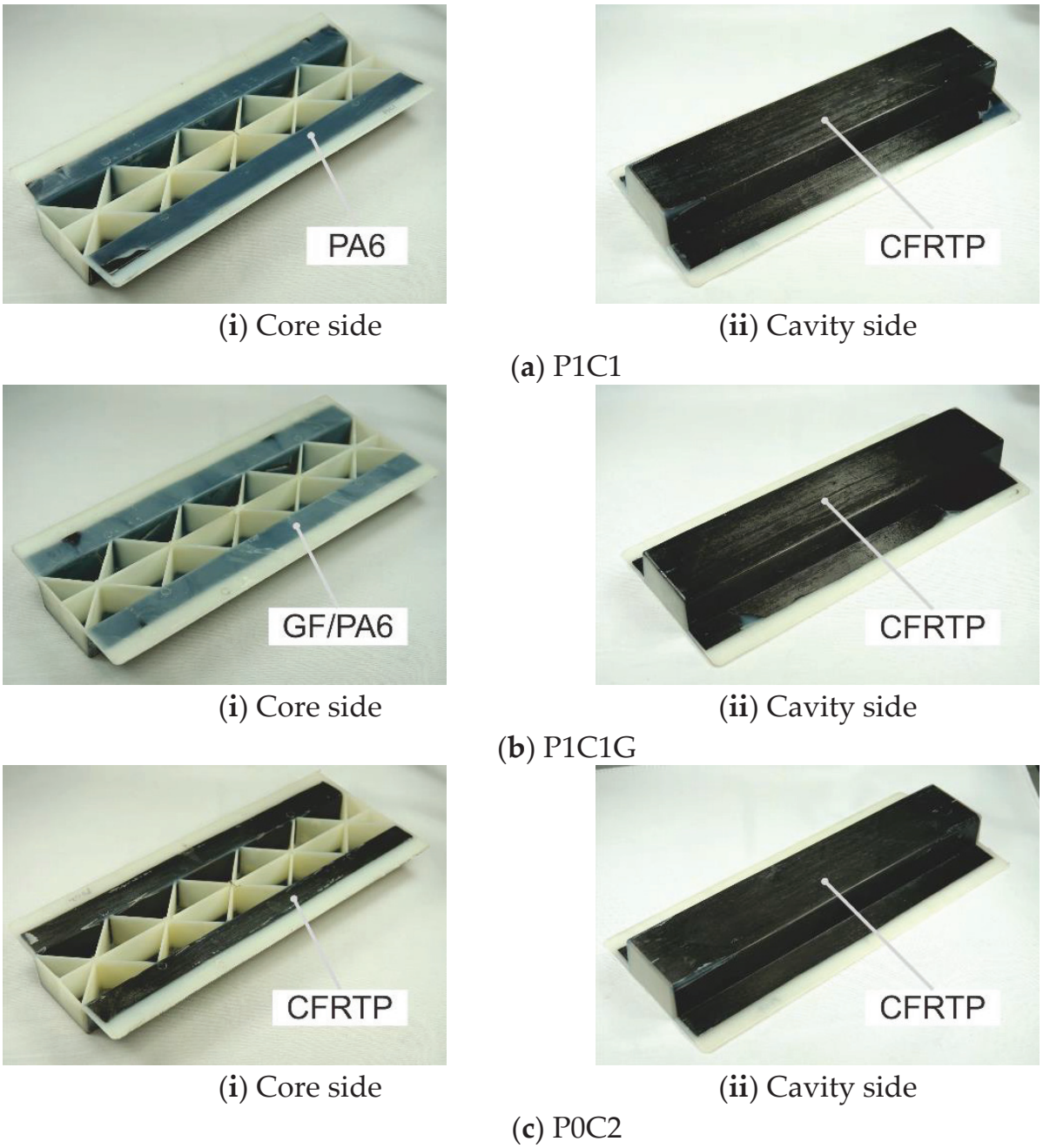

(**i**) Core side (**ii**) Cavity side

(**a**) P1C1

(**i**) Core side (**ii**) Cavity side

(**b**) P1C1G

(**i**) Core side (**ii**) Cavity side

(**c**) P0C2

Figure 2. Molded hat-shaped parts.

Table 1. Composition of hat-shaped parts.

	Resin Layer [mm]		CFRTP Laminate [mm]	Experiment	FEM Analysis
	PA6	GF/PA6			
P1C1	1	-	1	○	○
P1C1G	-	1	1	○	○
P0C2	-	-	2	○	○
P0C1	-	-	1	-	○
P0C1G	-	-	1	-	○

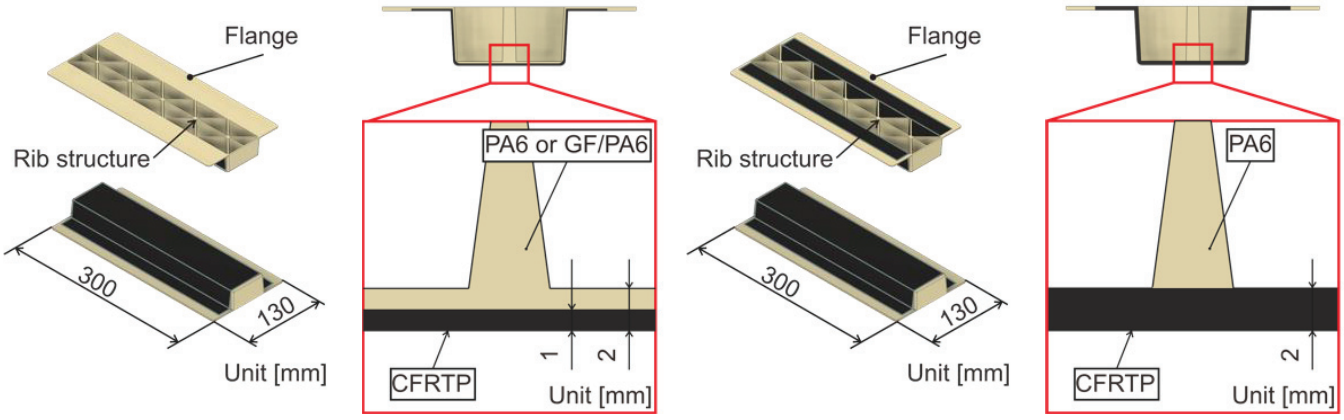

(**i**) Overview (**ii**) Cross section (**i**) Overview (**ii**) Cross section

(**a**) P1C1, P1C1G (**b**) P0C2

Figure 3. Schematic drawing of hat-shaped parts. (the red square in the figure is a magnified view of the rib root).

2.2. T-Shaped Tensile Tests

The bond strength at the rib root of each hat-shaped part was evaluated by a tensile test using a universal testing instrument (5566, Instron, Norwood, MA, USA) with a T-shaped specimen cut out, as shown in Figure 4. With reference to the previous studies [12,13,20], T-shaped tensile tests were conducted. T-shaped tensile tests were also performed on specimens of P1C1 and P1C1G in which the resin layer at the rib root was removed using abrasive paper, as shown in Figure 5. These specimens are called P0C1 and P0C1G, respectively. To reduce displacement in the direction of tensile loading, aluminum tabs were bonded to the laminates of the test specimens using epoxy adhesive. The displacement speed was set to 1.7×10^{-5} m/s (1.0 mm/min), and the bond strength was calculated by dividing the maximum load in the obtained load–displacement curve by the cross-sectional area, without considering the R at the rib root, regardless of the failure position. The cross section of each specimen was observed using a digital microscope (VHX-5000, Keyence, Osaka, Japan).

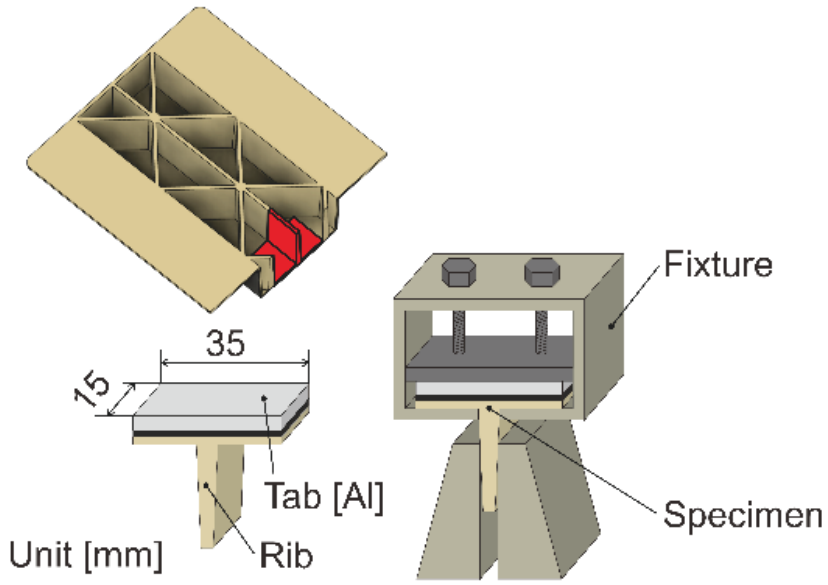

Figure 4. Schematic drawing of T-shaped specimen and tensile test.

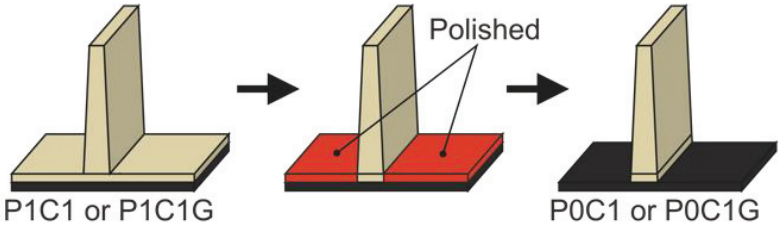

Figure 5. Removal process of the resin layer at the rib root.

2.3. Three-Point Bending Tests of Hat-Shaped Parts

The mechanical properties of each hat-shaped part were evaluated by a three-point bending test using a universal testing instrument (Autograph AGX-250 kN, Shimadzu Corporation, Kyoto, Japan) with the surface material on the tensile side, as shown in the schematic diagram in Figure 6. The displacement speed was set to 5.3×10^{-5} m/s (3.2 mm/min), the span length of the support was 240 mm, and the slope of the obtained load–displacement curve from the time when the hat-shaped part was loaded to the displacement of 0.96 mm was calculated as the stiffness of the entire part. The bending behavior of each hat-shaped part during the test was observed using a digital video camera (FDR-AX45, SONY, Tokyo, Japan).

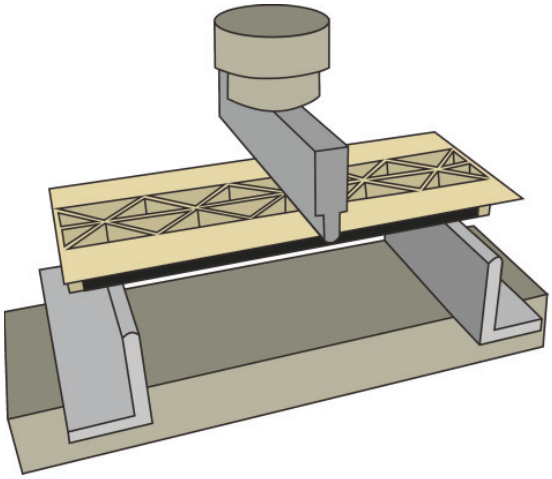

Figure 6. Schematic drawing of three-point bending test.

2.4. Three-Point Bending FEM Analysis of Hat-Shaped Parts

FEM analysis was performed by Solid Mechanics (structural mechanics module) using the COMSOL Multiphysics® (Stockholm, Sweden) simulation software. An example of an FEM model is shown in Figure 7. The mesh was generated with tetrahedral elements. The displacement in the –Z direction was applied to the FEM model at the line segment assuming the indenter on the core side, and the displacement in the Z direction was constrained at the two-line segments assuming the support on the cavity side. The shapes of the FEM models are the same as those of P1C1, P1C1G, and P0C2 fabricated in Section 2.1, and structures are shown in Figure 8a,b. A convex surface material with a thickness of 2 mm was divided into 1 mm sections; for P1C1 and P1C1G, the core side was set as the resin layer and the cavity side was set as the laminate. In P0C2, both the core and cavity sides were set as the laminate. To evaluate the effect of the resin layer at the rib root on the mechanical properties, analyses were also performed for P0C1 and P0C1G with the resin layer at the rib root removed, as shown in Figure 8c. Table 2 shows the material properties of each material used in the FEM model. Young's modulus of PA6 resin, glass fiber-reinforced PA6 resin, and CFRTP laminate in the Z direction was evaluated by load–unload tests using a dynamic ultra micro hardness tester (DUH-211, Shimadzu Corporation, Kyoto, Japan). Young's modulus of CFRTP laminates in the X and Y directions was calculated from

displacements obtained by FEM analysis of the tensile tests using an FEM model of a strip specimen complying with JIS K 7164. The FEM model was created using the same structure as the CFRTP laminate explained in Section 2.1. Other material properties were based on catalog values [21–24]. In this study, the reaction force and displacement acting on the line segment assuming an indenter were obtained by three-point bending FEM analysis; the stiffness was calculated as shown in Section 2.3 and compared with the experimental values. The principal stress distribution for the cross section of the parts shown in Figure 9 and the principal strain distribution for the sides of the parts were obtained, and the specific stiffness was calculated by dividing the stiffness by the density.

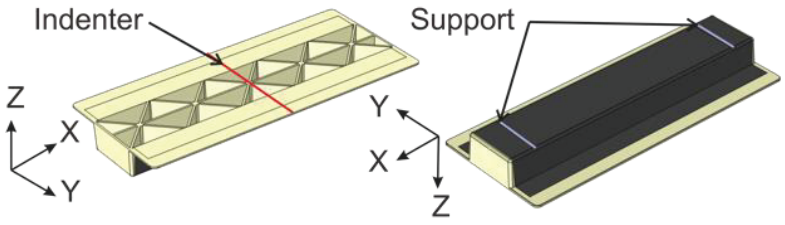

(**a**) Core side (**b**) Cavity side

Figure 7. Schematic drawing of FEM model for P1C1, P1C1G.

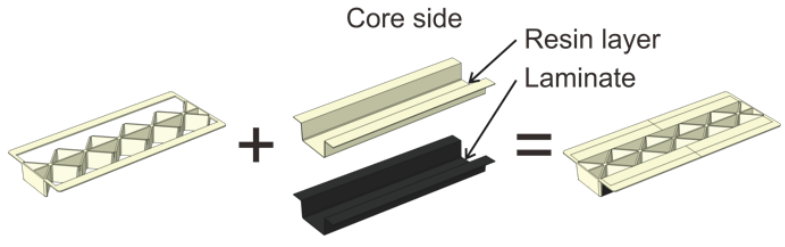

(**a**) P1C1, P1C1G

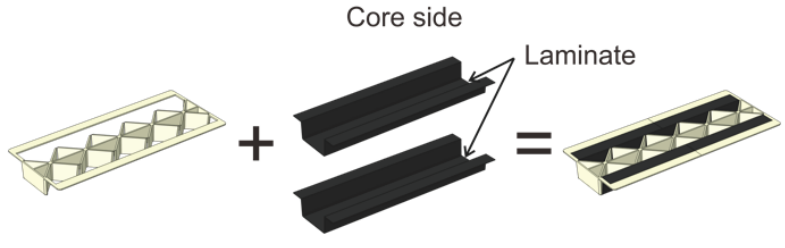

(**b**) P0C2

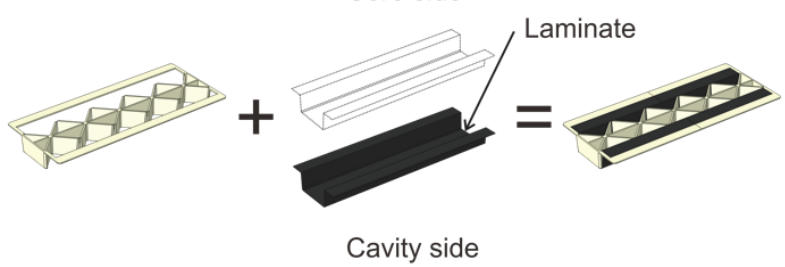

(**c**) P0C1, P0C1G

Figure 8. Composition of FEM models.

Table 2. Material properties.

Material \ Property	Young's Modulus [GPa]			Shear Modulus [GPa]			Poisson Ratio	Density [kg/m^3]
	E_X	E_Y	E_Z	G_X	G_Y	G_Z		
PA6		2.3					0.3	1140 [21]
GF/PA6		3.7					0.3	1360 [22]
CFRTP laminate	79	40	1.8	30	15	0.7	0.3	1505 [23,24]

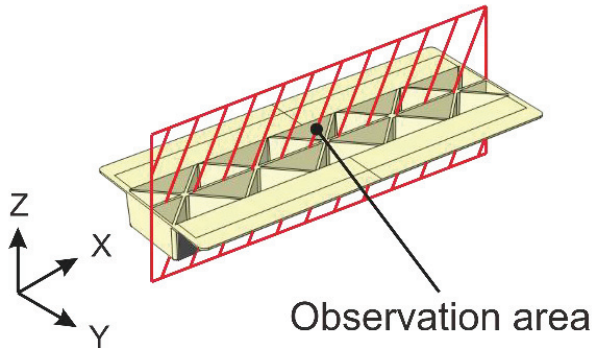

Figure 9. Cross-sectional observation area of FEM model.

2.5. Cost Evaluation of Hat-Shaped Parts

The costs of the injection and surface materials used to fabricate each hat-shaped part are the values shown in Table 3. These costs were our purchase prices. The molded part costs were calculated using the material costs shown in Table 3, using the volumes of the injection part, laminate, and resin layer calculated by CAD software and the density of the materials. The results of the cost calculations for each hat-shaped part are shown in Table 4. In this study, the cost of materials only was evaluated, without considering labor, equipment, or molding costs, and the relationship between the specific stiffness calculated by FEM analysis and the cost of each hat-shaped part was evaluated.

Table 3. Cost of materials.

Material	Cost [yen/kg]
PA6	0.60×10^3
GF/PA6	1.2×10^3
CF/Phenoxy prepreg	29×10^3

Table 4. Cost of molded parts.

Molded Part	Cost [yen]
P1C1	2.0×10^3
P1C1G	2.1×10^3
P0C2	3.9×10^3
P0C1	2.0×10^3
P0C1G	2.1×10^3

3. Results and Discussion

3.1. T-Shaped Tensile Test

Figure 10 shows the results of the observation of the molded P1C1 and P1C1G from the core side, respectively. Whitened areas were observed where the CFRTP laminate and the resin layer appeared to be peeling off. For clarity, the peeled areas are shown in red in the right-side figures of Figure 10. Although for P1C1, which used neat PA6 resin as the injection material, a peeled area was observed, no peeling was observed for P1C1G, which used glass fiber-reinforced PA6 resin as the injection material. Cross-sectional observations

of the cut specimens of P1C1 and P0C2 are shown in Figure 11. P0C2, which used a 2 mm thick CFRTP laminate, showed that the press pressure caused the laminate to flow into the ribs in contrast to P1C1, which had a resin layer. Although not shown here, P1C1G, P0C1, and P0C1G, like P1C1, showed no laminate flow into the ribs.

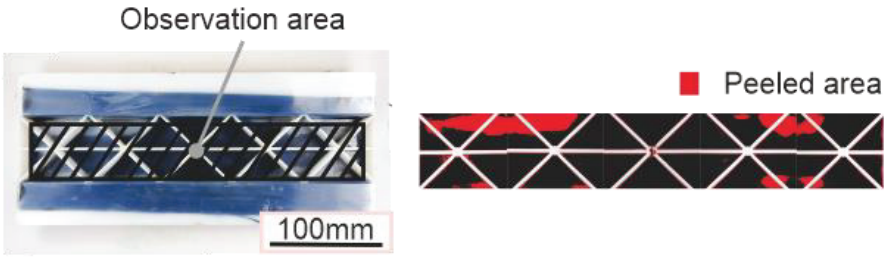

(**a**) P1C1

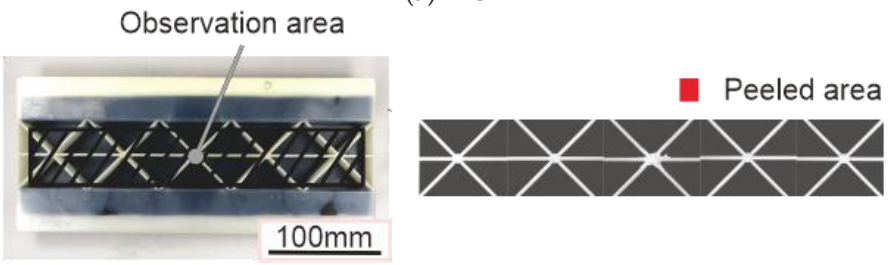

(**b**) P1C1G

Figure 10. Molded parts after the eject process and their schematic diagrams.

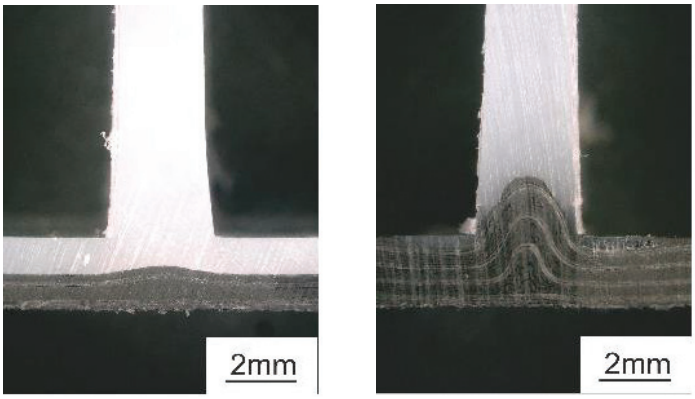

(**a**) P1C1 (**b**) P0C2

Figure 11. Magnified cross-sectional view of T-shaped specimens.

Figure 12 shows the results of the bond strength at the rib roots obtained from the T-shaped tensile test. The bond strengths of P1C1 and P1C1G with a resin layer at the rib root were 129% and 52% higher than those of P0C1 and P0C1G without a resin layer, respectively. The bond strength of P1C1 was not significantly different from that of P0C2. The bond strengths of P1C1G and P0C1G using glass fiber-reinforced PA6 resin as the injection material were 90% and 186% higher than those of P1C1 and P0C1 using neat PA6 resin, respectively. In general, the stress was concentrated at the rib roots. In the case of P1C1 and P1C1G, which had a resin layer, the stress dispersed at the interface due to the resin layer. As a result, P1C1 and P1C1G with a resin layer at the rib roots showed higher bond strengths than P0C1 and P0C1G without a resin layer. Previously, the authors reported that, in hybrid molding, the more the laminate flows into the ribs, the higher the bond strength is [12,13]. In this study, P0C2, which used 2 mm thick CFRTP laminates and did not have a resin layer, increased the bond strength due to the inflow into the ribs of the laminate. Therefore, it is considered that the bonding strength of P0C2 was equivalent to that of P1C1 with a resin layer. The mold shrinkage rate [21,22] of the materials used in

injection molding was 1.4% in the machine direction and 1.5% in the transverse direction for the neat PA6 resin, while the glass fiber-reinforced PA6 resin had lower values of 0.2% in the machine direction and 0.7% in the transverse direction. As shown in Figure 10b, the use of glass fiber-reinforced PA6 resin as the injection material prevented peeling of the bonding area due to its low mold shrinkage rate. It was reported that, in the case of joints between injection materials and metals, the smaller the amount of peeling in the bonding area, the higher the bond strength is and there is a correlation between the two [15]. These results suggest that P1C1G, which had a lower mold shrinkage rate, can be used to mold parts that exhibit higher bond strength than P1C1.

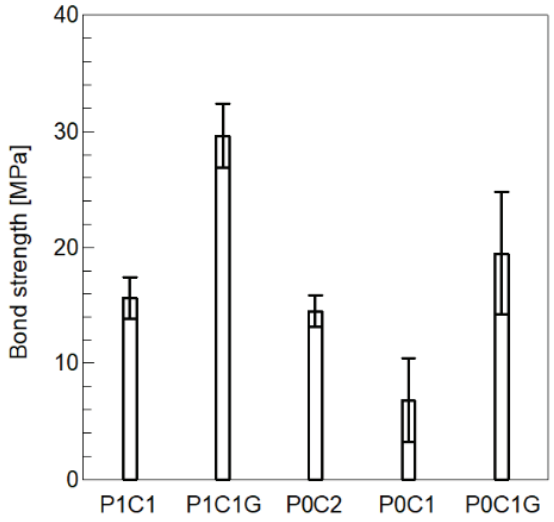

Figure 12. Tensile strength of molded parts obtained by T-shaped tensile tests. (N = 5, mean ± S.D).

3.2. Three-Point Bending Tests of Hat-Shaped Parts

Some examples of load–displacement curves obtained from three-point bending tests are shown in Figure 13. The stiffness and maximum load calculated from these results are shown in Figure 14. The stiffness of P1C1G was 70% higher than that of P1C1 and not significantly different from that of P0C2. The maximum load of P0C2 was 85% higher than that of P1C1, and the maximum load of P1C1G was 74% higher than that of P1C1.

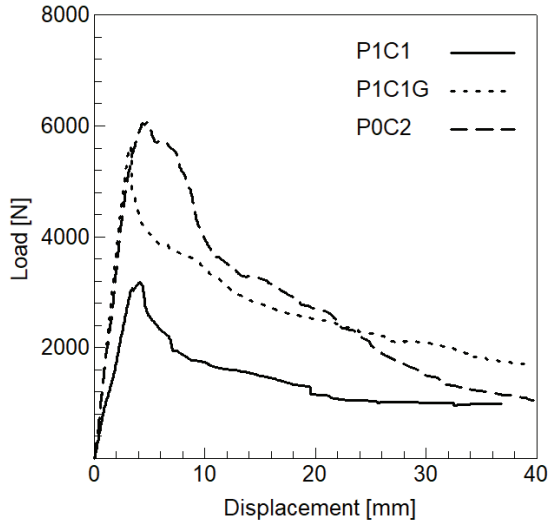

Figure 13. Load–displacement curve of three-point bending tests.

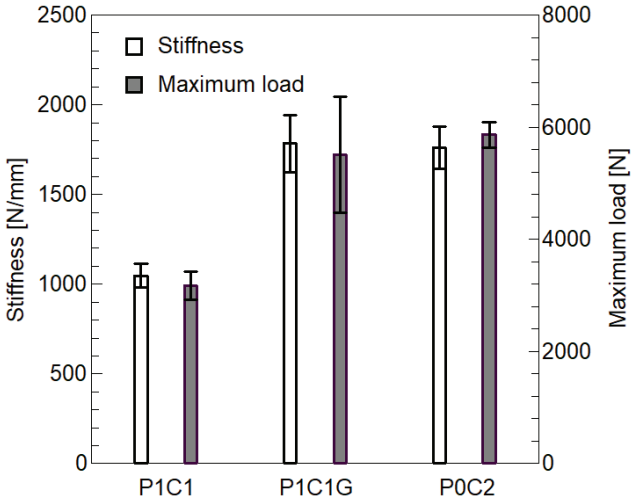

Figure 14. Stiffness and maximum load of molded parts obtained by three-point bending tests. (N = 5, mean ± S.D).

The use of glass fiber-reinforced PA6 resin, which has a high Young's modulus, in the injection material showed that P1C1G exhibited higher stiffness than P1C1. A study on the bending properties of hat-shaped parts reported that the thicker the laminate, the higher the stiffness [25]; in this study, P0C2, with a thicker laminate of 2 mm CFRTP, showed higher stiffness than P1C1. Figure 15 shows a side observation of P1C1 after the three-point bending test; the white arrows indicate the direction of crack propagation. At maximum load, a crack was observed in the CFRTP laminate at the back of the flange, followed by crack propagation to the side of the part. Although not shown here, cracks in the laminates were observed in P1C1G and P0C2 as well as in P1C1. Figure 14 suggests that the use of a high-strength laminate for the surface material resulted in a higher maximum load for P0C2 than that for P1C1. As shown in Figure 15, the laminate cracked around 3.5 mm displacement, showing the maximum load in both P1C1 and P1C1G. However, there was a significant difference in the maximum load of P1C1 and P1C1G. The reasons for this difference are discussed in detail in Section 3.3.

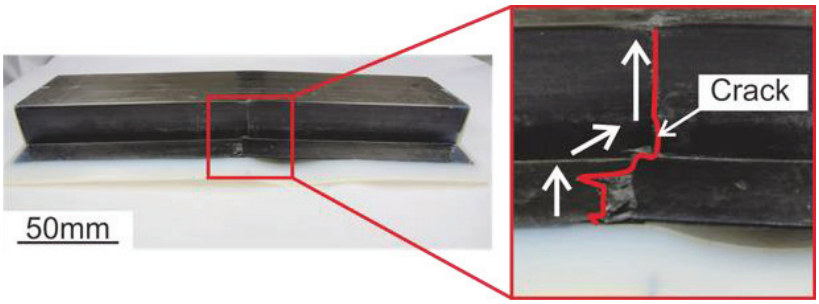

Figure 15. Observation of the side of P1C1 after three-point bending tests (the red square in the figure is a magnified view of the crack area).

3.3. Three-Point Bending FEM Analysis of Hat-Shaped Parts

The stiffness of each hat-shaped part obtained by FEM analysis is shown in Figure 16 with the experimental values. For P1C1G and P0C2, the analytical values were within the standard deviation, showing that the modeling performed with excellent accuracy. On the other hand, for P1C1, the analytical value was not within the standard deviation of the experimental values and was high. As shown in Figure 10a, peeling between the CFRTP laminate and the resin layer on the surface at P1C1 is considered to be the one reason for these lower experimental values. Figure 17 shows the observed bending behavior of P1C1 at a displacement of 0.96 mm after loading in a three-point bending test. The resin layer

was observed to have peeling at the flange just below the indenter. In the FEM model of P1C1, the bonding conditions between the laminate and the resin layer were not considered, which may have lowered the stiffness.

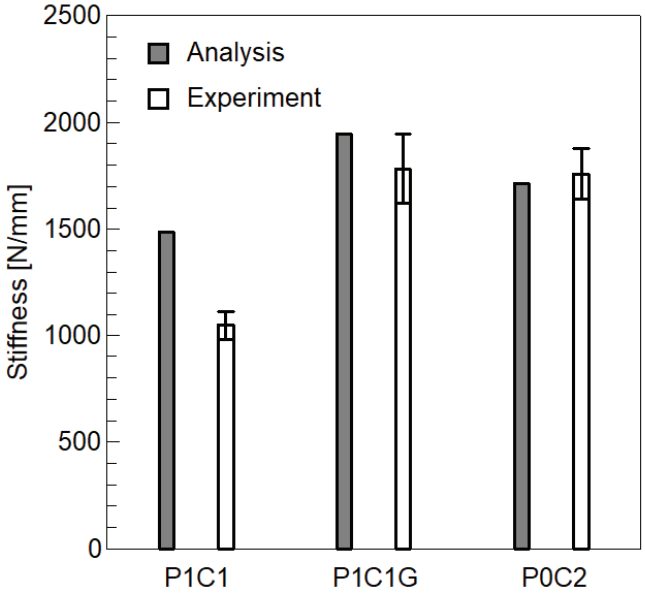

Figure 16. Stiffness of experimental and analytical results.

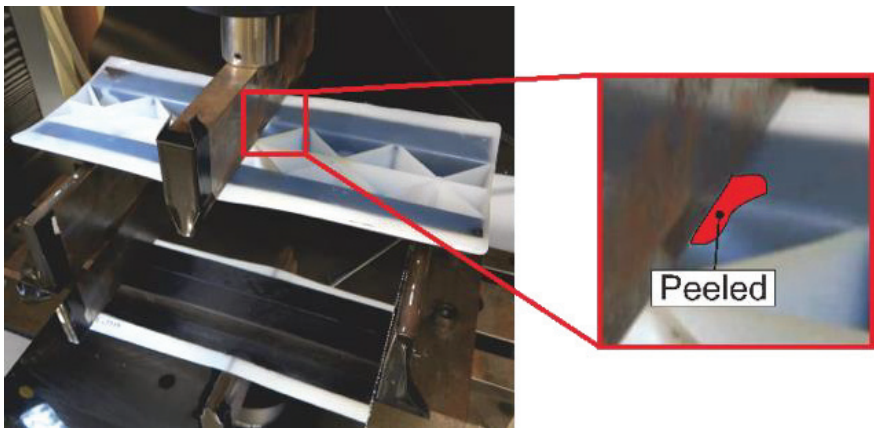

Figure 17. Observation of bending behavior of P1C1 (the red square in the figure is a magnified view of peeled area) (displacement = 0.96 mm).

The principal stress distributions and the principal strain distributions of each model obtained by FEM analysis are shown in Figure 18. In the principal stress distribution of P1C1G and P0C1G using glass fiber-reinforced PA6 resin as the injection material, we observed higher stress in the ribs just below the indenter than in P1C1, P0C2, and P0C1 using neat PA6 resin. The cause of the significant difference in the maximum loads for P1C1 and P1C1G in Section 3.2 may be due to the glass fiber-reinforced PA6 resin, which increased the stiffness of the ribs and prevented deformation. In the principal strain distribution of P0C2, P0C1, and P0C1G, which had no resin layer, the strain was concentrated at the place where the ribs were located. On the other hand, P1C1 and P1C1G with the resin layer were observed to prevent the concentration of strain. The resin layer is considered to have dispersed the load applied to the interface and prevented the concentration of strain.

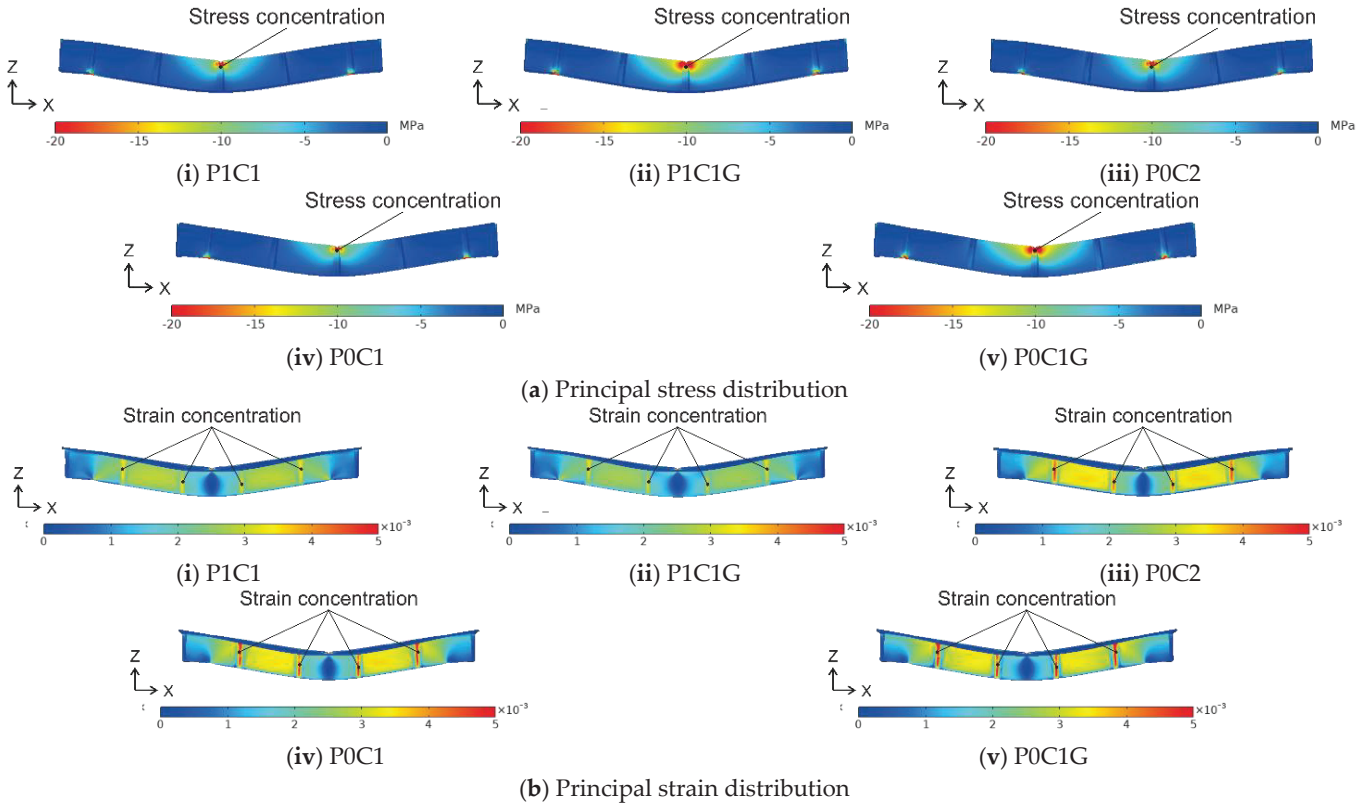

Figure 18. Analyzed principal stress and principal strain distributions of FEM models (displacement = 0.96 mm).

The specific stiffness calculated by dividing the stiffness of each hat-shaped part by the density is shown in Figure 19. The specific stiffness of P1C1 and P1C1G with a resin layer at the rib root was 38% and 42% higher than that of P0C1 and P0C1G without a resin layer, respectively. The resin layer is considered to have increased the sectional secondary moment, resulting in high specific stiffness. Therefore, if the wall thickness can be expanded, a molded part with excellent stiffness can be fabricated by adding a resin layer at the rib root. In this study, the P1C1G with a 1 mm thick CFRTP laminate on the top surface of the outer shell and a 1 mm glass fiber-reinforced PA6 resin layer by injection showed the highest specific stiffness.

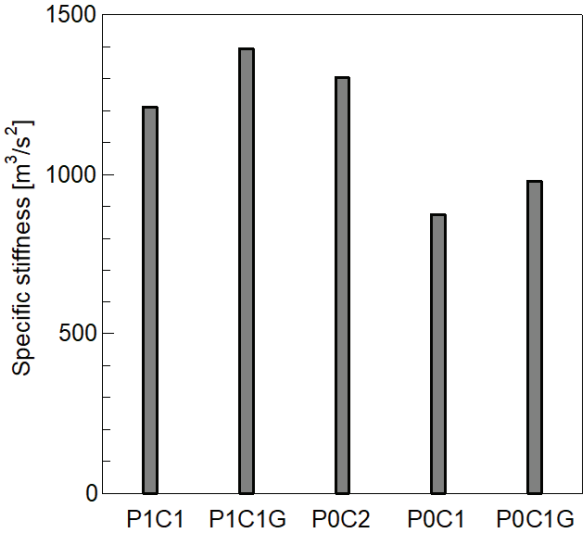

Figure 19. Specific stiffness of FEM models.

In this study, only the stiffness was obtained by the FEM models. The next step would be to construct the FEM model for fracture analysis. In this case, the Cohesive Zone Model (CZM) in the FEM analysis would be one solution to obtain more accurate simulation results [20,26].

3.4. Cost Evaluation of Hat-Shaped Parts

The relationship between material cost and specific stiffness for each hat-shaped part calculated by FEM analysis is shown in Figure 20. The cost of P1C1 and P1C1G with a resin layer at the rib root was almost the same as that of P0C1 and P0C1G without a resin layer. The specific stiffness of P1C1 and P1C1G was 38% and 42% higher than that of P0C1 and P0C1G, respectively. By adding a resin layer to the rib roots, molded parts with excellent specific stiffness can be fabricated at a small increase in cost. Among these, P1C1G, which had a 1 mm thick CFRTP laminate on the top surface of the outer shell and a 1 mm glass fiber-reinforced PA6 resin layer by injection molding, achieved a 7% higher specific stiffness at a 47% lower cost than P0C2, which used a 2 mm thick CFRTP laminate for the outer shell.

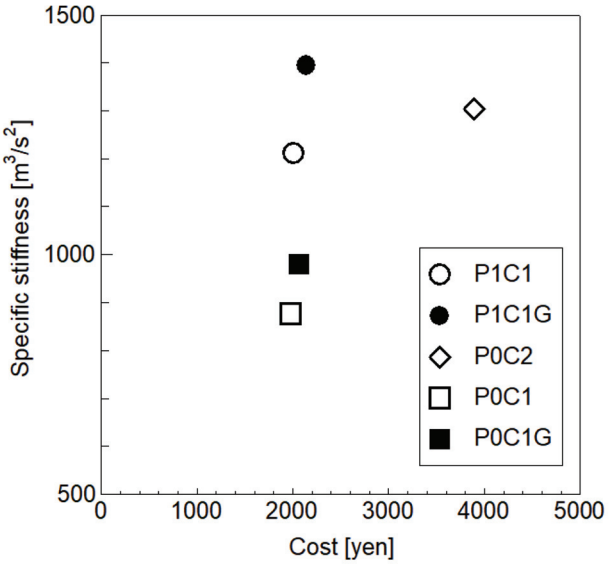

Figure 20. Relationship between material cost and specific stiffness.

4. Conclusions

In this study, CFRTP hat-shaped parts with neat PA6 or glass fiber-reinforced resin layers at the rib roots were fabricated by press-injection hybrid molding. T-shaped tensile and three-point bending tests at the rib root were performed to assess the bond strength between the surface material and the ribs and to clarify their effects on stiffness. Furthermore, a three-point bending FEM analysis was performed to clarify the effect of the resin layer at the rib roots on the mechanical properties and the relationship between material cost and mechanical properties. The investigation yielded the following conclusions:

1. In T-shaped tensile tests at the rib roots, molded parts with neat and fiber-reinforced resin layers at the rib roots showed 129% and 52% higher bond strengths than those without resin layers, respectively. The use of glass fiber-reinforced PA6 resin showed a lower molding shrinkage rate, suggesting that it prevents peeling of the bonded area, resulting in higher bond strength than that of the neat PA6 resin.
2. In the CFRTP hat-shaped parts with a resin layer at the rib root, the use of glass fiber-reinforced PA6 resin as an injection material enables the fabrication of a molded part that shows the same stiffness as that of a molded part using a 2 mm thick CFRTP laminate for the outer shell.
3. The three-point bending FEM analysis of a CFRTP hat-shaped part showed that the addition of a resin layer prevents the concentration of strain where the ribs of the

surface material are located. The model with the use of a 1 mm thick CFRTP laminate for the outer shell and glass fiber-reinforced PA6 resin as the injection material showed the best specific stiffness in this study.

4. By adding a resin layer to the rib root, molded parts with excellent specific stiffness can be fabricated with a small increase in cost. A model with a resin layer using glass fiber-reinforced PA6 resin as the injection material showed low cost and excellent specific stiffness.

Author Contributions: Conceptualization, K.T.; data curation, M.T.; funding acquisition, K.T.; investigation, M.T.; methodology, K.T.; project administration, K.T.; resources, K.T.; supervision, K.T.; validation, K.T. and M.T.; visualization, M.T.; writing—original draft, M.T.; writing—review and editing, K.T. All authors have read and agreed to the published version of the manuscript.

Funding: This research was partially supported by Individual Research Allowances of Doshisha University.

Data Availability Statement: Data are contained within the article.

Conflicts of Interest: The authors declare no conflicts of interest.

References

1. Ureshino, Y. Weight reduction and joining Technology for multi-material automobile. *J. Surf. Finish. Soc. Jpn.* **2022**, *73*, 380–383. [CrossRef]
2. Ishikawa, T. Overview of carbon fiber reinforced composites (CFRTP) applications to automotive structural parts,-focused on thermoplastic CFRP-. *J. Jpn. Soc. Precis. Eng.* **2015**, *81*, 489–493. [CrossRef]
3. Wan, Y.; Takahashi, J. Developed of carbon fiber-reinforced thermoplastics for mass-produced automotive applications in Japan. *J. Compos. Sci.* **2021**, *5*, 86. [CrossRef]
4. Terada, K. Carbon fiber reinforced thermo plastics-currently, applications and forecast. *J. Jpn. Soc. Precis. Eng.* **2015**, *81*, 485–488. [CrossRef]
5. Lee, J.M.; Kim, B.M.; Ko, D.C. Multi-material forming using DP780 and CFRTP. *Procedia Manuf.* **2018**, *15*, 1716–1721. [CrossRef]
6. Guo, Q.; Xiao, B.; Ohsawa, I.; Fujita, M.; Takahashi, J. Numerical analysis and optimization of CFRTP hat-stiffened structure. In Proceedings of the ECCM18—18th European Conference on Composite Materials, Athens, Greece, 25–28 June 2018; pp. 1–8.
7. Limaye, M.; Pradeep, S.A.; Kothari, A.; Savla, S.; Agha, A.; Pilla, S.; Li, G. Thermoforming process effects on structural performance of carbon fiber reinforced thermoplastic composite parts through a manufacturing to response pathway. *Compos. Part B* **2022**, *235*, 109728. [CrossRef]
8. Fiorotto, M.; Lucchetta, G. Experimental investigation of a new hybrid molding process to manufacture high-performance composites. *Int. J. Mater. Form.* **2013**, *6*, 179–185. [CrossRef]
9. Kang, T.-H.; Lee, J.-W.; Kim, J.-H.; Ahn, T.-M.; Ko, D.-C. Design of center pillar with composite reinforcements using hybrid molding method. *Material* **2021**, *14*, 2047. [CrossRef]
10. Ohishi, M.; Ohtani, A.; Nakai, A. Effect of heating condition for prepreg sheet and injection resin on interfacial properties between prepreg and injection part in hybrid molding. *Seikei-Kakou* **2017**, *29*, 135–141. [CrossRef]
11. Asanuma, N. Applying direct injection molding process and hybrid molding system to CFRP molding. *Seikei-Kakou* **2015**, *27*, 89–93. [CrossRef]
12. Tanaka, K.; Tokura, D.; Katayama, T.; Ishikawa, T.; Tomioka, M. Evaluation of mechanical property of press and injection hybrid molded CF/PA6 using cut prepreg sheets. *J. Soc. Mater. Sci.* **2016**, *65*, 713–720. [CrossRef]
13. Tanaka, K.; Harada, Y.; Katayama, T.; Ishikawa, T.; Tomioka, M. Press and injection hybrid using CF/PP unidirectional slit prepreg and evaluation of boding strength at rib root. *J. Soc. Mater. Sci.* **2016**, *65*, 721–726. [CrossRef]
14. Wan, Y.; Takahashi, J. Tensile and compressive properties of chopped carbon fiber tapes reinforced thermoplastics with different fiber lengths and molding pressures. *Compos. Part A* **2016**, *87*, 271–281. [CrossRef]
15. Seto, M.; Tanaka, H.; Katayama, M.; Itakura, M.; Yamabe, M. Influence of reinforced fiber on joining strength in metal-resin joining injection molded products. *Seikei-Kakou* **2016**, *28*, 427–433. [CrossRef]
16. Akkerman, R.; Bouwman, M.; Wijskamp, S. Analysis of the Thermoplastic Composite Overmolding Process: Interface Strength. *Front. Mater.* **2020**, *7*, 27. [CrossRef]
17. Paramasivam, A.; Timmaraju, M.V.; Velmurugan, R. Influence of Preheating on the Fracture Behavior of Over-Molded Short/Continuous Fiber Reinforced Polypropylene Composites. *J. Compos. Mater.* **2021**, *55*, 4387–4397. [CrossRef]
18. Hartley, W.D.; McCann, J.; Davis, S.; Hocker, T.; Bobba, S.; Verghese, N.; Bajaj, D.; Yu, H.Z.; Dillard, D.A. Fracture Characterization of Composite adhesion. *J. Thermoplast. Compos. Mater.* **2022**, *35*, 977–997. [CrossRef]
19. Jiang, Q.; Takayama, T.; Nishioka, A. Impact energy dissipation and quantitative models of injection molded short fiber-reinforced thermoplastics. *Polymers* **2023**, *15*, 4297. [CrossRef] [PubMed]
20. Giusti, R.; Lucchetta, G. Cohesive Zone Modeling of the Interface Fracture in Full-Thermoplastic Hybrid Composites for Lightweight Application. *Polymers* **2023**, *15*, 4459. [CrossRef] [PubMed]

21. UBE Corporation Website. Available online: https://ube.es/wp-content/uploads/2021/12/TDS_UBE-NYLON-1015B_Injection.pdf (accessed on 18 July 2023).
22. UBE Corporation. Available online: https://www.ube.com/contents/jp/chemical/nylon/chemical_injection/1015gc6.html (accessed on 18 July 2023).
23. Mitsubishi Chemical Group Corporation. Available online: https://www.m-chemical.co.jp/carbon-fiber/product/tow/ (accessed on 18 July 2023).
24. Gabriel Phenoxies, Inc. Available online: https://www.gabrielchem.com/wp-content/uploads/GPI-SDS-US-PHENOXY-RESIN-PELLETS-Version-5.pdf (accessed on 18 July 2023).
25. Dhaliwal, G.S.; Newaz, G.M. Experimental and numerical investigation of flexural behavior of hat sectioned aluminum/carbon fiber reinforced mixed material composite beam. *Compos. Part B Eng.* **2020**, *182*, 107642. [CrossRef]
26. Ghabezi, P.; Farahani, M. Effects of Nanoparticles on Nanocomposites Mode I and II Fracture: A Critical Review. *Rev. Adhes. Adhes.* **2017**, *5*, 414–435. [CrossRef]

Journal of
Composites Science

MDPI

Article

Buckling Analysis for Carbon and Glass Fibre Reinforced Hybrid Composite Stiffened Panels

Haoting Han and Chensong Dong *

School of Civil and Mechanical Engineering, Curtin University, Perth, WA 6845, Australia
* Correspondence: c.dong@curtin.edu.au; Tel.: +61-(8)-92669204

Abstract: Composite laminated structural panels are widely used in various industries such as aerospace and machinery because of their light weight, large specific stiffness, and strong fatigue resistance. As a typical engineering structure, the composite stiffened plate is designed to enhance the bearing capacity of the laminated plate. In this study, composite stiffened panels reinforced by carbon and/or E-glass fibres are modelled by finite element analysis (FEA) using Ansys. Nonlinear structural analysis is employed to find the critical buckling load. Three different skin layups, i.e., $[45°/-45°/90°/0°]_S$, $[90°/0°/90°/0°]_S$, and $[60°/-30°/90°/0°]_S$, are studied. For each ply angle combination, different ply material combinations are studied. The cost and weight of each combination formed by applying different ply materials to the skin and stiffeners are studied. The results show that hybrid reinforcement in the stiffened panels reduces costs and maintains high buckling loads. Carbon/epoxy composites as the outer layers also reduce costs and maintain acceptable buckling loads without compromising the overall performance. Customized composite designs in terms of cost and weight can be achieved while maintaining critical buckling loads.

Keywords: composite; hybrid; stiffened panel; buckling

1. Introduction

In recent years, the pursuit of lightweight and high-strength materials has led to significant advancements in the field of composite materials. Among these, hybrid composites, integrating diverse fibres such as carbon and glass, have emerged as promising candidates for structural applications [1]. One critical aspect of their performance is the buckling behaviour, especially in the context of stiffened panels. Stiffened panels play a crucial role in aerospace, automotive, and marine structures, where their ability to withstand compressive loads is of paramount importance [2]. Fu et al. [3] previously studied the impact characteristics of a reinforced sandwich of functionally graded porous materials with a hyperbolic shell with a concave-angled honeycomb auxetic core. The results showed that reinforced structures have significant advantages in impact energy absorption. This provides important reference and guidance for the optimal design and application of such structures.

Buckling failure in composite structures refers to the sudden, catastrophic collapse of a structure due to compressive loads exceeding the critical buckling load. Unlike homogeneous materials, composites exhibit complex failure modes, influenced by the interplay of various constituent materials. A buckle can be generally defined as a compression (or shear) failure in a feature (web or flange) or column that occurs in multiples of wavelengths over the whole length of the feature. When a panel is in the buckled state, it continues to carry shear load (usually a significantly greater load than the load at which the feature buckles) and the structure can be said to have residual strength in the post-buckled state. However, a buckled panel or web cannot continue to carry a compression load after it has buckled. Another type of failure related to buckling is crippling failure. A cripple is a failure, of a corner feature or compound shape that is not reversible upon the removal

of the load. A crippling failure is usually considered an ultimate failure with no residual strength remaining after failure and occurs within a very local area rather than over a significant length [4].

The factors affecting the buckling of composites include material anisotropy, fibre–matrix interaction, geometric imperfections, and environmental effects [5]. Composite materials are anisotropic, meaning their properties vary with direction. The orientation of the fibres significantly affects the buckling behaviour. The interaction between reinforcing fibres and the matrix material influences how loads are transmitted and distributed within the composite. For a composite structure, any deviations from an idealized, perfectly straight structure can lead to localized stress concentrations, promoting buckling initiation. Additionally, exposure to environmental factors, such as moisture or temperature variations, can impact the composite's mechanical properties and contribute to buckling.

When designing a composite structure with buckling in consideration, the proper selection and arrangement of laminate layers play a crucial role in preventing or mitigating buckling. The fibre orientation and stacking sequence are key considerations. Understanding and applying appropriate boundary conditions are essential for accurate buckling predictions. The choice of support conditions significantly influences the critical buckling load.

The buckling of composite stiffened plates has been studied experimentally [6–8]. Most studies have considered axial compression loads [6,7]. Some studies have also considered shear loads [8]. Lanzi [6] conducted a numerical and experimental investigation into the post-buckling behaviour of composite stiffened panels. Orifici et al. [7] explored compression and post-buckling damage growth and collapse analysis of flat composite stiffened panels. Bai et al. [8] contributed to the field by studying the dynamic buckling behaviour of a J-stiffened composite panel under in-plane shear.

Numerical methods based on the finite element method [6–10] have been employed to predict the buckling of composite stiffened plates. Chen and Guedes Soares [9] focused on the reliability assessment of the post-buckling compressive strength of laminated composite plates and stiffened panels under axial compression. Guo et al. [10] delved into the buckling behaviour of stiffened laminated plates, providing valuable insights into their structural response.

Research has been performed for the optimisation of the buckling/postbuckling of stiffened composite panels [11–14]. Ye et al. [11] optimised the distribution and stacking sequence of sub-stiffeners to improve the critical buckling load without adding weight. Bisagni and Lanzi [12] developed an optimisation procedure based on a global approximation strategy and genetic algorithms. The structure response is given by a system of neural networks trained by means of FEA. Bacarreza et al. [13] presented a multilevel optimization including progressive failure analysis and robust design optimization for composite stiffened panels, in which the ultimate load that a post-buckled panel can bear is maximized for a chosen weight. This method is a novel robust multi-objective approach for structural sizing of composite stiffened panels at different design stages. Chu et al. [14] investigated the weight minimisation of stiffened panels simultaneously optimising sizing, layout, and topology under stress and buckling constraints. An effective topology optimisation parameterisation is presented using multiple level-set functions.

Hybrid composites comprising two or more types of fibre have received significant attention in engineering design because of the potential of achieving balanced properties. One common type of hybrid composite is the carbon and glass fibre reinforced hybrid composite. Previous research on this material suggested that the flexural strength could be improved via hybridisation [15,16]. The main reason is that glass fibre has higher strain-to-failure than carbon fibre, and consequently, the strain-to-failure is increased due to the inclusion of glass fibre [17]. Rajpurohit et al. [18] showed positive hybrid effects in tension and compression. Zhang et al. [19] showed the carbon/glass interlayer hybrid composite had improved low velocity impact performance. The existence of hybrid effect can be potentially useful for achieving a balanced cost and weight optimal composite material. It

is shown carbon and glass fibre reinforced hybrid composites have been used in windsurf boards and wind turbine blades [20].

It is shown from the literature that little research has been performed on the effect of fibre hybridisation on the buckling of composites. Ranganathan and Mantena [21] investigated the effects of hybridisation on the buckling characteristics of flat pultruded glass-graphite/epoxy composite beams. It was shown that that buckling strengths improved with increase in graphite fibre content. Ragheb [22] investigated the effectiveness of utilizing hybridisation to improve the local buckling capacity of pultruded Fibre Reinforced Polymer (FRP) wide flange I-beams loaded in bending. Ahmed and Rajput [23] studied the buckling behaviour of interlayer hybrid I-shape composite panels composed of one natural and two synthetic unidirectional fabrics combined with epoxy resin. The results show that high buckling loads can be obtained by placing high-strength and high-stiffness material layers (Carbon/epoxy) on the top and bottom of I-shape beams. It was shown that significant increases in the local buckling load of the beam could be gained if the glass fibre mat laminates of the beam were replaced by carbon fibre ones, especially those located near the outer surface of the beam. No research has been performed on the effect of hybridisation on the buckling of complex composite stiffened panels. This study focuses on the buckling analysis of hybrid composite stiffened panels, exploring the effect of hybridisation on the buckling characteristics. Additionally, the cost and weight are considered. It is shown that fibre hybridisation can significantly reduce the cost.

2. Materials and Methods

2.1. Material Properties

In this study, hybrid composites are developed by reinforcing an epoxy matrix with unidirectional carbon fibre fabrics and unidirectional E-glass fibre fabrics. Epoxy resins are widely used in composites because of their high strength (tensile, compressive, and flexural), good chemical resistance, fatigue resistance, corrosion resistance, and electrical resistance [24]. Typical values of the properties of carbon and E-glass fibres and epoxy resin are given in Table 1 [25]. The detailed properties of carbon/epoxy and E-glass/epoxy composites are given in Table 2.

Table 1. Typical values of the properties of carbon and E-glass fibres and epoxy resin.

Material	Tensile Modulus (GPa)	Tensile Strength (MPa)	Density (g/cm^3)	Cost ($/litre)
High strength carbon fibre	230	4900	1.8	151.2
E-glass fibre	72	3450	2.58	10.8
Epoxy	3.1	69.6	1.09	26.2

Table 2. Detailed properties of carbon/epoxy and E-glass/epoxy composites.

Property	Carbon/Epoxy	E-Glass/Epoxy
Longitudinal modulus (GPa)	150.59	37.55
Transverse modulus (GPa)	7.82	8.69
Longitudinal–transverse Poisson's ratio	0.235	0.250
Transverse–transverse Poisson's ratio	0.398	0.305
Longitudinal–transverse shear modulus (GPa)	3.21	3.24
Transversetransverse shear modulus (GPa)	2.80	3.33
Tensile strength (MPa)	3208.1	1474.8
Compressive strength (MPa)	1320.4	613.9

The density of the hybrid composite reinforced by carbon and glass fibres (ρ_c) can be derived based on the Rule of Mixtures (RoM) [26] as follows:

$$\rho_c = \left[\rho_{fc}V_{fc} + \rho_m\left(1 - V_{fc}\right)\right]f_c + \left[\rho_{fg}V_{fg} + \rho_m\left(1 - V_{fg}\right)\right]f_g \quad (1)$$

where ρ_{fc}, ρ_{fg}, and ρ_m are the densities of carbon fibre, glass fibre, and the matrix, respectively; V_{fc} and V_{fg} are the fibre volume fractions for carbon/epoxy and glass/epoxy plies, respectively; and f_c and f_g are the volume fractions of carbon/epoxy and glass/epoxy plies, respectively.

The material cost of the hybrid composite (C_c) is given by

$$C_c = \left[C_{fc}V_{fc} + C_m\left(1 - V_{fc}\right)\right]f_c + \left[C_{fg}V_{fg} + C_m\left(1 - V_{fg}\right)\right]f_g \quad (2)$$

where C_{fc}, C_{fg}, and C_m are the costs of carbon fibre, glass fibre, and the matrix, respectively.

2.2. FEA-Based Model

The composite panels in this study are modelled by FEA using Ansys. Composite materials are defined using Ansys ACP, and nonlinear structural analysis is employed for buckling analysis. The FEA-based modelling approach has been proven to be valid by previous studies [27,28].

A partially cylindrical composite shell containing four stiffeners similar to a previous study [29] is studied. The radius of curvature is 381 mm, the overall length/width is 356 mm, and the height of stiffeners is 33 mm. A shell FEA model is created using Ansys Workbench, as shown in Figure 1. The skin contains 8 plies and each stiffener contains 16 plies. The ply thickness is 0.125 mm for all plies.

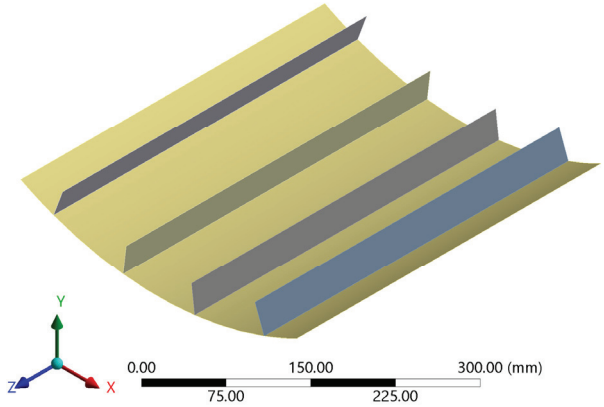

Figure 1. A partially cylindrical composite shell containing four stiffeners.

The layup for the stiffeners is fixed at $[[45°/-45°/90°/0°]_S]_2$, and three different ply angle layups, $[45°/-45°/90°/0°]_S$, $[90°/0°/90°/0°]_S$, and $[60°/-30°/90°/0°]_S$, are applied to the skin. For each ply angle layup combination, 12 different ply material combinations, as shown in Table 3, are applied to the skin and stiffeners, respectively. When hybrid layups are applied to the skin, the material of outer four layers is different from that of the inner four layers. Likewise, when hybrid layups are applied to the skin, the material of outer eight layers is different from that of the inner eight layers.

The composite panel is fixed at the bottom and subjected to an axial compressive load at the top, where from the top to bottom is in the positive z direction. The left and right edges of the composite panel are simply supported. The setting of the boundary conditions is shown in Table 4, where 1 represents being free, and 0 represents being constrained.

Table 3. Ply materials for each ply angle layup combination.

Ply Material Combination	Skin	Stiffeners
1	Carbon/epoxy	Carbon/epoxy
2	Carbon/epoxy	E-glass/epoxy
3	E-glass/epoxy	Carbon/epoxy
4	E-glass/epoxy	E-glass/epoxy
5	Carbon/epoxy	Hybrid (E-glass outer)
6	Carbon/epoxy	Hybrid (Carbon outer)
7	E-glass/epoxy	Hybrid (E-glass outer)
8	E-glass/epoxy	Hybrid (Carbon outer)
9	Hybrid (E-glass outer)	Carbon/epoxy
10	Hybrid (Carbon outer)	Carbon/epoxy
11	Hybrid (E-glass outer)	E-glass/epoxy
12	Hybrid (Carbon outer)	E-glass/epoxy

Table 4. The setting of curved stiffened plate boundary conditions.

Displacement Constraints	Top	Bottom	Left Side	Right Side
X	0	0	1	1
Y	0	0	0	0
Z	1	0	1	1

Nonlinear static analysis is conducted with progressively increasing loads to find the load levels at which the structure would fail.

3. Results

For all the ply material combinations given in Table 3, the critical buckling loads for all the skin ply angle layups are shown in Table 5. Similar trends are found for all the skin ply angle layups.

Table 5. Summary of critical buckling loads.

Ply Material Combination	Critical Buckling Load (kN)		
	$[45°/-45°/90°/0°]_S$	$[90°/0°/90°/0°]_S$	$[60°/-30°/90°/0°]_S$
1	30.14	36.80	32.74
2	30.06	36.26	32.04
3	14.34	17.06	15.23
4	13.85	16.35	14.84
5	30.04	36.64	32.50
6	30.10	36.73	32.72
7	13.77	16.73	14.87
8	14.09	17.00	14.99
9	17.96	18.56	19.15
10	26.56	33.08	28.85
11	18.23	19.43	18.69
12	24.63	31.89	26.67

Combinations 1 to 4 of the data in Table 5 are consistent with SudhirSastry's [29] previous research model parameters. It can be seen that under the three different skin ply angle layups, the results of each ply material combination of this study all show a buckling load from large to small, such as 1 > 2 > 3 > 4, in which the carbon/epoxy stiffened panel has the highest buckling load. This is consistent with the results of previous studies.

For skin ply angle layup $[45°/-45°/90°/0°]_S$, when both the skin and stiffeners are made of carbon/epoxy plies, the critical buckling load is 30,140 N, and the buckled shape

is shown in Figure 2. The contours show the y displacement in mm. The maximum displacement is 5.50 mm.

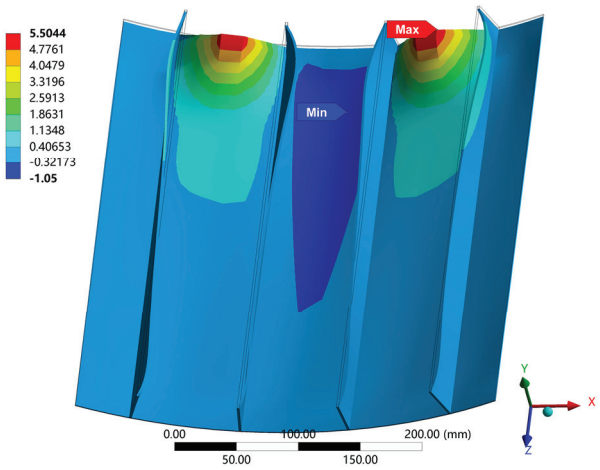

Figure 2. Buckled shape for carbon/epoxy skin and carbon/epoxy stiffeners for $[45°/-45°/90°/0°]_S$ skin.

When the skin is made of carbon/epoxy plies and the stiffeners are made of E-glass/epoxy plies, the critical buckling load is 30,060 N, and the buckled shape is shown in Figure 3. The contours show the y displacement in mm. The maximum displacement is 7.45 mm. Compared to all the carbon/epoxy composites, when the stiffeners are made of E-glass/epoxy composite, the critical buckling load only decreases slightly by 0.27%.

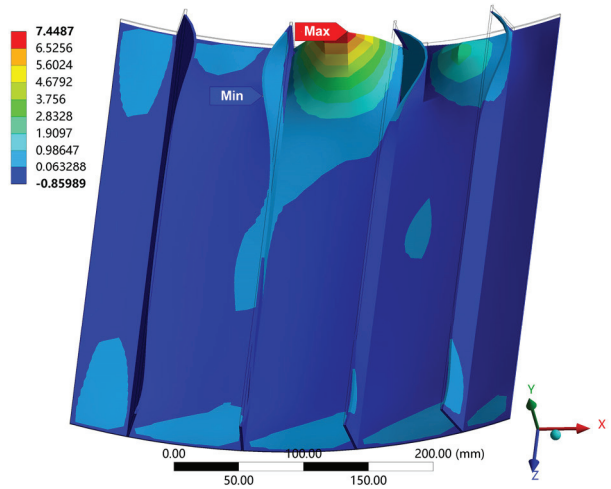

Figure 3. Buckled shape for carbon/epoxy skin and E-glass/epoxy stiffeners for $[45°/-45°/90°/0°]_S$ skin.

When the skin is made of E-glass/epoxy plies and the stiffeners are made of carbon/epoxy plies, the critical buckling load is 14,340 N, and the maximum displacement is 6.91 mm. When both the skin and stiffeners are made of E-glass/epoxy plies, the critical buckling load is 13,850 N, and the maximum displacement is 6.92 mm. The buckled shapes are similar to Figure 2. Compared to all the carbon/epoxy composites, the critical buckling load decreases significantly for both cases. The all E-glass/epoxy composite has the lowest critical buckling load. This is in agreement with previous research [29].

When the skin is made of carbon/epoxy plies and the stiffeners are made of hybrid plies with E-glass/epoxy plies as outer layers, the critical buckling load is 30,040 N, and the maximum displacement is 7.42 mm. The buckled shape is similar to that shown in Figure 2. When the stiffeners are made of hybrid plies with carbon/epoxy plies as the outer layers,

the critical buckling load is 30,100 N, and the maximum displacement is 6.76 mm. The buckled shape is similar to Figure 3. It is seen that the critical buckling loads are similar for these two cases, and similar to that of the all carbon/epoxy composite.

When the skin is made of E-glass/epoxy plies and the stiffeners are made of hybrid plies with E-glass/epoxy plies as the outer layers, the critical buckling load is 13,770 N, and the maximum displacement is 5.51 mm. When the stiffeners are made of hybrid plies with carbon/epoxy plies as the outer layers, the critical buckling load is 14,090 N, and the maximum displacement is 5.58 mm. The buckled shapes are similar to Figure 2. It is seen that the critical buckling loads are similar for these two cases, and similar to that of the all E-glass/epoxy composite.

When the skin is made of hybrid plies with E-glass/epoxy plies as the outer layers, and the stiffeners are made of carbon/epoxy plies, the critical buckling load is 17,960 N, and the maximum displacement is 4.63 mm. When the skin is made of hybrid plies with carbon/epoxy plies as the outer layers, and the stiffeners are made of carbon/epoxy plies, the critical buckling load is 26,560 N, and the maximum displacement is 6.65 mm. The buckled shape is similar to that shown in Figure 2.

When the skin is made of hybrid plies with E-glass/epoxy plies as the outer layers, and the stiffeners are made of E-glass/epoxy plies, the critical buckling load is 18,230 N, and the maximum displacement is 5.00 mm; when the skin is made of hybrid plies with carbon/epoxy plies as the outer layers, and the stiffeners are made of E-glass/epoxy plies, the critical buckling load is 24,630 N, and the maximum displacement is 6.50 mm. The buckled shape is similar to that shown in Figure 2.

In summary, it is shown that the critical buckling load mostly depends on the layup of the skin. The all carbon/epoxy composite has the highest critical buckling load. When hybrid composites are used for the skin, carbon/epoxy plies should be placed as the outer layers. Compared to the all carbon/epoxy skin, the critical buckling load decreases slightly by about 12%.

When the layup of the skin is changed to $[90^\circ/0^\circ/90^\circ/0^\circ]_S$, the buckled shape becomes more complex. When the skin is made of hybrid plies with E-glass/epoxy plies as the outer layers, and the stiffeners are made of E-glass/epoxy plies, the buckled shape is of that shown in Figure 4.

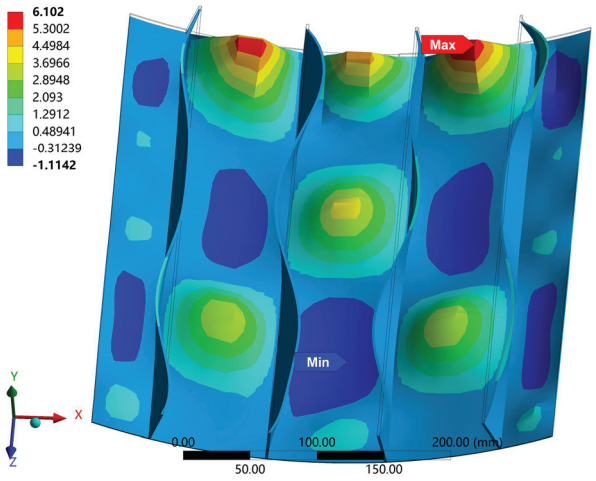

Figure 4. Buckled shape for hybrid skin with E-glass/epoxy plies as outer layers and E-glass/epoxy stiffeners for $[90^\circ/0^\circ/90^\circ/0^\circ]_S$ skin.

When the layup of the skin is changed to $[60^\circ/-30^\circ/90^\circ/0^\circ]_S$, similar buckled shapes compared to those of $[45^\circ/-45^\circ/90^\circ/0^\circ]_S$ are found.

It is shown that when the curved stiffened plate is made of carbon/epoxy, and the layups of the skin and the stiffeners are $[90^\circ/0^\circ/90^\circ/0^\circ]_s$ and $[[45^\circ/-45^\circ/0^\circ/90^\circ]_s]_2$, respectively, the highest critical buckling load is achieved, which is 36,800 N.

Using Equations (1) and (2), the overall cost and weight for each combination is calculated, as shown in Table 6.

Table 6. Overall cost and weight.

	Ply Material Combination	Cost ($)	Weight (g)
High critical buckling load	1	25.52	368.45
	2	16.57	396.96
	6	21.04	382.7
Middle critical buckling load	10	19.43	387.85
	12	10.48	416.36
Low critical buckling load	3	13.34	407.25
	4	4.39	435.77
	8	8.87	421.54

It is seen from Table 6 that the cost of the stiffened panel decreases with an increasing amount of glass fibre being used, but the weight increases. The hybridisation of stiffeners in stiffened plates can significantly cut costs while maintaining high critical buckling loads. Additionally, combinations 9, 10, and 1 can be interpreted as being generated by applying more carbon fibre to the skin of combination 3. An increase in the critical buckling load is observed with the increase in the carbon fibre content, which is consistent with previous research by Ranganathan et al. [21] on the effect of hybridisation with carbon fibres on the buckling behaviour of pultruded glass FRP flat plates. Notably, replacing the E-glass/epoxy layers of the skin with carbon/epoxy ones, especially those located near the outer surfaces of the skin, significantly improves the critical buckling load. This suggests that optimal improvements in the buckling load are observed when carbon fibre is positioned on the outer surfaces of the stiffened plate—a conclusion in line with Ragheb's research [22] on the effectiveness of hybridisation in improving the local buckling capacity of pultruded I-beams, where enhanced buckling loads were also recorded with the surface application of carbon layers.

When carbon fibre is partially replaced by glass fibre in an all the carbon curved composite stiffened plates, each 1% increase in weight corresponds to a cost reduction of $1.157. The integration of hybrid stiffeners in carbon stiffened plates proves to be a highly effective strategy, resulting in a notable 17.55% reduction in costs. Importantly, this cost optimisation is achieved while retaining robust buckling loads, exhibiting minimal decreases ranging from 0.06% to 0.73%.

Moreover, extending the hybridisation approach to the skin (carbon surface) yields even more substantial cost savings, with a reduction of 23.86%. Despite this, the buckling loads remain within acceptable limits, showcasing moderate decreases ranging from 10.11% to 11.89%. Consequently, the adoption of hybrid composites in stiffened plates emerges as an economically viable solution, ensuring not only significant cost efficiency but also maintaining satisfactory buckling performance. This approach provides valuable flexibility for design considerations, allowing for informed trade-offs in pursuit of optimal solutions.

Although the focus of this study is stiffened plates, the consistent findings across different structures suggest the general applicability of these conclusions. In this study, the introduction of hybridisation with carbon/epoxy being the outer layers can significantly reduce the cost while maintaining an acceptable buckling load, without undermining the overall high buckling performance.

4. Conclusions

A study on the effect of fibre hybridisation on the buckling of composite stiffened panels is presented in this paper. Various layups in terms of the ply angle and ply material are studied. It is shown that the hybridisation of stiffeners in stiffened plates can significantly cut costs while maintaining high critical buckling loads. The introduction of

hybridisation with carbon/epoxy as the outer layers can significantly reduce the cost while maintaining an acceptable buckling load, without undermining the overall high buckling performance. Likewise, placing carbon/epoxy on the skin surface of stiffened panels can effectively increase buckling loads at a low cost. In addition, stiffeners are not the main load-bearing components of stiffened plate structures. Applying hybrid composites to stiffened plates allows for cost-effective solutions, offering flexibility in design trade-offs.

This paper focuses exclusively on modifying the skin layup of the stiffened plate in the composite material and the ply materials of both the skin and stiffeners to investigate their impact on the overall buckling. Notably, other influential variables affecting the stiffened plate of the composite materials, such as the load action mode, aspect ratio, thickness, height of stiffeners, and boundary conditions, are not examined in this study. Recognizing that these variables can significantly influence the overall buckling load of the plate, future research should broaden its scope to yield more comprehensive results beneficial for engineering design.

Moreover, it is important to note that post-buckling analysis is not addressed in this paper. When structural buckling occurs due to boundary constraints, tensile stress is generated on the middle surface. Consequently, the plate surface remains undamaged despite buckling and retains additional load-bearing capacity, constituting the post-buckling phenomenon. Given the substantial deflection observed during this phase, the post-buckling of the plate poses a geometrically nonlinear problem. To address this, future research could employ nonlinear stability theory to conduct a detailed analysis of the post-buckling problem. The complete deformation process, including the load–displacement path curve before and after instability, needs to be obtained. Conducting a comprehensive post-buckling analysis of the stiffened plate structure in subsequent research endeavours will contribute valuable data to enhance our understanding of its behaviour.

Author Contributions: Conceptualization, C.D.; methodology, H.H. and C.D.; software, H.H. and C.D.; validation, H.H. and C.D.; formal analysis, H.H. and C.D.; investigation, H.H. and C.D.; resources, H.H. and C.D.; data curation, H.H. and C.D.; writing—original draft preparation, H.H.; writing—review and editing, C.D.; visualization, H.H. and C.D.; supervision, C.D.; project administration, C.D. All authors have read and agreed to the published version of the manuscript.

Funding: This research received no external funding.

Data Availability Statement: Data are contained within the article.

Conflicts of Interest: The authors declare no conflicts of interest.

References

1. Swolfs, Y.; Gorbatikh, L.; Verpoest, I. Fibre hybridisation in polymer composites: A review. *Compos. Part A Appl. Sci. Manuf.* **2014**, *67*, 181–200. [CrossRef]
2. Ni, X.; Prusty, B.; Hellier, A. Buckling and post-buckling of isotropic and composite stiffened panels: A review on optimisation (2000–2015). *Int. J. Marit. Eng.* **2016**, *158*, A-251–A-267. [CrossRef]
3. Fu, T.; Hu, X.; Yang, C. Impact response analysis of stiffened sandwich functionally graded porous materials doubly-curved shell with re-entrant honeycomb auxetic core. *Appl. Math. Model.* **2023**, *124*, 553–575. [CrossRef]
4. Abbott, R. *Analysis and Design of Composite and Metallic Flight Vehicle Structures*; Abbott Aerospace SEZC Ltd.: Collingwood, ON, Canada, 2016.
5. Qi, D.; Sun, Q.; Zhang, S.; Wang, Y.; Zhou, X. Buckling Analysis of a Composite Honeycomb Reinforced Sandwich Embedded with Viscoelastic Damping Material. *Appl. Sci.* **2022**, *12*, 10366.
6. Lanzi, L. A numerical and experimental investigation on composite stiffened panels into post-buckling. *Thin-Walled Struct.* **2004**, *42*, 1645–1664. [CrossRef]
7. Orifici, A.C.; de Zarate Alberdi, I.O.; Thomson, R.S.; Bayandor, J. Compression and post-buckling damage growth and collapse analysis of flat composite stiffened panels. *Compos. Sci. Technol.* **2008**, *68*, 3150–3160. [CrossRef]
8. Bai, R.; Lei, Z.; Wei, X.; Tao, W.; Yan, C. Numerical and experimental study of dynamic buckling behavior of a J-stiffened composite panel under in-plane shear. *Compos. Struct.* **2017**, *166*, 96–103. [CrossRef]
9. Chen, N.-Z.; Guedes Soares, C. Reliability assessment of post-buckling compressive strength of laminated composite plates and stiffened panels under axial compression. *Int. J. Solids Struct.* **2007**, *44*, 7167–7182. [CrossRef]

10. Guo, M.-W.; Harik, I.E.; Ren, W.-X. Buckling behavior of stiffened laminated plates. *Int. J. Solids Struct.* **2002**, *39*, 3039–3055. [CrossRef]
11. Ye, Y.; Zhu, W.; Jiang, J.; Xu, Q.; Ke, Y. Design and optimization of composite sub-stiffened panels. *Compos. Struct.* **2020**, *240*, 112084. [CrossRef]
12. Bisagni, C.; Lanzi, L. Post-buckling optimisation of composite stiffened panels using neural networks. *Compos. Struct.* **2002**, *58*, 237–247. [CrossRef]
13. Bacarreza, O.; Aliabadi, M.H.; Apicella, A. Robust design and optimization of composite stiffened panels in post-buckling. *Struct. Multidiscip. Optim.* **2015**, *51*, 409–422. [CrossRef]
14. Chu, S.; Featherston, C.; Kim, H.A. Design of stiffened panels for stress and buckling via topology optimization. *Struct. Multidiscip. Optim.* **2021**, *64*, 3123–3146. [CrossRef]
15. Dong, C.; Ranaweera-Jayawardena, H.A.; Davies, I.J. Flexural properties of hybrid composites reinforced by S-2 glass and T700S carbon fibres. *Compos. Part B Eng.* **2012**, *43*, 573–581. [CrossRef]
16. Papa, I.; Boccarusso, L.; Langella, A.; Lopresto, V. Carbon/glass hybrid composite laminates in vinylester resin: Bending and low velocity impact tests. *Compos. Struct.* **2020**, *232*, 111571. [CrossRef]
17. Manders, P.W.; Bader, M.G. The strength of hybrid glass/carbon fibre composites. *J. Mater. Sci.* **1981**, *16*, 2233–2245. [CrossRef]
18. Rajpurohit, A.; Joannès, S.; Singery, V.; Sanial, P.; Laiarinandrasana, L. Hybrid effect in in-plane loading of carbon/glass fibre based inter- and intraply hybrid composites. *J. Compos. Sci.* **2020**, *4*, 6.
19. Zhang, C.; Rao, Y.; Li, Z.; Li, W. Low-velocity impact behavior of interlayer/intralayer hybrid composites based on carbon and glass non-crimp fabric. *Materials* **2018**, *11*, 2472. [CrossRef]
20. Swolfs, Y.; Verpoest, I.; Gorbatikh, L. Recent advances in fibre-hybrid composites: Materials selection, opportunities and applications. *Int. Mater. Rev.* **2019**, *64*, 181–215. [CrossRef]
21. Ranganathan, S.; Mantena, P.R. Axial loading and buckling response characteristics of pultruded hybrid glass-graphite/epoxy composite beams. *J. Reinf. Plast. Compos.* **2003**, *22*, 671–679. [CrossRef]
22. Ragheb, W.F. Hybridization effectiveness in improving local buckling capacity of pultruded i-beams. *Mech. Adv. Mater. Struct.* **2010**, *17*, 448–457. [CrossRef]
23. Ahmad, S.; Rajput, L. Buckling analysis of inter-ply hybrid composite plate. *Mater. Today Proc.* **2020**, *21*, 1313–1319. [CrossRef]
24. Bilyeu, B.; Brostow, W.; Menard, K.P. Epoxy thermosets and their applications I: Chemical structures and applications. *J. Mater. Educ.* **1999**, *21*, 281–286.
25. Kalantari, M.; Dong, C.; Davies, I.J. Multi-objective robust optimisation of unidirectional carbon/glass fibre reinforced hybrid composites under flexural loading. *Compos. Struct.* **2016**, *138*, 264–275. [CrossRef]
26. Schubel, P. Cost analysis in using non-crimp fabric composites in engineering applications. In *Non-Crimp Fabric Composites*; Lomov, S.V., Ed.; Woodhead Publishing: Sawston, UK, 2011; pp. 494–510.
27. Dong, C. Flexural properties of symmetric carbon and glass fibre reinforced hybrid composite laminates. *Compos. Part C Open Access* **2020**, *3*, 100047. [CrossRef]
28. Yeter, E.; Erkliğ, A.; Bulut, M. Hybridization effects on the buckling behavior of laminated composite plates. *Compos. Struct.* **2014**, *118*, 19–27. [CrossRef]
29. SudhirSastry, Y.B.; Budarapu, P.R.; Madhavi, N.; Krishna, Y. Buckling analysis of thin wall stiffened composite panels. *Comput. Mater. Sci.* **2015**, *96*, 459–471. [CrossRef]

MDPI AG
Grosspeteranlage 5
4052 Basel
Switzerland
Tel.: +41 61 683 77 34

Journal of Composites Science Editorial Office
E-mail: jcs@mdpi.com
www.mdpi.com/journal/jcs

Academic Open
Access Publishing

mdpi.com

ISBN 978-3-7258-5872-9